frontiers | Research Topics

Cell death in cancer immunology

Edited by
Laura Senovilla, Laura Mondragón Martínez and Shensi Shen

Published in
Frontiers in Immunology
Frontiers in Oncology

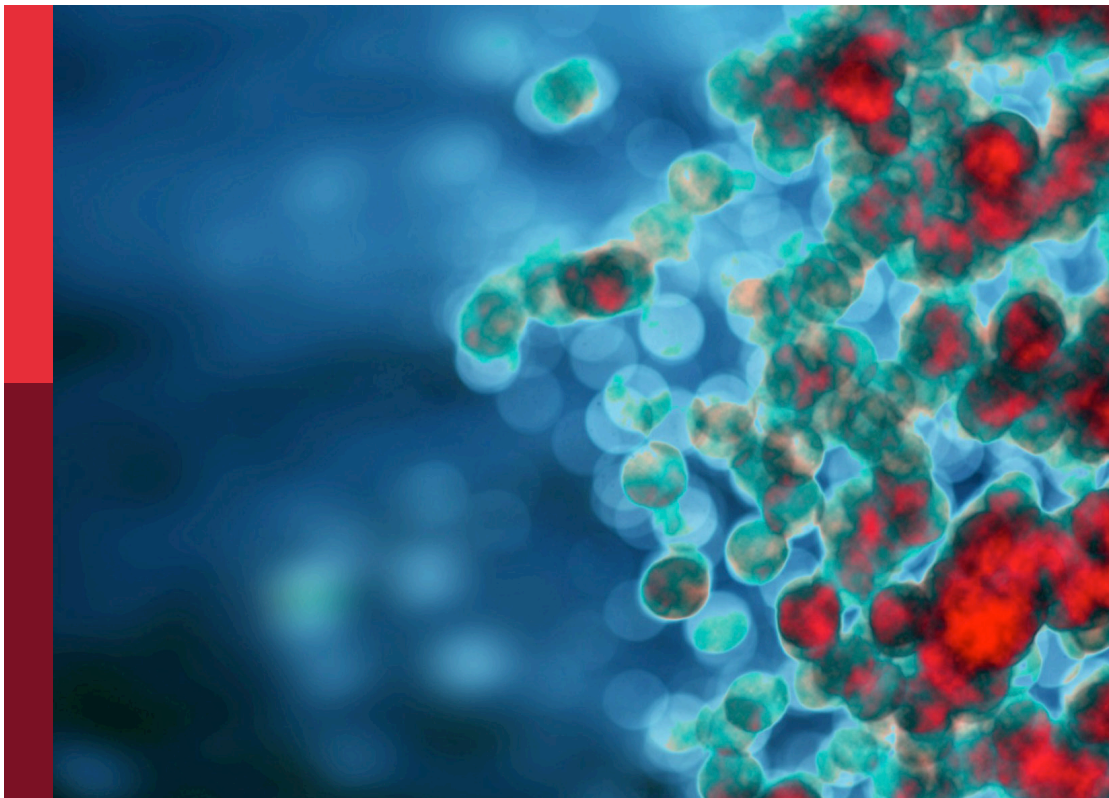

ISSN 1664-8714
ISBN 978-2-8325-5749-5
DOI 10.3389/978-2-8325-5749-5

About Frontiers

Frontiers is more than just an open access publisher of scholarly articles: it is a pioneering approach to the world of academia, radically improving the way scholarly research is managed. The grand vision of Frontiers is a world where all people have an equal opportunity to seek, share and generate knowledge. Frontiers provides immediate and permanent online open access to all its publications, but this alone is not enough to realize our grand goals.

Frontiers journal series

The Frontiers journal series is a multi-tier and interdisciplinary set of open-access, online journals, promising a paradigm shift from the current review, selection and dissemination processes in academic publishing. All Frontiers journals are driven by researchers for researchers; therefore, they constitute a service to the scholarly community. At the same time, the *Frontiers journal series* operates on a revolutionary invention, the tiered publishing system, initially addressing specific communities of scholars, and gradually climbing up to broader public understanding, thus serving the interests of the lay society, too.

Dedication to quality

Each Frontiers article is a landmark of the highest quality, thanks to genuinely collaborative interactions between authors and review editors, who include some of the world's best academicians. Research must be certified by peers before entering a stream of knowledge that may eventually reach the public - and shape society; therefore, Frontiers only applies the most rigorous and unbiased reviews. Frontiers revolutionizes research publishing by freely delivering the most outstanding research, evaluated with no bias from both the academic and social point of view. By applying the most advanced information technologies, Frontiers is catapulting scholarly publishing into a new generation.

What are Frontiers Research Topics?

Frontiers Research Topics are very popular trademarks of the *Frontiers journals series*: they are collections of at least ten articles, all centered on a particular subject. With their unique mix of varied contributions from Original Research to Review Articles, Frontiers Research Topics unify the most influential researchers, the latest key findings and historical advances in a hot research area.

Find out more on how to host your own Frontiers Research Topic or contribute to one as an author by contacting the Frontiers editorial office: frontiersin.org/about/contact

Cell death in cancer immunology

Topic editors

Laura Senovilla — Institute of Biology and Molecular Genetics, Spanish National Research Council (CSIC), Spain

Laura Mondragón Martínez — Josep Carreras Leukaemia Research Institute (IJC), Spain

Shensi Shen — Sichuan University, China

Citation

Senovilla, L., Martínez, L. M., Shen, S., eds. (2024). *Cell death in cancer immunology*. Lausanne: Frontiers Media SA. doi: 10.3389/978-2-8325-5749-5

Table of contents

frontiers | Frontiers in Oncology

TYPE Editorial
PUBLISHED 19 November 2024
DOI 10.3389/fonc.2024.1504738

OPEN ACCESS

EDITED AND REVIEWED BY
Peter Brossart,
University of Bonn, Germany

*CORRESPONDENCE
Laura Mondragón
lmondragon@carrerasresearch.org
Shensi Shen
shenshensi@wchscu.cn
Laura Senovilla
laurasenovilla@hotmail.com

RECEIVED 01 October 2024
ACCEPTED 15 October 2024
PUBLISHED 19 November 2024

CITATION
Mondragón L, Shen S and Senovilla L (2024) Editorial: Cell death in cancer immunology. *Front. Oncol.* 14:1504738. doi: 10.3389/fonc.2024.1504738

Editorial: Cell death in cancer immunology

Laura Mondragón[1]*, Shensi Shen[2]* and Laura Senovilla[3,4,5]*

[1]T Cell Lymphoma Group, Josep Carreras Leukaemia Research Institute (IJC), Badalona, Spain, [2]Institute of Thoracic Oncology and Department of Thoracic Surgery, National Clinical Research Centre for Geriatrics, West China Hospital, Sichuan University, Chengdu, China, [3]Unidad de Excelencia Instituto de Biomedicina y Genética Molecular (IBGM), Universidad de Valladolid-Spanish National Research Council (CSIC), Valladolid, Spain, [4]Centre de Recherche des Cordeliers, Equipe Labellisée par la Ligue Contre le Cancer, Université Paris Cité, Sorbonne Université, Inserm U1138, Institut Universitaire de France, Paris, France, [5]Metabolomics and Cell Biology Platforms, Institut Gustave Roussy, Villejuif, France

KEYWORDS

immunotherapy, immunogenic cell death, prognosis predictive models, biomarkers, vaccines

Editorial on the Research Topic
Cell death in cancer immunology

The relationship between cell death and cancer immunology has been studied for decades with different approaches, as cell death plays a crucial immunomodulatory role in tumor initiation, progression and metastasis (1). Research has focused on understanding the immune system's role in tumor cell resistance to cell death; discerning how cell death paradoxically promotes immunosuppression and tumor progression; explaining the mechanisms by which cell death induces tumor immunogenicity; studying the immunomodulatory effects of dead or dying tumor cells on tumor microenvironment; and investigating how various immunotherapies trigger tumor cell death.

Given the complex interplay between cancer immunology and cell death, this Research Topic of fourteen articles highlights the latest advances in the field through three reviews and eleven original studies. These works can be categorized into two main axes: 1) the development of prognostic models using machine learning, multiomics and patient datasets, and 2) the identification and validation of new biomarkers and therapies focused on the activation of the immune system.

In the last decades, the rise of "omic" technologies has enabled the development of clinical prediction models aimed at improving medical decision-making, enhancing patient's outcomes, and identifying novel biomarkers and therapeutic targets. In the ongoing quest for better treatments and ways to overcome cancer cell death resistance and immune evasion, new cell death mechanisms linking these processes have been discovered, offering fresh new strategies to combat cancer.

This is the case of disulfidptosis, a recently described new form of cell death caused by disulfide stress (2). Disulfides are produced in response to oxidative stress to help maintain the secondary, tertiary, and quaternary structures of proteins by acting as inter- and intra-subunit cross-links. Excessive intracellular accumulation of disulfides solute carrier family 7 member 11 (SLC7A11) induces, together with glucose starvation, aberrant disulfide bonds formation between actin cytoskeleton, causing its collapse in a particular and orderly manner. Overexpression of SLC7A11 and GLUT inhibitors has proved to inhibit tumor

growth, which may contribute to the development of a new therapeutic strategy against cancer.

Consequently, multiple works have been undertaken to answer these questions in the last months, mostly by predictive models development. In this sense, Li et al. make use of 20 diagnosed-related groups (DRGs) and LASSO and Cox regression analysis to provide, among other immune cell infiltration patterns, a new potential therapeutic target: POU Class 4 Homeobox 1 (POU4F1), which promotes cell proliferation, migration and, most importantly, disulfidptosis in colon adenocarcinoma (COAD) patients. In a broader application, Wang et al. also develop a similar analysis making use of disulfidptosis-related genes identified from CRISPR–Cas9 screenings leading to the identification of neuronal acetylcholine receptor subunit alpha-5 (CHRNA5) as a potential therapeutic target due to its impact on cell proliferation, migration, and disulfidptosis in the context of lung adenocarcinoma (LUAD). Finally, Zhang et al. focused on Methods Public datasets to develop a prognostic model for LUAD to predict patient's survival and the efficacy of immune checkpoint blockage considering the expression of disulfidptosis-related genes.

Yang et al. also explore disulfidptosis and immune microenvironment to develop a new prognostic model to identify therapeutic targets for hepatocellular carcinoma (HCC) utilizing bulk ribonucleic acid (RNA) sequencing, spatial transcriptomic (ST) and single-cell RNA sequencing. Their findings reveal that N-myc downregulated gene 1 (NDRG1) influences macrophage differentiation and enables tumor cells to evade the immune system. Similarly, Zheng et al. leverage RNA sequencing data and clinical information from HCC patients in the *The Cancer Genome Atlas* (TCGA) to create a predictive model for chemotherapy sensitivity and immunotherapy efficacy in HCC.

To finish the first axis, ferroptosis, a form of cell death dependent on iron and characterized by the accumulation of lipid peroxides, and fatty acid metabolism (FAM) in the tumor microenvironment (TME), is reviewed by Guo et al. in the context of ovarian cancer and its role in tumor suppression (3, 4). Ferroptosis role in the onset, progression, and incidence of ovarian cancer and their synergy with immunotherapy is defined together with new potential treatments based on these facts. Then, Zhu et al. explore the relationship between ferroptosis and patients outcome in colorectal cancer (CRC) with the objective of anticipating immunotherapy effectiveness. They make use of TCGA and GEO databases to create the FeFAMscore, which proved that ferroptosis regulators and FAM-related genes not only enhance immune activation, but they also contribute to immune escape. Finally, Wang et al. describe the generation of the PANoptosis-model, based on PANoptosis cell death, which is initiated by innate immune sensors and driven by caspases and receptor-interacting protein kinases (RIPKs) through the so-called PANoptosome complexes. They make use of clinical and single-cell data from breast cancer patients and validate them by means of immunohistochemistry (IHC) assays, proving how this model can help in predicting breast cancer prognosis and treatment personalization.

Regarding the second set of articles of this Research Topic, Shabrish et al. takes profit of cell-free chromatin particles (cfChPs) circulating in blood of cancer patients or that have been released by dying cancer cells, which upon internalization by healthy cells can modulate the activation of immune checkpoints, providing a novel form of immunotherapy of cancer. Verhaar et al. make use of MHC class I chain related-proteins A and B (MICA, MICB) glycoproteins present on the surface of epithelial and hematopoietic cancer cells and that bind to natural killer group 2D (NKG2D) and activate the immune system. By means of nanobodies, Verhaar et al. surface-dispose MICA together with the Maytansine derivative DM1, selectively killing MICA positive tumor cells *in vitro*.

Additionally, with the goal of providing a long-term cancer protection, Wang et al. review therapeutic strategies to enhance the immunogenicity of dying tumor cells leading to achieve more effective and sustained immune activation. They focus on strategies for inducing ICD and designing vaccines that introduce more immunogenic antigens and stimulating factors. Complementing this review, Budhu et al. provide a practical approach, addressing the common issue of immunotherapy failure due to the lack of immune infiltrates in tumor. They compare the effectiveness of anti-PD1 therapy combined with radiation therapy (RT), vascular targeted photodynamic therapy (VTP) and cryoablation (Cryo), demonstrating that these tumor destruction methods can indeed improve therapy outcomes by eliciting different immune responses.

Taking into account the effect of damage-associated molecular patterns (DAMPs) and certain cytokines and chemokines in ICD, Naessens et al. explore the intricate role of CX3CL1 in immunogenic apoptosis induced by mitoxantrone (MTX) in cancer cells. CX3CL1, which exerts a role in cellular signaling and immune cell interactions, has been denoted as a "find me" signal that stimulates chemotaxis of immune cells towards dying cells, facilitating efferocytosis and antigen presentation. Its role in ICD in melanoma and fibrosarcoma cells is described by studying its role upon the activation of an adaptive immune response against cancer cells undergoing ICD.

To conclude this Research Topic focused on non-invasive biomarkers for better diagnostics and prognostics in CRC and liver cancer, de Castro et al. provide a revision on advanced cytometry panels covering over 40 parameters (computational cytometry) that make use of elemental mass spectrometry to detect metal-conjugated antibodies bound to antigens of interest on single cells. This next generation flow cytometry platform can be applied to the study of the immune system and the search of novel biomarkers to aid in diagnosis and prognosis, and to even predict clinical response to different treatments.

We believe that, collectively, these fifteen contributions in "Cell Death in Cancer Immunology" will provide a comprehensive description of current genomic strategies for the development of

new prognostic methods based on the study of molecular, immunological, and therapeutic aspects of cancer cell death, and potential development of new biomarkers for therapeutic gain in the context of immune system activation.

Author contributions

LM: Writing – original draft, Writing – review & editing. SS: Writing – review & editing. LS: Writing – review & editing.

Conflict of interest

SS reports personal fees from Agence nationale de la recherche France, Krebsliga Schweiz Switzerland, KWF Kankerbestrijding Netherlands, Austrian Research.

The remaining authors declare that the research was conducted in the absence of any commercial or financial relationships that could be construed as a potential conflict of interest.

The author(s) declared that they were an editorial board member of Frontiers, at the time of submission. This had no impact on the peer review process and the final decision.

Publisher's note

References

1. Galluzzi L, Kepp O, Hett E, Kroemer G, Marincola FM. Immunogenic cell death in cancer: concept and therapeutic implications. *J Transl Med*. (2023) 21:162. doi: 10.1186/s12967-023-04017-6

2. Liu X, Nie L, Zhang Y, Yan Y, Wang C, Colic M, et al. Actin cytoskeleton vulnerability to disulfide stress mediates disulfidptosis. *Nat Cell Biol*. (2023) 25:404–14. doi: 10.1038/s41556-023-01091-2

3. Stockwell BR. Ferroptosis turns 10: Emerging mechanisms, physiological functions, and therapeutic applications. *Cell*. (2022) 185:2401–21. doi: 10.1016/j.cell.2022.06.003

4. Stockwell BR, Angeli JPF, Bayir H, Bush AI, Conrad M, Dixon S, et al. Ferroptosis: a regulated cell death nexus linking metabolism, redox biology, and disease. *Cell*. (2017) 171:273–85. doi: 10.1016/j.cell.2017.09.021

frontiers | Frontiers in Immunology

TYPE Original Research
PUBLISHED 03 January 2024
DOI 10.3389/fimmu.2023.1294677

OPEN ACCESS

EDITED BY
Laura Senovilla,
Spanish National Research Council (CSIC), Spain

REVIEWED BY
Luis Castro-Sánchez,
CONACYT-Universidad de Colima, Mexico
Ezgi Eryilmaz,
Bursa Uludağ University, Türkiye
Jian Wang,
Tianjin Medical University Cancer Institute and Hospital, China

*CORRESPONDENCE
Jianfan Wen
wenjianfan927@163.com
Yifeng He
gzhyf001@163.com
Juan Duan
gzdj1019@163.com
Xiancheng Zeng
zxcq12333@163.com

†These authors have contributed equally to this work

RECEIVED 15 September 2023
ACCEPTED 11 December 2023
PUBLISHED 03 January 2024

CITATION
Yang T, Liu J, Liu F, Lei J, Chen S, Ma Z, Ke P, Yang Q, Wen J, He Y, Duan J and Zeng X (2024) Integrative analysis of disulfidptosis and immune microenvironment in hepatocellular carcinoma: a putative model and immunotherapeutic strategies. *Front. Immunol.* 14:1294677. doi: 10.3389/fimmu.2023.1294677

Integrative analysis of disulfidptosis and immune microenvironment in hepatocellular carcinoma: a putative model and immunotherapeutic strategies

Ti Yang[1,2†], Junhao Liu[1†], Fang Liu[3†], Jiashun Lei[1,2], Siliang Chen[4], Zengxin Ma[1,2], Peifeng Ke[5], Qiaolan Yang[1], Jianfan Wen[1*], Yifeng He[6*], Juan Duan[5*] and Xiancheng Zeng[1,2*]

[1]Department of Hepatobiliary-pancreatic&hernia Surgery, Guangdong Second Provincial General Hospital, Guangzhou, Guangdong, China, [2]The Second School of Clinical Medicine, Southern Medical University, Guangzhou, Guangdong, China, [3]The First School of Clinical Medicine, Southern Medical University, Guangzhou, Guangdong, China, [4]Department of Interventional Radiology, Guangdong Second Provincial General Hospital, Guangzhou, Guangdong, China, [5]Guangdong Provincial Hospital of Chinese Medicine, The Second Affiliated Hospital of Guangzhou University of Chinese Medicine, Guangzhou, Guangdong, China, [6]Department of General Management, Guangdong Second Provincial General Hospital, Guangzhou, Guangdong, China

Background: Hepatocellular carcinoma (HCC) is a malignant tumor with a high rate of recurrence and m metastasis that does not respond well to current therapies and has a very poor prognosis. Disulfidptosis is a novel mode of cell death that has been analyzed as a novel therapeutic target for HCC cells.

Methods: This study integrated bulk ribonucleic acid (RNA) sequencing datasets, spatial transcriptomics (ST), and single-cell RNA sequencing to explore the landscape of disulfidptosis and the immune microenvironment of HCC cells.

Results: We developed a novel model to predict the prognosis of patients with HCC based on disulfidptosis. The model has good stability, applicability, and prognostic and immune response prediction abilities. N-myc downregulated gene1 (NDRG1) may contribute to poor prognosis by affecting macrophage differentiation, thus allowing HCC cells to evade the immune system.

Conclusion: Our study explores the disulfidptosis of HCC cells through multi-omics and establishes a new putative model that explores possible targets for HCC treatment.

KEYWORDS

HCC, disulfidptosis, putative model, immune microenvironment, NDRG1

1 Introduction

Liver cancer is the third most common cause of cancer deaths worldwide, accounting for 8.3% of the overall cancer mortality (1). Hepatocellular carcinoma (HCC) accounts for about 85%-90% of all primary liver malignancies (2). Although new therapies have emerged, like immunotherapy, targeted therapy, and radiation therapy, the five-year survival of advanced HCC is less than 15% (3). New immune checkpoint inhibitors, such as Nivolumab, Atezolizumab, and Ipilimumab, are currently on the market, but their therapeutic efficacy is not promising, possibly due to immune escape (4). A lack of effective treatment has prompted a search for new biomarkers.

Programmed cell death is associated with numerous pathophysiological processes, including tumor progression and alterations in the surrounding immune microenvironment (5). Several new cell death models have recently arisen: apoptosis, cuproptosis, ferroptosis, necroptosis, lysosome-dependent cell death, immunogenic cell death, and autophagy-dependent cell death (6, 7). Liu et al. recently discovered a new mode of cell death: disulfidptosis. In glucose-starved cells overexpressing solute carrier family 7 member 11 (SLC7A11), disulfidestress caused by excessive intracellular cystine accumulation can cause rapid cell death (8). Normal disulfide bonds between cytoskeletal proteins are disrupted by accumulation of disulfide material, leading to collapse of the histone skeleton and cell death. Glucose transporter inhibitors trigger disulfidptosis and suppress tumor proliferation.

The bulk ribonucleic acid (RNA) sequencing is the average messenger RNA (mRNA) expression in all cells, which does not reflect the state of single cells in the tissue. Single-cell RNA sequencing (scRNA-seq) enables a detailed analysis of the tumor microenvironment heterogeneity at the single-cell resolution level (9, 10). However, scRNA-seq fails to preserve the tissues' spatial structures. The complicated cellular interactions that transpire across the entire tissue space cannot be accurately deciphered. The advent of spatial transcriptomics (ST) technology facilitates the spatial exploration of gene expression and preserves cell arrangements during multicellular tissue analysis. Thus, combining single-cell technology with ST may detect details regarding heterogeneous cell populations and provide insight into spatial tissue organization (11, 12).

In our study, we employed a multi-omics strategy to investigate the landscape ofdisulfidptosis in HCC. We constructed a survival prognostic model using bulk RNA sequencing and confirmed the model has good prognostic and immune response prediction abilities. Importantly, our findings revealed elevated expression levels of N-myc downregulated gene1 (NDRG1) was expressed more in tumor macrophages and promoted Polarization of M2-type macrophages. These findings provide a theoretical basis for exploring effective biomarkers in HCC and improving the efficacy of anti-tumor immune therapy. Outline of the study design is shown in Figure 1.

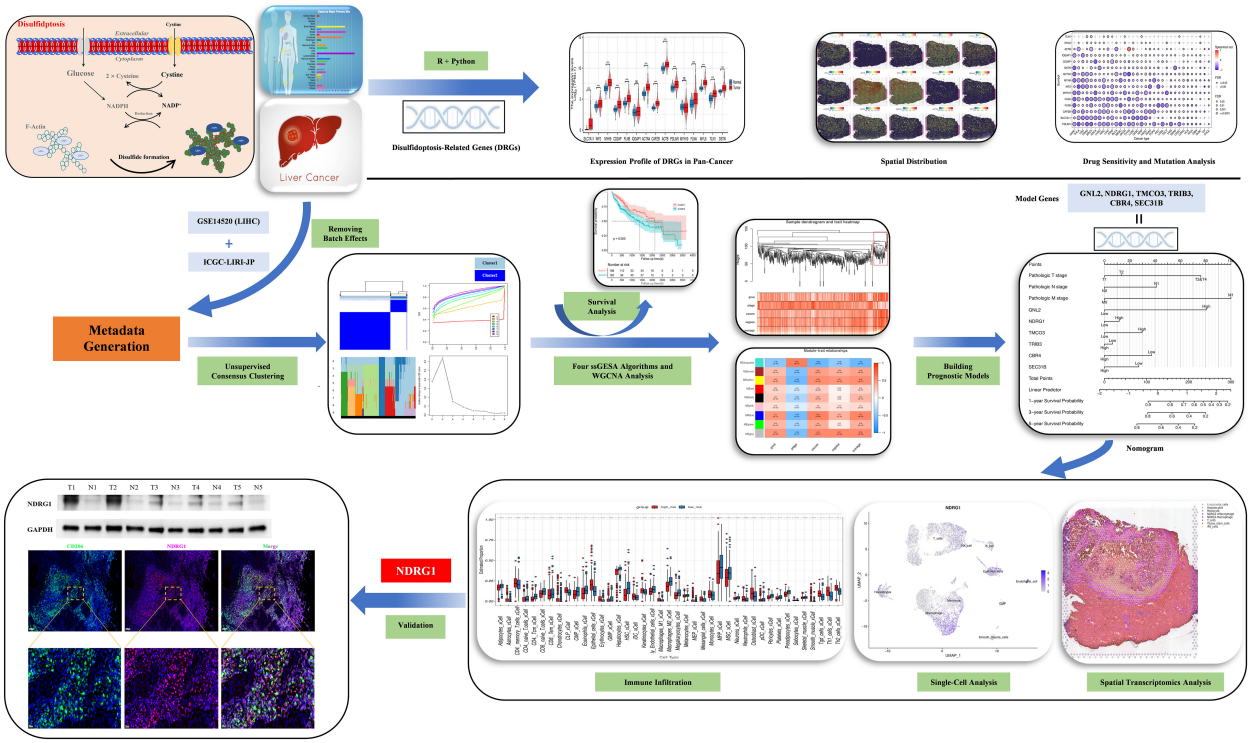

FIGURE 1
Study flow chart.

2 Results

2.1 The expression of disulfidptosis related genes in pan-cancer

We established a protein-protein correlation network with 15 DRGs (Figure 2A), which was derived from previous research (8) and identified SLC7A11 as a key player within this network. Furthermore, we employed the Single-sample Gene Set Enrichment Analysis (ssGSEA) algorithm to assess the disulfidptosis score in pan-cancer. The results revealed a positive normalized enrichment score, indicating upregulation of disulfidptosis. In bladder urothelial carcinoma (BLCA), the normalized enrichment score was negative and disulfidptosis was downregulated (Figure 2B). In HCC, the expression levels of SLC7A11, inverted formin 2 (INF2), myosin heavy chain 9 (MYH9), CD2 associated protein (CD2AP), filamon B (FLNB), actinin alpha 4 (ACTN4), capping actin protein of muscle Z-line subunit beta (CAPZB), actin B (ACTB), PDZ and LIM domain 1 (PDLIM1), filamin A (FLNA), myosin light polypeptide 6 (MYL6), talin 1 (TLN1), and destrin (DSTN) were remarkably higher than the normal tissues. MYH10 and Ras GTPase-activating-like protein (IQGAP1) (Figure 2C) were not higher, although this difference was not statistically significant. We then evaluated the expression of DRGs in tissue sections using ST analysis. Generally, DRGs were highly expressed around and in tumors, except for MYH9 and MYH10 (Figure 2D). To investigate their mutations, we downloaded copy number variation (CNV) and single nucleotide variants (SNV) data from the The Cancer Genome Atlas (TCGA) database. Figure 2E displays the positions of CNV changes in DRGs on their corresponding chromosomes. Despite the high frequency of deletions in MYH10 and FLNA, CNVs were still common and mostly involved in amplification (Figure 2F). We then analyzed the prevalence of SNV in 15 DRGs and found that 31 (8.54%) of 367 liver hepatocellular carcinoma (LIHC) samples showed mutations in the DRGs. Among them, IQGAP1, FLNB, and TLN1 had the maximum mutation frequency (2%), followed by MYH10, INF2, and FLN1, while others displayed no obvious mutations (Figure 2G). Thus, our results suggest that DRGs may act in pan-cancer onset and progression.

2.2 Methylation levels and drug sensitivity of DRGs

Figure 3A shows the methylation levels of DRGs in pan-cancer. CD2AP had the lowest methylation level in uterine corpus endometrial carcinoma (UCEC), and IQGAP1 had the highest methylation level in UCEC. Except for ACTB in Thymoma and Ovarian Cancer, the methylation levels of DRGs in pan-cancer had different degrees of negative correlation with mRNA expression (Figure 3B). Drug sensitivity prediction against DRGs using two drug sensitivity databases revealed that the drugs with the strongest predictive sensitivity in the GDSC were FK866, WZ3105, Ispinesib Mesylate, and SB52334. In the Cancer Therapeutics Response Portal (CTRP) database, the drugs with strong predictive sensitivity were

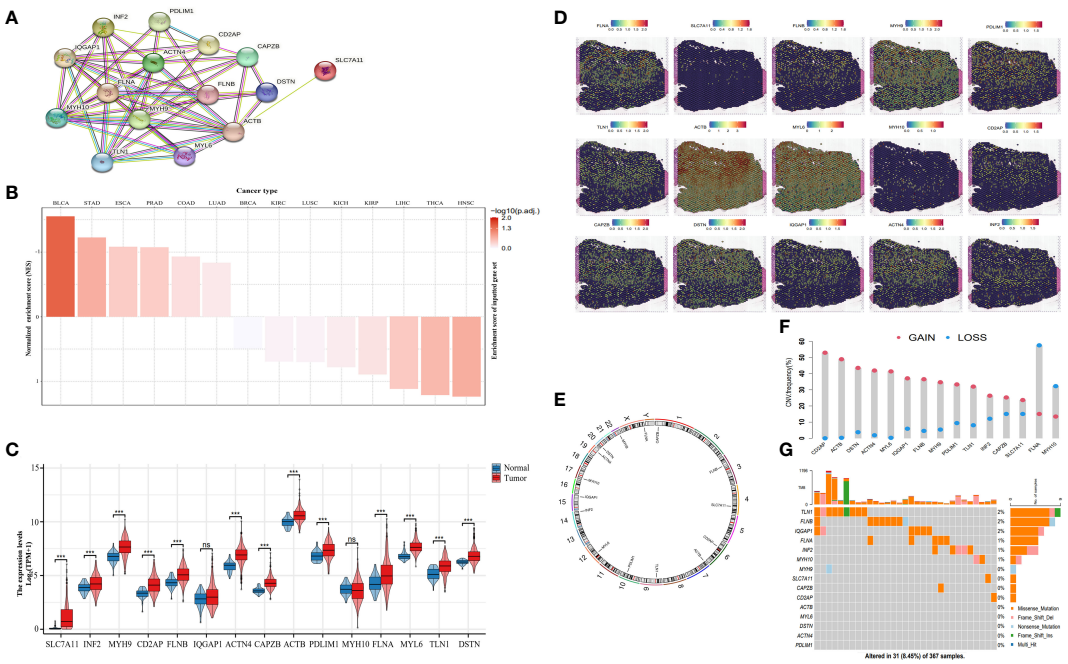

FIGURE 2
Landscape of DRGs in pan-cancer. **(A)** The correlation network of the 15 DRGs. **(B)** The enrichment score of DRGs in pan-cancer. **(C)** The different expression of DRGs between HCC and normal tissue. **(D)** Spatial expression levels of DRGs in HCC tissue sections. **(E)** The location of the CNV alteration of the changes in DRGs in 23 chromosomes. **(F)** The frequency of CNV variation in DRGs (blue: CNV deletion; red: CNV amplification). **(G)** Analysis of SNV in DRGs. ns, not statistically significant; *P< 0.05; **P< 0.01; ***P< 0.001; ****P< 0.0001.

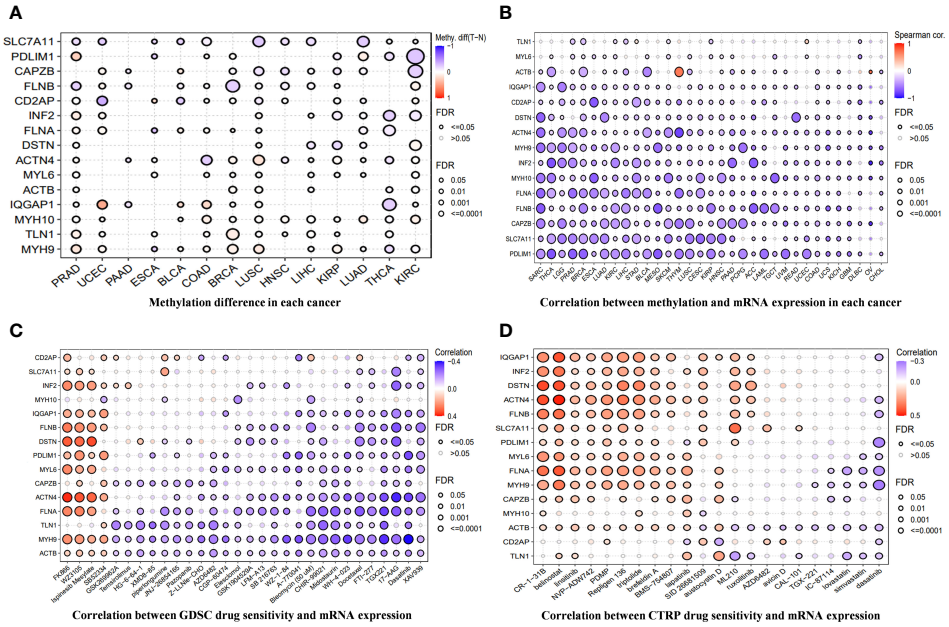

FIGURE 3
(A) The differences in methylation of DRGs in each cancer. **(B)** The correlation between methylation across different cancer types and the mRNA expression of DRGs. **(C, D)** A drug-sensitive analysis aimed at DRGs based on GDSC and CTRP.

CR-1-31B, belinostat, Palmitoyl-DL-carnitine hydrochloride (PDMP), Repligen 136, and triptolide (Figures 3C, D).

2.3 Identification and exploration of DRGs in HCC

An unsupervised consistent cluster analysis of patients with HCC based on the expression of DRGs yielded two disulfidptosis subgroups (Figures 4A–D). We performed principal component analysis (PCA) and uniform manifold approximation and projection (UMAP) analyses and observed that the two clusters were separated in space (Figures 4E, F). Survival analyses for both groups of patients indicated a significant difference in their survival time (Figure 4G), with cluster1 showing a better prognosis. Similar clustering modes were noted in the TCGA dataset (Supplementary Figure 1A–D). The results of different datasets were highly consistent, further demonstrating the reliability and stability of our typing.

2.4 Disulfidptosis score and weighted gene co-expression network analysis

We utilized the "gene set variation analysis (GSVA)" R package to apply the "gsva," "plage," "zscore," and "ssgsea" algorithms to score gene expression in the metadata associated with disulfidptosis. The average value of these scores was calculated. Pearson's correlation method and the mean linkage method were employed to correlate the dendrograms of the samples with disulfidptosis score traits (Figure 5A). To construct co-expression networks, we performed co-expression analysis with a soft threshold of 18 (scale-free $R^2 = 0.9$) to ensure a scale-free network. The dendrograms of all differentially expressed genes were clustered based on the differential measure (1-TOM) (Figures 5B, C). Through hierarchical clustering, a total of nine units were identified. Among these units, we selected the blue module, which exhibited the highest correlation with the disulfidptosis score, as the clinically significant module for further analysis. Within the blue module, we identified 753 phenotypic genes (Figure 5D).

2.5 Construction and verification of the blue module-based prognostic signature

We performed a univariate Cox regression analysis on 753 phenotypic genes and screened 507 candidate genes with prognostic values (Supplementary Figure·2). After performing a LASSO regression analysis (Figures 6A–C) and multivariate Cox regression analysis, we obtained a six-gene model. G protein nucleolar 2 (GNL2), NDRG1, transmembrane and coiled-coil domains 3 (TMCO3), tribbles pseudokinase 3 (TRIB3), carbonyl reductase 4 (CBR4), and SEC31 homolog B, COPII coat complex component (SEC31B) were the prognostic indicators for establishing a risk model with a C-index of 0.717. Based on the median risk score, we classified patients into low- (n = 223) and high-risk groups (n = 222).

We plotted and compared survival analysis and recipient work characteristic curves to determine the accuracy of the prognostic characteristic predictions. According to the Kaplan-Meier analysis, overall survival (OS) was considerably longer in the low-risk group versus the high-risk group (Figure 6D). The results of the study

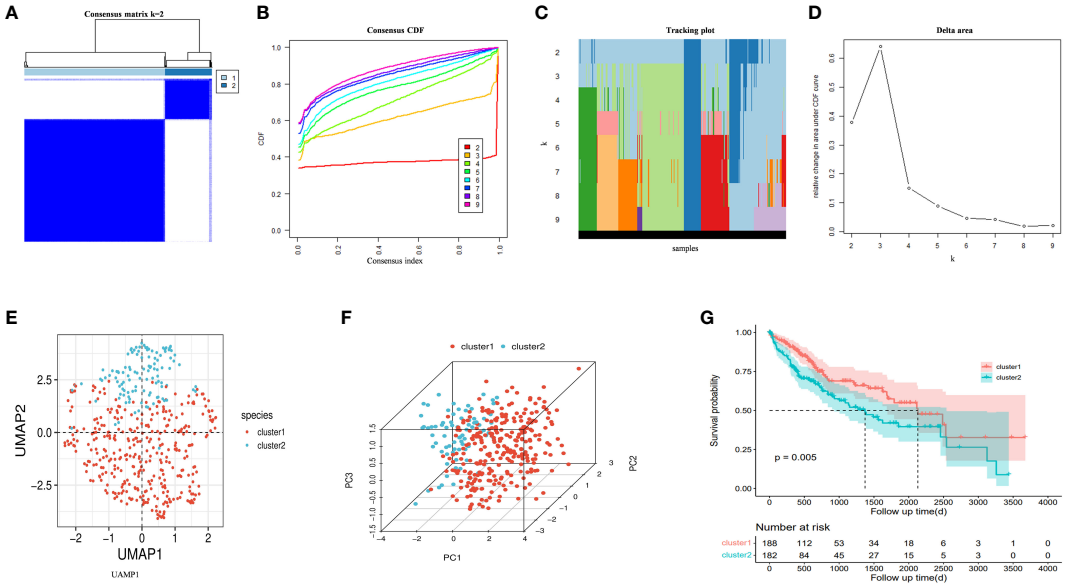

FIGURE 4
(A) An unsupervised consensus clustering heatmap. **(B)** The plot of the relative area changes from k = 2 to 9 under the cumulative distribution function (CDF) curve. **(C)** Consistent CDF plot. **(D)** Tracing plot of the clustered samples. **(E)** Principal Component Analysis. **(F)** Uniform Manifold Approximation and Projection Analysis. **(G)** The OS curves between clusters.

indicated that in the metadata cohort, the area under the receiver operating characteristic (ROC) curve of the risk model for one-, three-, and five-year OS was 0.739, 0.757, and 0.712, respectively. (Figure 6E). According to the decision curve analysis (DCA), the risk model predicted favorable net clinical benefits for OS at one, three, and five years in patients with HCC (Figures 6G–I). To further verify the model's general applicability, we conducted DCA analysis, ROC analysis, and Kaplan-Meier analysis on the model with the validation set TCGA-LIHC and GSE144269. The validation TCGA-LIHC process demonstrated the model's robustness and applicability. Notably, the survival analysis conducted using the model revealed a significant difference in

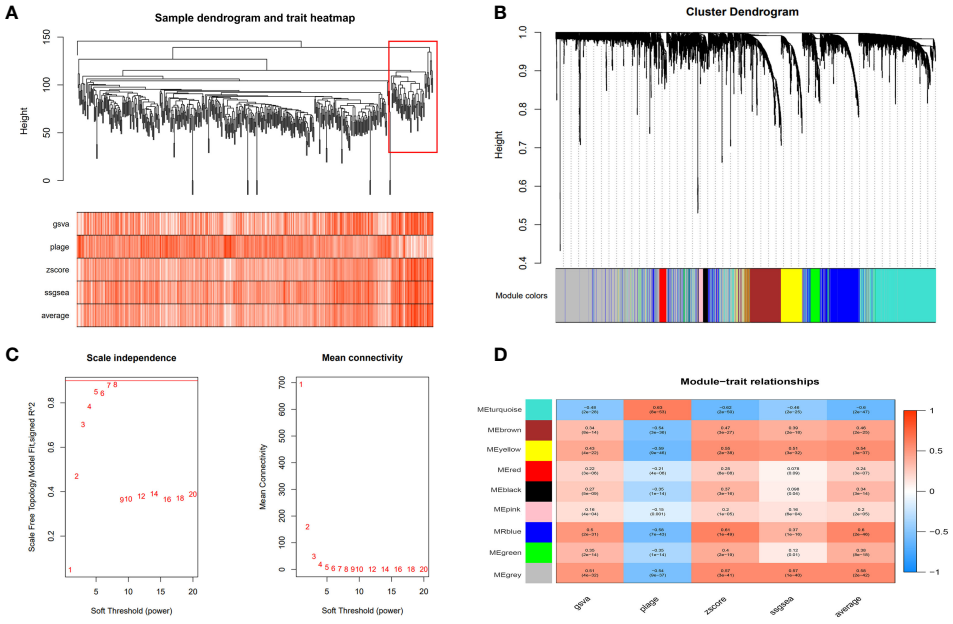

FIGURE 5
Weighted gene co-expression network analysis (WGCNA). **(A)** The cluster dendrogram of co-expression genes in HCC. The red boxes are dendrogram regions corresponding to disulfidptosis. **(B)** Cluster analysis of HCC samples to detect outliers (the white-to-red linear gradient color is associated with the disulfidptosis score, and the grey color indicates missing data). **(C)** Determination of soft-thresholding power in the WGCNA. **(D)** Module–trait relationships in HCC. Each cell contains the corresponding correlation and P-value.

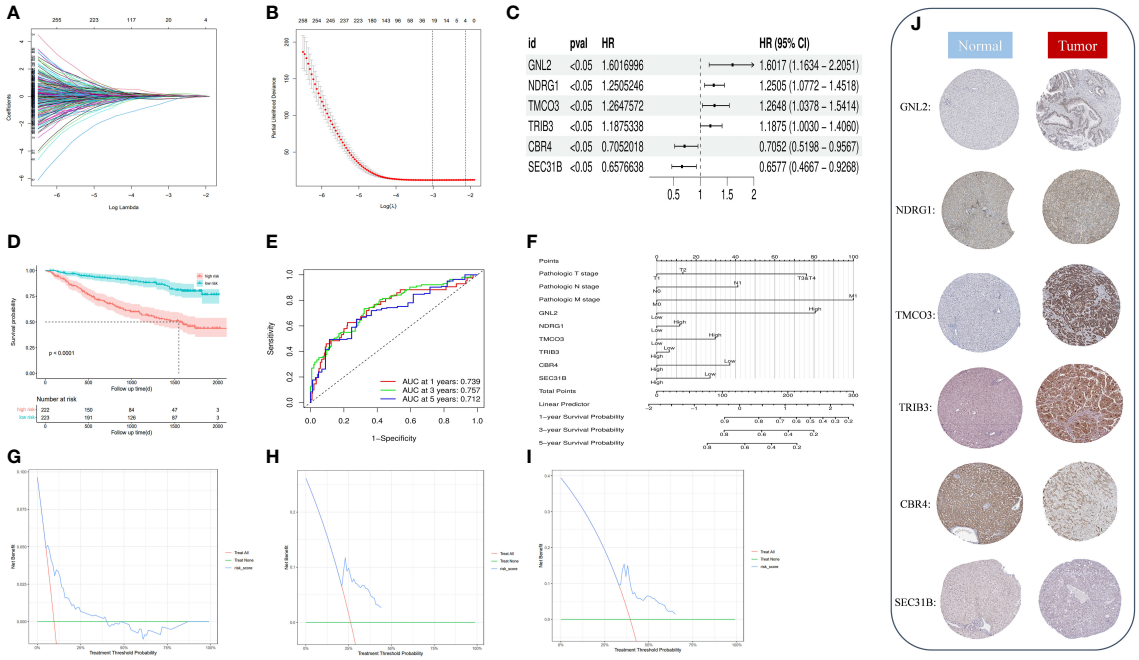

FIGURE 6
(A) Identification of optimal variables through LASSO regression with 10-fold cross-validatio. **(B)** The solution path was plotted according to coefficients against the L1 norm. **(C)** The forest plot shows the hazard ratios and 95% confidence intervals of signature genes from the multivariate Cox regression analysis. **(D)** We plotted the OS curves between high-risk and low-risk groups based on the prognostic signature. **(E)** The time-dependent ROC curves. **(F)** We constructed a nomogram model to predict the one-year, three-year, and five-year OS of HCC patients. **(G–I)** DCA for the one-year **(G)**, three-year **(H)**, and five-year **(I)** OS of the risk model. **(J)** Representative immunohistochemical staining images of GNL, NDRG1, TMCO3, TRIB3, CBR4, and SEC31B in normal and tumor tissues were retrieved from the HPA (https://www.proteinatlas.org/, accessed: January 2023).

survival between the high and low-risk groups (P = 0.00091) (Supplementary Figure 1E). Furthermore, the model's performance was evaluated using ROC curves in the validation set. The area under the curve (AUC) values for 1, 3, and 5 years were determined to be 0.721, 0.650, and 0.656 (Supplementary Figure 1F), respectively. These results indicate the model's ability to accurately predict patient outcomes. Additionally, the decision curve analysis demonstrated that the model can provide substantial net clinical benefits in the validation set (Supplementary Figure 1G). To further validate the model's effectiveness, we obtained a new dataset, GSE144269, from the Gene Expression Omnibus (GEO) and conducted another round of validation. Remarkably, the results from this validation set confirmed the previous findings, showing a significant difference in survival between the high and low-risk groups (P = 0.029) (Supplementary Figure 1H). The ROC curves for the model in this validation set yielded AUC values of 0.681, 0.644, and 0.586 for predicting patient survival at 1, 3, and 5 years (Supplementary Figure 1I), respectively. Moreover, the DCA decision curve analysis indicated that the model can provide substantial net clinical benefits to patients (Supplementary Figure 1J). Overall, these validation efforts reinforce the reliability and clinical utility of the prognostic model.

By drawing forest plots of the multifactorial Cox regression analysis (Figure 6C), we identified SEC31B and CBR4 as the prognostic protective factors for HCC, whereas the other prognostic markers were risk factors. To characterize the protein expression levels of the signature gene in patients with HCC, we compared the protein expression profiles identified via immunohistochemical staining in the HPA database. These findings suggest that four of the factors in the prognostic profile (NDRG1, GNL2, TRIB3, and TMCO3) were overexpressed in HCC tissues (Figure 6J). High expression of SEC31B and CBR4 indicates a positive prognosis for HCC patients. We included pathologic staging in the risk score model and developed a nomogram model to predict one-, three-, and five-year OS (Figure 6F). These findings indicate that the model has favorable discriminatory power.

2.6 Tumor immune infiltration and GSVA analyses

To investigate the immune status of various risk groups and their immunotherapy response, we examined the association between risk models and infiltrating immune cells. We assessed differences in the immune status between risk groups by applying the "xCell" and inverse convolution algorithms. The high-risk group had relatively higher levels of Th2 cells, Th1 cells, iDC, neutrophils, Macrophages_M1 cells, and CD4 memory T cells. Levels of the CD8 naive T cells, CD4 Tcm, CD4 naive T cells, Macrophages M2, and CD8 Tem cells were lower (Figure 7A).

The tumor immune dysfunction and exclusion (TIDE) scores (Figure 7B, P< 0.0001) and exclusion scores (Figure 7D, P< 0.0001)

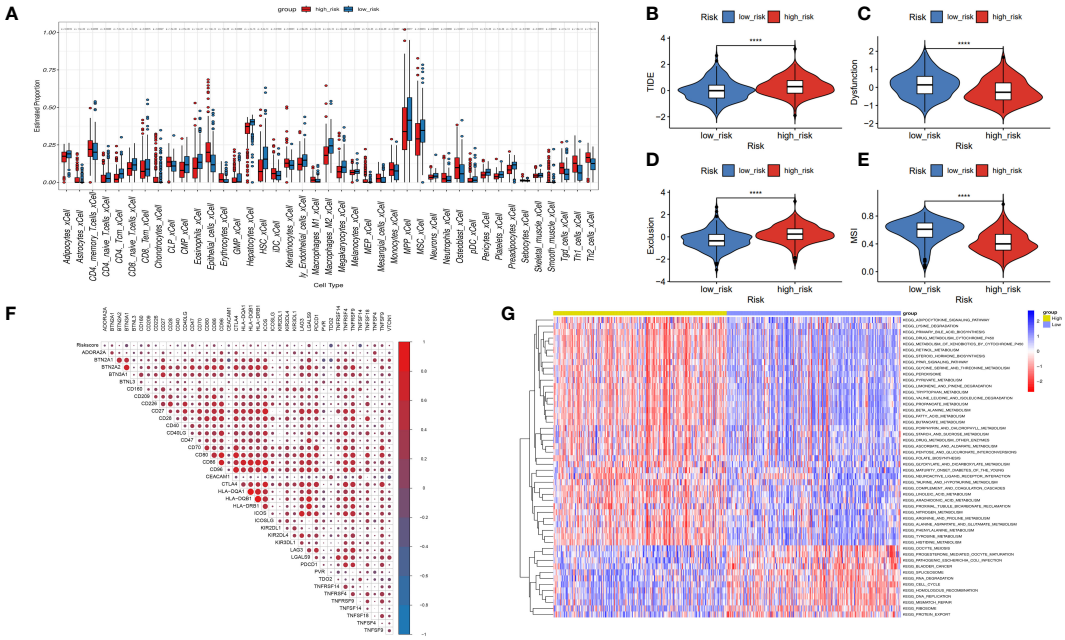

FIGURE 7
Correlation between risk model and immune function. **(A)** The box diagram displays the difference in immune infiltration between the high-risk and low-risk groups via the Cibersort Algorithm. **(B–E)** Response to immunotherapy in high- and low-risk patients. TIDE score, Dysfunction score, Exclusion score, MSI score. **(F)** Comparison of the expression relevance between risk score and immune checkpoint genes. **(G)** Comparison of the GSVA between the high- and low-risk groups.

were notably higher, and the dysfunction scores (Figure 7C, P< 0.0001) and microsatellite instability (MSI) scores (Figure 7E, P< 0.0001) were lower in the high-risk group versus the low-risk group. These outcomes suggest that risk scores in patients with HCC may indicate lower immune checkpoint blockade therapy efficacy. High-risk patients may become resistant to immunotherapy. Risk score may potentially be associated with overexpression of other immune checkpoint genes (ICGs), rather than the well-known PD-1 or CTLA4. Figure 7F shows the positive association between risk scores and CD209, CD47, CD86, LGALS9, TNFSF4, and TNFSF9. There was a negative association between risk and TDO2, and TNFSF14. Moreover, GSVA analysis indicated that the high-risk group had increased "HOMOLOGOUS_RECOMBINATION," "MISMATCH_REPAIR," "RNA_DEGRADATION," and "RNA_DEGRADATION" pathways (Figure 7G).

2.7 ScRNA and pseudotime analyses

We generated 21 subgroups through UMAP-based hierarchical clustering of GSE166635 and performed cell annotation using the "singleR" R package, resulting in the identification of 10 distinct cell subgroups (Figure 8A). By examining the expression of six genes across various cell types, we observed a significant differential expression of NDRG1 specifically in macrophages (Figure 8B). Furthermore, employing RNA rate-based trajectory analysis, we discovered that macrophages in GSE166635 differentiated into two distinct types. Notably, cluster 1 exhibited an initial high expression of NDRG1, as evident from the gradient heatmap (Figure 8C). The trajectory diagram (Figures 8D, E) revealed that cluster 1 differentiated into a subtype of macrophages. These findings suggest that the elevated expression of NDRG1 contributes to the polarization of macrophages.

To explore the immune landscape of disulfidptosis in different tissues, we selected the GSE149614 dataset. Following strict quality control, we analyzed samples from advanced patients and performed UMAP-based hierarchical clustering, resulting in the identification of 15 cell subgroups. Using the "singleR" R package and CellMarker, we annotated these subgroups as "NK cells, B cells, Endothelial cells, T cells, Tissue stem cells, Monocytes, Macrophages, Hepatocytes, and induced pluripotent stem (iPS)" (Figures 9A, B). Analysis of cell ratios in different tissue sources from patients with advanced HCC revealed that natural killer (NK) cells were predominant in normal tissues, while hepatocytes, monocytes, T cells, and iPS cells were predominantly present in tumor tissues. These results reflect the malignant, highly differentiated, and immune infiltrative characteristics of tumors (Figure 9H). Notably, NDRG1 exhibited differential expression across different tissues, with minimal expression in any cell subtypes of normal tissues and higher expression in macrophages of tumor tissues, lymphoid tissues, and portal carcinoma plugs (Figures 9C–G). These findings further validate our observations in GSE166635.

2.8 Cell-to-cell communication

Conventional bulk RNA sequencing data is limited in its ability to analyze cellular communication between different cell types. To

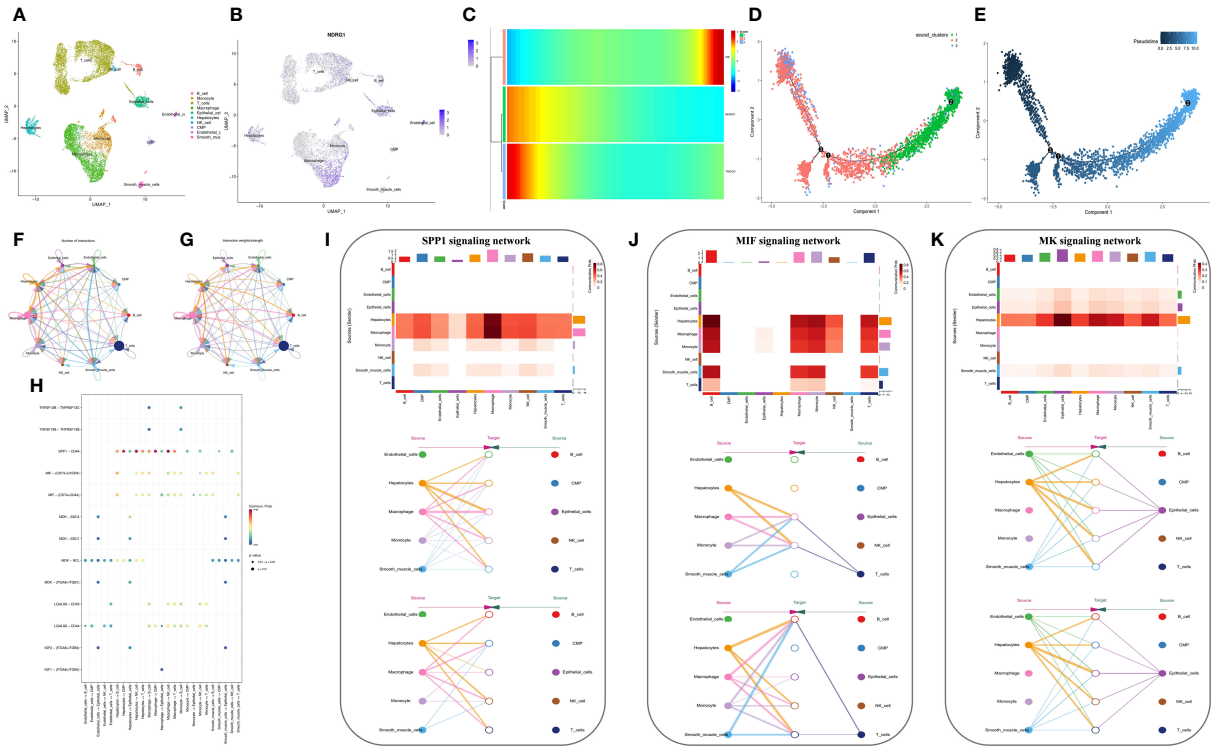

FIGURE 8
Analysis based on the GSE166635 dataset. **(A)** A UMAP of GSE166635. **(B)** The expression of NDRG1 in different cell clusters. **(C)** The trajectory inference was obtained by a monocle using the RNA velocities method. **(D, E)** A pseudotime analysis of macrophages. These graphs contain cells displayed in a trajectory dimensionality reduction algorithm, colored by group. **(D)** The heatmap showed gene expression (evaluated by the Z-value) as the transition during pseudotime dynamics. **(E)** The circle plots show the overview of cell-cell interaction numbers among cells. **(F)** The circle plot also shows the interaction strength among cells. **(G)** In the tumor tissues, broader arrows indicate stronger interactions. **(H)** An overview of cell-cell communication at the legend-receptor level. **(I-K)** A heatmap shows communication between different cell types in SPP1 **(I)**, MIF **(J)**, and MK **(K)** tumor signals. The hierarchy plots of the SPP1 **(I)**, MIF **(J)**, and MK **(K)** signaling pathway network show the sources and targets.

overcome this limitation, we employed the "cellchat" R package to investigate the pathways involved. Our analysis revealed replicative crosstalk between cells in the GSE166635 dataset (Figures 8F–H). Notably, hepatocytes and macrophages exhibited close intercellular connections and sent secreted phosphoprotein 1 (SPP1) signals to nearly all other cell types (Figure 8I). Additionally, hepatocytes, macrophages, monocytes, smooth muscle cells, and T-cells transmitted macrophage migration inhibitory factor (MIF) signals to monocytes, macrophages, and B cells (Figure 8J). Furthermore, endothelial cells, epithelial cells, and hepatocytes conveyed Midkine (MK) signals to all other cells (Figure 8K).

Next, we aimed to investigate the differential expression of NDRG1 in macrophages and its role in macrophage activation during cellular communication. To achieve this, we utilized the "AUCell," "UCell," "singscore," "ssgsea," and "AddModuleScore" algorithms (implemented through the "AUCell," "UCell," "irGSEA," and "GSVA" R packages) to compute disulfidptosis scores for advanced tumor tissues in the GSE149614 dataset. Subsequently, we classified the macrophages within the tumor tissue based on the median disulfidptosis score, resulting in two groups: Disulfidptosis score high macrophages (DSThighM) and Disulfidptosis score low macrophages (DSTlowM). DSThighM macrophages exhibited a close association with endothelial cells in terms of IL6-IL6ST, MFNG-NOTCH1, OSM-IL6ST, ADAM17-NOTCH1, VEGF1-FLT1, VEGF2-FLT1, and PDGFC-FLT1 ligand-receptor linkages. Furthermore, DSThighM macrophages and endothelial cells displayed a tight relationship in IGF1-INSR, CXCL12-CXCR4, and MFNG-NOTCH1 ligand-receptor pairs (Figure 9I). In terms of signaling pathways, DSThighM macrophages and hepatocytes exhibited high activity in Toxoplasmosis, Th17 cell differentiation, and EGFR tyrosine kinase inhibitor resistance. Conversely, the MAPK signaling pathway and focal adhesion were highly active in DSThighM macrophages and endothelial cells. Pathogenic Escherichia coli infection, non-alcoholic fatty liver disease, and human cytomegalovirus infection were closely associated with the autocrine level of DSThighM macrophages. Moreover, the Janus kinase (JAK)-signal transducer and activator of transcription (STAT) signaling pathway and chemokine signaling pathway were highly active in both DSThighM and DSTlowM macrophages (Figure 9J). Figure 9K illustrates the strength of cellular connections among different cell types.

2.9 Disulfidptosis landscape at the spatial transcriptome level

Based on the expression or non-expression of NDRG1, we classified macrophages into two groups: NDRG1+Macrophages

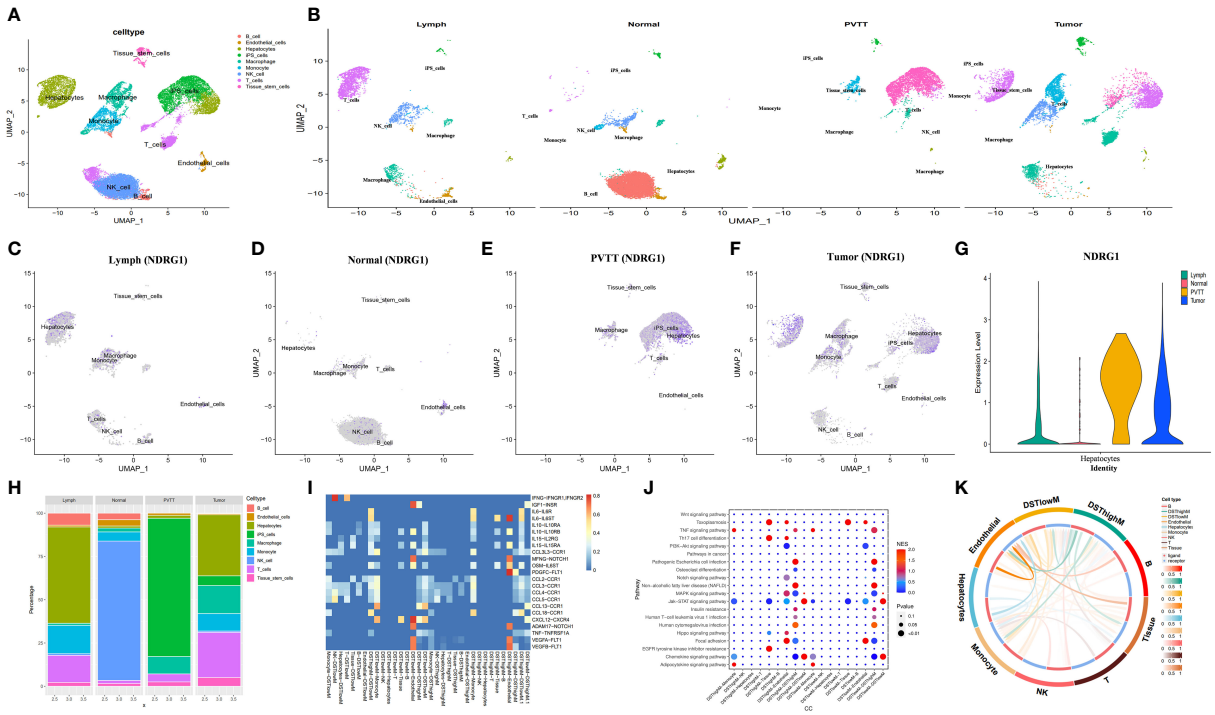

FIGURE 9
Analysis based on the GSE149614 dataset. **(A)** The UMAP of GSE149614. **(B)** The UMAP of GSE149614 is split by tissues. **(C–G)** The expression of NDRG1 in different tissues. **(H)** Cell infiltration level in various tissues inferred by scRNA-seq. **(I)** Heatmap of ligand-receptor pairs of immune pathways among different cell types in tumor tissues. **(J)** Dot plot of signaling pathways among different cell types in tumor tissues. **(K)** Circle plots showing the overview of cell-cell interaction numbers in tumor tissues.

and NDRG1-Macrophages. To annotate the spatial patches, we examined the DRGs of each cluster and HE-stained sections, resulting in the identification of eight major clusters: tissue stem cells, endothelial cells, monocytes, T-cells, iPS cells, hepatocytes, NDRG1-Macrophage cells, and NDRG1+Macrophage cells (Figures 10A, B). Notably, T-cells, monocytes, and macrophages exhibited increased accumulation within tumors. Comparatively, NDRG1+Macrophage cells were predominantly located in the tumor center, indicating that this subpopulation has a tendency to target the tumor center through chemotaxis. This observation, combined with previous single-cell typing, supports the notion that NDRG1+Macrophage subpopulations specifically migrate towards the tumor center (Figure 10C). To assess active metabolism within the tumor region at the ST level, we employed the "scMetabolism" R package, revealing metabolic activity patterns (Figure 10D).

Furthermore, through scoring the co-expression of ligand-receptor pairs, we discovered a close association between NDRG1 +Macrophages, liver-type cells, and tissue stem cells. Notably, three immunologically relevant ligand-receptor pairs, including major histocompatibility complex, class I, A-amyloid beta precursor-like protein 2 (HLA-A_APLP2), biglycan-toll-like receptor 4 (BGN_TLR4), and β2 microglobulin-human leukocyte antigen-F (B2M_HLA-F), were significantly co-expressed in the tumor centers and at the junction of tumors and normal tissues (Figure 11B). This finding highlights the existence of cellular communication between different cell types at the spatial transcriptional level. Specifically, tissue stem cells (defined as tumor cells through tissue sections) exhibited close communication with NDRG1+Macrophages and hepatocytes (Figure 11A).

2.10 Prognostic gene expression

To validate the robustness of our prognostic model, we performed an in-depth investigation into the potential relevance of NDRG1 in HCC. We meticulously examined the expression levels of this prognostic gene in human tissue samples. Through qRT-PCR analysis, we observed significantly elevated NDRG1 expression in tumor tissues (Figure 12A). Furthermore, to corroborate these findings at the protein level, we conducted Western blotting and IHC analyses, both of which confirmed the heightened protein expression of NDRG1 in tumor tissues (Figures 12B–E). These compelling results unequivocally demonstrate the upregulation of NDRG1 in HCC tissues, further emphasizing its potential significance in the context of HCC prognosis.

2.11 Co-expression of NDRG1, macrophages, and tumor cells

To elucidate the role of NDRG1 in the immune microenvironment, we collected specimens from patients with HCC. Multicolor immunofluorescence results demonstrated a significant elevation and co-localization of CD206 and NDRG1

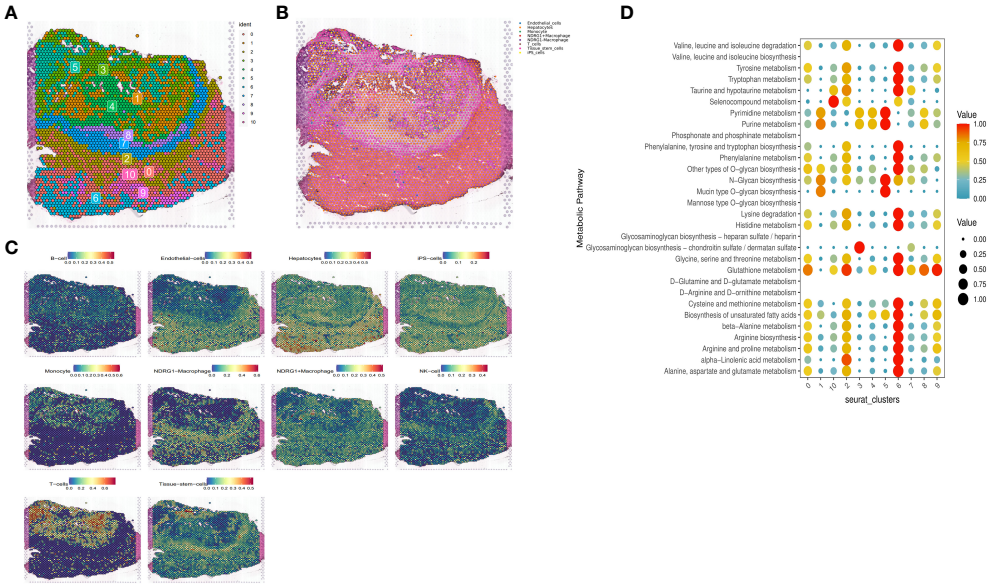

FIGURE 10
Expression of selected genes in the tissue sections. HE-stained images of HCC tissue sections labeled with eight cell clusters. **(A)** Dimensionality reduction clustering of spots on tissue slices. **(B)** Spatial distribution and expression levels of different cell types on tissue sections. **(C)** Spatial expression levels of different cell types in HCC tissue sections. **(D)** The metabolic status of different cell clusters.

expression in hepatocellular carcinoma tissues compared to paracancerous tissues (Figures 12F–H). These findings suggest that the high expression of NDRG1 in tumor tissues may induce the concentration of M2-type macrophages towards the tumor center, thereby facilitating immune escape and ultimately resulting in a poorer prognosis for patients with HCC.

3 Discussion

Recent developments in immunotherapy, molecularly targeted agents, and neoadjuvant chemotherapy have resulted in improved treatments for HCC. However, the prognosis for the long-term survival of patients continues to be poor. There is an urgent need for more sensitive and reliable prognostic indicators to monitor the progression of HCC and assess patient survival.

Disulfidptosis is a new method of controlling tumor cell development (8). To investigate disulfidptosis in HCC, we carried out a comprehensive analysis of ST, sc-RNA seq, and bulk RNA sequencing. First, we obtained 15 DRGs from Liu's study and performed unsupervised consensus clustering, PCA, and UMAP. We then divided patients with liver cancer into two clusters and performed a survival analysis to find cluster 2, which had a poorer prognosis. Next, we used four algorithms to score disulfidptosis in patients with liver cancer and WGCNA to calculate the score for the blue modules most strongly related to disulfidptosis.

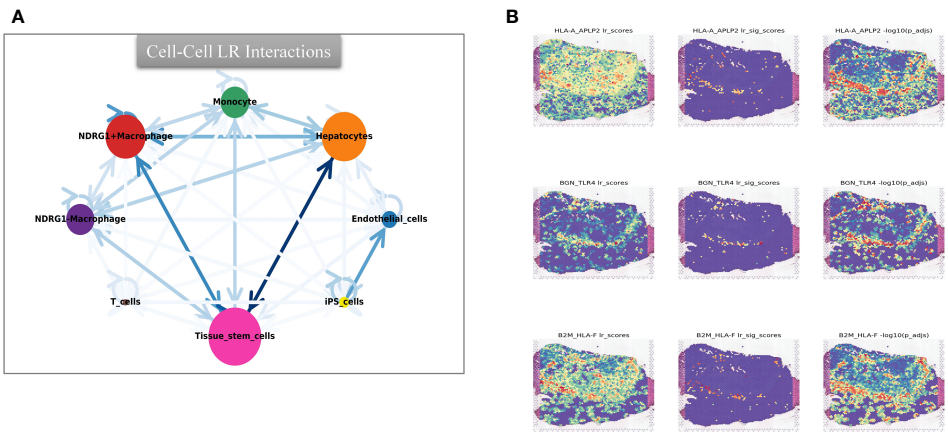

FIGURE 11
Intercellular cmmunication and ligand-rceptor analysis. **(A)** Intercellular communication at the ST level. **(B)** Ligand-receptor analysis at the ST level, including HLA-A_APLP2, BGN_TLR4, and B2M_HLA-F.

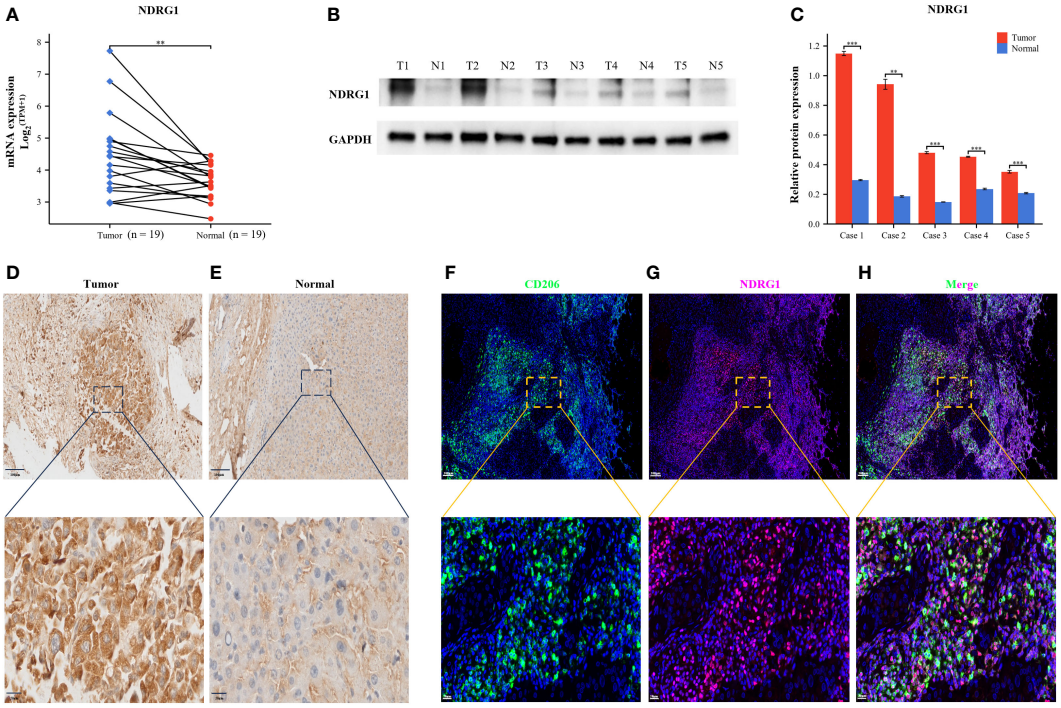

FIGURE 12
Validation of NDRG1 Expression in Hepatocellular Carcinoma. **(A)** NDRG1 mRNA expression profile in Patients with Hepatocellular Carcinoma. **(B)** NDRG1 protein expression profile in Patients with Hepatocellular Carcinoma. **(C)** Bar chart of relative expression levels of NDRG1 protein. **(D, E)** Immunohistochemical staining analysis of NDRG1 in tumor and normal liver tissues. **(F–H)** Immunofluorescence confocal microscopy analysis of CD206 and NDRG1 expression in HCC tissue.

We then subjected the genes within the modules to multivariate Cox regression, LASSO regression, and univariate Cox regression analyses. Through these analyses, we identified six genes that are closely associated with liver cancer prognosis and constructed a prognostic model. Based on the median score, we categorized patients into low- and high-risk groups. The performance of the model was assessed using survival analysis, receiver operating characteristic analysis, and decision curve analysis, demonstrating its robustness and accuracy. In the study by Li (13), a prognostic model was constructed using different disulfidptosis modes to analyze differentially expressed genes. The AUC values under the ROC curve of the model were only 0.689 and 0.659 for 3-year and 5-year predictions, respectively. Additionally, in Yang's study, although they utilized the WGCNA algorithm to construct a prognostic model, it only focused on identifying modules most correlated with clinical features and did not thoroughly analyze the expression patterns of disulfidptosis in liver cancer patients and the AUC values of the model's 3-year and 5-year ROC curves are 0.739 and 0.685, respectively, which are also not as good as our model's (14). In our study, for the first time, we calculated the disulfidptosis scores of liver cancer patients using four different algorithms from the ssGSEA package. We then identified the module with the highest correlation to the average disulfidptosis score using WGCNA (Figure 5). The prognostic model constructed based on this module exhibited better clinical predictive ability, with AUC values of 0.739, 0.757, and 0.712 for 1-year, 3-year, and 5-year predictions, respectively. Furthermore, we conducted an immune infiltration analysis and observed that the high-risk population exhibited upregulation in various cell types, including CLP, epithelial cells, iDC, osteoblasts, type 1 T helper (Th1) cells, and the type 2 T helper (Th2) cell pathway. Conversely, CD4 memory T cells, Th1 cells, Th2 cells, Macrophages_M1 cells, and neutrophils were more likely to infiltrate the high-risk groups. Notably, CD4 T cells have the ability to produce significant amounts of IL-22 cytokines (15), which have been implicated in driving HCC progression by promoting tumor cell proliferation (16). Additionally, cancer cells can influence memory CD4 T cells to express and release IL-1 in an IL-22-dependent manner, thereby facilitating tumor growth (17). Regulatory T cells (Tregs), a subset of immunosuppressive T cells, are commonly enriched in various cancer types and contribute to immune evasion by tumors. In the context of human breast cancer (BC), Tregs predominantly originate from naive CD4 T cells. The presence of Tregs is closely associated with an abundance of naive CD4 T cells, which serves as a prognostic indicator for poor outcomes in BC patients (18).

The lack of effector memory T cells (CD8 Tem) and central memory T cells (CD4 Tcm) explains immune incompetence and exhaustion in high-risk patients (19). Interestingly, high-risk patients are infiltrated with a higher number of M1, Th1, and Th2 macrophages. M1 macrophages secrete multiple inflammatory factors to sustain a prolonged inflammatory environment and recruit and initiate T cells early in tumor progression (20). We noted that high-risk patients were more prone to immune escape and immune rejection by TIDE analysis. We derived some potential

immunotherapy targets by analyzing the relationship between the immune checkpoints and risk score.

Research has revealed that hepatocytes and macrophages frequently signal MIF and SPP1 to associate with other cell types. SPP1 is a sialic acid-rich chemokine-like glycoprotein that is overexpressed in a variety of cancers, including pancreatic cancer (21). Studies have demonstrated that an interaction between CD44 and SPP1 induces cell signaling and modulates tumor cell activation, motility, and adhesion, resulting in cancer progression and metastasis (22). MIF acts as a critical player in cell proliferation, tumorigenesis, and metastasis. MIF can activate the PI3K and MAPK pathways and modulate apoptosis, differentiation, proliferation, cell survival, and cancer progression (23). Midkine (MK), a cancer mediator that is highly expressed in a wide range of human malignancies, modulates cell growth, survival, migration, metastasis, and angiogenesis (24).

We performed scRNA-seq and spatial transcriptional analysis and found that the disulfidptosis score was higher in tumor cells and endothelial cells. NDRG1 was barely expressed in the normal tissues and highly expressed in the macrophages of metastatic lymph nodes, portal vein tumor thrombus (PVTT), and primary tumors. NDRG1 may promote tumor progression by affecting macrophage differentiation, as observed by pseudotime analysis, and is mostly involved in immune and oncogenic pathways. We validated this via ST.

NDRG1, commonly referred to as a metastasis suppressor protein, is expressed across various tumor types. This intracellular protein is composed of 394 amino acids, weighs 43 kD, and exhibits multiple isoforms (25). NDRG1 is actively involved in various cellular processes, such as DNA repair, immunity, and stress response. Additionally, NDRG1 plays pleiotropic roles depending on the type of cancer (26). In recent years, cancer immunotherapy has made significant progress, providing new opportunities for the treatment of liver cancer. However, the immune tolerance characteristics of the liver and the immunosuppressive tumor microenvironment (TME) in HCC have collectively hindered the development of effective anti-tumor immune responses against HCC. The presence of an immunosuppressive TME in liver cancer may be attributed to the accumulation of cells with negative regulatory immune activity, such as M2-polarized tumor-associated macrophages (27). Research has shown that tumor-associated macrophages (TAMs) in the tumor microenvironment are primarily composed of M2-type macrophages, which promote the expression of IL-1α, IL-1β, VEGF-A, and VEGF-C, thereby facilitating tumor growth and tumor angiogenesis/lymphangiogenesis (28). Additionally, several studies have confirmed that NDRG1 is highly expressed in macrophages within the tumor microenvironment (29). Observations have been made of a significant decrease in the serum levels of macrophage colony-stimulating factor (M-CSF) and macrophage-related cytokines in NDRG1 knockout mice (30). The deficiency of NDRG1 has been shown to attenuate the differentiation of macrophage lineage cells, leading to a suppression of bone remodeling and inflammatory angiogenesis (30). Mechanistically, NDRG1 interacts with the orphan nuclear receptor Nur77 and inhibits the transcriptional activity of NF-κB (nuclear factor Kappa B) (31). However, the loss of NDRG1 activates the NF-κB pathway, leading to the induction of epithelial-mesenchymal transition in prostate cancer (32). In their study, Chang et al. found that NF-κB activity is typically upregulated in classical M1 macrophages, while M2 macrophages are believed to have lower NF-κB activity and exhibit strong immunosuppressive effects (33). These findings indicate that NDRG1 may regulate macrophage polarization through the NF-κB pathway, ultimately leading to immune evasion. CD206, also known as an alternative activated macrophage marker, is a membrane glycoprotein expressed on the surface of macrophages, particularly M2 macrophages (34). Our multicolor immunofluorescence results have revealed a significant elevation and co-localization of CD206 and NDRG1 in hepatocellular carcinoma tissues. This further supports the close relationship between NDRG1 expression and macrophage differentiation. Tumor-associated macrophages (TAMs) account for more than 50% of all cells in tumors and play a crucial role as immune cells within the tumor microenvironment (35). Therapeutic strategies that incorporate or target TAMs have emerged as a promising and novel approach for anticancer therapy (36). On the other hand, one of the challenges in immunotherapy is the presence of immune suppressor cells in the tumor microenvironment, which can counteract the immune system's attack on tumor cells. Research has found that tumor cells also induce immune tolerance by manipulating cells of the innate immune system, including polarizing macrophages into tumor-friendly M2 phenotypes and neutrophils into N2 phenotypes (37). Based on the findings from these studies, combined with our own research results, we speculate that NDRG1 may have a potential role in enhancing the efficacy of immunotherapy and reducing immunotherapy resistance. We aim to advance gene diagnosis and gene therapy into the early stages of cancer treatment, discovering more effective combination or sequential treatment strategies. Through future clinical research, we hope to gradually refine prognostic models to identify high-risk patients with poor prognosis in HCC. Targeted gene testing will be conducted on high-risk patients, and gene technology will be utilized for personalized treatment, either through specific knockout of NDRG1 or the design of NDRG1-targeted inhibitors. This approach may potentially reduce the M2/M1 ratio of tumor-associated macrophages in the tumor microenvironment, thereby preventing immune escape of cancer cells and improving the efficacy of immunotherapy and patient prognosis. However, further experimental validation is needed to confirm this hypothesis and extend it to other types of cancer.

In terms of limitations, our research lacks clinical data to evaluate the correlation between NDRG1 and immune therapy response as well as survival rates. Furthermore, the specific mechanisms underlying the interaction of NDRG1 with target genes and downstream signaling events require further investigation. These gaps will impede the translation of our findings into clinical applications, limiting the potential to provide valuable insights for personalized treatment and patient stratification.

In summary, the immediate research priorities following from these findings would involve further mechanistic studies, validation in preclinical models, identification of therapeutic targets,

exploration of combination therapies, and clinical translation. These efforts could potentially lead to the development of novel therapeutic strategies for improving immune responses and treating HCC.

4 Conclusion

Our study provides the first comprehensive analysis of a disulfidptosis pattern in HCC in a large sample of the transcriptome, single-cell transcriptome, and spatial transcriptomics levels. We constructed a novel putative model that suggests high expression of the key factor NDRG1 may contribute to macrophage polarization, infiltration into the tumor center, and ultimately lead to a poor prognosis.

5 Materials and methods

5.1 Data acquisition and preprocessing

We obtained clinical information and bulk RNA sequencing data of HCC patients from various sources. The GEO14520, GSE144269, International Cancer Genome Consortium-Liver Cancer in Japan (ICGC-LIRI-JP), and TCGA Liver Hepatocellular Carcinoma (TCGA-LIHC) datasets were downloaded from the Gene Expression Omnibus database (https://www.ncbi.nlm.nih.gov/geo/), the ICGC data portal (https://dcc.icgc.org/), and TCGA data portal (https://www.cancer.gov/tcga/), respectively. For single-cell RNA sequencing (scRNA-seq) data of HCC, we downloaded the GSE149614 and GSE166635 datasets from the GEO database (https://www.ncbi.nlm.nih.gov/geo/). The GSE166635 dataset contains tumor scRNA-seq data from two HCC patients, while the GSE146914 dataset includes four relevant sites from 10 patients with different stages of PVTT, primary tumor, non-tumor liver, and metastatic lymph node. To acquire spatial transcriptome (ST) information for HCC tissue sections, we accessed the Single-Cell Colorectal Cancer Liver Metastases (CRLM) Atlas web portal (http://www.cancerdiversity.asia/scCRLM). The DRGs were obtained from Liu's article (https://doi.org/10.1038/s41556-023-01091-2). After addressing batch effects, we integrated the GSE14520 and ICGC-LIRI-JP datasets, resulting in the formation of metadata. This metadata was used as the training set, while the TCGA-LIHC and GSE144269 datasets served as independent validation sets. All of the bulk transcriptome data were transformed logarithmically and transformed to transcripts per million (TPM) before analysis.

5.2 Expression analysis of disulfidptosis related genes in pan-cancer

We investigated the expression patterns of DRGs across a diverse range of tumor types using the Gene Set Cancer Analysis dataset (GSCALite) (http://bioinfo.life.hust.edu.cn/web/GSCALite/). Specifically, we examined the genomic locations of CNV mutations in DRGs on the 23 chromosome pairs, as well as CNV mutations and SNV in liver cancer. To visualize these findings, we employed R (Version 4.2.0) to generate graphical representations for 15 selected DRGs. Furthermore, we retrieved the protein-protein interaction network of the DRGs from the STRING database (https://string-db.org/cgi/input.pl) and visualized it using Cytoscape 3.9.

5.3 Methylation and drug sensitivity of DRGs

We conducted an analysis of DNA methylation levels in the pan-cancer using the GSCALite website, specifically focusing on the DNA methylation levels of DRGs. Additionally, we investigated the correlation between mRNA expression and DRG methylation levels across different tumor types. Furthermore, we performed a drug sensitivity analysis of DRGs using two databases: the Cancer Therapeutics Response Portal (CTRP) and the Genomics of Drug Sensitivity in Cancer (GDSC) databases.

5.4 Unsupervised consensus clustering for DRGs on patients with hepatocellular carcinomas

To explore the different disulfidptosis patterns of HCC, we applied the "ConsensusClusterPlus" R package to determine the subgroups of patients with HCC based on DRGs. We also verified the discriminatory degree of the categorization using the UMAP and PCA dimensionality reduction. Then, we subjected clusters to a survival analysis by applying the "survival" R package.

5.5 Disulfidptosis score and the weighted gene co-expression network analysis for the disulfidptosis-related module

In our study on HCC, we initially utilized four scoring methods from the "GSVA" R package to assess the disulfidptosis status. The average value of these scores was then used to represent the disulfidptosis characteristics of liver cancer patients (38, 39). Subsequently, we employed the WGCNA method to identify gene modules that were highly correlated, as well as the interconnections between these modules and their associations with disulfidptosis scores. This analysis aimed to identify potential therapeutic targets or candidate biomarkers. To construct the gene co-expression network, we utilized the "WGCNA" R package and selected modules that exhibited the strongest correlation with disulfidptosis in HCC (39). Prior to the analysis, we pre-processed the sample data and removed any outliers. We then constructed a correlation matrix using the "WGCNA" R package. By determining the optimal soft threshold, we transformed the correlation matrix into an adjacency matrix and subsequently built a topological overlap matrix (TOM). Through hierarchical clustering based on the TOM dissimilarity metric, genes with similar expression patterns were grouped into gene modules using

average association. The module that exhibited the strongest correlation with disulfidptosis was selected as the critical module for further analysis.

5.6 Construction and verification of the DRG-based prognostic signature

We constructed and verified the prognostic characteristics of patients with HCC for key module genes from the WGCNA that are closely associated with disulfidptosis. First, we screened the prognosis-associated genes in the metadata training set by applying univariate Cox regression ("survival" R package). We then conducted a multivariate Cox regression and least absolute shrinkage and selection operator (LASSO) regressions ("glmnet" R package) to minimize the candidate genes and create a prognostic signature. We calculated the risk score by multiplying the regression coefficient (b) from the multivariate Cox regression by a linear combination of gene expression levels. The risk score calculation formula is:

$$Risk\ \ Score = \sum_{i=1}^{n} Coefficient(\beta_i) * x_i$$

Per the median risk score, we classified patients with HCC into low- and high-risk groups. We then drew time-dependent ROC curves ("pROC" R package) and Kaplan-Meyer survival curves ("survival" and "survminer") to detect the clinical model's prognostic value. We validated the new model's robustness and assessed the prognostic value with TCGA-LIHC and GSE144269. Using the Human Protein Atlas database (HPA) (https://www.proteinatlas.org), we compared the protein expression patterns of the signature HCC genes to normal tissue. We built a predictive nomogram model ("survival" and "rms" R packages) incorporating tumor Tumor, Node, Metastasis (TNM) pathologic staging to predict the one-, three-, and five-year OS probability of patients with HCC based on the multivariate Cox regression analysis results. In addition, we conducted a DCA to determine the model's net clinical benefits on OS at one, three, and five years for patients with HCC.

5.7 Tumor immune infiltration and GSVA analyses

To assess the tumor microenvironment across different risk groups, we employed the xCell algorithm (40). Furthermore, we obtained exclusion scores, dysfunction scores, and TIDE scores from the TIDE website (http://tide.dfci.harvard.edu/) (41). In order to evaluate the response to immunotherapy in the high- and low-risk groups, we compiled a list of 40 ICGs based on the literature (42). We then conducted a correlation analysis between the risk scores and the ICGs using the "corrplot" R package. Additionally, we utilized the "GSVA" R package to examine the expression patterns of different risk profiles in the Kyoto Encyclopedia of Genes and Genomes (KEGG) signaling pathway. For this analysis, we retrieved the C2 (C2.cp.Kegg.v7.4.symbols.gmt) gene set from the Molecular Signatures Database and generated a heatmap to visualize the results.

5.8 Analysis of scRNA-seq data

First, we utilized the "Seurat" package to generate objects and performed quality control measures to filter out lower-quality cells. Specifically, we applied the following criteria: cells with fewer than 200 or more than 4000 expressed genes were excluded, and cells with more than 10% of unique molecular identifiers (UMIs) mapped to mitochondrial genes were also excluded. We retained only genes that were expressed in at least three cells. Next, we normalized the data and identified the top 3000 highly variable genes using the "FindVariableFeatures" function. Principal component analysis (PCA) was then performed on the scRNA-seq data using these 3000 genes. For visualization and clustering purposes, we retained the first 16 and 22 principal components for GSE149614 and GSE166635, respectively, and applied the UMAP algorithm. To address batch effects between samples, we employed the harmony method (v0.1.0) to remove these effects and integrate the Seurat objects into a single dataset. Subsequently, we performed cell clustering using the "FindClusters" function in the "Seurat" package, with a resolution parameter set to 0.7. To annotate the cells, we utilized the "singleR" package and CellMarker 2.0 (http://bio-bigdata.hrbmu.edu.cn/CellMarker).

5.9 Cell-cell interaction and pseudotime analyses at single-cell level

To investigate cell-cell interactions, we employed the "CellChat" R package (43) and utilized its "cellchat" function. Our analysis involved utilizing ScRNA-seq count files and cell type-specific markers as input data. Using this approach, we examined the expression of receptors in one cell type and ligands in another. By assessing the presence of ligand-receptor interactions, we quantified the enrichment of such interactions between pairs of cell types. This analysis provided insights into the extent of communication and signaling between different cell types. To evaluate the cell-type specificity of a particular ligand-receptor complex, we identified P-values based on the proportion of mean values greater than or equal to the actual mean. We utilized a P-value threshold of< 0.05 to select important cell-cell interactions.

In parallel, we employed a pseudotime analysis of the scRNA-seq data to measure the evolutionary trajectory of macrophages in GSE166635. This analysis entailed mapping the high-dimensional gene expression data onto a one-dimensional quantity called pseudotime. We inferred cell fates and revealed the cellular trajectories. We utilized the "Monocle" R packages (Version 2.26.0) (44, 45), which can provide insight into the cellular developmental trajectory but cannot accurately determine the origin and direction of this developmental process.

5.10 Spatial transcriptomics data analysis

We processed and visualized the ST data using the "Seurat" R package. To ensure data comparability, we integrated the ST data using the SCT approach and subsequently performed clustering of

similar ST sites using PCA. Specifically, we established filtering criteria, including a gene count between 300 and 6000, a mitochondrial ratio below 15%, and the exclusion of genes expressed in fewer than 10 spots. Then, we used the sctransform normalization method and PCA dimensionality reduction is performed first, and then the top 20 dimensions are selected for clustering and umap dimensionality reduction. Cell clusters were annotated based on hematoxylin and eosin (HE) staining sections and genes exhibiting high variability within each cluster. The spatial expression of DRGs was visualized using the SpatialDimPlot function. Furthermore, we conducted deconvolution using the "spacexr" package and utilized the "spotlight" R packages to identify cell types at specific spatial spots. Subsequently, we employed the "scMetabolism" R package to evaluate the metabolic activity of the spatial transcriptional data on slices (46) Additionally, we utilized the Python "stlearn" package to visualize and analyze cell-cell interactions, as well as score the co-expression of ligand-receptor pairs in the tissue slice.

5.11 Human specimens

We obtained 19 HCC pairs and adjacent non-cancerous specimens from the Department of Hepatobiliary-pancreatic & Hernia Surgery at Guangdong Second Provincial General Hospital. The study was authorized by the Medical Research Ethics Committee of Guangdong Second Provincial General Hospital, and all of the participants provided written informed consent. Following specimen isolation, we rapidly froze the liver tissue in liquid nitrogen and stored it at a temperature of -80°C to ensure preservation and prevent degradation.

5.12 Quantitative reverse transcription polymerase chain reaction

We extracted the total RNA with Trizol reagent (Invitrogen, Carlsbad, CA, USA), and synthesized the cDNA through the ABI 7500 Fast System (Applied Biosystems, Rockville, MD, USA). We used α-Tubulin as the reference gene. The relative expression level of the relevant gene was 2- [(Ct of gene) – (Ct of α-tubulin)], in which Ct stands for the threshold cycle. Primer sequences for amplification were as below: NDRG1 (47), forward primer, 5'-CTGCACCTGTTCATCAATGC-3' and reverse primer, 5'-AGAGAAGTGACGCTGGAACC-3'.

5.13 Western blotting

The HCC tissue samples were lysed using a radioimmunoprecipitation assay buffer containing 1% phenylmethylsulfonyl fluoride (PMSF, Beyotime, Shanghai, China). Western blotting was performed following a previously described protocol. Primary antibodies specific to NDRG1 (1:5000, T57079S, Abmart) and an anti-glyceraldehyde-3-phosphate dehydrogenase (GAPDH) antibody (1:5000, Proteintech) were used, with GAPDH serving as a control. The obtained results were subjected to semi-quantitative analysis using ImageJ software.

5.14 Immunocytochemistry

To evaluate the expression of NDRG1 protein, we performed immunohistochemistry (IHC) experiments. Fresh human tissues were fixed overnight in 10% formalin, followed by dehydration, embedding in paraffin, and sectioning. The sections were then dewaxed and hydrated accordingly. Antigen retrieval was performed using citrate, and peroxidase activity in liver samples was blocked with 3% H_2O_2. The primary antibodies against NDRG1 (1:500, T57079S, Abmart) were incubated overnight at 4°C. Subsequently, the slides were incubated with a secondary antibody at 37°C for one hour. A 3,3'-diaminobenzidine (DAB) color development kit was employed, followed by hematoxylin restaining. Finally, the slides were dehydrated, rendered transparent, and sealed with neutral treacle. We then viewed the slides under a microscope, and two experienced pathologists conducted double-blind readings to identify the staining intensity and the percentage of positive cells, which was scored as follows:< 5% was scored as 0, 5%-25% was scored as 1, 26%-50% was scored as 2, 51%-75% was scored as 3, and 76%-100% was scored as 4. Moreover, we assessed staining intensity as follows: 0, 1, 2, and 3 for colorless, light yellow, tan, and brown, respectively. Lastly, We acquired the final score by multiplying the staining intensity score by the percentage of positive cells. Scores of 0, 1-4, 5-8, and 9-12 were negative (-), weakly positive (+), positive (++), and strongly positive (++++), respectively.

5.15 Immunofluorescence

For immunofluorescence staining, we utilized a multiplex immunofluorescence staining kit (abs50012, absin, Shanghai, China) and followed the instructions provided by the manufacturer. Antibodies against NDRG1 (1:500, T57079S, Abmart) and CD206 (1:500, TD4149S, Abmart) were incubated at room temperature for one hour. Subsequently, the slides were incubated with anti-rabbit/mouse IgG conjugated with HRP for 15 minutes at room temperature, followed by incubation with fluorophore-conjugated tyramine molecules (PPD 650, PPD 570, or PPD 520) for 15 minutes. Finally, the nuclei were stained using DAPI.

5.16 Statistical analysis

We conducted data analysis and visualization using the R software (Version 4.2.0, https://www.r-project.org/) and Python software (Version 3.9.0, https://www.python.org/). To compare two groups and two or more groups, we employed the Wilcoxon rank-sum test and the Kruskal-Wallis test, respectively. Categorical variables were compared using Fisher's exact test or the chi-square test. Differences in survival curves were assessed using the log-rank test. We performed a Spearman's correlation test to determine the

correlations between the two variables. Statistical significance was determined at a significance level of $P< 0.05$.

Data availability statement

The datasets presented in this study can be found in online repositories. The names of the repository/repositories and accession number(s) can be found in the article/Supplementary Material.

Ethics statement

The studies involving human participants were reviewed and approved by The Medical Research Ethics Committee of Guangdong Second People's Hospital. The patients/participants provided their written informed consent to participate in this study. Written informed consent was obtained from the individual(s) for the publication of any potentially identifiable images or data included in this article.

Author contributions

TY: Data curation, Investigation, Methodology, Software, Writing – original draft. JLi: Formal Analysis, Writing – original draft. FL: Investigation, Software, Writing – original draft. JLe: Software, Supervision, Writing – original draft. SC: Resources, Visualization, Writing – original draft. ZM: Project administration, Visualization, Writing – original draft. PK: Investigation, Methodology, Software, Writing – original draft. QY: Funding acquisition, Investigation, Writing – original draft. JW: Conceptualization, Investigation, Writing – review & editing. YH: Conceptualization, Data curation, Writing – review & editing. JD: Conceptualization, Data curation, Formal analysis, Funding acquisition, Writing – review & editing. XZ: Conceptualization, Funding acquisition, Investigation, Methodology, Writing – original draft, Writing – review & editing.

Funding

The author(s) declare financial support was received for the research, authorship, and/or publication of this article. This research was supported by Guangdong Natural Science Foundation (no. 2018A0303130184), in part by Project of Administration of Traditional Chinese Medicine of Guangdong Province of China (no. 20242004), Funding by Science and Technology Projects in Guangzhou (no. 202201020270 and no.SL2024A03J01183), Hospital Fund of Guangdong Second Provincial General Hospital (no. 3D-A2020005), Youth Research Foundation of Guangdong Second Provincial General Hospital (no. YQ2020-003), and 3D Printing Project of Guangdong Second Provincial General Hospital (no. 3D-D2020020).

Conflict of interest

The authors declare that the research was conducted in the absence of any commercial or financial relationships that could be construed as a potential conflict of interest.

Publisher's note

All claims expressed in this article are solely those of the authors and do not necessarily represent those of their affiliated organizations, or those of the publisher, the editors and the reviewers. Any product that may be evaluated in this article, or claim that may be made by its manufacturer, is not guaranteed or endorsed by the publisher.

Supplementary material

The Supplementary Material for this article can be found online at: https://www.frontiersin.org/articles/10.3389/fimmu.2023.1294677/full#supplementary-material

SUPPLEMENTARY FIGURE 1
Validation of the putative model. **(A–D)** Unsupervised consensus clustering. TCGA-LIHC **(E)** We plotted the OS curves between the high-risk and low-risk groups based on the prognostic signature. **(F)** The time-dependent ROC curves. **(G)** DCA for the validation data. GSE144269 **(H)** We plotted the OS curves between the high-risk and low-risk groups based on the prognostic signature. **(I)** The time-dependent ROC curves. **(J)** DCA for the validation data.

SUPPLEMENTARY FIGURE 2
The forest plot shows the hazard ratios and 95% confidence intervals of the signature genes from the univariate Cox regression analysis.

References

1. Sung H, Ferlay J, Siegel RL, Laversanne M, Soerjomataram I, Jemal A, et al. Global Cancer Statistics 2020: Globocan estimates of incidence and mortality worldwide for 36 cancers in 185 countries. *CA: Cancer J Clin* (2021) 71(3):209–49. doi: 10.3322/caac.21660

2. Zou H, Li M, Lei Q, Luo Z, Xue Y, Yao D, et al. Economic burden and quality of life of hepatocellular carcinoma in greater China: A systematic review. *Front Public Health* (2022) 10:801981. doi: 10.3389/fpubh.2022.801981

3. Villanueva A. Hepatocellular carcinoma. *New Engl J Med* (2019) 380(15):1450–62. doi: 10.1056/NEJMra1713263

4. Pinter M, Jain RK, Duda DG. The current landscape of immune checkpoint blockade in hepatocellular carcinoma: A review. *JAMA Oncol* (2021) 7(1):113–23. doi: 10.1001/jamaoncol.2020.3381

5. Koren E, Fuchs Y. Modes of regulated cell death in cancer. *Cancer Discovery* (2021) 11(2):245–65. doi: 10.1158/2159-8290.Cd-20-0789

6. Galluzzi L, Vitale I, Aaronson SA, Abrams JM, Adam D, Agostinis P, et al. Molecular mechanisms of cell death: recommendations of the nomenclature committee on cell death 2018. *Cell Death Differentiation* (2018) 25(3):486–541. doi: 10.1038/s41418-017-0012-4

7. Tang D, Kang R, Berghe TV, Vandenabeele P, Kroemer G. The molecular machinery of regulated cell death. *Cell Res* (2019) 29(5):347–64. doi: 10.1038/s41422-019-0164-5

8. Liu X, Nie L, Zhang Y, Yan Y, Wang C, Colic M, et al. Actin cytoskeleton vulnerability to disulfide stress mediates disulfidptosis. *Nat Cell Biol* (2023) 25(3):404–14. doi: 10.1038/s41556-023-01091-2

9. Lei Y, Tang R, Xu J, Wang W, Zhang B, Liu J, et al. Applications of single-cell sequencing in cancer research: progress and perspectives. *J Hematol Oncol* (2021) 14 (1):91. doi: 10.1186/s13045-021-01105-2

10. Lavie D, Ben-Shmuel A, Erez N, Scherz-Shouval R. Cancer-associated fibroblasts in the single-cell era. *Nat Cancer* (2022) 3(7):793–807. doi: 10.1038/s43018-022-00411-z

11. Ståhl PL, Salmén F, Vickovic S, Lundmark A, Navarro JF, Magnusson J, et al. Visualization and analysis of gene expression in tissue sections by spatial transcriptomics. *Sci (New York NY)* (2016) 353(6294):78–82. doi: 10.1126/science.aaf2403

12. Rao A, Barkley D, França GS, Yanai I. Exploring tissue architecture using spatial transcriptomics. *Nature* (2021) 596(7871):211–20. doi: 10.1038/s41586-021-03634-9

13. Li XM, Liu SP, Li Y, Cai XM, Zhang SB, Xie ZF. Identification of disulfidptosis-related genes with immune infiltration in hepatocellular carcinoma. *Heliyon* (2023) 9 (8):e18436. doi: 10.1016/j.heliyon.2023.e18436

14. Yang L, Zhang W, Yan Y. Identification and characterization of a novel molecular classification based on disulfidptosis-related genes to predict prognosis and immunotherapy efficacy in hepatocellular carcinoma. *Aging* (2023) 15(13):6135–51. doi: 10.18632/aging.204809

15. Dudakov JA, Hanash AM, van den Brink MR. Interleukin-22: immunobiology and pathology. *Annu Rev Immunol* (2015) 33:747–85. doi: 10.1146/annurev-immunol-032414-112123

16. Kuang DM, Xiao X, Zhao Q, Chen MM, Li XF, Liu RX, et al. B7-H1-expressing antigen-presenting cells mediate polarization of protumorigenic th22 subsets. *J Clin Invest* (2014) 124(10):4657–67. doi: 10.1172/jci74381

17. Voigt C, May P, Gottschlich A, Markota A, Wenk D, Gerlach I, et al. Cancer cells induce interleukin-22 production from memory cd4(+) T cells via interleukin-1 to promote tumor growth. *Proc Natl Acad Sci United States America* (2017) 114 (49):12994–9. doi: 10.1073/pnas.1705165114

18. Su S, Liao J, Liu J, Huang D, He C, Chen F, et al. Blocking the recruitment of naive cd4(+) T cells reverses immunosuppression in breast cancer. *Cell Res* (2017) 27 (4):461–82. doi: 10.1038/cr.2017.34

19. Oliveira G, Wu CJ. Dynamics and specificities of T cells in cancer immunotherapy. *Nat Rev Cancer* (2023) 23(5):295–316. doi: 10.1038/s41568-023-00560-y

20. Aras S, Zaidi MR. Tameless traitors: macrophages in cancer progression and metastasis. *Br J Cancer* (2017) 117(11):1583–91. doi: 10.1038/bjc.2017.356

21. Zhao H, Chen Q, Alam A, Cui J, Suen KC, Soo AP, et al. The role of osteopontin in the progression of solid organ tumour. *Cell Death Dis* (2018) 9(3):356. doi: 10.1038/s41419-018-0391-6

22. Rao G, Wang H, Li B, Huang L, Xue D, Wang X, et al. Reciprocal interactions between tumor-associated macrophages and cd44-positive cancer cells via osteopontin/cd44 promote tumorigenicity in colorectal cancer. *Clin Cancer Res* (2013) 19(4):785–97. doi: 10.1158/1078-0432.Ccr-12-2788

23. Koh HM, Kim DC. Prognostic significance of macrophage migration inhibitory factor expression in cancer patients: A systematic review and meta-analysis. *Medicine* (2020) 99(32):e21575. doi: 10.1097/md.0000000000021575

24. Filippou PS, Karagiannis GS, Constantinidou A. Midkine (Mdk) growth factor: A key player in cancer progression and a promising therapeutic target. *Oncogene* (2020) 39(10):2040–54. doi: 10.1038/s41388-019-1124-8

25. Park KC, Menezes SV, Kalinowski DS, Sahni S, Jansson PJ, Kovacevic Z, et al. Identification of differential phosphorylation and sub-cellular localization of the metastasis suppressor, ndrg1. *Biochim Biophys Acta Mol Basis Dis* (2018) 1864 (8):2644–63. doi: 10.1016/j.bbadis.2018.04.011

26. Park KC, Paluncic J, Kovacevic Z, Richardson DR. Pharmacological targeting and the diverse functions of the metastasis suppressor, ndrg1, in cancer. *Free Radical Biol Med* (2020) 157:154–75. doi: 10.1016/j.freeradbiomed.2019.05.020

27. Yeung OW, Lo CM, Ling CC, Qi X, Geng W, Li CX, et al. Alternatively activated (M2) macrophages promote tumour growth and invasiveness in hepatocellular carcinoma. *J Hepatol* (2015) 62(3):607–16. doi: 10.1016/j.jhep.2014.10.029

28. Watari K, Shibata T, Kawahara A, Sata K, Nabeshima H, Shinoda A, et al. Tumor-derived interleukin-1 promotes lymphangiogenesis and lymph node metastasis through M2-type macrophages. *PloS One* (2014) 9(6):e99568. doi: 10.1371/journal.pone.0099568

29. Nishie A, Masuda K, Otsubo M, Migita T, Tsuneyoshi M, Kohno K, et al. High expression of the cap43 gene in infiltrating macrophages of human renal cell carcinomas. *Clin Cancer Res* (2001) 7(7):2145–51. Available at: https://pubmed.ncbi.nlm.nih.gov/11448934/

30. Watari K, Shibata T, Nabeshima H, Shinoda A, Fukunaga Y, Kawahara A, et al. Impaired differentiation of macrophage lineage cells attenuates bone remodeling and inflammatory angiogenesis in ndrg1 deficient mice. *Sci Rep* (2016) 6:19470. doi: 10.1038/srep19470

31. Zhang G, Qin Q, Zhang C, Sun X, Kazama K, Yi B, et al. Ndrg1 signaling is essential for endothelial inflammation and vascular remodeling. *Circ Res* (2023) 132 (3):306–19. doi: 10.1161/circresaha.122.321837

32. Lian Z, Chang T, Ma S, Li J, Zhang H, Wang X, et al. Mir-96-5p induced ndrg1 deficiency promotes prostate cancer migration and invasion through regulating the nf-Kb signaling pathway. *Cancer Biomarkers Sect A Dis Markers* (2022) 35(1):83–98. doi: 10.3233/cbm-210072

33. Chang CP, Su YC, Lee PH, Lei HY. Targeting nfkb by autophagy to polarize hepatoma-associated macrophage differentiation. *Autophagy* (2013) 9(4):619–21. doi: 10.4161/auto.23546

34. Gao ZS, Zhang CJ, Xia N, Tian H, Li DY, Lin JQ, et al. Berberine-loaded M2 macrophage-derived exosomes for spinal cord injury therapy. *Acta Biomaterialia* (2021) 126:211–23. doi: 10.1016/j.actbio.2021.03.018

35. Zhao C, Cheng Y, Huang P, Wang C, Wang W, Wang M, et al. X-ray-guided in situ genetic engineering of macrophages for sustained cancer immunotherapy. *Advanced Mater (Deerfield Beach Fla)* (2023) 35(14):e2208059. doi: 10.1002/adma.202208059

36. Duan Z, Luo Y. Targeting macrophages in cancer immunotherapy. *Signal Transduction Targeted Ther* (2021) 6(1):127. doi: 10.1038/s41392-021-00506-6

37. Popper HH. Manipulation of the immune system by non-small cell lung cancer and possible therapeutic interference. *Cancer Drug Resistance (Alhambra Calif)* (2020) 3(4):710–25. doi: 10.20517/cdr.2020.40

38. Hänzelmann S, Castelo R, Guinney J. Gsva: gene set variation analysis for microarray and rna-seq data. *BMC Bioinf* (2013) 14:7. doi: 10.1186/1471-2105-14-7

39. Zhang B, Horvath S. A general framework for weighted gene co-expression network analysis. *Stat Appl Genet Mol Biol* (2005) 4(1):1701–45. doi: 10.2202/1544-6115.1128

40. Aran D, Hu Z, Butte AJ. Xcell: digitally portraying the tissue cellular heterogeneity landscape. *Genome Biol* (2017) 18(1):220. doi: 10.1186/s13059-017-1349-1

41. Jiang P, Gu S, Pan D, Fu J, Sahu A, Hu X, et al. Signatures of T cell dysfunction and exclusion predict cancer immunotherapy response. *Nat Med* (2018) 24(10):1550–8. doi: 10.1038/s41591-018-0136-1

42. Hu FF, Liu CJ, Liu LL, Zhang Q, Guo AY. Expression profile of immune checkpoint genes and their roles in predicting immunotherapy response. *Briefings Bioinf* (2021) 22(3):211–2. doi: 10.1093/bib/bbaa176

43. Jin S, Guerrero-Juarez CF, Zhang L, Chang I, Ramos R, Kuan CH, et al. Inference and analysis of cell-cell communication using cellchat. *Nat Commun* (2021) 12(1):1088. doi: 10.1038/s41467-021-21246-9

44. Trapnell C, Cacchiarelli D, Grimsby J, Pokharel P, Li S, Morse M, et al. The dynamics and regulators of cell fate decisions are revealed by pseudotemporal ordering of single cells. *Nat Biotechnol* (2014) 32(4):381–6. doi: 10.1038/nbt.2859

45. Cao J, Spielmann M, Qiu X, Huang X, Ibrahim DM, Hill AJ, et al. The single-cell transcriptional landscape of mammalian organogenesis. *Nature* (2019) 566(7745):496–502. doi: 10.1038/s41586-019-0969-x

46. Wu Y, Yang S, Ma J, Chen Z, Song G, Rao D, et al. Spatiotemporal immune landscape of colorectal cancer liver metastasis at single-cell level. *Cancer Discovery* (2022) 12(1):134–53. doi: 10.1158/2159-8290.Cd-21-0316

47. Aikemu B, Shao Y, Yang G, Ma J, Zhang S, Yang X, et al. Ndrg1 regulates filopodia-induced colorectal cancer invasiveness via modulating cdc42 activity. *Int J Biol Sci* (2021) 17(7):1716–30. doi: 10.7150/ijbs.56694

frontiers | Frontiers in Immunology

TYPE Original Research
PUBLISHED 11 January 2024
DOI 10.3389/fimmu.2023.1331491

OPEN ACCESS

EDITED BY
Laura Senovilla,
Spanish National Research Council (CSIC), Spain

REVIEWED BY
Tahir Bashir Dar,
Cedars Sinai Medical Center, United States
Nahum Puebla-Osorio,
University of Texas MD Anderson Cancer Center, United States

*CORRESPONDENCE
Indraneel Mittra
imittra@actrec.gov.in

RECEIVED 01 November 2023
ACCEPTED 18 December 2023
PUBLISHED 11 January 2024

CITATION
Shabrish S, Pal K, Khare NK, Satsangi D, Pilankar A, Jadhav V, Shinde S, Raphael N, Sriram G, Lopes R, Raghuram GV, Tandel H and Mittra I (2024) Cell-free chromatin particles released from dying cancer cells activate immune checkpoints in human lymphocytes: implications for cancer therapy. *Front. Immunol.* 14:1331491. doi: 10.3389/fimmu.2023.1331491

Cell-free chromatin particles released from dying cancer cells activate immune checkpoints in human lymphocytes: implications for cancer therapy

Snehal Shabrish[1,2], Kavita Pal[1,2], Naveen Kumar Khare[1,2], Dharana Satsangi[1,2], Aishwarya Pilankar[1,2], Vishalkumar Jadhav[1,2], Sushma Shinde[1,2], Nimisha Raphael[1,2], Gaurav Sriram[1,2], Relestina Lopes[1,2], Gorantla V. Raghuram[1,2], Harshali Tandel[1,2] and Indraneel Mittra[1,2]*

[1]Translational Research Laboratory, Advanced Centre for Treatment, Research and Education in Cancer, Tata Memorial Centre, Mumbai, India, [2]Homi Bhabha National Institute, Mumbai, India

Immune checkpoint blockade is the exciting breakthrough in cancer, but how immune checkpoints are activated is unknown. We have earlier reported that cell-free chromatin particles (cfChPs) that circulate in blood of cancer patients, or those that are released locally from dying cancer cells, are readily internalized by healthy cells with biological consequences. Here we report that treatment of human lymphocytes with cfChPs isolated from sera of cancer patients led to marked activation of the immune checkpoints PD-1, CTLA-4, LAG-3, NKG2A, and TIM-3. This finding was corroborated *in vivo* in splenocytes of mice when cfChPs were injected intravenously. Significant upregulation of immune checkpoint was also observed when isolated lymphocytes were exposed to conditioned medium containing cfChPs released from hypoxia-induced dying HeLa cells. Immune checkpoint activation could be down-regulated by pre-treating the conditioned media with three different cfChPs deactivating agents. Down-regulation of immune checkpoints by cfChPs deactivating agents may herald a novel form of immunotherapy of cancer.

KEYWORDS

cell death, cellular stress, immunotherapy, cancer, cell-free chromatin deactivators

Introduction

Immune checkpoint molecules prevent the immune system from indiscriminately attacking self-cells. Immunologically altered cancer cells, on the other hand, can protect themselves from elimination by activating immune checkpoints (1). Consequently, targeting activated immune checkpoints with specific inhibitors is being widely used in

the treatment of cancer (2, 3). Several immune checkpoint inhibitors have now been approved by FDA for the treatment of a variety of cancers (4). Although much has been reported on immune checkpoint biology and immune therapy, how immune checkpoints are activated by lymphocytes has not been elucidated.

Several hundred billion to a trillion cells die in the body everyday (5, 6) and the fragmented chromosomal material in the form of cell-free chromatin particles (cfChPs) enter into the extracellular compartment of the body, including into the circulation (7–9). We have earlier reported that cfChPs that circulate in blood of cancer patients, and those that are released locally from dying cancer cells, can readily enter into healthy cells to activate two hallmarks of cancer viz. DNA damage and inflammation (10, 11). Since immune escape by the way of activation of immune checkpoints is another critical hallmark of cancer (12), we investigated whether cfChPs might be the agents that also activate immune checkpoints in human lymphocytes. We approached this question in several ways: 1) by directly treating isolated human T-cells with cfChPs isolated from sera of cancer patients; 2) by intravenously injecting cfChPs isolated from sera of cancer patients into mice; and 3) by using a co-culture system wherein human T cells were exposed to conditioned medium containing cfChPs released from hypoxia-induced dying HeLa cells.

Materials and methods

Institutional ethics approval

This study was approved by Institutional Ethics Committee (IEC) of Advanced Centre for Treatment, Research and Education in Cancer (ACTREC), Tata Memorial Centre (TMC) for collection of blood (10mL) from cancer patients and healthy volunteers for isolation of cfChPs and lymphocytes respectively (Approval no. 900520). All participants signed a written informed consent form which was approved by the IEC.

Animal ethics approval

The experimental protocol of this study was approved by the Institutional Animal Ethics Committee (IAEC) of Advanced Centre for Treatment, Research and Education in Cancer (ACTREC), Tata Memorial Centre (TMC) (Approval no. 12/2020). The experiments were carried out in compliance with the IAEC animal safety guidelines, and with those of ARRIVE guidelines.

ACTREC- IAEC maintains respectful treatment, care and use of animals in scientific research. It aims that the use of animals in research contributes to the advancement of knowledge following the ethical and scientific necessities. All scientists and technicians involved in this study have undergone training in ethical handling and management of animals under supervision of FELASA certified attending veterinarian. Inbred female C57Bl/6 mice were obtained from our Institutional Animal Facility. All mice were maintained in covenant with Institutional Animal Ethics Committee (IAEC) standards. Animals were euthanized at appropriate time points under CO_2 atmosphere by cervical dislocation under supervision of FELASA trained animal facility personnel.

Collection of blood samples for cfChPs and lymphocyte isolation

For lymphocyte culture, peripheral blood samples from healthy adult volunteers were collected using Vacutainer TM tubes (Becton-Dickinson Vacutainer Systems, Franklin Lakes, NJ, U.S.A.) containing sodium heparin anticoagulant. For isolation of cfChPs blood was collected from cancer patients in plain vacutainer (VACUETTE blood collection tube Serum Clot Activator PREMIUM).

Isolation of cfChPs from human sera

cfChPs were isolated from sera of cancer patients according to a protocol described by us earlier (11). In order to maintain inter-experimental consistency, pooled serum (typically from ~5 individuals) was used to isolate cfChPs and were quantified in terms of their DNA content as estimated by the Pico-green quantification assay.

Fluorescent dual labelling of cfChPs

cfChPs were fluorescently dually labelled in their DNA by Platinum Bright 550 (red) and in their histone H4 with ATTO-TEC 488 (green) according to a protocol described by us earlier (11).

PBMC isolation

Peripheral blood mononuclear cells (PBMC) were isolated using Ficoll-Hypaque according to standard procedures.

FACs sorting

PBMCs were stained with FITC-conjugated anti-human CD4 antibody (clone PRA-T4, BD Biosciences Pharmingen, San Jose, CA, USA) and PerCP-conjugated anti-human CD8 antibody (clone SK1, BD Biosciences Pharmingen, San Jose, CA, USA) or with FITC-conjugated anti-human CD3 antibody (clone UCHT1, BD Biosciences Pharmingen, San Jose, CA, USA). Cells were sorted on FACS Aria III (BD Biosciences, San Jose, CA, USA). Data were analyzed using FACS Diva software (version 4.0.1.2; Becton, Dickinson and Company). Sorted cells were seeded in 24-well plates and were allowed to rest overnight at 37°C in humidified atmosphere of 5% CO_2 prior to stimulation.

Preparation of cfChPs deactivating agents

The cfChPs deactivating agents used in our study were: 1) anti-histone antibody complexed nanoparticles (CNPs) (13);

2) DNase I from bovine pancreas was procured from Sigma-Aldrich, and 3) a novel pro-oxidant combination of Resveratrol and Copper(R-Cu), which can deactivate/degrade cfChPs via the medium of free-radicals (14–17). The concentrations of R and Cu used in this study were 1mM and 0.0001mM respectively (14).

Treatment of lymphocytes with cfChPs isolated from sera of cancer patients

Sorted $CD4^+$T cells and $CD8^+$T cells were plated at a density of $5x10^5$ in 24-well plates containing 1ml of DMEM. After overnight culture, cells were treated with cfChPs (10ng equivalent of DNA) isolated from sera of cancer patients and used for determining upregulation of immune checkpoints.

Procedure for collecting conditioned media from hypoxia induced dying HeLa cells

A dual chamber system was used to generate conditioned medium containing cfChPs released from dying cells. HeLa cells (~$1x10^5$) were seeded on ThinCert® Cell Culture Inserts (pore size 400nm) containing 1.5ml of DMEM and were placed in 6-well culture plate and were incubated overnight at 37°C. The 6-well plate with Thincert® Inserts was transferred to a hypoxia chamber with 1% O_2 for 48h to induce hypoxic cell death. Sufficient DMEM (~700 µl) was added to the lower chamber of the 6-well plate such that the medium touched the lower surface of the ThinCert® Inserts and plates were placed at 37°C in humidified atmosphere of 5% CO_2 for 48h under normoxic conditions. This procedure allowed cfChPs <400 nm in size released from the hypoxic HeLa cells to seep into the medium in the lower chamber. Post-incubation, conditioned media from the wells was pooled and was used for further experiments.

Fluorescent dual labelling of HeLa cells

HeLa cells were dually labeled in their histones (H2B) and DNA. Histone H2B labelling was done for 36h using CellLight® Histone 2BGFP (Thermo Fisher Scientific, MA, USA) and DNA labeling was done for 24h using BrdU (10 µM Sigma Chemicals, MO, USA). The procedure for dual labelling of culture cells has been described by us earlier (10). Dually labeled HeLa cells were seeded on ThinCert® Cell Culture Inserts and cultured in hypoxic conditions (1% O_2) for 48h. Two hundred and fifty micro-liters of conditioned media containing cfChPs <400nm that had seeped into the lower chamber of the insert was applied to isolated PBMCs in a time course experiment (2h, 4h and 6h). Cells were then washed and processed for fluorescence microscopy to detect presence of fluorescent signals of BrdU and histone H2BGFP in the recipient PBMCs.

Treatment of cells with conditioned media collected from hypoxic HeLa cells

Conditioned media from hypoxia treated HeLa cells was collected as described above. Sorted T cells were plated at a density of $5x10^5$ in 24-well plate containing 250µL of DMEM media. After overnight culture, cells were treated with 250µL of conditioned media and a time course analysis using qRT-PCR was performed to determine up-regulation of immune checkpoint. In order to confirm that the active agents in the hypoxic media were cfChPs released from the dying HeLa cells, the hypoxic media was pre-treated for 1h with the following cfChPs inhibitors: 1) CNPs (25µg of anti-H4 IgG conjugated nanoparticles) in 125 µL of phosphate buffer; 2) DNase I in PBS to achieve a final concentration of 0.05U/mL; 3) R:Cu in distilled water to achieve a final molar ratio of 1 mM R: 0.0001 mM Cu).

Analyses of immune checkpoints

qRT-PCR

Evaluation of immune checkpoints was performed using qRT-PCR following treatment of human lymphocytes with cfChPs or with media of hypoxic dying HeLa cells as described above. The time points for analyses were: 0h, 30min, 6h, 12h, 24h, 36h and 48h. Appropriate untreated control cells for each time point were analyzed in parallel. Total RNA was isolated using RNeasy Mini Kit (Qiagen, Hilden, Germany) and approximately 1 µg of isolated RNA was converted to cDNA using RT^2 First Strand Kit (Qiagen, Hilden, Germany). cDNA was diluted (1:10) and used in 10µl reaction volume in duplicates. Real-time PCR was carried out using SYBR Select Master Mix (Applied Biosystems, CA, USA) and all the samples were assayed on a QuantStudioTM 12K Flex Real-Time PCR System (ThermoFisher) using a 384-well block in duplicates. Data were analyzed using a comparative C_T method and fold change in mRNA expression was calculated as $2^{(-\Delta\Delta C_T)}$.

Immunofluorescence

For detection of immune checkpoints expression, immunofluorescence analysis for five immune checkpoints was performed at peak time points of mRNA expression following treatment of cells. Methodological details of immunofluorescence have been described by us earlier (10). Briefly, slides were mounted with vectashield mounting medium with DAPI (Vector Laboratories) and analyzed on Applied Spectral Imaging system as described by us earlier (10). All experiments were performed in duplicate, and 500 cells were analyzed in each case. Results were expressed as mean ± SEM.

Flow cytometry

After 72hrs of cfChPs treatment, PBMCs were labelled with the following antibodies; anti-CD3-FITC (clone:UCHT1), anti-CD-8 PerCP (clone:SK1), anti-PD-1-BV421 (clone:EH12.1), anti-CTLA-4-PE-CF594 (clone:BN13), anti-LAG-3-BUV395 (clone:T47-530),

anti-NKG2A-BV421 (clone:131411) and anti-TIM-3-BV786 (clone:7D3). All antibodies were purchased from Becton Dickinson Biosciences, San Jose, CA, USA. Cells were incubated for 20mins in dark at room temperature followed by PBS wash. Samples were acquired on FACSAria III cytometer (Becton Dickinson, USA) and analyzed with *FlowJo*™ *v10.6 Software* (ThreeStar Inc, USA). Lymphocytes were gated on forward and side scatter parameters. At least 20,000 cells were acquired. Untreated T cells reveal a basal expression of immune checkpoints which increases following treatment. Therefore, to determine an increase in percent positive cells, the difference between negative and positive expression was defined by the fluorescence minus one (FMO) method.

In vivo studies

Intravenous injection of cfChPs into mice

For the *in vivo* study, 21 mice (3 per group, 7 groups) were injected with cfChPs (100ng dissolved in saline for each mouse) and 3 mice acted as untreated controls. Mice were sacrificed under anesthesia at 6h, 12h, 18h, 24h, 48h, 72h and 96h after cfChPs injection and spleen was removed.

Preparation of mouse splenocytes

The spleens were minced with a sharp sterile blade, placed in a 40-m nylon cell strainer and pressed with the plunger of a syringe. Splenocytes were suspended in RPMI-1640 supplemented with 5% FBS. Red blood cells were lysed with 1XBD Pharmlyse, washed, and splenocytes were re-suspended in 5% FBS in PBS.

Analysis of activation of immune checkpoints in splenocytes by flow cytometry

One million splenocytes were stained for 20 min in the dark with the following antibodies: CD3-APC-Cy7 (Clone: 17A2), CD4-FITC (Clone : GK1.5), CD8-APC (Clone:53-6.7), PD-1-BV510 (Clone:29F.1A12), CTLA-4-PE (Clone : UC10-4B9), NKG2A-PE (Clone:16A11), Tim-3-BV421 (Clone : RMT3-23) and LAG-3-PerCP-Cy5.5 (Clone:C9B7W). All antibodies were purchased from BioLegend company (USA). Samples were acquired on BD FACS Aria III (Becton Dickinson, USA) and analyzed with *FlowJo*™ *v10.6 Software* (ThreeStar Inc, USA) as described above.

Statistical analysis

All data are presented as Mean ± Standard Error of Mean (SEM). Statistical analysis was performed using GraphPad Prism 8 (GraphPad Software, Inc., USA, Version 8.0). Data were compared using Student's t-test (two tailed, unpaired), one-way ANNOVA and Bonferroni's multiple comparisons test. $p < 0.05$ was taken as the level of significance.

Results

cfChPs are readily internalized by human lymphocytes

In the context of our first approach i.e. of treating lymphocytes with cfChPs from cancer patients, we revisited our earlier experiments wherein we had shown that cfChPs are readily internalized by mouse fibroblast cells (11). We confirm using fluorescent microscopy that, like in case of fibroblast cells, treatment of lymphocytes with dually fluorescently labelled cfChPs, in their DNA with Platinum Bright 550 and in their histones with ATTO-TEC-488, results in their rapid uptake within 2h (Supplementary Figure 1).

cfChPs isolated from sera of cancer patients activate immune checkpoints in human lymphocytes

We have earlier reported that cfChPs that circulate in blood of cancer patients, and those that are released locally from dying cancer cells, can readily enter into healthy cells to activate two hallmarks of cancer viz. DNA damage and inflammation (10, 11). Since immune escape by the way of activation of immune checkpoints is another critical hallmark of cancer (12), we investigated whether cfChPs might be the agents that also activate immune checkpoints in human lymphocytes. To investigate this possibility, we treated sorted $CD4^+$T and $CD8^+$T cells with cfChPs (10ng) from cancer patients and performed a time course analyses using qRT-PCR to detect 5 immune checkpoints. All five immune checkpoints, viz. PD-1, CTLA-4, LAG-3, NKG2A and TIM-3, were found to be markedly up-regulated, albeit at different time points (Figure 1A). We validated the above finding of immune checkpoint expression by two methods: 1) by immune-florescence at peak time points of mRNA expression following cfChPs treatment, and 2) by flow cytometry at 72 h. (Figures 1B, C; Supplementary Figures 2A, B, D, E; Supplementary Table 1).

cfChPs activate immune checkpoints as a stress response by lymphocytes

We wondered whether immune checkpoint activation might be a stress response of the cell to DNA damage inflicted by cfChPs (10, 11). To this end, we examined six different stress markers that are involved in transcriptional regulation of immune checkpoints (18–20) viz. c-Jun, c-Fos, NFKB, JunB, EGR-1 and FosB by qRT-PCR after treating PBMCs with cfChPs (10ng) isolated from sera of cancer patients. A time-course analysis revealed marked activation of all six stress markers, albeit at different time points (Figure 2). These data provided suggestive evidence that cfChPs that circulate in blood of cancer patients activate immune checkpoints in human T cells ostensibly as a response to cellular stress.

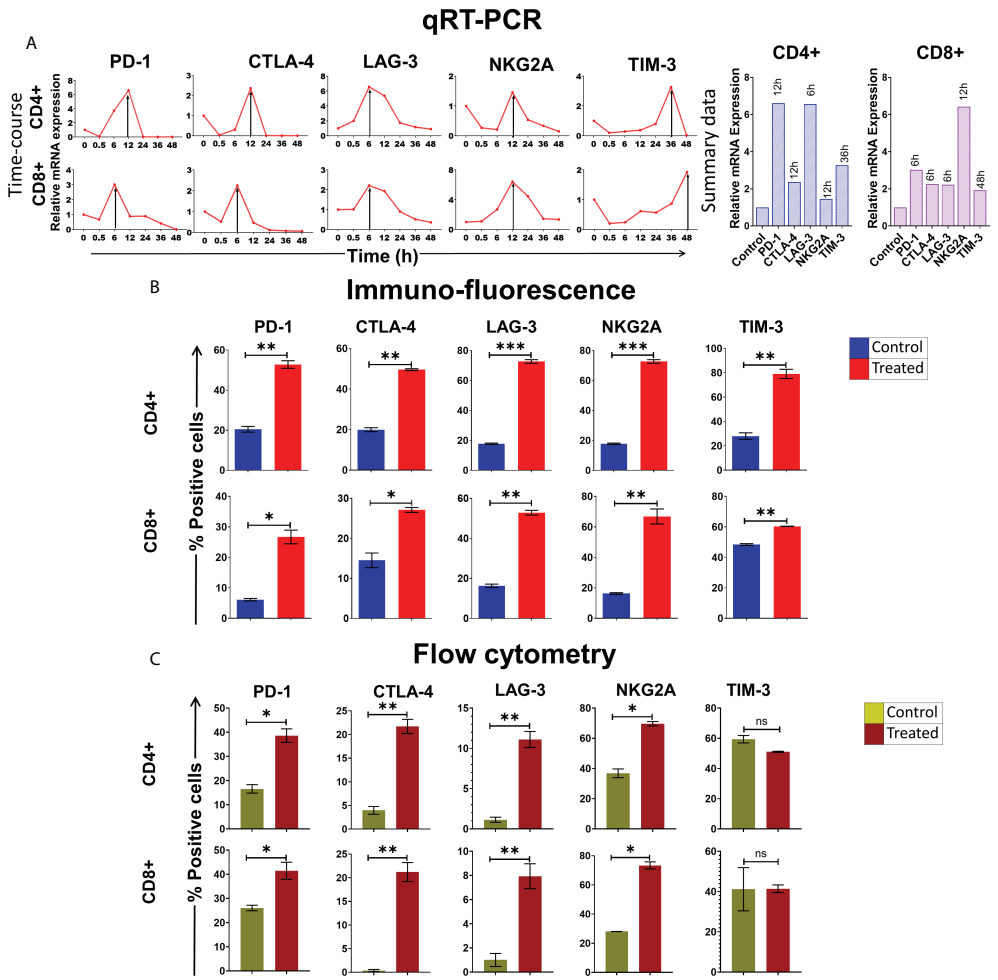

FIGURE 1
Upregulation of immune checkpoints on human lymphocytes following treatment of cfChPs isolated from sera of cancer patients. **(A)** Line graphs showing time course analysis of mRNA expression of immune checkpoints detected by qRT-PCR in purified CD4+T cells and CD8+T cells treated with cfChPs (10ng). The expression fold change was analyzed using a comparative C_T method [2^(-$\Delta\Delta C_T$)]. The histograms represent relative mRNA expression at respective peak time points on CD4+T cells and CD8+T cells. **(B)** Histograms depict the results of quantitative Immunofluorescence (IF) analysis of percent positive cells for immune checkpoints on CD4+T and CD8+T-cells at peak time points of mRNA expression. Five hundred cells were examined in duplicate slides and percent biomarker-positive cells were recorded. **(C)** Histograms depict the results of quantitative flow cytometry analysis of surface expression of immune checkpoint on CD4+T and CD8+T-cells at 72hrs post cfChPs treatment. All experiments were performed in duplicates and histograms represent mean ± SEM values. Statistical analyses were performed using a two-tailed student's unpaired t-test (GraphPad Prism 8). * p<0.05, ** p<0.01, *** p<0.001.

cfChPs upregulate immune checkpoints *in vivo*

We next examined if cfChPs could activate immune checkpoints *in vivo*. Intravenous injection into mice of cfChPs (100ng) isolated from sera of cancer patients led to marked activation of several immune checkpoints in their splenocytes. A time course analysis by flow cytometry of isolated splenocytes detected significant increased surface expression of four out of five immune checkpoints on $CD4^+$T and $CD8^+$T cells. Time points at which immune checkpoints were activated were variable, viz. PD-1 at 6h, CTLA-4 at 6h, NKG2A at 6h and LAG-3 at 24h. Expression of TIM-3 was not detected on T cells in experiments lasting 96h (Figure 3). The variability in time-points of immune checkpoint activation on mouse splenocytes could be attributed to their distinct expression on different cell populations. For example, PD-1 is largely expressed on activated T and B cells and on monocytes; CTLA-4 is expressed on activated T-cells; LAG-3 is expressed on activated T, B, NK, DCs and monocytes; NKG2A is expressed on CD8+T and NK cells, while TIM-3 is expressed on monocytes, NK cells, Th1, Tc1 and Treg cells (21, 22).

cfChPs released from dying HeLa cells are readily internalized by human lymphocytes

To confirm the above findings in another experimental setting, we devised a method in which isolated T-cells were exposed to conditioned medium containing cfChPs released from hypoxia-induced dying HeLa cells. Such an experimental setting provides further confirmation of the effect of cfChPs on immune checkpoint activation in a more physiological situation as it utilizes cfChPs that has been naturally released into the culture medium from hypoxia

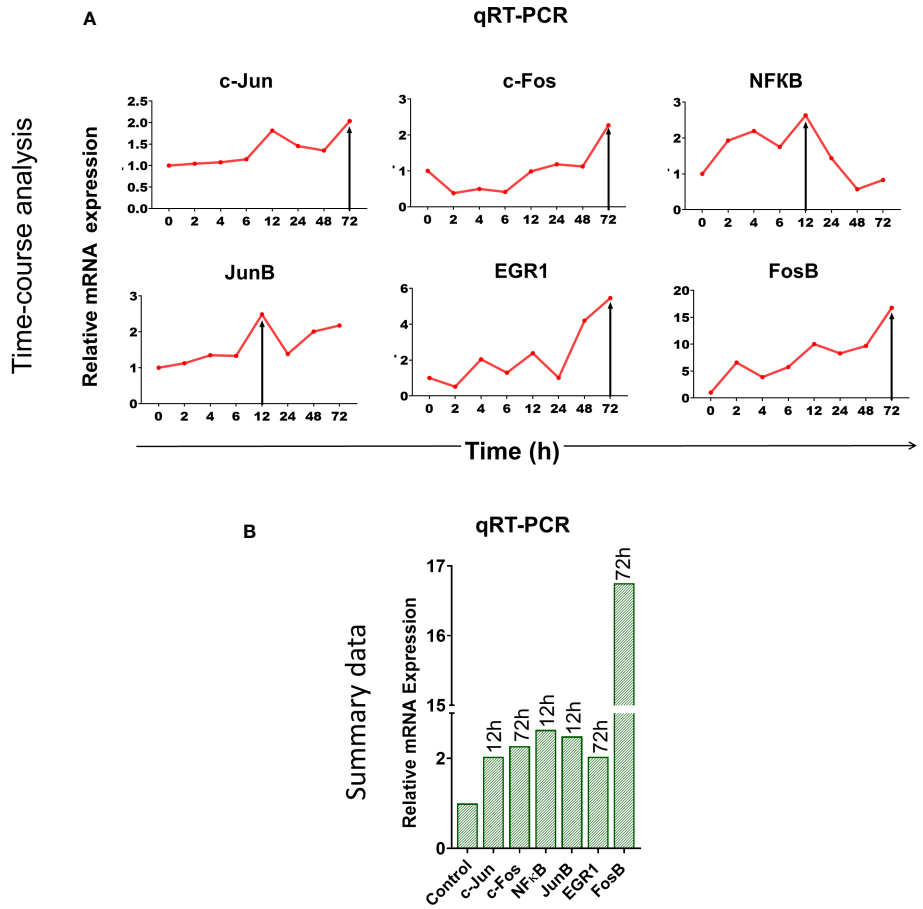

FIGURE 2
Upregulation of stress-related markers in human PBMCs following treatment of cfChPs isolated from sera of cancer patients. mRNA expression of six stress-related markers in PBMCs was detected by qRT-PCR and analyzed using a comparative C_T method. **(A)** Line graphs represent results of time-course analyses calculated as expression fold [2^(-$\Delta\Delta C_T$)]. **(B)** Histograms represent relative mRNA expression of stress-related markers at respective peak time points.

induced dying HeLa cells. As a first step, we confirmed that cfChPs released from dying cells are internalized by T-cells. For this, we fluorescently dually labelled HeLa cells in their DNA with BrdU and in their histones with CellLight® Histone 2BGFP (please see Methods) and induced them to undergo apoptosis in a hypoxia chamber for 48h. The culture medium containing dually labelled cfChPs released from the dying HeLa cells was passed through a porous membrane (pore size ~400nm). Isolated human T-cells were incubated in the filtered conditioned medium for 4h (please see Methods). Fluorescence microscopy at 4h detected copious presence of dually labelled cfChPs within PBMCs which had accumulated in their nuclei (Figure 4A).

cfChPs released from dying HeLa cells activate immune checkpoints

Having confirmed that cfChPs released from dying HeLa cells are readily internalized by T-cells, we performed our next experiments using conditioned medium of hypoxia-induced dying but unlabeled HeLa cells. A time course analysis using qRT-PCR revealed marked up-regulation of all five immune checkpoints and six stress markers described above (Supplementary Figure 3).

Activation of immune checkpoint is abrogated by cfChPs deactivating agents

To confirm that cfChPs in the conditioned media were indeed the immune checkpoint activating agents, we pre-treated the conditioned media with three different cfChPs inactivating agents. These included anti-histone antibody complexed nanoparticles (CNPs) which inactivate cfChPs by binding to histones (13); DNase I, which inactivates cfChPs by degrading its DNA component; and a newly described pro-oxidant combination of the nutraceuticals Resveratrol and metallic Copper (R-Cu) which degrades cfChPs through the medium of free radicals (14, 15, 23–25). Immunofluorescence analysis were performed at the peak time point of mRNA expression as defined by qRT-PCR and flow cytometry was performed at 72h after treatment (Supplementary Figure 3). We found a highly significant reduction in expression of all three immune checkpoints examined, namely, PD-1, CTLA-4

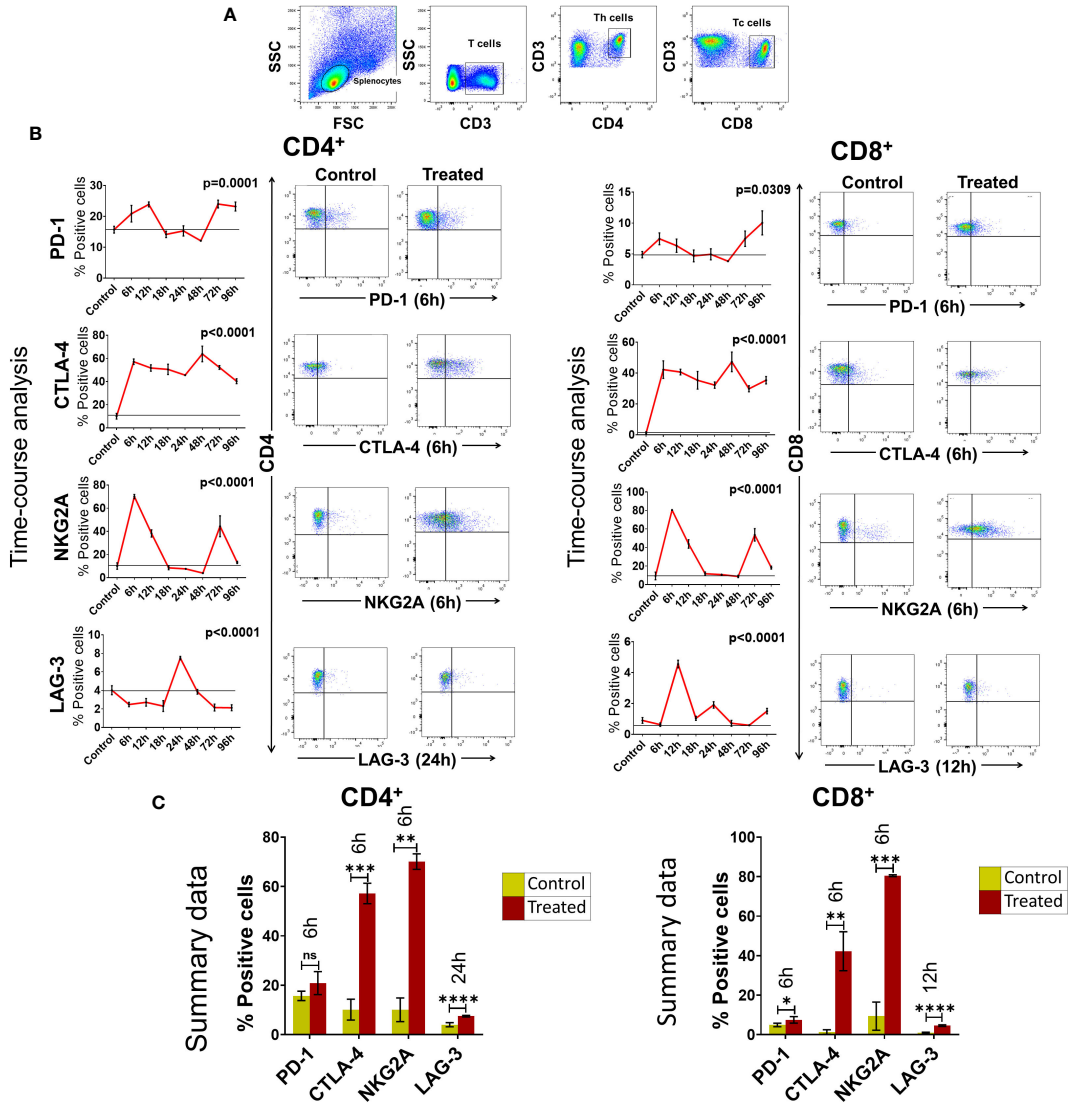

FIGURE 3
Upregulation of immune checkpoints on splenic lymphocytes of mice following intravenous injection of cfChPs (100ng) isolated from sera of cancer patients. **(A)** Gating of splenic lymphocytes on forward/side scatter, T-cells were identified by using CD3 antibodies, Th cells were identified by using CD4 antibodies and Tc cells were identified by using CD8 antibodies. **(B)** Line graphs showing results of time course analysis of surface expression of various immune checkpoints on $CD4^+$T cells and $CD8^+$T cells by flow cytometry (N=3 at each time point) (left-hand panels). Representative flow cytometry plots at respective peak time points are given in right- hand panels. Percent expression of each immune checkpoint was compared with untreated controls. **(C)** Histograms represent immune checkpoint expression on CD4+T cells and CD8+T cells at respective peak time points determined by flow cytometry in control and treated mouse splenocytes. Statistical analyses were performed using Bonferroni's multiple comparisons test (GraphPad Version 8) to compare immune checkpoint expression on T-cells at different time-points in response to cfChPs. A two-tailed unpaired student's *t*-test was used to compare immune checkpoint expression on T-cells of untreated and treated mice at peak time points of expression. * p<0.05, ** p<0.01, *** p<0.001, **** p<0.0001.

and LAG-3 (Figures 4B, C; Supplementary Figure 4). We specifically focused on these three immune checkpoints because inhibitors against these have been approved for clinical use.

Discussion

Cancer immunotherapy is considered to be a new breakthrough in cancer treatment (4). However, how immune checkpoints are regulated has not been elucidated. We have shown here that cfChPs that circulate in the blood of cancer patients, or those that are released naturally from dying cancer cells, are readily internalized by human lymphocytes leading them to activate immune checkpoints. Cell death has been long associated with immune modulation (26, 27), however, the underlying mechanism(s) remains unclear. Our results suggest that cfChPs that emerge from dying cells to enter into the circulation, or those that are released locally from the dying cells, is the missing link between cell death and immune response.

We wondered whether stress markers that are involved in transcriptional regulation of immune checkpoints (18–20) might be involved in the cfChPs induced activation of immune

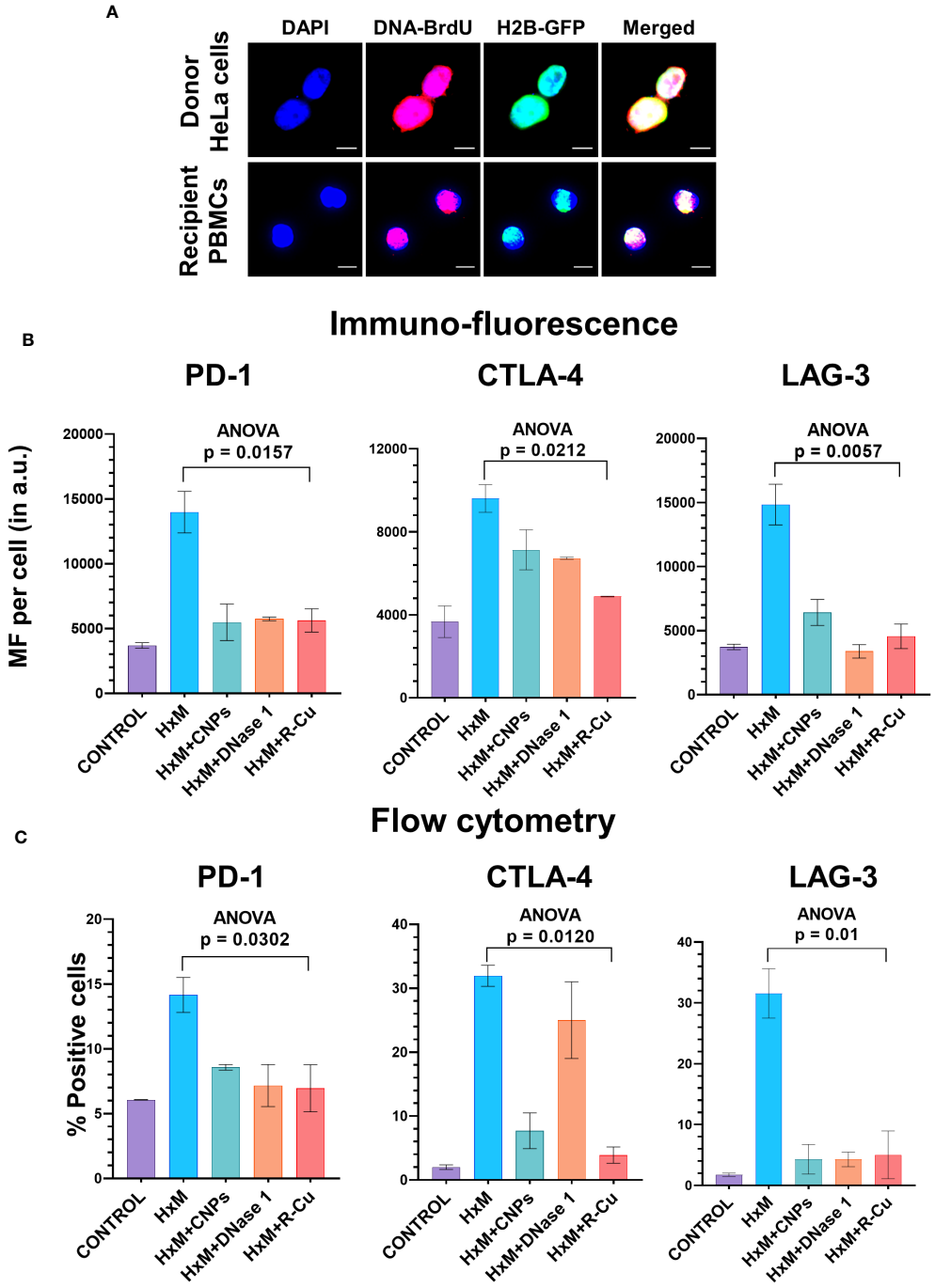

FIGURE 4
Upregulation of immune checkpoints by cfChPs released from hypoxia- induced dying HeLa cells and their abrogation by cfChPs deactivating agents. **(A)** Uptake by PBMCs of fluorescent cfChPs released from fluorescently dually labelled dying HeLa cells in their DNA with BrdU and in their histones with CellLight® Histone 2BGFP. A dual chamber system of Thincert®Cell Inserts was used and cfChPs released from hypoxia-induced dying HeLa cells were collected from the lower chamber (200uL) and added to PBMCs as described in the methods section. Fluorescence microscopy at 4h detected copious presence of dually labelled cfChPs, released from dying HeLa cells, within the nuclei of PBMCs; **(B)** Results of quantitative IF analysis of upregulation of three immune checkpoints at peak time points of mRNA expression (Figure 3A) and their inhibition by concurrent treatment with the cfChPs deactivators, viz. CNPs, DNase I and R-Cu; **(C)** Results of quantitative flow cytometry analysis of upregulation of three immune checkpoints at peak time points of mRNA expression (Figure 3A) and their inhibition by concurrent treatment with the cfChPs deactivators, viz. CNPs, DNase I and R-Cu. Experiments were performed in duplicates. Results are represented as mean ± SEM values and data were analyzed using one-way ANOVA (GraphPad Prism 8).

checkpoints. To this end we show here cfChPs treatment of lymphocytes leads to simultaneous activation of multiple stress markers namely, c-Jun, c-Fos, NFKB, JunB, EGR-1 and FosB.

Abrogation of immune checkpoint activation by the three cfChPs deactivating agents, provided further evidence for the involvement of cfChPs in immune checkpoint activation and suggesting therapeutic possibilities. If confirmed *in vivo*, prevention of immune checkpoints activation may herald the prospect of a novel form of immunotherapy which simultaneously downregulates multiple immune checkpoints all at once. Above all, cfChPs deactivating agents are likely to be far less toxic and less expensive than the immunotherapeutic agents that are currently in use.

Several immune checkpoint inhibitors are currently approved for clinical use. These inhibitors specifically target PD-1 (Pembrolizumab, Nivolumab and Cemiplimab), CTLA-4 (Ipilimumab and tremelimumab) and LAG-3 (Relatlimab) (28). However, each of these agents is specific for a single immune checkpoint, and all of them are associated with considerable toxicity. Their high cost limits their use in countries with limited resources. The three cfChPs deactivating agents used in our study hold the promise of being alternatives to the immune checkpoint inhibitors, especially because of their ability to down-regulate multiple immune checkpoints simultaneously. Of the three agents, CNPs and DNase I, being proteins, are likely to be therapeutically less attractive. On the other hand, a combination of Resveratrol and copper (R-Cu), being commonly used nutraceuticals, would be more attractive, especially since it has already been shown to be effective in multiple therapeutic indications in humans (23–25). For example, the administration of R-Cu to patients with advanced oral cancer down-regulated five immune check-points in the tumor infiltrating lymphocytes (25), immediately suggesting its therapeutic potential in other human cancers. In addition, R-Cu treatment significantly down-regulated nine additional hall-marks of cancer that have been defined by Hanahan and Weinberg (25, 29). R-Cu would have the added advantage of reducing toxic side effects in case it is used as an adjunct to chemotherapy (23, 24). Taken together, these findings make R-Cu a worthy alternative to immune checkpoint inhibitors with which it should be compared in well-designed randomized clinical trials for the treatment of cancer.

Data availability statement

The original contributions presented in the study are included in the article/Supplementary Material. Further inquiries can be directed to the corresponding author.

Ethics statement

The studies involving humans were approved by Institutional Ethics Committee (IEC) of Advanced Centre for Treatment, Research and Education in Cancer (ACTREC), Tata Memorial Centre (TMC). The studies were conducted in accordance with the local legislation and institutional requirements. The participants provided their written informed consent to participate in this study. The animal study was approved by Institutional Animal Ethics Committee (IAEC) of Advanced Centre for Treatment, Research and Education in Cancer (ACTREC), Tata Memorial Centre (TMC) (Approval no. 12/2020). The study was conducted in accordance with the local legislation and institutional requirements.

Author contributions

SSha: Conceptualization, Data curation, Formal analysis, Investigation, Methodology, Writing – original draft, Writing – review & editing. KP: Data curation, Methodology, Writing – review & editing. NK: Methodology, Writing – review & editing. DS: Methodology, Writing – review & editing. AP: Methodology, Writing – review & editing. VJ: Methodology, Writing – review & editing. SShi: Methodology, Writing – review & editing. NR: Methodology, Writing – review & editing. GS: Methodology, Writing – review & editing. RL: Methodology, Writing – review & editing. GR: Data curation, Methodology, Supervision, Writing – review & editing. HT: Methodology, Writing – review & editing. IM: Conceptualization, Funding acquisition, Project administration, Supervision, Writing – original draft, Writing – review & editing.

Funding

The author(s) declare financial support was received for the research, authorship, and/or publication of this article. This study was supported by the Department of Atomic Energy, Government of India, through its grant CTCTMC to Tata Memorial Centre awarded to IM. The funder had no role in the preparation, review, or approval of the manuscript and decision to submit the manuscript for publication.

Acknowledgments

The authors thank flow cytometry facility at ACTREC-TMC for their technical support. The authors thank Dr. Rajan Basak for his guidence in qRT-PCR.

Conflict of interest

The authors declare that the research was conducted in the absence of any commercial or financial relationships that could be construed as a potential conflict of interest.

Publisher's note

All claims expressed in this article are solely those of the authors and do not necessarily represent those of their affiliated

organizations, or those of the publisher, the editors and the reviewers. Any product that may be evaluated in this article, or claim that may be made by its manufacturer, is not guaranteed or endorsed by the publisher.

Supplementary material

The Supplementary Material for this article can be found online at: https://www.frontiersin.org/articles/10.3389/fimmu.2023.1331491/full#supplementary-material

SUPPLEMENTARY FIGURE 1
Rapid internalization by human PBMCs of cfChPs isolated from sera of cancer patients. cfChPs were dually labelled in their DNA and histones with Platinum Bright 550 (red) and ATTO-TEC-488 (green), respectively. Fluorescently dually labeled cfChPs (10ng) when added to PBMCs, fluorescent microscopy detected accumulation of dual labelled cfChPs in their nuclei at 2h.

SUPPLEMENTARY FIGURE 2
Representative IF images showing upregulation of five immune checkpoints at peak time points of mRNA expression in **(A)** $CD4^+$T cells and **(B)** $CD8^+$T cells following treatment with cfChPs isolated from sera of cancer patients. Scale bars = 20μm; **(C)** Representative flow cytometry plots of PBMCs showing the gating strategy; **(D)** upregulation of surface expression of immune checkpoint expressions on $CD4^+$T cells following 72hrs treatment with cfChPs isolated from sera of cancer patients and; **(E)** upregulation of surface expression of immune checkpoint expressions on $CD8^+$T cells following 72hrs treatment with cfChPs isolated from sera of cancer patients.

SUPPLEMENTARY FIGURE 3
Time-course analysis using qRT-PCR to determine the point of maximum expression of immune checkpoints and stress markers following treatment of PBMCs with conditioned media containing cfChPs released from hypoxia-induced dying HeLa cells. **(A)** Upregulation of immune checkpoints and **(B)** upregulation stress related markers.

SUPPLEMENTARY FIGURE 4
Abrogation of immune checkpoints by cfChPs deactivators **(A)** Representative IF images showing immune checkpoint expression in T cells following treatment of PBMCs with conditioned media containing cfChPs released from hypoxia-induced dying HeLa cells. Pre-treatment of conditioned medium with CNPs (25μg), DNase I (0.005U) and R-Cu ($1:10^{-4}$) significantly reduced the expression of immune checkpoints. **(B)** Representative flow cytometry plots showing immune checkpoint expression in T cells following treatment of PBMCs with conditioned media containing cfChPs released from hypoxia-induced dying HeLa cells. Pre-treatment of conditioned medium with CNPs (25μg), DNase I (0.005U) and R-Cu ($1:10^{-4}$) significantly reduced the expression of immune checkpoints.

References

1. Zhang Y, Zheng J. Functions of immune checkpoint molecules beyond immune evasion. *Adv Exp Med Biol* (2020) 1248:201–26. doi: 10.1007/978-981-15-3266-5_9

2. Dyck L, Mills KHG. Immune checkpoints and their inhibition in cancer and infectious diseases. *Eur J Immunol* (2017) 47(5):765–79. doi: 10.1002/eji.201646875

3. Jiang X, Liu G, Li Y, Pan Y. Immune checkpoint: The novel target for antitumor therapy. *Genes Dis* (2021) 8(1):25–37. doi: 10.1016/j.gendis.2019.12.004

4. Wojtukiewicz MZ, Rek MM, Karpowicz K, Górska M, Polityńska B, Wojtukiewicz AM, et al. Inhibitors of immune checkpoints—PD-1, PD-L1, CTLA-4—new opportunities for cancer patients and a new challenge for internists and general practitioners. *Cancer Metastasis Rev* (2021) 40(3):949–82. doi: 10.1007/s10555-021-09976-0

5. Fliedner TM, Graessle D, Paulsen C, Reimers K. Structure and function of bone marrow hemopoiesis: mechanisms of response to ionizing radiation exposure. *Cancer Biother Radiopharm* (2002) 17(4):405–26. doi: 10.1089/108497802760363204

6. Sender R, Milo R. The distribution of cellular turnover in the human body. *Nat Med* (2021) 27(1):45–8. doi: 10.1038/s41591-020-01182-9

7. Holdenrieder S, Stieber P, Bodenmüller H, Fertig G, Fürst H, Schmeller N, et al. Nucleosomes in serum as a marker for cell death. *Clin Chem Lab Med* (2001) 39 (7):596–605. doi: 10.1515/CCLM.2001.095

8. Holdenrieder S, Stieber P. Clinical use of circulating nucleosomes. *Crit Rev Clin Lab Sci* (2009) 46(1):1–24. doi: 10.1080/10408360802485875

9. van der Vaart M, Pretorius PJ. The origin of circulating free DNA. *Clin Chem* (2007) 53(12):2215–5. doi: 10.1373/clinchem.2007.092734

10. Mittra I, Samant U, Sharma S, Raghuram GV, Saha T, Tidke P, et al. Cell-free chromatin from dying cancer cells integrate into genomes of bystander healthy cells to induce DNA damage and inflammation. *Cell Death Discovery* (2017) 3(1):17015. doi: 10.1038/cddiscovery.2017.15

11. Mittra I, Khare NK, Raghuram GV, Chaubal R, Khambatti F, Gupta D, et al. Circulating nucleic acids damage DNA of healthy cells by integrating into their genomes. *J Biosci* (2015) 40(1):91–111. doi: 10.1007/s12038-015-9508-6

12. Mortezaee K. Immune escape: A critical hallmark in solid tumors. *Life Sci* (2020) 258:118110. doi: 10.1016/j.lfs.2020.118110

13. Rekha MR, Pal K, Bala P, Shetty M, Mittra I, Bhuvaneshwar GS, et al. Pullulan-histone antibody nanoconjugates for the removal of chromatin fragments from systemic circulation. *Biomaterials* (2013) 34(27):6328–38. doi: 10.1016/j.biomaterials.2013.05.019

14. Subramaniam S, Vohra I, Iyer A, Nair NK, Mittra I. A paradoxical synergism between Resveratrol and copper (II) with respect to degradation of DNA and RNA. *F1000Research* (2015) 4:1145. doi: 10.12688/f1000research.7202.1

15. Mittra I, Pal K, Pancholi N, Shaikh A, Rane B, Tidke P, et al. Prevention of chemotherapy toxicity by agents that neutralize or degrade cell-free chromatin. *Ann Oncol* (2017) 28(9):2119–27. doi: 10.1093/annonc/mdx318

16. Kirolikar S, Prasannan P, Raghuram GV, Pancholi N, Saha T, Tidke P, et al. Prevention of radiation-induced bystander effects by agents that inactivate cell-free chromatin released from irradiated dying cells. *Cell Death Dis* (2018) 9(12):1–16. doi: 10.1038/s41419-018-1181-x

17. Mittra Id I, Pal K, Pancholi N, Tidke P, Siddiqui S, Rane B, et al. Cell-free chromatin particles released from dying host cells are global instigators of endotoxin sepsis in mice. *PloS One* (2020) 15(3):e0229017. doi: 10.1371/journal.pone.0229017

18. Venkatraman S, Meller J, Hongeng S, Tohtong R, Chutipongtanate S. Transcriptional regulation of cancer immune checkpoints: emerging strategies for immunotherapy. *Vaccines* (2020) 8(4):735. doi: 10.3390/vaccines8040735

19. Merhi M, Ahmad F, Taib N, Inchakalody V, Uddin S, Shablak A, et al. The complex network of transcription factors, immune checkpoint inhibitors and stemness features in colorectal cancer: A recent update. *Semin Cancer Biol* (2023) 89:1–17. doi: 10.1016/j.semcancer.2023.01.001

20. Wang B, Guo H, Yu H, Chen Y, Xu H, Zhao G. The role of the transcription factor EGR1 in cancer. *Front Oncol* (2021) 11. doi: 10.3389/fonc.2021.642547

21. Datar I, Sanmamed MF, Wang J, Henick BS, Choi J, Badri T, et al. Expression analysis and significance of PD-1, LAG-3, and TIM-3 in human non–small cell lung cancer using spatially resolved and multiparametric single-cell analysis. *Clin Cancer Res* (2019) 25(15):4663–73. doi: 10.1158/1078-0432.CCR-18-4142

22. Shibru B, Fey K, Fricke S, Blaudszun A-R, Fürst F, Weise M, et al. Detection of immune checkpoint receptors – A current challenge in clinical flow cytometry. *Front Immunol* (2021) 12. doi: 10.3389/fimmu.2021.694055

23. Agarwal A, Khandelwal A, Pal K, Khare NK, Jadhav V, Gurjar M, et al. A novel pro-oxidant combination of resveratrol and copper reduces transplant related toxicities in patients receiving high dose melphalan for multiple myeloma (RESCU 001). *PloS One* (2022) 17(2):e0262212. doi: 10.1371/journal.pone.0262212

24. Ostwal V, Ramaswamy A, Bhargava P, Srinivas S, Mandavkar S, Chaugule D, et al. A pro-oxidant combination of resveratrol and copper reduces chemotherapy-related non-haematological toxicities in advanced gastric cancer: results of a prospective open label phase II single-arm study (RESCU III study). *Med Oncol* (2022) 40(1):17. doi: 10.1007/s12032-022-01862-1

25. Pilankar A, Singhavi H, Raghuram GV, Siddiqui S, Khare NK, Jadhav V, et al. A pro-oxidant combination of resveratrol and copper down-regulates hallmarks of cancer and immune checkpoints in patients with advanced oral cancer: Results of an exploratory study (RESCU 004). *Front Oncol* (2022) 12. doi: 10.3389/fonc.2022.1000957

26. Riera Romo M. Cell death as part of innate immunity: Cause or consequence? *Immunology* (2021) 163(4):399–415. doi: 10.1111/imm.13325

27. Rock KL, Kono H. The inflammatory response to cell death. *Annu Rev Pathol* (2008) 3:99–126. doi: 10.1146/annurev.pathmechdis.3.121806.151456

28. Marin-Acevedo JA, Kimbrough EO, Lou Y. Next generation of immune checkpoint inhibitors and beyond. *J Hematol Oncol* (2021) 14(1):45. doi: 10.1186/s13045-021-01056-8

29. Hanahan D, Weinberg RA. Hallmarks of cancer: the next generation. *Cell* (2011) 144(5):646–74. doi: 10.1016/j.cell.2011.02.013

frontiers | Frontiers in Immunology

TYPE Original Research
PUBLISHED 05 March 2024
DOI 10.3389/fimmu.2024.1359204

OPEN ACCESS

EDITED BY
Laura Senovilla,
Spanish National Research Council (CSIC), Spain

REVIEWED BY
David Bernardo,
University of Valladolid, Spain
Lei Li,
University of Otago, New Zealand

*CORRESPONDENCE
Qing Ni
13985527762@163.com
Tao Wang
wangtaoGPPH@gzu.edu.cn

†These authors have contributed equally to this work

RECEIVED 21 December 2023
ACCEPTED 20 February 2024
PUBLISHED 05 March 2024

CITATION
Wang S, Li Z, Hou J, Li X, Ni Q and Wang T (2024) Integrating PANoptosis insights to enhance breast cancer prognosis and therapeutic decision-making.
Front. Immunol. 15:1359204.
doi: 10.3389/fimmu.2024.1359204

Integrating PANoptosis insights to enhance breast cancer prognosis and therapeutic decision-making

Shu Wang[1†], Zhuolin Li[1,2†], Jing Hou[1], Xukui Li[3,4], Qing Ni[1*] and Tao Wang[3,4*]

[1]Department of Breast Surgery, Guizhou Provincial People's Hospital, Guiyang, Guizhou, China, [2]Medical College, Guizhou University, Guiyang, Guizhou, China, [3]Research Laboratory Center, Guizhou Provincial People's Hospital, Guiyang, Guizhou, China, [4]NHC Key Laboratory of Pulmonary Immune-related Diseases, Guizhou Provincial People's Hospital, Guizhou University, Guiyang, Guizhou, China

Background: Despite advancements, breast cancer outcomes remain stagnant, highlighting the need for precise biomarkers in precision medicine. Traditional TNM staging is insufficient for identifying patients who will respond well to treatment.

Methods: Our study involved over 6,900 breast cancer patients from 14 datasets, including in-house clinical data and single-cell data from 8 patients (37,451 cells). We integrated 10 machine learning algorithms in 55 combinations and analyzed 100 existing breast cancer signatures. IHC assays were conducted for validation, and potential immunotherapies and chemotherapies were explored.

Results: We pinpointed six stable Panoptosis-related genes from multi-center cohorts, leading to a robust Panoptosis-model. This model outperformed existing clinical and molecular features in predicting recurrence and mortality risks, with high-risk patients showing worse outcomes. IHC validation from 30 patients confirmed our findings, indicating the model's broader applicability. Additionally, the model suggested that low-risk patients benefit more from immunotherapy, while high-risk patients are sensitive to specific chemotherapies like BI-2536 and ispinesib.

Conclusion: The Panoptosis-model represents a major advancement in breast cancer prognosis and treatment personalization, offering significant insights for effectively managing a wide range of breast cancer patients.

KEYWORDS

breast cancer, PANoptosis, machine learning, immunotherapy, BI-2536

Introduction

Breast cancer remains a significant health challenge globally, being one of the leading causes of cancer-related deaths among women (1). Despite advancements in early detection and treatment strategies aiming to reduce recurrence and mortality, the battle against breast cancer continues (2). The quest for improved prognosis and therapeutic outcomes is ongoing, with early diagnosis playing a crucial role in enhancing survival rates (3).

Recent scientific developments have shed light on PANoptosis, a sophisticated form of programmed cell death that integrates elements of pyroptosis, apoptosis, and necroptosis (4). This process is crucial for maintaining the body's balance and defending against diseases by removing harmful cells (5). Intriguingly, PANoptosis has been implicated in the progression of various diseases, including cancer, highlighting its potential as a target for innovative treatments (6). For example, research has indicated that manipulating PANoptosis pathways could influence the development of tumors and the effectiveness of cancer therapies (7).

Despite the known significance of programmed cell death mechanisms like apoptosis in cancer, the specific contributions of PANoptosis to breast cancer progression and patient outcomes remain underexplored (8). While prognostic models based on PANoptosis-related genes have shown promise in other cancers, a dedicated model for breast cancer prognosis is yet to be established (9). This gap underscores the need for a deeper understanding of PANoptosis in breast cancer, which could unlock new avenues for diagnosis and treatment (10).

This study aims to bridge this gap by conducting a thorough analysis of breast cancer samples from the TCGA-BRCA and GEO datasets. By employing cutting-edge single-cell sequencing technologies and a comprehensive set of machine learning techniques, we have identified critical PANoptosis-related genes associated with breast cancer outcomes. Using these insights, we developed a novel prognostic model that categorizes breast cancer patients into distinct risk groups, offering a new tool for predicting survival and guiding treatment decisions. Our model's effectiveness was rigorously tested across multiple datasets, and we further investigated the molecular and immunological profiles of the risk categories identified, providing a comprehensive view of the implications of PANoptosis in breast cancer.

Materials and methods

Data acquisition

The foundation of our research involved the compilation of PANoptosis genes, encompassing elements of pyroptosis, apoptosis, and necroptosis, which were meticulously curated from GeneCards, GSEA gene sets, KEGG pathways, and relevant literature (11, 12). This curation process yielded a comprehensive list of genes integral to the PANoptosis pathway, detailed in Supplementary Table S1.

The training dataset was assembled from the TCGA database, which included gene profiles, mutational data, and clinical information from breast cancer cases. Samples without survival data were carefully excluded from the dataset to ensure data completeness and accuracy.

To enhance the robustness of our findings and validate our model, we obtained additional datasets from the Gene Expression Omnibus (GEO) database and MetaGxData (13). These validation datasets were comprised of samples from various studies, namely GSE93601, GSE76250, GSE70947, GSE20685, GSE131769, GSE96058, GSE20711, GSE24450, GSE202203, GSE21653, GSE86166, GSE48391, GSE88770 and PNC. This comprehensive approach allowed us to validate our results across diverse datasets and strengthen the reliability of our findings.

Single-cell analysis

Single-cell RNA sequencing data for breast cancer was sourced from the GEO database (accession number GSE161529) as the basis for our single-cell analysis (14). Our preprocessing protocol began with the elimination of genes that were not expressed in any samples, specifically those with zero counts across all cells. This step was critical to focus our analysis on active genetic elements within the samples. We then normalized the gene expression matrix. This normalization process, conducted using the "SCTransform" function within the Seurat R package, allowed for the correction of technical variances and the stabilization of variance across features. Subsequent dimensionality reduction techniques, including PCA, tSNE, and UMAP, were employed to distill the high-dimensional data into a more interpretable form, facilitating the identification of cellular phenotypes and states. Cell populations were categorized using the "FindNeighbors" and "FindClusters" functions, which are instrumental in discerning the heterogeneity within the cell populations. We augmented our quality control measures by identifying and removing doublets with the DoubletFinder R package, further ensuring the integrity of our dataset (15).

Following these rigorous quality control measures, we retained approximately 37,451 cells for subsequent analyses. The final step involved cell type assignment; a task made efficient using Celltypist (16). This comprehensive approach ensured the robust processing and analysis of the single-cell data, setting a strong foundation for our research endeavors.

CellChat analysis

For the investigation of intercellular communication within the tumor microenvironment, we utilized the "CellChat" R package, which allows for the analysis of cell-cell interactions based on ligand-receptor pairs (17). We constructed CellChat objects for each group using their respective UMI count matrices. The "CellChatDB.human" database was employed as the reference for known ligand-receptor interactions, enabling us to analyze the complex signaling networks within our samples. Using the default settings within CellChat, we performed a comparative analysis of the interaction counts and strengths between different cell types. To

synthesize this information across groups, we merged the individual CellChat objects using the "mergeCellChat" function. This step was crucial for aggregating data to observe broader trends in cell communication. Differences in interaction number and strength among specific cell types across groups were visualized using the "netVisual_diffInteraction" function. We ascertained variations in signaling pathways through the "rankNet" function and depicted the spread of signaling gene expression across groups with "netVisual_bubble" and "netVisual_aggregate" functions.

Functional analyses

To elucidate the complex landscape of differential PANoptosis-related gene expression between tumor and normal tissues, we utilized the GO and KEGG databases for a thorough assessment of associated functional activities and pathways (18, 19). The Enrichplot package within R was employed to visualize the results of this enrichment analysis. In parallel, the clusterProfiler algorithm facilitated Gene Set Enrichment Analysis (GSEA) to distinguish the biological functions between distinct breast cancer risk subgroups identified by our model (20). We established a False Discovery Rate (FDR) below 0.05 to denote statistical significance, enhancing the robustness of our findings by performing 1,000 permutations for each analysis. This comprehensive approach allowed us to identify key functional pathways differentially activated in our PANoptosis-related gene sets, providing insight into the molecular underpinnings of breast cancer pathology and prognosis.

Establishment of the PANoptosis score

To uncover the significance of PANoptosis in BC, a systematic methodology was adopted. This exploration commenced with a differential analysis, specifically comparing gene expression patterns between tumor and normal tissues using the TCGA-BRCA dataset.

To visually depict the outcomes of differential gene expression, we employed a heatmap, effectively illustrating the observed disparities. Concurrently, we analyzed gene correlations, utilizing the igraph package. The crucial PANoptosis Score was then meticulously calculated. This calculation was based on the differentially expressed PANoptosis-related genes. In this effort, we utilized the ssGSEA algorithm for bulk data analysis (21), while for single-cell data, we employed the Ucell algorithm (22). This dual approach ensured a comprehensive and robust assessment of the PANoptosis Score, facilitating a deeper understanding of its role in breast cancer.

Development and validation of the PANoptosis-model

In constructing a prognostic model for breast cancer based on PANoptosis, we followed the analytical workflow established by Liu et al. (23). We integrated ten classical computational algorithms, including Random Forest (RSF), Least Absolute Shrinkage and Selection Operator (LASSO), Gradient Boosting Machine (GBM), Survival Support Vector Machine (Survival-SVM), Supervised Principal Components (SuperPC), Ridge Regression, Partial Least Squares Regression for Cox (plsRcox), CoxBoost, Stepwise Cox, and Elastic Network (Enet). each bringing unique strengths in dimensionality reduction and variable selection, as detailed in Supplementary Table S2. The TCGA-BRCA dataset served as the training cohort, with the combination of these algorithms being used to create the prognostic signature. We then evaluated the model's predictive power using the average concordance index (C-index) across five external test cohorts from the GEO database. This process allowed us to identify the most effective prognostic model for breast cancer, which we refer to as the PANoptosis-model:

$$riskscore = \sum_{i=1}^{n}(\beta_i \times Exp_i)$$

Where 'n' represents the number of PANoptosis genes, 'Exp' signifies the PANoptosis gene profile, and 'β' denotes the multi-Cox coefficient.

This model calculates a risk score based on the expression profile of PANoptosis genes and their respective coefficients derived from multivariate Cox regression. Patients from the TCGA-BRCA dataset were stratified into different risk groups according to these scores. The generalizability of the risk score was then validated using additional external datasets, which served as independent test cohorts. Kaplan-Meier survival analysis, conducted with R v4.2, was employed to discern survival differences between the risk groups, with a p-value of less than 0.05 indicating statistical significance. This meticulous approach ensured that the PANoptosis-model was robustly validated and capable of accurately predicting patient outcomes.

Genomic character analysis

To unravel the genomic alteration disparities between the PANoptosis-model subgroups, we conducted an extensive examination of mutation and Copy Number Alteration (CNA) data within the TCGA-BRCA dataset.

We initiated this analysis by extracting the raw mutation file and proceeded to calculate the Tumor Mutation Burden (TMB) for each sample. To provide insights into the genetic landscape, we visually represented the top 28 genes utilizing the maftools package. Following the methodology described by Wang et al. (24), we employed the deconstructSigs package to derive mutational signatures unique to each patient. Notably, we highlighted four signatures with notable occurrence frequencies in BRCA: SBS1, SBS3, SBS11, and SBS12.

Furthermore, we selected the top 5 regions exhibiting a high-level CNA frequency. Particular attention was given to genes within chromosomes 13q34, including CDK19, SOBP, ATG5, and FYN. This comprehensive analysis provided valuable insights into the genomic alterations within the PANoptosis-model subgroups.

Estimation of TME variations

We collected five algorithms [MCPcounter (25), xCell (26), CIBERSORT (27), quanTIseq (28), and TIMER (29)] to estimate

the abundance of diverse immune cells through different risk score groups using the IOBR package (30). Furthermore, we utilized ESTIMATE and TIDE to assess the composition, structure, and state of the tumor microenvironment (31, 32). This analysis provided crucial insights into the biological traits and prognosis of the tumor. Finally, the expression features of multiple immune checkpoints were also quantified to explore the immune state, preliminary predicting therapeutic sensitivity to ICIs therapy.

Selections of therapeutic targets and agents

For estimating drug targets and predicting chemotherapeutic responses, we obtained comprehensive target data for 6,125 compounds from the Drug Repurposing Hub (https://clue.io/repurposing), resulting in 2,249 distinct drug targets after removing duplicates (33). We used Spearman correlation analysis to identify potential drug targets associated with unfavorable prognosis by correlating the gene expression of targetable genes with risk scores (correlation coefficient > 0.25, P< 0.05). Subsequently, we correlated CERES scores with risk scores for brain cell lines from CCLE, identifying genes (correlation coefficient < -0.2, P< 0.05) associated with poor prognosis dependence (34).

To predict drug responses accurately, we leveraged CTRP and PRISM datasets, which contain extensive drug screening and molecular data across cancer cell lines. We performed differential expression analyses between bulk and cell line samples. For drug response prediction, we employed the reliable ridge regression model within the pRRophetic package. This model was trained on expression profiles and drug response data from solid Cancer Cell Lines (CCLs) and exhibited robust performance, validated by default 10-fold cross-validation (35).

Additionally, we conducted a Supplementary Connectivity Map (CMap) analysis to assess the therapeutic potential of candidate agents in BC (36). We performed differential gene expression analysis between tumor and normal tissue samples and then submitted the top 300 genes (150 up-regulated and 150 down-regulated) to the dedicated CMap website (https://clue.io/query). This analysis drew on gene expression signatures from CMap v1 and the LINCS database. Negative connectivity scores indicated the potential therapeutic efficacy of perturbations in the disease context.

Human sample collection and IHC staining

In this study, we obtained specimens from a cohort of 30 patients diagnosed with BC at the Guizhou Provincial People's Hospital. These specimens were collected during surgical procedures. Hematoxylin and eosin (HE) staining was applied to the specimens based on established protocols. Diagnostic evaluations were independently conducted by two pathologists. Comprehensive cohort details are provided in Supplementary Table S3.

Immunohistochemistry (IHC) was conducted on paraffin-embedded samples, adhering to methods outlined in our earlier publications (37, 38). The antibodies utilized are enumerated in Supplementary Table S4. Evaluation was consistent with established protocols and scoring guidelines. Two pathologists independently assessed protein expression levels, consistent with the methodology described in our previous work (38).

qRT-PCR and patient stratification

RNA was isolated from breast cancer samples using TRIzol reagent (Invitrogen, Carlsbad, CA, USA). This was followed by the synthesis of cDNA and qRT-PCR procedures, employing GoScript reverse transcriptase and Master Mix (Promega), following the manufacturer's instructions. Data were captured using the CFX96 Touch Real-Time PCR Detection System (BioRad, Hercules, CA, USA). The relative quantification of gene expression was performed with the $2^{-\Delta\Delta Cq}$ method, normalizing against GAPDH as the reference gene.

Patient stratification into low-risk and high-risk categories was achieved through the evaluation of gene expression levels, applying a specific threshold based on the PANoptosis-model's equation.

Statistical analysis

Data processing and statistical analysis were conducted using R software (version 4.2.3). We applied the Wilcoxon signed-rank test to evaluate expression differences between BC patients and controls. Pearson and Spearman correlation analyses were utilized to determine statistical correlations between parametric and non-parametric variables, respectively. Significance was established at a p-value< 0.05, with gradations indicated as *p< 0.05, **p< 0.01, ***p< 0.001, ****p< 0.0001.

Results

Differential expression of PANoptosis genes in breast cancer tissues

The overall design of this study is displayed in Figure 1. We identified 52 pyroptosis genes, 581 apoptosis genes, 101 necroptosis genes, and 28 potential PANoptosis genes. To comprehensively evaluate the expression landscape of PANoptosis-related genes in BC, we conducted differential gene expression analysis comparing tumor samples to normal counterparts within the TCGA-BRCA dataset. The heatmap depiction underscores a pervasive pattern of dysregulated PANoptosis gene expression within BC samples, delineating a stark contrast between malignant and non-malignant tissue profiles (Supplementary Figure S1A; Supplementary Table S5). In our subsequent analysis, we discerned 61 genes with prognostic significance within the realm of PANoptosis, segregating these into four distinct clusters of expression (as depicted in Figure 2A). A particularly compelling positive correlation emerged between IFNG and FASLG within cluster A (cor = 0.84, P-value< 0.001), suggesting a concerted

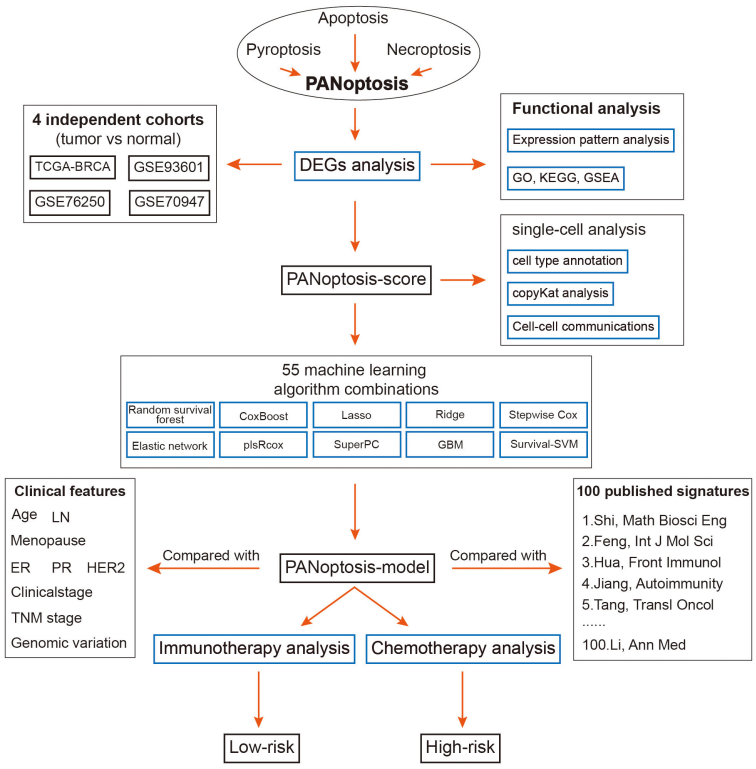

FIGURE 1
The overall flow of this study.

regulatory mechanism at play. Similarly, cluster B showcased a noteworthy synergistic expression pattern between YWHAZ and CD24 (cor = 0.300, P-value< 0.001). In stark contrast, cluster D revealed an intriguing negative correlation between POU4F1 and SIAH2 (cor = -0.34, P-value< 0.001), hinting at an intricate antagonistic interaction pertinent to BC progression (Figure 2A).

Further refining our investigative scope, we introduced a novel metric, the PANoptosis-score, crafted to quantify the cumulative activity of PANoptosis pathways within BC. Our scrutiny extended across the foundational TCGA-BRCA dataset and was corroborated by analyses within three ancillary datasets (GSE93601, GSE76250, and GSE70947). The data cohesively pointed to an elevated PANoptosis-score in BC patients relative to normal groups, a finding consistently replicated across all datasets examined (Figures 2B–E). The enrichment analyses were conducted to clarify the function and pathways of these genes within BC patients. The Proteomaps indicated that these differentially expressed genes related to PANoptosis displayed strong relationships with 15 top roles, such as signal transduction, signaling molecules and interaction, and transcription. Massive signaling pathways were exhibited including IL19, IL16, PDX1 and IL33 (Supplementary Figure S1B).

Based on the background that tumor microenvironment (TME) participates in the progression of tumors, the association between the PANoptosis-score and 26 infiltrated immune cells was further elaborated as unraveled in Figure 2F, of which Th1 cells, Tregs and M1 macrophages were positively infiltrated with PANoptosis-score in BC patients, in contrast, taking M2 macrophages as an example, 11 immune cells were negatively correlated with PANoptosis-score. According to the correlation analysis results from Figures 2G, H, it was confirmed that the PANoptosis-score exhibited a positive relevance with $CD8^{+}$T cells, but a negative relation to M2 macrophages.

Single-cell analysis reveals PANoptosis dynamics in BC

To further assess the PANoptosis features in BC, the single-cell transcriptome analysis was performed, of which a total of eight patients and two groups (tumor and normal) were enrolled in this analysis (Figures 3A, B). We then grouped them into fifteen cell clusters and identified seven cell types (Figures 3C, D). The bar chart clearly and intuitively presented the proportion of seven cell types in normal and BC tissues, of which three cell types, including T cells, macrophages, and epithelial cells, accounted for far over fifty percent in tumor tissues relative to the normal tissues, and conversely, Pericytes, fibroblasts and endothelial cells occupied higher proportion in normal tissues (Figure 3E). To accurately observe the distribution of these cells, they were individually annotated by their biomarkers. For example, T cells were marked by IL7R, CD36 was specifically expressed in the surface of endothelial cells, and fibroblasts were exclusively annotated by COL1A1 and PFGFRA, in addition, CD68, CD14, RGS5 and EPCAM were the markers of macrophages, Pericytes and epithelial cells, respectively (Figure 3G). Moreover, the mRNA expression levels of massive protein molecules

10.3389/fimmu.2024.1359204

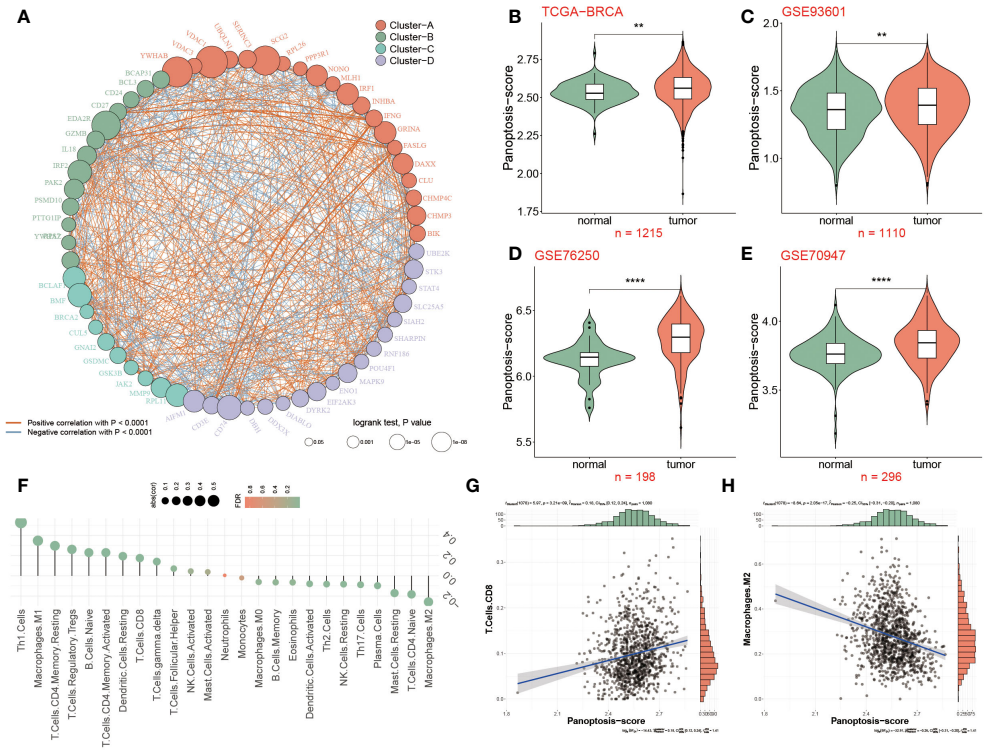

FIGURE 2
Differential expression of PANoptosis genes in breast cancer tissues. **(A)** 61 differentially expressed PANoptosis genes were categorized into four cell clusters (A, B, C, and D), and this network revealed the complicated relationships between these genes. The red or blue line represented a positive or negative correlation. The larger the circle, the stronger the impact of a single gens on BC. **(B)** The PANoptosis-score was compared among two groups in the TCGA-BRCA dataset, **(C–E)** Validation datasets of GSE93601 **(C)**, GSE76250 **(D)** and GSE70947 **(E)** for PANoptosis-score. **(F)** Relevance of PANoptosis-score and immune cell infiltration. **(G, H)** The correlation between PANoptosis-score and $CD8^{+}$T cells and M2 macrophages. **P<0.01, ****P < 0.0001.

were observed across these seven cells (Figure 3H), revealing that these specifically expressed molecules served as potential biomarkers for corresponding cell types.

Subsequently, the Ucell algorithm was applied for the calculation of the PANoptosis-score among diverse cells as shown in Figure 3F as well as it was outlined that this score existed notable distinctions in separate cell types. The mountain map plainly and separately unfolded the divergence of the PANoptosis-score among these seven cell types, finding that this score was distinctive in each cell subtype, and noting that epithelial cells, endothelial cells and fibroblasts possessed higher PANoptosis-score (Figure 3I). We further utilized copykat algorithms to identify the tumor cell from epithelial cells in tumor tissues (Figure 3J). Corresponding with the results of bulk sequence, in epithelial cells, the PANoptosis-scores of tumor-aneuploid exceeded the score in normal and tumor-diploid samples, suggesting that the extent of PANoptosis was tightly correlated with the development of tumor.

Deciphering the variations of cell-cell interactions within BC patients

To clarify the interaction status among these seven cell types (epithelial cells, endothelial cells, B cells, T cells, plasma cells, macrophages, and fibroblasts) in two groups, the bar chart revealed that the numbers and strength of cell-cell interaction in normal groups outperformed BC patients (Figure 4A). Subsequently, the network map visually displayed the interaction among seven cells, hence it was found that these three cells, including epithelial cells, fibroblasts and endothelial cells, had stronger interaction in normal populations, accompanied by a weak interaction relationship with the other four cells, such as macrophages, plasma cells, T cells and B cells, in contrast to BC patients (Figure 4B). Ulteriorly, the interaction of each intracellular pathway within distinctive groups was identified, witnessing that most of the signaling pathways were notably active in normal populations, such as SELE, ANGPT, CCL, ANGPTL, and other twenty pathways, whereas the activation of seven pathways, namely APP, MIF, MK, ESAM, PECAM1, CD99 and SPP1, primarily occurred in BC patients (Figure 4C).

To accurately identify the cell groups in dynamic situations where the received or submitted signals were changed, the comparison based on the outgoing and incoming interaction strength was developed in 4D space. According to this result, it was displayed that epithelial cells, endothelial cells and fibroblasts were classified as primary sources and targets for normal populations, while the chief sources of BC patients were macrophages and plasma cells, indicating the potential that they

10.3389/fimmu.2024.1359204

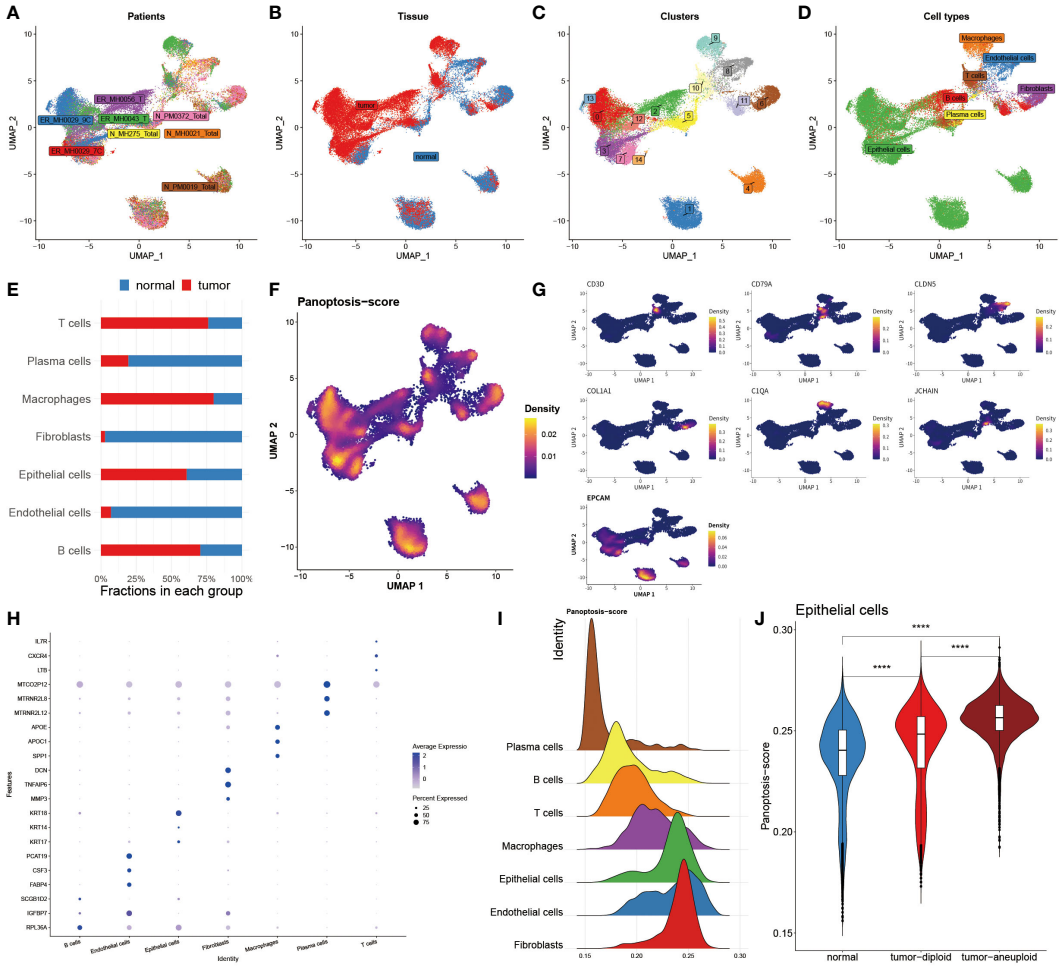

FIGURE 3
Single-cell analysis reveals PANoptosis dynamics in BC. **(A)** Distribution of cells collected from 8 patients. **(B)** Distribution of cells from tumor and normal tissues. **(C)** Distribution of 15 cell clusters. **(D)** Distribution of 7 annotated cell types. **(E)** Bar chart unveiling the proportion of 7 immune cells in two groups. **(F)** PANoptosis activity in each cell. **(G)** Specific marker genes for each immune cell. **(H)** Top three marker genes in each immune cell. **(I)** Mountain map exhibiting PANoptosis-score in each cell type. **(J)** Violin map revealing the difference of PANoptosis-score among normal tissues, tumor-diploid, and tumor-aneuploid in epithelial cells. ****P < 0.0001.

partook in the progression of BC (Figure 4D). Additionally, we further examined the strong interaction probability among T cells, B cells, plasma cells and macrophages. It was seen that the interaction obtained between CDL6A2 and CD44 and ITGAV +ITGB8 exclusively belonged to normal groups, while the interplay between CD44 and SPP1, FN1 merely occurred in BC patients (Figure 4E).

Machine learning approaches to develop a prognostic PANoptosis model

In the TCGA dataset and other five testing cohorts, 55 combined algorithms were leveraged to establish the PANoptosis-model, as well as obtained the mean C-index value of each algorithm for each combination (Figure 5A). As the result unveiled, the mean C-index of the RSF algorithm was highest compared with other algorithm combinations, emphasizing that this algorithm was competent to recruit prognostic genes and construct a predictive model (Figure 5A). To ensure the effectiveness of the subsequent established predictive model, the random forest model was deployed, as well a smaller generalization error (or OOB error) was strongly demanded. It was seen that OOB error was continuously decreasing and dynamic equilibrium between 0.4 and 0.38 (Figure 5B). Meanwhile, based on the analysis of random forest, we ultimately recruited six of the most significant genes pertinent to PANoptosis, namely, CD24, BMF, DAPK2, GNAI3, NR4A2 and SRC, which could be utilized to construct a prognostic model further (Figure 5C):

$$riskscore = CD24 \times 0.3459 + BMF \times 0.1461 - DAPK2 \times 0.1456 - GNAI3 \times 0.0007 - NR4A2 \times 0.0413 - SRC \times 0.1437$$

Consequently, two subgroups were successfully divided according to multivariate coefficient of the six genes, of which the low-risk group was superior in prognosis, accompanied by longer OS and more alive people, which was in contrast to the high-risk

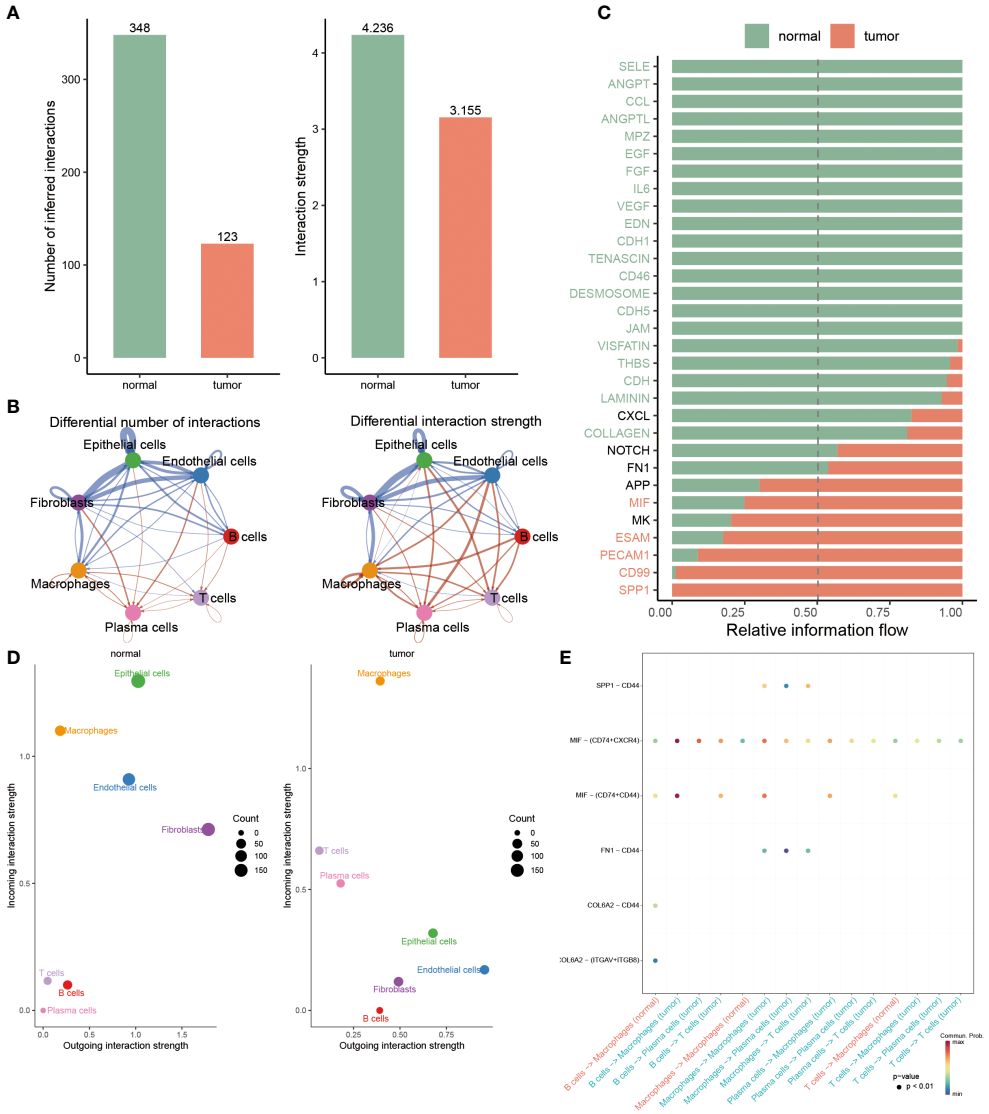

FIGURE 4
Deciphering the variations of cell-cell interactions within BC patients. **(A)** Comparison of interaction number and strength of multiple cell types between two groups. **(B)** Detailed cell communications among each cell type. **(C)** The bar chart signifies the proportion of massive signaling pathways from diverse cell types in each population. **(D)** Identifying the distinctions of interaction strength of incoming outgoing in separate groups. **(E)** Dot plot revealing the distribution of multiple signaling molecules in B cells, macrophages, T cells and plasma cells between normal and tumor samples.

group. Moreover, the expression profiles of these six genes were visualized, of which SRC, NR4A2 and DAPK2 were exceedingly abundant in low-risk populations, while GNAI3, BMF and CD24 exhibited higher expression levels in the high-risk patients (Figure 5D). Furthermore, the PANoptosis-model predicted the survival probability of separate-risk patients, displaying that low-risk patients possessed longer OS than high-risk BC patients (Figure 5E). The analysis of the Kernel-smoothing hazard also reflected the fact that the high-risk patients possessed a higher probability of BC recurrence compared to low-risk BC patients according to the hazard values (Figure 5F). Ultimately, the ROC curve evaluated the predictive ability of this model, since the range of AUC value was between 0.603 and 0.613, demonstrating that it was a robust and reliable prognostic model (Figure 5G).

Predictive performance of the PANoptosis prognostic model

The univariate and multivariate Cox regression analyses were resorted to evaluate the independence of our prognostic model and other clinical factors. The result from univariate Cox analysis indicated that these indicators, including risk score, menopause, stage, T, N and M, were capable of exerting influences on the survival rate of BC patients. Interestingly, the multivariate Cox regression analysis interpreted that risk score and age conformed to the criteria ($P < 0.05$), demonstrating that our PANoptosis-model was equipped with independence of prediction for BC patients (Figure 6A). Since the stage is a valuable reference in clinical practice, we then established a PANoptosis-nomogram to precisely

10.3389/fimmu.2024.1359204

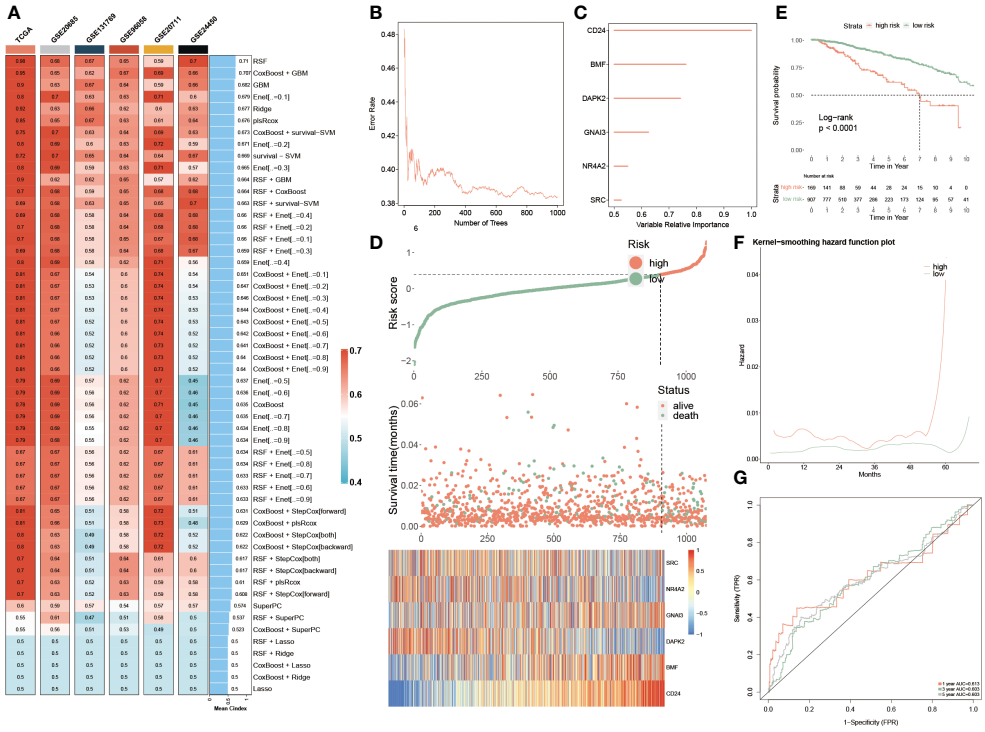

FIGURE 5
Machine learning approaches to develop a prognostic PANoptosis model. **(A)** The C-indexes of the 55 machine-learning algorithm combinations in the six testing cohorts. (TCGA, GSE20685, GSE131769, GSE96058, GSE2071 and GSE24450). **(B)** The forest model showcases the error rate in several different trees. **(C)** The importance of each significant PANoptosis gene. **(D)** The difference in OS, and survival status between two groups. Heatmap quantifying the expression levels of six PANoptosis genes in distinctive populations. **(E)** KM survival illustrates the survival probability in these two groups. **(F)** The kernel-smoothing hazard function plot demonstrates the correlation between relapse hazard and moths in two populations. **(G)** The ROC curves visualize the AUC values of the PANoptosis-model at one-, three-, and five-year.

predict the survival probability for BC patients at one-, three-, and five-year, which is composed of risk score, stage and age (Figure 6B). As the calibration curves illuminated, the nomogram-predicted OS was extremely consistent with the observed OS, confirming the accuracy of this nomogram (Figure 6C). In addition, the decision curve analysis (DCA) and the Hosmer-Lemeshow analysis continued to be conducted to enhance the nomogram persuasiveness. The DCA manifested that the net benefit of the PANoptosis-model curve far outweighed the other two curves, representing the efficiency of this model (Figure 6D). Similarly, its salient performance was again validated via the Hosmer-Lemeshow analysis, due to the result that the PANoptosis-nomogram curve did not exist apparent distinction with the ideal curve (P = 0.132) (Figure 6E), implying a superb predictive capability of this model. According to these data, it was summarized that the PANoptosis-nomogram had terrific potential and value for clinical application.

We also observed the predictive performance of eleven factors via the ROC curve, of which except for ER (AUC = 0.42) and PR (AUC = 0.4), the AUC value< 0.5, the good predictive potential of other factors was demonstrated (AUC > 0.5, Figure 6F). The C-index is a fundamental approach to appraise the predictive capability of distinctive models. We proceeded to assess the predictive efficacy of our model against 100 published signatures through C-index evaluation across the training cohort and ten testing cohorts. Remarkably, our PANoptosis-model demonstrated consistently higher precision compared to other models in the majority of the cohorts, underscoring model's robustness (Supplementary Figure S2).

Genomic alterations and their prognostic implications in PANoptosis

The above findings had preliminarily mentioned genetic alterations in two groups, to deeply analyze these diversities between two populations, we introduced multi-omics analysis to inspect the genetic variations within separate groups (Figure 7A). It was observed that the tumor mutational burden (TMB) of low-risk patients was comparatively lower in comparison to the high-risk populations. Moreover, this finding was again emphasized via the findings from Figures 7B, C. In Figure 7B, we calculated and visualized the TMB value, of which a lower TMB value was detected in low-risk patients instead of in high-risk populations (P< 0.05). Additionally, the TP53 mutational frequency was individually calculated among these two groups, respectively, as well as a higher proportion of the TP53 MUT was discovered in high-risk patients, which accounted for 58% and far surpassed the 38% of low-risk patients (Figure 7C). These three mutational signatures of SBS12, SBS1 and SBS11 primarily occurred in high-risk patients. Secondly, it was also detected that the mutation frequency of other genes, such as PIK3A, TTN, HMCN1 and CCDC168, also showed obvious

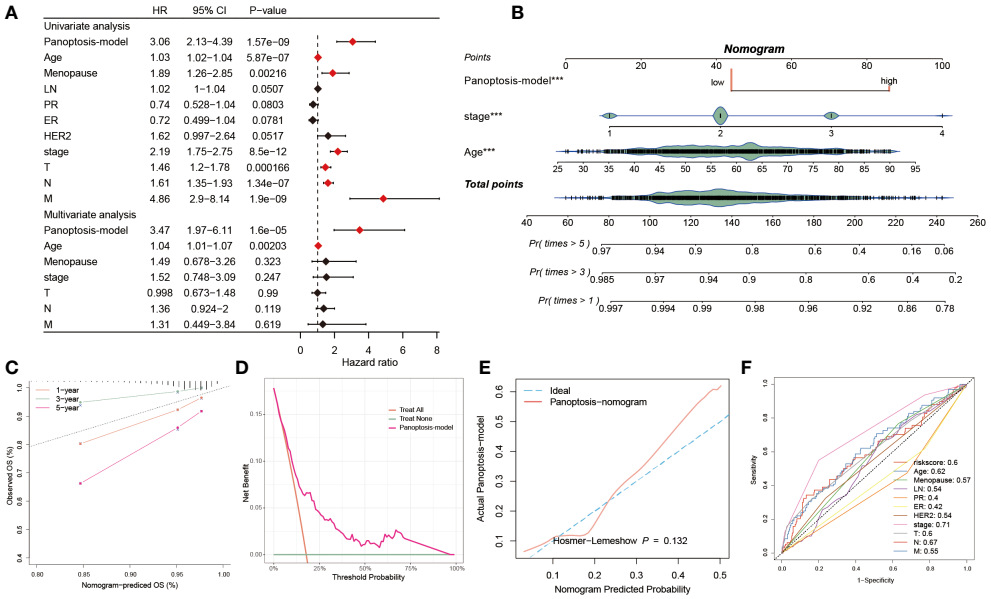

FIGURE 6
Predictive performance of the PANoptosis prognostic model. **(A)** The univariate Cox regression analysis comprised of risk score, age, menopause, LN, PR, ER, HER2, stage, T, N, and M, and the multivariate Cox regression analysis composed of risk score, age, menopause, stage, T, N, and M. **(B)** The establishment of a PANoptosis-nomogram made up of risk score, stage, and age. **(C)** The calibration curves assess the correctness of this nomogram prediction for OS at 1-, 3-, and 5-year. **(D)** The PANoptosis-model possesses higher net benefit and threshold probability than treat all and treat none. **(E)** The Hosmer-Lemeshow curve of PANoptosis-nomogram plotted by actual PANoptosis-model and nomogram predicted probability. **(F)** 11 ROC curves respectively unfolding the corresponding AUC values of the risk score and ten clinicopathological indexes. ***P < 0.001.

heterogeneity between these two populations. Besides, the amplification of 3p25.1, 6q21 and 13q34, as well as the deletion of 1p21.2, 17p12, 17q21.31 and 19p13.3 were identified in high-risk patients. These results were demonstrated due to the gain of oncogenic genes CDK19, SOBP, ATG5 and FYN in chr6q21 (Figure 7A). After that, the expression levels of six PANoptosis-related genes were quantified, as the heatmap showcased that SRC, DAPK2 and NR4A2 were primarily up-regulated in low-risk BC patients, while other three PANoptosis genes had higher expression levels in other risk patients (Figure 7D). Subsequently, the relevance between the risk score and survival status (Figure 7E) and tumor grade (Figure 7F) was explained, respectively. The risk score presented a remarkably positive correlation with status and grade, hinting that PANoptosis was pivotal in BC development. Ultimately, we compared the enrichment divergences of landmark pathways between two populations using GSEA analysis, of which five signaling pathways related to the immunoreaction had lower abundances in the high-risk patients, such as T cell-mediated cytotoxicity, antigen processing and presentation of peptide antigen, taking the positive regulation of epithelial cell differentiation pathway as an example, these five pathways, which were involved in cell development, were dramatically down-regulated in the low-risk patients (Figure 7G).

Tumor microenvironment evaluations using the PANoptosis model

Due to the significance of the TME in tumor development, we explored the immune discrepancies between these two populations using multiple methods, including CIBERSORT, xCell, MCP counter, TIMER and quanTIseq, to deeply analyze the prognostic mechanisms. We observed that a majority of immune cell types were prominently distributed in low-risk BC patients, such as neutrophil cells, monocyte cells, $CD4^{+}$T cells and NK cells, and a minority of cells were found in the high PANoptosis-score patients, for instance, pDC cells, Tregs, and dendritic cells (Figure 8A). Consistent with immune infiltration, low-risk patients possessed a higher abundance of ICIs compared to high-risk patients, accompanied by a favorable prognosis (Figure 8B). To further assess the TME variation and validate the analyzed results, we performed IHC staining based on key cell markers and ICIs in-house collected samples, the representative IHC images and statical results are shown in Figures 8C, D.

Prognostic implications of PANoptosis for ICIs therapy response

Through the evaluation of TME, it was speculated that low-risk BC patients may be superior in response to immunotherapy based on more immune cell infiltration and higher expression levels of ICIs genes, consequently demanding further validation. It is well-known that TIDE has been widely utilized to examine the efficiency of immunotherapy, and it typified a negative relevance with the responsiveness. Here, higher Dysfunction values were observed in low-risk patients, but there were no prominent differences in the TIDE and Exclusion scores between these two patients (P > 0.05) (Figure 9A). The survival probabilities included four combinations

10.3389/fimmu.2024.1359204

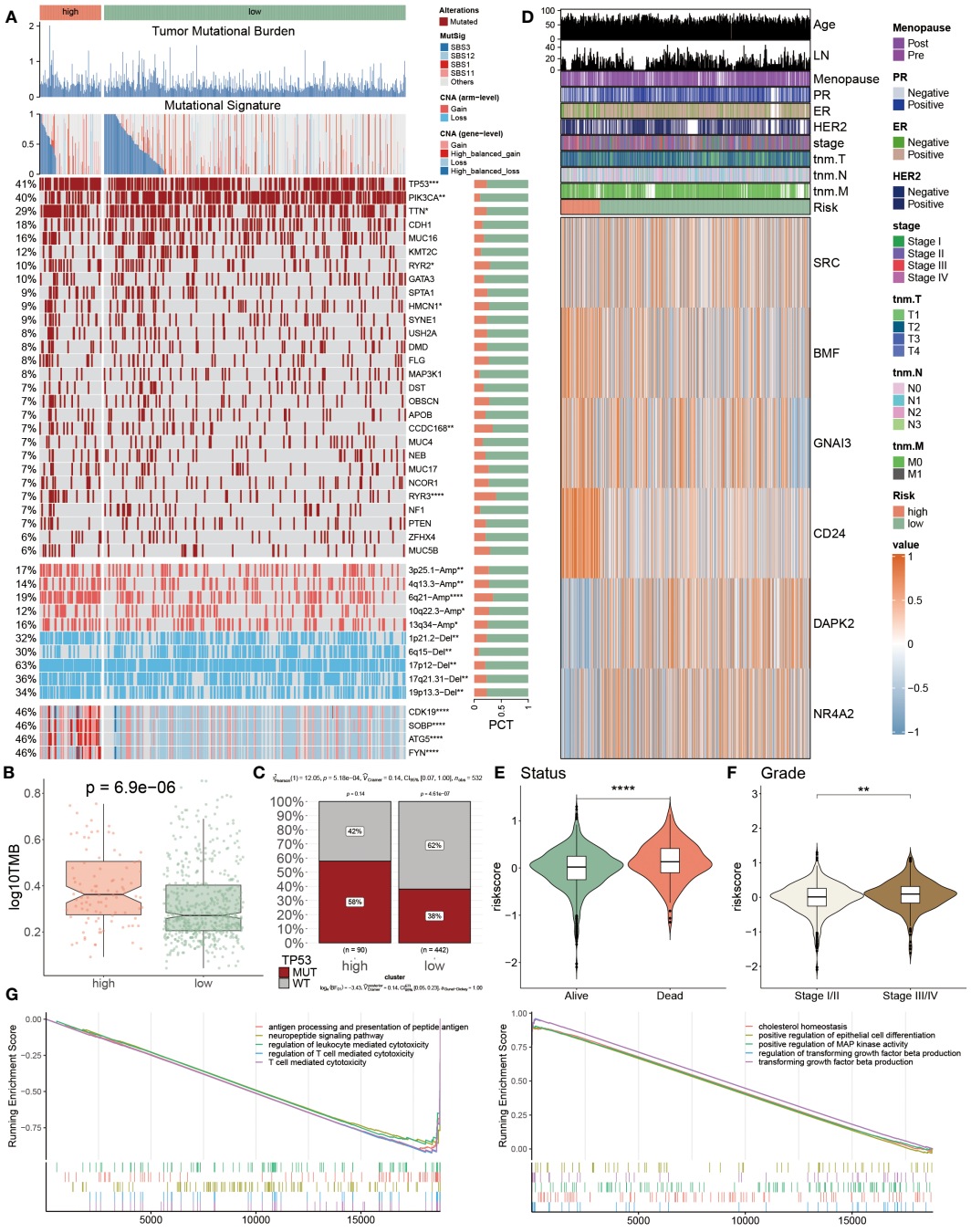

FIGURE 7
Genomic alterations and their prognostic implications in PANoptosis. **(A)** Genomic alteration landscape according to PANoptosis-model, including TMB, mutational signature, mutated frequencies of top 28 genes, CNV alteration and the distribution of selected genes in Chr6p21; Bar chart visualized the proportion. **(B)** The logarithmic value of TMB was computed in each group. **(C)** The TP53 MUT separately accounted for 58% and 38% in high- and low-risk patients, and similarly the percentages of WT were 42% and 62% between them, respectively **(D)** The heatmap presenting the expression profiling of five important PANoptosis genes in distinct populations and other clinicopathological factors, such as age, LN, stage, and HER2. **(E, F)** The violin charts individually indicated the association of risk score and status **(E)** and grade **(F)**. **(G)** GSEA analyses results from the high-risk subgroup compared with the low-risk one. *P<0.05, **P<0.01, ***P<0.001, ****P < 0.0001.

that were separately evaluated as shown by four KM survival curves, suggesting that low-risk score and high TIDE were superior in the outcome than other combinations, which claimed that low-risk patients with high TIDE value implied the further improvement of prognosis effect and risk score played a domain and decisive role (Figure 9B).

We estimated the tumor immunogenicity characteristics according to these indexes including CTA score, recombination defect, wound healing and proliferation, since their dysregulation could furnish new impetus for the development of tumors. As the outcomes exhibited, these four indexes displayed sensibly positive relations with the risk score, proposing that high-risk BC patients

10.3389/fimmu.2024.1359204

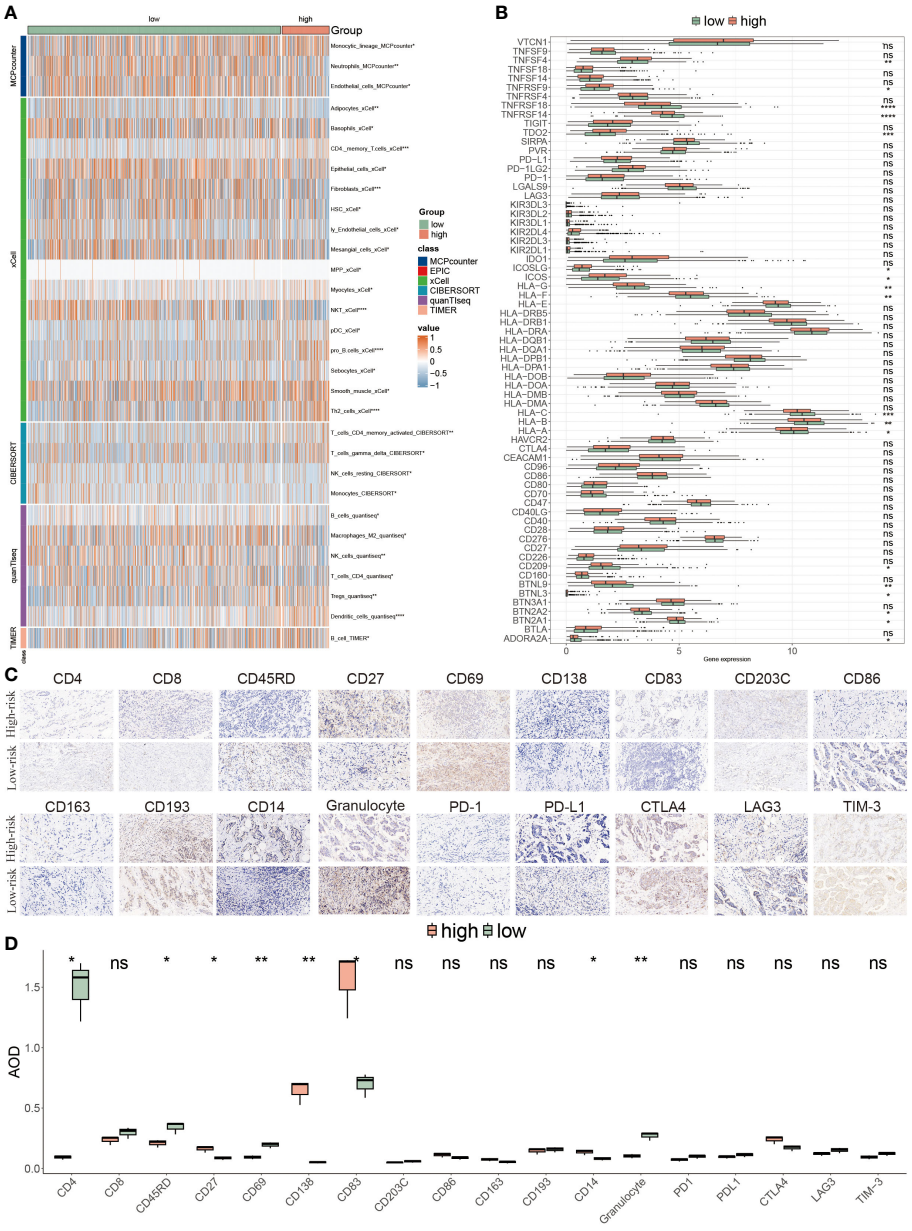

FIGURE 8
Tumor microenvironment evaluations using the PANoptosis model. **(A)** The distribution of multiple infiltrated immune cells derived from five algorithms (xCell, CIBERSORT, quanTIseq, TIMER) in two populations. **(B)** The expression features of massive immune checkpoints in these two risk-score subgroups. **(C)** IHC images of infiltrated immune cells and ICIs targeting the representative makers. **(D)** Statistical result of **(C)**. *P<0.05, **P<0.01, ***P<0.001, ****P < 0.0001. ns, not significant.

possessed inferior prognoses (Figure 9C). Until now, it has not been determined which groups were more suitable for ICIs therapy, so we introduced the IPS score from the TCGA dataset to diagnose. It was emphasized that the IPS scores were all extremely high in low-risk BC patients, representing that this group was more likely to acquire benefits from immunotherapy, no matter what alone or combined therapy methods were (Figure 9D). Ultimately, the assessment of response to PD1, PDL1, CTLA4 and MAGE-A3 treatment provided the immunotherapy chance for high-risk populations, but this group was merely limited to response to anti-PD-1 and MAGE-A3 treatments (P< 0.05) (Figure 9E). Collectively, the PANoptosis-model predicted the responsiveness to ICIs therapy between distinctive groups, as well as low-risk BC patients were more beneficial for this treatment in clinical.

Chemotherapy response and PANoptosis signatures

While novel therapeutic approaches, including targeted therapy, have been explored, chemotherapy remains an essential option for clinical cancer treatment. Therefore, it is imperative to employ the PANoptosis model to predict chemotherapy response in BC patients, to improve the prognosis, especially for high-risk BC

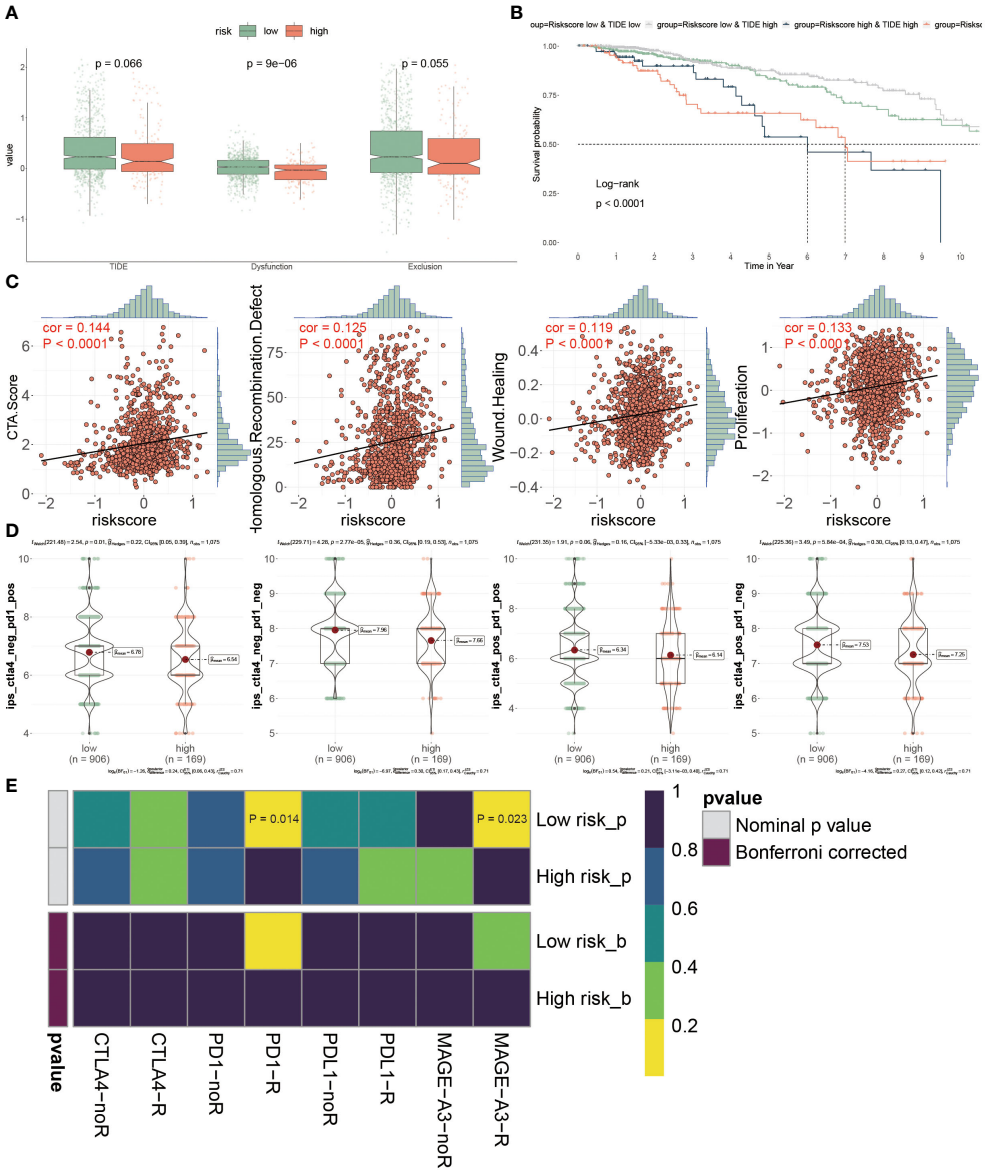

FIGURE 9
Prognostic implications of PANoptosis for icis therapy response. **(A)** Differences of TIDE value, dysfunction value and exclusion value in low- and high- risk populations. **(B)** To compare the OS of four combinations composed of (low or high) TIDE and (low or high) risk score, individually. **(C)** The relevance of the risk score and CTA score, recombination defect, wound healing and proliferation. **(D)** IPS (Immunophenoscore) value of each combination among two risk groups. **(E)** Putative ICIs therapy response in two risk BC patients.

patients. The identification of therapeutic targets is deemed a pivotal measurement to breaking undruggable dilemmas. So, Spearman's correlation analysis was utilized to select, finding that four proteins had a higher abundance in high-risk patients, which also indicated that this group was more prone to chemotherapy. Moreover, the CERES scores also supported the finding that these four proteins were considered therapeutic targets for high-risk BC patients (Figure 10A). Meanwhile, the candidate drug targeting these four anti-cancer drugs was characterized as having higher drug sensitivity (Figure 10B). Together, ACTB, SLC15A1, SLC5A6, and SQLE were recommended as potential therapeutic targets.

In the following, we continued to identify underlying drugs from PRISM and CTRP datasets. This study displayed that a total of six candidate compounds were listed, among them ispinesib and LY2606368 compounds from the PRISM dataset (Figure 10C), and the CTRP dataset including SB-743921, paclitaxel, BI-2536 and GSK461364 compounds (Figure 10D). We also found that lower AUC value was reported in high-risk patients, hinting a better responsiveness to chemotherapy in this population. Since the above finding was unable to determine the most superior drugs, therefore, a multiple-perspective analysis was further conducted. Among them, the clinical status, experimental evidence, mRNA expression levels and CMap score of these six compounds were disclosed, based on the criterion CMap score< -35, concluding that only BI-2536 and ispinesib were ultimately chosen as therapeutic drugs for high-risk BC populations (Figure 10E; Supplementary Table S6).

10.3389/fimmu.2024.1359204

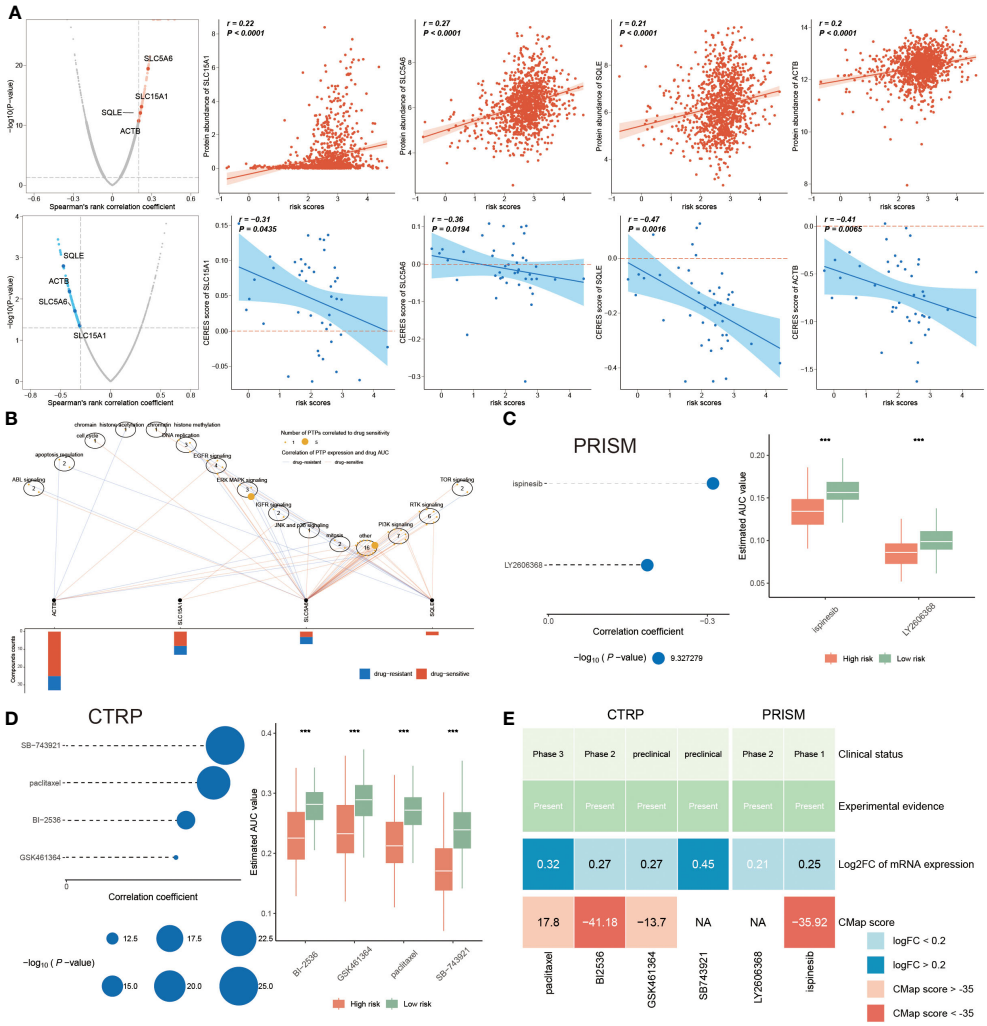

FIGURE 10
Chemotherapy response and PANoptosis signatures. **(A)** The left plots illuminating the spearman's rank correlation coefficient of five candidates, among them the red and blue plots signifying the positive and negative correlations, respectively. Correspondingly, the right scatter plots separately denoting the relevance between the risk score and each candidate' protein abundance and CERES score. **(B)** Spearman correlation between mRNA expression of potential targets and drug sensitivity across cancer cell line. **(C, D)** Correlation coefficients of two compounds from PRISM dataset **(C)** and of four compounds gotten from CTRP **(D)**, of which the larger circle, the lower *P*-value. Accordingly, the right boxplot illustrating the remarkable distinction of AUC value between these two risk groups in each compound. **(E)** A multiple-perspective analysis was constituted by clinical status, experimental evidence, mRNA expression and CMap score of six compounds. ***P < 0.001.

Discussion

Our investigation into the role of PANoptosis in breast cancer marks a significant stride toward refining prognostic tools and personalizing patient care. By developing a risk score rooted in the intricate mechanisms of PANoptosis—encompassing pyroptosis, apoptosis, and necroptosis—we've unveiled a multifaceted perspective on tumor biology and patient outcomes. This approach not only sheds light on the underlying processes driving breast cancer progression but also sets the stage for targeted therapeutic strategies that could dramatically alter the clinical landscape.

The introduction of our PANoptosis-based risk score has the potential to revolutionize treatment paradigms in breast cancer care. By accurately stratifying patients according to their risk, we can pave the way for more nuanced treatment strategies—those at higher risk might benefit from innovative, aggressive treatments earlier in their disease course, while lower-risk patients could avoid unnecessary side effects from overtreatment. Moreover, our findings underscore the potential of targeting the PANoptosis pathway as a novel therapeutic avenue, offering hope for treatments that could inhibit tumor growth and metastasis more effectively.

Crucially, our study illuminates the complex relationship between PANoptosis and key processes in cancer development. While our analysis provides valuable insights into PANoptosis and its association with breast cancer prognosis, we did not directly investigate its relationship with EMT or other specific pathways involved in cancer metastasis. However, the identification of key PANoptosis-related genes and their prognostic significance underscores the potential of further research in these areas. Future studies could explore how these

genes interact within the broader network of cancer progression mechanisms, potentially uncovering novel targets for therapeutic intervention. Understanding how PANoptosis intersects with other cellular processes to drive or inhibit cancer spread is essential for developing targeted interventions that could halt progression and improve survival outcomes.

While our study represents a pivotal step forward, we must acknowledge the limitations inherent in our current model, most notably the exclusion of molecular subtypes of breast cancer. This oversight is significant; the diversity of breast cancer at the molecular level profoundly influences both prognosis and therapeutic response. Future iterations of our research will need to incorporate these subtypes to fully capture the complexity of breast cancer and refine the applicability of our risk score in diverse clinical contexts.

Looking forward, integrating our PANoptosis-based risk score with molecular subtyping and other biomarkers could yield a robust, multifactorial tool for breast cancer prognosis and treatment planning. Collaborative research efforts that bridge basic science and clinical practice are essential for translating these insights into tangible benefits for patients. Moreover, exploring the potential of combination therapies that target both PANoptosis pathways and other key drivers of tumor growth and resistance may offer new hope for challenging cases of breast cancer.

In sum, our study contributes a vital piece to the puzzle of breast cancer prognosis and treatment, highlighting the importance of PANoptosis in shaping patient outcomes. While challenges remain in translating these findings into clinical practice, the promise of more personalized, effective treatment strategies based on our understanding of PANoptosis offers a new horizon in breast cancer care. As we move forward, expanding the scope of our research to address the limitations identified and exploring the full therapeutic potential of targeting PANoptosis will be crucial in our ongoing battle against breast cancer.

Data availability statement

The datasets presented in this study can be found in online repositories. The names of the repository/repositories and accession number(s) can be found in the article/Supplementary Material.

Ethics statement

The studies involving humans were approved by Ethics Committee of Guizhou Provincial People's Hospital (approved number: 2023-070). The studies were conducted in accordance with the local legislation and institutional requirements. The participants provided their written informed consent to participate in this study.

Author contributions

SW: Data curation, Formal analysis, Writing – original draft. ZL: Investigation, Resources, Visualization, Writing – original draft. JH: Methodology, Resources, Writing – original draft. XL: Investigation, Resources, Writing – original draft. QN: Funding acquisition, Methodology, Supervision, Writing – review & editing. TW: Conceptualization, Formal analysis, Funding acquisition, Visualization, Writing – original draft, Writing – review & editing.

Funding

The author(s) declare financial support was received for the research, authorship, and/or publication of this article. This study was supported by the Talent Fund of Guizhou Provincial People's Hospital ([2022]-33), National Natural Science Foundation of China (82272656), and Scientific Research Fund of Guizhou Provincial People's Hospital (GZSYQN[2021]16).

Conflict of interest

The authors declare that the research was conducted in the absence of any commercial or financial relationships that could be construed as a potential conflict of interest.

Publisher's note

Supplementary material

The Supplementary Material for this article can be found online at: https://www.frontiersin.org/articles/10.3389/fimmu.2024.1359204/full#supplementary-material

References

1. Sung H, Ferlay J, Siegel RL, Laversanne M, Soerjomataram I, Jemal A, et al. Global cancer statistics 2020: GLOBOCAN estimates of incidence and mortality worldwide for 36 cancers in 185 countries. *CA Cancer J Clin*. (2021) 71:209–49. doi: 10.3322/caac.21660

2. Siegel RL, Miller KD, Jemal A. Cancer statistics, 2020. *CA Cancer J Clin*. (2020) 70:7–30. doi: 10.3322/caac.21590

3. Smith RA, Andrews KS, Brooks D, Fedewa SA, Manassaram-Baptiste D, Saslow D, et al. Cancer screening in the United States, 2019: A review of current American Cancer Society guidelines and current issues in cancer screening. *CA Cancer J Clin*. (2019) 69:184–210. doi: 10.3322/caac.21557

4. Samir P, Malireddi RKS, Kanneganti TD. The PANoptosome: A deadly protein complex driving pyroptosis, apoptosis, and necroptosis (PANoptosis). *Front Cell Infect Microbiol*. (2020) 10:238. doi: 10.3389/fcimb.2020.00238

5. Malireddi RKS, Tweedell RE, Kanneganti TD. PANoptosis components, regulation, and implications. *Aging*. (2020) 12:11163–4. doi: 10.18632/aging.103528

6. Ocansey DKW, Qian F, Cai P, Ocansey S, Amoah S, Qian Y, et al. Current evidence and therapeutic implication of PANoptosis in cancer. *Theranostics*. (2024) 14:640–61. doi: 10.7150/thno.91814

7. Chen X, Kang R, Kroemer G, Tang D. Broadening horizons: the role of ferroptosis in cancer. *Nat Rev Clin Oncol*. (2021) 18:280–96. doi: 10.1038/s41571-020-00462-0

8. Wong RS. Apoptosis in cancer: from pathogenesis to treatment. *J Exp Clin Cancer Res CR*. (2011) 30:87. doi: 10.1186/1756-9966-30-87

9. Johnson DE, O'Keefe RA, Grandis JR. Targeting the IL-6/JAK/STAT3 signalling axis in cancer. *Nat Rev Clin Oncol*. (2018) 15:234–48. doi: 10.1038/nrclinonc.2018.8

10. Yu T, Cheng W, Zhang J, Wang T, Liu Y, Duan Y, et al. Identification of a PANoptosis-related gene signature for predicting the prognosis, tumor microenvironment and therapy response in breast cancer. *J Cancer*. (2024) 15:428–43. doi: 10.7150/jca.90113

11. Tang D, Kang R, Berghe TV, Vandenabeele P, Kroemer G. The molecular machinery of regulated cell death. *Cell Res*. (2019) 29:347–64. doi: 10.1038/s41422-019-0164-5

12. Zou Y, Xie J, Zheng S, Liu W, Tang Y, Tian W, et al. Leveraging diverse cell-death patterns to predict the prognosis and drug sensitivity of triple-negative breast cancer patients after surgery. *Int J Surg*. (2022) 107:106936. doi: 10.1016/j.ijsu.2022.106936

13. Gendoo DMA, Zon M, Sandhu V, Manem VSK, Ratanasirigulchai N, Chen GM, et al. MetaGxData: clinically annotated breast, ovarian and pancreatic cancer datasets and their use in generating a multi-cancer gene signature. *Sci Rep*. (2019) 9:8770. doi: 10.1038/s41598-019-45165-4

14. Pal B, Chen Y, Vaillant F, Capaldo BD, Joyce R, Song X, et al. A single-cell RNA expression atlas of normal, preneoplastic and tumorigenic states in the human breast. *EMBO J*. (2021) 40:e107333. doi: 10.15252/embj.2020107333

15. McGinnis CS, Murrow LM, Gartner ZJ. DoubletFinder: doublet detection in single-cell RNA sequencing data using artificial nearest neighbors. *Cell Syst*. (2019) 8:329–337.e4. doi: 10.1016/j.cels.2019.03.003

16. Domínguez Conde C, Xu C, Jarvis LB, Rainbow DB, Wells SB, Gomes T, et al. Cross-tissue immune cell analysis reveals tissue-specific features in humans. *Science*. (2022) 376:eabl5197. doi: 10.1126/science.abl5197

17. Jin S, Guerrero-Juarez CF, Zhang L, Chang I, Ramos R, Kuan CH, et al. Inference and analysis of cell-cell communication using CellChat. *Nat Commun*. (2021) 12:1088. doi: 10.1038/s41467-021-21246-9

18. Ashburner M, Ball CA, Blake JA, Botstein D, Butler H, Cherry JM, et al. Gene ontology: tool for the unification of biology. The Gene Ontology Consortium. *Nat Genet*. (2000) 25:25–9. doi: 10.1038/75556

19. Kanehisa M, Sato Y, Kawashima M, Furumichi M, Tanabe M. KEGG as a reference resource for gene and protein annotation. *Nucleic Acids Res*. (2016) 44:D457–62. doi: 10.1093/nar/gkv1070

20. Yu G, Wang LG, Han Y, He QY. clusterProfiler: an R package for comparing biological themes among gene clusters. *OMICS*. (2012) 16:284–7. doi: 10.1089/omi.2011.0118

21. Hänzelmann S, Castelo R, Guinney J. GSVA: gene set variation analysis for microarray and RNA-seq data. *BMC Bioinf*. (2013) 14:7. doi: 10.1186/1471-2105-14-7

22. Andreatta M, Carmona SJ. UCell: Robust and scalable single-cell gene signature scoring. *Comput Struct Biotechnol J*. (2021) 19:3796–8. doi: 10.1016/j.csbj.2021.06.043

23. Liu Z, Guo C, Dang Q, Wang L, Liu L, Weng S, et al. Integrative analysis from multi-center studies identities a consensus machine learning-derived lncRNA signature for stage II/III colorectal cancer. *EBioMedicine*. (2022) 75:103750. doi: 10.1016/j.ebiom.2021.103750

24. Wang L, Liu Z, Liang R, Wang W, Zhu R, Li J, et al. Comprehensive machine-learning survival framework develops a consensus model in large-scale multicenter cohorts for pancreatic cancer. *Elife*. (2022) 11:e80150. doi: 10.7554/eLife.80150

25. Becht E, Giraldo NA, Lacroix L, Buttard B, Elarouci N, Petitprez F, et al. Estimating the population abundance of tissue-infiltrating immune and stromal cell populations using gene expression. *Genome Biol*. (2016) 17:218. doi: 10.1186/s13059-016-1070-5

26. Aran D, Hu Z, Butte AJ. xCell: digitally portraying the tissue cellular heterogeneity landscape. *Genome Biol*. (2017) 18(1):220. doi: 10.1186/s13059-017-1349-1

27. Newman AM, Liu CL, Green MR, Gentles AJ, Feng W, Xu Y, et al. Robust enumeration of cell subsets from tissue expression profiles. *Nat Methods*. (2015) 12:453–7. doi: 10.1038/nmeth.3337

28. Finotello F, Mayer C, Plattner C, Laschober G, Rieder D, Hackl H, et al. Molecular and pharmacological modulators of the tumor immune contexture revealed by deconvolution of RNA-seq data. *Genome Med*. (2019) 11:34. doi: 10.1186/s13073-019-0638-6

29. Li T, Fan J, Wang B, Traugh N, Chen Q, Liu JS, et al. TIMER: A web server for comprehensive analysis of tumor-infiltrating immune cells. *Cancer Res*. (2017) 77:e108–10. doi: 10.1158/0008-5472.Can-17-0307

30. Zeng D, Ye Z, Shen R, Yu G, Wu J, Xiong Y, et al. IOBR: multi-omics immuno-oncology biological research to decode tumor microenvironment and signatures. *Front Immunol*. (2021) 12:687975. doi: 10.3389/fimmu.2021.687975

31. Yoshihara K, Shahmoradgoli M, Martinez E, Vegesna R, Kim H, Torres-Garcia W, et al. Inferring tumour purity and stromal and immune cell admixture from expression data. *Nat Commun*. (2013) 4:2612. doi: 10.1038/ncomms3612

32. Jiang P, Gu S, Pan D, Fu J, Sahu A, Hu X, et al. Signatures of T cell dysfunction and exclusion predict cancer immunotherapy response. *Nat Med*. (2018) 24:1550–8. doi: 10.1038/s41591-018-0136-1

33. Corsello SM, Bittker JA, Liu Z, Gould J, McCarren P, Hirschman JE, et al. The Drug Repurposing Hub: a next-generation drug library and information resource. *Nat Med*. (2017) 23:405–8. doi: 10.1038/nm.4306

34. Meyers RM, Bryan JG, McFarland JM, Weir BA, Sizemore AE, Xu H, et al. Computational correction of copy number effect improves specificity of CRISPR-Cas9 essentiality screens in cancer cells. *Nat Genet*. (2017) 49:1779–84. doi: 10.1038/ng.3984

35. Yang C, Huang X, Li Y, Chen J, Lv Y, Dai S. Prognosis and personalized treatment prediction in TP53-mutant hepatocellular carcinoma: an in silico strategy towards precision oncology. *Brief Bioinform*. (2021) 22(3):bbaa164. doi: 10.1093/bib/bbaa164

36. Lamb J, Crawford ED, Peck D, Modell JW, Blat IC, Wrobel MJ, et al. The Connectivity Map: using gene-expression signatures to connect small molecules, genes, and disease. *Science*. (2006) 313:1929–35. doi: 10.1126/science.1132939

37. Wang T, Li T, Li B, Zhao J, Li Z, Sun M, et al. Immunogenomic landscape in breast cancer reveals immunotherapeutically relevant gene signatures. *Front Immunol*. (2022) 13:805184. doi: 10.3389/fimmu.2022.805184

38. Wang T, Ba X, Zhang X, Zhang N, Wang G, Bai B, et al. Nuclear import of PTPN18 inhibits breast cancer metastasis mediated by MVP and importin β2. *Cell Death Dis*. (2022) 13:720. doi: 10.1038/s41419-022-05167-z

frontiers | Frontiers in Immunology

TYPE Original Research
PUBLISHED 14 March 2024
DOI 10.3389/fimmu.2024.1368586

OPEN ACCESS

EDITED BY
Laura Senovilla,
Spanish National Research Council (CSIC), Spain

REVIEWED BY
Eva M. Galvez,
Spanish National Research Council (CSIC), Spain
Pooria Safarzadeh Kozani,
Tarbiat Modares University, Iran

*CORRESPONDENCE
Hidde L. Ploegh
hidde.ploegh@childrens.harvard.edu

RECEIVED 10 January 2024
ACCEPTED 29 February 2024
PUBLISHED 14 March 2024

CITATION
Verhaar ER, Knoflook A, Pishesha N, Liu X, van Keizerswaard WJC, Wucherpfennig KW and Ploegh HL (2024) MICA-specific nanobodies for diagnosis and immunotherapy of MICA$^+$ tumors. *Front. Immunol.* 15:1368586. doi: 10.3389/fimmu.2024.1368586

MICA-specific nanobodies for diagnosis and immunotherapy of MICA$^+$ tumors

Elisha R. Verhaar[1,2], Anouk Knoflook[1], Novalia Pishesha[3,4], Xin Liu[1], Willemijn J. C. van Keizerswaard[1], Kai W. Wucherpfennig[5] and Hidde L. Ploegh[1,2]*

[1]Boston Children's Hospital, Harvard Medical School, Boston, MA, United States, [2]Department of Cell and Chemical Biology, Leiden University Medical Centre, Leiden, Netherlands, [3]Division of Immunology, Boston Children's Hospital, Boston, MA, United States, [4]Department of Pediatrics, Harvard Medical School, Boston, MA, United States, [5]Department of Cancer Immunology and Virology, Dana-Farber Cancer Institute, Boston, MA, United States

MICA and MICB are Class I MHC-related glycoproteins that are upregulated on the surface of cells in response to stress, for instance due to infection or malignant transformation. MICA/B are ligands for NKG2D, an activating receptor on NK cells, CD8$^+$ T cells, and γδ T cells. Upon engagement of MICA/B with NKG2D, these cytotoxic cells eradicate MICA/B-positive targets. MICA is frequently overexpressed on the surface of cancer cells of epithelial and hematopoietic origin. Here, we created nanobodies that recognize MICA. Nanobodies, or VHHs, are the recombinantly expressed variable regions of camelid heavy chain-only immunoglobulins. They retain the capacity of antigen recognition but are characterized by their stability and ease of production. The nanobodies described here detect surface-disposed MICA on cancer cells *in vitro* by flow cytometry and can be used therapeutically as nanobody-drug conjugates when fused to the Maytansine derivative DM1. The nanobody-DM1 conjugate selectively kills MICA positive tumor cells *in vitro*.

KEYWORDS

MICA, NKG2D, NKG2D ligands, cancer, nanobodies, VHHs, immuno-oncology, nanobody drug conjugate

1 Introduction

The Class I MHC-like molecules MICA and MICB are stress-induced surface glycoproteins, absent from healthy cells but upregulated on virus-infected or malignantly transformed human cells (1). MICA/B are ligands for NKG2D, an activating receptor on NK cells, CD8$^+$ T cells, and γδ T cells (2). Upon engagement of NKG2D, these cytotoxic cells can eradicate MICA-positive targets, assisted by secretion of cytokines (3–5). Elevated levels of MICA/B occur in hematopoietic malignancies, as well as in epithelial solid tumors such as colorectal cancer (6), ovarian cancer (7), cervical cancer (8), breast cancer (9), pancreatic

cancer (10), melanoma (11) and cholangiocarcinoma (12). MICA/B are thus considered possible targets for immunotherapy.

Nanobodies, a registered trademark, are also referred to as VHHs. They are the smallest immunoglobulin fragments that retain the capacity of antigen binding. They are the recombinantly expressed variable regions of camelid heavy chain-only immunoglobulins (13). Nanobodies have a short circulatory half-life, are poorly immunogenic, and show excellent tissue penetration compared to conventional full-sized immunoglobulins (14, 15). Many nanobodies do not require disulfide bonds for their stability, nor do they depend on glycosylation for expression. They are therefore easily and affordably produced in prokaryotic cells (16–18). Nanobodies have proven valuable as the point of departure for the construction of PET imaging agents (19–24), nanobody-drug conjugates (25–27), and chimeric antigen receptors in cell-based therapies (28–38).

Because MICA is expressed on stressed and cancerous cells, the ability to detect such aberrations *in vivo* would be an important diagnostic tool to detect premalignant and malignant lesions. Here, we report the generation of nanobodies that recognize MICA, and apply these nanobodies to detect surface-bound MICA *in vitro* by flow cytometry. Fused to the microtubule inhibitor Maytansine (DM1), these nanobodies can be used therapeutically as nanobody-drug conjugates.

2 Materials and methods

2.1 Alpaca immunization and phage library construction

We immunized an alpaca with 250 ug of the purified extracellular portion of MICA*009 (obtained by baculovirus expression in the lab of K.W. Wucherpfennig (39)) comprising the α1, α2, and α3 domains in alum adjuvant, followed by 3 booster injections at 2-week intervals. Immunizations were carried out by Camelid Immunogenics. The immune response of the animal was checked by immunoblot (Supplementary Figure 1). Briefly, 1 µg of antigen was resolved by SDS PAGE and transferred to a PVDF membrane. The membrane was incubated with at 1:5000 dilution of alpaca serum collected 2 weeks after the last boost. HRP-linked goat-anti-llama (0.05 µg/mL; Bethyl, NC9656984) was used as the secondary antibody. Membranes were developed with ECL Western Lightning Plus. Mononuclear cells from peripheral blood of the immunized alpaca were isolated by Ficoll gradient separation. The VHH library was generated according to an established protocol (Maas et al., 2007). Briefly, RNA was extracted (RNeasy RNA purification kit, Qiagen) and cDNA was prepared (Superscript III first-strand synthesis system, Invitrogen). The DNA sequences from conventional and heavy-chain only Ig genes are not distinguishable based on the use of specific primers, but two distinct hinge regions are generated between the VHH domain and the CH2 region. We amplified the VHH repertoire from the alpaca using VHH-specific primers that target these hinge sequences (Supplementary Table 1). We pooled the VHH PCR products and ligated them into a phagemid vector in-frame with the pIII gene of the M13 phagemid to construct a phagemid library display. We performed two rounds of panning against MICA*009 immobilized on an ELISA plate, following previously described protocols (40).

2.2 Production of recombinant VHHs and sortase reactions

DNA from positive clones was sequenced and 9 clones were selected for further characterization. The relevant VHH sequences were subcloned into a pHEN6 expression vector with C-terminal modifications, so that each nanobody sequence included an LPETG motif recognized by sortase A, followed by a $(His)_6$-tag to facilitate recovery and purification. Briefly, VHH sequences were amplified from the phagemid vector by PCR (primers in Supplementary Table 1) and the pHEN6 vector was linearized using the NcoI and BstEII restriction enzymes. Gibson assembly was performed following manufacturer's directions (Gibson Assembly® Master Mix, NEB). Positive VHH clones were expressed in WK6 *E.Coli* in terrific broth and periplasmic protein expression was activated by induction with isopropyl β-D-thiogalactopyranoside (1 mM) at an OD600 of 0.6. VHHs were harvested from the periplasm by osmotic shock. The C-terminal $(His)_6$-tag allows purification of the recombinant proteins using Ni-NTA agarose beads (Qiagen), followed by FPLC purification on an S75 column by FPLC (ÄKTA, Cytiva Life Sciences). Sortase reactions were performed by incubating each nanobody with a 10-fold molar excess of GGG-nucleophile in the presence of 25 µM Sortase 7M (41) overnight at 4°C. Because the LPETG sequence is cleaved during transpeptidation, the $(His)_6$-tag immediately C-terminal of the LPETG motif is lost. This allows enrichment of the desired modified product by depletion of His-tagged sortase and unreacted nanobody on a NiNTA matrix, while the unbound fraction contains the modified nanobody.

2.3 Competitive ELISA and estimation of binding affinity

An ELISA was performed to determine the concentration at which each biotinylated nanobody showed ~80% binding to recombinant MICA*009 (5 mg/mL) immobilized on an ELISA plate. Biotinylated nanobody at a concentration that yielded 80% of the maximum attainable binding value was then mixed with a 500-fold excess of unlabeled competitor nanobody and allowed to compete for binding to 5 µg/mL MICA*009 coated on an ELISA plate. Plates were incubated with streptavidin-HRP (0.00025 µg/mL) for 45-60 minutes at room temperature. After addition of TMB substrate, absorbance was read out at 450 nm on a Spectramax iD5 plate reader (Molecular Devices). If the unlabeled nanobody binds to an epitope distinct from that recognized by the biotinylated nanobody, no diminution of the signal at 450 nm is expected. Nanobodies that recognize the same epitope as that seen by the biotinylated nanobody will show a reduction in the signal at 450nm.

We estimated the binding affinity of VHH-A1 and VHH-H3 by performing an ELISA as previously described (42). Briefly, we incubated plates coated with 100µL PBS containing 2.5 µg/mL

recombinant MICA*009 or GFP as negative control with biotinylated VHH-A1 and VHH-H3 in various concentrations (10-fold serial dilutions; 0.000001 nM – 1000 nM). Streptavidin-HRP at 0.00025 µg/mL was used as detection agent. After addition of TMB substrate, absorbance was read at 450 nm on a Spectramax iD5 plate reader (Molecular Devices). Binding affinity was estimated by calculating the IC50 obtained from three experimental replicates with each sample added in duplicates. Recombinant MICA*009 was produced by transfection of EXPI-293 cells with pcDNA3.1(+) vector encoding for extracellular MICA*009 containing a C-terminal LPETG sortase motif followed by a His (6)-tag to facilitate recovery and purification on a NiNTA matrix (Supplementary Figure 2). EXPI-293 cells were transfected using the ExpiFectamine™ 293 Transfection Kit, according to manufacturer's directions (Gibco).

2.4 Cell culture

B16F10 and EL-4 cells and their MICA$^+$ transfectants were a gift from the lab of Kai Wucherpfennig. B16F10 cells were cultured in complete DMEM (DMEM with 4.5 g/L glucose, substituted with 10% Fetal Bovine Serum (FBS) and 100 U/mL penicillin/streptomycin). EL-4 cells were cultured in complete RPMI 1640 (RPMI 1640, substituted with 10% FBS and 100 U/mL penicillin/streptomycin). Cells were maintained at optimal densities in a humidified 5% CO2 incubator at 37°C.

2.5 Flow cytometry

EL-4 WT and MICA$^+$ cells, or B16F10 WT and MICA$^+$ cells, were stained with biotinylated VHH-A1 and VHH-H3 for 30 minutes on ice, washed, and incubated with a cocktail of Streptavidin-conjugated PE at 0.0025 µg/mL (Invitrogen) and 2 µg/mL propidium iodide (Life technologies) for EL-4 or LIVE/DEAD™ Fixable Violet Dead Cell Stain Kit (Invitrogen) for B16F10, both according to manufacturer's directions for 30 minutes on ice. Cells were analyzed on an LSR Fortessa flow cytometer (BD Biosciences). Gating strategies were based on cell lines stained with the appropriate controls, where single cells and live cells were appropriately selected.

2.6 VHH-drug conjugate creation and *in vitro* cytotoxicity assays

VHH-DM1 was produced in a sortase-mediated transpeptidation reaction. Briefly, 500-1000 µg of VHH containing a C-terminal LPETG-motif was mixed with a 10-fold molar excess of GGG-DM1 and incubated with 25 µM Sortase for 16 hours at 4°C. GGG-DM1 was produced in-house by modifying a GGG-peptide linker to contain a maleimide group and allowing it to react with the thiol group on DM1 (Broadpharm) (Supplementary Figure 3A). Unreacted VHH and Sortase, both containing a $(His)_6$-tag, were depleted by incubation with NiNTA agarose (Qiagen or Prometheus). Excess free GGG-DM1 was removed by desalting on a PD-10 desalting column (Cytiva). We plated 4000 cells/well in a 96-well plate and incubated cells with serial 3-fold dilutions of VHH-drug adduct or free DM4 (Broadpharm), a structural analog of DM1 (Supplementary Figure 3B) at 37°C in a humidified 5% CO2 atmosphere. After 72 hours, we measured cell viability by CellTiter GloTM assay according to the manufacturer's directions (Promega). For co-culture experiments, MICA expression was determined after a 72-hour incubation. Each treatment was performed in duplicate. For flow cytometry, the duplicate wells of each condition were combined, and the cell mixture was stained with 0.0006 µg/mL biotinylated anti-human MICA/B antibody (Clone 6D4, Biolegend) for 30 minutes on ice. Cells were washed and incubated with Streptavidin-conjugated PE at 0.0025 µg/mL (Invitrogen) and LIVE/DEAD™ Fixable Violet Dead Cell Stain Kit according to manufacturer's directions (Invitrogen) for 30 minutes on ice. Cells were washed and viability and MICA positivity were determined by flow cytometry on an LSR Fortessa flow cytometer (BD Biosciences).

2.7 Statistical analysis

All statistical analysis was performed with GraphPad Prism 8. Flow cytometry data was analyzed with FlowJo (v10.8.1 and v10.9.0).

3 Results

3.1 Alpaca immunization and phage display panning yields MICA-specific nanobodies

We immunized an alpaca with purified recombinant MICA*009 in alum adjuvant, followed by 3 booster injections at 2-week intervals. We checked the immune response of the animal by immunoblot using serum samples collected prior to each boost. Having recorded a positive response after the 3rd boost, construction of a phage display library, followed by screening for MICA-reactive hits, yielded positive clones. DNA from positive clones was sequenced and 9 clones were selected for further characterization. Because nanobodies interact with their antigen mainly via their CDR3 region, and to a lesser extent via the germline-encoded CDR1 and CDR2 (43), we chose clones that were unique in their CDR3. A detailed comparison of the nanobody clones based on sequence similarity in the framework and CDR regions is described in the caption of Figure 1.

Relevant VHH sequences were subcloned into a pHEN6 expression vector to encode a VHH product with C-terminal modifications, so that each VHH sequence included an LPETG motif at its C-terminus, recognized by sortase A, and a $(His)_6$-tag to facilitate recovery and purification (Figure 1). This arrangement enables the installation of fluorophores, biotin, and other substituents by a site-specific and efficient sortase-catalyzed transpeptidation reaction (41). Because the LPETG sequence is cleaved during transpeptidation, the $(His)_6$-tag immediately C-terminal of the LPETG motif is lost. This allows enrichment of the desired modified product by depletion of His-tagged sortase and

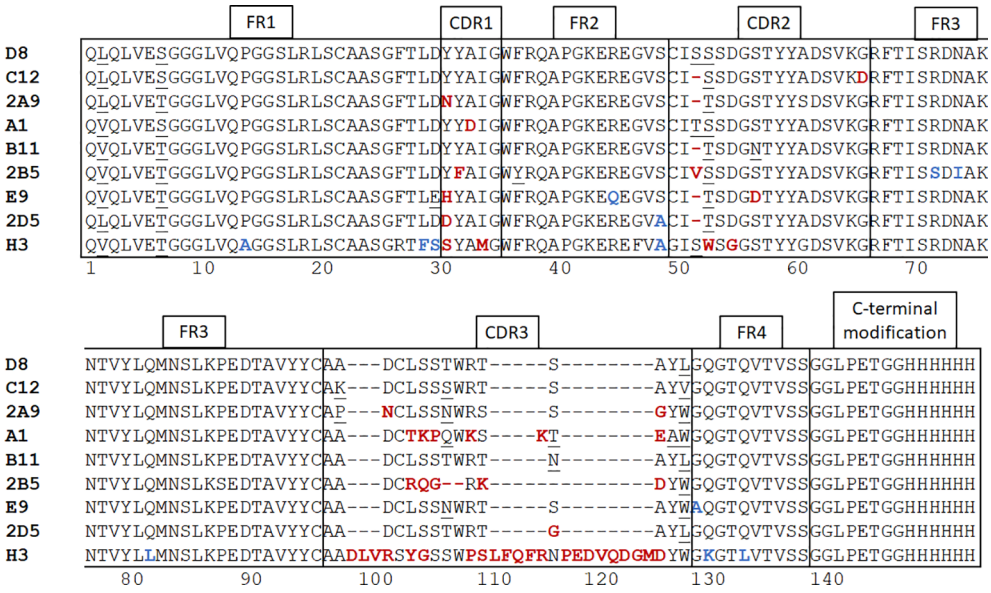

FIGURE 1
Alpaca immunization and nanobody panning. After construction of a phage display library and screening for positive clones with plate-based panning, nanobody sequences were determined and 9 unique clones were selected. Neutral amino acid substitutions attributable to somatic hypermutations are underscored. Unique substitutions in framework regions are highlighted in blue and in CDR's are highlighted in red. Nanobodies harboring such mutations are more likely derived from different germline V regions rather than somatic hypermutation. The framework regions of nanobodies D8 and C12 are identical. The alpaca IGHHV-3-3*01 gene is the possible germline version of these nanobodies (44). The single difference of VHH A1 with D8 and C12 in its framework regions is an L2V substitution. A1 may thus be derived from the same germline V gene as D8 and C12 by a single (somatic) point mutation. The framework regions of nanobodies 2A9 and 2D5 are mostly identical to each other, with a single S49A substitution between them. Nanobody E9 has both a D29E and a R45Q substitution, indicating that E9 may be derived from a different V gene. In comparison with the other MICA-specific nanobodies, H3 has the largest number of differences in its framework regions and is clearly derived from a different germline V gene, likely the alpaca IGHHV3-1*01 (44). The CDR1 and CDR2 regions are mostly conserved. The most obvious deviation is a deletion at position 53 in VHH C12, B11, 2A9, 2D5, and E9. The MICA-specific nanobodies have CDR3 regions of 13-16 amino acids, but H3 has a 31-residue CDR3. Except for VHH H3, A1 and 2B5, the remaining CDR3 regions are enriched for the sequence "AxDCLSSxWRx". The VHH sequences were subcloned into the pHen6 expression vector and modified at the C-terminus to contain an LPETG motif and $(His)_6$ tag.

unreacted nanobody on a NiNTA matrix, while the unbound fraction contains the modified nanobody.

3.2 Nanobodies recognize recombinant MICA and surface-exposed MICA on cancer cells

To determine whether the isolated MICA-specific nanobodies recognized similar or distinct epitopes on MICA, we performed cross-competition experiments by ELISA. Competition of unlabeled nanobodies with a biotinylated nanobody for binding to MICA showed that this set of nanobodies recognizes two distinct epitopes, one defined by the H3 nanobody and the second by all the other nanobodies. None of the nanobodies compete for binding with the 7C6 monoclonal antibody, an agent that inhibits shedding of MICA (45) (Figure 2A). Typically, not all nanobodies are suitable for use in immunoblotting experiments, but the biotinylated versions of A1 and H3 yielded a strong and specific signal in immunoblots on recombinant MICA (Figure 2B). The binding affinities of VHH-A1 and VHH-H3 are both in the nanomolar range, at ~0.2 and ~0.4 nM for A1 and H3 respectively (Figure 2C), as estimated by ELISA assay. By examining the binding of the A1 and H3 nanobodies to a subset of MICA/B allelic products, available in purified form, we conclude that the A1 and H3 nanobodies recognize the MICA*008 and MICA*009 alleles (Figure 2D) which, combined, cover 51.1% of the Caucasian population (46). To verify that A1 and H3 also recognize surface-disposed MICA, we used B16F10 transfectants that express MICA*009, and EL-4 transfectants that express MICA*008, with B16F10 and EL-4 wild type cells serving as negative controls. Both A1 and H3 showed excellent staining of the MICA transfectants by flow cytometry and yielded no signal for the untransfected parental cell lines (Figure 2E) with a significant difference determined by mean fluorescence intensity (MFI) (Figure 2F). Gating strategies are shown in Supplementary Figure 4.

3.3 Anti-MICA nanobodies fused to Maytansine (DM1) for targeted cytotoxicity of $MICA^+$ cancer cells

The reactivity of VHH-A1 and VHH-H3 make them appealing candidates for the construction of nanobody-drug conjugates. To test this, we ligated the Maytansine derivative DM1, a microtubule disrupting agent, to VHH-A1 or to a VHH that targets mouse MHC-II ($VHH_{MHC\text{-}II}$) (47) as a negative control via a sortase-mediated transpeptidation reaction (Figure 3A) and confirmed successful ligation with SDS-PAGE (Figure 3B). We performed an *in*

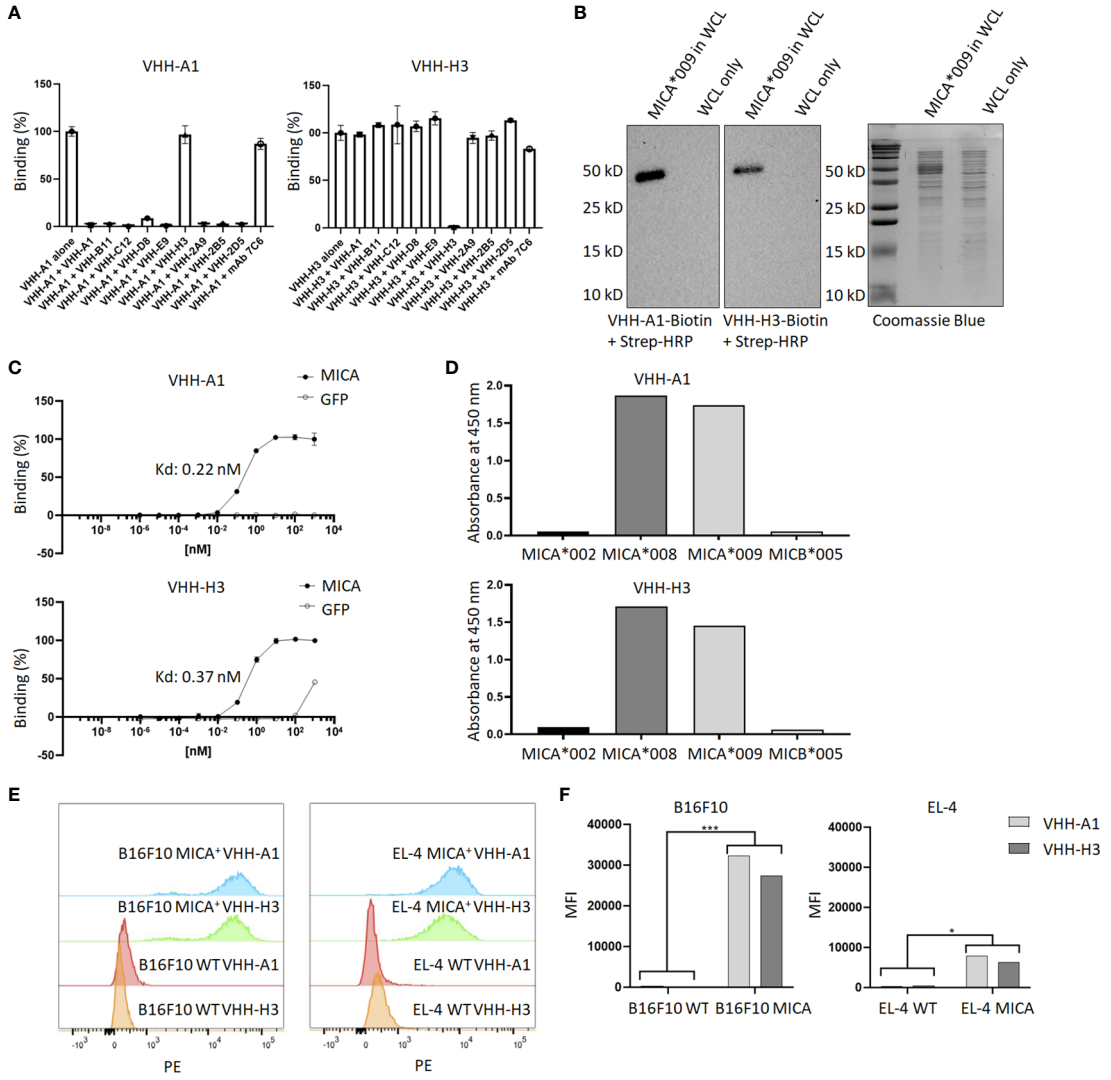

FIGURE 2
Characterization of MICA-specific VHHs. **(A)** Cross-competition ELISA shows that VHH-A1 and VHH-H3 recognize distinct epitopes on MICA. Neither VHH cross-competes for binding with the monoclonal antibody 7C6. **(B)** VHH-A1 and VHH-H3 recognize MICA in immunoblot. 500 ng recombinant MICA*009 in non-specific *E. coli* whole cell lysate (WCL) was separated by SDS-PAGE and transferred to a PVDF membrane. Blots were stained with 1 µg/mL biotinylated VHH-A1 or VHH-H3 respectively. Detection with strep-HRP (0.3 ng/mL) shows a clear signal for both VHHs. **(C)** Binding affinity as estimated by ELISA coated with 2.5 µg/mL recombinant MICA*009, or GFP as the negative control. Estimated Kd values are 0.22 nM and 0.37 nM for VHH-A1 and VHH-H3 respectively. **(D)** ELISA coated with different recombinant MICA alleles shows that VHH-A1 and VHH-H3 both recognize MICA*008 and MICA*009. **(E)** Flow cytometry with biotinylated VHH-A1 and VHH-H3, using streptavidin-conjugated PE as secondary agent, shows a clear signal in the PE channel for MICA$^+$ EL-4 and B16F10 cells, but not for the WT cells, indicating recognition of membrane-disposed MICA on the surface of cells by both nanobodies. Gating strategies for flow cytometry are shown in Supplementary Figure 4. **(F)** We calculated the MFI after flow cytometry. The MFI of B16F10 WT cells was 394 for VHH-A1 and 299 for VHH-H3. The MFI of B16F10 MICA$^+$ cells was 23430 for VHH-A1 and 27411 for VHH-H3. The MFI of EL-4 WT was 310 for VHH-A1 and 511 for VHH-H3. MFI of EL-4 MICA$^+$ cells was 7955 for VHH-A1 and 6417 for VHH-H3. We averaged the MFI from the WT or MICA$^+$ cells and determined a significant difference in nanobody staining of WT versus MICA$^+$ cells ($p = 0.00713$ for B16F10; $p = 0.0128$ for EL-4, calculated by multiple T-test).

vitro cytotoxicity assay by titration of $VHH_{MHC\text{-}II}$-DM1, VHH_{A1}-DM1, or free DM4 (a functional analog of DM1) on EL-4 WT and MICA$^+$ cells. EL-4 MICA$^+$ cells were sensitive to VHH_{A1}-DM1, with a stronger cytotoxic effect at lower doses of the VHH-drug conjugate compared to $VHH_{MHC\text{-}II}$-DM1, as estimated by IC50. The IC50 of VHH_{A1}-DM1 treated EL-4 MICA$^+$ cells was comparable to that of cells treated with free DM4. Similarly treated WT cells showed no obvious reduction in viability with either nanobody-drug conjugate (Figure 3C).

To further validate selectivity of VHH_{A1}-DM1 for MICA$^+$ cells, we co-cultured EL-4 WT and EL-4 MICA$^+$ cells at a 1:1 ratio, and added VHH_{MHCII}-DM1, VHH_{A1}-DM1, or free DM4 at different concentrations. We determined the ratio of viable EL-4 WT and EL-4 MICA$^+$ cells after 72 hours by flow cytometry using a live/dead cell stain. We stained the MICA$^+$ cells in the co-culture with a biotinylated αMICA mAb, using streptavidin-conjugated PE as secondary reagent. Gating on live cells and MICA$^+$ cells showed specific elimination of MICA$^+$ cells at adduct concentrations between 1.71 nM and 416 nM for VHH_{A1}-DM1. A difference in ratio between WT and MICA$^+$ cells was not observed in cells treated with VHH_{MHCII}-DM1 or free DM4. Because WT cells proliferate slightly faster than MICA$^+$ cells in culture,

10.3389/fimmu.2024.1368586

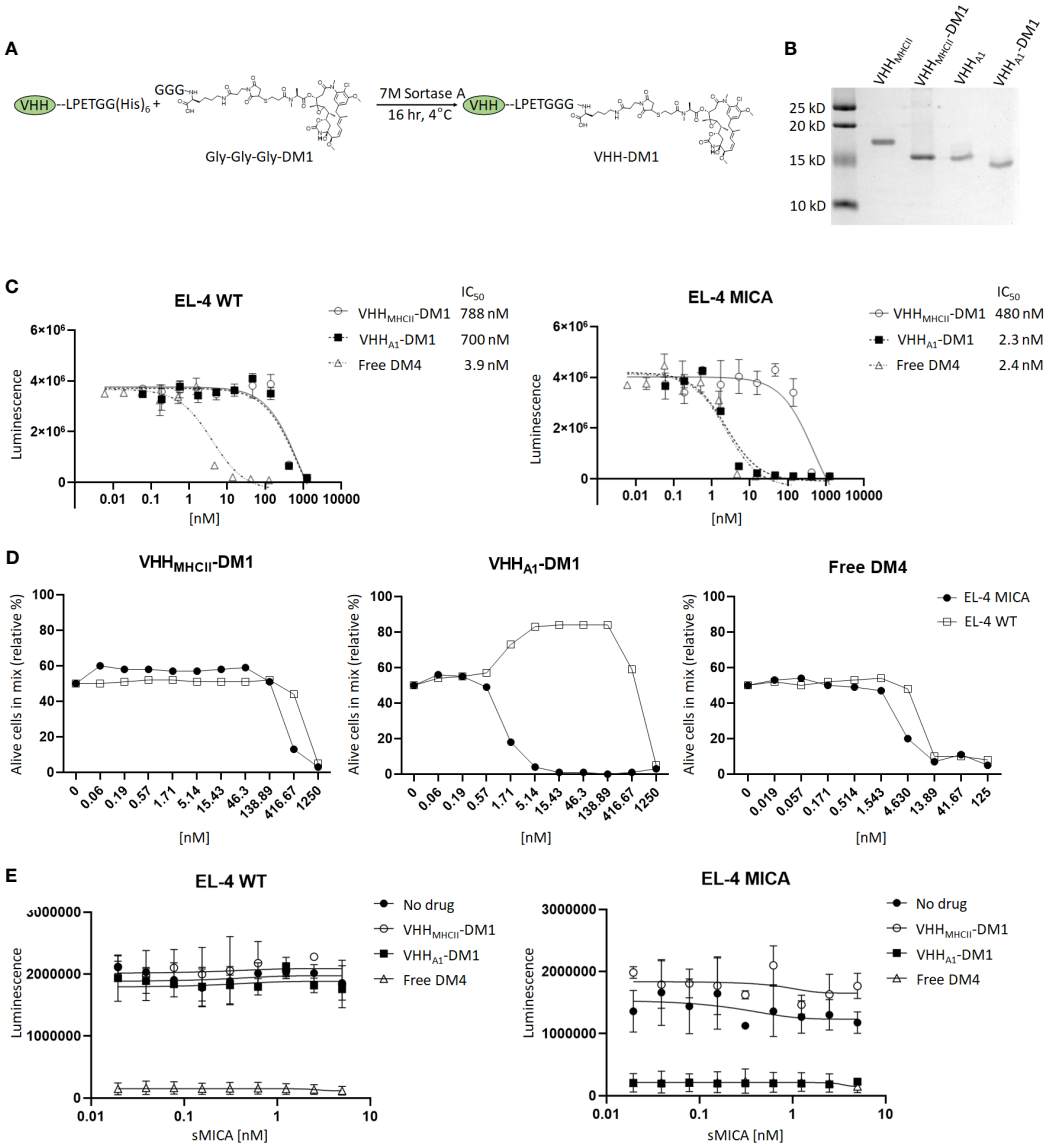

FIGURE 3
Anti-MICA VHHs as nanobody-drug conjugate with the Maytansine derivative DM1. **(A)** We ligated the microtubule inhibitor Maytansine GGG-DM1 to VHH-A1 or VHH_{MHC-II} as non-targeting control through sortase-mediated transpeptidase reaction. **(B)** Because GGG-DM1 has a slight positive charge, the modified VHHs will migrate slightly lower on the SDS-PAGE gel compared to the unmodified VHHs. **(C)** The *in vitro* cytotoxicity assay was performed with limited dilutions of VHH_{MHC-II}-DM1, VHH_{A1}-DM1, or free DM4 on EL-4 WT cells and their $MICA^+$ counterparts. After incubation for 72 hours, we measured cell viability by CellTiter Glo™ assay. $MICA^+$ cells treated with VHH_{A1}-DM1 showed a significant reduction in IC_{50}, and thus a reduction in viability with smaller amounts of drug added, compared to similarly treated WT cells, or cells treated with the non-targeting VHH_{MHCII}-DM1. **(D)** We co-cultured EL-4 WT and EL-4 $MICA^+$ cells at a 1:1 ratio and added VHH_{MHCII}-DM1, VHH_{A1}-DM1, or free DM4 at different concentrations. Viability of EL-4 WT and $MICA^+$ cells was determined using a live/dead cell stain. $MICA^+$ cells were stained with a biotinylated anti-MICA mAb, using streptavidin-PE as secondary agent. Gating on live cells and PE showed elimination of $MICA^+$ cells at VHH-drug adduct concentrations between 1.71 nM and 416 nM for VHH_{A1}-DM1. A difference in [WT : MICA] was not observed in cells treated with VHH_{MHCII}-DM1 or free DM4. Gating strategies for flow cytometry are shown in Supplementary Figure 5. **(E)** We incubated EL-4 WT and $MICA^+$ cells with 2.5 nM of VHH_{MHCII}-DM1, VHH_{A1}-DM1, or free DM4 in the presence of sMICA (two-fold dilutions; 0-5 nM/0-170 ng/mL) for 72 hours. We measured viability by CellTiter Glo™ assay. We did not observe a decreased effect on cytotoxicity of VHHA1-DM1 on $MICA^+$ cells with addition of sMICA in the medium.

the distribution shifted to ~65% WT and 35% $MICA^+$ cells after 72 hours in culture. Thus, numbers were normalized according to the percentage of cells of either line in the untreated ("0 nM") group (Figure 3D). Gating strategies are shown in Supplementary Figure 5.

Tumor cells can downregulate surface expression of MICA through shedding, mediated by proteolytic cleavage at the α3 domain. Increased levels of soluble MICA (sMICA) in the serum of patients are associated with poor prognosis and worse disease progression (10, 48–50). To address the possible competition of sMICA for binding with the anti-MICA nanobody, we performed an *in vitro* cytotoxicity assay. EL-4 WT and $MICA^+$ cells were incubated with VHH_{MHCII}-DM1, VHH_{A1}-DM1, or free DM4 at a fixed concentration of 2.5 nM, in the presence of sMICA at various concentrations (serial 2-fold dilutions; 0-5 nM/0-170 ng/mL). We

observed no reduction in cytotoxicity of VHH_{A1}-DM1 on $MICA^+$ cells upon addition of sMICA to the medium (Figure 3E). Publications report concentrations of sMICA in the serum of $MICA^+$ patients in the range of 0.1-15 ng/mL (51–53) which is at least 10-fold lower than the sMICA concentration in our competition assay. We thus expect little to no impact of sMICA in patients' serum on the ability of these nanobodies to target membrane-bound MICA *in vivo*.

4 Discussion

MICA and MICB are Class I MHC-related proteins expressed on stressed and cancerous cells. Their presence can serve not only as a diagnostic marker but may also be exploited as a target for therapy. While the typical immunoglobulins exert their functional properties through Fc effector functions, their size compromises efficient tissue penetration. Nanobodies offer an appealing alternative to immunoglobulins for the purpose of launching an immune attack on MICA-positive tumors. Nanobodies are characterized by their small size, showing superior tissue penetration compared to intact immunoglobulins, and ease of production and modification (14, 15, 17, 18). Lastly, nanobodies are poorly immunogenic, presumably because of their considerable sequence homology with human V_H regions (44). Because nanobodies lack an Fc portion, for them to exert cytotoxic activity they require functionalization, for example with a cytotoxic drug creating a nanobody-drug conjugate, as done here for the VHH-DM1 adducts. Compared to antibody-drug conjugates using conventional immunoglobulins, the small size of the nanobody allows superior penetration into tumor tissue. Furthermore, owing to the relatively short circulatory half-life, the nanobody-drug conjugate that is not bound to its target will be eliminated more quickly from the circulation, resulting in less systemic cytotoxicity by slow release of the drug attached to the antibody-drug conjugate.

We produced and characterized in further detail two nanobodies, A1 and H3, that recognize the MICA alleles *008 and *009 with nM affinities. An analysis of the MICA-specific nanobodies shows that they are unique sequences, thus the isolated nanobodies were likely derived from a few different germline V genes (see Figure 1 and legend). The germline sequences of the V genes of the (outbred) alpaca used for immunization are not known. We can only compare the sequences of the MICA-specific nanobodies with each other, and with reference germline sequences from unrelated alpacas.

The alpaca IGHHV-3-3*01 gene is the possible germline version of the D8 and C12 nanobodies (44). The single difference of VHH A1 with D8 and C12 in its framework regions is an L2V substitution, thus A1 may be derived from the same germline V gene as D8 and C12 by somatic mutation. Nanobody E9 has a D29E and an R45Q substitution, indicating that E9 may be derived from a different V gene. In comparison with the other MICA-specific nanobodies, H3 has the largest number of differences in its framework regions and is clearly derived from a different germline V gene, likely the alpaca IGHHV3-1*01 (44).

Highly similar CDR regions, specifically CDR3, imply recognition of related antigens (54–57). For the MICA-specific nanobodies, the CDR1 and CDR2 regions are mostly conserved. The most obvious deviation in the CDR2 region is a deletion at position 53 in VHH C12, B11, 2A9, 2D5, and E9. Somatic hypermutation can produce deletions and insertions in V genes (58–60) but given the overall similarity in framework regions, the use of a distinct V gene that lacks residue 53 is the more plausible explanation. Except for H3, A1 and 2B5, the remaining CDR3 regions are enriched for the sequence "AxDCLSSxWRx".

We show that these nanobodies bind to surface-disposed MICA on cells and can thus be used for diagnostic and therapeutic purposes. The specific targeting of $MICA^+$ cells make them suitable candidates as diagnostic markers, as building blocks for nanobody-drug conjugate, or for the construction of chimeric antigen receptors (29, 30, 37, 61). MICA and MICB are highly polymorphic in the human population, with hundreds of alleles for MICA and MICB identified so far (46, 62). The isolated nanobodies were tested for recognition of the MICA alleles *002, *008 and *009, and MICB allele *005. Of the tested alleles, the nanobodies recognize MICA*008 and MICA*009, which together cover over 50% of the investigated German population (46). Expanding the nanobody pool to cover a larger portion of the alleles of MICA and MICB should be considered. We recognize the limitations of using a $MICA^+$ cell line obtained by transfection. The availability of a suitable patient-derived cell line that expresses the correct alleles of MICA is a limiting factor, an issue worth exploring in future research.

We created a nanobody-drug conjugate by conjugating the microtubule inhibitor DM1 to VHH-A1. We show increased cytotoxicity of $MICA^+$ tumor cells compared to WT tumor cells *in vitro*, with efficacy comparable to that of free drug but with much higher specificity for $MICA^+$ cells. The production of these nanobody adducts should be scaled up for testing on *in vivo* tumor models. The creation of different VHH-drug combinations, for example by inclusion of DNA damaging agents or other cytotoxic drugs (63, 64), or even radiopharmaceuticals for targeted radiotherapy (65, 66), deserves consideration as well.

Cleavage of the α3 domain involving the disulphide isomerase ERp5 and ADAM-type proteases such as ADAM10 and ADAM17 (48–50, 67, 68), and thus shedding of the MICA/B from the cancer cell surface, may lead to immune evasion and failure to be recognized by NKG2D-positive cytotoxic cells. The monoclonal antibody 7C6 inhibits the shedding of MICA/B, and thus increases the density of MICA/B proteins on the surface of tumor cells (45) Although we saw no reduction in efficacy of VHH_{A1}-DM1 on $MICA^+$ cells upon addition of sMICA to the medium, the combination of anti-MICA nanobody adducts with the 7C6 antibody might therefore be therapeutically more attractive than either treatment alone.

Data availability statement

The datasets presented in this study can be found in online repositories. The names of the repository/repositories and accession number(s) can be found below: 10.6084/m9.figshare.25289806.

Ethics statement

The animal study was approved by IACUC University of Massachusetts Amherst. The study was conducted in accordance with the local legislation and institutional requirements.

Author contributions

EV: Writing – original draft, Visualization, Validation, Supervision, Methodology, Investigation, Formal analysis, Data curation, Conceptualization. AK: Writing – review & editing, Investigation, Data curation. NP: Writing – review & editing, Resources, Investigation. XL: Writing – review & editing, Resources. WvK: Writing – review & editing, Investigation. KW: Writing – review & editing, Resources. HP: Writing – review & editing, Writing – original draft, Supervision, Project administration, Funding acquisition, Conceptualization.

Funding

The author(s) declare that financial support was received for the research, authorship, and/or publication of this article. This research was supported by the NIH Pioneer Grant (DP1AI150593-05) to HP and an R01 from NCI (CA238039) to KW.

Acknowledgments

We gratefully acknowledge Dr. Thomas Balligand for helpful discussions.

Conflict of interest

Author KW serves on the scientific advisory boards of DEM BioPharma, Solu Therapeutics, D2M Biotherapeutics and Nextechinvest. He is a co-founder of Immunitas Therapeutics and receives sponsored research funding from Novartis and Fate Therapeutics.

The remaining authors declare that the research was conducted in the absence of any commercial or financial relationships that could be construed as a potential conflict of interest.

Publisher's note

Supplementary material

The Supplementary Material for this article can be found online at: https://www.frontiersin.org/articles/10.3389/fimmu.2024.1368586/full#supplementary-material

References

1. Agaugue S, Hargreaves A, De Sousa P, De Waele P, Gilham D. The high expression of NKG2D ligands on tumor and the lack of surface expression on healthy tissues provides a strong rationale to support NKG2D-based therapeutic approaches for cancer. *Ann Oncol.* (2018) 29:viii420. doi: 10.1093/annonc/mdy288.052

2. Bauer S, Groh V, Wu J, Phillips JH, Lanier LL, Spies T. Activation of NK cells and T cells by NKG2D, a receptor for stress-inducible MICA. *Sci (1979).* (1999) 285:727–9. doi: 10.1126/science.285.5428.727

3. Fuertes MB, Domaica CI, Zwirner NW. Leveraging NKG2D ligands in immuno-oncology. *Front Immunol.* (2021) 12:713158. doi: 10.3389/fimmu.2021.713158

4. Zingoni A, Molfetta R, Fionda C, Soriani A, Paolini R, Cippitelli M, et al. NKG2D and its ligands: "One for all, all for one." *Front Immunol.* (2018) 9:476. doi: 10.3389/fimmu.2018.00476

5. Raulet DH, Gasser S, Gowen BG, Deng W, Jung H. Regulation of ligands for the NKG2D activating receptor. *Annu Rev Immunol.* (2013) 31:413–41. doi: 10.1146/annurev-immunol-032712-095951

6. McGilvray RW, Eagle RA, Watson NFS, Al-Attar A, Ball G, Jafferji I, et al. NKG2D ligand expression in human colorectal cancer reveals associations with prognosis and evidence for immunoediting. *Clin Cancer Res.* (2009) 15:6993–7002. doi: 10.1158/1078-0432.CCR-09-0991

7. Li K, Mandai M, Hamanishi J, Matsumura N, Suzuki A, Yagi H, et al. Clinical significance of the NKG2D ligands, MICA/B and ULBP2 in ovarian cancer: high expression of ULBP2 is an indicator of poor prognosis. *Cancer Immunology Immunotherapy.* (2009) 58:641–52. doi: 10.1007/s00262-008-0585-3

8. Cho H, Chung JY, Kim S, Braunschweig T, Kang TH, Kim J, et al. MICA/B and ULBP1 NKG2D ligands are independent predictors of good prognosis in cervical cancer. *BMC Cancer.* (2014) 14:1–11. doi: 10.1186/1471-2407-14-957

9. de Kruijf EM, Sajet A, van Nes JG, Putter H, THBM Smit V, Eagle RA, et al. NKG2D ligand tumor expression and association with clinical outcome in early breast cancer patients: an observational study (2012). Available online at: http://www.biomedcentral.com/1471-2407/12/24.

10. Chen J, Xu H, Zhu XX. Abnormal expression levels of sMICA and NKG2D are correlated with poor prognosis in pancreatic cancer. *Ther Clin Risk Manag.* (2015) 12:11–8. doi: 10.2147/TCRM.S96869

11. Vetter CS, Groh V, thor Straten P, Spies T, Brocker E-B, Becker JC. Expression of stress-induced MHC class I related chain molecules on human melanoma. *J Invest Dermatol.* (2002) 118:600–5. doi: 10.1046/j.1523-1747.2002.01700.x

12. Tsukagoshi M, Wada S, Yokobori T, Altan B, Ishii N, Watanabe A, et al. Overexpression of natural killer group 2 member D ligands predicts favorable prognosis in cholangiocarcinoma. *Cancer Sci.* (2016) 107:116–22. doi: 10.1111/cas.12853

13. Hamers-Casterman C, Atarhouch T, Muyldermans S, Robinson G, Hammers C, Bajyana Songa E, et al. Naturally occurring antibodies devoid of light chains. *Nature1.* (1993) 363:446–8.

14. Fang T, Lu X, Berger D, Gmeiner C, Cho J, Schalek R, et al. Nanobody immunostaining for correlated light and electron microscopy with preservation of ultrastructure. *Nat Methods.* (2018) 15:1029–32. doi: 10.1016/j.physbeh.2017.03.040

15. Tijink BM, Laeremans T, Budde M, Stigter-Van Walsum M, Dreier T, De Haard HJ, et al. Improved tumor targeting of anti-epidermal growth factor receptor Nanobodies through albumin binding: Taking advantage of modular Nanobody technology. *Mol Cancer Ther.* (2008) 7:2288–97. doi: 10.1158/1535-7163.MCT-07-2384

16. Kijanka M, Dorresteijn B, Oliveira S, Van Bergen En Henegouwen PMP. Nanobody-based cancer therapy of solid tumors. *Nanomedicine.* (2015) 10:161–74. doi: 10.2217/nnm.14.178

17. Van Der Linden RHJ, Frenken LGJ, De Geus B, Harmsen MM, Ruuls RC, Stok W, et al. Comparison of physical chemical properties of llama VHH antibody fragments and mouse monoclonal antibodies. *Biochim Biophys Acta.* (1999) 1431:37–46. doi: 10.1016/S0167-4838(99)00030-8

18. Tanha J, Xu P, Chen Z, Ni F, Kaplan H, Narang SA, et al. Optimal design features of camelized human single-domain antibody libraries. *J Biol Chem.* (2001) 276:24774–80. doi: 10.1074/jbc.M100770200

19. Rashidian M, Keliher EJ, Dougan M, Juras PK, Cavallari M, Wojtkiewicz GR, et al. Use of 18F-2-fluorodeoxyglucose to label antibody fragments for immuno-positron emission tomography of pancreatic cancer. *ACS Cent Sci.* (2015) 1:142–7. doi: 10.1021/acscentsci.5b00121

20. Ingram JR, Dougan M, Rashidian M, Knoll M, Keliher EJ, Garrett S, et al. PD-L1 is an activation-independent marker of brown adipocytes. *Nat Commun.* (2017) 8:1–15. doi: 10.1038/s41467-017-00799-8

21. Rashidian M, LaFleur MW, Verschoor VL, Dongre A, Zhang Y, Nguyen TH, et al. Immuno-PET identifies the myeloid compartment as a key contributor to the outcome of the antitumor response under PD-1 blockade. *PNAS.* (2019) 116:16971–80. doi: 10.1073/pnas.1905005116

22. Van Elssen CHMJ, Rashidian M, Vrbanac V, Wucherpfennig KW, El Habre Z, Sticht J, et al. Noninvasive imaging of human immune responses in a human xenograft

model of graft-versus-host disease. *J Nucl Med*. (2017) 58:1003–8. doi: 10.2967/jnumed.116.186007

23. Jailkhani N, Ingram JR, Rashidian M, Rickelt S, Tian C, Mak H, et al. Noninvasive imaging of tumor progression, metastasis, and fibrosis using a nanobody targeting the extracellular matrix. *PNAS*. (2019) 116:14181–90. doi: 10.1073/pnas.1817442116

24. Fang T, Van Elssen CHMJ, Duarte JN, Guzman JS, Chahal JS, Ling J, et al. Targeted antigen delivery by an anti-class II MHC VHH elicits focused αmUC1(Tn) immunity. *Chem Sci*. (2017) 8:5591–7. doi: 10.1039/c7sc00446j

25. Altintas I, Heukers R, van der Meel R, Lacombe M, Amidi M, Van Bergen En Henegouwen PMP, et al. Nanobody-albumin nanoparticles (NANAPs) for the delivery of a multikinase inhibitor 17864 to EGFR overexpressing tumor cells. *J Controlled Release*. (2013) 165:110–8. doi: 10.1016/j.jconrel.2012.11.007

26. Fang T, Duarte JN, Ling J, Li Z, Guzman JS, Ploegh HL. Structurally-defined αMHC-II nanobody-drug conjugates: Therapeutic and imaging platforms for B-cell lymphoma. *Angewandte Chemie Int Edition*. (2016) 55:2416–20. doi: 10.1016/j.pep.2015.11.007.Simple

27. Bachran C, Schröder M, Conrad L, Cragnolini JJ, Tafesse FG, Helming L, et al. The activity of myeloid cell-specific VHH immunotoxins is target-, epitope-, subset- and organ dependent. *Sci Rep*. (2017) 7:2–11. doi: 10.1038/s41598-017-17948-0

28. Hajari Taheri F, Hassani M, Sharifzadeh Z, Behdani M, Arashkia A, Abolhassani M. T cell engineered with a novel nanobody-based chimeric antigen receptor against VEGFR2 as a candidate for tumor immunotherapy. *IUBMB Life*. (2019) 71:1259–67. doi: 10.1002/iub.2019

29. De Munter S, Ingels J, Goetgeluk G, Bonte S, Pille M, Weening K, et al. Nanobody based dual specific CARs. *Int J Mol Sci*. (2018) 19:1–11. doi: 10.3390/ijms19020403

30. Xie YJ, Dougan M, Jailkhani N, Ingram J, Fang T, Kummer L, et al. Nanobody-based CAR T cells that target the tumor microenvironment inhibit the growth of solid tumors in immunocompetent mice. *PNAS*. (2019) 116:7624–31. doi: 10.1073/pnas.1817147116

31. Xie YJ, Dougan M, Ingram JR, Pishesha N, Fang T, Momin N, et al. Improved antitumor efficacy of chimeric antigen receptor T cells that secrete single-domain antibody fragments. *Cancer Immunol Res*. (2020) 8:518–30. doi: 10.1158/2326-6066.CIR-19-0734

32. You F, Wang Y, Jiang L, Zhu X, Chen D, Yuan L, et al. A novel CD7 chimeric antigen receptor-modified NK-92MI cell line targeting T-cell acute lymphoblastic leukemia. *Am J Cancer Res*. (2019) 9:64–78.

33. Hambach J, Riecken K, Cichutek S, Schütze K, Albrecht B, Petry K, et al. Targeting CD38-expressing multiple myeloma and burkitt lymphoma cells *in vitro* with nanobody-based chimeric antigen receptors (Nb-CARs). *Cells*. (2020) 9:1–14. doi: 10.3390/cells9020321

34. Rajabzadeh A, Ahmadvand D, Salmani MK, Rahbarizadeh F, Hamidieh AA. A VHH-based anti-MUC1 chimeric antigen receptor for specific retargeting of human primary T cells to MUC1-positive cancer cells. *Cell J*. (2021) 22:502–13. doi: 10.22074/cellj.2021.6917

35. Jamnani FR, Rahbarizadeh F, Shokrgozar MA, Mahboudi F, Ahmadvand D, Sharifzadeh Z, et al. T cells expressing VHH-directed oligoclonal chimeric HER2 antigen receptors: Towards tumor-directed oligoclonal T cell therapy. *Biochim Biophys Acta (BBA) - Gen Subj*. (2014) 1840:378–86. doi: 10.1016/j.bbagen.2013.09.029

36. Rahbarizadeh F, Ahmadvand D, Moghimi S. CAR T-cell bioengineering: Single variable domain of heavy chain antibody targeted CARs. *Adv Drug Delivery Rev*. (2019) 141:41–6. doi: 10.1016/j.addr.2019.04.006

37. Bao C, Gao Q, Li LL, Han L, Zhang B, Ding Y, et al. The application of nanobody in CAR-T therapy. *Biomolecules*. (2021) 11:1–18. doi: 10.3390/biom11020238

38. Zajc CU, Salzer B, Taft JM, Reddy ST, Lehner M, Traxlmayr MW. Driving CARs with alternative navigation tools – the potential of engineered binding scaffolds. *FEBS J*. (2021) 288:2103–18. doi: 10.1111/febs.15523

39. Badrinath S, Dellacherie MO, Li A, Zheng S, Zhang X, Sobral M, et al. A vaccine targeting resistant tumours by dual T cell plus NK cell attack. *Nature*. (2022) 606:992–8. doi: 10.1038/s41586-022-04772-4

40. Pardon E, Laeremans T, Triest S, Rasmussen SGF, Wohlkönig A, Ruf A, et al. A general protocol for the generation of Nanobodies for structural biology. *Nat Protoc*. (2014) 9:674–93. doi: 10.1038/nprot.2014.039

41. Jeong HJ, Abhiraman GC, Story CM, Ingram JR, Dougan SK. Generation of Ca2+-independent sortase A mutants with enhanced activity for protein and cell surface labeling. *PloS One*. (2017) 12:1–10. doi: 10.1371/journal.pone.0189068

42. Beatty JD, Beatty BG, Vlahos WG. Measurement of monoclonal antibody affinity by non-competitive enzyme immunoassay. *J Immunol Methods*. (1987) 100:173–9. doi: 10.1016/0022-1759(87)90187-6

43. Truong TTT, Huynh VQ, Vo NT, Nguyen HD. Studying the characteristics of nanobody CDR regions based on sequence analysis in combination with 3D structures. *J Genet Eng Biotechnol*. (2022) 20:1–13. doi: 10.1186/s43141-022-00439-9

44. Klarenbeek A, El Mazouari K, Desmyter A, Blanchetot C, Hultberg A, de Jonge N, et al. Camelid Ig V genes reveal significant human homology not seen in therapeutic target genes, providing for a powerful therapeutic antibody platform. *MAbs*. (2015) 7:693–706. doi: 10.1080/19420862.2015.1046648

45. De Andrade LF, En Tay R, Pan D, Luoma AM, Ito Y, Badrinath S, et al. Antibody-mediated inhibition of MICA and MICB shedding promotes NK cell-driven tumor immunity. *Sci (1979)*. (2018) 359:1537–42. doi: 10.1126/science.aao0505

46. Klussmeier A, Massalski C, Putke K, Schäfer G, Sauter J, Schefzyk D, et al. High-throughput MICA/B genotyping of over two million samples: workflow and allele frequencies. *Front Immunol*. (2020) 11:314. doi: 10.3389/fimmu.2020.00314

47. Fang T, Duarte JN, Ling J, Li Z, Guzman JS, Ploegh HL. Structurally defined αMHC-II nanobody-drug conjugates: A therapeutic and imaging system for B-cell lymphoma. *Angewandte Chemie - Int Edition*. (2016) 55:2416–20. doi: 10.1002/anie.201509432

48. Kaiser BK, Yim D, Chow I-T, Gonzales S, Dai Z, Mann HH, et al. Disulphide-isomerase-enabled shedding of tumour-associated NKG2D ligands. *Nature*. (2007) 447:482–6. doi: 10.1038/nature05768

49. Salih HR, Rammensee H-G, Steinle A. Cutting edge: down-regulation of MICA on human tumors by proteolytic shedding. *J Immunol*. (2002) 169:4098–102. doi: 10.4049/jimmunol.169.8.4098

50. Xing S, Ferrari de Andrade L. NKG2D and MICA/B shedding: a 'tag game' between NK cells and Malignant cells. *Clin Transl Immunol*. (2020) 9:1–10. doi: 10.1002/cti2.1230

51. Hervier B, Ribon M, Tarantino N, Mussard J, Breckler M, Vieillard V, et al. Increased concentrations of circulating soluble MHC class I-related chain A (sMICA) and sMICB and modulation of plasma membrane MICA expression: potential mechanisms and correlation with natural killer cell activity in systemic lupus erythematosus. *Front Immunol*. (2021) 12:633658. doi: 10.3389/fimmu.2021.633658

52. Li JJ, Pan K, Gu MF, Chen MS, Zhao JJ, Wang H, et al. Prognostic value of soluble MICA levels in the serum of patients with advanced hepatocellular carcinoma. *Chin J Cancer*. (2013) 32:141–8. doi: 10.5732/cjc.012.10025

53. Arai J, Otoyama Y, Fujita K, Goto K, Tojo M, Katagiri A, et al. Baseline soluble MICA levels act as a predictive biomarker for the efficacy of regorafenib treatment in colorectal cancer. . *BMC Cancer*. (2022) 22:1–10. doi: 10.1186/s12885-022-09512-5

54. Henry Dunand CJ, Wilson PC. Restricted, canonical, stereotyped and convergent immunoglobulin responses. *Philos Trans R Soc Lond B Biol Sci*. (2015) 370:1–8. doi: 10.1098/rstb.2014.0238

55. Tian C, Hromatka BS, Kiefer AK, Eriksson N, Noble SM, Tung JY, et al. Genome-wide association and HLA region fine-mapping studies identify susceptibility loci for multiple common infections. *Nat Commun*. (2017) 8:1–13. doi: 10.1038/s41467-017-00257-5

56. Tsuji I, Vang F, Dominguez D, Karwal L, Sanjali A, Livengood JA, et al. Somatic hypermutation and framework mutations of variable region contribute to anti-zika virus-specific monoclonal antibody binding and function. *J Virol*. (2022) 96:1–18. doi: 10.1128/jvi.00071-22

57. Klein F, Diskin R, Scheid JF, Gaebler C, Mouquet H, Georgiev IS, et al. Somatic mutations of the immunoglobulin framework are generally required for broad and potent HIV-1 neutralization. *Cell*. (2013) 153:126–38. doi: 10.1016/j.cell.2013.03.018

58. Briney BS, Willis JR, Crowe JE. Location and length distribution of somatic hypermutation-associated DNA insertions and deletions reveals regions of antibody structural plasticity. *Genes Immun*. (2012) 13:523–9. doi: 10.1038/gene.2012.28

59. Wilson PC, De Bouteiller O, Liu Y-J, Potter K, Banchereau J, Capra JD, et al. Somatic Hypermutation Introduces Insertions and Deletions into Immunoglobulin V Genes (1998). Available online at: http://www.jem.org.

60. Bemark M, Neuberger MS. By-products of immunoglobulin somatic hypermutation. *Genes Chromosomes Cancer*. (2003) 38:32–9. doi: 10.1002/gcc.10241

61. Albert S, Arndt C, Feldmann R, Bergmann R, Bachmann D, Koristka S, et al. A novel nanobody-based target module for retargeting of T lymphocytes to EGFR-expressing cancer cells via the modular UniCAR platform. *Oncoimmunology*. (2017) 6:1–17. doi: 10.1080/2162402X.2017.1287246

62. Koskela S, Tammi S, Clancy J, Lucas JAM, Turner TR, Hyvarinen K, et al. MICA and MICB allele assortment in Finland. *HLA Immune Response Genet*. (2023) 102:52–61. doi: 10.1111/tan.15023

63. Fuentes-Antrás J, Genta S, Vijenthira A, Siu LL. Antibody–drug conjugates: in search of partners of choice. *Trends Cancer*. (2023) 9:339–54. doi: 10.1016/j.trecan.2023.01.003

64. Fu Y, Ho M. DNA damaging agent-based antibody-drug conjugates for cancer therapy. *Antib Ther*. (2018) 1:43–53. doi: 10.1093/abt/tby007

65. Milenic DE, Brady ED, Brechbiel MW. Antibody-targeted radiation cancer therapy. *Nat Rev Drug Discovery*. (2004) 3:488–98. doi: 10.1038/nrd1413

66. Lin M, Paolillo V, Le DB, Macapinlac H, Ravizzini GC. Monoclonal antibody based radiopharmaceuticals for imaging and therapy. *Curr Probl Cancer*. (2021) 45. doi: 10.1016/j.currproblcancer.2021.100796

67. Liu G, Atteridge CL, Wang X, Lundgren AD, Wu JD. Cutting edge: the membrane type matrix metalloproteinase MMP14 mediates constitutive shedding of MHC class I chain-related molecule A independent of A disintegrin and metalloproteinases. *J Immunol*. (2010) 184:3346–50. doi: 10.4049/jimmunol.0903789

68. Waldhauer I, Goehlsdorf D, Gieseke F, Weinschenk T, Wittenbrink M, Ludwig A, et al. Tumor-associated MICA is shed by ADAM proteases. *Cancer Res*. (2008) 68:6368–76. doi: 10.1158/0008-5472.CAN-07-6768

frontiers | Frontiers in Immunology

TYPE Review
PUBLISHED 29 April 2024
DOI 10.3389/fimmu.2024.1389173

OPEN ACCESS

EDITED BY
Shensi Shen,
Sichuan University, China

REVIEWED BY
Daoming Zhu,
Southern Medical University, China
Joanna Rossowska,
Polish Academy of Sciences, Poland

*CORRESPONDENCE
Leilei Bao
annabao212@126.com
Quangang Zhu
zhuqg@shskin.com
Zongguang Tai
taizongguang@126.com

†These authors have contributed equally to this work

RECEIVED 21 February 2024
ACCEPTED 10 April 2024
PUBLISHED 29 April 2024

CITATION
Wang J, Ma J, Xie F, Miao F, lv L, Huang Y, Zhang X, Yu J, Tai Z, Zhu Q and Bao L (2024) Immunogenic cell death-based cancer vaccines: promising prospect in cancer therapy. *Front. Immunol.* 15:1389173. doi: 10.3389/fimmu.2024.1389173

Immunogenic cell death-based cancer vaccines: promising prospect in cancer therapy

Jiandong Wang[1,2,3,4†], Jinyuan Ma[3,4†], Fangyuan Xie[2†], Fengze Miao[3,4], Lei lv[2], Yueying Huang[2], Xinyue Zhang[3,4], Junxia Yu[1,2,3], Zongguang Tai[3,4*], Quangang Zhu[3,4*] and Leilei Bao[2*]

[1]School of Pharmacy, Bengbu Medical College, Bengbu, Anhui, China, [2]Department of Pharmacy, Third Affiliated Hospital of Naval Medical University, Shanghai, China, [3]Shanghai Skin Disease Hospital, School of Medicine, Tongji University, Shanghai, China, [4]Shanghai Engineering Research Center of External Chinese Medicine, Shanghai, China

Tumor immunotherapy is a promising approach for addressing the limitations of conventional tumor treatments, such as chemotherapy and radiotherapy, which often have side effects and fail to prevent recurrence and metastasis. However, the effectiveness and sustainability of immune activation in tumor immunotherapy remain challenging. Tumor immunogenic cell death, characterized by the release of immunogenic substances, damage associated molecular patterns (DAMPs), and tumor associated antigens, from dying tumor cells (DTCs), offers a potential solution. By enhancing the immunogenicity of DTCs through the inclusion of more immunogenic antigens and stimulating factors, immunogenic cell death (ICD) based cancer vaccines can be developed as a powerful tool for immunotherapy. Integrating ICD nanoinducers into conventional treatments like chemotherapy, photodynamic therapy, photothermal therapy, sonodynamic therapy, and radiotherapy presents a novel strategy to enhance treatment efficacy and potentially improve patient outcomes. Preclinical research has identified numerous potential ICD inducers. However, effectively translating these findings into clinically relevant applications remains a critical challenge. This review aims to contribute to this endeavor by providing valuable insights into the *in vitro* preparation of ICD-based cancer vaccines. We explored established tools for ICD induction, followed by an exploration of personalized ICD induction strategies and vaccine designs. By sharing this knowledge, we hope to stimulate further development and advancement in the field of ICD-based cancer vaccines.

KEYWORDS

immunogenic cell death, cancer vaccine, dying tumor cells, immunotherapy, nanoinducers

1 Introduction

Cancer remains the most formidable disease globally, with over 19,292,789 new cases and approximately 9,958,133 cancer-related deaths recorded worldwide each year (1). As is well-known, tumor cells primarily evade immune surveillance by downregulating tumor-associated antigens (TAAs) and tumor-specific antigens (TSAs), and releasing soluble antigens and MHC molecules (2). Therefore, tumor immunotherapy has emerged as a crucial therapeutic approach for suppressing both primary and metastatic tumors. Moreover, immunotherapy can confer long-term immune protection for the body (3). Immune checkpoint blockade (ICB) represents a novel groundbreaking tumor immunotherapy that targets two key immune checkpoint pathways programmed cell death protein 1/programmed death ligand 1 (PD-1/PD-L1) and cytotoxic T lymphocyte-associated protein 4/B7 (CTLA-4/B7). By disrupting the mechanisms of tumor immune resistance, ICB can effectively promote antigen-specific T-cell immune responses. Currently, more than ten ICB drugs have been approved by the FDA for the treatment of a broad spectrum of tumors, offering new hope in the fight against cancer (4). However, the efficacy of ICB drugs appears to be less than satisfactory against late-stage patients in relevant clinical trials, with only a few patients benefiting from these treatments (5).

Cancer vaccines represent a promising emerging approach in tumor immunotherapy, offering extensive application prospects (6). The complexity of the preparation process, coupled with insufficient antigenic immune effects and immune cell dysfunction, have emerged as the primary factors limiting the development of cancer vaccines (7, 8). Nonetheless, the identification of immunogenic cell death (ICD) as a distinct form of tumor-regulated cell demise has offered new prospects to overcome the limitations hampering the advancement of cancer vaccines (9). In this regard, the capacity of chemotherapy, radiotherapy, photothermal therapy, and sonodynamic therapy to induce ICD, as evidenced in recent studies, could present a novel approach for reshaping conventional methods in oncology (10). It is now understood that the importance of ICD-based cancer vaccines lies in the *in vivo* application of ICD nanomedicine inducers and the production of dying tumor cells (DTCs) *in vitro* during tumor treatment (Figure 1).

ICD, induced by the chronic release and exposure of damage-associated molecular patterns (DAMPs) including calreticulin (CRT), adenosine triphosphate (ATP), high mobility histone 1 (HMGB1), heat shock protein (HSP) activates the recruitment and activation functions of neutrophils, macrophages, and dendritic cells. This orchestrated immune response associated within the tumor microenvironment exhibits characteristics akin to vaccination, a concept gaining significant traction within the research community (11). Simultaneously, during the study of ICD induction against tumor cells *in vitro*, it has been discovered that a substantial number of immunogenic DTCs are generated following ICD induction. These DTCs possess a strong ability to release immunogenic substances, such as DAMPs, which continuously trigger a potent immune stress response, remodel the immune microenvironment, and enhance the body's immune surveillance capabilities. In summary, "ICD-based cancer vaccines" offer advantages such as broad-spectrum antigens and diverse induction conditions, which can mitigate numerous adverse factors in the development and application of cancer vaccines. Overall, the advent of ICD-based cancer vaccines has demonstrated significant potential for the immunotherapy of relevant tumors (12).

However, the pursuit of efficient and stable methods for ICD induction remains critical for developing and evaluating relevant ICD-stimulating nanomedicines. Since ICD inducers and induction strategies are key focuses in ICD-based cancer vaccine research, this review highlights recent advancements in ICD-based cancer vaccines from both *in vivo* and *in vitro* perspectives. Our goal is to provide more reliable preparation protocols and strategies for ICD-based cancer vaccines, thereby promoting their continued development and application. A crucial area of investigation for these vaccines, compared to other immunotherapies, lies in their potential to address tumor recurrence in long-term survivors of metastatic and invasive cancers To achieve curative potential, we advocate for the synergistic combination of immune-stimulating tools with ICD-based cancer vaccine therapy.

2 The role of ICD in anti-cancer immunity

Well-documented by numerous studies, immunogenic cell death plays a critical role in generating an immunogenic tumor phenotype, effectively overcoming immunosuppressive effects of a non-immunoreactive tumor microenvironment (TME).ICD is characterized by CRT exposure, ATP release, and leakage of HMGB1 and HSP (13). These processes facilitate the uptake of TAAs by adaptive immune cells, triggering a broad-spectrum antigen-specific immune response, promoting DC maturation,

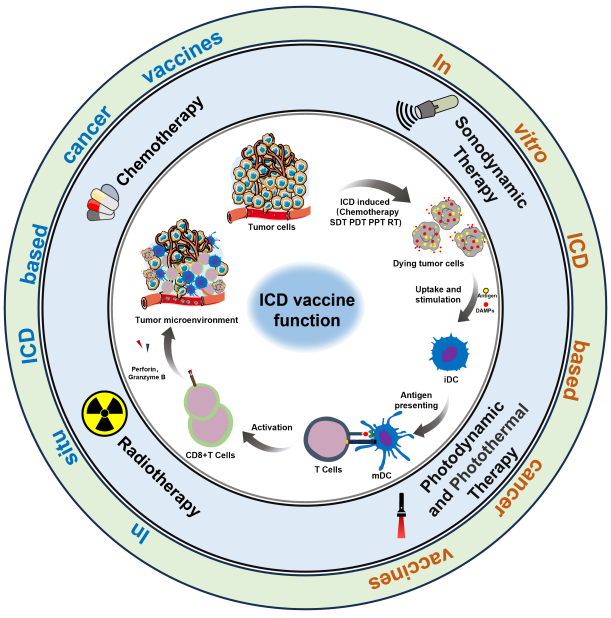

FIGURE 1
ICD-based cancer vaccines utilize methods to induce anti-cancer immunity within the TME.

and enhancing the search for DTCs (14). Furthermore, ICB therapy relies on the production and activation of tumor antigen-specific T cells. Consequently, the release of specific antigens from ICD tumor cells is crucial for reshaping the TME and has been validated in the combination of ICB with chemotherapy and radiotherapy. The recruitment of adaptive immune cells, neutrophils, macrophages, and NK cells all can activate innate effector mechanisms (15).

Immunogenic substances released during ICD can be classified into constitutive DAMPs (cDAMPs) and inducible DAMPs (iDAMPs). cDAMPs consist of immune-stimulating molecules such as CRT, ATP, HMGB1, and HSP, which are expressed prior to tumor cell death (16). iDAMPs are endogenous molecules produced by underlying mechanisms during tumor cell death, primarily including cytotoxic T-lymphocytes (CTLs) with CD3+, CD4+, and CD8+, releasing interferon-α (IFN-α), granzymes, lysins, and perforins (17). In this respect, CRT and HSP emit eat-me signals. CRT-CD91 and HSP90-CD91 interactions promote endocytosis signals in tumor cells, inducing antigen presentation and specific CTL responses. Additionally, the release of tumor necrosis factor-α (TNF-α) and interleukin-6 (IL-6) (18); ATP emit energy signals, ATP-P2RY2 binding is involved in the recruitment of monocytes or macrophages, neutrophils, and promoting DC maturation (19); HMGB1, aided by chemokines, binds to pattern recognition receptor (PRR) (P2RX7, P2RY2), CD91, CD40, and Toll-like receptor 4 (TLR4) receptors on the surface of antigen-presenting cells (APCs) (20). Upon the functional activation of APCs, those APCs exposed to TAA and TSA immunostimulants initiate cross-presentation to CD4+/CD8+ T cells, enhancing DC antigen presentation and CTLs proliferation (14). Consequently, the transition from a "cold" to a "hot" tumor immune microenvironment occurs, accompanied by changes in the secretion levels of immunostimulatory and immunosuppressive factors (up-regulation of IFN-γ, TNF-α, and IL-12; down-regulation of IL-4, IL-6, and IL-10), as well as the depletion of myeloid-derived suppressor cells (MDSCs), regulatory T cells (Tregs), and tumor-associated macrophages 2 (TAM2) (21). The above studies overlap in their assertion that ICD, as an in-situ vaccine, possesses potential immunomodulatory abilities and holds great value in reversing the TME and improving the efficacy of tumor immunotherapy.

3 Inducers of *in situ* ICD-based cancer vaccines

Over the years, a multitude of ICD inducers have been developed, especially when integrated with nanotechnology, to boost the effectiveness of ICDs. Administering ICD nano-inducers to the tumor site not only averts degradation and premature active ingredient release but also enhances their penetration and retention capabilities (EPR) (22). Presently, the primary driving methods of ICDs encompass chemotherapy, photodynamic, photothermal, radiotherapy, and sonodynamic therapies Table 1. Thus, a comprehensive investigation of ICD induction mechanisms and inducers holds substantial importance in advancing the development of "*in situ* ICD-based cancer vaccines". The release of cancer cell immunogenic antigens induced by ICD and the presentation of these antigens by APCs constitute the fundamental stages of the "cancer vaccine-like function" observed *in vivo* (Figure 2). We introduce the ICD induction methods with some latest research to provide more evidence in the field of ICD-vaccine.

3.1 Chemotherapy-induced ICD-based cancer vaccines

Chemotherapeutic agents that have been shown to be effective for ICD induction include: Idarubicin; Epirubicin, Doxorubicin (DOX) (23), Mitoxantrone, Oxaliplatin (Oxp) (25), Bortezomib, Cyclophosphamide, and Paclitaxel (PTX) (27, 47). Studies have demonstrated that the induction of ICD by chemotherapeutic agents, particularly anthracyclines, is accompanied by phenomena such as the unfolded protein response within the endoplasmic reticulum (ER) and the generation of reactive oxygen species (ROS). These events are primarily caused by the DNA damage induced by chemotherapeutic agents to secondary structures, including the cytoplasm (28). Chemotherapy-induced ICD can also lead to the release of CRT, ATP, HMGB1, CXCL1, and CXCL2, which ultimately induces an immune stress response, triggering a sustained antitumor effect (48).

In experiments exploring the use of chemotherapeutic nanomedicines for ICD induction, some researchers employed nanoprecipitation technology to develop and design nanomedicines (called Nano-Folox), which contain Oxp derivatives and FnA. Nano-Folox not only induced ICD, but also synergistically interacted with free 5-Fu to induce a shift from cold to hot tumors. This ultimately led to a significant inhibition of tumor growth in CRC mouse models (29). Liu et al. synthesized liposomes carrying Oxp and coupled with indoximod (IND) precursors; the nanoparticles not only enhanced the ability of Oxp to induce ICD in pancreatic ductal carcinoma (PDAC) but also stimulated antitumor immune responses in PDAC (49). In recent years, researchers have designed nanoplatforms integrating OXA with polyethylene glycolated photosensitizer (PS) prodrugs, exhibiting good stability in blood circulationand able to complete drug release and ICD induction under near-infrared (NIR) irradiation. They also explored the enhancing effect of CD47 blockade on tumor ICD induction (50). Xie et al. designed nanoparticles MDP NPs self-assembled from DOX, MnO2 nanoparticles, Fe3+, and PEG-polyphenol ligands, which could enhance DOX-based tumor ICD induction and achieve high expression of TAAs, DC maturation, and infiltration of tumor-specific T-cells (51). Some researchers have constructed ROS-responsive polymers (R-SIP) using hydrophilic polyethylene glycol (PEG) and a hydrophobic self-immolative backbone, loaded with DOX. This nanoparticle could release DOX in response to spontaneous depolymerization of ROS and undergo depolymerization to produce azoquinone methyl ether derivatives that significantly deplete GSH, increase the level of oxidative stress, and ultimately enhance the induction of ICD in oncological treatments (52).

10.3389/fimmu.2024.1389173

TABLE 1 ICD-based cancer vaccines with common inducers.

ICD-induced methods	Inducer	Inducer structural formula	Detection of ICD based biomarkers	Ref.
Chemotherapy	Doxorubicin	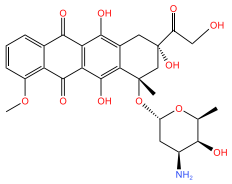	CRT, HMGB1, ATP	(23, 24)
	Oxaliplatin	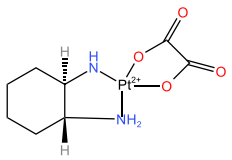	HMGB1	(25, 26)
	Paclitaxel	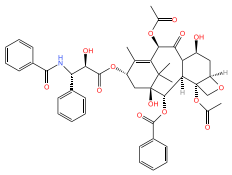	CRT	(27, 28)
	5-Fluorouracil	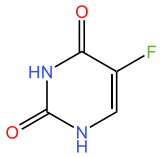	CRT, ATP, HMGB1	(29)
	KP-1339	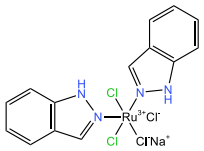	CRT, ATP, HMGB1	(30)
PDT	Chlorine a6	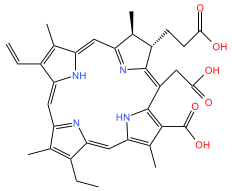	CRT, ATP, HMGB1	(31, 32)
	Hypericin	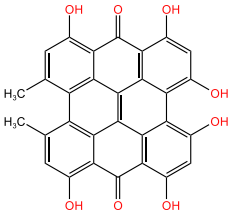	CRT, ATP, HMGB1	(33)
	5-ALA	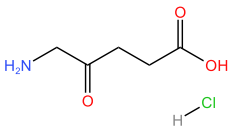	CRT, ATP, HMGB1, HSP	(34, 35)

(Continued)

10.3389/fimmu.2024.1389173

TABLE 1 Continued

ICD-induced methods	Inducer	Inducer structural formula	Detection of ICD based biomarkers	Ref.
	Rose Bengal	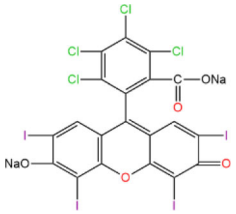	CRT, ATP, HMGB1, HSP	(36)
PPT	ICG	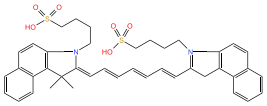	CRT	(37)
	PDA	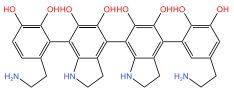	CRT, ATP, HMGB1	(38)
	IR780	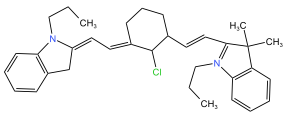	CRT, ATP, HMGB1	(39)
	CuS		CRT, ATP, HMGB1	(40)
	ZnO		CRT, ATP, HMGB1	(41)
SDT	IR780	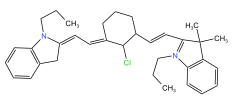	CRT, ATP, HMGB1	(42, 43)
	Perfluorocarbon	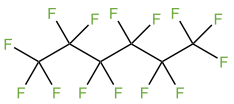	CRT, HMGB1	(44)
	ICG	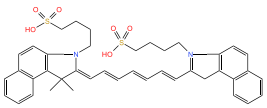	CRT, ATP, HMGB1	(38)
Others	CUR	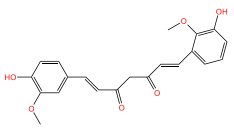	CRT, ATP, HMGB1	(45)
	Icaritin	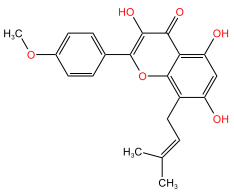	CRT, ATP, HMGB1	(46)

3.2 PDT-induced ICD-based cancer vaccines

PDT has shown effectiveness in inducing tumor cell death, solidifying its role as a viable clinical application in oncology. Currently, photosensitizers with the ability to induce cell death include Hypericin (33), 5-ALA (34), and Rose-Bengal acetate (36). The induction of ICD in tumor cells during PDT treatment is primarily attributed to the generation of intracellular ROS under NIR irradiation, which occurs after photosensitizer aggregation in the ER, causing disruptions in ER homeostasis, elevating calcium levels in the ER, and losing SERCA2 function. Mitochondrial dysfunction, characterized by oxidative damage to mtDNA and BAX/BAK-mediated apoptosis, triggers a series of events culminating in immunogenic stress. This process begins with the release of ATP and exposure of CRT on the mitochondrial surface. Subsequently, DAMPs, such as heat shock protein 70 (HSP70), are released, initiating a localized inflammatory response. Ultimately,

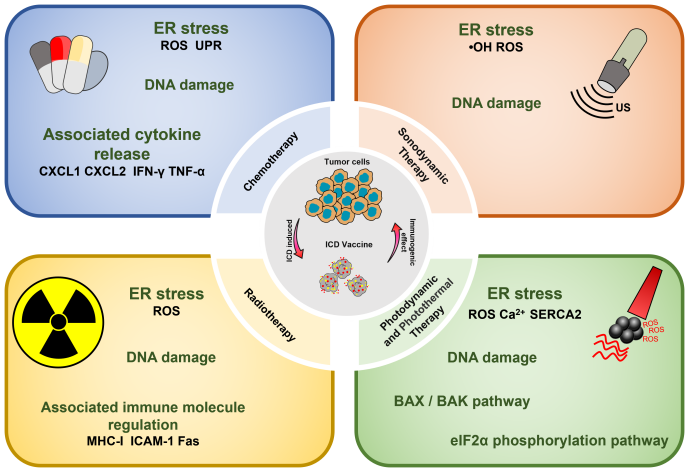

FIGURE 2
Overview of ICD-based cancer vaccines and the associated mechanisms involved in ICD regulation.

these events contribute to the development of an immunogenic stress response (53). Beyond the intrinsic properties of the photosensitizer, the ROS generation and ICD-inducing effects can be severely limited by the constraints of hypoxia and insufficient tumor penetration in the TME (54). Therefore, it is crucial to address adverse factors in the TME to enhance ICD induction by PDT. Several strategies can be employed for this purpose, such as inducing mitochondrial damage that causes ER disorders and calcium overload (55); utilizing oxygen carriers like hemoglobin (Hb) as catalysts for ROS generation, and modifying the targeting effect of ER-targeting pardaxin (FAL) to enable more drugs to be internalized into the ER, thus increasing the efficacy of PDT (37).

Studies onPDT-induced ICD have explored the use of a smart semiconductor polymer nano-immunomodulator (SPNI) that could be activated under acidic TME. When it was used in the therapeutic process, SPNI exerted a photodynamic effect, directly ablating tumors and inducing ICD when exposed to NIR light treatment, while R837 promoted DC maturation and pro-inflammatory cytokine secretion (56). Qiu et al. incorporated the photosensitizer Chlorin e6 (Ce6) doped with the chemotherapeutic agent 10-hydroxycamptothecin (HCPT) into calcified nanocarriers CHC NPs. CHC NPs can generate ROS, causing mitochondrial dysfunction and inducing the ICD. This phenomenon is also crucial to compensate for the lack of results from insufficient immunogenic tumor microenvironment (ITME) in HCPT treatment (31). Zhu et al. demonstrated that a platelet membrane fusion liposome nanovesicle system (named TFL) loaded with type I AIE photosensitizer TBP-2. In this study, TBP-2 has the potential to increase the incidence of cuproptosis and induce the vaccine-function in tumor site (57, 58).

3.3 PTT-induced ICD-based cancer vaccines

PTT is a potential non-invasive treatment strategy that converts NIR energy into heat by photothermal agents, ultimately leading to tumor ablation. Interestingly, it was found that PTT could induce ICD and assume a role akin to a vaccine (59). The types of photothermal agents that can induce the photothermal effect at present include (1) precious metals Au, Ag, Pt, etc., which have high photothermal conversion efficiency and imaging; (2) Carbon materials graphene, carbon nanorods, with large photothermal conversion area but poor NIR absorption; (3) Metal and non-metal compounds, CuS, ZnS; with high photothermal and low cost; (4) Organic and inorganic nanomaterials. The ICD-inducing ability of PTT therapy may be attributed to several factors. Firstly, the photothermal agent initiates temperature changes at the tumor site, leading to a Fenton-like reaction, peroxidation reaction, and direct induction of H_2O_2 production in the TME (60). These results in intracellular Ca^{2+} overload within tumor organelles (61). The process involves mitochondria damage including reduced membrane potential and the generation of mitochondrial reactive oxygen species (mtROS) and the up-regulation of the PERK-mediated eukaryotic initiation factor 2α (eIF2α) phosphorylation pathway. Disruption of the ER structure is a hallmark of ICD. This process ultimately culminates in the release of a significant amount of DAMPs into the cytoplasm (62).

In recent years, the catalytic properties of Fenton metals, particularly copper and iron, have emerged as crucial mechanisms for inducing cell death processes termed copper death and iron death. The utilization of photo-activated copper, exhibiting exceptional photo-oxidation and reduction catalytic efficiency has ushered in a new era of photosensitizers. This advancement has significantly contributed to the burgeoning research in innovative photodynamic and photothermal therapies for tumors (63). One approach involves the synthesis of multifunctional nanoplatforms, such as Cu-PDA-FA, by combining polydopamine (PDA) with Cu^{2+} through chelation technology. Cu-PDA-FA not only induces ICD and cancer vaccine-like effects but also amplifies the efficiency of conversion (38). Some researchers designed CaO_2 and Cu_2Se conjugates, which showed the ability to induce ICD after being activated by NIR-II. Indeed, the Ca^{2+} overload in the ER enhances

the immune activation capacity. Reinforcing this concept, research on photothermal materials (40). Zinc oxide (ZnO) has been identified as an efficient drug carrier responsive to tumor pH that significantly inhibits tumor growth. Building on these findings, scientists have designed a multifunctional composite nanoplatform (AuNP@mSiO2@DOX-ZnO) to harness the synergistic therapeutic effects. This platform could promote ICD, maturation of DCs, and proliferation of effector T cells, ultimately preventing tumor growth and metastasis (41). Ran et al. designed nano-platforms PBDB-T NPs using the organic photovoltaic material PBDB-T through a nanoprecipitation method. PBDB-T NPs exhibited favorable photothermal therapeutic effects and the ability to induce ICD. Importantly, they increased the efficiency of DAMPs production after mild-temperature PTT (mPTT) treatment (64). Tian et al. developed a mesoporous polydopamine nanoparticle MPDA. IR-780@MPDA not only induced ICD-activated CTLs in a therapeutic 4T1-homozygous mouse model under NIR treatment, but it also demonstrated its utility for *in vivo* photoacoustic (PA) imaging, as evidenced by the PA imaging tracings (39).

3.4 SDT-induced ICD-based cancer vaccines

It is well-established that SDT enables the concentration of ultrasound energy at the tumor site, leveraging the cavitation effect to elevate local temperatures and enhance drug decomposition. This process can generate free radicals and produce ROS under the action of endogenous substances in the cell, thereby achieving the purpose of local killing of the tumor. SDT offers several advantages, inducing high tissue penetration, low invasiveness, high controllability, and low costs (65). Consequently, SDT is safer than the traditional means of tumor treatment, such as chemotherapy, radiotherapy, and can minimize damage to normal tissues during the treatment process. Furthermore, ultrasound (US) has an ideal depth of tissue penetration (10 cm), which greatly mitigates the inhibitory effects of hypoxia, low pH, and other unfavorable factors in complex TME, which confers SDT a stronger ICD induction effect (66).

In recent years, a new type of calreticulin nanoparticles (CRT-NP) has been developed, which can be activated by focused ultrasound (FUS) and induce ICD during melanoma immunotherapy. The CRT-NP *in vivo* therapeutic study of CRT-NP benefits from the non-invasiveness of has the advantage of ultrasound, couple with a thermal effect that transforms the TME to enhance TAA release, HSP expression, and up-regulation of CRT to stimulate tumor immune stress response (67). Some researchers designed perfluorocarbon nanoparticles (LIP-PFH NPs), which also exhibited tumor suppression effect and ICD induction effect on breast cancer cells by SDT (68). Besides, researchers have synthesized mitochondria-targeted liposome nanoparticles (MLipRIR NPs), which could be activated by ultrasound and released R162 that disrupted the glutaminolysis pathway in mitochondria and down-regulates glutathione peroxidase (GPx) enzyme expression. At the same time, IR780 generated large amounts of ROS in response to US treatment, disrupting normal mitochondrial function and inducing ICD (42). Building on the discovery that a combined photodynamic and sonodynamic therapy(PSDT) reduces sonosensitizer dose and energy loss, Zheng et al. developed the OIX-NP. This nanoparticle comprises poly(lactic-co-glycolic acid) (PLGA) encapsulating oxygen-carrying perfluoropentane (PFP), an ICG near-infrared dye and an Oxp chemoinducer. The OIX-NP not only efficiently induce ICD, but also demonstrated significant potential for imaging applications (44).

3.5 RT-induced ICD-based cancer vaccines

It has been reported that RT can accumulate energy in the tumor site by using high-energy X-rays, Y-rays, or other isoelectronic radiation (IR). Then RT induces DNA damage, destroying double-stranded DNA (dsDNA), leading to ICD. This process results in the release of key signaling molecules, including CRT, HSP70 and HMGB1, within the TME (69). The induction of ICD by RT mainly involves the up-regulation of histocompatibility complex I (MHC-I) molecule, intercellular adhesion molecule-1, and factor-related apoptosis (Fas) (70). This process contributes to the so-called "distant effect" and inhibits the development of metastasis. Thus, RT has the potential to act as an in-situ vaccine (71, 72).

While radiotherapy is a mainstay of local tumor treatment, its effectiveness in controlling distant tumor spread is limited. However, the recent discovery of RT's ability to induce ICD offers a promising avenue to revitalize RT therapy. Importantly, research suggests that the degree of immune modulation within the tumor microenvironment by RT is dependent on the radiation dose (73). He et al. found that gold nanoparticles AuNPs were able to increase the expression of phosphorylated eIF2α (p-eIF2α) in G422 glioblastoma cells under RT treatment, promote eIF2α protein phosphorylation, and induce ICD. The study also verified the ICD-inducing ability of AuNPs under RT treatment in a therapeutic G422 tumor-bearing mice model (74).

4 *In vitro* induction of DTCs for cancer vaccines

"ICD-based cancer vaccines" involve DTCs for re-infusion vaccination *in vivo*, ultimately leading to tumor therapy. DTCs, produced after treatment with ICD inducers, exhibit excellent immunogenicity (Figure 3). In this respect, studies have reported that ICD-based cancer vaccines can induce robust immune activation in mouse models during prophylactic vaccination trials *in vivo* (75). ICD-based cancer vaccines offer a distinct advantage by inducing a comprehensive tumor cell antigen expression profile. This eliminates the dependence on a single antibody for recognition, a major hurdle in conventional immunotherapy. By promoting the expression of diverse tumor antigens, ICD vaccines significantly reduce the risk of tumor cells evading immune attack during treatment. The rationale behind this approach lies in the ability of ICD inducers to stimulate the spontaneous production of

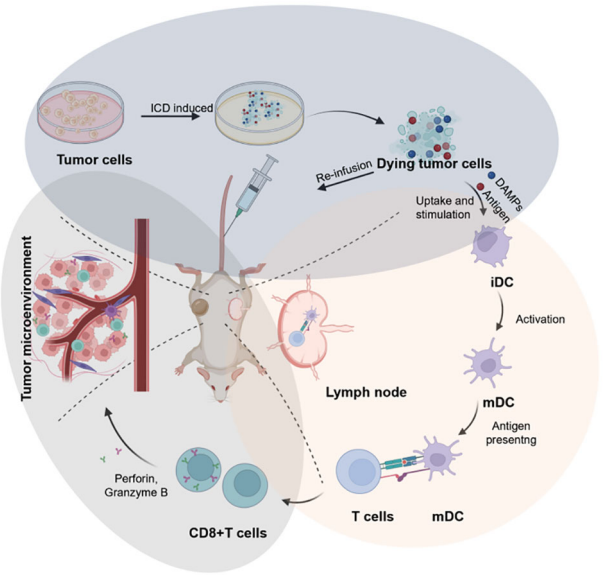

FIGURE 3
Schematic illustration of the design of cancer vaccines inspired by DTCs for eliciting humoral and cellular immunity, which can be broken into three key stages: the preparation of ICD-based cancer vaccines (blue circle), the immune activation include DC maturation and antigen presentation (red circle), and the immune effect of CD8 +T cells in TME for anti-tumor therapy (grey circle). Created by © 2023 BioRender.

relevant antigens, DAMPs, and immune activation molecules within tumor cells. This comprehensive immune response translates to potent antitumor effects, establishment of long-term immune memory against the tumor, and aligns perfectly with the evolving paradigm of immunotherapy, which seeks to integrate preventive and therapeutic strategies.

Studies have explored various methods for the preparation of ICD-based cancer vaccines include: One approach utilizes chemotherapy. Qing et al. demonstrated that DOX can induce tumor cells to become dendritic cell activators. They employed liquid nitrogen cryogenics to generate frozen dying tumor cells (FDTs), which achieved a 38% tumor elimination rate in the MC100 peritoneal carcinoma mouse model. Furthermore, in combination with cytokines IL-12 and aPD-L1, they achieved 100% eradication in the peritoneal metastasis model of colorectal carcinoma (76). Li et al. showed that tumor antigens CIAs induced by chemotherapeutic agents *in vitro*, triggering an immune response and demonstrating synergistic effects with anti-PD-1 therapy (77). Another approach involves using radiotherapy. Researchers have successfully prepared nano-vaccines *in vitro* using RT-induced tumor cells. These vaccines demonstrated efficacy in treating metastatic tumors and enhanced immunotherapeutic effects when combined with anti-PD-1 treatment (78).Although research on ICD inducers and strategies is more advanced, the development of ICD-based cancer vaccines *in vitro* is still in the preliminary stage. However, achieving high efficiency and low cost remains crucial research criteria for ICD-based cancer vaccines. Therefore, investigating whether photodynamic and sonodynamic therapy can be an ideal induction for ICD-based cancer vaccines is expected to be a worthy direction for more researchers to explore. Given the promising results of ICD induction using chemotherapy and radiotherapy, investigating the potential of PDT and SDT as triggers for ICD-based cancer vaccines warrants further exploration. we posit that the personalized design of these ICD-based cancer vaccines holds immense potential for advancing clinical translation in antitumor immunotherapy translation. As an example, previously mentioned strategies like encapsulating patient-specific nanoparticles and obtaining DC activators from tumors offer valuable avenues for personalization. While current personalized cancer vaccine development primarily focus on immune cells loaded with immune-stimulating agents, future breakthroughs lie in utilizing specific immune elements to create novel and highly effective therapeutic strategies.

5 ICD related clinical cancer therapy

In clinical immunotherapy studies involving non-small cell lung cancer, hepatocellular carcinoma, breast cancer, bladder cancer, melanoma, squamous carcinoma, and other solid tumors, the induction of ICD has demonstrated the ability to enhance the presentation function of APCs such as DCs, deplete Treg cells, and activate the vitality of immune cytotoxic effector cells. Thess combined effects ultimately lead to improved efficacy in tumor therapy.

As summarized in (Table 2), clinical trials have primarily focused on chemotherapy and radiotherapy for inducing ICD, demonstrating its clinical applicability. Researchers have further shown that physical treatments, like cryoablation, can also trigger ICD, potentially improving cost-effectiveness and clinical translation efficiency. However, significant progress is needed to develop and translate ICD-based cancer vaccines for clinical use. Therefore, exploring novel therapeutic approaches based on ICD-based cancer vaccines research and establishing a system to comprehensively evaluate the types and levels of immunogenic substance generated by ICD are crucial next steps.

6 Discussion and conclusion

The immunological adjuvant effect of ICD is now understood to be intricately linked to the exposure and release of cellular DAMPs. These DAMPs include exposed CRT, secreted ATP, ANXA1, TNF-α, and HMGB1, as well as phosphorylated eIF2α. However, additional valuable markers likely remain undiscovered. For example, low levels of autophagy can both protect cells and limit the release of immunogenic substances, while potentially increasing the risk of oncogenicity during treatment. Mounting evidence suggests that tumor autophagy, once thought to be similar to apoptosis, can also impact the effectiveness of antitumor immunotherapy. As expected, the autophagy inducer called STF-62247 (STF) can effectively convert protective autophagy into ICD, thereby enhancing antitumor immune activation. Furthermore, the uncertainty surrounding conventional methods of inducing ICD and determining the optimal dosage of ICD inducers makes it challenging to accurately quantify the release of associated immunogenic DAMPs. As ICD-based cancer

10.3389/fimmu.2024.1389173

TABLE 2 Clinical studies about tumor treatment based on ICD.

ICD-based treatment form	Tumor type	Intervention	Aims of the study	Identifier
Combination of chemotherapy	Ovarian Cancer	Carboplatin-pegylated Liposomal Doxorubicin (PLD) or Doxorubicin Combination Chemotherapy with Tocilizumab and Pegylated Interferon Alpha (Peg-Intron)	Feasibility of the Combination of Chemotherapy (Carbo/Caelyx or Carbo/ Doxorubicin) With Tocilizumab (mAb IL-6R) and Peg-Intron in Patients With Recurrent Ovarian Cancer	NCT01637532
	Hepatocellular carcinoma	Envafolimab; Lenvatinib combined with TACE PD-L1 inhibitor	Envafolimab, Lenvatinib Combined With TACE in the Treatment of Unresectable Locally Advanced Hepatocellular Carcinoma	NCT05582109
	Head and Neck Cancer	Digoxin	Potentiation of Cisplatin-based Chemotherapy by Digoxin in Advanced Unresectable Head and Neck Cancer Patients	NCT02906800
	Colorectal Cancer Metastatic	Capecitabine; Oxaliplatin; Bevacizumab; Pembrolizumab	Chemotherapy and Immunotherapy as Treatment for MSS Metastatic Colorectal Cancer With High Immune Infiltrate	NCT04262687
	Cholangiocarcinoma	Novel combination of chemotherapy and immunotherapy	Durvalumab and Tremelimumab With Platinum-based Chemotherapy in Intrahepatic Cholangiocarcinoma	NCT04989218
	Non-small Cell Lung Cancer	Nivolumab; Oxaliplatin; Ipilimumab	Nivolumab and Ipilimumab in CombinationWith Immunogenic Chemotherapy for Patients With Advanced NSCLC	NCT04043195
	Rectal Neoplasms	Oxaliplatin; Capecitabine and Anti-PD-1 monoclonal antibody	Rectal Artery Infusion Chemotherapy Combined With Anti-PD1 Antibody for MSS LARC	NCT05307198
	Colorectal Cancer Metastatic	Nivolumab FLOX	METIMMOX: Colorectal Cancer METastasis - Shaping Anti-tumor IMMunity by OXaliplatin	NCT03388190
	Non-small Cell Lung Cancer	Atezolizumab and Vinorelbine	Trial to Evaluate Safety and Efficacy of Vinorelbine With Metronomic Administration in Combination With Atezolizumab as Second-line Treatment for Patients With Stage IV Non-small Cell Lung Cancer	NCT03801304
	Solid Tumor	SQZ-AAC-HPV; Ipilimumab; Nivolumab	Study of SQZ-AAC-HPV in Patients With HPV16+ Recurrent, Locally Advanced or Metastatic Solid Tumors	NCT04892043
	Mycosis Fungoides	Cemiplimab	BIOmarker-guided Study to Evaluate the Efficacy and Safety of cemipLimab for advanced Cutaneous T-cell Lymphoma	NCT05538988
	Squamous Cell Carcinoma of the Head and Neck	Atezolizumab and UCPVax	Combination of UCPVax Vaccine and Atezolizumab for the Treatment of Human Papillomavirus Positive Cancers	NCT03946358
	Solid Tumor	RAPA-201 Rapamycin Resistant T Cells and Chemotherapy Prior to RAPA-201 Therapy	RAPA-201 Therapy of Solid Tumors	NCT05144698
	Melanoma	Ipilimumab and Nivolumab	Isolated Hepatic Perfusion in Combination With Ipilimumab and Nivolumab in Patients With Uveal Melanoma Metastases	NCT04463368
	Hepatocellular Carcinoma	Nivolumab and SIR-Spheres	A Study of the Safety and Antitumoral Efficacy of Nivolumab After SIRT for the Treatment of Patients With HCC	NCT03380130
		Olaparib; MEDI4736; Bevacizumab		NCT02734004

(Continued)

TABLE 2 Continued

ICD-based treatment form	Tumor type	Intervention	Aims of the study	Identifier
	Ovarian Breast SCLC Gastric Cancers		A Phase I/II Study of MEDI4736 in Combination With Olaparib in Patients With Advanced Solid Tumors	
Combination of Radiotherapy	Non- Small Cell Lung Cancer	High-dose radiotherapy alone or concurrent cisplatin-doublet therapy	Detection of Circulating Biomarkers of Immunogenic Cell Death	NCT02921854
	Non-small Cell Lung Cancer	Radiotherapy and atezolizumab/tiragolumab	Study of Stereotactic Ablative Radiotherapy Followed by Atezolizumab/ Tiragolumab in Treatment-naive Patients With Metastatic Non-small Cell Lung Cancer	NCT05034055
	Advanced Solid Tumors	Stereotactic Body Radiotherapy; navoximod and NLG802 (indoximod Prodrug)	Safety of Navoximod and NLG802 With Stereotactic Body Radiotherapy Treatment of Advanced Solid Tumors	NCT05469490
	Esophageal Squamous Cell Carcinoma	Radiotherapy combined with immune checkpoint inhibitors	Hybrid Dose-fraction Radiotherapy for Metastatic Non-small Cell Lung Cancer	NCT05348668
	Urinary Bladder Neoplasms	radiotherapy and Tislelizumab	Comprehensive Bladder Preservation Therapy on Patients With Muscle Invasive Bladder Cancer	NCT05445648
	Biliary Tract Neoplasms; Liver Cancer; Hepatocellular Carcinoma	Durvalumab and Tremelimumab combined with Trans-arterial Catheter Chemoembolization Radiofrequency Ablation Cryoablation	A Pilot Study of Combined Immune Checkpoint Inhibition in Combination With Ablative Therapies in Subjects With Hepatocellular Carcinoma or Biliary Tract Carcinomas	NCT02821754
	Melanoma	Radiotherapy and lpilimumab	Trial of SBRT With Concurrent Ipilimumab in Metastatic Melanoma	NCT02406183
Others	Breast Cancer	Cryoablation	To Detect Cryoimmunologic Response Induced by Early Breast Cancer Ultrasound-guided Cryoablation	NCT05727813
	Esophageal Cancer	Cryotherapy	Cryotherapy for Locally Advanced Esophageal Cancer	NCT04248582
	Bladder Cancer	Mitomycin C	To Detect Immunogenic Cell Death as a Novel Mechanism of Mitomycin C Activity in Bladder Cancer	NCT04256616
	Thymic Epithelial Tumor; Recurrent Thymoma Thymic Cancer	PT-112	PT-112 in Subjects With Thymoma and Thymic Carcinoma	NCT05104736

therapy gains wider acceptance in clinical settings, it becomes increasingly important to select closely correlated assay secretions for screening ICD inducers that possess efficient induction capabilities for future development of ICD-based cancer vaccines.

Meanwhile, the development of safer and more reliable *in vitro* systems for ICD-based cancer vaccines, as well as the elimination of unfavorable factors *in vivo*, are areas that warrant attention and in-depth exploration. While some personalized ICD-based cancer vaccine research has been discussed above, providing potential mechanisms for their effectiveness, the activation of immunity by cancer vaccines is a complex process. For instance, studies have demonstrated that targeting the STING pathway can activate innate immune signaling in immune-infiltrating cells and within tumor cells, ultimately inducing ICD. However, the effectiveness of STING pathway activation within tumor cells may vary depending on the tumor type., Nanotechnology offers a potential solution by enhancing the delivery of STING activators to cells, thereby improving their efficacy (79). The involvement of the CXCL12/CXCR4 signaling pathway also plays a role in various physiological processes, such as tumor survival, invasion, metastasis, angiogenesis, and the creation of hypoxic environments (80). Additionally, CXCR4 expression can facilitate the transportation of MDSCs in different tumors, leading to the creation of an immunosuppressive TME and immune resistance (81). In gliomas, blocking CXCR4 signaling using nanoparticles loaded with CXCR4 inhibitors can reduce the infiltration of immunosuppressive MDSC and trigger an adaptive immune response (82).

In recent years, immunotherapy has made remarkable strides in the treatment of cancer, particularly with the emergence of cancer vaccines based on immune cell death. These vaccines hold great promise for expanding and enhancing tumor immunotherapy. In

this article, we expounded on the mechanisms of ICD as a potent tool for regulating TME and explored the vast potential of ICD-based cancer vaccines. The successful clinical application of ICD-based cancer vaccines necessitates a rigorous evaluation of their therapeutic value. Therefore, we advocate for the identification of more robust clinical evaluation indicators, particularly those that assess the efficacy of ICD induction by these vaccines. A comprehensive assessment of both safety and efficacy is paramount in determining the transformative potential of this approach in cancer treatment. Further exploration of the intricate mechanisms underlying ICD and its role in tumor immunotherapy is crucial to unlocking the full potential of this innovative strategy. Our ongoing research endeavors to contribute to the expanding body of knowledge surrounding ICD-based cancer vaccines and ultimately pave the way for their successful translation into clinical practice through meticulous evaluation and analysis. In conclusion, the utilization of immunogenic patterns generated by ICD in tumor cells represents a paradigm shift in the field of tumor immunotherapy. By advancing the development of disease-specific cancer vaccines, we can harness the full potential of this approach to significantly improve treatment outcomes for cancer patients. Rigorous evaluation and analysis are essential to ensure the clinical relevance and applicability of these vaccines, ultimately leading to improved patient outcomes on a global scale.

Author contributions

JW: Software, Visualization, Writing – original draft, Writing – review & editing. JM: Investigation, Supervision, Writing – review & editing. FX: Supervision, Writing – review & editing. FM: Supervision, Writing – review & editing. LL: Supervision, Writing – review & editing. YH: Investigation, Writing – review & editing. XZ: Supervision, Writing – review & editing. JY: Supervision, Writing – review & editing. ZT: Supervision, Writing – review & editing. QZ: Funding acquisition, Writing – review & editing. LB: Funding acquisition, Supervision, Writing – review & editing.

Funding

The author(s) declare financial support was received for the research, authorship, and/or publication of this article. This review was financially supported by the National Natural Science Foundation of China (No. 82073385, 82172706 and 82003295), Natural Science Foundation of Shanghai (No. 23ZR1478100).

Conflict of interest

The authors declare that the research was conducted in the absence of any commercial or financial relationships that could be construed as a potential conflict of interest.

Publisher's note

References

1. Sung H, Ferlay J, Siegel RL, Laversanne M, Soerjomataram I, Jemal A, et al. Global cancer statistics 2020: GLOBOCAN estimates of incidence and mortality worldwide for 36 cancers in 185 countries. *CA Cancer J Clin May*. (2021) 71:209–49. doi: 10.3322/caac.21660

2. Villadangos JA, Schnorrer P. Intrinsic and cooperative antigen-presenting functions of dendritic-cell subsets in *vivo*. *Nat Rev Immunol Jul*. (2007) 7:543–55. doi: 10.1038/nri2103

3. Ribas A, Wolchok JD. Cancer immunotherapy using checkpoint blockade. *Science. Mar 23*. (2018) 359:1350–5. doi: 10.1126/science.aar4060

4. Topalian SL, Forde PM, Emens LA, Yarchoan M, Smith KN, Pardoll DM. Neoadjuvant immune checkpoint blockade: A window of opportunity to advance cancer immunotherapy. *Cancer Cell*. (2023) 41:1551–66. doi: 10.1016/j.ccell.2023.07.011

5. Brahmer JR, Tykodi SS, Chow LQ, Hwu WJ, Topalian SL, Hwu P, et al. Safety and activity of anti-PD-L1 antibody in patients with advanced cancer. *N Engl J Med*. (2012) 366:2455–65. doi: 10.1056/NEJMoa1200694

6. Chen KS, Reinshagen C, Van Schaik TA, Rossignoli F, Borges P, Mendonca NC, et al. Bifunctional cancer cell-based vaccine concomitantly drives direct tumor killing and antitumor immunity. *Sci Transl Med*. (2023) 15:eabo4778. doi: 10.1126/scitranslmed.abo4778

7. Tanyi JL, Bobisse S, Ophir E, Tuyaerts S, Roberti A, Genolet R, et al. Personalized cancer vaccine effectively mobilizes antitumor T cell immunity in ovarian cancer. *Sci Transl Med*. (2018) 10:436. doi: 10.1126/scitranslmed.aao5931

8. Wang T, Wang D, Yu H, Feng B, Zhou F, Zhang H, et al. A cancer vaccine-mediated postoperative immunotherapy for recurrent and metastatic tumors. *Nat Commun*. (2018) 9:1532. doi: 10.1038/s41467-018-03915-4

9. Kroemer G, Galassi C, Zitvogel L, Galluzzi L. Immunogenic cell stress and death. *Nat Immunol*. (2022) 23:487–500. doi: 10.1038/s41590-022-01132-2

10. Choi B, Choi H, Yu B, Kim DH. Synergistic local combination of radiation and anti-programmed death ligand 1 immunotherapy using radiation-responsive splintery metallic nanocarriers. *ACS Nano*. (2020) 14:13115–26. doi: 10.1021/acsnano.0c04701

11. Obeid M, Tesniere A, Ghiringhelli F, Fimia GM, Apetoh L, Perfettini JL, et al. Calreticulin exposure dictates the immunogenicity of cancer cell death. *Nat Med*. (2007) 13:54–61. doi: 10.1038/nm1523

12. Huang Z, Wang Y, Yao D, Wu J, Hu Y, Yuan A. Nanoscale coordination polymers induce immunogenic cell death by amplifying radiation therapy mediated oxidative stress. *Nat Commun*. (2021) 12:145. doi: 10.1038/s41467-020-20243-8

13. Apetoh L, Ghiringhelli F, Tesniere A, Criollo A, Ortiz C, Lidereau R, et al. The interaction between HMGB1 and TLR4 dictates the outcome of anticancer chemotherapy and radiotherapy. *Immunol Rev*. (2007) 220:47–59. doi: 10.1111/j.1600-065X.2007.00573.x

14. Ghiringhelli F, Apetoh L, Tesniere A, Aymeric L, Ma Y, Ortiz C, et al. Activation of the NLRP3 inflammasome in dendritic cells induces IL-1beta-dependent adaptive immunity against tumors. *Nat Med*. (2009) 15:1170–8. doi: 10.1038/nm.2028

15. Garg AD, Vandenberk L, Fang S, Fasche T, Van Eygen S, Maes J, et al. Pathogen response-like recruitment and activation of neutrophils by sterile immunogenic dying cells drives neutrophil-mediated residual cell killing. *Cell Death Differ*. (2017) 24:832–43. doi: 10.1038/cdd.2017.15

16. Galluzzi L, Vitale I, Aaronson SA, Abrams JM, Adam D, Agostinis P, et al. Molecular mechanisms of cell death: recommendations of the Nomenclature Committee on Cell Death 2018. *Cell Death Differ*. (2018) 25:486–541. doi: 10.1038/s41418-017-0012-4

17. Wang Q, Ju X, Wang J, Fan Y, Ren M, Zhang H. Immunogenic cell death in anticancer chemotherapy and its impact on clinical studies. *Cancer Lett*. (2018) 438:17–23. doi: 10.1016/j.canlet.2018.08.028

18. Panaretakis T, Kepp O, Brockmeier U, Tesniere A, Bjorklund A, Chapman DC, et al. Mechanisms of pre-apoptotic calreticulin exposure in immunogenic cell death. *EMBO J*. (2009) 28:578–90. doi: 10.1038/emboj.2009.1

19. Martins I, Wang Y, Michaud M, Ma Y, Sukkurwala AQ, Shen S, et al. Molecular mechanisms of ATP secretion during immunogenic cell death. *Cell Death Differ*. (2014) 21:79–91. doi: 10.1038/cdd.2013.75

20. Apetoh L, Ghiringhelli F, Tesniere A, Obeid M, Ortiz C, Criollo A, et al. Toll-like receptor 4-dependent contribution of the immune system to anticancer chemotherapy and radiotherapy. *Nat Med*. (2007) 13:1050–9. doi: 10.1038/nm1622

21. Ahmed A, Tait SWG. Targeting immunogenic cell death in cancer. *Mol Oncol*. (2020) 14:2994–3006. doi: 10.1002/1878-0261.12851

22. Irvine DJ, Hanson MC, Rakhra K, Tokatlian T. Synthetic nanoparticles for vaccines and immunotherapy. *Chem Rev*. (2015) 115:11109–46. doi: 10.1021/acs.chemrev.5b00109

23. Banstola A, Pandit M, Duwa R, Chang JH, Jeong JH, Yook S. Reactive oxygen species-responsive dual-targeted nanosystem promoted immunogenic cell death against breast cancer. *Bioeng Transl Med*. (2023) 8:e10379. doi: 10.1002/btm2.10379

24. Liu M, Hao L, Zhao D, Li J, Lin Y. Self-assembled immunostimulatory tetrahedral framework nucleic acid vehicles for tumor chemo-immunotherapy. *ACS Appl Mater Interfaces*. (2022) 14:38506–14. doi: 10.1021/acsami.2c09462

25. Bains SJ, Abrahamsson H, Flatmark K, Dueland S, Hole KH, Seierstad T, et al. Immunogenic cell death by neoadjuvant oxaliplatin and radiation protects against metastatic failure in high-risk rectal cancer. *Cancer Immunol Immunother*. (2020) 69:355–64. doi: 10.1007/s00262-019-02458-x

26. Kim NR, Kim YJ. Oxaliplatin regulates myeloid-derived suppressor cell-mediated immunosuppression via downregulation of nuclear factor-kappaB signaling. *Cancer Med*. (2019) 8:276–88. doi: 10.1002/cam4.1878

27. Tang X, Rao J, Yin S. PD-L1 knockdown via hybrid micelle promotes paclitaxel induced Cancer-Immunity Cycle for melanoma treatment. *Eur J Pharm Sci*. (2019) 127:161–74. doi: 10.1016/j.ejps.2018.10.021

28. Vanmeerbeek I, Sprooten J, De Ruysscher D. Trial watch: chemotherapy-induced immunogenic cell death in immuno-oncology. *Oncoimmunology*. (2020) 9:1703449. doi: 10.1080/2162402X.2019.1703449

29. Guo J, Yu Z, Sun D, Zou Y, Liu Y, Huang L. Two nanoformulations induce reactive oxygen species and immunogenetic cell death for synergistic chemo-immunotherapy eradicating colorectal cancer and hepatocellular carcinoma. *Mol Cancer*. (2021) 20:10. doi: 10.1186/s12943-020-01297-0

30. Zhang F, Chen F, Yang C. Coordination and redox dual-responsive mesoporous organosilica nanoparticles amplify immunogenic cell death for cancer chemoimmunotherapy. *Small*. (2021) 17:e2100006. doi: 10.1002/smll.202100006

31. Qiu W, Liang M, Gao Y. Polyamino acid calcified nanohybrids induce immunogenic cell death for augmented chemotherapy and chemo-photodynamic synergistic therapy. *Theranostics*. (2021) 11:9652–66. doi: 10.7150/thno.64354

32. Ding D, Zhong H, Liang R. Multifunctional nanodrug mediates synergistic photodynamic therapy and MDSCs-targeting immunotherapy of colon cancer. *Adv Sci (Weinh)*. (2021) 8:e2100712. doi: 10.1002/advs.202100712

33. Garg AD, Dudek AM, Ferreira GB. ROS-induced autophagy in cancer cells assists in evasion from determinants of immunogenic cell death. *Autophagy*. (2013) 9:1292–307. doi: 10.4161/auto.25399

34. Sun Z, Zhao M, Wang W. 5-ALA mediated photodynamic therapy with combined treatment improves anti-tumor efficacy of immunotherapy through boosting immunogenic cell death. *Cancer Lett*. (2023) 554:216032. doi: 10.1016/j.canlet.2022.216032

35. Ji J, Fan Z, Zhou F. Improvement of DC vaccine with ALA-PDT induced immunogenic apoptotic cells for skin squamous cell carcinoma. *Oncotarget*. (2015) 6:17135–46. doi: 10.18632/oncotarget.3529

36. Jin F, Qi J, Liu D, You Y, Shu G, Du Y, et al. Cancer-cell-biomimetic Upconversion nanoparticles combining chemo-photodynamic therapy and CD73 blockade for metastatic triple-negative breast cancer. *J Control Release* (2021) 337:90–104. doi: 10.1016/j.jconrel.2021.07.021

37. Li W, Yang J, Luo L. Targeting photodynamic and photothermal therapy to the endoplasmic reticulum enhances immunogenic cancer cell death. *Nat Commun*. (2019) 10:3349. doi: 10.1038/s41467-019-11269-8

38. Xu N, Hu A, Pu X. Cu-Chelated polydopamine nanoparticles as a photothermal medium and "immunogenic cell death" inducer for combined tumor therapy. *J Mater Chem B*. (2022) 10:3104–18. doi: 10.1039/D2TB00025C

39. Tian Y, Younis MR, Tang Y. Dye-loaded mesoporous polydopamine nanoparticles for multimodal tumor theranostics with enhanced immunogenic cell death. *J Nanobiotechnology*. (2021) 19:365. doi: 10.1186/s12951-021-01109-7

40. Feng X, Lin T, Chen D. Mitochondria-associated ER stress evokes immunogenic cell death through the ROS-PERK-eIF2alpha pathway under PTT/CDT combined therapy. *Acta Biomater*. (2023) 160:211–24. doi: 10.1016/j.actbio.2023.02.011

41. Zhang Y, Guo C, Liu L. ZnO-based multifunctional nanocomposites to inhibit progression and metastasis of melanoma by eliciting antitumor immunity via immunogenic cell death. *Theranostics*. (2020) 10:11197–214. doi: 10.7150/thno.44920

42. Ren J, Zhou J, Liu H. Ultrasound (US)-activated redox dyshomeostasis therapy reinforced by immunogenic cell death (ICD) through a mitochondrial targeting liposomal nanosystem. *Theranostics*. (2021) 11:9470–91. doi: 10.7150/thno.62984

43. Zheng J, Sun Y, Long T. Sonosensitizer nanoplatform-mediated sonodynamic therapy induced immunogenic cell death and tumor immune microenvironment variation. *Drug Deliv. Dec*. (2022) 29:1164–75. doi: 10.1080/10717544.2022.2058653

44. Zheng J, Sun J, Chen J. Oxygen and oxaliplatin-loaded nanoparticles combined with photo-sonodynamic inducing enhanced immunogenic cell death in syngeneic mouse models of ovarian cancer. *J Control Release*. (2021) 332:448–59. doi: 10.1016/j.jconrel.2021.02.032

45. Dai Z, Tang J, Gu Z. Eliciting immunogenic cell death via a unitized nanoinducer. *Nano Lett*. (2020) 20:6246–54. doi: 10.1021/acs.nanolett.0c00713

46. Xiao Y, Yao W, Lin M. Icaritin-loaded PLGA nanoparticles activate immunogenic cell death and facilitate tumor recruitment in mice with gastric cancer. *Drug Deliv*. (2022) 29:1712–25. doi: 10.1080/10717544.2022.2079769

47. Song Q, Yin Y, Shang L. Tumor microenvironment responsive nanogel for the combinatorial antitumor effect of chemotherapy and immunotherapy. *Nano Lett*. (2017) 17:6366–75. doi: 10.1021/acs.nanolett.7b03186

48. Jiang M, Zeng J, Zhao L. Chemotherapeutic drug-induced immunogenic cell death for nanomedicine-based cancer chemo-immunotherapy. *Nanoscale*. (2021) 13:17218–35. doi: 10.1039/D1NR05512G

49. Lu J, Liu X, Liao YP. Nano-enabled pancreas cancer immunotherapy using immunogenic cell death and reversing immunosuppression. *Nat Commun*. (2017) 8:1811. doi: 10.1038/s41467-017-01651-9

50. Zhou F, Feng B, Yu H. Tumor microenvironment-activatable prodrug vesicles for nanoenabled cancer chemoimmunotherapy combining immunogenic cell death induction and CD47 blockade. *Adv Mater*. (2019) 31:e1805888. doi: 10.1002/adma.201805888

51. Xie L, Wang G, Sang W. Phenolic immunogenic cell death nanoinducer for sensitizing tumor to PD-1 checkpoint blockade immunotherapy. *Biomaterials*. (2021) 269:120638. doi: 10.1016/j.biomaterials.2020.120638

52. Jeon J, Yoon B, Dey A. Self-immolative polymer-based immunogenic cell death inducer for regulation of redox homeostasis. *Biomaterials*. (2023) 295:122064. doi: 10.1016/j.biomaterials.2023.122064

53. Garg AD, Krysko DV, Vandenabeele P, Agostinis P. The emergence of phox-ER stress induced immunogenic apoptosis. *Oncoimmunology*. (2012) 1:786–8. doi: 10.4161/onci.19750

54. Deng H, Zhou Z, Yang W. Endoplasmic reticulum targeting to amplify immunogenic cell death for cancer immunotherapy. *Nano Lett*. (2020) 20:1928–33. doi: 10.1021/acs.nanolett.9b05210

55. Huang C, Lin B, Chen C. Synergistic reinforcing of immunogenic cell death and transforming tumor-associated macrophages via a multifunctional cascade bioreactor for optimizing cancer immunotherapy. *Adv Mater Dec*. (2022) 34:e2207593. doi: 10.1002/adma.202207593

56. Liu J, He S, Luo Y. Tumor-microenvironment-activatable polymer nano-immunomodulator for precision cancer photoimmunotherapy. *Adv Mater*. (2022) 34:e2106654. doi: 10.1002/adma.202106654

57. Chen H, Luo X, Huang Q. Platelet membrane fusion liposome loaded with type I AIE photosensitizer to induce chemoresistance cancer pyroptosis and immunogenic cell death for enhancing cancer immunotherapy. *Chem Eng J*. (2023) 476:146276. doi: 10.1016/j.cej.2023.146276

58. Ning S, Lyu M, Zhu D. Type-I AIE photosensitizer loaded biomimetic system boosting cuproptosis to inhibit breast cancer metastasis and rechallenge. *ACS Nano*. (2023) 17:10206–17. doi: 10.1021/acsnano.3c00326

59. Guo R, Wang S, Zhao L. Engineered nanomaterials for synergistic photo-immunotherapy. *Biomaterials*. (2022) 282:121425. doi: 10.1016/j.biomaterials.2022.121425

60. Zhu D, Chen H, Huang C. H2O2 self-producing single-atom nanozyme hydrogels as light-controlled oxidative stress amplifier for enhanced synergistic therapy by transforming "Cold" Tumors. *Advanced Funct Materials*. (2022) 32:2110268. doi: 10.1002/adfm.202110268

61. Wang X, Zhong X, Lei H. Hollow cu2Se nanozymes for tumor photothermal-catalytic therapy. *Chem Materials*. (2019) 31:6174–86. doi: 10.1021/acs.chemmater.9b01958

62. Zhou J, Lei M, Peng XL, Wei DX, Yan LK. Fenton reaction induced by fe-based nanoparticles for tumor therapy. *J BioMed Nanotechnol*. (2021) 17:1510–24. doi: 10.1166/jbn.2021.3130

63. Beaudelot J, Oger S, Perusko S. Photoactive copper complexes: properties and applications. *Chem Rev*. (2022) 122:16365–609. doi: 10.1021/acs.chemrev.2c00033

64. Ran J, Liu T, Song C, et al. Rhythm mild-temperature photothermal therapy enhancing immunogenic cell death response in oral squamous cell carcinoma. *Adv Healthc Mater*. (2023) 12:e2202360. doi: 10.1002/adhm.202202360

65. Canavese G, Ancona A, Racca L, Canta M, Dumontel B, Barbaresco F, et al. Nanoparticle-assisted ultrasound: A special focus on sonodynamic therapy against cancer. *Chem Eng J*. (2018) 340:155–72. doi: 10.1016/j.cej.2018.01.060

66. Bilmin K, Kujawska T, Grieb P. Sonodynamic therapy for gliomas. Perspectives and prospects of selective sonosensitization of glioma cells. *Cells*. (2019) 8:11. doi: 10.3390/cells8111428

67. Sethuraman SN, Singh MP, Patil G, et al. Novel calreticulin-nanoparticle in combination with focused ultrasound induces immunogenic cell death in melanoma to enhance antitumor immunity. *Theranostics*. (2020) 10:3397–412. doi: 10.7150/thno.42243

68. Sethuraman SN, Singh MP, Patil G, Li S, Fiering S, Hoopes PJ, et al. Phase-transformation nanoparticle-mediated sonodynamic therapy: an effective modality to enhance anti-tumor immune response by inducing immunogenic cell death in breast cancer. *Int J Nanomedicine*. (2021) 16:1913–26. doi: 10.2147/IJN.S297933

69. Galluzzi L, Buque A, Kepp O, Zitvogel L, Kroemer G. Immunogenic cell death in cancer and infectious disease. *Nat Rev Immunol*. (2017) 17:97–111. doi: 10.1038/nri.2016.107

70. Schaue D, Ratikan JA, Iwamoto KS, McBride WH. Maximizing tumor immunity with fractionated radiation. *Int J Radiat Oncol Biol Phys*. (2012) 83:1306–10. doi: 10.1016/j.ijrobp.2011.09.049

71. Rodriguez-Ruiz ME, Vitale I, Harrington KJ, Melero I, Galluzzi L. Immunological impact of cell death signaling driven by radiation on the tumor microenvironment. *Nat Immunol*. (2020) 21:120–34. doi: 10.1038/s41590-019-0561-4

72. Sharabi AB, Lim M, DeWeese TL, Drake CG. Radiation and checkpoint blockade immunotherapy: radiosensitisation and potential mechanisms of synergy. *Lancet Oncol*. (2015) 16:e498–509. doi: 10.1016/S1470-2045(15)00007-8

73. Demaria S, Formenti SC. Radiation as an immunological adjuvant: current evidence on dose and fractionation. *Front Oncol*. (2012) 2:153. doi: 10.3389/fonc.2012.00153

74. He C, Ding H, Li L, Chen J, Mo X, Ding Y, et al. Gold nanoparticles enhance the ability of radiotherapy to induce immunogenic cell death in glioblastoma. *Int J Nanomedicine*. (2023) 18:5701–12. doi: 10.2147/IJN.S419712

75. Fan Y, Kuai R, Xu Y, Ochyl LJ, Irvine DJ, Moon JJ. Immunogenic cell death amplified by co-localized adjuvant delivery for cancer immunotherapy. *Nano Lett*. (2017) 17:7387–93. doi: 10.1021/acs.nanolett.7b03218

76. Qin X, Yang T, Xu H, Zhang R, Zhao S, Kong L, et al. Dying tumor cells-inspired vaccine for boosting humoral and cellular immunity against cancer. *J Control Release*. (2023) 359:359–72. doi: 10.1016/j.jconrel.2023.05.044

77. omrat Li R, Hao Y, Roche K, Chen G, Pan W, Wang AZ, et al. Chemotherapy-induced nanovaccines implement immunogenicity equivalence for improving cancer chemoimmunotherapy. *Biomaterials*. (2023) 301:122290. doi: 10.1016/j.biomaterials.2023.122290

78. Min Y, Roche KC, Tian S, Eblan MJ, McKinnon KP, Caster JM, et al. Antigen-capturing nanoparticles improve the abscopal effect and cancer immunotherapy. *Nat Nanotechnol*. (2017) 12:877–82. doi: 10.1038/nnano.2017.113

79. Chattopadhyay S, Liu YH, Fang ZS, Lin CL, Lin JC, Yao BY, et al. Synthetic immunogenic cell death mediated by intracellular delivery of STING agonist nanoshells enhances anticancer chemo-immunotherapy. *Nano Lett*. (2020) 20:2246–56. doi: 10.1021/acs.nanolett.9b04094

80. Huang X, Xiong M, Jin Y, Deng C, Xu H, An C, et al. Evidence that high-migration drug-surviving MOLT4 leukemia cells exhibit cancer stem cell-like properties. *Int J Oncol*. (2016) 49:343–51. doi: 10.3892/ijo.2016.3526

81. Gupta SK, Lysko PG, Pillarisetti K, Ohlstein E, Stadel JM. Chemokine receptors in human endothelial cells. Functional expression of CXCR4 and its transcriptional regulation by inflammatory cytokines. *J Biol Chem*. (1998) 273:4282–7. doi: 10.1074/jbc.273.7.4282

82. Alghamri MS, Banerjee K, Mujeeb AA, Mauser A, Taher A, Thalla R, et al. Systemic delivery of an adjuvant CXCR4-CXCL12 signaling inhibitor encapsulated in synthetic protein nanoparticles for glioma immunotherapy. *ACS Nano*. (2022) 16:8729–50. doi: 10.1021/acsnano.1c07492

Glossary

DAMPs	damage-associated molecular patterns
DTCs	dying tumor cells
ICD	immunogenic cell death
TAAs	tumor-associated antigens
TSAs	tumor-specific antigens
ICB	Immune checkpoint blockade
PD-1/PD-L1	programmed cell death protein 1/programmed death ligand 1
CTLA-4/B7	cytotoxic T lymphocyte-associated protein 4/B7
CRT	calreticulin
ATP	adenosine triphosphate
HMGB1	high mobility histone 1
HSP	heat shock protein
cDAMPs	constitutive DAMPs
iDAMPs	inducible DAMPs
TME	tumor microenvironment
CTLs	cytotoxic T-lymphocytes
IFN-α	interferon-α
TNF-α	tumor necrosis factor-α
IL-6	interleukin-6
PRR	pattern recognition receptor
TLR4	Toll-like receptor 4
APCs	antigen-presenting cells
MDSCs	myeloid-derived suppressor cells
Tregs	regulatory T cells
TAM2	tumor-associated macrophages 2
EPR	enhances penetration and retention
DOX	Doxorubicin
Oxp	Oxaliplatin
PTX	Paclitaxel
IND	indoximod
PDAC	pancreatic ductal carcinoma
PS	photosensitizer
R-SIP	ROS-responsive polymers
PEG	polyethylene glycol
ER	endoplasmic reticulum
ROS	reactive oxygen species
GSH	glutathione
NIR	near-infrared

(Continued)

Continued

Cas9-Cdk5	CRISPR/Cas9-Cdk5 plasmid
HSP70	heat shock protein 70
Hb	hemoglobin
FAL	ER-targeting pardaxin
SPNI	semiconductor polymer nano-immunomodulator
Ce6	Chlorin e6
HCPT	hydroxycamptothecin
ITME	insufficient immunogenic tumor microenvironment
mtROS	mitochondrial reactive oxygen species
TLR7	Toll-like receptor 7
poly (ethylene glycol)-block	poly(2-(diisopropylamino)ethyl methacrylate)
PBEs	phenylboronic acid esters
PPa	photosensitizer pheophorbide a
aPD-L1	anti-PD-L1 antibody
eIF2α	eukaryotic initiation factor 2α
PDA	polydopamine
ZnO	Zinc oxide
PA	photoacoustic
BSA	bovine serum albumin
mPTT	mild-temperature PTT
US	ultrasound
CRT-NP	calreticulin nanoparticles
FUS	focused ultrasound
LIP-PFH NPs	perfluorocarbon nanoparticles
MLipRIR NPs	mitochondria-targeted liposome nanoparticles
GPx	glutathione peroxidase
PFH	perfluoro hexane
EOC	epithelial ovarian cancer
PSDT	PDT/SDT treatment modality
PLGA	poly (lactic-co-glycolic acid)
PFP	perfluoropentane
IR	isoelectronic radiation
dsDNA	destroying double-stranded DNA
MHC-I	mainly involves the up-regulation of histocompatibility complex I
Fas	factor-related apoptosis
H@Gd-NCPs	Hemin@ Gd3+/5′ -GMP NCPs
5′-GMP	5′-guanosine monophosphate
Gd-NCPs	Gd3+/5′-GMP NCPs

(Continued)

Continued

p-eIF2α	phosphorylated eIF2α
FDTs	frozen dying tumor cells
LNs	lymph nodes
PLD	Carboplatin-pegylated Liposomal Doxorubicin
Peg-Intron	Pegylated Interferon Alpha
SBRT	Stereotactic Body Radiotherapy
TACE	Trans-arterial Catheter Chemoembolization
RFA	Radiofrequency Ablation
STF	STF-62247

frontiers | Frontiers in Immunology

TYPE Original Research
PUBLISHED 22 May 2024
DOI 10.3389/fimmu.2024.1371831

OPEN ACCESS

EDITED BY
Laura Senovilla,
Spanish National Research Council (CSIC), Spain

REVIEWED BY
Manik Kuvalekar,
Baylor College of Medicine, United States
Zhirui Zeng,
Guizhou Medical University, China

*CORRESPONDENCE
Jianxiang Li
aljxcr@suda.edu.cn

RECEIVED 17 January 2024
ACCEPTED 02 May 2024
PUBLISHED 22 May 2024

CITATION
Wang J, Liu K, Li J, Zhang H, Gong X, Song X, Wei M, Hu Y and Li J (2024) Identifying and assessing a prognostic model based on disulfidptosis-related genes: implications for immune microenvironment and tumor biology in lung adenocarcinoma. *Front. Immunol.* 15:1371831. doi: 10.3389/fimmu.2024.1371831

Identifying and assessing a prognostic model based on disulfidptosis-related genes: implications for immune microenvironment and tumor biology in lung adenocarcinoma

Jin Wang, Kaifan Liu, Jiawen Li, Hailong Zhang, Xian Gong, Xiangrong Song, Meidan Wei, Yaoyu Hu and Jianxiang Li*

School of Public Health, Suzhou Medical College of Soochow University, Jiangsu, Suzhou, China

Introduction: Lung cancer, with the highest global mortality rate among cancers, presents a grim prognosis, often diagnosed at an advanced stage in nearly 70% of cases. Recent research has unveiled a novel mechanism of cell death termed disulfidptosis, which is facilitated by glucose scarcity and the protein SLC7A11.

Methods: Utilizing the least absolute shrinkage and selection operator (LASSO) regression analysis combined with Cox regression analysis, we constructed a prognostic model focusing on disulfidptosis-related genes. Nomograms, correlation analyses, and enrichment analyses were employed to assess the significance of this model. Among the genes incorporated into the model, CHRNA5 was selected for further investigation regarding its role in LUAD cells. Biological functions of CHRNA5 were assessed using EdU, transwell, and CCK-8 assays.

Results: The efficacy of the model was validated through internal testing and an external validation set, with further evaluation of its robustness and clinical applicability using a nomogram. Subsequent correlation analyses revealed associations between the risk score and infiltration of various cancer types, as well as oncogene expression. Enrichment analysis also identified associations between the risk score and pivotal biological processes and KEGG pathways. Our findings underscore the significant impact of CHRNA5 on LUAD cell proliferation, migration, and disulfidptosis.

Conclusion: This study successfully developed and validated a robust prognostic model centered on disulfidptosis-related genes, providing a foundation for predicting prognosis in LUAD patients.

KEYWORDS

disulfidptosis, LASSO, prognostic model, lung cancer, immune infiltration

1 Introduction

Lung cancer remains the leading cause of cancer-related death worldwide, and its mortality accounts for approximately 18% of all types of cancer (1). Non–small cell lung cancer (NSCLC) is the most common lung cancer subtype, and it comprises two major histological types: lung squamous cell carcinoma (LUSC) and lung adenocarcinoma (LUAD). In addition to conventional therapies such as surgery, chemotherapy and radiotherapy, targeted therapy and immunotherapy for lung cancer have also developed rapidly in recent years. However, these therapies can only benefit some patients and have many limitations, such as side effects and high costs (2, 3). Nearly 70% of patients with NSCLC are initially diagnosed at a locally advanced stage and suffer from a poor prognosis (4). The 5-year survival rate is less than 3% for patients with advanced NSCLC (5). Therefore, exploring new diagnostic and prognostic markers is an important way to improve the early diagnosis and prognosis of lung cancer.

In the past few years, an increasing number of forms of cell death have been discovered, providing more possibilities for humans to combat various diseases (6). Activating specific forms of death through agonist treatment can provide new strategies for cancer treatment. Recent research has revealed a novel form of cell death, disulfidptosis, which is a form of cell death induced by glucose deficiency and SLC7A11 (7, 8). Specifically, disulfidptosis was triggered when cells with high SLC7A11 protein expression were subjected to glucose starvation. Treatment with glucose transporter (GLUT) inhibitors can induce disulfidptosis in cancer cells with high SLC7A11 expression without significant toxicity to normal tissues, thus effectively inhibiting tumor growth (7). This new form of death opens new doors for the development of cancer treatment strategies. Although the basic concept of disulfidptosis has been proposed, its detailed mechanisms remain unclear, especially its role across different cell types and under disease conditions. Currently, GLUT inhibitors are the only known inducers of disulfidptosis, highlighting the limited understanding of their mechanisms and therapeutic targets (9).

In this study, disulfidptosis-related genes (DRGs) identified from CRISPR–Cas9 screenings were obtained from a previous study (8), and they were used to establish a prognostic model based on the LUAD dataset in the TCGA database and another LUAD dataset in the GEO database using the least absolute contact and selection operator (LASSO) and Cox regression analysis (Figure 1). The model-derived risk factors were further analyzed for associations with immune cell infiltration, tumor suppressor gene expression, tumor-related biological functions and drug sensitivity. Moreover, the key genes in the model were further validated by *in vitro* assays.

2 Methods

2.1 Data collection

The LUAD data of 572 patients, including 59 normal tissues adjacent to cancer tissues, 513 tumor tissues and corresponding clinical information, were retrieved from The Cancer Genome Map (TCGA) database. The expression profile and clinical results are open and accessible. To validate the prognostic model based on the TCGA LUAD cohort, another LUAD dataset (GSE13213) was retrieved from the Gene Expression Omnibus (GEO) database as an external validation dataset. The GSE13213 (10) dataset contains gene expression data and prognosis information for 117 primary lung adenocarcinoma samples.

The disulfidptosis-related genes (DRGs) were extracted via CRISPR–Cas9 screening from a previous study (8). Genes with |normZ values| > 2 and P values< 0.05, including 399 suppressors and 409 synergists, were further screened to construct a prognostic model.

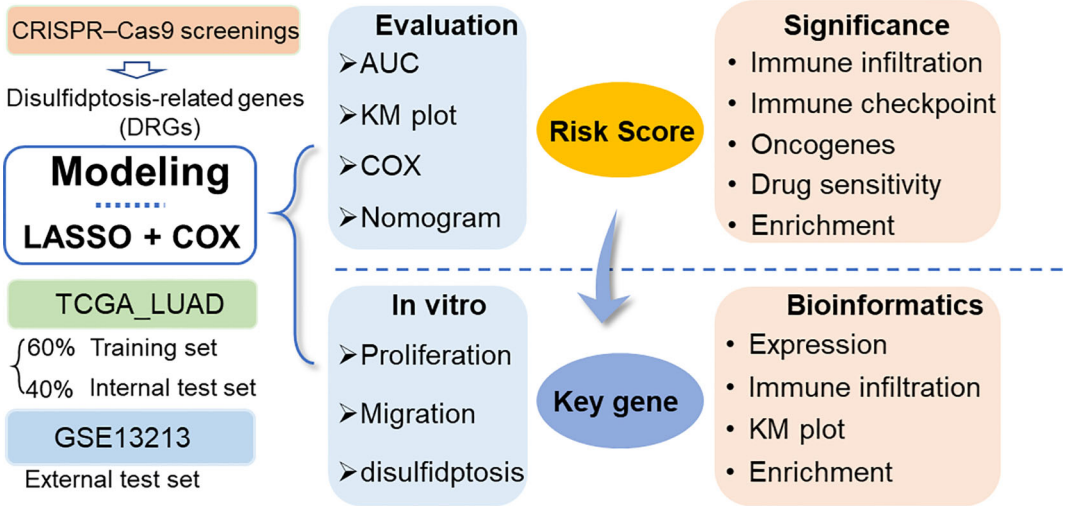

FIGURE 1
Workflow diagram of this study. DRGs: disulfidptosis-related genes. LASSO, least absolute contact and selection operator. AUC, area under the curve; TCGA, cancer genome map; LUAD, lung adenocarcinoma.

2.2 Prognostic model construction and validation

The chi-square test was used to analyze the differences between the training set, the internal test set and the total dataset in terms of sex, age, tumor stage, depth of invasion (T), lymph node metastasis (N), distal metastasis (M) status and smoking history. The univariate Cox model was used to study the relationship between continuous expression levels of DRGs and OS. The risk ratio (HR) and P value from the univariate Cox regression analysis were used to identify candidate survival-related DRGs. DRGs with an HR > 1 were considered risky DRGs, and those with an HR< 1 were defined as protective DRGs. DRGs that met the criterion of a P value<0.05 were identified as survival-related DRGs and further included in LASSO and multivariate Cox regression analyses to construct a prognostic model. The risk score for each LUAD patient was calculated based on the expression of DRGs (Exp_i) and Cox coefficients ($coef_i$) Risk score = $\sum_{i=1}^{n} Exp_i \times coef_i$. All patients in each dataset were divided into high- or low-risk groups according to the median value. K–M plots were generated to evaluate patient survival in each dataset between the high- and low-risk groups. Moreover, multivariate Cox regression analysis was performed to estimate whether the risk score was independent of clinicopathological features. To investigate the performance of the prognostic model in predicting LUAD patient outcomes, the area under the curve (AUC) of the ROC curve (AUC) was calculated. In addition, the expression of each MRG in the model and its correlation with clinicopathological features were also analyzed.

All analyses were performed with R software (version 4.3.1) and the corresponding fundamental package. The "care" package was used to randomly divide the patients into two datasets at a ratio of 6:4 according to their survival status, which were used as training sets and internal test sets, respectively. The "glmnet" package was used for LASSO regression model analysis. In addition, the "survival" and "survminer" packages were used to perform univariate and multivariate Cox analyses and to generate Kaplan–Meier plots. The "TimeROC" package was used to generate the time-dependent receiver operating characteristic (ROC) curve, and the "survivalROC" package was used to calculate the area under the curve (AUC). Nomogram plots were generated with the "rms" package.

2.3 Enrichment analysis

Based on the correlation analysis between the risk score and all mRNAs, gene set enrichment analysis (GSEA) was further performed by using the "ClusterProfiler" package of R software (version 4.3.1).

In addition, the differentially expressed genes (DEGs) between the low and high groups were identified based on the R package "limma" with the thresholds of log(fold change) >1 and P value< 0.05. The DEGs were further input into the DAVID online tool (https://david.ncifcrf.gov/) for pathway and biological process enrichment.

2.4 Correlation analysis

To further explore the biological role and clinical significance of the DRG prognostic model, correlation analysis was performed between the risk score and the expression of oncogenes, tumor mutation burden (TMB), immune regulatory gene expression, immune cell infiltration and tumor immune dysfunction and exclusion (TIDE) score. Correlation analysis was performed with the Spearman method based on the "psych" package.

The oncogenes were extracted from the ONGene database (http://www.ongene.bioinfo-minzhao.org) (11). A total of 73 immunomodulatory genes (IMGs) (12) were extracted from previous studies. The immune cell infiltration score was calculated by using the XCELL algorithm (13). Moreover, the TIDE score, dysfunction score and exclusion score of each patient in the datasets were predicted using the TIDE online tool (http://tide.dfci.harvard.edu/) following standard procedures (14).

The Genomics of Drug Sensitivity in Cancer (GDSC) database was developed by the Sanger Research Institute to collect data on the sensitivity and response of tumor cells to drugs (15). "OncoPredict" was used to calculate the drug sensitivity of each sample in the training and validation datasets based on the GDSC V2.0 database (16).

2.5 shRNA and overexpression plasmid construction

CHRNA5 shRNA sequences were designed according to BLOCK-iT™ RNAi Designer (https://rnaidesigner.thermofisher.com/rnaiexpress), and the annealed double-stranded shRNA was cloned and inserted into the pGreen vector. After testing the knockdown efficiency of several candidate shRNAs, the sequence 5'-GGGTCACTATGGAGTTCAAAG-3' targeting *CHRNA5* and the sequence 5'-GCAGCTGAAATATCCTAAACT-3' targeting FTO were selected for subsequent experiments. A scrambled nonspecific control shRNA (shNC) was also cloned and inserted into the same vector and used as a negative control. For overexpression, the full-length coding sequence of *CHRNA5* was amplified and cloned and inserted into the pCDH plasmid.

2.6 Cell culture and transfection

The human lung cancer cell lines A549 and H1299 were purchased from the American Type Culture Collection (ATCC). All cells were cultured in DMEM (Thermo Fisher Scientific, Inc.) supplemented with 10% FBS (Thermo Fischer Scientific, Inc.) at 37°C in the presence of 5% CO2.

GC cells were seeded in 6-well plates in each well and grown for 24 h. Then, the cells were transfected with 2.5 μg of shCHRNA5 or shNC using Lipofectamine 6000 reagent (Beyotime, China) following the manufacturer's protocol.

2.7 Cell proliferation and migration assays

For cell proliferation, lung cancer cells were initially seeded into 6-well plates. These cells were then incubated with 10 μM EdU for 2 hours. Next, the cells were stabilized with 4% paraformaldehyde and permeabilized using 0.3% Triton X-100, a process conducted in a PBS environment. A subsequent step involved incubating the cells with a click reaction solution, a product provided by the Beyotime Institute of Biotechnology in China. Within a 24-hour timeframe, images of the cells were obtained using an inverted fluorescence microscope, and the resulting data were analyzed with the assistance of NIH ImageJ software (version 1.8.0).

In terms of the cell migration assay, cells from each group were methodically placed in the upper chambers of each Transwell membrane (Corning, Inc., USA). Next, 1 ml of medium without FBS and 2 ml of complete medium were added to the bottom chamber. After a 24-hour incubation period at 37°C in an environment with 5% CO2, the cells were stabilized in methanol and stained with 0.5% crystal violet for 30 minutes. The final stage involved washing the cells in the upper chamber with phosphate-buffered saline (PBS, provided by Gibco, USA) three times. The cells were then imaged using a microscope and evaluated with NIH ImageJ software (version 1.8.0).

2.8 Western blot

Total protein from lung cancer cells was extracted using RIPA lysis buffer (Beyotime, China). Protein concentrations were quantified via an Enhanced BCA Kit (Beyotime, China). The proteins, in equivalent quantities, were separated via SDS–PAGE, and 30 μg of each protein was transferred onto a PVDF membrane (Millipore Sigma, Billerica, MA). After blocking with 5% BSA, the membranes were incubated at 4°C overnight with the following primary antibodies: anti-E-cadherin (CDH1, ProteinTech Group, Inc., USA) and anti-N-cadherin (CDH2, ProteinTech Group, Inc., USA), both at a 1:1,000 dilution. Anti-GAPDH (1:1,000 dilution, Cell Signaling Technology Inc., USA) was used as a loading control. The membranes were then incubated with HRP-labeled secondary antibodies for 2 hours at room temperature and subsequently washed three times with TBST. The protein bands were visualized using an enhanced chemiluminescence (ECL) substrate and the GeneTools GBox system (Syngene) and were scanned and quantified with ImageJ software (National Institutes of Health, NIH).

2.9 Disulfidptosis assays

Glucose-free DMEM was used to simulate glucose deprivation conditions. When CHRNA5 was knocked down or overexpressed in cells, the culture medium was replaced with glucose-free medium, and the regulatory effect of the gene on dysfildptosis was determined by measuring cell viability and apoptosis.

2.10 Statistical analysis

Statistical analyses were conducted using GraphPad V8.3.0 software (GraphPad Software, LLC), and the data are presented as the means ± standard deviations. To ascertain the existence of statistically significant differences between the means of two or more groups, Student's t test and analysis of variance (ANOVA) were employed. All the statistical tests were two-tailed, and a P value less than 0.05 was considered to indicate statistical significance.

3 Manuscript formation

3.1 Data collection

Three LUAD cohorts and corresponding clinical data were obtained from the TCGA and GEO databases. The demographic and clinical data for the training, internal testing and independent validation sets are summarized in Table 1. After filtering out the samples with missing clinical information from the TCGA LUAD dataset, a total of 504 LUAD patients, including 183 living patients and 321 patients who died at the end of follow-up, were included in this study (median follow-up: 2.474 years). This dataset was randomly divided into a training set (n = 303, 60%) and an internal testing set (n = 201, 40%). As expected, no significant differences were found in the major clinicopathological features between the training, testing and entire TCGA LUAD datasets (Table 1). In addition, this study also included a GEO dataset (GSE13213) including 117 LUAD patients, which included 41.88% of deaths at the end of follow-up (median follow-up time was 5.306 years).

3.2 Construction and validation of the prognostic model according to the DEGs in LUAD patients

Based on the CRISPR–Cas9 screenings, a total of 808 DRGs were screened with the criteria of |normZ values| > 2 and P value< 0.05 (Supplementary Figure 1). Forty prognosis-related DRGs were identified based on the TCGA training set using univariate Cox regression analysis (Figure 2A). Consequently, LASSO-penalized Cox analysis further identified 20 DRGs for multivariate analysis (Supplementary Figures 2A-B). The multivariate Cox proportional hazard model was built stepwise using the likelihood-ratio forward method to reach the highest significance. Hence, 14 DRGs were further screened to construct a risk model to assess the prognostic risk of patients with LUAD: risk score = (0.577 × GNG12 Exp) + (0.358 × UQCRB Exp) + (0.317 × AP3B1 Exp) + (0.313 × SLC35E3 Exp) + (0.298 × CHD1L Exp) + (0.237 × DDIT4 Exp) + (0.219 × KCNJ14 Exp) + (0.204 × CHRNA5 Exp) + (0.180 × LEFTY1 Exp) + (-0.119 × LAX1 Exp) + (-0.265 × SLC46A3 Exp) + (-0.288 × MYO6 Exp) + (-0.445 × IVD Exp) + (-0.456 × GDPD1 Exp) (Figure 2B). ROC curves demonstrated that the risk score serves as a significant

TABLE 1 Clinical features of the LUAD patients in the training set, testing set and validation set.

Characteristics	TCGA-LUAD				GSE13213 n = 117
	Training set (60%) n = 303	Testing set (40%) n = 201	All data n = 504	χ2 P value	
Gender					
female	162 (53.47%)	108 (53.73%)	270 (53.57%)	0.998	57 (48.72%)
male	141 (46.53%)	93 (46.27%)	234 (46.43%)		60 (51.28%)
Age					
≤60	95 (31.99%)	63 (31.98%)	158 (31.98%)	1.000	52 (44.44%)
>60	202 (68.01%)	134 (68.02%)	336 (68.02%)		65 (55.56%)
M					
M0	206 (93.64%)	129 (92.14%)	335 (93.06%)	0.863	
M1	14 (6.36%)	11 (7.86%)	25 (6.94%)		
N					
N0	195 (66.33%)	129 (65.82%)	324 (66.12%)	0.993	87 (74.36%)
N1/2/3	99 (33.67%)	67 (34.18%)	166 (33.88%)		30 (25.64%)
T					
T1/2	258 (85.15%)	180 (89.55%)	438 (86.90%)	0.357	104 (88.89%)
T3/4	45 (14.85%)	21 (10.45%)	66 (13.10%)		13 (11.11%)
Stage					
Stage I/II	239 (78.88%)	151 (75.12%)	390 (77.38%)	0.615	79 (67.52%)
Stage III/IV	64 (21.12%)	50 (24.88%)	114 (22.62%)		38 (32.48%)
Smoke history					
Nonsmoke	120 (39.60%)	80 (39.80%)	200 (39.68%)	0.999	
Smoke	183 (60.40%)	121 (60.20%)	304 (60.32%)		
OS time					
≤2	171 (56.44%)	114 (56.72%)	285 (56.55%)	0.998	13 (11.11%)
>2	132 (43.56%)	87 (43.28%)	219 (43.45%)		104 (88.89%)
OS					
Live	188 (62.05%)	133 (66.17%)	321 (63.69%)	0.641	68 (58.12%)
Dead	115 (37.95%)	68 (33.83%)	183 (36.31%)		49 (41.88%)

predictor of the OS of LUAD patients, with AUCs greater than 0.730 at 1-5 years (Figure 2C). Samples in the training set were classified into low- and high-risk groups based on the median value of the risk score. KM survival analysis indicated that the low-risk group had significantly favorable OS for LUAD patients (Figure 2D). The distribution of risk scores between the low-risk and high-risk groups and the survival status and survival time of patients in the two different risk groups are depicted in Figure 2E. The relative expression of the 14 DRGs for each patient is shown in Figure 2F.

To further verify the accuracy and reliability of the prognostic model obtained from the training set, we applied it to the internal testing set and other independent validation cohorts, *viz*. GSE13213. By using the same prognostic model, the classifier could also successfully subdivide patients in the internal testing set (n = 201) into high-risk or low-risk groups with marked differences in overall survival (P = 0.008; Supplementary Figure 3). In addition, the same observation was also found in the entire TCGA LUAD dataset (training set and internal testing set, Figure 3A), as well as in the GSE13213 validation cohort (Figure 3B). Additionally, ROC curves indicated that the risk score was an effective predictor of the OS of LUAD patients in both the TCGA LUAD (Figure 3C) and GSE13213 (Figure 3E) datasets, with AUCs greater than 0.750. Consistent with the results demonstrated in the training set, the KM survival analysis indicated that the DRG risk score

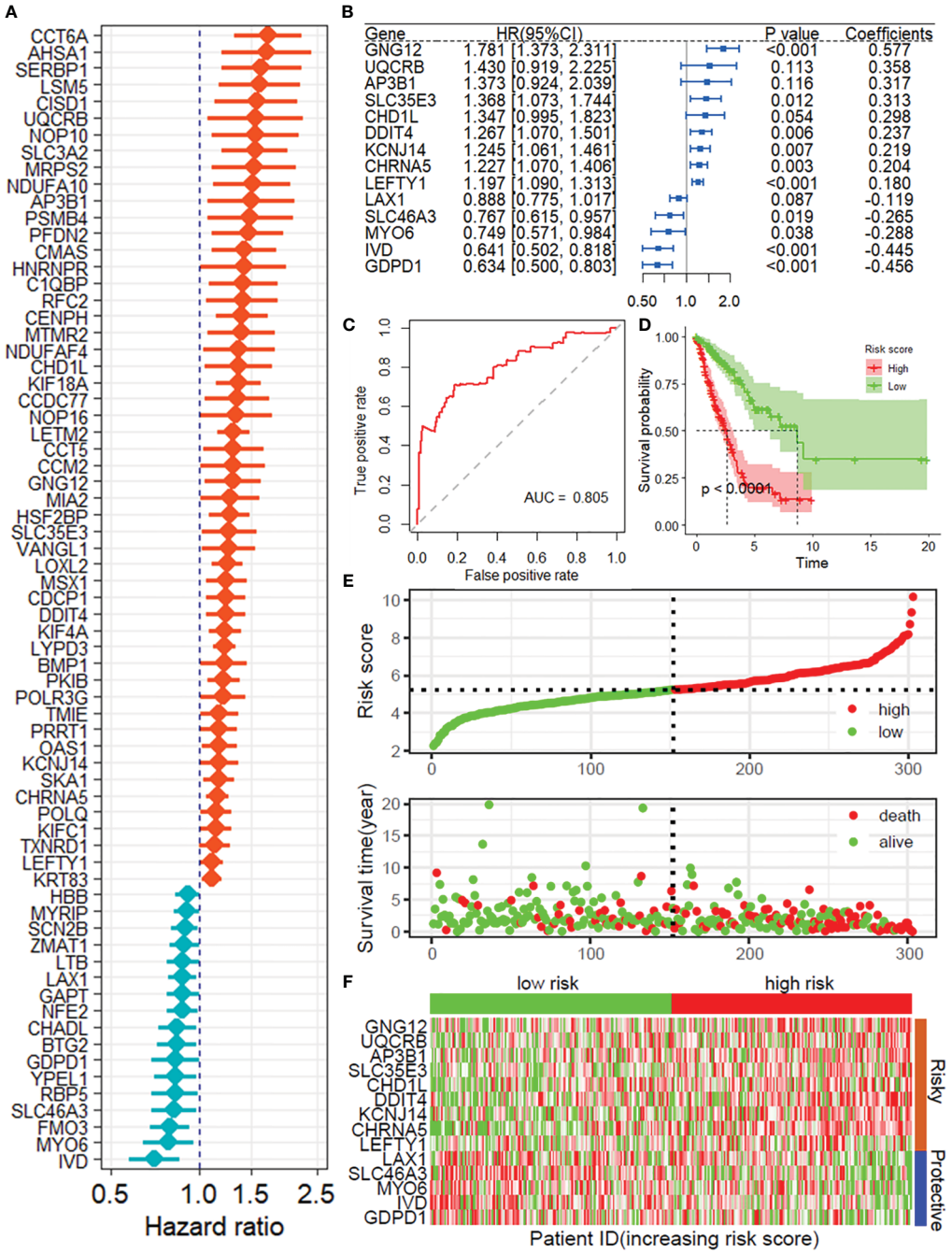

FIGURE 2
Construction of the prognostic model of DRGs. **(A)** Univariate Cox regression analysis for the selection of DRGs correlated with the OS of LUAD patients. **(B)** Forest plot showing the multivariate Cox regression analysis of 14 DRGs. **(C)** ROC curves for 1-year OS in the training set. **(D)** K–M curve of OS in the training group. **(E)** Risk score distribution and survival status of the training group. **(F)** Heatmap showing the expression of 14 DRGs in the training group. DRGs, disulfidptosis-related genes; OS, Overall survival; ROC, receiver operating characteristic curve.

was a significant risk factor for OS in LUAD patients in the above 2 datasets (all $P< 0.001$, Figure 3D, F). Importantly, when the other 3 survival indicators, namely, disease-specific survival (DSS), disease-free interval (DFI) and progression-free interval (PFI), were considered, Kaplan–Meier curves and receiver operating characteristic (ROC) curves indicated that the low-risk group had significantly favorable outcomes for LUAD patients (Supplementary Figure 4).

3.3 The DRG risk score is independent of clinical features

As depicted in Supplementary Table 1, the DRG risk score was related to several clinicopathological features in the TCGA-LUAD dataset, including sex, lymph node metastasis, invasion depth and stage. To assess whether the risk score is an independent indicator in

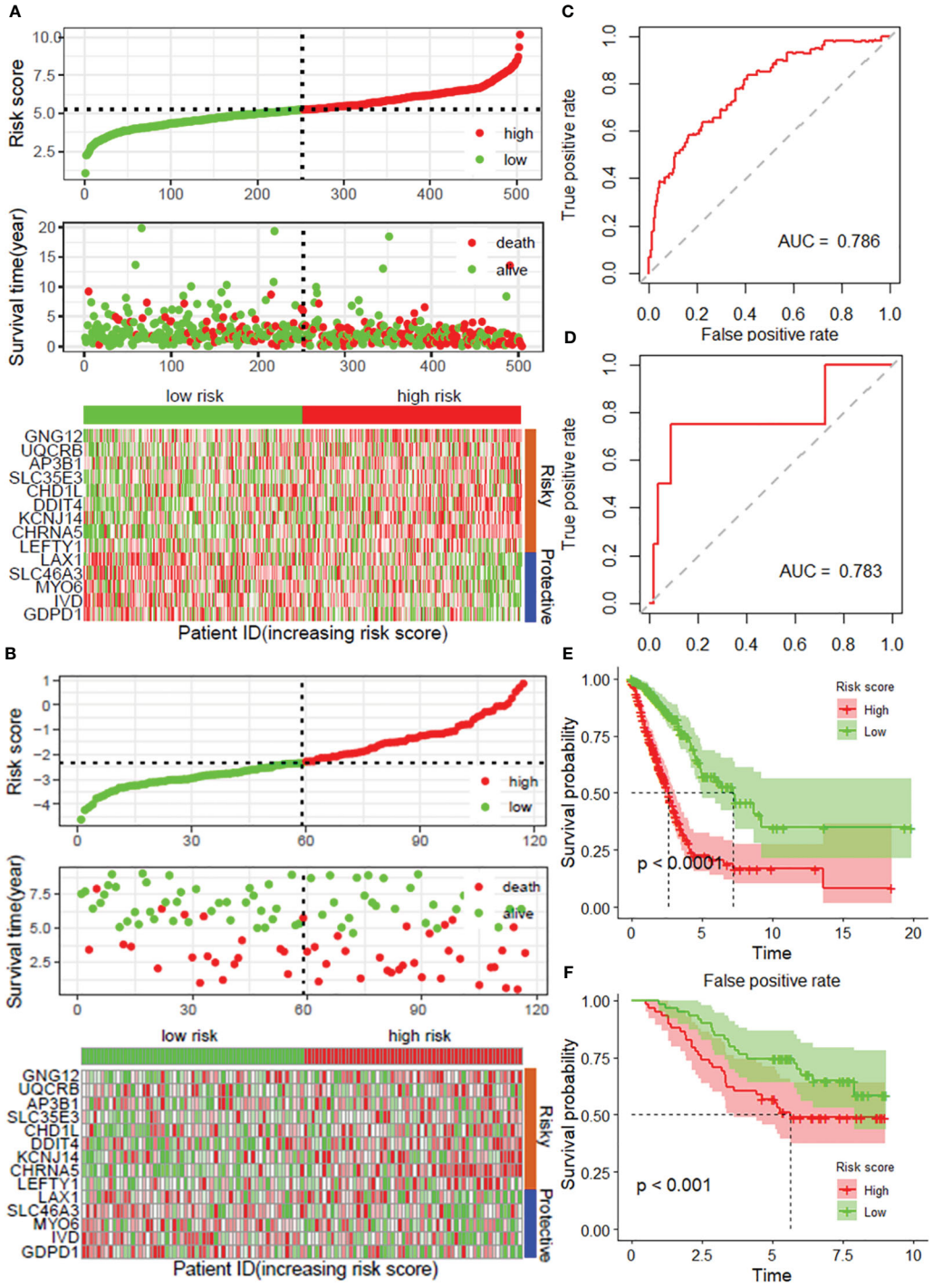

FIGURE 3
Validation of the prognostic model with 14 DRGs constructed from the training dataset. Risk score distribution, survival status and expression of 14 DRGs in the TCGA-LUAD dataset **(A)** and external validation datasets, *viz*. and GSE31213 **(B)**. ROC curves for overall survival in the TCGA-LUAD **(C)** and GSE31213 **(D)** datasets. K–M curves of OS in the TCGA-LUAD **(E)** and GSE13213 **(F)** datasets. DRGs, disulfidptosis-related genes; ROC, dependent receiver operating curve; TCGA, the cancer genome map; LUAD, lung adenocarcinoma.

LUAD patients, the effect of each clinicopathologic feature on OS was analyzed by univariate Cox regression (Figure 4A). As shown in Figure 4B, after multivariable adjustment, the risk score remained a powerful and independent factor in the entire TCGA-LUAD dataset. Moreover, the risk score was verified as an independent factor based on the GSE13213 dataset (Supplementary Figures 5A–B). The discrepancies in OS stratified by lymph node metastasis (N) and invasion depth (T) stage were analyzed between the low- and high-risk groups in the entire TCGA-LUAD dataset. According to the subgroups classified by N and T stage, the OS of the low-risk group was superior to that of the high-risk group (Supplementary Figures 6A-D).

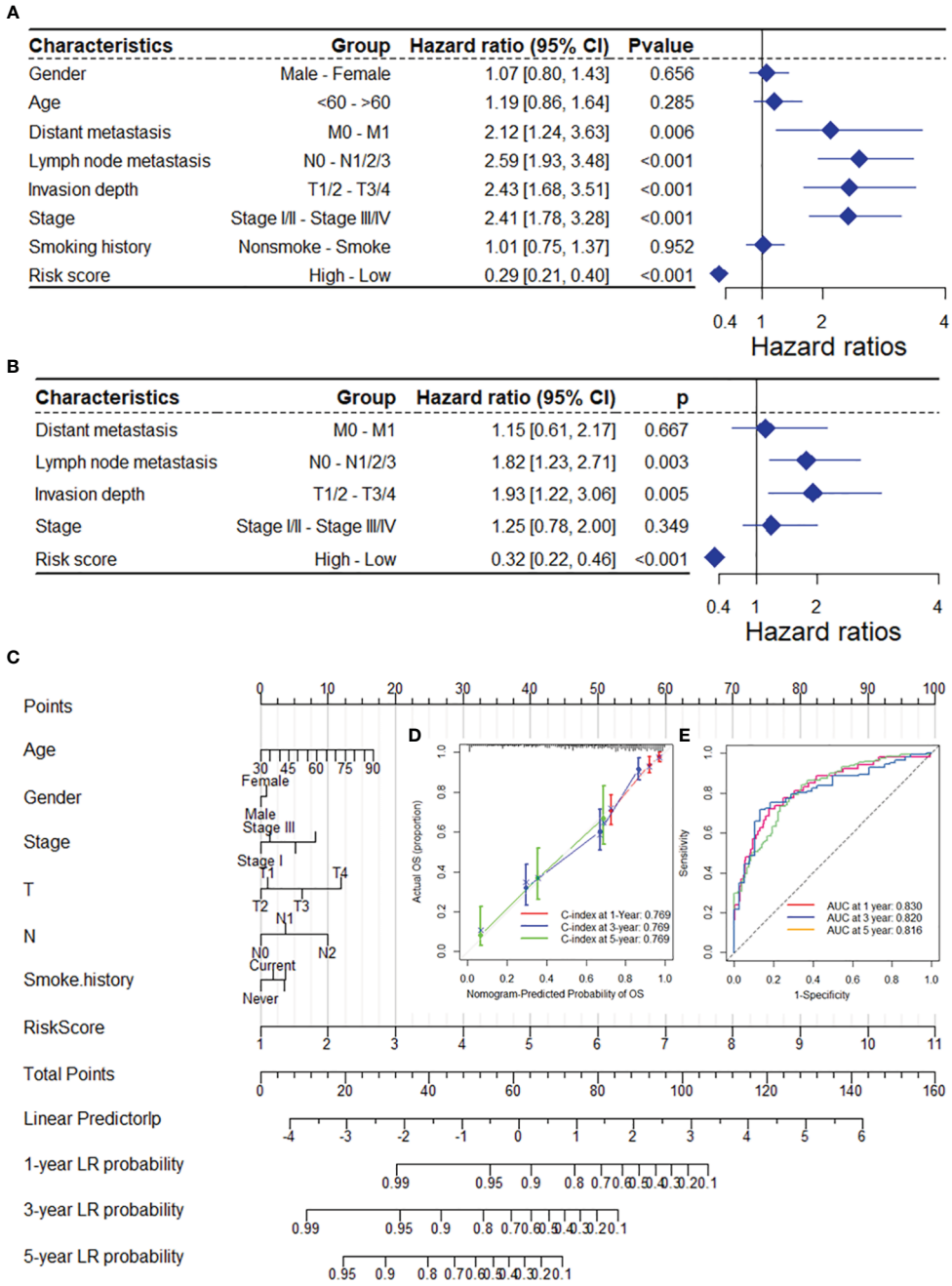

FIGURE 4
The DRG risk score was an independent prognostic factor for OS in the TCGA-LUAD dataset. Univariate **(A)** and multivariate **(B)** Cox regression analyses of the risk score and clinicopathological features for overall survival in the TCGA-LUAD dataset. **(C)** The nomogram consists of the 14-gene risk score and 6 clinical indicators based on the TCGA-LUAD dataset. The points from these variables are combined, and the locations of the total points are determined. The total points projected on the bottom scales indicate the probabilities of 1-year, 3-year and 5-year overall survival. Calibration plots **(D)** and receiver operating characteristic (ROC) curves **(E)** were used to validate the prognostic nomogram constructed based on the TCGA-LUAD dataset. DRGs, disulfidptosis-related genes; ROC, dependent receiver operating curve; TCGA, the cancer genome map; LUAD, lung adenocarcinoma.

To ensure the robustness and practicability of the 14-DRG prognostic model, a prognostic nomogram for predicting overall survival in LUAD patients was established using the TCGA-LUAD and GSE13213 datasets (Figure 4C and Supplementary Figure 5C). Major clinicopathological features and risk scores were included in the nomogram. The nomogram was internally validated by computing the bootstrap C-index (≥ 0.700 both in TCGA-LUAD and GSE13213) and a calibration plot (Figure 4C and Supplementary Figure 6E). The ROC curve confirmed that the score calculated based on the nomogram was highly predictive of overall survival, with AUCs of 0.830 and 0.905 at 1 year in the TCGA-LUAD cohort and GSE13213 cohort, respectively (Figure 4C and Supplementary Figure 6F).

3.4 The DRG risk score is associated with the immune landscape

Based on the XCELL algorithm and TCGA-LUAD dataset, the DRG risk score was found to be associated with infiltration of multiple immune cell types (Figure 5A), including CD4+ T cells, Th2 cells, common lymphoid progenitors, mast cells, and B cells, as well as the microenvironment and immune score. Additionally, the risk score was associated with infiltration of many types of immune cells, as was the immune score based on the GSE13213 dataset (Figure 5B). In addition, a significant negative correlation between the risk score and dysfunction score was found based on the TIDE algorithm in the TCGA-LUAD dataset (r = -0.239), and the low-risk group had a higher TIDE score (Figure 5F). A positive correlation was found between the exclusion score and the risk score (r = 0.457), and the high-risk group had the highest score (Figure 5G). After comprehensive consideration of the dysfunction and exclusion scores, a positive correlation was found between the TIDE score and the risk score (r = 0.169), and the high-risk group had a higher score (Supplementary Figures 7A-B). Additionally, the same results were found in the GSE13213 validation dataset (Supplementary Figures 7C-H). Overall, the TIDE results suggest that the DRG risk score may be associated with poorer immune checkpoint inhibition therapeutic efficacy.

3.5 DRG risk score is associated with cancer progression

Correlation analysis revealed that the DRG risk score was significantly related to multiple oncogenes in both the TCGA-LUAD (Figure 6A) and GSE13213 (Figure 6B) datasets. After the intersection of the oncogenes correlated with the risk score in both datasets, 35 positively correlated and 4 negatively correlated oncogenes were identified (Figure 6C), including FOSL1, FOXM1, CDK1, and CCNB2. By analyzing the differentially expressed genes (DEGs) between the high-risk and low-risk groups in the TCGA-LUAD and GSE13213 datasets, we obtained a total of 554 genes that were upregulated in both datasets and 401 genes that were downregulated (Supplementary Figure 8). The enrichment analysis revealed that these DEGs were significantly enriched in several important biological processes and pathways, including lung alveolus development, G2/M transition of mitotic cell cycle, extracellular matrix organization, cell proliferation, DNA replication, cell adhesion and immune response (Figure 6D), as well as drug metabolism, ABC transporters, p53 signaling pathway, ECM-receptor interaction, cell cycle and PI3K-Akt signaling pathway (Figure 6E). Moreover, GSEA was performed to investigate the biological processes and pathways potentially related to the DRG risk score. As depicted in Figure 6F, the DRG risk score was related to multiple cancer-related biological processes, including DNA replication, recombination repair, double-strand break repair, cell cycle checkpoint signaling and the B-cell receptor signaling pathway, as well as other vital processes, in both the TCGA-LUAD and GSE13213 datasets (Figure 6G). Additionally, the risk score was related to several cancer-associated pathways (Figure 6H), mainly the proteasome, cell cycle, DNA replication, mismatch repair and RNA degradation pathways, as well as other crucial pathways (Figure 6I).

3.6 CHRNA5 contributes to lung cancer progression

Among these DRGs in the constructed risk model, CHRNA5 had a high normalized Z score (normZ = 2.23, Figure 7A) and the highest correlation with SLC7A11 (r = 0.432, Figures 7B-C). Survival analysis revealed that patients with lower CHRNA5 expression had longer overall survival in both the TCGA-LUAD datasets (Supplementary Figure 9A). When considering disease-specific survival and progression-free survival, a better prognosis was found for patients with low CHRNA5 expression (Supplementary Figures 9B-C). CHRNA5 expression was greater in tumors than in normal tissues in multiple LUAD datasets (Figure 7D). Further correlation analysis revealed that CHRNA5 expression was significantly correlated with multiple oncogenes (Figure 7E). Additionally, CHRNA5 expression was positively correlated with the sensitivity to several antitumor drugs (Figure 7F). Correlation analysis of immune cell infiltration revealed that CHRNA5 was significantly correlated with several cell types (Figure 7G), including DC4+ T cells (Th1/2), cancer-associated fibroblasts (Figure 7H), monocytes, mast cells, and M2 macrophages, as well as the microenvironment, stroma and immune score. Moreover, CHRNA5 expression was correlated with tumor stemness in the TCGA-LUAD cohort (Figure 7I). GSEA further demonstrated that CHRNA5 is related to many cancer-related KEGG pathways (Figures 7J-K) and biological processes (Supplementary Figure 9D), including the cell cycle (NES = 2.868), DNA replication (NES = 2.586), the JAK-STAT signaling pathway (NES = -2.198) and cell adhesion molecules (NES = -2.823), as well as several other vital terms.

3.7 CHRNA5 regulates proliferation, migration and disulfidptosis in LUAD cells

To evaluate the biological function of CHRNA5 in LUAD cells, we constructed shRNA plasmids to knock down CHRNA5 and a plasmid to overexpress CHRNA5 (Supplementary Figure 10). EdU assays revealed that CHRNA5 knockdown attenuated LUAD cell proliferation, while CHRNA5 overexpression amplified proliferation in A549 and H1299 cells (Figures 8A-B). The transwell migration assay indicated that CHRNA5 knockdown significantly reduced cell migration, while CHRNA5 overexpression significantly increased cell migration (Figures 8C-D). The western blotting results demonstrated that CHRNA5 knockdown significantly promoted CDH1 expression (Figures 8E-F) but inhibited CDH2 expression (Figure 8G). Conversely, CHRNA5 overexpression resulted in the upregulation of CDH2 and the downregulation of CDH1 (Figures 8E-G). To further evaluate the synergistic role of CHRNA5 in disulfidptosis, we used glucose-deprived medium to culture LUAD cells. The results of the CCK-8 assay revealed that

10.3389/fimmu.2024.1371831

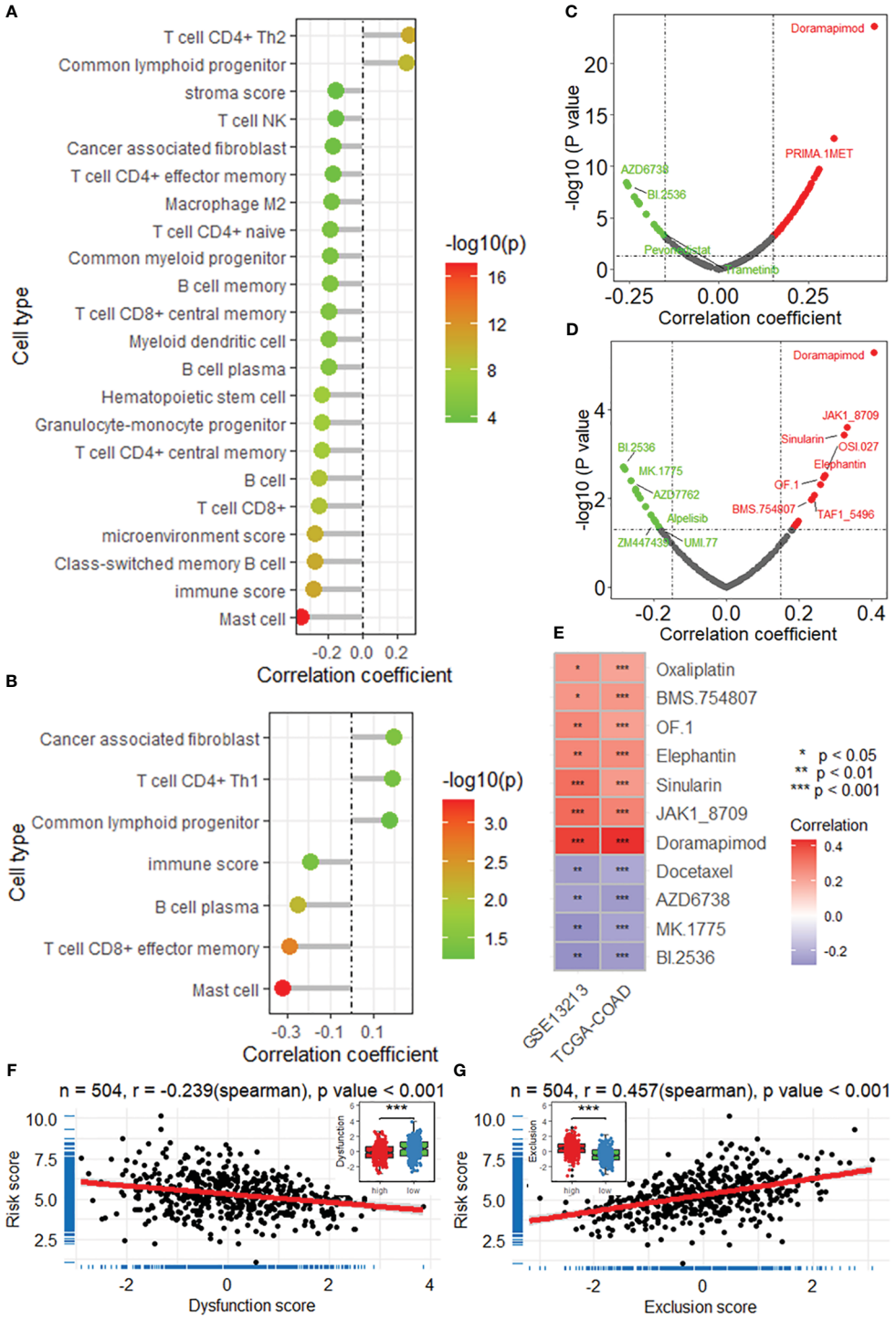

FIGURE 5
The DRG risk score is correlated with the immune landscape. Lollipop plots showing the results of the correlation analysis between the risk score and immune cell infiltration based on the XCELL algorithm in the TCGA-LUAD **(A)** and GSE13213 **(B)** datasets. Scatter plots showing the results of the correlation analysis between the risk score and sensitivity to antitumor drugs in the TCGA-LUAD **(C)** and GSE13213 **(D)** datasets. **(E)** Heatmap showing the intersection of the drugs significantly correlated with the risk score. *, **, *** represent P value of correlation analysis less than 0.05, 0.01, 0.001, respectively. Correlation analysis between the risk score and dysfunction score **(F)** and exclusion score **(G)**. ***, P value of t-test < 0.001 betweenh igh and low risk groups. DRGs, disulfidptosis-related genes; TCGA, the cancer genome map; LUAD, lung adenocarcinoma.

10.3389/fimmu.2024.1371831

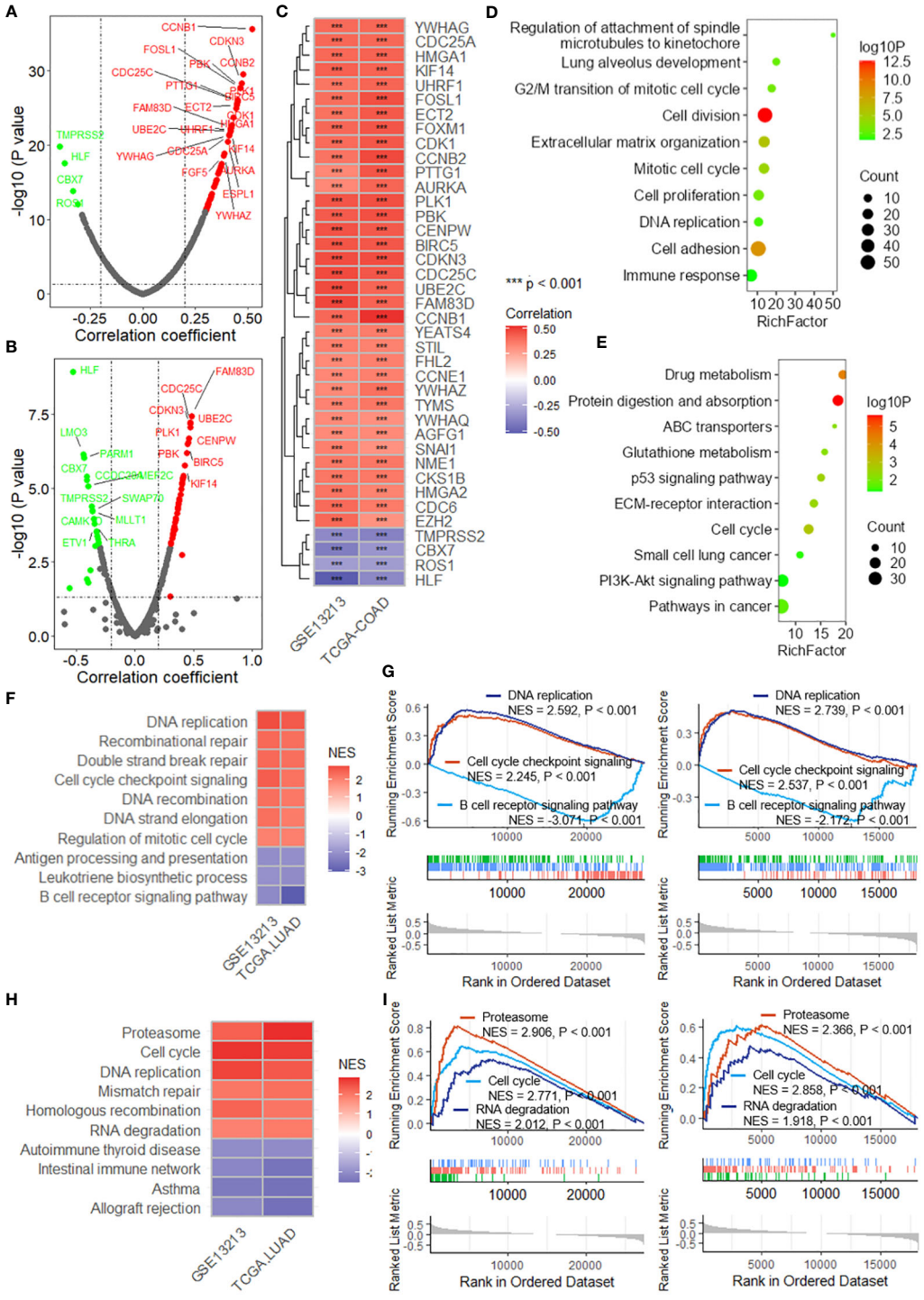

FIGURE 6
The DRG risk score is associated with cancer progression. Scatter plots showing the results of the correlation analysis between the risk score and oncogenes in the TCGA-LUAD **(A)** and GSE13213 **(B)** datasets. **(C)** Heatmap showing the intersection of the oncogenes significantly correlated with the risk score. *** represent P value of correlation analysis less than 0.001. Lollipop plots showing the enrichment analysis of the differentially expressed genes between the high-risk group and low-risk group for biological processes **(D)** and KEGG pathways **(E)**. **(F)** Heatmap showing the intersecting biological processes in the TCGA-LUAD and GSE13213 datasets based on GSEA. **(G)** GSEA plots showing the enrichment results of three biological processes related to the risk score. **(H)** Heatmap showing the intersecting biological processes in the TCGA-LUAD and GSE13213 datasets based on GSEA. **(I)** GSEA plots showing the enrichment results of three biological processes related to the risk score. GSEA, gene set enrichment analysis; TCGA, the cancer genome map; LUAD, lung adenocarcinoma.

10.3389/fimmu.2024.1371831

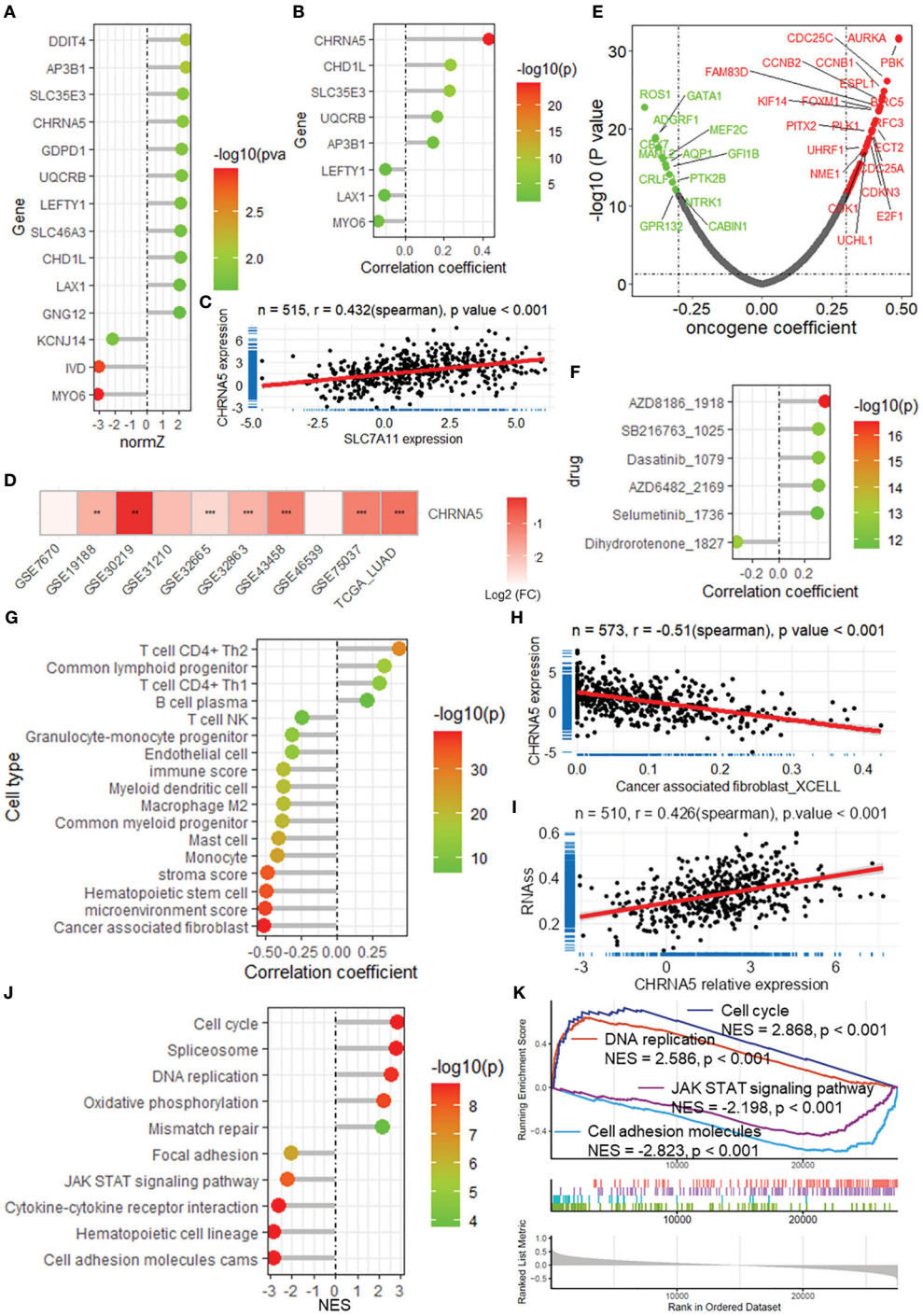

FIGURE 7
CHRNA5 is highly expressed in LUAD and is related to cancer progression. **(A)** The lollipop plot shows the normalized Z score of the DRGs in the risk model. **(B)** The lollipop plot shows the correlation between SLC7A11 and the DRGs in the risk model. **(C)** Scatter plot showing the correlation between the expression of SLC7A11 and CHRNA5. **(D)** Heatmap showing the change in CHRNA5 expression in tumors compared with normal tissue in multiple datasets. ** and *** represent P value of t-test less than 0.01 and 0.001 between tumor and normal groups, respectively. **(E)** Volcano plot showing the results of the correlation analysis between the expression of CHRNA5 and that of oncogenes. **(F)** Lollipop plot showing the correlation between CHRNA5 and antitumor drug sensitivity. **(G)** Lollipop plot showing the correlation between CHRNA5 and immune cell infiltration. **(H)** Scatter plot showing the correlation between SLC7A11 expression and the infiltration of cancer-associated fibroblasts in the TCGA-LUAD dataset. **(I)** Scatter plot showing the correlation between SLC7A11 expression and tumor stemness calculated by the RNA-seq algorithm based on the TCGA-LUAD dataset. Lollipop plot **(J)** and GSEA plot **(K)** showing the results of GSEA of CHRNA5 for KEGG pathways. GSEA, gene set enrichment analysis; DRGs, disulfidptosis-related genes; TCGA, the cancer genome map; LUAD, lung adenocarcinoma.

10.3389/fimmu.2024.1371831

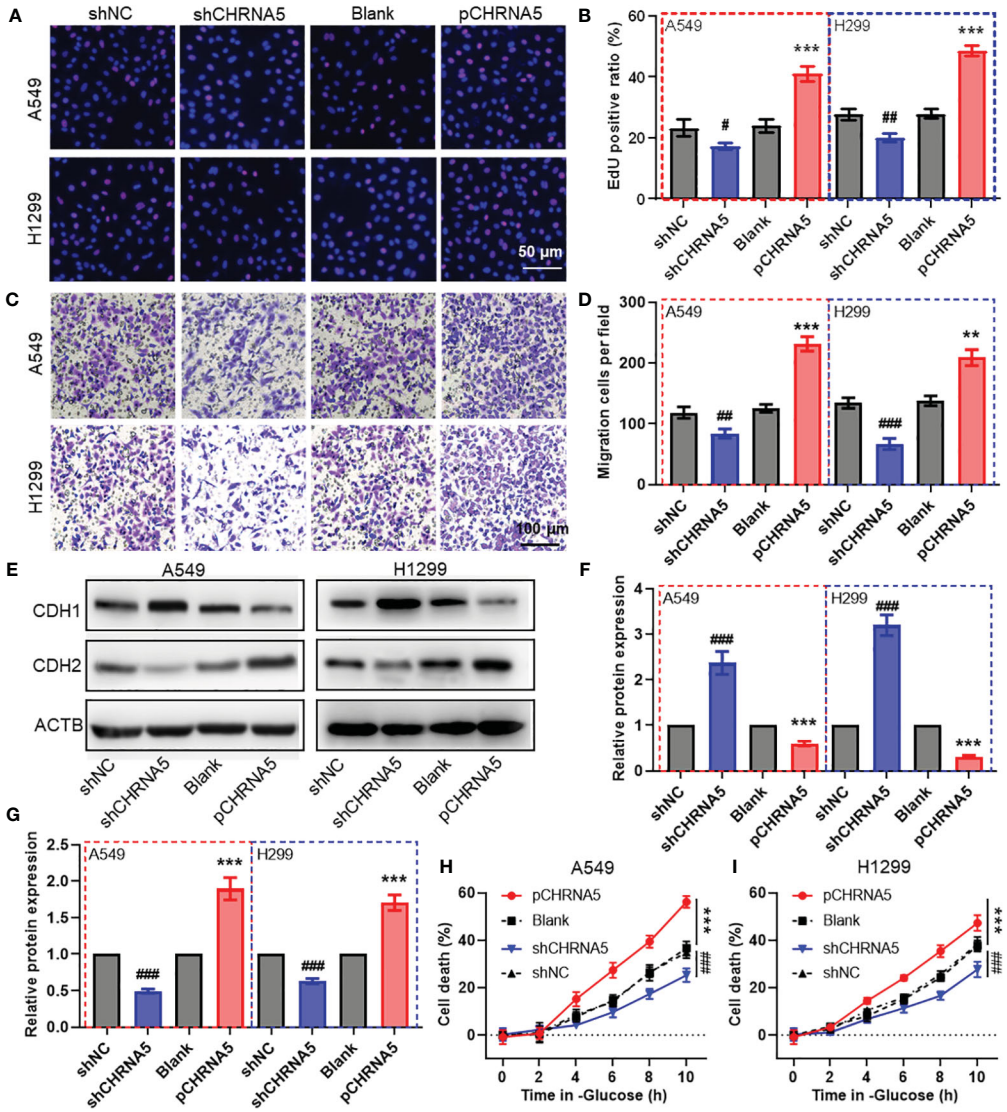

FIGURE 8
CHRNA5 promotes cell proliferation, migration and disulfidptosis in LUAD. Representative images **(A)** and the quantified results **(B)** of the EdU cell proliferation assay in LUAD cells with CHRNA5 knockdown or knockdown. Representative images **(C)** and the quantified results **(D)** of the transwell cell migration assay in LUAD cells with CHRNA5 knockdown or knockdown. Representative images **(E)** and the quantified results **(F-G)** of western blotting for CDH1 and CDH2 in LUAD cells with CHRNA5 knockdown or expression. A CCK-8 assay was used to measure the cell death induced by glucose deprivation in A549 **(H)** and H1299 **(I)** cells with CHRNA5 knockdown or expression. LUAD, lung adenocarcinoma. #, ## and ### represent P value less than 0.05, 0.01 and 0.001 versus shNC group, respectively. ** and *** represent P value less than 0.05, 0.01 and 0.001 versus Blank group, respectively.

CHRNA5 knockdown significantly attenuated cell death induced by glucose deprivation, while CHRNA5 overexpression significantly amplified cell death (Figures 8H-I).

4 Discussion

Disulfidptosis is a new form of regulated cell death in cancers with high SLC7A11 expression under glucose starvation conditions, providing a novel therapeutic strategy for treating malignant tumors (7, 8). Here, we established a prognosis prediction model based on DRGs using LASSO and Cox regression analysis and further screened a key gene in the model, CHRNA5, for functional analysis in lung cancer cells.

Recently, several studies have built risk prediction models for different cancers, including cervical cancer (17), bladder cancer (18, 19), colorectal cancer (20) and lung cancer (21, 22), based on DRGs. With respect to lung cancer, a previous study identified 465 DRGs based on correlation analysis and established a 21-gene-based risk prediction model with an AUC = 0.747 at 1 year (22). Additionally, another study devised a 7-gene-based model with an AUC = 709 at 1 year (21). Compared to these studies, the present study established

a risk prediction model with an AUC of 0.805 in lung cancer based on DRGs obtained from CRISPR/Cas9 screening. The superiority of this model was further validated in internal testing and external validation sets, with AUCs of 0.786 and 0.783, respectively. The robustness and practicability of this model were measured by the nomogram, and the nomogram based on the risk score showed better prediction accuracy, with an AUC = 0.830. These results revealed that our DRG risk score model has good predictive accuracy and certain practical value.

The tumor microenvironment (TME) has attracted increasing attention due to its important role in tumor immunosuppression, distant metastasis and drug resistance (23). The TME is mainly composed of tumor cells, infiltrating immune cells, cancer-related stromal cells, endothelial cells and other components (24, 25). The generation and progression of tumors largely depend on external signals received from the surrounding immune cells and nonimmune cells of the TME (26). Our correlation analysis revealed that the risk score was positively correlated with the immune score, microenvironment score and infiltration of mast cells and other cell types. Mast cells are located at the edge of the tumor and TME, usually around blood vessels (27), and have both protumor and antitumor properties. After activation and degranulation, they become highly proinflammatory and actively recruit cells from the innate immune system, mainly neutrophils, macrophages, and eosinophils, as well as cells from the acquired immune system (B cells and T cells), to coordinate antitumor immune responses (28). In contrast, they may also support angiogenesis and MMP9 degradation in the ECM and promote metastasis by releasing VEGF, which is beneficial for tumor progression (28). In addition, the risk score is also correlated with dysfunction and exclusion of T cells, as is the TIDE score, which can predict the clinical response to cancer immunotherapy (14). Further GSEA revealed that the risk score was correlated with DNA replication, the cell cycle, cell adhesion and the immune response, as well as several vital KEGG pathways. Moreover, positive correlations were found between the risk score and the expression of multiple oncogenes and the sensitivity to several antitumor drugs. These results suggest that our DRG risk prediction model may serve as a potential indicator for the prediction of immune microenvironment homeostasis, the evaluation of immune checkpoint blockade therapy, and the evaluation of the biological functional status of tumors.

Among the 14 DRGs included in the risk prediction model, we selected CHRNA5, which had a high normalized Z score based on CRISPR screening and the highest correlation with SLC7A11, to further investigate its regulation of biological function and disulfidptosis in LUAD cells. CHRNA5, a member of the nicotinic acetylcholine receptor superfamily, is a key modulator of nicotine-dependent lung cancer and other malignancies (29, 30). CHRNA5 accelerates lung cancer progression via the MAPK and VEGF pathways (31), influences melanoma growth via Notch1 regulation (32), and promotes radioresistance in oral squamous cell carcinoma by modulating E2F transcription factors (33). In this study, we found that CHRNA5 might function as an oncogene, as evidenced by its upregulation in lung cancer and its positive correlation with oncogene expression. Moreover, survival analysis indicated that patients with high CHRNA5 expression generally have a poorer prognosis. Furthermore, *in vivo* experiments revealed that knocking down CHRNA5 significantly reduced both cell proliferation and migration in LUAD cells. We also investigated its regulatory role in disulfidptosis under glucose-deprived conditions. The results revealed that CHRNA5 knockdown inhibited cell death induced by glucose deprivation, whereas CHRNA5 overexpression enhanced cell death. These findings underscore the significant influence of CHRNA5 on the proliferation and migration of LUAD cells, as well as on disulfidptosis.

In conclusion, our study successfully established and validated a robust risk prediction model rooted in disulfidptosis-related genes (DRGs) for LUAD patients. Notably, this risk score is associated with the homeostasis of the immune microenvironment and the biological function of tumors. CHRNA5, a critical component of this model, has been confirmed to enhance cell proliferation, migration, and disulfidptosis in LUAD cells.

Data availability statement

The original contributions presented in the study are included in the article/Supplementary Material. Further inquiries can be directed to the corresponding author.

Author contributions

JW: Conceptualization, Funding acquisition, Investigation, Methodology, Project administration, Resources, Software, Writing – original draft. KL: Data curation, Methodology, Software, Validation, Writing – original draft. JWL: Methodology, Writing – review & editing. HZ: Software, Validation, Writing – review & editing. XG: Data curation, Software, Validation, Writing – review & editing. XS: Resources, Writing – review & editing. MW: Software, Writing – review & editing. YH: Resources, Writing – review & editing. JNL: Conceptualization, Project administration, Supervision, Writing – review & editing.

Funding

The author(s) declare financial support was received for the research, authorship, and/or publication of this article. This study was funded by the China Postdoctoral Science Foundation (Project No. 2023M732527) and the National Natural Science Foundation of China (Project No. 82373613). The study was also supported by the Jiangsu Key Laboratory of Preventive and Translational Medicine for Major Chronic Non-communicable Diseases as well as the Priority Academic Program Development of Jiangsu Higher Education Institutions (PAPD).

Conflict of interest

The authors declare that the research was conducted in the absence of any commercial or financial relationships that could be construed as a potential conflict of interest.

Publisher's note

All claims expressed in this article are solely those of the authors and do not necessarily represent those of their affiliated organizations, or those of the publisher, the editors and the reviewers. Any product that may be evaluated in this article, or claim that may be made by its manufacturer, is not guaranteed or endorsed by the publisher.

Supplementary material

The Supplementary Material for this article can be found online at: https://www.frontiersin.org/articles/10.3389/fimmu.2024.1371831/full#supplementary-material

References

1. Sung H, Ferlay J, Siegel RL, Laversanne M, Soerjomataram I, Jemal A, et al. Global cancer statistics 2020: GLOBOCAN estimates of incidence and mortality worldwide for 36 cancers in 185 countries. *CA Cancer J Clin*. (2021) 71:209–49. doi: 10.3322/caac.21660

2. Kroschinsky F, Stölzel F, von Bonin S, Beutel G, Kochanek M, Kiehl M, et al. New drugs, new toxicities: severe side effects of modern targeted and immunotherapy of cancer and their management. *Crit Care*. (2017) 21:89. doi: 10.1186/s13054-017-1678-1

3. Cukier P, Santini FC, Scaranti M, Hoff AO. Endocrine side effects of cancer immunotherapy. *Endocr Relat Cancer*. (2017) 24:T331–T47. doi: 10.1530/ERC-17-0358

4. Bodor JN, Boumber Y, Borghaei H. Biomarkers for immune checkpoint inhibition in non-small cell lung cancer (NSCLC). *Cancer*. (2020) 126:260–70. doi: 10.1002/cncr.32468

5. Ozkaya S, Findik S, Dirican A, Atici AG. Long-term survival rates of patients with stage IIIB and IV non-small cell lung cancer treated with cisplatin plus vinorelbine or gemcitabine. *Exp Ther Med*. (2012) 4:1035–8. doi: 10.3892/etm.2012.714

6. Santagostino SF, Assenmacher C-A, Tarrant JC, Adedeji AO, Radaelli E. Mechanisms of regulated cell death: current perspectives. *Veterinary Pathol*. (2021) 58:596–623. doi: 10.1177/03009858211005537

7. Liu X, Olszewski K, Zhang Y, Lim EW, Shi J, Zhang X, et al. Cystine transporter regulation of pentose phosphate pathway dependency and disulfide stress exposes a targetable metabolic vulnerability in cancer. *Nat Cell Biol*. (2020) 22:476–86. doi: 10.1038/s41556-020-0496-x

8. Liu X, Nie L, Zhang Y, Yan Y, Wang C, Colic M, et al. Actin cytoskeleton vulnerability to disulfide stress mediates disulfidptosis. *Nat Cell Biol*. (2023) 25:404–14. doi: 10.1038/s41556-023-01091-2

9. Zheng P, Zhou C, Ding Y, Duan S. Disulfidptosis: a new target for metabolic cancer therapy. *J Exp Clin Cancer Res*. (2023) 42:103. doi: 10.1186/s13046-023-02675-4

10. Tomida S, Takeuchi T, Shimada Y, Arima C, Matsuo K, Mitsudomi T, et al. Relapse-related molecular signature in lung adenocarcinomas identifies patients with dismal prognosis. *J Clin Oncol*. (2009) 27:2793–9. doi: 10.1200/JCO.2008.19.7053

11. Zhao M, Kim P, Mitra R, Zhao J, Zhao Z. TSGene 2.0: an updated literature-based knowledgebase for tumor suppressor genes. *Nucleic Acids Res*. (2016) 44:D1023–31. doi: 10.1093/nar/gkv1268

12. Charoentong P, Finotello F, Angelova M, Mayer C, Efremova M, Rieder D, et al. Pan-cancer immunogenomic analyses reveal genotype-immunophenotype relationships and predictors of response to checkpoint blockade. *Cell Rep*. (2017) 18:248–62. doi: 10.1016/j.celrep.2016.12.019

13. Aran D, Hu Z, Butte AJ. xCell: digitally portraying the tissue cellular heterogeneity landscape. *Genome Biol*. (2017) 18:220. doi: 10.1186/s13059-017-1349-1

14. Jiang P, Gu S, Pan D, Fu J, Sahu A, Hu X, et al. Signatures of T cell dysfunction and exclusion predict cancer immunotherapy response. *Nat Med*. (2018) 24:1550–8. doi: 10.1038/s41591-018-0136-1

15. Yang W, Soares J, Greninger P, Edelman EJ, Lightfoot H, Forbes S, et al. Genomics of Drug Sensitivity in Cancer (GDSC): a resource for therapeutic biomarker discovery in cancer cells. *Nucleic Acids Res*. (2013) 41:D955–61. doi: 10.1093/nar/gks1111

16. Maeser D, Gruener RF, Huang RS. oncoPredict: an R package for predicting in vivo or cancer patient drug response and biomarkers from cell line screening data. *Brief Bioinform*. (2021) 22:bbab260. doi: 10.1093/bib/bbab260

17. Liu L, Liu J, Lyu Q, Huang J, Chen Y, Feng C, et al. Disulfidptosis-associated LncRNAs index predicts prognosis and chemotherapy drugs sensitivity in cervical cancer. *Sci Rep*. (2023) 13:12470. doi: 10.1038/s41598-023-39669-3

18. Xue W, Qiu K, Dong B, Guo D, Fu J, Zhu C, et al. Disulfidptosis-associated long non-coding RNA signature predicts the prognosis, tumor microenvironment, and immunotherapy and chemotherapy options in colon adenocarcinoma. *Cancer Cell Int*. (2023) 23:218. doi: 10.1186/s12935-023-03065-8

19. Hu G, Yao H, Wei Z, Li L, Yu Z, Li J, et al. A bioinformatics approach to identify a disulfidptosis-related gene signature for prognostic implication in colon adenocarcinoma. *Sci Rep*. (2023) 13:12403. doi: 10.1038/s41598-023-39563-y

20. Chen H, Yang W, Li Y, Ma L, Ji Z. Leveraging a disulfidptosis-based signature to improve the survival and drug sensitivity of bladder cancer patients. *Front Immunol*. (2023) 14:1198878. doi: 10.3389/fimmu.2023.1198878

21. Qi C, Ma J, Sun J, Wu X, Ding J. The role of molecular subtypes and immune infiltration characteristics based on disulfidptosis-associated genes in lung adenocarcinoma. *Aging (Albany NY)*. (2023) 15:5075–95. doi: 10.18632/aging.204782

22. Huang J, Zhang J, Zhang F, Lu S, Guo S, Shi R, et al. Identification of a disulfidptosis-related genes signature for prognostic implication in lung adenocarcinoma. *Comput Biol Med*. (2023) 165:107402. doi: 10.1016/j.compbiomed.2023.107402

23. Chen F, Zhuang XQ, Lin LY, Yu PF, Wang Y, Shi YF, et al. New horizons in tumor microenvironment biology: challenges and opportunities. *BMC Med*. (2015) 13:45. doi: 10.1186/s12916-015-0278-7

24. Giraldo NA, Sanchez-Salas R, Peske JD, Vano Y, Becht E, Petitprez F, et al. The clinical role of the TME in solid cancer. *Brit J Cancer*. (2019) 120:45–53. doi: 10.1038/s41416-018-0327-z

25. Li HC, Fan XL, Houghton J. Tumor microenvironment: The role of the tumor stroma in cancer. *J Cell Biochem*. (2007) 101:805–15. doi: 10.1002/jcb.21159

26. Hui L, Chen Y. Tumor microenvironment: Sanctuary of the devil. *Cancer Lett*. (2015) 368:7–13. doi: 10.1016/j.canlet.2015.07.039

27. Tamma R, Guidolin D, Annese T, Tortorella C, Ruggieri S, Rega S, et al. Spatial distribution of mast cells and macrophages around tumor glands in human breast ductal carcinoma. *Exp Cell Res*. (2017) 359:179–84. doi: 10.1016/j.yexcr.2017.07.033

28. Hempel HA, Cuka NS, Kulac I, Barber JR, Cornish TC, Platz EA, et al. Low intratumoral mast cells are associated with a higher risk of prostate cancer recurrence. *Prostate*. (2017) 77:412–24. doi: 10.1002/pros.v77.4

29. Benowitz NL. Nicotine addiction. *N Engl J Med*. (2010) 362:2295–303. doi: 10.1056/NEJMra0809890

30. Chen LS, Baker T, Hung RJ, Horton A, Culverhouse R, Hartz S, et al. Genetic risk can be decreased: quitting smoking decreases and delays lung cancer for smokers with high and low CHRNA5 risk genotypes - A meta-analysis. *EBioMedicine*. (2016) 11:219–26. doi: 10.1016/j.ebiom.2016.08.012

31. Niu XM, Lu S. Acetylcholine receptor pathway in lung cancer: New twists to an old story. *World J Clin Oncol*. (2014) 5:667–76. doi: 10.5306/wjco.v5.i4.667

32. Dang N, Meng X, Qin G, An Y, Zhang Q, Cheng X, et al. α5-nAChR modulates melanoma growth through the Notch1 signaling pathway. *J Cell Physiol*. (2020) 235:7816–26. doi: 10.1002/jcp.29435

33. Lin CH, Lee HH, Kuei CH, Lin HY, Lu LS, Lee FP, et al. Nicotinic acetylcholine receptor subunit alpha-5 promotes radioresistance via recruiting E2F activity in oral squamous cell carcinoma. *J Clin Med*. (2019) 8:1454. doi: 10.3390/jcm8091454

frontiers | Frontiers in Oncology

TYPE Review
PUBLISHED 29 May 2024
DOI 10.3389/fonc.2024.1407580

OPEN ACCESS

EDITED BY
Shensi Shen,
Sichuan University, China

REVIEWED BY
Mohamed Jemaà,
Lund University, Sweden
Guillaume Beyrend,
Université de Lille, France

*CORRESPONDENCE
Sara Cuesta-Sancho
sara.cuesta.uva@gmail.com
David Bernardo
d.bernardo.ordiz@gmail.com

†These authors have contributed equally to this work and share first authorship

‡These authors have contributed equally to this work and share senior authorship

RECEIVED 26 March 2024
ACCEPTED 10 May 2024
PUBLISHED 29 May 2024

CITATION
G. de Castro C, G. del Hierro A, H-Vázquez J, Cuesta-Sancho S and Bernardo D (2024) State-of-the-art cytometry in the search of novel biomarkers in digestive cancers. *Front. Oncol.* 14:1407580. doi: 10.3389/fonc.2024.1407580

State-of-the-art cytometry in the search of novel biomarkers in digestive cancers

Carolina G. de Castro[1†], Alejandro G. del Hierro[1†], Juan H-Vázquez[1], Sara Cuesta-Sancho[1*‡] and David Bernardo[1,2*‡]

[1]Mucosal Immunology Lab, Institute of Biomedicine and Molecular Genetics (IBGM), University of Valladolid and Consejo Superior de Investigaciones Científicas (CSIC), Valladolid, Spain, [2]Centro de Investigaciones Biomedicas en Red de Enfermedades Infecciosas (CIBERINFEC), Madrid, Spain

Despite that colorectal and liver cancer are among the most prevalent tumours in the world, the identification of non-invasive biomarkers to aid on their diagnose and subsequent prognosis is a current unmet need that would diminish both their incidence and mortality rates. In this context, conventional flow cytometry has been widely used in the screening of biomarkers with clinical utility in other malignant processes like leukaemia or lymphoma. Therefore, in this review, we will focus on how advanced cytometry panels covering over 40 parameters can be applied on the study of the immune system from patients with colorectal and hepatocellular carcinoma and how that can be used on the search of novel biomarkers to aid or diagnose, prognosis, and even predict clinical response to different treatments. In addition, these multiparametric and unbiased approaches can also provide novel insights into the specific immunopathogenic mechanisms governing these malignant diseases, hence potentially unravelling novel targets to perform immunotherapy or identify novel mechanisms, rendering the development of novel treatments. As a consequence, computational cytometry approaches are an emerging methodology for the early detection and predicting therapies for gastrointestinal cancers.

KEYWORDS

spectral cytometry, mass cytometry, colorectal cancer, hepatocellular carcinoma, computational cytometry, biomarkers, gastric cancer

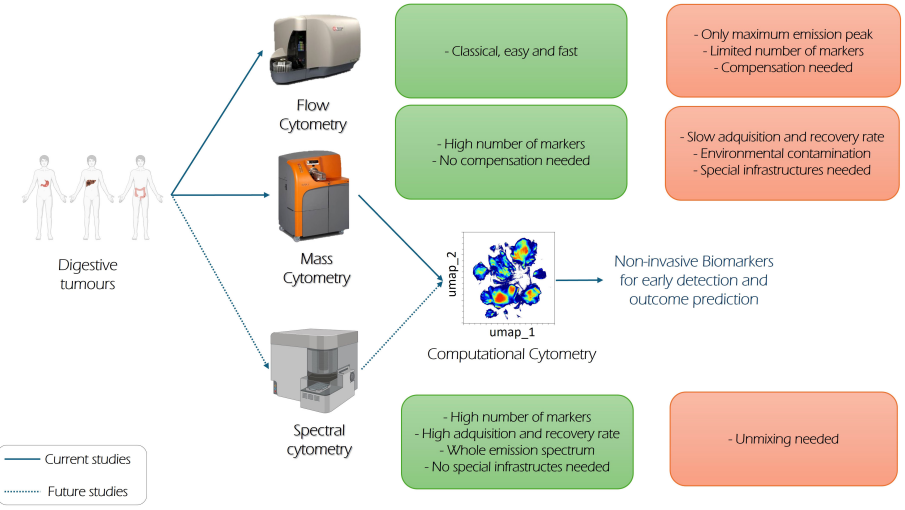

GRAPHICAL ABSTRACT

1 Digestive tumours

Currently, and according to the International Agency for Research on Cancer (1), the most prevalent cancers in the world are lung, breast, colorectal, prostate, stomach, and liver cancers, respectively. Although lung cancer is currently the one with the highest mortality, tumours within the gastrointestinal tract (colorectal, liver, and stomach) are the most prevalent ones when considering overall incidence and mortality. Among them, colorectal cancer (CRC) is actually the second global cause (1) of cancer-related mortality. Most of the CRC cases are adenocarcinoma, and 60%–65% of them are sporadic, 25% have a CRC family case without any hereditary syndrome, and 5% of them are caused by a cancer hereditary syndrome such as non-polyposis colorectal cancer (or Lynch syndrome) and familial adenomatous polyposis (FAP). Lynch syndrome is caused by mutations in genes encoding mismatch DNA repairing proteins, while FAP is due to mutations in the tumour suppressor gene *APC*. Moreover, colorectal cancer can be subdivided based on microsatellite stability (MSS) and microsatellite instability (MSI) due to this deficiency of mismatch repairing proteins. MSI tumours have better prognosis, as they can be easily treated with immunotherapy than MSS tumours (2–4). While there are more several factors such as aging or location (right side CRC has worse survival than the left side) (5) underlying its development, the most relevant risk contributors include modifiable elements such as obesity, sedentary lifestyle, low fruit and vegetable intake, red meat consumption, and smoking and alcoholic habits. Its frequency is higher in economically developed countries, although it is also increasing in westernised developing societies (6–8). Indeed, in 2022, colorectal cancer was the most diagnosed tumour and the second leading cause of cancer death in Europe (9). Its 5-year survival rate ranges from 10% to 90% depending on the stage at diagnose with a better prognosis if it is diagnosed at earlier stages. Screening methods include faecal occult blood test or double contrast barium enema, which are subsequently followed (if positive) by a colonoscopy (10).

Gastric cancer is the fifth most common tumour (1) in the world, and, as CRC, most of them are adenocarcinoma (11). It is usually classified as cardia gastric (upper stomach) and non-cardia gastric cancer (mid and distal stomach) having both different risk factors and epidemiological patterns (12). Of the gastric cancer cases, 90% are due to environmental factors while the remaining 10% have a familiar component. Hereditary diffuse gastric cancer, which has a worse survival than sporadic gastric tumours, is commonly caused by germinal mutations in *CDH1* gene, which codes E-cadherin protein. Hereditary Peutz–Jeghers syndrome predisposes to early-onset gastric cancer. Lynch syndrome also increases the lifetime risk of developing it (13–17). Whereas non-cardia gastric cancer is related to smoking and deficient diet, cardia class correlates with obesity and gastroesophageal reflux disease (18). Despite overall predisposing factors including dietary factors (like high consumption of processed meats, smoked foods, and high salt diets) (19), *Helicobacter pylori* infection is responsible for almost 90% of distal gastric cancers. Indeed, the International Agency for Research on Cancer labels this bacterium as a human carcinogen due to its correlation with gastric cancer, as it provokes gastritis, which can derive on stomach atrophy, metaplasia, and dysplasia. Its 5-year survival rate for early stages is 75.4% (20), so screening analysis, such as esophagogastroduodenoscopy, are usually implemented.

Last, but not the least, liver cancer remains the sixth most common tumour (1) worldwide. As opposed to both colorectal and gastric cancer, this one is a remarkable heterogeneous disease that has been redefined over time. However, hepatocellular carcinoma is its most frequent histological manifestation appearing in approximately 90% of the cases (21). Risk factors include alcohol abuse, diabetes, exposure to aflatoxin, and genetic predisposition.

Nevertheless, almost 80% (22) of hepatocellular carcinoma are associated with hepatitis B/C virus infection. In addition, high-risk groups include patients with non-alcoholic fatty liver and cirrhosis. The Barcelona Clinic for Liver Cancer (BCLC) classifies hepatocellular carcinoma status and determine treatments options based on it (from 0 to D). Another common indicator is the MELD model (Model for End-stage Liver Disease), which examines the bilirubin, creatinine, and International Normalised Ratio (INR) from each patient to predict the 3-month mortality with a statistical confidence of 80%, in order to prioritise those patients who need an earlier transplant (23). Although early stages of hepatocellular carcinoma are treatable, only 20% of diagnosed patients survive more than 1 year. Liquid biopsies such as cell-free DNA or α-fetoprotein are being studied as potential early detection biomarkers, but further research is required (22, 24, 25).

Given therefore the aggressive nature of digestive tumours, there is no doubt that early diagnosis is still the best weapon to fight them. In this regard, the identification of novel biomarkers can provide novel tools not only to aid on their diagnosis and predict their subsequent prognosis (26–30) but also unveil novel targets to perform immune therapy. However, although this has been partially achieved in the gastric one given the role that *H. pylori* infection elicits on its trigger, such goal remains elusive for both CRC and liver cancer.

Regarding hepatocellular carcinoma (HCC), alpha-fetoprotein (AFP) is widely used combined with abdominal ultrasound in order to determine HCC illness. However, it is also true that targeted therapies are essential for the treatment of hepatocellular carcinoma (HCC), yet tackling this type of cancer is challenging owing to its molecular heterogeneity. Some predictive biomarkers based on gene polymorphisms (like VEGFD), serum protein levels, or clinical predictors such as hypertension can be used to identify responders to sorafenib or levantinib, both of which serve as first-line systemic therapies (31). However, it is obvious that more studies are needed to obtain new biomarkers with utility in the clinical practice.

Related to CRC, clinicians focus on DNA signatures to design treatment options. As previously stated, high MSI is the phenotype of 15% colorectal tumours. These tumours typically do not metastasise and show poor response to chemotherapy. Despite this, they have a better clinical course than MSS tumours because of the higher production of neoantigens, making them more susceptible to treatment with immunotherapy (32). Other therapeutic strategies focus on the MAPK pathway status. RAS, which controls cells proliferation, is often mutated in CRC (33), and monoclonal antibodies (mAbs) anti-EFGR as cetuximab are typically used to stop the abnormal signalling. Other mAbs like encorafenib targets KRAF, which is usually mutated in CRC, and it is used when anti-EFGR are not effective, as it is downstream in the MAPK pathway (32). Focusing on liquid biopsies, several serum proteins such as carcinoembryonic antigen (CEA) are found in CRC. However, they do not correlate significantly with prognosis or survival rates. New approaches also investigate circulating tumour cells and circulating tumour DNA in the blood. In contrast with CEA and other serum proteins, these markers correlate with treatment response and survival rates, making them desirable biomarkers to study in depth before starting a therapeutic option (32, 34, 35).

Building from the current needs, this manuscript will therefore focus on the utility that flow cytometry elicits on the search of novel biomarkers with aid on the clinical practise of digestive tumours.

2 Conventional and mass cytometry

Conventional flow cytometry (CFC) is a fluorescence-based technique, which allows the immunotyping of immune cells at single-cell resolution, which has been used in the clinical setting for over 50 years (36). In addition, it is currently used for B- and T-cell leukaemia and lymphoma immunophenotyping, helping to identify their optimal treatment. However, given that CFC is based on the use of fluorochrome-labelled specific antibodies, the maximum number of fluorochromes—and therefore markers—which can be analysed by classical CFC, is restricted to the number of available channels in the equipment. Therefore, conventional cytometers in the clinical setting do not usually provide more than 8 or 10 channels, hence limiting the number of parameters that can be analysed. Although that has been recently overridden by the development of novel equipment, which display up to 20 channels and, therefore, can identify up to 20 markers at the same time (37), the development of CFC panels using more than 15 markers simultaneously requires advanced skills to compensate the fluorescence among the different markers. In addition, fluorochromes with a similar emission wavelength or close emission peaks cannot be combined in the same panel, hence limiting the capacity to perform complex panels.

In order to overcome these limitations, mass cytometry or CyTOF (cytometry time-of-flight) allows the analysis of over 40 markers at the single-cell level. That can be achieved because, as opposed to CFC, antibodies are tagged with heavy metals (like stable lanthanide isotopes) instead of fluorochromes, so cells are characterised based on atomic weight (38). Therefore, mass cytometry has proven to be highly valuable in the deep characterisation of immune cells (39) given its ability to identify over 40 parameters within a single cell (40, 41), rendering it a "pseudo-omic" technique (38), which has allowed the identification of novel biomarkers (42–46).

3 Computational cytometry

The capacity, however, of developing complex panels with over 40 parameters in a single-cell comes with a cost. Although flow cytometry data analyses are traditionally performed following a hierarchical gating strategy of serial selections in two-dimensional plots, this approach is time consuming, subjective, and can be also influenced by the operator's experience and biases. In addition, the amount of obtained data with complex panels is exponentially increased. Therefore, when addressing complex panels, it becomes obvious that novel unbiased approaches are required in order to address the whole variability (47, 48). Thus, computational approaches based on unsupervised algorithms have emerged to address such complexity (49).

To that end, preliminary data cleaning (either with an unsupervised cleaning algorithm or with manual removal) is essential to remove outlier events due to abnormal flow behaviours resulting from clogs and other common technical problems. Once that has been performed, a subsequent unbiased exploratory approach can be performed on the dataset in an efficient and reproducible way. Dimensionality reduction algorithms, which are commonly used to perform an unsupervised and exploratory cytometry analysis, organise the data based on the protein expression levels, projecting all the variables into two or three dimensions. T-distributed Stochastic Neighbour Embedding (t-SNE) focuses on the non-linear differences between cells in protein marker expression to create a two-dimension map retaining the local data structure. However, the global distances are not reliable, and the number of cells that it can support is limited (50). Hence, it is common to perform a randomised method of event downsizing to a given dataset called "Downsampling" or "Subsampling". Although this entails the possibility of losing under-represented populations along the way, it is possible to perform a subsequent unsupervised analysis by directly addressing the previously identified populations of interest, allowing the use of a larger number of events from these populations, which would confer greater robustness to the results. In addition, it is possible to implement the hierarchical analysis as a way of validating the results obtained, thus avoiding the loss of information that would involve doing the process in reverse (50, 51). Hierarchical Stochastic Neighbour Embedding (H-SNE) overcomes t-SNE because it allows to achieve dimension reduction algorithm without subsampling, becoming a solid and powerful single-cell analysis method (52). Given that t-SNE quadratically scales its computation time in function of the number of cells being analysed, another algorithm option is the Uniform Manifold Approximation and Projection (UMAP), which has a faster computation time than t-SNE, preserves better the global data structure, and attaches additional data to an existing plot, reasons why it has a powerful clinical monitoring impact (for instance, comparing a treatment efficacy) (50). However, such approaches have certain issues, such as the absence of a standardised and agreed-upon pipeline protocol (due to his novelty) or the inability to eliminate subjectivity in the analysis steps and the technical limitations. Although computational cytometry approaches become more widespread, they are a highly computationally demanding method (50, 51).

In spite of that, results obtained by computational cytometry approaches are data-driven and operator-independent, hence increasing their reproducibility, comparability, and accuracy, which, altogether, allow the identification of novel cell subsets related to a specific condition that otherwise may have gone unnoticed (50, 51) so they can be further analysed (and isolated) following directed hierarchical gating approaches.

4 Mass cytometry and colorectal cancer

Mass cytometry and computational cytometry have been used in several studies involving mouse models to better understand patient's cancer and improve their therapeutic options. For instance, although PD-1/PD-L1 is a promising immunotherapy based on the inhibition of these immune checkpoints, not all patients derive benefit from this treatment; hence, it may need to be enhanced by other immune checkpoint blockade (ICB). Beyrend et al. (53) generated a CRC mouse model treated with PBS or PD-L1 therapy, and their tumour-infiltrating lymphocytes (TILs) were analysed by computational and mass cytometry. They found that the PD-L1 group showed a distinct T-cell subset expressing LAG-3 (inhibitory molecule) and ICOS (activating molecule). These findings suggest that enhancing antitumour immunity could be achieved by targeting LAG-3 or ICOS. Moreover, Krieg et al. (54) found that the complement component 3a receptor (C3aR) was downregulated in patients with CRC independently of their MSS or MSI status. Despite the role of the C3a–C3aR interaction in maintaining homeostasis and creating a tumour-free microenvironment, their CRC model lacking C3aR demonstrated that their protumourogenic faecal microbiota induced a significant immune infiltrate, which could be targeted with ICB. In addition, macrophages in CRC, known as tumour-associated macrophages (TAMs), can develop a proinflammatory (M1) or anti-inflammatory (M2) phenotype, leading this last one to T-cell exhaustion and poor prognosis (55). MS4A4A is a transmembrane protein related to these events, and it serves as a biomarker for the M2 phenotype (56); however, the role in CRC of TAMs and MS4A4A remains unclear. Using murine models, Li et al. (57) showed that MS4A4A induces polarisation towards the M2 phenotype, leading to T-cell exhaustion and a poor prognosis. Blocking MS4A4A with anti-MS4A4A detained CRC progression and enhanced the efficacy of anti-PD-1 therapy.

On this wise, Tang et al. (58) found that colon cancer mice injected with IFN-γ and anti-PD-1 had reduced tumour growth and less amount of M2 macrophages; however, they also observed an upregulation of LAG-3 in response to anti-PD-1 therapy.

Oncolytic virus therapy is a kind of nanomaterial used to treat cancer. Zhang et al. (59) designed a protein nanocage with the structure of hepatitis B virus and CpG motifs, which are immunostimulatory. Using a CRC murine model, they found by mass cytometry that after being exposed to the nanocages, the tumour microenvironment was modified having a higher expression of CD8 (cytotoxic) T cells and decreasing the T-cell exhaustion. The treatment led to enhanced antitumour immunity.

Specifically focused in the human setting, the application of novel and complex multiparametric panels in the CRC setting by CyTOF has proved that there is a huge immune diversity between different patients and within each individual, not only between the blood and the intestinal immune infiltrate but also between the affected and non-affected tissue (60). In addition, certain circulating immune cells such as monocytes and NK cells subsets are altered during perioperative period (61), confirming that CRC requires a personalised approach.

Mass cytometry has, for instance, proved that the pregnane X receptor mediates the mechanisms of oxaliplatin therapy resistance in tumour cells by eliminating the drug from the cells (62). In addition, and following the first cycle of oxaliplatin chemotherapy, patients reduce their total NK cell numbers due to a specific

decrease in the $CD56^{dim}CD16^{-}$ subset. In a similar manner, the $CD16^{+}$ NK fraction was also reduced due the presence of several proinflammatory cytokines (IL-2, IL-15, and IL-18), which ultimately leads to lose their cytotoxic activity (63). In addition, Ting Zhang et al. (64) have shown that although $EpCAM^{+}CD4^{+}$ T-cell subsets can infiltrate the tumour in a CCR5- and CCR6-dependent manner, they nevertheless displayed an exhausted and immunosuppressive phenotype, as they were both not only $PD\text{-}1^{+}$ but also $PD\text{-}L1^{+}$. Not surprisingly, and given its immune-suppressive effect, such cell subset has become the target for immune checkpoint blockade therapies. In addition, Yang Luo et al. (65) found that high levels of circulating T-cell co-expressing $CD103^{+}CD39^{+}$ predict clinical response to such immune checkpoint inhibitors.

In line with the above, Tsunenori et al. (66) proved that IL-6 produced by stromal and tumour cells correlated with lower T_{reg} ($CD4^{+}FOXP3^{+}$) cells in the tumour microenvironment. In addition, IL-6 serum levels positively correlated with enhanced levels of myeloid-derived suppressor cells (MDSCs) and effector regulatory T-cells (eT_{reg}), two types of immunosuppressive cell subsets, while high levels of IL-6 in the tumour microenvironment correlates with immune evasion and a debilitated antitumour activity. In a similar manner, eT_{reg} (defined as $BLIMP\text{-}1^{+}FOXP3^{+}$) were increased in the tumour infiltrate. These cells can be further divided into $FOXP3^{lo}$ and $FOXP3^{hi}$. In addition, higher levels of the first subset in the tumour infiltrate correlate with good outcomes while the later correlate with bad prognosis. Therefore, and given that eT_{reg} cells have been associated with both good and bad prognosis in CRC, it seems obvious that further investigation is required in order to specifically identify the specific subset, which can be used as a therapeutic target (67).

Cytokeratin 20 (CK20) is a common biomarker used to determine CRC tumour stage and histological grade. In addition, its expression on tumour cells is related to poor prognosis, whereas its absence indicates a less-invasive cancer (68). Despite that, terminally differentiated epithelial cells have a lower proportion of CK20 expression in CRC tissues referred to controls, while its expression also differs, within CRC patients, based on the tumour microsatellite stability. This reveals the necessity of fully understanding the colorectal cancer status of the patients in each of its different stages (69).

On the other hand, it is obvious that the gut microbiota can also modulate the outcome of immune responses in CRC (70). Indeed, mucosa-associated invariant T cells (MAIT) cells recognise bacterial riboflavin antigens following presentation by the non-classic histocompatibility complex MR1. Building from that, Shamin Li et al. (71) found that tumour-infiltrating MAIT cells are $CD39^{+}$ and display an increased expression of exhaustion markers $PD\text{-}1^{+}$ and $CTL4^{+}$ coupled with lower cytokine production. Together, these suggest that chronic activation of MAIT cells induces the expression of CD39 together with senescence markers leading to T-cell exhaustion. In addition, *Fusobacterium nucleatum* induces CD39 expression on MAIT in a TCR-dependent manner, hence providing a mechanism by which such bacteria are bad prognosis factors in CRC.

One of the most advantageous locations for identifying biomarkers are liquid biopsies like peripheral blood where we have PBMCs. Kong et al. (72) studied the differences between immune subsets during CRC development. Through mass cytometry and computational analysis, they revealed that central memory $CD4^{+}$ T cells, switched B cells, $CD16^{-}$ NK cells, monocytes, and basophils were increased in adenocarcinoma compared with adenoma and healthy controls, while double-negative T cells were decreased in adenoma and adenocarcinoma. Moreover, effector $CD4^{+}$ T cells and naive B cells were higher in CRC patients with lymph node metastasis, while basophils and unswitched B cells were lower.

Mass cytometry can also monitor the effects of a clinical trial in the patient's immune system. Monjazeb et al. (73) performed mass cytometry to evaluate the immune impact on the patients of a phase 2 trial of combined anti-CTLA-4 and anti-PD-1 therapy. They found that patient's PBMCs had a lower amount of $CD4^{+}$ and $CD8^{+}$ T cells compared with patients treated with two different radiation regimens (with generally no differences between them). This included activation markers such as CXCR3 or ICOS.

Yang et al. (74) decided to use mass cytometry among other exploratory methods to study primary liver cancers and liver metastases from other cancers including CRC. They found that hepatic metastatic CRC had higher levels of $CD4^{+}$ T_{reg}, $LAG\text{-}3^{+}CD4^{+}$ T-cells, $CD27^{+}PD\text{-}1^{+}CD8^{+}$ T-cells, and lower levels of $CD57^{+}PD\text{-}1^{+}CD8^{+}$ T cells than non-hepatic metastatic CRC. Circulating levels of this immune subsets have therefore the potential to be considered as novel biomarkers to predict patients with a higher probability of subsequently developing metastases.

5 Mass cytometry and liver cancer

Mass cytometry has also been implemented in the context of liver cancer and its main variant, hepatocellular carcinoma (HCC). The full comprehension of HCC illness becomes complicated due to its heterogeneity. In addition, although there is a wide range of different treatments based on tumour stage, they however do not always translate into clinical remission (75); it appears mandatory to explore new targets and therapeutic options (21). Moreover, mass cytometry approaches can be also applied as diagnostic tools. Hence, a complex panel applied on blood samples can identify several immune disturbances, which can be used to allow an early detection of different solid tumours including HCC (56).

Animal models of HCC are often used to study this condition through mass cytometry. In the search of new proposing target markers for therapies, research in mice revealed that GDF15 protein induces enhancement of T_{reg} through CD48 (76), and this leads to immunosuppression in HCC; blockade of this protein could potentially be translated to human therapies. When studying effectiveness of treatments, it was found that SUMOylation levels are higher in HCC liver than in normal liver tissues. Subsequently, it was proved that inhibition of this process enhances antitumour activity and could be a therapeutic option (77). In another study using mice, it was found that "M2-like" tumour-associated macrophages are more prevalent in a specific type of mouse model resistant to anti-anti-PD-1 therapy (78). However, the conclusion highlights the wide diversity in the immune tumour

microenvironments among preclinical models, in addition to the intrinsic heterogeneity of HCC in humans. It seems imperative to expand studies in mouse models to obtain translational results for humans. Therefore, in this review, we will focus on human studies.

Focused on the human setting, potential new therapeutic strategies could benefit from mass cytometry studies regarding HCC cells mechanisms. For example, it has been revealed that tumour cells and their intrinsic activation of β-catenin pathway results in the recruitment of MDSC and the formation of immune "desert" phenotype, which could be a potential treatment strategy option (79). However, immune system description regarding HCC involves not only novel immunotherapy targets but also prognosis and evolution biomarkers and cell subsets. Undeniably, the role of NK cells remain fundamental for immunity and especially in cancer (80). Indeed, $CD56^{+}$ and $CD56^{dim}$ NK cells may be useful as immunotherapies targets for HCC patients, as they have impairment phenotypes in hepatocarcinoma affected from different aetiologies, especially in non-alcoholic fatty liver disease (NAFLD) patients (21, 81).

In HCC, it is also possible to explore the patient's immunity depending on the stage or type of development that they have achieved. Although patients with HCC who successfully had a transplant are scarce, they display a unique immune fingerprint, since mass cytometry approaches have shown that such differential immune profile can be used to stratify and predict patients with risk of recurrence, which can be very helpful when designing patient treatment (82).

Also building from mass cytometry results, it has been proven that the $CD161^{+}/CD161^{-}$ ratio within peripheral $CD8^{+}PD\text{-}1^{+}$ T cells predicts subsequent disease outcome with better prognosis with higher ratios (83). Specifically focused on the tissue (affected, non-affected, and border area), although PD-1 expression does not predict the outcome of the patients, it is actually the balance between tissue resident memory and $PD\text{-}1^{+}$ exhausted T cells that is relevant for such outcome, since a high tissue resident memory/exhausted T-cell ratio in tumour microenvironment determines positive patient prognosis (84, 85). Better prognosis conditions are expected from HCC patients who have a non-terminally exhausted phenotype in tumour-resident memory T cells, which are specific to HBV response (86), and also for those patients with enriched $CD4^{+}CD8^{+}$ T cells, especially if they are expressing PD-1 and located in leading-edge regions (87).

When focusing on ongoing therapies, radiofrequency ablation is the primary first-line treatment option for HCC patients who are not eligible for surgery. Aiming to study its effects on tumour immune response, a mass cytometry study revealed that decreased levels of $CD8^{+}$ effector and memory T cells, among others, correlated with a worst immune response against tumour cells (88). As for current therapy options, immune checkpoint inhibitors (including PD-1/PD-L1) have reached long-term response rates of 14%–20% in HCC patients. However, there is no information about patients who would benefit from this treatment due to its aetiology. In addition, CyTOF analyses revealed that neither viral aetiology nor the current viral status in HCC patients were variables to consider when deciding to prescribe PD-1 inhibitor therapy (89). On the other hand, the use of threonine tyrosine kinase inhibitor changes the proportion of circulating immune subsets before following treatment, with bigger changes on patients with a better outcome (90). Another scenario in which immune activation occurs, leading to a favourable response in HCC patients, is Yttrium90-Radioembolisation treatment (91). There are other types of uncommon treatments under study, such as the use of compound 2,5-dimethylcelecoxib (92), which has proven an increased infiltrate of NK cells within HCC tumours, resulting in favourable prognosis and suggesting its potential as a therapy target.

In summary, HCC pathology, heterogeneity, and treatment response have been broadly studied by CyTOF. Some immune cell subsets like CD56 NK cells or the $CD161^{+}/CD161^{-}$ ratio within $CD8^{+}PD\text{-}1^{+}$ T cells may indeed be useful to stratify patients based on their aetiology and their subsequent outcome, while other subsets can predict clinical response to immune checkpoint inhibitors.

6 Future perspectives and remarks

Mass cytometry has undoubtedly shown a great potential in the study of human gastrointestinal tumours. Nevertheless, it is also true that although this approach overcomes most of the CFC approaches, it also has some specific handicaps (41, 93).

The main one is the low acquisition rate, as it only allows to acquire approximately 500 cells per second instead of more than 10,000 in CFC. In addition, it is an expensive technique, since the costs of not only the equipment but also the special reagents and labelling compounds are significantly higher than those in flow cytometry. In a similar manner, cell vaporisation is an irreversible process and restricts the potential for subsequent *ad hoc* sorting. Likewise, due to lower cell recovery, there is a decrease in sensitivity for detecting low abundance proteins. Last, but not the least, as with a classical sorter, the equipment requires operation by a highly trained person, hence limiting its widespread accessibility.

An alternative to overcome these limitations is spectral cytometry, which combines the principal features of CyTOF while abrogating its handicaps. Therefore, as opposed to the CFC, spectral cytometry provides a measure of the entire fluorescence emission spectrum. That way, classical issues associated with CFC compensation and autofluorescence issues are reduced through a concrete unmixing algorithm (94). In addition, as it uses fluorochromes, reagents are usually cheaper, since it is not the same ones used in CFC. Moreover, its acquisition speed is high (up to 30,000 events per second) (95). Overall, these are even more attractive features, especially considering that comparable results can be expected from both procedures (96).

However, both spectral and mass cytometry data must offer high-quality, reliable, and robust information to be considered valid. Hence, a careful panel design and validation, titration, and optimisation of antibodies and reference controls are required.

Having said that, and given the properties of mass cytometry, it is also true that the implementation of novel panels is usually faster in that approach, since no unmixing controls are required to optimise a panel. Either way, sample staining on both approaches should always include normalisation control and correct equipment handling (97). On the contrary, both mass and spectral cytometry are capable of performing complex panels of up to 40 parameters (47). As a consequence, all the known immune cell subsets can be identified in a given sample by using these techniques. Hence, the ability to obtain such a wide range of information from each analysis provides a major reason to implement these approaches, spectral or mass cytometry, in various types of studies, especially in those aimed at discovering new biomarkers needed for some illnesses. In this regard, Table 1 summarises the different aspects to take into consideration before considering mass or spectral cytometry approaches. Therefore, it seems obvious that spectral cytometry overtakes the approaches performed by mass cytometry, as it is faster, cheaper, and requires a smaller sample size. Indeed, there are several issues that need to be addressed in the near future for both CRC and HCC, and they may be overcome when using different types of approaches, for example spectral cytometry studies, which, to the best of our knowledge, have not been performed in this context.

In addition, these techniques provide a high-resolution single-cell analysis, so the more parameters can be detected on cancer cells, the more specific will be the exploration of the tumour heterogeneity. The classification of the function and phenotype of the immune cells leads to an accurate examination of the altered cellular process, early diagnosis and detection, and prediction of therapy response. The integration of cytometry, proteomics, and genomics technologies will bring a promising precision medicine in order to improve patients' outcomes and life expectancy (98).

7 Conclusions

The only current approach for CRC diagnosis and monitoring is the use of regular colonoscopies, which, however, are not only invasive and uncomfortable for the patients but also expensive and time consuming for the health systems. On the other hand, regarding HCC, most of its current knowledge has been obtained from murine models, which, although essential to deepen our understanding on such disease, they may not always translate into the human setting (99, 100). Therefore, given the large amount of information that computational cytometry approaches provide, these approaches will allow the identification of novel (and better) biomarkers to aid on CRC or HCC diagnosis, monitoring, or even predicting disease outcome. In addition, given that both mass and spectral cytometry usually focus on the study of the immune system, they may not only identify biomarkers but also provide novel insights into the specific pathogenic mechanisms potentially unravelling novel targets to perform immunotherapy or identify novel mechanisms, hence rendering to the development of novel treatments.

TABLE 1 Conventional mass and spectral cytometry features.

	Conventional Flow Cytometry	Mass Cytometry	Spectral Cytometry
Parameters capability	Up to 30	>60	Up to 50
Cell labelling	Fluorochrome	Heavy metal	Fluorochrome
Cell throughout	>10,000 events/second	500 events/second	30,000 events/second
Detection	Fluorescence (maximum peak emission)	Mass spectrometry	Fluorescence (whole spectrum)

Author contributions

CG: Methodology, Writing – original draft. AG: Methodology, Writing – original draft. JH: Methodology, Writing – original draft. SC: Supervision, Writing – review & editing. DB: Supervision, Writing – review & editing.

Funding

The author(s) declare financial support was received for the research, authorship, and/or publication of this article. CC and AH are currently funded by the Spanish Association Against Cancer (Asociación Española Contra el Cáncer—AECC). The lab is currently funded by the Spanish Ministry of Science (PID2019–104218RB-I00), Programa Estratégico Instituto de Biología y Genética Molecular (IBGM Junta de Castilla y León. Ref. CVC8485), and the European Commission—NextGenerationEU (Regulation EU 2020/2094), through CSIC's Global Health Platform (PTI Salud Global).

Conflict of interest

The authors declare that the research was conducted in the absence of any commercial or financial relationships that could be construed as a potential conflict of interest.

Publisher's note

References

1. IARC. Home. Available online at: https://www.iarc.who.int/ (Accessed September 13, 2022).

2. Keum N, Giovannucci E. Global burden of colorectal cancer: emerging trends, risk factors and prevention strategies. *Nat Rev Gastroenterol Hepatol*. (2019) 16:713–32. doi: 10.1038/s41575–019-0189–8

3. Jasperson KW, Tuohy TM, Neklason DW, Burt RW. Hereditary and familial colon cancer. *Gastroenterology*. (2010) 138:2044–58. doi: 10.1053/j.gastro.2010.01.054

4. Li K, Luo H, Huang L, Luo H, Zhu X. Microsatellite instability: a review of what the oncologist should know. *Cancer Cell Int*. (2020) 20:16. doi: 10.1186/s12935–019-1091–8

5. Bufill JA. Colorectal cancer: evidence for distinct genetic categories based on proximal or distal tumor location. *Ann Intern Med*. (1990) 113:779–88. doi: 10.7326/0003–4819-113–10-779

6. Center MM, Jemal A, Smith RA, Ward E. Worldwide variations in colorectal cancer. *CA Cancer J Clin*. (2009) 59:366–78. doi: 10.3322/caac.20038

7. Jemal A, Bray F, Center MM, Ferlay J, Ward E, Forman D. Global cancer statistics. *CA Cancer J Clin*. (2011) 61:69–90. doi: 10.3322/caac.20107

8. Arnold M, Sierra MS, Laversanne M, Soerjomataram I, Jemal A, Bray F. Global patterns and trends in colorectal cancer incidence and mortality. *Gut*. (2017) 66:683–91. doi: 10.1136/gutjnl-2015–310912

9. Observatorio AECC. Available online at: https://observatorio.contraelcancer.es/.

10. Schreuders EH, Ruco A, Rabeneck L, Schoen RE, Sung JJY, Young GP, et al. Colorectal cancer screening: a global overview of existing programmes. *Gut*. (2015) 64:1637–49. doi: 10.1136/gutjnl-2014–309086

11. Vishwanath A, Krishna S, Manudhane AP, Hart PA, Krishna SG. Early-onset gastrointestinal Malignancies: an investigation into a rising concern. *Cancers (Basel)*. (2024) 16:1553. doi: 10.3390/cancers16081553

12. Japanese Gastric Cancer Association. Japanese classification of gastric carcinoma: 3rd English edition. *Gastric Cancer*. (2011) 14:101–12. doi: 10.1007/s10120-011-0041-5

13. Dong E, Duan L, Wu BU. Racial and ethnic minorities at increased risk for gastric cancer in a regional US population study. *Clin Gastroenterol Hepatol*. (2017) 15:511–7. doi: 10.1016/j.cgh.2016.11.033

14. Setia N, Wang CX, Lager A, Maron S, Shroff S, Arndt N, et al. Morphologic and molecular analysis of early-onset gastric cancer. *Cancer*. (2021) 127:103–14. doi: 10.1002/cncr.33213

15. Figueiredo J, Melo S, Carneiro P, Moreira AM, Fernandes MS, Ribeiro AS, et al. Clinical spectrum and pleiotropic nature of CDH1 germline mutations. *J Med Genet*. (2019) 56:199–208. doi: 10.1136/jmedgenet-2018–105807

16. Carneiro F, Oliveira C, Suriano G, Seruca R. Molecular pathology of familial gastric cancer, with an emphasis on hereditary diffuse gastric cancer. *J Clin Pathol*. (2008) 61:25–30. doi: 10.1136/jcp.2006.043679

17. Takahashi M, Sakayori M, Takahashi S, Kato T, Kaji M, Kawahara M, et al. A novel germline mutation of the LKB1 gene in a patient with Peutz-Jeghers syndrome with early-onset gastric cancer. *J Gastroenterol*. (2004) 39:1210–4. doi: 10.1007/s00535-004-1474-y

18. Thrift AP, Wenker TN, El-Serag HB. Global burden of gastric cancer: epidemiological trends, risk factors, screening and prevention. *Nat Rev Clin Oncol*. (2023) 20:338–49. doi: 10.1038/s41571–023-00747–0

19. Ilic M, Ilic I. Epidemiology of stomach cancer. *World J Gastroenterol*. (2022) 28:1187–203. doi: 10.3748/wjg.v28.i12.1187

20. National Cancer Institute. Cancer Stat Facts: Stomach Cancer. Available online at: https://seer.cancer.gov/statfacts/html/stomach.html (Accessed May 2, 2024).

21. Yoshida Y, Yoshio S, Yamazoe T, Mori T, Tsustui Y, Kawai H, et al. Phenotypic characterization by single-cell mass cytometry of human intrahepatic and peripheral NK cells in patients with hepatocellular carcinoma. *Cells*. (2021) 10:1495. doi: 10.3390/cells10061495

22. Li L, Wang H. Heterogeneity of liver cancer and personalized therapy. *Cancer Lett*. (2016) 379:191–7. doi: 10.1016/j.canlet.2015.07.018

23. Luo X, Leanza J, Massie AB, Garonzik-Wang JM, Haugen CE, Gentry SE, et al. MELD as a metric for survival benefit of liver transplantation. *Am J Transplant*. (2018) 18:1231–7. doi: 10.1111/ajt.14660

24. Kulik L, El-Serag HB. Epidemiology and management of hepatocellular carcinoma. *Gastroenterology*. (2019) 156:477–491.e1. doi: 10.1053/j.gastro.2018.08.065

25. Johnson P, Zhou Q, Dao DY, Lo YMD. Circulating biomarkers in the diagnosis and management of hepatocellular carcinoma. *Nat Rev Gastroenterol Hepatol*. (2022) 19:670–81. doi: 10.1038/s41575-022-00620-y

26. Ahlquist DA. Universal cancer screening: revolutionary, rational, and realizable. *NPJ Precis Oncol*. (2018) 2:23. doi: 10.1038/s41698-018-0066-x

27. Cohen JD, Li L, Wang Y, Thoburn C, Afsari B, Danilova L, et al. Detection and localization of surgically resectable cancers with a multi-analyte blood test. *Sci (1979)*. (2018) 359:926–30. doi: 10.1126/science.aar3247

28. Martínez-Bosch N, Cristóbal H, Iglesias M, Gironella M, Barranco L, Visa L, et al. Soluble AXL is a novel blood marker for early detection of pancreatic ductal adenocarcinoma and differential diagnosis from chronic pancreatitis. *EBioMedicine*. (2022) 75:103797. doi: 10.1016/j.ebiom.2021.103797

29. Hüttenhain R, Soste M, Selevsek N, Röst H, Sethi A, Carapito C, et al. Reproducible quantification of cancer-associated proteins in body fluids using targeted proteomics. *Sci Transl Med*. (2012) 4:142ra94-142ra94. doi: 10.1126/scitranslmed.3003989

30. Beretov J, Wasinger VC, Millar EKA, Schwartz P, Graham PH, Li Y. Proteomic analysis of urine to identify breast cancer biomarker candidates using a label-free LC-MS/MS approach. *PloS One*. (2015) 10:e0141876. doi: 10.1371/journal.pone.0141876

31. Wang Y, Deng B. Hepatocellular carcinoma: molecular mechanism, targeted therapy, and biomarkers. *Cancer Metastasis Rev*. (2023) 42:629–52. doi: 10.1007/s10555–023-10084–4

32. Crutcher M, Waldman S. Biomarkers in the development of individualized treatment regimens for colorectal cancer. *Front Med (Lausanne)*. (2022) 9:1062423. doi: 10.3389/fmed.2022.1062423

33. Wan M-L, Wang Y, Zeng Z, Deng B, Zhu B-S, Cao T, et al. Colorectal cancer (CRC) as a multifactorial disease and its causal correlations with multiple signaling pathways. *Biosci Rep*. (2020) 40(3):BSR20200265. doi: 10.1042/BSR20200265

34. Kidess E, Heirich K, Wiggin M, Vysotskaia V, Visser BC, Marziali A, et al. Mutation profiling of tumor DNA from plasma and tumor tissue of colorectal cancer patients with a novel, high-sensitivity multiplexed mutation detection platform. *Oncotarget*. (2015) 6:2549–61. doi: 10.18632/oncotarget.3041

35. Krebs MG, Metcalf RL, Carter L, Brady G, Blackhall FH, Dive C. Molecular analysis of circulating tumour cells-biology and biomarkers. *Nat Rev Clin Oncol*. (2014) 11:129–44. doi: 10.1038/nrclinonc.2013.253

36. Bendall SC, Nolan GP, Roederer M, Chattopadhyay PK. A deep profiler's guide to cytometry. *Trends Immunol*. (2012) 33:323–32. doi: 10.1016/j.it.2012.02.010

37. Monaco G, Chen H, Poidinger M, Chen J, de Magalhães JP, Larbi A. flowAI: automatic and interactive anomaly discerning tools for flow cytometry data. *Bioinformatics*. (2016) 32:2473–80. doi: 10.1093/bioinformatics/btw191

38. Bjornson ZB, Nolan GP, Fantl WJ. Single-cell mass cytometry for analysis of immune system functional states. *Curr Opin Immunol*. (2013) 25:484–94. doi: 10.1016/j.coi.2013.07.004

39. Bandura DR, Baranov VI, Ornatsky OI, Antonov A, Kinach R, Lou X, et al. Mass cytometry: technique for real time single cell multitarget immunoassay based on inductively coupled plasma time-of-flight mass spectrometry. *Anal Chem*. (2009) 81:6813–22. doi: 10.1021/ac901049w

40. Spitzer MH, Nolan GP. Mass cytometry: single cells, many features. *Cell*. (2016) 165:780–91. doi: 10.1016/j.cell.2016.04.019

41. Millian DE, Saldarriaga OA, Wanninger T, Burks JK, Rafati YN, Gosnell J, et al. Cutting-edge platforms for analysis of immune cells in the hepatic microenvironment—Focus on tumor-associated macrophages in hepatocellular carcinoma. *Cancers (Basel)*. (2022) 14:1861. doi: 10.3390/cancers14081861

42. DiGiuseppe JA, Wood BL. Applications of flow cytometric immunophenotyping in the diagnosis and posttreatment monitoring of B and T lymphoblastic leukemia/lymphoma. *Cytometry B Clin Cytom*. (2019) 96:256–65. doi: 10.1002/cyto.b.21833

43. Krieg C, Nowicka M, Guglietta S, Schindler S, Hartmann FJ, Weber LM, et al. High-dimensional single-cell analysis predicts response to anti-PD-1 immunotherapy. *Nat Med*. (2018) 24:144–53. doi: 10.1038/nm.4466

44. Gadalla R, Noamani B, MacLeod BL, Dickson RJ, Guo M, Xu W, et al. Validation of cyTOF against flow cytometry for immunological studies and monitoring of human cancer clinical trials. *Front Oncol*. (2019) 9:415. doi: 10.3389/fonc.2019.00415

45. Rochigneux P, Lisberg A, Garcia A, Granjeaud S, Madroszyk A, Fattori S, et al. Mass cytometry reveals classical monocytes, NK cells, and ICOS+ CD4+ T cells associated with pembrolizumab efficacy in patients with lung cancer. *Clin Cancer Res*. (2022) 28:5136–48. doi: 10.1158/1078–0432.CCR-22–1386

46. Anandan S, Thomsen LCV, Gullaksen S-E, Abdelaal T, Kleinmanns K, Skavland J, et al. Phenotypic characterization by mass cytometry of the microenvironment in ovarian cancer and impact of tumor dissociation methods. *Cancers (Basel)*. (2021) 13:755. doi: 10.3390/cancers13040755

47. Park LM, Lannigan J, Jaimes MC. OMIP-069: forty-color full spectrum flow cytometry panel for deep immunophenotyping of major cell subsets in human peripheral blood. *Cytometry A*. (2020) 97:1044–51. doi: 10.1002/cyto.a.24213

48. Conrad VK, Dubay CJ, Malek M, Brinkman RR, Koguchi Y, Redmond WL. Implementation and validation of an automated flow cytometry analysis pipeline for human immune profiling. *Cytometry Part A*. (2019) 95:183–91. doi: 10.1002/cyto.a.23664

49. Saeys Y, Van Gassen S, Lambrecht BN. Computational flow cytometry: Helping to make sense of high-dimensional immunology data. *Nat Rev Immunol*. (2016) 16:449–62. doi: 10.1038/nri.2016.56

50. Keyes TJ, Domizi P, Lo Y, Nolan GP, Davis KL. A cancer biologist's primer on machine learning applications in high-dimensional cytometry. *Cytometry Part A*. (2020) 97:782–99. doi: 10.1002/cyto.a.24158

51. Diggins KE, Ferrell PB, Irish JM. Methods for discovery and characterization of cell subsets in high dimensional mass cytometry data. *Methods*. (2015) 82:55–63. doi: 10.1016/j.ymeth.2015.05.008

52. van Unen V, Höllt T, Pezzotti N, Li N, Reinders MJT, Eisemann E, et al. Visual analysis of mass cytometry data by hierarchical stochastic neighbour embedding reveals rare cell types. *Nat Commun*. (2017) 8:1740. doi: 10.1038/s41467–017-01689–9

53. Beyrend G, van der Gracht E, Yilmaz A, van Duikeren S, Camps M, Höllt T, et al. PD-L1 blockade engages tumor-infiltrating lymphocytes to co-express targetable activating and inhibitory receptors. *J Immunother Cancer*. (2019) 7:217. doi: 10.1186/s40425–019-0700–3

54. Krieg C, Weber LM, Fosso B, Marzano M, Hardiman G, Olcina MM, et al. Complement downregulation promotes an inflammatory signature that renders colorectal cancer susceptible to immunotherapy. *J Immunother Cancer*. (2022) 10: e004717. doi: 10.1136/jitc-2022–004717

55. Gentles AJ, Newman AM, Liu CL, Bratman SV, Feng W, Kim D, et al. The prognostic landscape of genes and infiltrating immune cells across human cancers. *Nat Med*. (2015) 21:938–45. doi: 10.1038/nm.3909

56. Mattiola I, Tomay F, De Pizzol M, Silva-Gomes R, Savino B, Gulic T, et al. The macrophage tetraspan MS4A4A enhances dectin-1-dependent NK cell-mediated resistance to metastasis. *Nat Immunol*. (2019) 20:1012–22. doi: 10.1038/s41590-019-0417-y

57. Li Y, Shen Z, Chai Z, Zhan Y, Zhang Y, Liu Z, et al. Targeting MS4A4A on tumour-associated macrophages restores CD8+ T-cell-mediated antitumour immunity. *Gut*. (2023) 72:2307–20. doi: 10.1136/gutjnl-2022–329147

58. Tang Y, Wei J, Ge X, Yu C, Lu W, Qian Y, et al. Intratumoral injection of interferon gamma promotes the efficacy of anti-PD1 treatment in colorectal cancer. *Cancer Lett*. (2024) 588:216798. doi: 10.1016/j.canlet.2024.216798

59. Zhang Q, Dong J, Wang J, Wang J, Wang C, Li Y, et al. Integration of protein nanocage with cpG motifs: A virus-mimicked core-shell nanostructure to ignite antitumor immunity. *Small*. (2023) 19:e2301281. doi: 10.1002/smll.202301281

60. Di J, Liu M, Fan Y, Gao P, Wang Z, Jiang B, et al. Phenotype molding of T cells in colorectal cancer by single-cell analysis. *Int J Cancer*. (2020) 146:2281–95. doi: 10.1002/ijc.32856

61. Zhou C, Wang Z, Jiang B, Di J, Su X. Monitoring pre- and post-operative immune alterations in patients with locoregional colorectal cancer who underwent laparoscopy by single-cell mass cytometry. *Front Immunol*. (2022) 13:807539. doi: 10.3389/fimmu.2022.807539

62. Dong Y, Wang Z, Xie G, Li C, Zuo W, Meng G, et al. Pregnane X receptor is associated with unfavorable survival and induces chemotherapeutic resistance by transcriptional activating multidrug resistance-related protein 3 in colorectal cancer. *Mol Cancer*. (2017) 16:71. doi: 10.1186/s12943–017-0641–8

63. Shinko D, McGuire HM, Diakos CI, Pavlakis N, Clarke SJ, Byrne SN, et al. Mass cytometry reveals a sustained reduction in CD16+ Natural killer cells following chemotherapy in colorectal cancer patients. *Front Immunol*. (2019) 10:2584. doi: 10.3389/fimmu.2019.02584

64. Zhang T, Lv J, Tan Z, Wang B, Warden AR, Li Y, et al. Immunocyte profiling using single-cell mass cytometry reveals epCAM+ CD4+ T cells abnormal in colon cancer. *Front Immunol*. (2019) 10:1571. doi: 10.3389/fimmu.2019.01571

65. Luo Y, Zong Y, Hua H, Gong M, Peng Q, Li C, et al. Immune-infiltrating signature-based classification reveals CD103+CD39+ T cells associate with colorectal cancer prognosis and response to immunotherapy. *Front Immunol*. (2022) 13:1011590. doi: 10.3389/fimmu.2022.1011590

66. Yamamoto T, Tsunedomi R, Nakajima M, Suzuki N, Yoshida S, Tomochika S, et al. IL-6 levels correlate with prognosis and immunosuppressive stromal cells in patients with colorectal cancer. *Ann Surg Oncol*. (2023) 30:5267–77. doi: 10.1245/s10434-023-13527-y

67. Norton SE, Ward-Hartstonge KA, McCall JL, Leman JKH, Taylor ES, Munro F, et al. High-dimensional mass cytometric analysis reveals an increase in effector regulatory T cells as a distinguishing feature of colorectal tumors. *J Immunol*. (2019) 202:1871–84. doi: 10.4049/jimmunol.1801368

68. Lassmann S, Bauer M, Soong R, Schreglmann J, Tabiti K, Nährig J, et al. Quantification of CK20 gene and protein expression in colorectal cancer by RT-PCR and immunohistochemistry reveals inter- and intratumour heterogeneity. *J Pathol*. (2002) 198:198–206. doi: 10.1002/path.1196

69. Simmons AJ, Scurrah CR, McKinley ET, Herring CA, Irish JM, Washington MK, et al. Impaired coordination between signaling pathways is revealed in human colorectal cancer using single-cell mass cytometry of archival tissue blocks. *Sci Signal*. (2016) 9:rs11-rs11. doi: 10.1126/scisignal.aah4413

70. Helmink BA, Khan MAW, Hermann A, Gopalakrishnan V, Wargo JA. The microbiome, cancer, and cancer therapy. *Nat Med*. (2019) 25:377–88. doi: 10.1038/s41591–019-0377–7

71. Li S, Simoni Y, Becht E, Loh CY, Li N, Lachance D, et al. Human tumor-infiltrating MAIT cells display hallmarks of bacterial antigen recognition in colorectal cancer. *Cell Rep Med*. (2020) 1:100039. doi: 10.1016/j.xcrm.2020.100039

72. Kong X-X, Xu J-S, Hu Y-T, Jiao Y-R, Chen S, Yu C-X, et al. Circulation immune cell landscape in canonical pathogenesis of colorectal adenocarcinoma by CyTOF analysis. *iScience*. (2024) 27:109229. doi: 10.1016/j.isci.2024.109229

73. Monjazeb AM, Giobbie-Hurder A, Lako A, Thrash EM, Brennick RC, Kao KZ, et al. A randomized trial of combined PD-L1 and CTLA-4 inhibition with targeted low-dose or hypofractionated radiation for patients with metastatic colorectal cancer. *Clin Cancer Res*. (2021) 27:2470–80. doi: 10.1158/1078–0432.CCR-20–4632

74. Yang S, Qian L, Li Z, Li Y, Bai J, Zheng B, et al. Integrated multi-omics landscape of liver metastases. *Gastroenterology*. (2023) 164:407–423.e17. doi: 10.1053/j.gastro.2022.11.029

75. Chen Z, Xie H, Hu M, Huang T, Hu Y, Sang N, et al. Recent progress in treatment of hepatocellular carcinoma. *Am J Cancer Res*. (2020) 10:2993–3036.

76. Wang Z, He L, Li W, Xu C, Zhang J, Wang D, et al. GDF15 induces immunosuppression via CD48 on regulatory T cells in hepatocellular carcinoma. *J Immunother Cancer*. (2021) 9:e002787. doi: 10.1136/jitc-2021–002787

77. Wang Z, Pan B, Su L, Yu H, Wu X, Yao Y, et al. SUMOylation inhibitors activate anti-tumor immunity by reshaping the immune microenvironment in a preclinical model of hepatocellular carcinoma. *Cell Oncol (Dordr)*. (2024) 47:513–32. doi: 10.1007/s13402-023-00880-z

78. Zabransky DJ, Danilova L, Leatherman JM, Lopez-Vidal TY, Sanchez J, Charmsaz S, et al. Profiling of syngeneic mouse HCC tumor models as a framework to understand anti-PD-1 sensitive tumor microenvironments. *Hepatology*. (2023) 77:1566–79. doi: 10.1002/hep.32707

79. Wang K, Wu J, Yang Z, Zheng B, Shen S, Wang R-R, et al. Hyperactivation of β-catenin signal in hepatocellular carcinoma recruits myeloid-derived suppressor cells through PF4-CXCR3 axis. *Cancer Lett*. (2024) 586:216690. doi: 10.1016/j.canlet.2024.216690

80. Sajid M, Liu L, Sun C. The dynamic role of NK cells in liver cancers: role in HCC and HBV associated HCC and its therapeutic implications. *Front Immunol*. (2022) 13:887186. doi: 10.3389/fimmu.2022.887186

81. Sakamoto Y, Yoshio S, Doi H, Mori T, Matsuda M, Kawai H, et al. Increased frequency of dysfunctional siglec-7–CD57+PD-1+ Natural killer cells in patients with non-alcoholic fatty liver disease. *Front Immunol*. (2021) 12:603133. doi: 10.3389/fimmu.2021.603133

82. Wei X, Xie W, Yin W, Yang M, Khan AR, Su R, et al. Prediction of tumor recurrence by distinct immunoprofiles in liver transplant patients based on mass cytometry. *Am J Cancer Res*. (2022) 12:4160–76.

83. Li Z, Zheng B, Qiu X, Wu R, Wu T, Yang S, et al. The identification and functional analysis of CD8+PD-1+CD161+ T cells in hepatocellular carcinoma. *NPJ Precis Oncol*. (2020) 4:28. doi: 10.1038/s41698–020-00133–4

84. Barsch M, Salié H, Schlaak AE, Zhang Z, Hess M, Mayer LS, et al. T-cell exhaustion and residency dynamics inform clinical outcomes in hepatocellular carcinoma. *J Hepatol*. (2022) 77:397–409. doi: 10.1016/j.jhep.2022.02.032

85. Chew V, Lai L, Pan L, Lim CJ, Li J, Ong R, et al. Delineation of an immunosuppressive gradient in hepatocellular carcinoma using high-dimensional proteomic and transcriptomic analyses. *Proc Natl Acad Sci USA*. (2017) 114:E5900–9. doi: 10.1073/pnas.1706559114

86. Cheng Y, Gunasegaran B, Singh HD, Dutertre C-A, Loh CY, Lim JQ, et al. Non-terminally exhausted tumor-resident memory HBV-specific T cell responses correlate with relapse-free survival in hepatocellular carcinoma. *Immunity*. (2021) 54:1825–1840.e7. doi: 10.1016/j.immuni.2021.06.013

87. Zheng B, Wang D, Qiu X, Luo G, Wu T, Yang S, et al. Trajectory and functional analysis of PD-1high CD4+CD8+ T cells in hepatocellular carcinoma by single-cell cytometry and transcriptome sequencing. *Adv Sci (Weinh)*. (2020) 7:2000224. doi: 10.1002/advs.202000224

88. Zhao Y, Yang T, Ouyang Y, Rao W, Liu K, Zheng J, et al. Radiofrequency ablation plays double role in immunosuppression and activation of PBMCs in recurrent hepatocellular carcinoma. *Front Immunol*. (2024) 15:1339213. doi: 10.3389/fimmu.2024.1339213

89. Ho WJ, Danilova L, Lim SJ, Verma R, Xavier S, Leatherman JM, et al. Viral status, immune microenvironment and immunological response to checkpoint inhibitors in hepatocellular carcinoma. *J Immunother Cancer*. (2020) 8:e000394. doi: 10.1136/jitc-2019–000394

90. Chan CY-K, Chiu DK-C, Yuen VW-H, Law C-T, Wong BP-Y, Thu KL, et al. CFI-402257, a TTK inhibitor, effectively suppresses hepatocellular carcinoma. *Proc Natl Acad Sci*. (2022) 119:1–11. doi: 10.1073/pnas.2119514119

91. Chew V, Lee YH, Pan L, Nasir NJM, Lim CJ, Chua C, et al. Immune activation underlies a sustained clinical response to Yttrium-90 radioembolisation in hepatocellular carcinoma. *Gut*. (2019) 68:335–46. doi: 10.1136/gutjnl-2017–315485

92. Pan B, Chen Z, Zhang X, Wang Z, Yao Y, Wu X, et al. 2,5-dimethylcelecoxib alleviated NK and T-cell exhaustion in hepatocellular carcinoma via the gastrointestinal microbiota-AMPK-mTOR axis. *J Immunother Cancer*. (2023) 11:e006817. doi: 10.1136/jitc-2023–006817

93. Newell EW, Cheng Y. Mass cytometry: blessed with the curse of dimensionality. *Nat Immunol*. (2016) 17:890–5. doi: 10.1038/ni.3485

94. Niewold P, Ashhurst TM, Smith AL, King NJC. Evaluating spectral cytometry for immune profiling in viral disease. *Cytometry Part A*. (2020) 97:1165–79. doi: 10.1002/cyto.a.24211

95. Mondelo-Macía P, León-Mateos L, Bernardo D, Díaz-Peña R. Top-of-the-art cytometry as a novel tool to aid in lung cancer immunotherapy. *Transl Lung Cancer Res*. (2023) 12:957–61. doi: 10.21037/tlcr-23–80

96. Ferrer-Font L, Mayer JU, Old S, Hermans IF, Irish J, Price KM. High-dimensional data analysis algorithms yield comparable results for mass cytometry

and spectral flow cytometry data. *Cytometry A*. (2020) 97:824–31. doi: 10.1002/cyto.a.24016

97. Bonilla DL, Reinin G, Chua E. Full spectrum flow cytometry as a powerful technology for cancer immunotherapy research. *Front Mol Biosci*. (2021) 7:612801. doi: 10.3389/fmolb.2020.612801

98. Irish JM, Doxie DB. High-dimensional single-cell cancer biology. *Curr Top Microbiol Immunol*. (2014) 377:1–21. doi: 10.1007/82_2014_367

99. Bjornson-Hooper ZB, Fragiadakis GK, Spitzer MH, Chen H, Madhireddy D, Hu K, et al. A comprehensive atlas of immunological differences between humans, mice, and non-human primates. *Front Immunol*. (2022) 13:867015. doi: 10.3389/fimmu.2022.867015

100. Gibbons DL, Spencer J. Mouse and human intestinal immunity: Same ballpark, different players; Different rules, same score. *Mucosal Immunol*. (2011) 4:148–57. doi: 10.1038/mi.2010.85

frontiers | Frontiers in Oncology

TYPE Original Research
PUBLISHED 18 June 2024
DOI 10.3389/fonc.2024.1405486

OPEN ACCESS

EDITED BY
Laura Mondragón Martínez,
Josep Carreras Leukaemia Research Institute (IJC), Spain

REVIEWED BY
Franco Lugnani,
Hippocrates DOO, Slovenia
Robert Wesolowski,
Ohio State University, United States

*CORRESPONDENCE
Taha Merghoub
tmerghoub@med.cornell.edu
Jonathan A. Coleman
colemanj@mskcc.org

†These authors share first authorship

‡These authors share senior authorship

RECEIVED 22 March 2024
ACCEPTED 31 May 2024
PUBLISHED 18 June 2024

CITATION
Budhu S, Kim K, Yip W, La Rosa S, Jebiwott S, Cai L, Holland A, Thomas J, Preise D, Somma A, Gordon B, Scherz A, Wolchok JD, Erinjeri J, Merghoub T and Coleman JA (2024) Comparative study of immune response to local tumor destruction modalities in a murine breast cancer model. *Front. Oncol.* 14:1405486. doi: 10.3389/fonc.2024.1405486

Comparative study of immune response to local tumor destruction modalities in a murine breast cancer model

Sadna Budhu[1†], Kwanghee Kim[2†], Wesley Yip[3], Stephen La Rosa[2], Sylvia Jebiwott[2], Liqun Cai[4], Aliya Holland[1], Jasmine Thomas[2], Dina Preise[5], Alex Somma[2], Benjamin Gordon[2], Avigdor Scherz[5], Jedd D. Wolchok[1,6,7], Joseph Erinjeri[4], Taha Merghoub[1,7*‡] and Jonathan A. Coleman[2,3*‡]

[1]Swim Across America and Ludwig Collaborative Laboratory, Department of Pharmacology, Weill Cornell Medical Center, New York, NY, United States, [2]Department of Surgery, Memorial Sloan Kettering Cancer Center, New York, NY, United States, [3]Urology Service, Department of Surgery, Memorial Sloan Kettering Cancer Center, New York, NY, United States, [4]Department of Radiology, Memorial Sloan Kettering Cancer Center, New York, NY, United States, [5]Department of Plants and Environmental Sciences, The Weizmann Institute of Science, Rehovot, Israel, [6]Department of Immunology, Weill Cornell Medical Center, New York, NY, United States, [7]Department of Medicine, Parker Institute for Cancer Immunotherapy and Sandra and Edward Meyer Cancer Center, Weill Cornell Medical Center, New York, NY, United States

Introduction: Immunotherapy is revolutionizing the management of multiple cancer types. However, only a subset of patients responds to immunotherapy. One mechanism of resistance is the absence of immune infiltrates within the tumor. *In situ* vaccine with local means of tumor destruction that can induce immunogenic cell death have been shown to enhance tumor T cell infiltration and increase efficacy of immune checkpoint blockade.

Methods: Here, we compare three different forms of localize tumor destruction therapies: radiation therapy (RT), vascular targeted photodynamic therapy (VTP) and cryoablation (Cryo), which are known to induce immunogenic cell death, with their ability to induce local and systemic immune responses in a mouse 4T1 breast cancer model. The effects of combining RT, VTP, Cryo with anti-PD1 was also assessed.

Results: We observed that RT, VTP and Cryo significantly delayed tumor growth and extended overall survival. In addition, they also induced regression of non-treated distant tumors in a bilateral model suggesting a systemic immune response. Flow cytometry showed that VTP and Cryo are associated with a reduction in CD11b+ myeloid cells (granulocytes, monocytes, and macrophages) in tumor and periphery. An increase in CD8+ T cell infiltration into tumors was

observed only in the RT group. VTP and Cryo were associated with an increase in CD4+ and CD8+ cells in the periphery.

Conclusion: These data suggest that cell death induced by VTP and Cryo elicit similar immune responses that differ from local RT.

KEYWORDS

radiation therapy, vascular photodynamic therapy, cryoablation, immune checkpoint blockade, breast cancer

Introduction

Immunotherapies have shown great potential to control cancer by enhancing T cell responses to cancer antigens. Immune checkpoint blockade (ICB) targeting the cytotoxic T-lymphocyte associated protein 4 (CTLA-4), programmed cell death protein 1 (PD-1) and lymphocyte activating gene 3 (LAG-3) have been approved for treating multiple cancers, however, a large fraction of patients still do not respond to these therapies. This is mainly due to multiple mechanisms of immune resistance that may exist within tumors, such as the lack of T cell infiltration or immune desert tumor microenvironment (TME), low tumor mutation burden or an immunosuppressive TME. In poorly infiltrated tumors (cold tumors), enhancing tumor T cell infiltration by physically disrupting the tumor can be utilized using local ablation therapies, such as with radiation therapy (RT), vascular targeted photodynamic therapy (VTP), or cryoablation (Cryo). In highly infiltrated tumors (hot tumors), immune suppressive cells have been shown to play a major role in limiting the efficacy of anti-tumor immunity (1). The presence of high levels of immune suppressive cells such as myeloid derived suppressive cells (MDSCs) have been shown to correlate with poor prognosis and ICB resistance (2, 3). Combination strategies that can convert a cold tumor into a hot tumor while targeting the immunosuppressive TME are key to the design of therapeutic combinations that can overcome such resistance mechanisms.

Local ablative therapies have all been shown induce tumor cell death that can be immunogenic (4–6) because they not only release tumor antigens that can trigger an *in-situ* vaccination effect but also secreted factors such as danger associated molecular patterns (DAMPs) that can facilitate the maturation of antigen presenting cells (APCs) further enhancing the immune response to the cancer (7). In addition, inflammatory or secreted factors such as cytokines can recruit more immune cells into to the tumor microenvironment. The resulting outcome of immunogenic cell death in the context of cancer is activation of a tumor specific immune response in the host. Therefore, not only can the immune system recognize and kill the primary tumor but also distant metastases (termed the abscopal effect).

Prior studies have demonstrated that the abscopal effect of RT, in which localized RT causes distant tumors to regress, may be due to the release of tumor-antigens that can enhance the immunogenicity of tumors, which can then increase susceptibility to systemic immune-stimulating agents (8). This effect has been seen in the regression of a metastatic melanoma case treated with local RT, which enhanced systemic responses to an anti-CTLA-4 antibody (ipilimumab) (9). This co-occurred with increase in NY-ESO-1 expression and $CD4^{+}ICOS^{high}$ cells, both of which correlated with increased benefit from ipilimumab. In a recent clinical study of RT in combination with CTLA-4 blockade in chemo-refractory metastatic non-small-cell lung cancer (NSCLC) where anti-CTLA-4 antibodies had failed to demonstrate significant efficacy alone or in combination with chemotherapy, RT and CTLA-4 blockade showed objective responses in 18% patients and 31% disease control and induced systemic anti-tumor T cells (10). In preclinical breast cancer models, radiation controls tumor growth both directly through cell killing and indirectly through immune activation (11).

Another local therapy with both ablative and immunologic effects is VTP, a form of photodynamic therapy, which uses an intravenously administered photosensitizing agent (padeliporfin/TOOKAD Soluble/WST11; STEBA Biotech, Luxembourg) and near-infrared light to create radical oxygen species that lead to tumor vasculature collapse and subsequent tissue destruction (12). Photodynamic therapy, which is Food and Drug Administration-approved for several malignancies (13), has been reported to cause acute inflammation and increase tumor antigen presentation (14). Similarly, VTP treatment of preclinical models induces a defined local inflammatory response, including IFNγ production and infiltration of tumors by T cells and neutrophils in colon cancer models (15). In an orthotopic murine model of renal cell carcinoma that develops lung metastases, VTP in combination with anti-PD-1/PD-L-1 antibodies demonstrates superior anti-tumor activity as compared to checkpoint blockade alone and induces immune infiltration in primary and metastatic sites (16). Modulation of PD-L1 expression by VTP in human xenograft tumors was also observed.

An additional local ablation option is Cryo, which employs needle applicators (cryoprobes) to transmit pressurized argon and helium gases to the tumor to cause localized tissue freezing and thawing (17). As intracellular and extracellular fluid freezes, tissue destruction results from cell membrane disruption by ice crystals, cellular dehydration, and vascular thrombosis at temperatures below -20 to -40°C. Cryo induces cell lysis and leaves tumor proteins and tumor-associated antigens immunologically intact, different from hyperthermia-based ablation modalities (18). Cryo also results in the induction of both a

tumor-specific T cell response in the tumor draining lymph node (TDLN) and increased systemic NK cell activity, correlating with rejection of tumors upon re-challenge in a murine model of breast cancer (18). When performed in conjunction with CTLA-4 blockade, Cryo improved survival in a TRAMP C2 mouse model of prostate cancer, also generating intratumoral and systemic expansion of $CD8^+$ T cells against the SPAS-1 tumor-specific antigen (19). A safety/feasibility study of preoperative single-dose ipilimumab and/or Cryo in 19 women with early-stage breast cancer showed that this combination strategy increased Th1-cytokine production, peripheral T cell proliferation/activation, and intratumoral proliferation of effector T cells relative to regulatory T cells (20).

Since RT, VTP and Cryo are all clinically available treatment options for overlapping but also different indications, it is imperative to understand the immune modulatory effect of each therapy to delineate the best strategy in combination with immunotherapy. As each of these modes of treatment are given locally to the tumors only and have been shown to synergize well with immune modulatory agents, we compared the effects of three local ablation therapies: RT, Cryo and VTP using 4T1 triple negative murine breast cancer (TNBC) model. Unlike melanomas such as mouse B16 melanoma, 4T1 tumors have been shown to be poorly infiltrated by T cells but highly infiltrated with myeloid ($CD11b^+$) immune cells (2). These $CD11b^+$ myeloid cells in the spleens and tumors of 4T1 bearing mice display a MDSC phenotype and have been shown to be functionally immunosuppressive (2, 3). Thus, 4T1 tumors represent the classical T cell desert or immunologically "cold" tumors but highly immunosuppressive (enriched in MDSCs) that have been shown to contribute to the poor response of 4T1 tumors to ICB.

The main goal of this study is to measure how RT, VTP, or Cryo effect the innate and adaptive immune responses not only in the treated tumors but also on the immune system systemically. Our results demonstrate that immune modulation with RT, VTP, or Cryo therapy can generate potent local and systemic antitumor responses. These modalities may represent an effective strategy to treat poorly infiltrated or immunologically "cold" tumors known to be resistant to ICB by modulating the immunosuppressive TME along with systemic T cell activation to enhance therapeutic efficacy of ICB.

Materials and methods

Cell line

The murine breast cancer cell line 4T1 was maintained in RPMI medium supplemented with 10% FBS, 2 mM L-glutamine and penicillin with streptomycin.

In vivo studies

$2x10^5$ 4T1 cells were subcutaneously injected in the right hindlimb of BALB/cJ female mice (7–8 weeks old, JACKSON LABORATORY, Bar Harbor, ME) 12 days prior to RT, VTP and Cryo. For bilateral models, two sequential injections of $2x10^5$ 4T1 cells 12 days and 5 days prior to the treatments were administered in the mice. The mice bearing tumors were randomly assigned to different cohorts for further experiments. For efficacy studies (tumor growth and survival), n = 10 mice were used for each experimental group (Control, RT, VTP, Cryo +/- anti-PD1) and for *ex vivo* studies (e.g., flow cytometry, IHC, cytokines), n = 5 mice were used for each experimental group. Local tumor growth was monitored twice a week using caliper measurements (Perkin-Elmer, Waltham, MA). The tumor area/volume curves averaged at each time point per group are reported for as long as all mice in a group are alive. Overall survival curves of each treatment group were analyzed using the Kaplan–Meier estimator. The survival curves measure time from start of experiment to a tumor size of 2000 mm^3 (in which case the mouse needs to be euthanized) or death.

Tumor directed radiation therapy

A single dose of 15 Gy was used to irradiate 4T1 tumors. This dose was previously determined to be optimal for immune infiltration in a mouse B16 melanoma model (21). On day 12, mice were anesthetized with isoflurane and placed in a radiation jig where only the hindlimb is exposed (22). The right hindlimb bearing 4T1 tumors was irradiated with 15 Gy RT using the X-RAD 320 focus beam irradiator such that only the exposed hindlimb bearing the tumors receives the radiation.

WST-11 VTP

WST-11, a photosensitizer, was reconstituted in sterile 5% dextran in water at 2 mg/mL under light protected condition and the aliquots were stored at -20°C. At the time of VTP treatment, an aliquot was thawed and filtered through 0.2 µm disc syringe filter (Sartorius Stedin Biotech North America, Bohemia, NY). The mice were intravenously infused with WST-11 (9 mg/kg) for 5 min followed immediately by 10 minutes laser (Modulight, Tampere, Finland) illumination (755 nm, 100 mW/cm) through a 1 mm frontal diffuser fiber (MedLight S.A., Ecublens, Switzerland). The light field was set up to cover the entire tumor area plus 1 mm rim using red-light aiming beam.

Cryoablation

Visually guided cryoablation with 1.7 mm Per Cryo probes was used to treat tumors. Mice were anesthetized with a mixture of 100 mg/kg ketamine and 10 mg/kg xylazine, and the targeted area were shaved and cleaned with iodine and 70% alcohol swabs. A small cut in the skin was made to allow the cryoprobe tip to enter the tumor. Freeze cycle was discontinued when ice crystals encompassed the visible tumor and thaw cycles was discontinued when ice crystals were no longer visible. The treatment parameter was evaluated using single cycle at 20% freeze rate for up to 60 seconds. A control group was not ablated. After the treatment, mice were monitored

for bleeding or other complications according to the standard recovery procedure of the approved animal protocol.

Dosing schedule of anti-PD1

Animals received three doses of intraperitoneal (i.p.) injection of anti-PD1 (BioXCell, West Lebanon, NH; clone RMP1–14, 250 ug/mouse) on the same day of and 3- and 6-days post treatment.

Immunohistochemistry

Tumors and spleens from 3 mice/group were harvested 6 days after treatment with RT, VTP and Cryo. Tissues were then fixed in 10% buffered formalin (Fisher Scientific, Pittsburgh, PA), embedded in paraffin, sectioned at 5 micrometer thickness, and stained with hematoxylin-eosin (H&E), anti-mouse CD8 and CD11b antibodies. Slides were scanned and analyzed for immunoreactivity the image analysis platform HALO by Indica Labs (Albuquerque, NM). For quantification, heathy areas within tumors and spleens were selected in parallel sections based on H&E staining. 3–5 regions/slide were selected and the percent of $CD8^+$ and $CD11b^+$ area were calculated and normalized to tissue surface area.

Isolation of tumor-infiltrating cells and leukocytes and flow analysis

Spleens, LNs and tumors were prepared by mechanical dissociation through 40 and 100 µm cell strainers (BD Biosciences, Franklin Lakes, NJ) in RPMI supplemented with 7.5% FCS to isolate single cells. Red blood cells (RBCs) were lysed with ACK Lysing Buffer (Lonza, Basel, Switzerland) when required, all samples were washed and resuspended in FACS buffer (PBS without Ca^{++}/Mg^{++} supplemented with 0.5% BSA and 2mM EDTA). For staining for flow cytometry analysis, 100–200µL of single cell suspensions of each tissue were plated into two 96-well round bottom plates: one plate for T cell analysis (anti-CD45-Alexa 700, anti-CD8-PerCP-Cy5, anti-CD4-v450, anti-CD25-APC-Cy7, anti-CD62L-PE, anti-CD44-PE-Cy7, anti-FoxP3-APC, anti-Ki67-FITC, anti-Granzyme B PE-Texas Red, and a fixable viability dye eFluor506 (Invitrogen, Waltham, MA)) and one plate for myeloid cell analysis (anti-CD45-FITC, anti-CD11c-PE, anti-CD8-PE-Texas Red, anti-Ly6G-PerCP-Cy5, anti-Ly6C-PE-Cy7, anti-MHCII-v450, anti-CD86-APC, anti-CD11b-APC-Cy7, and the viability dye eFluor506). Cells were pelleted by spinning at 2,000 rpm for 5 mins. Cells were incubated in 100µL of 5 µg/ml Fc-block antibody (clone 2.4G2, BD Biosciences) for 20 mins on ice in FACS buffer. After Fc-block, cells were stained in FACS buffer containing fluorophore conjugated surface antibodies and for 20 mins on ice. Samples were then washed 2 times with 200µL FACS buffer. All intracellular staining were done using the Foxp3 fixation/permeabilization buffer according to the manufacturer's instructions. Events were acquired using a multi-channel flow cytometer (BD LSRII, BD Biosciences, San Diego, CA). FlowJo software V10 (FlowJo,LLC) was used to analyze all data. The gating strategies for each myeloid and T cell panel are shown in Supplementary Figures S2, S6. We identified the immune cell populations as follows: live cells – viability dye negative, total immune infiltrates $CD45^+$, total myeloid cells – $CD45^+CD11b^+$. Myeloid cells were subgated into Neutrophils/Granulocytes – $Ly6G^+$, Monocytes – $Ly6C^+$, Macrophages – $Ly6C^-Ly6G^-$. Antigen presenting cells (APCs/DCs) were identified as $CD45^+CD11c^+$MHC II^+ and subgated into cross-presenting DCs ($CD8^+$ DCs) – $CD8^+$, conventional DCs ($CD11b^+$ DCs) –$CD11b^+$, other DCs –$CD8^-$ $CD11b^-$. Additionally, we examine expression of two markers of antigen presentation (CD86 and MHC II) as activation markers on myeloid cell subsets. CD8 T cells were identified as $CD45^+$ $CD8^+$, CD4 Teff – $CD45^+$ $CD4^+$ $Foxp3^-$, CD4 Treg – $CD45^+$ $CD4^+$ $Foxp3^+$. For T cell differentiation states, naïve T cells were defined as $CD62L^+CD44^-$, central memory T cells as $CD62L^+CD44^+$, effector memory T cells as $CD62L^-CD44^+$. Additionally, we examined expression of several T cell activation markers: Ki67, Granzyme B, and CD25.

For intracellular cytokine staining (IFNγ and TNFα), single cell suspensions of tissues were plated in 96-well round bottom plates containing 200 µL RPMI supplemented with 10% FCS and stimulated with 1 µM PMA (Sigma, St. Louis, MO) and 1 µM Ionomycin (Sigma) for 30 mins at 37°C, then Brefeldin A (1000x dilution, BD Biosciences) and 10 µg/ml Monensin (Sigma) was added and incubated for an additional 5 hr at 37°C. The plates were chilled at 4°C and stained for surface and intracellular markers as described above.

Statistical analysis

Unless otherwise indicated p values were calculated using a 2-tailed Student's t test or two-way ANOVA-test. A p value of < 0.05 was considered statistically significant. p values comparing survival curves were calculated using the Log-rank (Mantel-Cox) test. Correlations of immune cell frequencies with tumor weight were done using Pearson's correlation. All graphs and statistical calculations were done using GraphPad Prism software and Microsoft Excel.

Results

RT, VTP and Cryo elicit anti-tumor responses in 4T1 murine breast cancer model

A summary comparing the kinetics and doses of RT, VTP and Cryo used in this study is listed in the table of Figure 1A. To examine the anti-tumor effects of three local ablation therapies, mice implanted with 4T1 breast tumor cells were treated with RT, VTP or Cryo according to the schedule outlined in Figure 1A. For the combination treatment with anti-PD-1, mice were also intraperitoneally administered with 3 doses of anti-PD1 antibody at 250 µg/mouse with the first dose given immediately after each treatment. Mice were monitored for tumor growth (Supplementary Figure S1; Figure 1B) and overall survival (Figure 1C). All three therapies delayed tumor growth, with VTP ($p<0.0001$) and Cryo

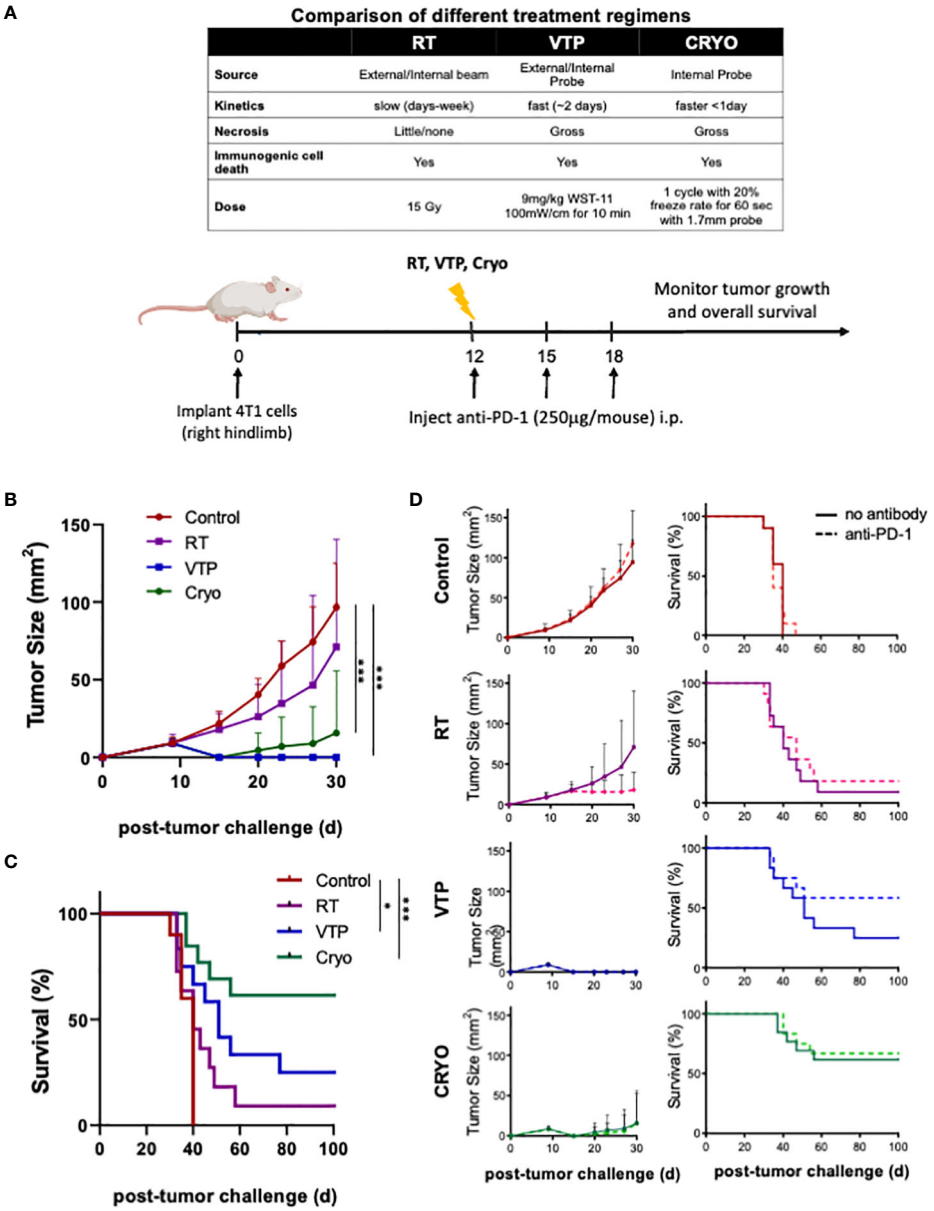

FIGURE 1
RT, VTP and Cryoablation elicit anti-tumor responses in 4T1 breast cancer. **(A)** Experiment schema of the comparative study with with RT, VTP and Cryo. 2 x 10^5 4T1 mouse breast cancer cells were injected subcutaneously in the hind limb of 6-8 week female Balbc mice (n=10 mice per group). 12 days later, mice were treated with RT, VTP or Cryo therapy. For combinations with anti-PD-1, mice were injected intraperitoneally with anti-PD-1 antibody every 3 days for a total of 3 doses. **(B)** Comparison average tumor growth and **(C)** overall survival of 4 cohorts relative to the control. **(D)** Comparison of the average tumor growth +/- SEM and overall survival for individual cohorts with and without anti-PD1 are shown. Statistics were calculated using student T-tests on day 30 for tumor growth and the Logrank method for survival: *p ≤ 0.05, ***p ≤ 0.005.

(p<0.0005) showing statistical significance. VTP and Cryo also improved overall survival (OS) of the animals compared to control group (VTP, p<0.05; Cryo, p<0.0005). RT showed a trend toward improved survival; however, this was not significant (p=0.139). One caveat in comparing these therapies is that treatment with RT and VTP regimens were aimed for suboptimal ablation of the tumors while the dose of Cryo in these studies was optimally ablative due to the nature of the procedure. The addition of anti-PD1 to each of these therapies further delayed tumor growth in a few tumors but had minimal effect on overall survival (Figure 1D). The cohort treated with VTP + anti-PD1 trended towards better survival than VTP alone however this difference was not significant (p=0.1663). OS in all three combination cohorts was improved compared to anti-PD1 monotherapy (RT combination vs. anti-PD-1, p<0.088; VTP combination vs. anti-PD-1, p<0.005; Cryo combination vs. anti-PD-1, p<0.0001). Some of the tumors treated with these therapies completely regressed in response to the therapies: two mice in VTP, 7 mice in Cryo, 6 mice in VTP + anti-PD1 combination and 7 mice in Cryo + anti-PD1 combination were tumor free at day 98 post treatment (Supplementary Figure S1).

RT, VTP and Cryo leads to activation of myeloid cells in the tumor, spleen and draining LN

To understand the changes in the TME after RT, VTP and Cryo, we performed flow cytometry analysis on tumors, tumor draining lymph nodes (LNs) and spleens isolated from animals treated with RT, VTP and Cryo according to the schedule outlined in Figure 2A. Identification of each innate immune cell population was determined using the gating strategy outlined in Supplementary Figure S2. We found a significant increase in the frequencies of viable CD45$^+$ total immune cells infiltrating the tumors at 3 days after RT, VTP and Cryo (Figure 2B). This effect diminished over time in the VTP and Cryo groups quickly however, RT showed different kinetics over time. The increases in immune cell infiltration in the tumor appears to mainly be due to an increase in CD11b$^+$ myeloid cells. We found an increase in CD11b$^+$ myeloid cells in the tumors at 3 days post all 3 treatments while CD11b$^+$ population in spleen and TDLN showed minimal increase (RT) or decrease (VTP & Cryo) (Figure 2C; Supplementary Figure S3). When CD11b+ cells are sub-gated into granulocytes (CD11b$^+$ Ly6G$^+$), monocytes (CD11b$^+$ Ly6C$^+$), and macrophages (CD11b$^+$ Ly6G$^-$Ly6C$^-$), (Supplementary Figure S2), we find that the majority of the cells infiltrating the tumors at day 3 are granulocytes and monocytes. These cells are decreased in the tumors treated with VTP and Cryo at 6- and 9-days post treatment. However, they remain higher in the RT treated tumors (Figure 2C). In addition, RT was associated with a significant ($p < 0.05$) increase in CD8$^+$ DCs in the tumors at 9 days after treatment (Figure 2C). This is consistent with previous reports that local RT activates cross-presenting DCs which elicits CD8$^+$ T cell activation (23, 24).

There was an increase although not significant in macrophages (CD11b$^+$Ly6G$^-$Ly6C$^-$F4/80$^+$) and antigen presenting cells (APCs: CD11c$^+$MHC II$^+$) in tumors 3 days after treatment with RT and Cryo, however there is a global decrease in these populations over time (Figure 2C). When we examine the correlations of all the innate cells with tumor burden (tumor weight at time of excision), we find that macrophages and APCs have the strongest positive correlation with tumor burden (Figure 2D), suggesting that these cells may help promote tumor progression. Of note, all the APC subtypes correlates positively with tumor burden whereas other immune subsets such as monocytes showed no correlation (Supplementary Figure S4). While we did observe a decrease in macrophages and APCs over time, the quality of these cells appears

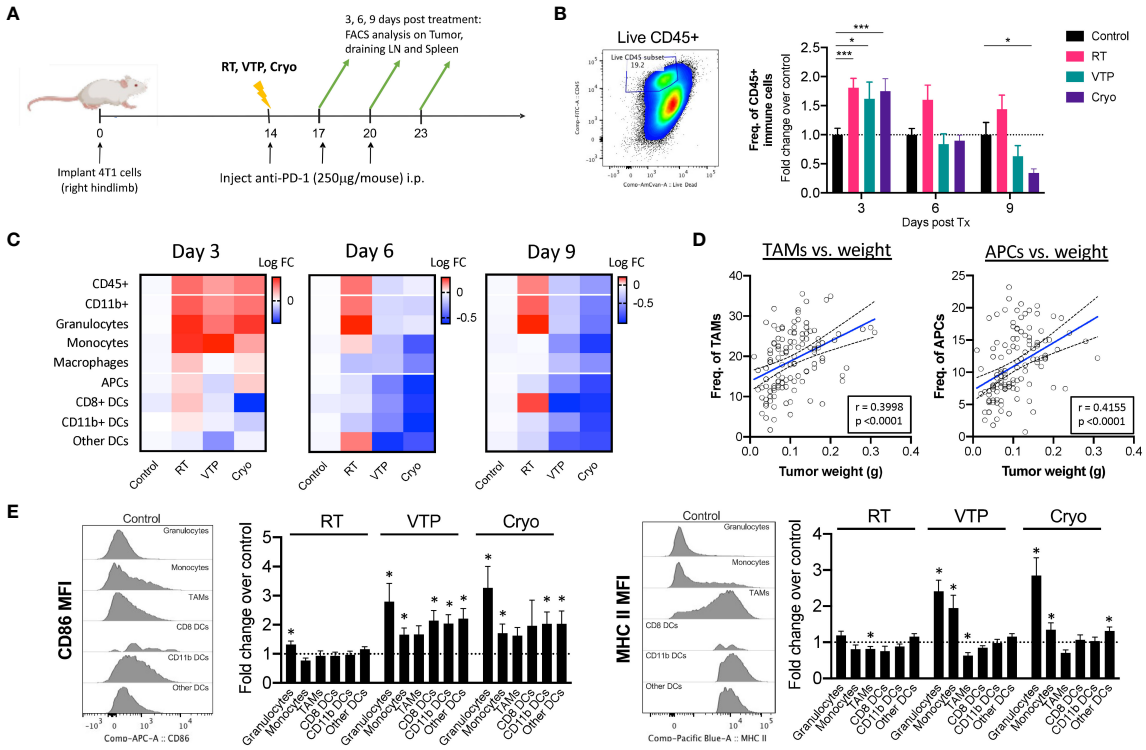

FIGURE 2
Activation of Myeloid cells in the tumor of animals treated with localized therapies. 2 x 10^5 4T1 mouse breast cancer cells were injected subcutaneously in the right hind limb of 6-8 week female Balbc mice (n=5 mice/group). 12 days later when the tumors reached 50-60mm2 in size, mice were treated with 15 Gy radiation (RT), VTP or Cryo therapy according to the doses listed in Figure 1A and methods. **(A)** Experiment schema of timeline of tumor challenge, treatment dates and tissue harvest for flow cytometry. **(B)** bivariate plot to show the gating strategy for total immune infiltrates in the tumors (live CD45$^+$) and fold change in The frequencies of CD45$^+$ cells of each treatment group represented at fold change over the control in the tumor at the indicated time points. **(C)** Heatmaps representing the log10 fold change (Log FC) of the immune cell populations in the tumor. **(D)** Pearson correlations of tumor burden (weight (g)) vs. frequencies of myeloid cells (as a % of CD45$^+$ cells) from experiments outlined in **(A)**. **(E)** Histogram plots showing relative expression levels of two activation markers associated with antigen presentation (CD86 and MHC II) on each myeloid cell in the tumor at day 3 post treatment. Bar graphs represent fold change in expression over the control group. Statistics were calculated using a student T-test: *p ≤ 0.05, ***p ≤ 0.005.

to be different after treatment with VTP and Cryo. In fact, most of the innate immune cells showed increased expression of markers associated with antigen presentation after treatment. All the innate cells examined show increased expression of CD86 (B7.2, the co-receptor for CD28 on T cells), however, only neutrophils and monocytes showed increased MHC II expression over the control. This is mainly because macrophages and all the subsets of APCs already express high levels of MHC II in the tumors and this expression does not change after treatment (Figure 2E, histogram plots).

Since RT, VTP and Cryo are all localized therapies given directly to the tumors, we sought to determine whether these therapies can elicit a systemic effect on innate immune cells. Consistent with that data from the tumors, we found a reduction of $CD11b^+$ population in the spleens (Supplementary Figure S5A) and tumor draining LNs (Supplementary Figure S5B) treated with VTP and Cryo. The effect was seen as early as 3 days post treatment and persists for up to 9 days post treatment. Similar decreases in APCs were seen in the LNs but not the spleens of treated animals. When we examined expression of activation markers involved in antigen presentation, we found that most of the innate cells in the LN and to a lesser extent in the spleen, showed an increase in expression of CD86 and MHC II. This expression peaks in the LN at 3 days after treatment in the RT groups, and 6 days after treatment with VTP and Cryo. This suggest that the kinetics for RT is different from VTP and Cryo.

RT, VTP and Cryo leads to activation of T cells in the tumor, spleen and draining LN

In addition to examining cells of the innate immune system, we conducted flow cytometry analysis on the adaptive immune system using markers for $CD8^+$ T cells, $CD4^+$ effector T cells (Teffs) and $CD4^+$ $Foxp3^+$ regulatory T cells (Tregs). Tumor bearing animals were treated according to the schedule outlined in Figure 1A and tumors, draining LNs and spleens were isolated and processed for flow cytometry according to the timeline in Figure 2A. Identification of T cell population and their activation/differentiation states were defined by the gating strategy outlined in Supplementary Figure S6. In addition to comparing the effects of RT, VTP and Cryo on the adaptive immune system, we also compared the effects of adding anti-PD-1 to each treatment since anti-PD-1 is known to affect T cell proliferation and activation.

We observed a global decrease in all T cell populations in the tumor at all 3 timepoints examined (Figure 3A, left and Supplementary Figure S7). The relative abundance of the effector T cells ($CD8^+$ T cells or $CD4^+$ Teffs) with respect to $CD4^+$ Tregs can be used to estimate immune responses to immunotherapies. In these experiments even though there is a decrease in these populations, we did observe an increase in the ratio of CD8:Treg and CD4:Treg at day 3 with VTP and Cryo. At day 9, the addition of anti-PD-1 significantly increased the ratio of CD8:Treg in the control, RT and VTP treated groups and there was a trend (not statistically significant) towards an increase in the Cyro group (Figure 3A, left and Supplementary Figure S7). This effect was especially striking in the RT group where an increase in both CD8:Treg and CD4:Treg was observed with the addition of anti-PD-1. In contrast to the tumors, we found a significant increase in both $CD8^+$ T cells and $CD4^+$ Teffs in the spleen of treated animals at all time points examined (Figure 3A, middle and Supplementary Figure S8). However, there was also an increase in $CD4^+$ Tregs which led to a decreased CD8:Treg and CD4:Treg ratio. In the tumor draining LNs, there was an early increase in $CD8^+$ T cells and $CD4^+$ Teffs coupled with an overall decrease in Tregs in all treatment groups. The net effect is an increase in CD8:Treg and CD4:Treg ratios (Figure 3A, right and Supplementary Figure S9). The addition of anti-PD-1 did not appear to significantly affect the T cell populations in the spleen or LNs.

When we examined the activation status of T cells in the tumor, spleen and LNs at all three time points, we found T cells were activated in the tumor and spleen with slightly different kinetics (Supplementary Figures S7, S8). No significant changes in T cell activation were observed in the draining LNs (Supplementary Figure S9). In some of the conditions, the tumors were at times too small to obtain enough data for statistical power, this was especially the case in the VTP and Cryo treated tumors. However, we did observe some significant changes in the samples which were analyzed. There was an early increase in T cell activation markers mainly on $CD8^+$ T cells among tumor samples at 3 days post therapy (Supplementary Figure S7). Notably, there was an increase in CD25 (the IL-2Rα chain) in the RT, VTP and Cryo groups. There was also an increase in the cytolytic protein, Granzyme B, expression in $CD8^+$ T cells in the RT groups. There was also a significant increase in effector memory (TEM) cells in all the treatment groups. The addition of anti-PD-1 did not significantly enhance the activation state of $CD8^+$ T cells or $CD4^+$ Teffs in the tumor at any of the time points examined.

There were some significant increases in T cell activation in the spleen at 6- and 9-days post treatment which was most striking in the VTP and Cryo groups (Supplementary Figure S8; Figure 3B). There was an increase in Granzyme B, and the proliferation marker Ki67 in both $CD8^+$ T cells and $CD4^+$ Teffs (Figures 3B, C; Supplementary Figure S10A). There was an increase in both central memory (TCM) and effector memory (TEM) $CD4^+$ Teffs at 9 days following all three treatments (Figures 3B, C; Supplementary Figure S10B). The addition of anti-PD-1 at this time point did not enhance the presence of TCM $CD4^+$ Teffs but did enhance the frequencies of TEM $CD4^+$ T cells. In addition, anti-PD-1 also enhanced Ki67 on $CD4^+$ Teffs in the RT and VTP groups at day 9 (Figure 3C). The addition of anti-PD-1 had the strongest effects on T cell activation in the spleen at day 3 post treatment where there was a significant increase in the expression of CD25 in both $CD8^+$ T cells and $CD4^+$ Teffs in the RT and VTP treated animals (Figure 3B; Supplementary Figure S10C). There was also an increase in TCM and/or TEM $CD8^+$ T cells and $CD4^+$ Teffs in all three groups with the strongest changes observed in the RT groups. On day 6, there was an increase in Ki67 in $CD8^+$ T cells and $CD4^+$ Teffs in animals treated with Cryo and anti-PD-1. In addition, at this time point VTP alone induced a significant increase in Granzyme B expression in both $CD8^+$ T cells and $CD4^+$ Teffs.

10.3389/fonc.2024.1405486

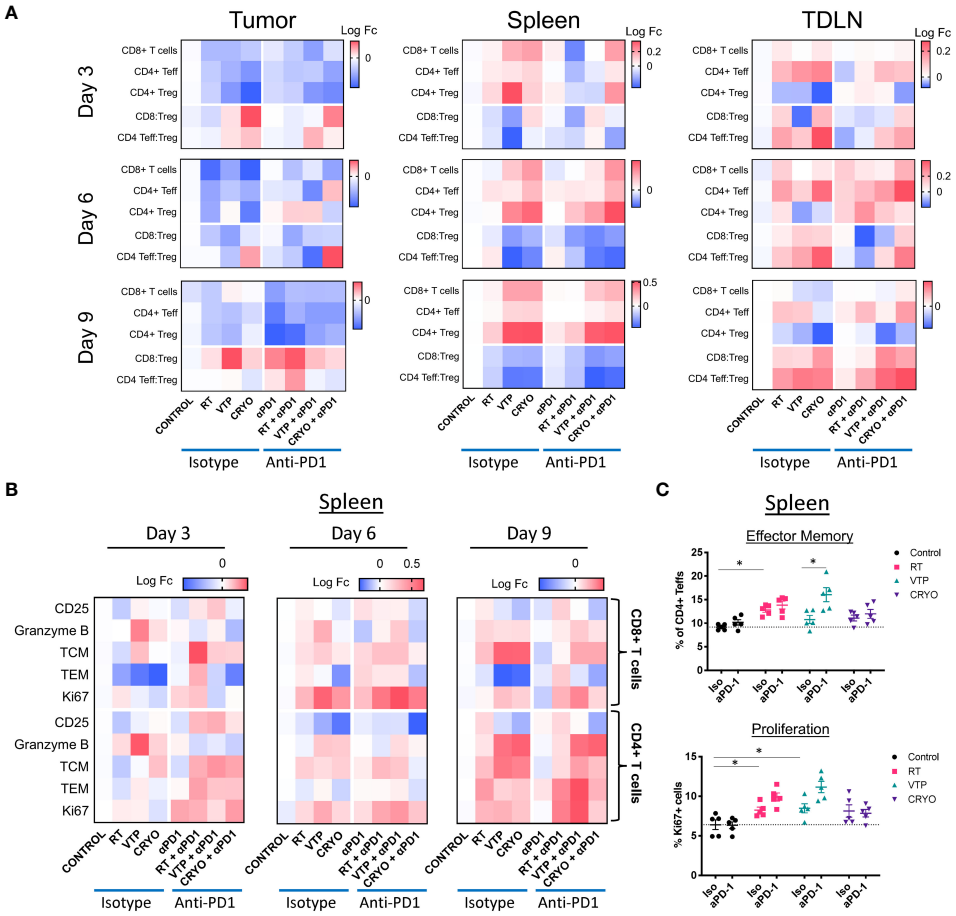

FIGURE 3
Activation of T cells in the tumor, spleen and draining LN of animals treated with localized therapies. 2 x 10^5 4T1 mouse breast cancer cells were injected subcutaneously in the right hind limb of 6-8 week female Balbc mice and treated with RT, VTP or Cryo therapy according to the doses and schedule in Figure 1A. 3, 6 and 9 days after the start of treatment, tumor, spleen and draining LNs were harvested and processed for flow cytometry. **(A)** Heatmaps represents the log10 fold change (Log FC) of the $CD8^+$ T cells, $CD4^+$ Teffs and $CD4^+$ Tregs as well as the CD8:Treg and CD4:Treg ratios in the tumor, spleen and LN at 3, 6, and 9 days post treatment. **(B)** Heatmaps represents the $\log_{10}$ fold change (Log FC) relative to the control group of T cell activation markers in the spleen with the indicated therapies. **(C)** Quantification of effector memory (Tem) and proliferating (Ki67+) $CD4^+$ Teffs ($CD4^+Foxp3^-$) in the spleen 9 days after treatment. *p ≤ 0.05.

In summary, the changes of T cell activation states in the spleen peaked 6–9 days post treatment with the monotherapies. These observations are highly significant because they show that localized treatments such as RT, VTP and Cryo can have systemic effects on the adaptive immune responses.

IHC analysis show a decrease in $CD11b^+$ myeloid cells and an increase in $CD8^+$ T cells in the spleens of animals treated with VTP and Cryo

While flow cytometry can give us a great deal of information on the breadth and depth of immune cells and their activation state, it cannot assess the spatial distribution of these cells throughout the tissues. To understand the spatial distribution of immune cells in 4T1 breast tumors, we performed immunohistochemistry (IHC) analysis on paraffin embedded sections of spleens and tumors from mice treated with RT, VTP and Cryo. Tumor bearing animals were treated according to the schema outlined in Figure 1A and tissues were harvested 6 days after treatment and processed for IHC. Serial paraffin sections were cut and stained with anti-CD8 and anti-CD11b and H&E. From the IHC data, we observed that 4T1 tumors which have not received any treatment are poorly infiltrated with $CD8^+$ T cells (Supplementary Figure S11; Figure 4A). On the contrary, these tumors are more heavily infiltrated by $CD11b^+$ myeloid cells, however, many of these cells appear to be confined to the stroma and necrotic tumor areas rather than tumor cell dense areas (Supplementary Figure S11). The density in $CD11b^+$ myeloid cells in the spleens of 4T1 tumor bearing mice also appear to be high in untreated animals (Supplementary Figure S12). These observations are in agreement with the flow cytometry data and previously published data that 4T1 tumors are poorly infiltrated by T cells and highly infiltrated with myeloid cells (2).

Analysis of the IHC data showed that 2/3 RT treated tumors and 1/3 VTP treated tumors showed an increase in CD8 infiltration relative to the control (Figures 4A, B). In the anti-PD-1 treated groups, 3/3 RT tumors showed significant increased CD8+ T cell

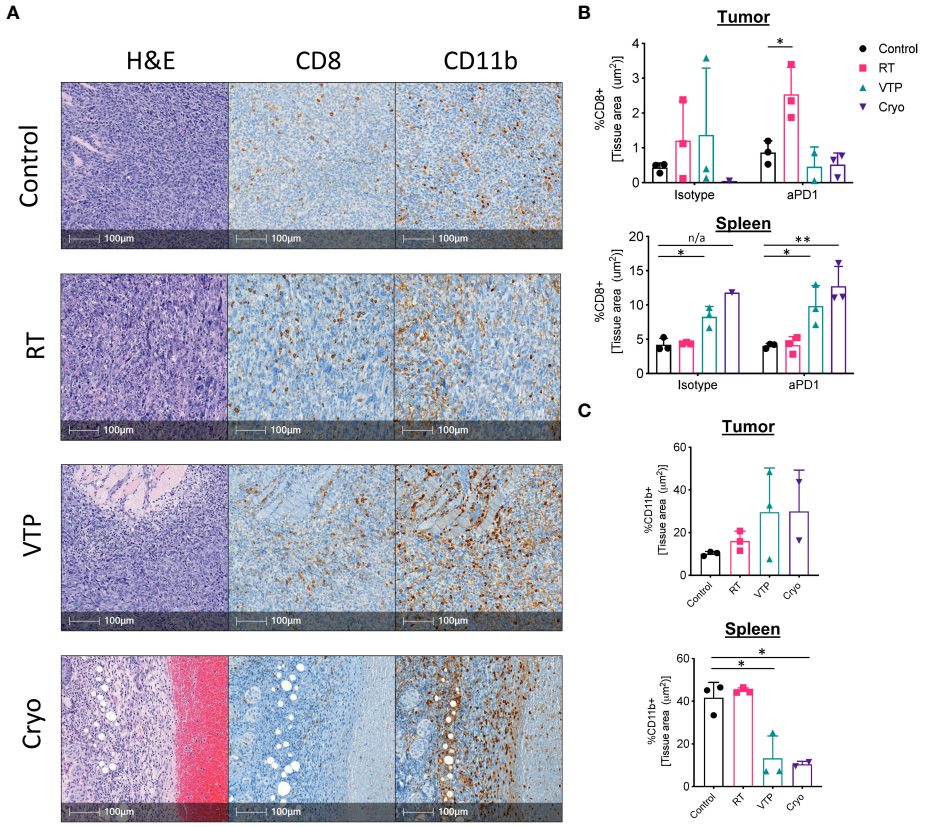

FIGURE 4
IHC analysis show an increase in CD11b$^+$ myeloid cells infiltrating the tumors of animals treated with RT, VTP and Cryoablation. 2 x 10^5 4T1 mouse breast cancer cells were injected subcutaneously in the right hind limb of 6-8 week female Balbc mice and treated with RT, VTP or Cryo therapy according to the doses and schedule in Figure 1A. 6 days after treatment, tumors and spleens were harvested and processed for immunohistochemistry (IHC). **(A)** Shown are representative images of serial sections for H&E, CD8 and CD11b for each treatment group. Bar = 100µm. **(B, C)** Relative densities of CD8 and CD11b expression in the tumor and spleens. Shown are % of tissue stained positive for each marker calculated and normalized per tissue area using the HALO Image Analysis Software. N=3 mice/group. Statistics were calculated using student's T-test: *p ≤ 0.05, **p ≤ 0.01. n/a means statistics could not be calculated since the Cryo group had only one analyzable tumor.

infiltration relative to the control or anti-PD-1 alone (Figure 4B). In agreement with the flow data (Figure 1C), we also observed a slight increase in CD11b$^+$ myeloid cell infiltration into the tumors treated with RT (Figure 4C). Because VTP and Cryo destroys the tumor tissue, it is difficult to get large enough healthy tumor areas to effectively quantify immune infiltrates. When the few healthy sections were analyzed, we did not observe any significant changes in CD8+ T cell infiltration into tumors treated with VTP and Cryo (Figures 4A, B). Similar to the flow data at early time points, we observed a trend towards an increase in CD11b$^+$ cells infiltrating tumors treated with VTP and Cryo (Figures 4A, C).

Remarkably, while VTP and Cryo did not appear to induce a T cell response in the tumors, they appear have a strong effect on T cells in the spleen as noted by larger T cell zones in the H&E sections and increased CD8$^+$ T cell in the IHC slides (Supplementary Figure S12, Figure 4B). In addition, VTP and Cryo significantly decrease the CD11b$^+$ myeloid population in the spleen (Supplementary Figure S12, Figure 4C). These data support the conclusion that that localized treatments such as VTP and Cryo can have systemic effects on the immune system.

RT, VTP and Cryo led to increased cytokine production by CD4+ and CD8+ T cells in the spleen

Our findings that T cell activation markers are increased on CD4$^+$ and CD8$^+$ T cells in the spleens of animals treated with localized therapies such as RT, VTP and Cryo suggests a systemic effect of these therapies on the adaptive immune system. To determine whether these phenotypic increases translate into a function change by T cells, we stimulated single cell suspensions isolated from the spleens of treated animals with PMA and Ionomycin in the presence of Golgi inhibitors (Brefeldin A and monensin) to examine the T cells' ability to produce pro-inflammatory cytokines such as interferon-gamma (IFNγ) and tumor necrosis factor-alpha (TNFα). We also examined if these T cells can produce both IFNγ and TNFα simultaneously. These polyfunctional T cells have been shown to be the most functional effector cells (25). We found that there was an increase in both IFNγ$^+$ and TNFα$^+$ CD4$^+$ and CD8$^+$ T cells as well as IFNγ$^+$TNFα$^+$ double positive polyfunctional T cells in the spleen in response to

RT, VTP and Cryo. The most robust increases seen in the VTP and Cryo groups (Figures 5A, B). The addition of anti-PD-1 to these treatments significantly increased the cytokine production of T cells in the RT groups but did not further enhance the effects of VTP and Cryo (Figure 5B). These data suggest that all three therapies elicited systemic effector T cell responses.

RT, VTP and Cryo delayed growth of secondary tumors in a bilateral tumor model

The finding that RT, VTP and Cryo can induce a systemic immune response suggest that these therapies may be capable of inducing an abscopal effect by controlling the growth of distant tumors or metastases. To assess whether these treatments can elicit regression of distant tumors, we used a bilateral tumor model where the tumor implanted at 12 days prior to treatment is treated and the second implanted at 7 days prior to treatment is left untreated (Figure 5C). We monitored growth of the treated and untreated tumors over time. We found that all three modalities (RT, VTP, Cryo) delayed the growth of both the treated and untreated tumors (Figure 5C) with Cryo having the greatest effect on the secondary tumors. However, the addition of anti-PD1 to the treatment did not affect the secondary tumor growth. This data is consistent with the fact that anti-PD1 has modest effects on enhancing activation of T cells when combined with these treatment regimens (Figures 3, 4A, B; Supplementary Figures S7–S9).

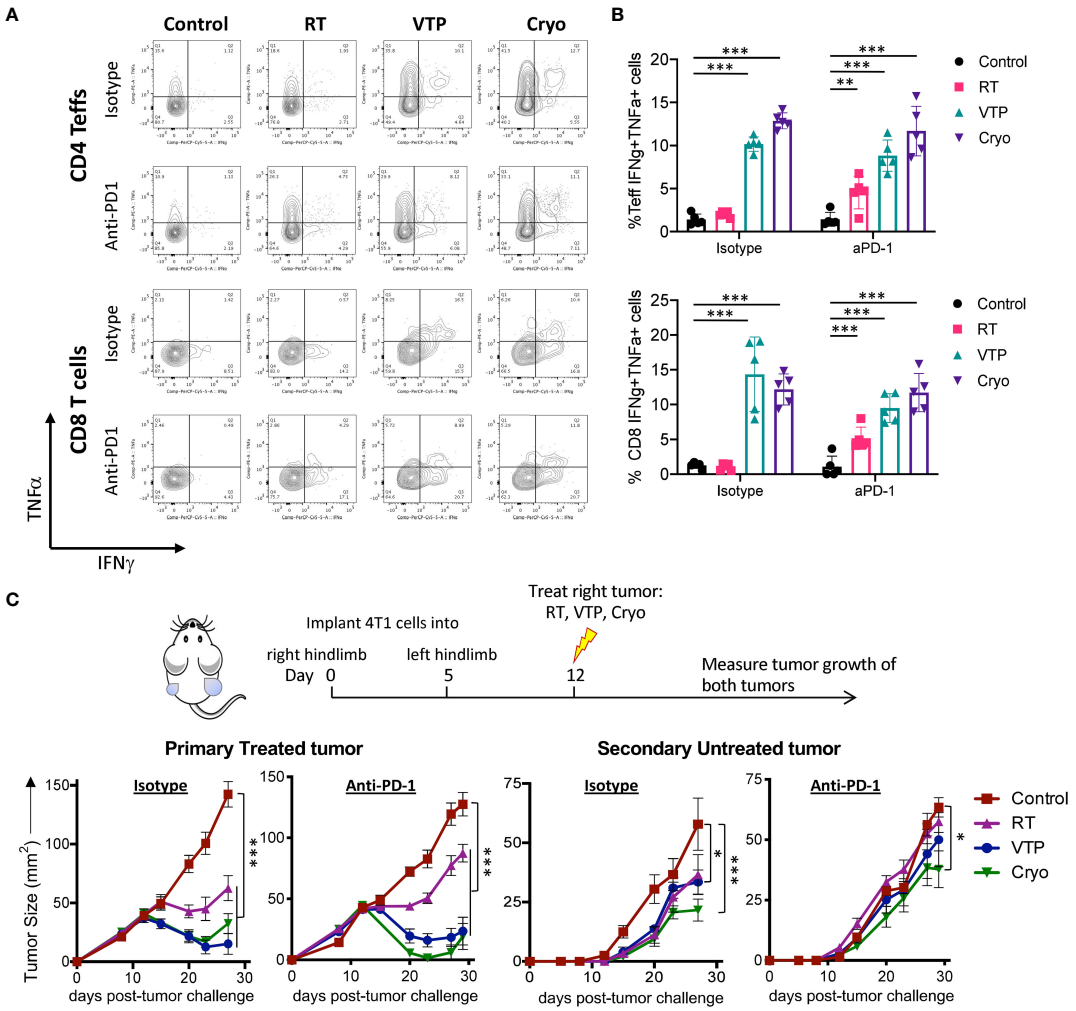

FIGURE 5
RT, VTP and Cryoablation incudes systemic T cell activation and promotes regression of secondary tumors. **(A, B)** 2 x 10^5 4T1 cells were injected subcutaneously in the right hind limb of 6-8 week female Balbc mice (5 mice/group) and treated with RT, VTP or Cryo therapy according to the doses and schedule in Figure 1A. 6 days after treatment, tumors, LNs and spleens were harvested and single cells suspension were stimulated with PMA/Ionomycin in the presence of Golgi inhibitors for 6hr then processed for intracellular cytokine staining (ICS). **(A)** Representative plots of IFNγ vs. TNFα by $CD4^+$ Teffs and $CD8^+$ T cells from the spleen. **(B)** Frequencies of $IFN\gamma^+TNF\alpha^+$ $CD4^+$ Teffs and $CD8^+$ T cells in the spleen. **(C)** 10^5 4T1 cells were injected subcutaneously in the right hind limb on day 0 and left flank on day 5 of female Balbc mice (10 mice/group). Twelve days after the initial tumor injection, the right hind limb tumors were treated with 15 Gy RT, VTP or Cryoablation as outlined in the treatment schedule. Tumor size was measured using calipers, shown are the average tumor size (mm^2) +/- SEM in both primary treated and secondary non-treated tumors. Statistics were calculated using a student T-test. For tumor growth curves, statistics were calculated on day 29 post tumor inoculation. *p ≤ 0.05, **p ≤ 0.01, ***p ≤ 0.005.

Discussion

Here we show that while RT, VTP and Cryo have been all shown to induce immunogenic cell death, they have differential effects on the adaptive and innate immune system. In general, VTP and Cryo have similar effects while RT appears to be different. One explanation for this may be the differences between the kinetics in which these treatments work. RT induces cell death through DNA damage and subsequent apoptosis or mitotic catastrophe, but these effects may take days to weeks to manifest, and the effects continue for weeks to months after therapy ends. Necrosis can be seen within tumors as well post RT, but at a relatively low frequency (26). There are parallel effects to the radiosensitive capillaries lined with endothelial cells, which dysregulates the balance of pro- and anti-inflammatory factors. Radiation-induced vascular damage increases the expression of ICAM-1 and E-selectin, which are adhesion molecules that mediate inflammatory reactions and promote recruitment of macrophages (27). The kinetics of VTP and Cryo are much more rapid and changes to the tumor (e.g., changes to the endothelium and tissue destruction) can be observed within hours of treatment. For VTP treatment, production of short-lived super oxide and hydroxyl radicals initiate rapid destruction of the targeted vasculature followed by coagulative necrosis of the tumors (12, 28). Recent studies using non-invasive optical imaging such as raster-scanning optoacoustic mesoscopy (RSOM) (28) and Multispectral Optoacoustic Tomography (MSOT) (29) have revealed that vascular destruction by VTP occurs from minutes up to an hour in subcutaneous murine tumor models (CT26 colon and RENCA renal tumor) followed by eschar, edema and tumor necrosis at 48 hours after VTP. By 5 days, there was no visible tumor detected at an optimal treatment condition. With Cryo, cellular damage and death is immediate through rapid freezing and thawing, with subsequent tissue necrosis. In the periphery of the treatment zone, further effect is seen with apoptotic cell death in tissue not exposed to immediately lethal temperatures. There is also evidence of a vascular effect, as ice crystal formation within blood vessels damages the endothelium, which comes into contact with platelets in the reperfusion period, leading to thrombus formation and delayed ischemia, as well as inflammatory cytokine release that increases vascular permeability (30). Additionally, the tumor growth delay induced by VTP and Cryo appears to be more rapid as seen in Figures 1B, D.

One of the most significant observations from this study is the decrease in myeloid cells after treatment with VTP and Cryo. The populations that we phenotypically defined as granulocytes and monocytes based on their expression of CD11b, Ly6G and Ly6C are also known as granulocytic MDSCs (G-MDSCs) and monocytic MDSCs (31). These populations when isolated from 4T1 tumors have been shown to be immunosuppressive (2, 3). VTP and Cryo significantly decrease the presence of MDSCs in 4T1 tumors and in the spleens of tumor bearing animals. This also correlated with an increase in $CD4^+$ and $CD8^+$ T cell responses such as increase in expression of T activation markers and cytokine production (Figures 5A, B). However, we observed mixed responses of Tregs with these different modalities. There was a decrease in Tregs in the tumors and draining LNs after treatment with all three therapies, which was linked to an increase in the effector:Treg ratios in both tissues with VTP and Cryo and in the LNs only with RT. However, there was an overall increase in Tregs in the spleens of treated animals in all three treatment modalities. Tregs have been shown to play a role in the recruitment of immunosuppressive myeloid cells in the tumors (32), therefore it is not surprising that both Tregs and MDSCs are decreased in the tumors after treatment with VTP and Cryo.

TNBC is also an attractive model for novel therapies such as VTP and Cryo. Unlike other subtypes of breast cancer, it has limited therapeutic options. We selected 4T1 breast cancer as the preclinical model for this study because it is one of the most well characterized models for TNBC. And like TNBC in patients, 4T1 tumors have been shown to be poorly responsive to ICB. While there are very few alternatives for preclinical models for TNBC other than 4T1, they are less characterized. Therefore, one potential limitation of this study is that we have only one model of TNBC. 4T1 tumors have poor T cell infiltration and high MDSC infiltration (2). Mechanisms that target immunosuppressive myeloid cells have been shown to re-sensitize 4T1 tumors to ICB (2). In this study, the decrease in myeloid cells after VTP and Cryo, while significant, did not sensitize 4T1 tumors to ICB with anti-PD-1 in concert with these treatments using this regimen. The antitumor efficacy of anti-PD-1 in combination with RT, VTP and Cryo was modest and for the most part not significant. Since 4T1 tumors are highly infiltrated by MDSC and immunosuppressive macrophages (2), we hypothesize that there are still significant amounts of the immunosuppressive cells remaining in the tumors to restrict the T cell responses induced by anti-PD1. On day 9 post therapy, there was approximately a 27% decrease with VTP and 66% decrease with Cryo of the total myeloid ($CD11b^+$) cells in the tumors on day 9. One way to potentially circumvent this problem is to combine these therapies with myeloid depleting or repolarizing regimens such as PI3K gamma inhibition (2) or CSF-1R blockade (33, 34).

We also found evidence of the abscopal effect, which is a phenomenon where localized treatment of a tumor causes regression of distant untreated metastatic tumors. This phenomenon has been extensively described in patients undergoing ionizing RT, and it is known that the immune system plays a major role. However, the abscopal effect is not limited to RT. In fact, any localized treatment can induce a systemic immune response that can regress secondary tumors. An important finding of this study is that tumor directed therapies such as RT, VTP and Cryo can control the growth of distal untreated tumors in a bilateral tumor model. The delay in growth of the distal untreated tumors by these therapies suggests that a systemic immune response to tumor antigen was induced by these modalities. Data from the spleen and LNs of treated animal also show activation of T cells in response to RT, VTP and Cryo. These include increase in T cell activation markers, memory markers and cytokine production. Similar to

what was observed in the single tumor models, the addition of anti-PD-1 did not have any significant effects of delaying growth of the secondary untreated tumors.

While we have demonstrated the variations in the immunomodulatory effects of these three local tumor ablation options, there are important differences in the clinical applicability of each treatment method, with implications on future therapeutic designs. RT can theoretically be used to target any tumor location within the body, but there are collateral damage risks to surrounding organs (26). Moreover, an important limitation to the usage of RT is the cumulative body dose limit, and so RT cannot be delivered to the same patient in indefinite amounts (35). In contrast, VTP, which has expanding indications with clinical trials investigating its utility in the treatment of prostate (36–38) (NCT03315754), esophageal (NCT03133650), and upper tract urothelial cancers (NCT04620239), has more tumor-selective properties by exploiting the increase in vasculature, and thus uptake of photosensitizer, within tumors. The treatment effect is not by direct cell damage, as seen with RT and Cryo, but by the creation of ROS that collapse the tumor vasculature. Thus, the risk of collateral damage is also less, which confers a particular advantage to the treatment of endoluminal tumors such as in the upper urothelial tract, where the consequences of collateral damage (ureteral stricture or obliteration and renal obstruction) are very high (39). Cryo has been applied to cervical, eye, kidney, liver, lung, and prostate cancers, and it is also an option for reducing bone pain and in local tumor control of bone and soft tissue oligometastasis (40–42). However, treatment is mostly done percutaneously or laparoscopically, which is a major limitation to Cryo since target tumors need to be reachable by the cryoprobe (30). In patients with underlying emphysema, cryoablation may increase the risk of pneumothorax and bleeding, which could be detrimental in patients with poor pulmonary reserve. Compared with heat-based thermal ablation therapies, VTP (non-thermal) and cryoablation (freezing) preserve the collagenous tissue and are safer options near large vasculature (43). Both therapies can be performed multiple times (VTP: UTUC Phase 1) and if necessary, can be followed by salvage therapies. Lastly, RT is typically fractionated into separate doses due to the slower proliferation of normal versus tumor tissues, which confers a survival advantage to normal tissue by better repairing sublethal radiation damage. However, this requires multiple doses of RT, typically over several weeks. On the other hand, VTP and Cryo can be performed in one outpatient sitting, albeit under sedation or anesthesia.

In summary, any means of local tumor destruction that was studied here can provide an *in-situ* vaccination effect that can generate a systemic adaptive immune response. The specificity and timing of each intervention should be taken into consideration when designing therapeutic interventions and combination therapies.

Data availability statement

The original contributions presented in the study are included in the article/Supplementary Material. Further inquiries can be directed to the corresponding authors.

Ethics statement

The animal study was approved by IACUC of Memorial Sloan Kettering Cancer Center. The study was conducted in accordance with the local legislation and institutional requirements.

Author contributions

SB: Writing – review & editing, Writing – original draft, Visualization, Methodology, Investigation, Formal analysis, Data curation, Conceptualization. KK: Writing – review & editing, Writing – original draft, Visualization, Validation, Methodology, Investigation, Formal analysis, Data curation, Conceptualization. WY: Writing – review & editing. SR: Writing – review & editing, Methodology, Investigation, Data curation. SJ: Writing – review & editing, Validation, Methodology, Investigation, Data curation. LC: Writing – review & editing, Methodology, Investigation, Data curation. AH: Methodology, Investigation, Formal analysis, Data curation, Writing – review & editing. JT: Methodology, Investigation, Data curation, Writing – review & editing. DP: Data curation, Writing – review & editing. ASo: Methodology, Investigation, Data curation, Writing – review & editing. BG: Methodology, Investigation, Data curation, Writing – review & editing. ASc: Methodology, Conceptualization, Writing – review & editing. JW: Supervision, Resources, Funding acquisition, Conceptualization, Writing – review & editing. JE: Resources, Methodology, Investigation, Writing – review & editing. TM: Methodology, Investigation, Funding acquisition, Formal analysis, Conceptualization, Writing – review & editing, Writing – original draft, Supervision, Resources. JC: Writing – review & editing, Writing – original draft, Supervision, Resources, Methodology, Investigation, Funding acquisition, Formal analysis, Conceptualization.

Funding

The author(s) declare financial support was received for the research, authorship, and/or publication of this article. This work was supported by Swim Across America, Ludwig Institute for Cancer Research, Parker Institute for Cancer Immunotherapy, the Breast Cancer Research Foundation, and the Thompson Family Foundation.

Acknowledgments

We would like to thank the Molecular Cytology Core Facility at MSK. We would like to thank Lucia Morgado Palacin for her input and editing of the manuscript.

Conflict of interest

TM is a consultant for Immunos Therapeutics, Daiichi Sankyo Co, TigaTx, Normunity and Pfizer; is a cofounder of and equity holder in IMVAQ Therapeutics; receives research funding from Bristol-Myers Squibb, and Realta; is an inventor on patent applications related to work on oncolytic viral therapy, alpha virus–based vaccine, neo antigen modeling, CD40, GITR, OX40, PD-1, and CTLA-4. JW is a consultant for: Apricity; Ascentage Pharma; AstraZeneca; BeiGene; Bicara Therapeutics; Bristol Myers Squibb; Daiichi Sankyo; Dragonfly; Imvaq; Larkspur; Takeda; Tizona; Trishula Therapeutics; Immunocore is on their Data Safety board. JW received Grant/Research Support from: Bristol Myers Squibb; Enterome. JW has Equity in: Apricity, Arsenal IO/ CellCarta; Ascentage; Imvaq; Linneaus, Larkspur; Georgiamune; Maverick; Tizona Therapeutics; Xenimmune.

The remaining authors declare that the research was conducted in the absence of any commercial or financial relationships that could be construed as a potential conflict of interest.

Publisher's note

All claims expressed in this article are solely those of the authors and do not necessarily represent those of their affiliated organizations, or those of the publisher, the editors and the reviewers. Any product that may be evaluated in this article, or claim that may be made by its manufacturer, is not guaranteed or endorsed by the publisher.

Supplementary material

The Supplementary Material for this article can be found online at: https://www.frontiersin.org/articles/10.3389/fonc.2024.1405486/full#supplementary-material

References

1. Gabrilovich DI, Ostrand-Rosenberg S, Bronte V. Coordinated regulation of myeloid cells by tumours. *Nat Rev Immunol*. (2012) 12:253–68. doi: 10.1038/nri3175

2. De Henau O, Rausch M, Winkler D, Campesato LF, Liu C, Cymerman DH, et al. Overcoming resistance to checkpoint blockade therapy by targeting PI3Kgamma in myeloid cells. *Nature*. (2016) 539:443–7. doi: 10.1038/nature20554

3. Dolcetti L, Peranzoni E, Ugel S, Marigo I, Fernandez Gomez A, Mesa C, et al. Hierarchy of immunosuppressive strength among myeloid-derived suppressor cell subsets is determined by GM-CSF. *Eur J Immunol*. (2010) 40:22–35. doi: 10.1002/eji.200939903

4. Galluzzi L, Kepp O, Kroemer G. Immunogenic cell death in radiation therapy. *Oncoimmunology*. (2013) 2:e26536. doi: 10.4161/onci.26536

5. Tan L, Shen X, He Z, Lu Y. The role of photodynamic therapy in triggering cell death and facilitating antitumor immunology. *Front Oncol*. (2022) 12:863107. doi: 10.3389/fonc.2022.863107

6. Wang M, Duan Y, Yang M, Guo Y, Li F, Wang J, et al. The analysis of immunogenic cell death induced by ablation at different temperatures in hepatocellular carcinoma cells. *Front Cell Dev Biol*. (2023) 11:1146195. doi: 10.3389/fcell.2023.1146195

7. Kroemer G, Galluzzi L, Kepp O, Zitvogel L. Immunogenic cell death in cancer therapy. *Annu Rev Immunol*. (2013) 31:51–72. doi: 10.1146/annurev-immunol-032712-100008

8. Tang C, Wang X, Soh H, Seyedin S, Cortez MA, Krishnan S, et al. Combining radiation and immunotherapy: a new systemic therapy for solid tumors? *Cancer Immunol Res*. (2014) 2:831–8. doi: 10.1158/2326-6066.CIR-14-0069

9. Postow MA, Callahan MK, Barker CA, Yamada Y, Yuan J, Kitano S, et al. Immunologic correlates of the abscopal effect in a patient with melanoma. *N Engl J Med*. (2012) 366:925–31. doi: 10.1056/NEJMoa1112824

10. Formenti SC, Rudqvist NP, Golden E, Cooper B, Wennerberg E, Lhuillier C, et al. Radiotherapy induces responses of lung cancer to CTLA-4 blockade. *Nat Med*. (2018) 24:1845–51. doi: 10.1038/s41591-018-0232-2

11. Markovsky E, Budhu S, Samstein RM, Li H, Russell J, Zhang Z, et al. An antitumor immune response is evoked by partial-volume single-dose radiation in 2 murine models. *Int J Radiat Oncol Biol Phys*. (2019) 103:697–708. doi: 10.1016/j.ijrobp.2018.10.009

12. Ashur I, Goldschmidt R, Pinkas I, Salomon Y, Szewczyk G, Sarna T, et al. Photocatalytic generation of oxygen radicals by the water-soluble bacteriochlorophyll derivative WST11, noncovalently bound to serum albumin. *J Phys Chem A*. (2009) 113:8027–37. doi: 10.1021/jp900580e

13. Brown SB, Brown EA, Walker I. The present and future role of photodynamic therapy in cancer treatment. *Lancet Oncol*. (2004) 5:497–508. doi: 10.1016/S1470-2045(04)01529-3

14. Castano AP, Mroz P, Hamblin MR. Photodynamic therapy and anti-tumour immunity. *Nat Rev Cancer*. (2006) 6:535–45. doi: 10.1038/nrc1894

15. Preise D, Oren R, Glinert I, Kalchenko V, Jung S, Scherz A, et al. Systemic antitumor protection by vascular-targeted photodynamic therapy involves cellular and humoral immunity. *Cancer Immunol Immunother*. (2009) 58:71–84. doi: 10.1007/s00262-008-0527-0

16. O'Shaughnessy MJ, Murray KS, La Rosa SP, Budhu S, Merghoub T, Somma A, et al. Systemic antitumor immunity by PD-1/PD-L1 inhibition is potentiated by vascular-targeted photodynamic therapy of primary tumors. *Clin Cancer Res*. (2018) 24:592–9. doi: 10.1158/1078-0432.CCR-17-0186

17. Georgiades C, Rodriguez R, Azene E, Weiss C, Chaux A, Gonzalez-Roibon N, et al. Determination of the nonlethal margin inside the visible "ice-ball" during percutaneous cryoablation of renal tissue. *Cardiovasc Intervent Radiol*. (2013) 36:783–90. doi: 10.1007/s00270-012-0470-5

18. Sabel MS, Nehs MA, Su G, Lowler KP, Ferrara JL, Chang AE. Immunologic response to cryoablation of breast cancer. *Breast Cancer Res Treat*. (2005) 90:97–104. doi: 10.1007/s10549-004-3289-1

19. Waitz R, Solomon SB, Petre EN, Trumble AE, Fasso M, Norton L, et al. Potent induction of tumor immunity by combining tumor cryoablation with anti-CTLA-4 therapy. *Cancer Res*. (2012) 72:430–9. doi: 10.1158/0008-5472.CAN-11-1782

20. McArthur HL, Diab A, Page DB, Yuan J, Solomon SB, Sacchini V, et al. A pilot study of preoperative single-dose ipilimumab and/or cryoablation in women with early-stage breast cancer with comprehensive immune profiling. *Clin Cancer Res*. (2016) 22:5729–37. doi: 10.1158/1078-0432.CCR-16-0190

21. Lugade AA, Moran JP, Gerber SA, Rose RC, Frelinger JG, Lord EM. Local radiation therapy of B16 melanoma tumors increases the generation of tumor antigen-specific effector cells that traffic to the tumor. *J Immunol*. (2005) 174:7516–23. doi: 10.4049/jimmunol.174.12.7516

22. Camphausen K, Moses MA, Menard C, Sproull M, Beecken WD, Folkman J, et al. Radiation abscopal antitumor effect is mediated through p53. *Cancer Res*. (2003) 63:1990–3.

23. Rodriguez-Ruiz ME, Rodriguez I, Garasa S, Barbes B, Solorzano JL, Perez-Gracia JL, et al. Abscopal effects of radiotherapy are enhanced by combined immunostimulatory mAbs and are dependent on CD8 T cells and crosspriming. *Cancer Res*. (2016) 76:5994–6005. doi: 10.1158/0008-5472.CAN-16-0549

24. Vanpouille-Box C, Alard A, Aryankalayil MJ, Sarfraz Y, Diamond JM, Schneider RJ, et al. DNA exonuclease Trex1 regulates radiotherapy-induced tumour immunogenicity. *Nat Commun*. (2017) 8:15618. doi: 10.1038/ncomms15618

25. Malandro N, Budhu S, Kuhn NF, Liu C, Murphy JT, Cortez C, et al. Clonal abundance of tumor-specific CD4(+) T cells potentiates efficacy and alters susceptibility to exhaustion. *Immunity*. (2016) 44:179–93. doi: 10.1016/j.immuni.2015.12.018

26. Baskar R, Lee KA, Yeo R, Yeoh KW. Cancer and radiation therapy: current advances and future directions. *Int J Med Sci*. (2012) 9:193–9. doi: 10.7150/ijms.3635

27. Venkatesulu BP, Mahadevan LS, Aliru ML, Yang X, Bodd MH, Singh PK, et al. Radiation-induced endothelial vascular injury: A review of possible mechanisms. *JACC Basic Transl Sci*. (2018) 3:563–72. doi: 10.1016/j.jacbts.2018.01.014

28. Brandis A, Mazor O, Neumark E, Rosenbach-Belkin V, Salomon Y, Scherz A. Novel water-soluble bacteriochlorophyll derivatives for vascular-targeted photodynamic therapy: synthesis, solubility, phototoxicity and the effect of serum proteins. *Photochem Photobiol*. (2005) 81:983–93. doi: 10.1562/2004-12-01-RA-389R1.1

29. Neuschmelting V, Kim K, Malekzadeh-Najafabadi J, Jebiwott S, Prakash J, Scherz A, et al. WST11 vascular targeted photodynamic therapy effect monitoring by multispectral optoacoustic tomography (MSOT) in mice. *Theranostics*. (2018) 8:723–34. doi: 10.7150/thno.20386

30. Erinjeri JP, Clark TW. Cryoablation: mechanism of action and devices. *J Vasc Interv Radiol*. (2010) 21:S187–91. doi: 10.1016/j.jvir.2009.12.403

31. Bronte V, Brandau S, Chen SH, Colombo MP, Frey AB, Greten TF, et al. Recommendations for myeloid-derived suppressor cell nomenclature and characterization standards. *Nat Commun*. (2016) 7:12150. doi: 10.1038/ncomms12150

32. Campesato LF, Budhu S, Tchaicha J, Weng CH, Gigoux M, Cohen IJ, et al. Blockade of the AHR restricts a Treg-macrophage suppressive axis induced by L-Kynurenine. *Nat Commun*. (2020) 11:4011. doi: 10.1038/s41467-020-17750-z

33. Holmgaard RB, Brachfeld A, Gasmi B, Jones DR, Mattar M, Doman T, et al. Timing of CSF-1/CSF-1R signaling blockade is critical to improving responses to CTLA-4 based immunotherapy. *Oncoimmunology*. (2016) 5:e1151595. doi: 10.1080/2162402X.2016.1151595

34. Lebdai S, Gigoux M, Alvim R, Somma A, Nagar K, Azzouzi AR, et al. Potentiating vascular-targeted photodynamic therapy through CSF-1R modulation of myeloid cells in a preclinical model of prostate cancer. *Oncoimmunology*. (2019) 8:e1581528. doi: 10.1080/2162402X.2019.1581528

35. Chandra RA, Keane FK, Voncken FEM, Thomas CR Jr. Contemporary radiotherapy: present and future. *Lancet*. (2021) 398:171–84. doi: 10.1016/S0140-6736(21)00233-6

36. Azzouzi AR, Vincendeau S, Barret E, Cicco A, Kleinclauss F, van der Poel HG, et al. Padeliporfin vascular-targeted photodynamic therapy versus active surveillance in men with low-risk prostate cancer (CLIN1001 PCM301): an open-label, phase 3, randomised controlled trial. *Lancet Oncol*. (2017) 18:181–91. doi: 10.1016/S1470-2045(16)30661-1

37. Gill IS, Azzouzi AR, Emberton M, Coleman JA, Coeytaux E, Scherz A, et al. Randomized trial of partial gland ablation with vascular targeted phototherapy versus active surveillance for low risk prostate cancer: extended followup and analyses of effectiveness. *J Urol*. (2018) 200:786–93. doi: 10.1016/j.juro.2018.05.121

38. Trachtenberg J, Weersink RA, Davidson SR, Haider MA, Bogaards A, Gertner MR, et al. Vascular-targeted photodynamic therapy (padoporfin, WST09) for recurrent prostate cancer after failure of external beam radiotherapy: a study of escalating light doses. *BJU Int*. (2008) 102:556–62. doi: 10.1111/j.1464-410X.2008.07753.x

39. Nogueira L, Tracey AT, Alvim R, Reisz P, Scherz A, Coleman JA, et al. Developments in vascular-targeted photodynamic therapy for urologic malignancies. *Molecules*. (2020) 25:5417. doi: 10.3390/molecules25225417

40. Bang HJ, Littrup PJ, Currier BP, Goodrich DJ, Aoun HD, Klein LC, et al. Percutaneous cryoablation of metastatic lesions from non-small-cell lung carcinoma: initial survival, local control, and cost observations. *J Vasc Interv Radiol*. (2012) 23:761–9. doi: 10.1016/j.jvir.2012.02.013

41. McMenomy BP, Kurup AN, Johnson GB, Carter RE, McWilliams RR, Markovic SN, et al. Percutaneous cryoablation of musculoskeletal oligometastatic disease for complete remission. *J Vasc Interv Radiol*. (2013) 24:207–13. doi: 10.1016/j.jvir.2012.10.019

42. Vaswani D, Wallace AN, Eiswirth PS, Madaelil TP, Chang RO, Tomasian A, et al. Radiographic local tumor control and pain palliation of sarcoma metastases within the musculoskeletal system with percutaneous thermal ablation. *Cardiovasc Intervent Radiol*. (2018) 41:1223–32. doi: 10.1007/s00270-018-1932-1

43. Kimm SY, Tarin TV, Monette S, Srimathveeravalli G, Gerber D, Durack JC, et al. Nonthermal ablation by using intravascular oxygen radical generation with WST11: dynamic tissue effects and implications for focal therapy. *Radiology*. (2016) 281:109–18. doi: 10.1148/radiol.2016141571

frontiers | Frontiers in Immunology

TYPE Original Research
PUBLISHED 19 June 2024
DOI 10.3389/fimmu.2024.1344637

OPEN ACCESS

EDITED BY
Laura Mondragón Martínez,
Josep Carreras Leukaemia Research Institute (IJC), Spain

REVIEWED BY
Ashok Palaniappan,
SASTRA University, India
Mingqing Zhang,
Tianjin Union Medical Center, China

*CORRESPONDENCE
Shaohua Wei
shaohuawei2010@sina.com
Jianfeng Gu
jscsgjf@sina.cn
Jinbing Sun
sunjb515@163.com

†These authors have contributed equally to this work and share first authorship

RECEIVED 26 November 2023
ACCEPTED 28 May 2024
PUBLISHED 19 June 2024

CITATION
Li M, Wang J, Zhao Y, Lin C, Miao J, Ma X, Ye Z, Chen C, Tao K, Zhu P, Hu Q, Sun J, Gu J and Wei S (2024) Identifying and evaluating a disulfidptosis-related gene signature to predict prognosis in colorectal adenocarcinoma patients.
Front. Immunol. 15:1344637.
doi: 10.3389/fimmu.2024.1344637

Identifying and evaluating a disulfidptosis-related gene signature to predict prognosis in colorectal adenocarcinoma patients

Ming Li[1,2†], Jin Wang[3†], Yuhao Zhao[4†], Changjie Lin[1], Jianqing Miao[1], Xiaoming Ma[1], Zhenyu Ye[1], Chao Chen[5], Ke Tao[2], Pengcheng Zhu[2], Qi Hu[2], Jinbing Sun[2*], Jianfeng Gu[2*] and Shaohua Wei[1*]

[1]Department of General Surgery, The Second Affiliated Hospital of Soochow University, Suzhou, China, [2]Department of General Surgery, Changshu Hospital Affiliated to Soochow University, The First People's Hospital of Changshu, Changshu, Jiangsu, China, [3]School of Public Health, Suzhou Medical College of Soochow University, Suzhou, Jiangsu, China, [4]Department of Biliary and Pancreatic Surgery, Renji Hospital Affiliated to Shanghai Jiaotong University School of Medicine, Shanghai, China, [5]Department of Breast Surgery, Fudan University Shanghai Cancer Center, Shanghai, China

Disulfidptosis, a regulated form of cell death, has been recently reported in cancers characterized by high SLC7A11 expression, including invasive breast carcinoma, lung adenocarcinoma, and hepatocellular carcinoma. However, its role in colon adenocarcinoma (COAD) has been infrequently discussed. In this study, we developed and validated a prognostic model based on 20 disulfidptosis-related genes (DRGs) using LASSO and Cox regression analyses. The robustness and practicality of this model were assessed via a nomogram. Subsequent correlation and enrichment analysis revealed a relationship between the risk score, several critical cancer-related biological processes, immune cell infiltration, and the expression of oncogenes and cell senescence-related genes. POU4F1, a significant component of our model, might function as an oncogene due to its upregulation in COAD tumors and its positive correlation with oncogene expression. *In vitro* assays demonstrated that POU4F1 knockdown noticeably decreased cell proliferation and migration but increased cell senescence in COAD cells. We further investigated the regulatory role of the DRG in disulfidptosis by culturing cells in a glucose-deprived medium. In summary, our research revealed and confirmed a DRG-based risk prediction model for COAD patients and verified the role of POU4F1 in promoting cell proliferation, migration, and disulfidptosis.

KEYWORDS

disulfidptosis, LASSO, prognostic model, cell senescence, POU4F1

Introduction

Colon adenocarcinoma (COAD) is the third most common cancer and has the second highest cancer-related mortality rate worldwide. Compared with USA and Japan, China has the highest all-age incidence for both sexes combined (1). Early-stage COAD has a 5-year survival rate of more than 90% after treatment; however, even after comprehensive treatment with surgery, radiotherapy, chemotherapy, molecular targeted therapy, and immunotherapy, for late-stage patients with distant metastases, the rate is still only 14% (2–4). In the clinical treatment of COAD, the TNM staging system has been the most commonly applied method for predicting patient prognosis in recent decades, but this method has limitations. Therefore, it is imperative to develop a molecular predictive system to help clinicians determine treatment options and drug choices for COAD patients.

Disulfidptosis is a form of regulated cell death (RCD) reported in cancers characterized by a high expression of solute carrier family 7 member 11 (SLC7A11) (5). Disulfidptosis mainly originates from the process by which nicotinamide adenine dinucleotide phosphate (NADPH) fails to reduce cystine to cysteine, which induces disulfide stress and actin cytoskeleton protein disulfide bond cross-linking and cytoskeleton contraction and ultimately induces disulfidptosis (6, 7). Disulfidptosis is triggered when cancer cells with high SLC7A11 expression are subjected to glucose starvation, and disulfidptosis-related genes (DRGs) were identified via CRISPR–Cas9 screening (8, 9). In preclinical models, treatment with a glucose transporter (GLUT) inhibitor can effectively inhibit glucose uptake, induce disulfidptosis in SLC7A11^{high}-expressing cancer cells, and limit the growth of SLC7A11^{high} cancer cells, such as UMRC6 kidney cell carcinoma xenografts in mice, which highlights the need for the development of cancer treatment strategies (8, 9). The interactions of tumor-related genes (TRGs) in the tumor microenvironment (TME) affect the survival, growth, migration, and adhesion of cancer cells. This study is based on the hypothesis that disulfidptosis, a form of cell death associated with high SLC7A11 expression, plays a significant role in colorectal adenocarcinoma (COAD) and can be used to predict prognosis through a specific gene signature based on DRGs.

Based on technological developments in transcriptomics and bioinformatics, such as CRISPR–Cas9 screening, bulk RNA-seq, and scRNA-seq, prognostic models of malignant tumors have been established to help determine the prognosis of cancer patients, but, to date, few DRG prognostic models of COAD have been reported. In our research, we constructed a molecular prognostic model for COAD based on DRGs by least absolute contact and selection operator (LASSO) and Cox regression analysis with transcriptomic and clinical data from COAD patients in the TCGA, GEO, and DRG databases. After accuracy and specificity validation, we constructed a novel disulfidptosis-related prognostic model that could predict the prognosis of COAD patients via the DRG-related risk score, which can be explained by the analyses of biological effects such as immune infiltration, specific tumorigenic pathways, and drug response and synergy. The aim of this study was to establish a solid platform for devising patient-specific treatment regimens and assisting clinicians in the prognostic assessment and clinical treatment of COAD patients. Additionally, the key gene POU4F1 in the model was further validated by *in vitro* assays.

Materials and methods

RNA-sequencing data and bioinformatics analysis data collection

The data and clinical information of 454 CRC patients and 92 normal colon tissue samples were obtained from the TCGA database (https://portal.gdc.cancer.gov). The data of 585 CRC patients and 19 nontumoral patients (GSE39582) were downloaded from the GEO database (https://www.ncbi.nlm.nih.gov/geo/). DRGs were extracted based on CRISPR–Cas9 screens from Gan's study (5). Genes, including 32 synergists and 63 suppressors, were identified according to the criteria of a |NormZ value| >2 and a *P*-value <0.05 for further construction of the prognostic model.

Construction and validation of a prognostic model based on DRGs

After the GSE39582 data were integrated, we used the "care" package to randomly subdivide the patients into two datasets at a ratio of 7:3 according to their survival status; these datasets were used as training sets and internal test sets, respectively. A total of 555 patients in the TCGA database were used as independent validation sets. DRGs downloaded and identified from CRISPR–Cas9 screenings were obtained from a previous study (5, 6). Gene expression data from the patients were used to identify DEGs, and least absolute shrinkage and selection operator (LASSO) regression analysis and multivariate Cox regression were used to construct the prognostic model. The risk score for each COAD patient was calculated based on the expression of DRGs (Exp_i) and Cox coefficients ($coef_i$), $Riskscore = \sum_{i=1}^{n} Exp_i \times coef_i$. We used the "glmnet" package for LASSO regression model analysis. Patients with COAD were divided into a high-risk group and a low-risk group according to the median risk score. We used the "survival" and "survminer" packages to perform univariate and multivariate Cox analyses, generate Kaplan–Meier plots, and estimate whether the risk score was an independent factor of clinicopathological features. To assess the prognosis of both groups, OS was analyzed via Kaplan–Meier curves. The prognostic ability of the risk model was evaluated by time-dependent receiver operating characteristic (ROC) curve analysis using the "survival ROC" software package. We investigated the ability of the prognostic model to predict the outcome of CRC patients by using the "TimeROC" package to generate a time-dependent receiver operating characteristic (ROC) curve. The area under the curve (AUC) of the ROC curve was calculated with the "survivalROC" package. Nomogram plots were generated with the "rms" package. To verify the DRG signature, the risk score of COAD patients in the TCGA dataset was used to verify the accuracy of the model. The risk score of COAD patients in the GSE39582 dataset was determined via the same method to verify the accuracy of the model.

Establishment of a prognostic nomogram for COAD

In the training set and test set, the associations between the DRG signatures and clinicopathological features were analyzed with the "rms" package. In addition, both univariate and multivariate Cox regression analyses were conducted to explore whether the risk score has an independent prognostic value in patients with COAD. The probabilities of 1-, 2-, 3-, 4-, and 5-year OS in COAD patients were assessed by clinical variables and risk scores. The accuracy of the nomogram was evaluated by the concordance index (CI) and calibration curve.

Determination of DRGs' differential expression

The differentially expressed genes (DEGs) were identified by the "limma" package with a |threshold of log (fold change)| >1 and a *P*-value <0.05 between the low and high groups.

Enrichment analysis

Based on the correlation analysis between the risk score and all mRNAs, gene set enrichment analysis (GSEA) was further performed by using the "ClusterProfiler" package of R software (version 4.3.1).

In addition, the differentially expressed genes (DEGs) between the low and high groups were identified based on the R package "limma" with the thresholds of log(fold change) >1 and *P*-value <0.05. The DEGs were further input into the DAVID online tool (https://david.ncifcrf.gov/) for pathway and biological process enrichment.

Correlation analysis

To further explore the biological function and clinical relevance of the DRG prognostic model, we performed a correlation analysis to evaluate the associations between the risk score and the expression of oncogenes, tumor mutation burden (TMB), immune regulatory gene expression, immune cell infiltration, and tumor immune dysfunction and exclusion (TIDE) score. This analysis utilized the Spearman method with the "psych" package.

Oncogene data were sourced from the ONGene database (http://www.ongene.bioinfo-minzhao.org) (10), while 73 immunomodulatory genes (IMGs) (11) were derived from earlier research. The immune cell infiltration score was calculated with the XCELL algorithm (12). Furthermore, the TIDE score, dysfunction score, and exclusion score for each dataset patient were estimated using the standard process with the TIDE online tool (http://tide.dfci.harvard.edu/) (13).

The Sanger Research Institute created the Genomics of Drug Sensitivity in Cancer database (GDSC) to gather information on tumor cell sensitivity and response to drugs (14). "OncoPredict" was employed to determine the drug sensitivity of each sample in the training and validation datasets, leveraging the GDSC V2.0 database (15).

Cell lines and culture

The human colon adenocarcinoma cell line SW480 (SW-480), which was isolated from the large intestine of a Dukes C colorectal cancer patient, was obtained from the National Collection of Authenticated Cell Culture at the Chinese Academy of Science (Shanghai, China). Colon adenocarcinoma HCT116 cells (ab255451) were isolated from the colon of an adult male with colon adenocarcinoma obtained from the Abcam Trading (Shanghai, China). The SW480 cells were cultured in DMEM supplemented with 10% fetal bovine serum (FBS) and 1% penicillin–streptomycin from Thermo Fisher Scientific (Shanghai, China). The HCT116 cells were cultured in McCoy's 5A medium supplemented with 10% FBS (Gibco) and 1% penicillin –streptomycin (Gibco). All cells were incubated at 37°C with 5% CO_2 for culture and passage unless otherwise stated. For the glucose deprivation experiments, cells were cultured in glucose-free DMEM supplemented with dialyzed FBS as previously described.

Short hairpin RNA construction, plasmid vectors, and transfection

The POU4F1 sequences of the primers used were as follows:

Forward: 5′ - ACGCACGAACTGAGTCGAAA - 3′
Reverse: 5′-CACTTCCCGGGATTGGAGAG-3′

The POU4F1 shRNA plasmid (sc-29839-SH) was purchased from Santa Cruz Biotechnology. The transfection of plasmid vectors was carried out in Opti-MEM (Invitrogen) using Lipofectamine 3000 reagent (Invitrogen) according to the manufacturer's transfection protocol.

Transwell migration assays and Transwell invasion assays

For the Transwell migration assay, cells were seeded in the upper chamber of a Transwell membrane (Corning, Inc., USA) with 200 µL of FBS-free medium, and 600 µL of complete medium was added to the lower chamber. After the cells were cultured at 37°C for 24 h, they were fixed with 4% paraformaldehyde and stained with 0.5% crystal violet solution. Subsequently, the cells in the upper chamber of the Transwell membrane were removed. Images of the migrated cells were captured under an inverted microscope and were then assessed using NIH ImageJ software (version 1.8.0).

Western blotting and antibodies

Total protein was extracted from cells by using RIPA lysis buffer (Beyotime, China) and quantitated by using Enhanced BCA Kit (Beyotime, China). Total protein (30 µg) was separated via SDS –PAGE and transferred onto PVDF Transfer Membranes (Thermo Fisher Scientific, China). After blocking with 5% BSA, the

membrane was incubated at 4°C overnight with primary antibodies against POU4F1 (PA5–41509) and beta-actin (MA5–15452), which were purchased from Thermo Fisher Scientific (Shanghai, China). Following the primary incubation, the membranes were incubated with HRP-labeled secondary antibodies. The protein bands were visualized using enhanced chemiluminescence (ECL) substrate and the GeneTools GBox (Syngene) system, the intensity of each band was quantified using ImageJ software (National Institutes of Health), and beta-actin was used as the internal control.

β-gal fluorescence imaging

The cell aging detection reagent SPiDER-β-gal was used for β-gal fluorescence staining. Briefly, after the cells were washed with wash buffer, SPiDER-β-gal staining solution was added. The plate was incubated in the dark for 15 min, and the cells were washed twice with PBS, followed by observation and imaging under a fluorescence microscope.

Disulfidptosis assay

Glucose-free DMEM was used to simulate glucose deprivation conditions. When POU4F1 was knocked down or overexpressed in cells, the culture medium was replaced with a glucose-free medium, and the regulatory effect of the gene on disulfidptosis was determined by measuring cell viability and apoptosis.

Statistical analysis

All statistical analyses were performed using R software (version 4.1.3). Continuous variables were tested by Student's *t*-test, while categorical variables were tested by chi-square test. A p-value <0.05 was considered significant.

Results

Data collection

Three COAD cohorts and corresponding clinical data were obtained from the TCGA and GEO databases (GSE39582). The demographic and clinical data for the training, internal testing, and independent validation sets are summarized in Table 1. After ruling out the samples with missing clinical information in the GEO (584 patients) dataset, the samples were randomly divided into a training set (n = 393, 70%) and an internal testing set (n = 168, 30%). As expected, no significant differences were found in the major clinicopathological features between the training, testing, and entire GEO datasets (p > 0.05) (Table 1).

Construction and validation of the DRG prognostic model in COAD patients

A total of 808 DRGs were screened with the criteria of |normZ values| >2 and *P*-value <0.05 based on the CRISPR–Cas9 screenings (Supplementary Figure S1). Using univariate Cox regression analysis, 95 prognosis-related DRGs were identified based on the GEO training set (Figure 1A). Consequently, LASSO-penalized Cox analysis further identified 20 DRGs for multivariate analysis (Figures 1B, C). The multivariate Cox proportional hazard model was built stepwise using the likelihood-ratio forward method to reach the highest significance. A total of 20 DRGs were further screened to construct a risk model to assess the prognostic risk of COAD patients: risk score = (1.057 × KIF7 Exp) + (1.005 × SLCO1C1 Exp) + (0.886 × MAFG Exp) + (0.751 × THSD7B Exp) + (0.747 × POU4F1 Exp) + (0.701 × ACAP2 Exp) + (0.668 × TM2D3 Exp) + (0.563 × RAB6B Exp) + (0.315 × ARC Exp) + (0.292 × GDPD3 Exp) + (0.265 × LETM2 Exp) + (-0.102 × CXCL13 Exp) + (-0.189 × AMACR Exp) + (-0.296 × OAS1 Exp) + (-0.394 × CCDC134 Exp) + (-0.457 × TXN2 Exp) + (-0.799 × CYB561D1 Exp) + (-0.805 × ADD1 Exp) + (-0.987 × C11of42 Exp) + (-1.092 × DIMT1 Exp) (Figure 1D). ROC curves demonstrated that the risk score serves as a significant predictor of the OS of COAD patients, with AUCs greater than 0.765 at 1–5 years (Figure 1E). K–M survival analysis indicated that the low-risk group had a significantly favorable overall survival for COAD patients (Figure 1F). The samples in the training set were classified into low-risk and high-risk groups based on the median value of the risk score (Figure 1G). The distribution of risk scores between the low-risk and high-risk groups and the survival status and survival time of patients in the two different risk groups are depicted. The relative expression of the 20 DRGs for each patient is shown in a heatmap (Figure 1H).

Prognostic value of the DRG model signature in the training cohort and validation cohort

According to the median risk score, the patients in the internal testing dataset and the entire GSE39582 dataset were divided into high-risk and low-risk groups. The patients in the low-risk group in both datasets had a significantly longer OS than did those in the high-risk group (p < 0.0001), with AUC values of 0.760 and 0.781, respectively (Supplementary Figures S2A, B, Figures 2A, B). According to the distribution of risk scores, the number of deaths in the high-risk group was significantly greater than that in the low-risk group (Supplementary Figure S2C, Figure 2C). The heatmap showed the differential expression of these 20 disulfidptosis-related risk genes between the low-risk group and the high-risk group (Supplementary Figure S2D, Figure 2D). The signature in the independent validation set also yielded the same result (Figures 2E–H).

10.3389/fimmu.2024.1344637

TABLE 1 Clinicopathological features of the GSE39682 and TCGA_COAD datasets.

Characteristics		GSE39582				TCGA_COAD
		Training	Testing	All	*P*-value	
Age	≤60	107 (27.23%)	50 (29.76%)	160 (27.40%)	0.808	160 (28.83%)
	>60	286 (72.77%)	118 (70.24%)	424 (72.60%)		395 (71.17%)
Gender	Female	179 (45.43%)	74 (44.05%)	263 (44.96%)	0.955	264 (47.57%)
	Male	215 (54.57%)	94 (55.95%)	322 (55.04%)		291 (52.43%)
Location	Proximal	153 (38.83%)	67 (39.88%)	232 (39.79%)	0.949	NA
	Distal	241 (61.17%)	101 (60.12%)	351 (60.21%)		
MMR	pMMR	306 (85.00%)	138 (88.46%)	459 (85.63%)	0.574	NA
	dMMR	54 (15.00%)	18 (11.54%)	77 (14.37%)		
TP53_MUT	WT	105 (43.21%)	54 (50.94%)	161 (45.87%)	0.410	NA
	MU	138 (56.79%)	52 (49.06%)	190 (54.13%)		
KRAS_MUT	WT	224 (58.79%)	101 (63.12%)	328 (60.18%)	0.643	NA
	MU	157 (41.21%)	59 (36.88%)	217 (39.82%)		
BRAF_MUT	WT	321 (89.92%)	138 (91.39%)	461 (90.04%)	0.865	NA
	MU	36 (10.08%)	13 (8.61%)	51 (9.96%)		
CIN_status	Negative	72 (22.22%)	36 (26.47%)	112 (23.28%)	0.616	NA
	Positive	252 (77.78%)	100 (73.53%)	369 (76.72%)		
TNM_stage	Stage I/II	202 (51.27%)	92 (54.76%)	309 (52.82%)	0.739	307 (55.12%)
	Stage III/IV	192 (48.73%)	76 (45.24%)	276 (47.18%)		250 (44.88%)
TNM_M	M0	338 (88.95%)	141 (88.12%)	499 (89.11%)	0.941	405 (83.51%)
	M1	42 (11.05%)	19 (11.88%)	61 (10.89%)		80 (16.49%)
TNM_N	N0	204 (51.78%)	95 (56.55%)	314 (53.68%)	0.576	326 (58.53%)
	N1/2/3	190 (48.22%)	73 (43.45%)	271 (46.32%)		231 (41.47%)
TNM_T	T1/2	36 (9.14%)	19 (11.31%)	61 (10.43%)	0.690	103 (18.49%)
	T3/4	358 (90.86%)	149 (88.69%)	524 (89.57%)		454 (81.51%)
OS	0	261 (66.24%)	110 (65.48%)	385 (66.49%)	0.970	412 (77.30%)
	1	133 (33.76%)	58 (34.52%)	194 (33.51%)		121 (22.70%)
OS.time	≤2	232 (58.88%)	100 (59.52%)	334 (57.69%)	0.884	266 (49.91%)
	>2	162 (41.12%)	68 (40.48%)	245 (42.31%)		267 (50.09%)

MMR, defective mismatch repair; OS, overall survival. NA, Not applicable.

DRG risk score is independent of clinical features

As depicted in Supplementary Table S1, the mitophagy risk score was related to several clinicopathological features in the GSE39582 dataset, including MMR, TNM_stage, TNM_M, TNM_N, and TNM_T. To assess whether the risk score is an independent indicator in COAD patients, the effect of each clinicopathological feature on OS was analyzed by univariate Cox regression (Figure 3A). As shown in Figure 3B, after multicollinearity test and multivariable adjustment, the risk score remained a powerful and independent factor in the GSE39582 dataset. Moreover, the risk score was verified as an independent factor based on the TCGA-COAD dataset (Supplementary Figures S3A, B). The discrepancies in OS stratified by M_stage and age were analyzed between the low-risk and high-risk groups in the GSE39582 and TCGA-COAD datasets. According to the subgroups classified by age and M stage, the OS of the low-risk score group was superior to that of the high-risk group (Figures 3C–F, Supplementary Figures S3C, D).

10.3389/fimmu.2024.1344637

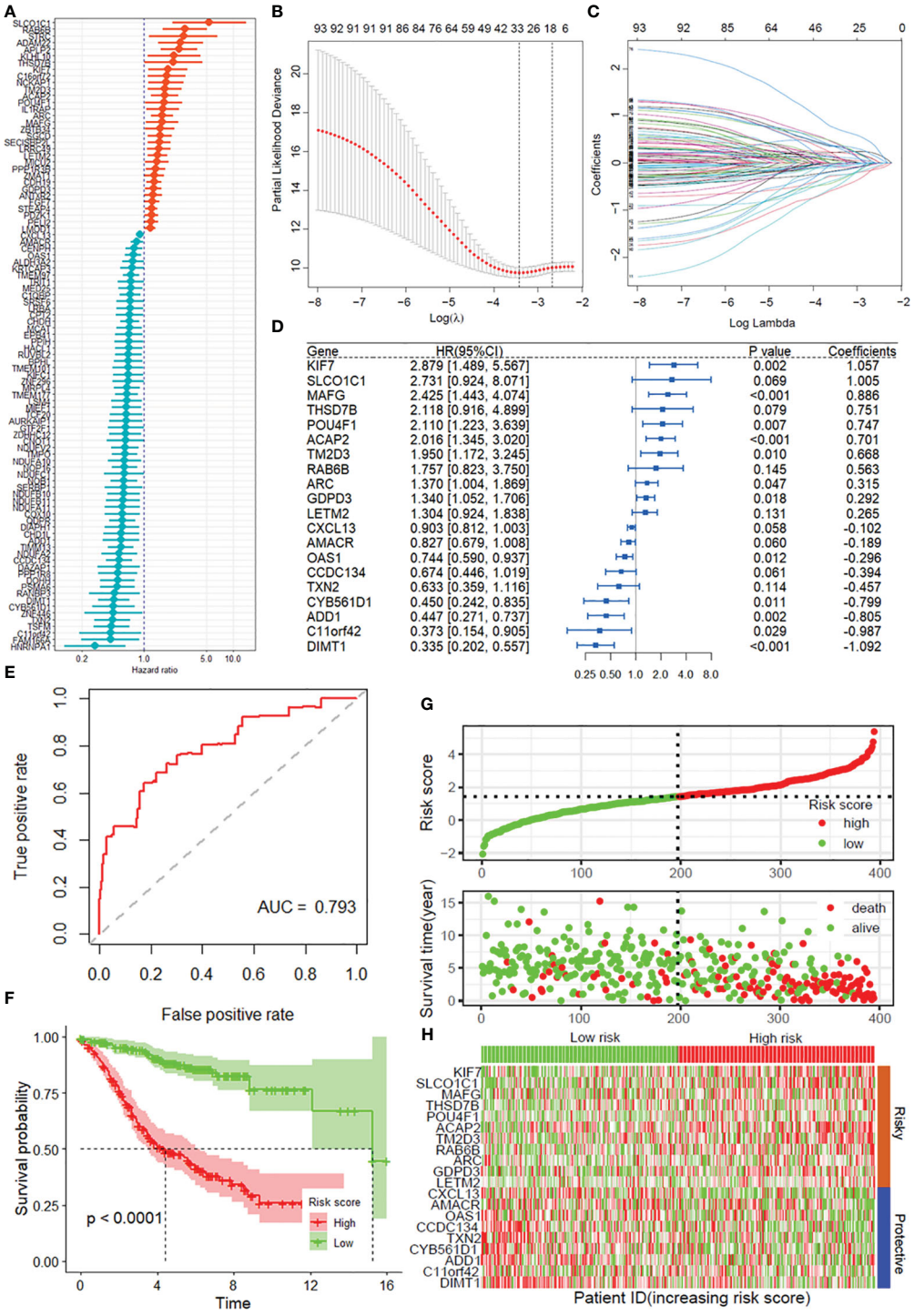

FIGURE 1
Construction of the DRG prognostic model of COAD. **(A)** Univariate Cox regression analysis for the selection of DRGs correlated with the overall survival (OS) of COAD patients. **(B, C)** LASSO-penalized Cox analysis revealed 20 DRGs related to overall survival. **(D)** Forest plot showing the multivariate Cox regression analysis of 20 DRGs. **(E)** ROC curves for 5-year OS in the training set. **(F)** Kaplan–Meier curve of overall survival in the training group. **(G)** Risk score distribution and survival status of the training group. **(H)** Heatmap showing the expression of genes in 20 DRGs in the training group. DRGs, disulfidptosis-related genes; ROC, receiver operating characteristic; COAD, colon adenocarcinoma.

To ensure the robustness and practicability of the 20-DRG prognostic model, a prognostic nomogram for predicting overall survival in COAD patients was established using the GSE31210 and TCGA-COAD datasets (Figure 4A, Supplementary Figure S4A). Major clinicopathological features and risk scores were included in the nomogram. The nomogram was internally validated by computing the bootstrap C-index (≥0.785 both in the GSE31210 and TCGA-COAD datasets) and a calibration plot (Figure 4B,

10.3389/fimmu.2024.1344637

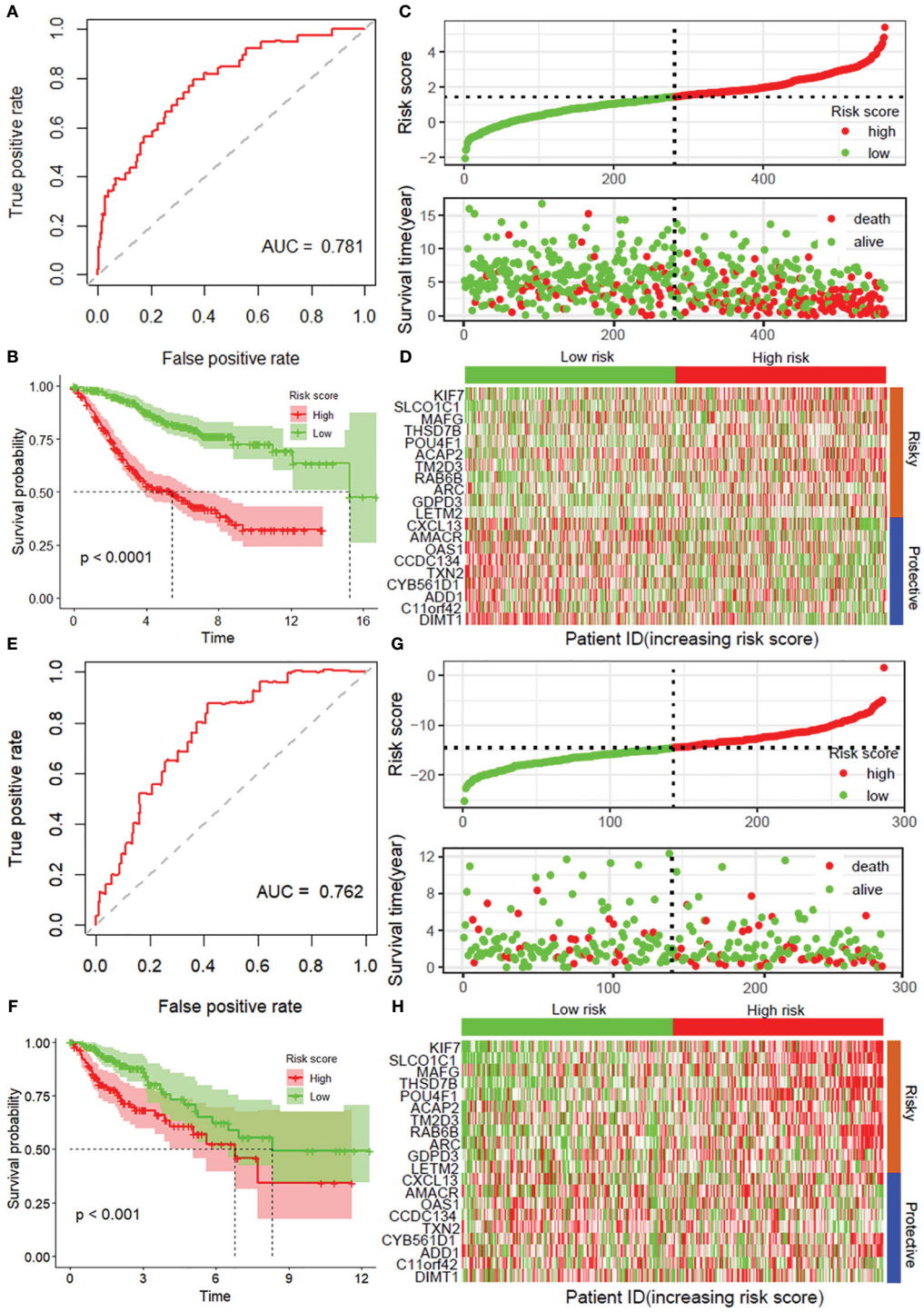

FIGURE 2
Validation of the prognostic model with 20 DRGs constructed from the training dataset. ROC curves for overall survival in the entire GSE39582 **(A)** and TCGA-COAD **(E)** datasets. K–M curves of overall survival in the entire GSE39582 **(B)** and TCGA-COAD **(F)** datasets. Risk score distribution and survival status in the entire GSE39582 dataset **(C)** and external validation dataset **(G)**. Heatmaps showing the expression of these 20 disulfidptosis-related risk genes between the low-risk group and the high-risk group in the entire GSE39582 dataset **(D)** and external validation dataset **(H)**. DRGs, disulfidptosis-related genes; ROC, receiver operating characteristic; COAD, colon adenocarcinoma.

Supplementary Figure S4B). The ROC curve confirmed that the score calculated based on the nomogram was highly predictive of overall survival, with AUCs of 0.845 and 0.862 at 1 year in the GSE31210 and TCGA-COAD cohorts, respectively (Figure 4C, Supplementary Figure S4C). The DCA for the nomogram is presented in Figure 4D. The nomogram provided a better net benefit than did the "treat-all" or "treat-none" schemes and the current TNM staging system.

10.3389/fimmu.2024.1344637

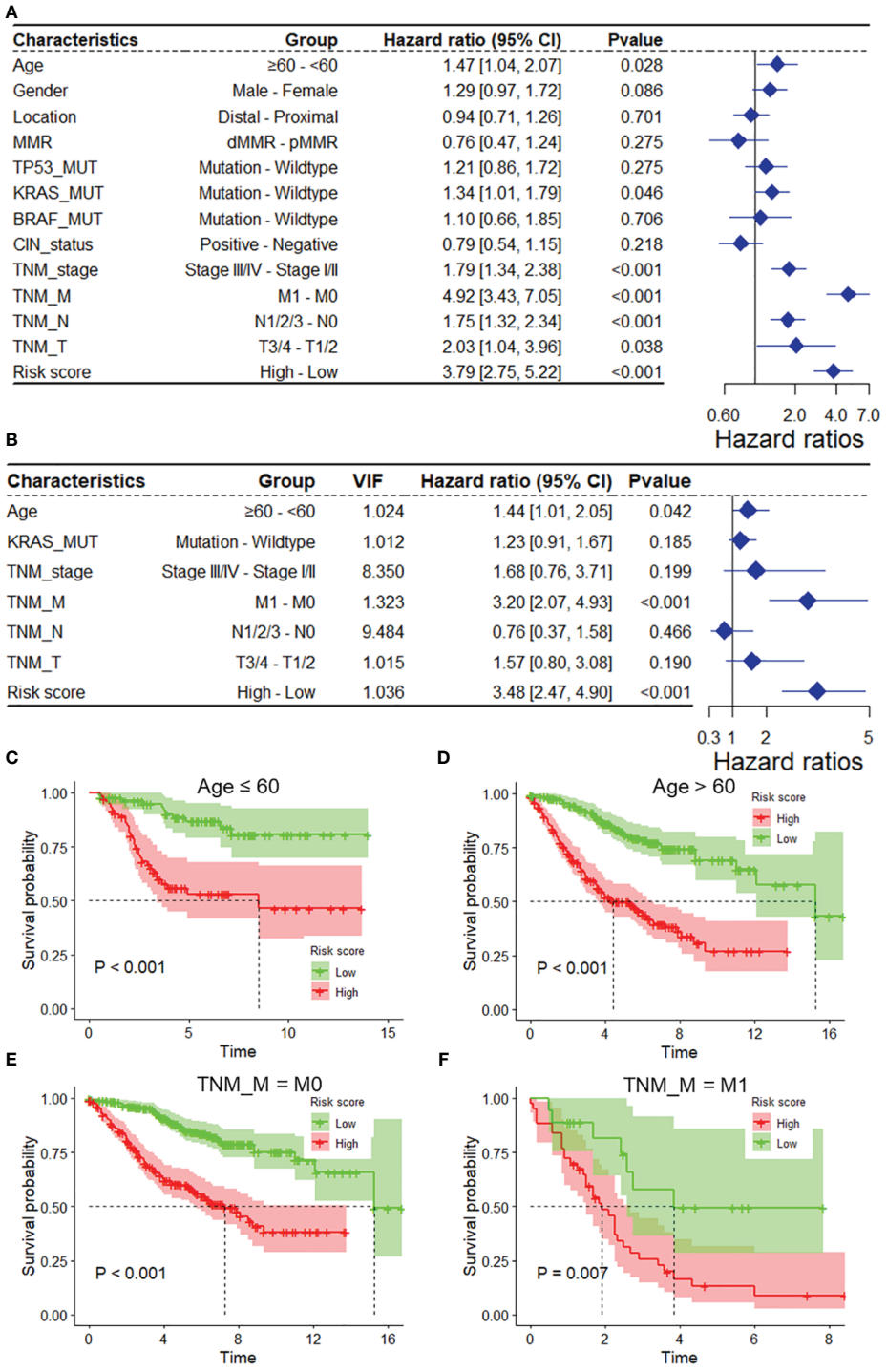

FIGURE 3
The DRG risk score was an independent prognostic factor for overall survival in the entire GSE39582 dataset. Univariate **(A)** and multivariate **(B)** Cox regression analyses of the risk score and clinicopathological features for overall survival in the entire GSE39582 dataset. **(C, D)** Kaplan–Meier analysis of overall survival stratified by the patients' age. **(E, F)** Kaplan–Meier analysis of overall survival stratified by TNM_M stage. DRGs, disulfidptosis-related genes; VIF, variance inflation factor.

DRG risk score correlated with immune cell infiltration

The single-sample gene set enrichment analysis package "XCELL" was used to quantify the infiltration of 24 immune cell types, and Spearman correlation analysis was used to assess the correlation of immune cell infiltration with the DRG risk score. The results revealed that the risk score was significantly correlated with the infiltration of multiple immune cell types in both the GEO39582 and TCGA-COAD datasets (Figures 5A, B). Specifically, we found a significant negative correlation between risk scores and T cells and the infiltration of CD4+ T cells (Th1), common lymphoid dendritic

10.3389/fimmu.2024.1344637

progenitors, and plasmacytoid dendritic cells in both datasets (Figure 5C). Additionally, the risk score was positively correlated with the infiltration of hematopoietic stem cells, endothelial cells, stroma score, cancer-associated fibroblasts, and common myeloid progenitors (Figure 5C). In addition, a correlation analysis revealed that the risk score was positively correlated with the expression of several immune checkpoint genes, mainly LILRB2, HAVCR2, SIRPA, TIGIT, CTLA4, and BTLA, in both datasets (Figures 5D–

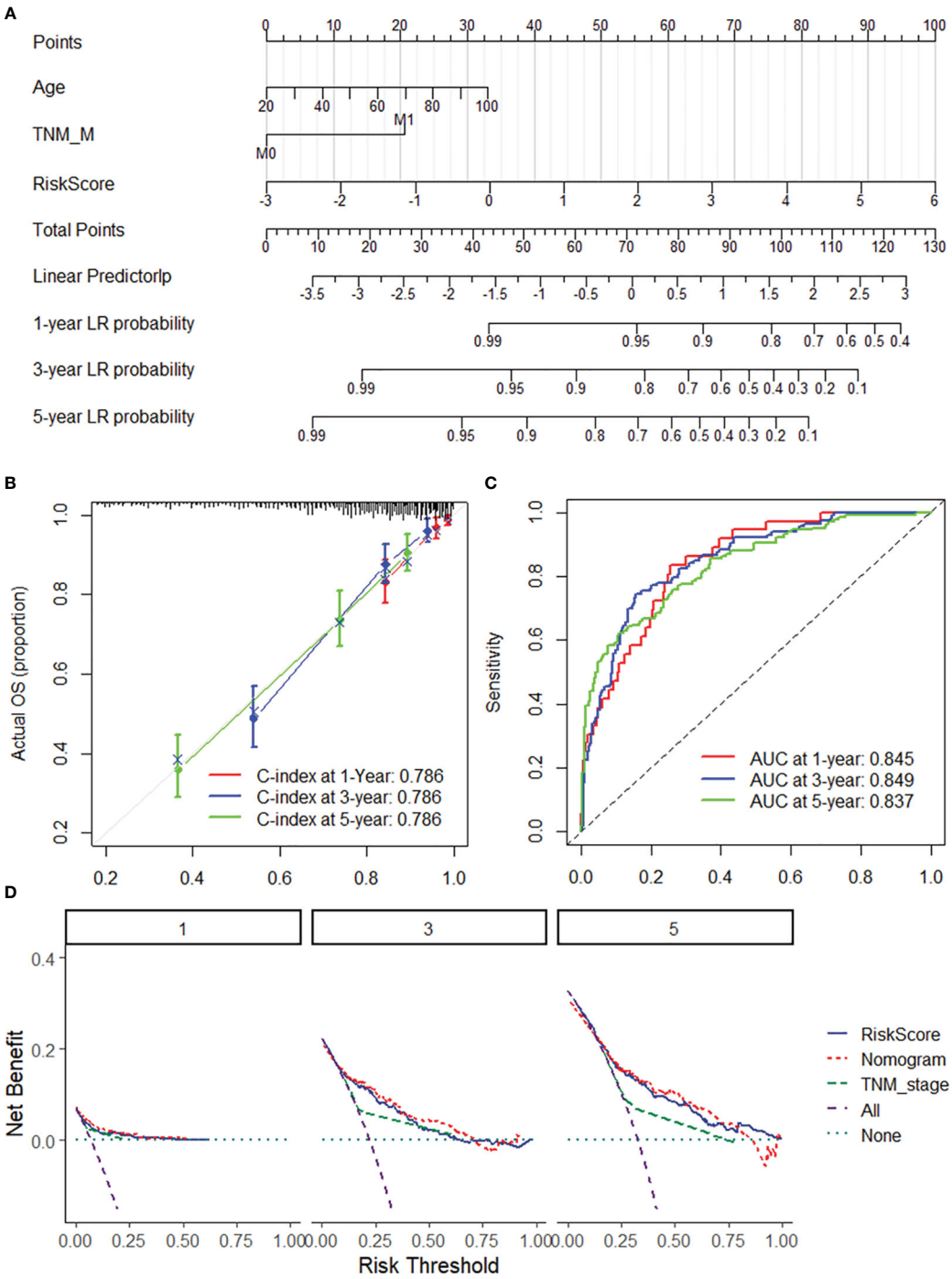

FIGURE 4
Nomogram for predicting the 1-y, 3-, and 5-year overall survival of COAD patients. **(A)** The nomogram consists of the 20-DRG risk scores and 12 clinical indicators based on the entire GSE39582 dataset. The points from these variables are combined, and the locations of the total points are determined. The total points projected on the bottom scales indicate the probabilities of 1-, 3-, and 5-year overall survival. **(B)** 1/3/5-year calibration plot validating the accuracy of the prognostic nomogram based on the GSE39582 dataset. **(C)** Kaplan–Meier curve of overall survival for the score calculated from the nomogram in the GSE39582 dataset. **(D)** DCA curves of the nomogram; the 20-DRG risk score and the TNM stage system for the prediction of OS prognosis at the 1-, 3-, and 5-year time points in the GSE39582 dataset. DRGs, disulfidptosis-related genes; COAD, colon adenocarcinoma; OS, overall survival; DCA, decision curve analysis.

F). As shown in Supplementary Figure S5, we found that the risk score was significantly correlated with the expression of multiple immune regulatory genes and the sensitivity to multiple antitumor drugs.

DRG risk score correlated with cancer progression

GSEA revealed that the DRG risk score was significantly correlated with several vital cancer-related biological processes (Figure 6A), mainly cytochrome complex assembly (NES = -3.47, Figure 6B), DNA replication initiation (NES = -3.43, Figure 6B), mitochondrial cytochrome c oxidase assembly, cell cycle DNA replication, and base excision repair. In addition, the risk score was related to several important KEGG pathways (Figure 6C), including DNA replication (NES = -3.79, Figure 6D), base excision repair (NES = -2.849, Figure 6D), mismatch repair, and ECM receptor interaction. Moreover, the correlation analysis demonstrated that the DRG risk score was significantly positively correlated with multiple oncogenes (N = 285, 40.2%, Figure 6E), including MIR99AHG (r = 0.558, Figure 6F), RUNX1T1 (r = 0.491, Figure 6G), MEIS1 (r = 0.490, Figure 6H), and PRDM6 (r = 0.485, Figure 5I). In addition, we found that the DRG risk score was positively correlated with many cell senescence-related genes (N = 95, 34.80%, Figure 6J), including EPHA3 (r = 0.504, Figure 6K), NOTCH3 (r = 0.490, Figure 6L), CPEB1 (r = 0.481, Figure 6M), and MYLK (r = 0.464, Figure 6N). These results revealed that the DRG risk score was correlated with multiple oncogenes and cell senescence-related genes as well as several cancer-related biological bioprocesses and KEGG pathways.

POU4F1 is highly expressed in COAD and is related to cancer progression

Among these DRGs in the constructed risk model, POU4F1 had the highest normalized Z score (Figure 7A). POU4F1 expression was greater in COAD tumor tissues than in normal tissues in the TCGA-COAD dataset (Figure 7B). Additionally, an increased expression of POU4F1 was detected in paired normal tissue specimens (Figure 7C). A survival analysis revealed that patients with lower POU4F1 expression had a longer overall survival in both the GSE395852 (Figure 7D) and TCGA-COAD (Figure 7E) datasets. When considering disease-specific survival and disease-free survival, a better prognosis was found for patients with low POU4F1 expression (Supplementary Figures S6A, B). A further correlation analysis revealed that POU4F1 expression was significantly correlated with multiple oncogenes in both the TCGA-COAD and GSE39582 datasets (Figure 7F, Supplementary Figures S6C, D), indicating that POU4F1 may serve as an oncogene in COAD. Additionally, POU4F1 expression was positively correlated with multiple cell senescence-related genes in both the TCGA-COAD and GSE39582 datasets (Figure 7G, Supplementary Figures S6E, F).

POU4F1 promotes cell proliferation, migration, and disulfidptosis in COAD

To evaluate the biological function of POU4F1 in COAD cells, we constructed shRNA plasmids to knock down POU4F1 and a plasmid to overexpress POU4F1 (Supplementary Figure S7). The CCK-8 assay demonstrated that POU4F1 knockdown significantly inhibited the proliferation of SW480 (Figure 8A) and HCT116 (Figure 8B) cells. Conversely, POU4F1 overexpression significantly promoted proliferation (Figures 8C, D). Additionally, the EdU assay revealed that POU4F1 knockdown attenuated COAD cell proliferation, while POU4F1 overexpression increased proliferation (Figures 8E, F). The Transwell migration assay indicated that POU4F1 knockdown significantly reduced the number of migrated cells, while POU4F1 overexpression significantly increased the number of migrated cells (Figures 8G, H). During cell senescence, the β-galactosidase (β-gal) staining assay demonstrated that POU4F1 knockdown significantly promoted β-gal expression (Figures 8I, J). To further evaluate the synergistic role of POU4F1 in disulfidptosis, we used a glucose-deprived medium to culture COAD cells. The results of the CCK-8 assay revealed that POU4F1 knockdown significantly attenuated cell death induced by glucose deprivation, while POU4F1 overexpression significantly amplified cell death (Figures 8K–N).

Discussion

Colorectal adenocarcinoma (COAD) has emerged as a significant global medical challenge attributed to environmental factors and genetic mutations and has an alarming increase in younger patients. Advances in gene sequencing technology and the accessibility of public genetic databases have enabled us to predict COAD prognosis by quantifying molecular prognostic markers and constructing prognostic models (16). Disulfidptosis, which is a newly recognized form of regulated cell death in cancers with high SLC7A11 expression under glucose starvation conditions, is a novel therapeutic strategy for treating malignant tumors (7, 8). In this study, we developed a prognosis prediction model based on disulfidptosis-related genes using LASSO and Cox regression analyses. Subsequently, we identified a key gene in this model, namely, POU4F1, for further functional analysis.

Risk prediction models have been developed for various cancers, including cervical cancer, bladder cancer, and colorectal cancer, based on disulfidptosis-related genes (DRGs). For colorectal cancer specifically, a previous study constructed a risk prediction model based on genes, achieving an AUC of 0.567 at 1 year (17). Another study developed a model based on four lncRNAs, with an AUC of 0.679 at 1 year (18). In comparison to these studies, our research established a risk prediction model with an AUC of 0.793 using DRGs based on DRGs obtained from CRISPR Cas9 screening results that Gan et al. published. The superiority of our model was further validated using internal testing and external validation sets, which achieved AUC values of 0.781 and 0.762, respectively. The robustness and practicality of our model were assessed using a

10.3389/fimmu.2024.1344637

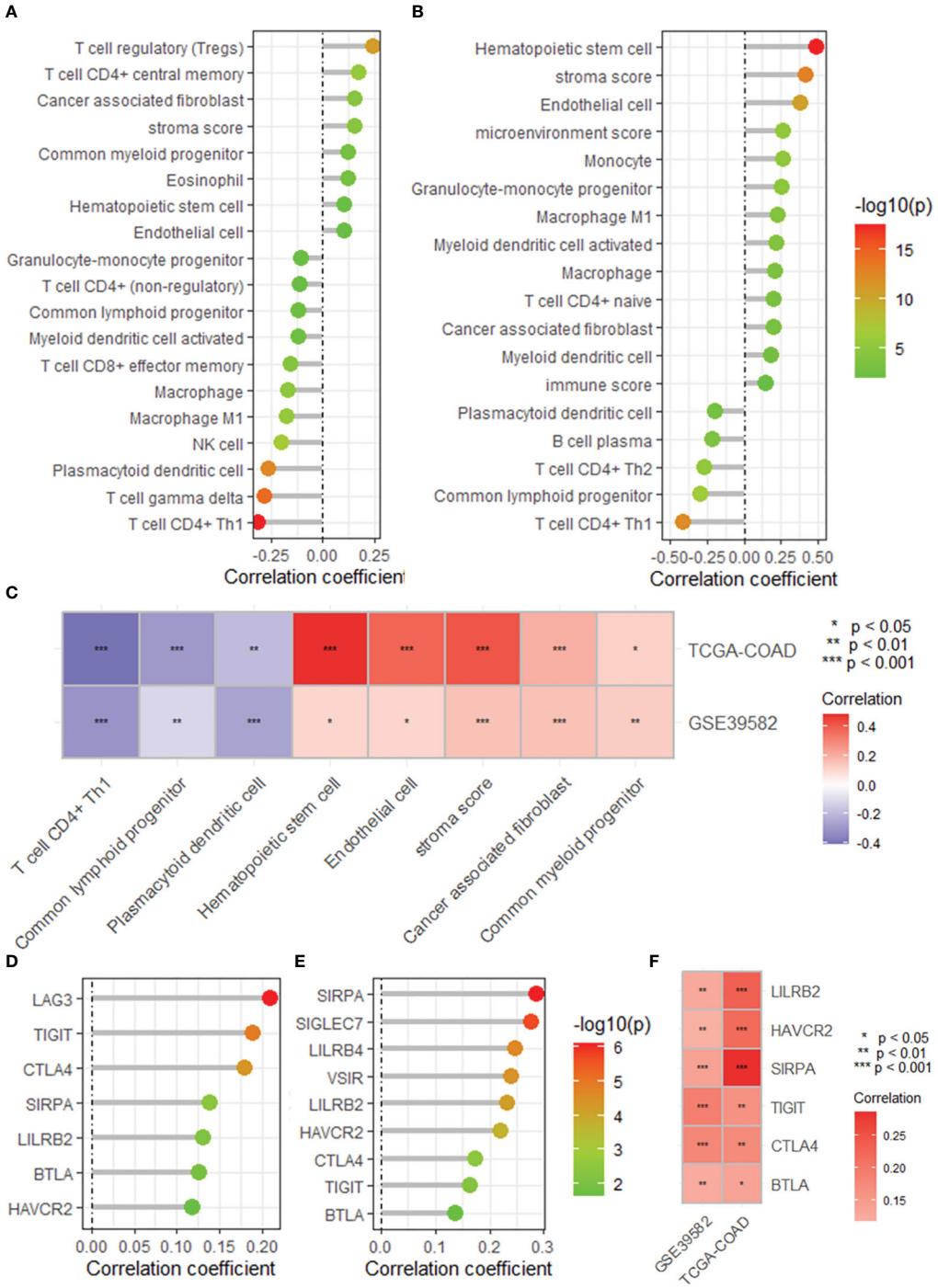

FIGURE 5
The DRG risk score correlated with immune cell infiltration and immune checkpoint gene expression. Lollipop plots showing the correlation between the risk score and the infiltration of immune cells calculated by the XCELL algorithm based on the GSE395852 **(A)** and TCGA-COAD **(B)** datasets. **(C)** Heatmap showing the intersection of the correlated immune cell types in the TCGA-COAD and GSE39582 datasets. Lollipop plots showing the correlation between the risk score and the expression of immune checkpoint genes based on the GSE395852 **(D)** and TCGA-COAD **(E)** datasets. **(F)** Heatmap showing the intersection of the correlated immune cell types in the TCGA-COAD and GSE39582 datasets. DRGs, disulfidptosis-related genes; COAD, colon adenocarcinoma.

nomogram, which demonstrated an improved prediction accuracy with an AUC of 0.845 based on the risk score. These results highlight the favorable predictive accuracy and practical value of our DRG prognostic model.

The tumor microenvironment (TME) has garnered significant attention due to its crucial role in tumor immunosuppression, distant metastasis, and drug resistance (19). The TME is primarily composed of tumor cells, infiltrating immune cells,

10.3389/fimmu.2024.1344637

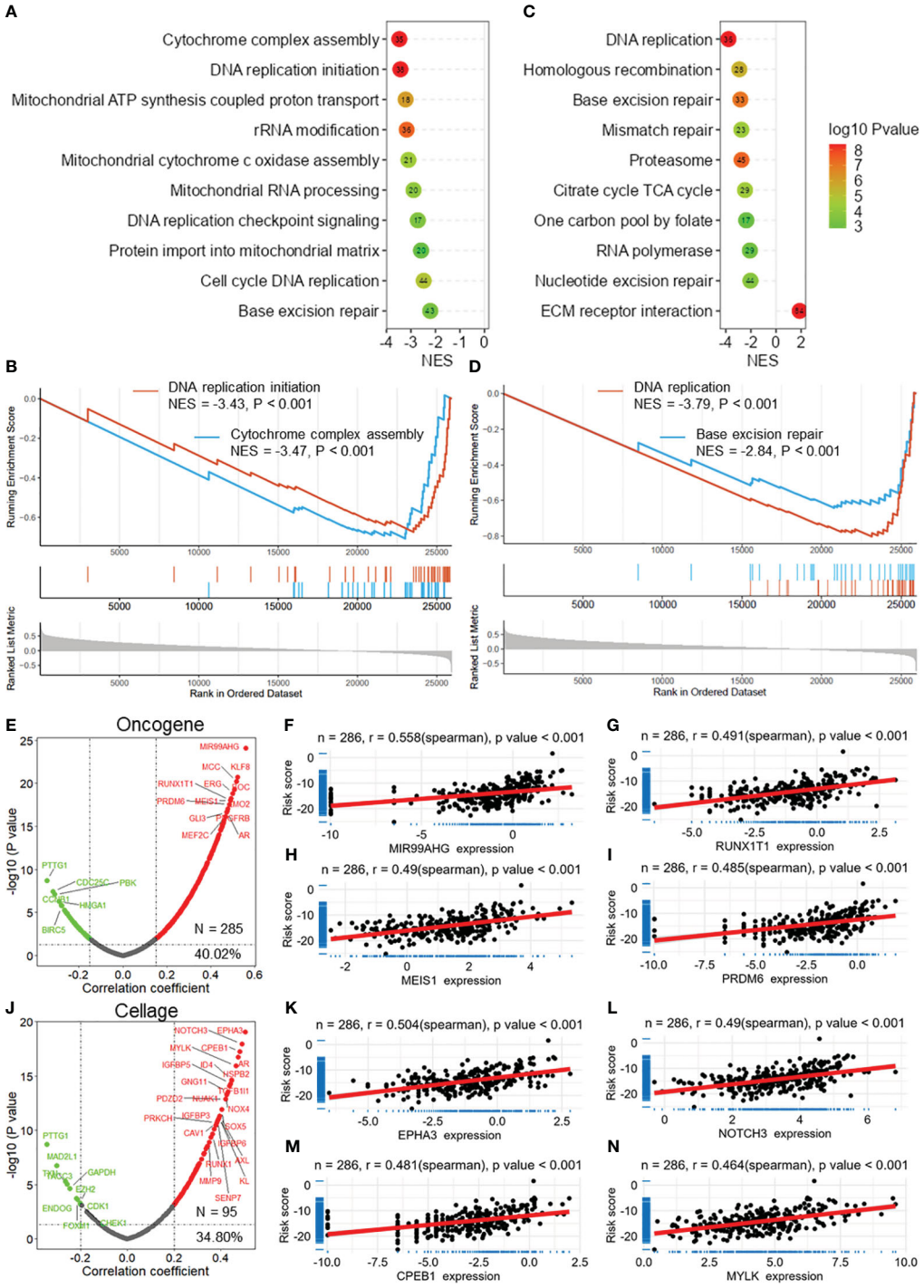

FIGURE 6
DRG risk score correlated with cancer progression. **(A)** Lollipop plots showing the results of GSEA for the biological processes associated with the DRG risk score. **(B)** GSEA plots showing that the risk score is related to DNA replication initiation and cytochrome complex assembly. **(C)** Lollipop plots showing the results of GSEA of the KEGG pathways associated with the DRG risk score. **(D)** GSEA plots showing that the risk score is related to DNA replication and base excision repair. **(E)** The volcano plot shows the results of the correlation analysis between the DRG risk score and oncogenes extracted from the ONGene database. Scatter plots showing the correlation between the risk score and MIR99AHG **(F)**, RUNX1T1 **(G)**, MEIS1 **(H)**, and PRDM6 **(I)**. **(J)** The volcano plot shows the results of the correlation analysis between the DRG risk score and cell senescence-related genes extracted from the ONGene database. Scatter plot showing the correlations between the risk score and EPHA3 **(K)**, NOTCH3 **(L)**, CPEB1 **(M)**, and MYLK **(N)** expression. GSEA, gene set enrichment analysis; DRGs, disulfidptosis-related genes.

10.3389/fimmu.2024.1344637

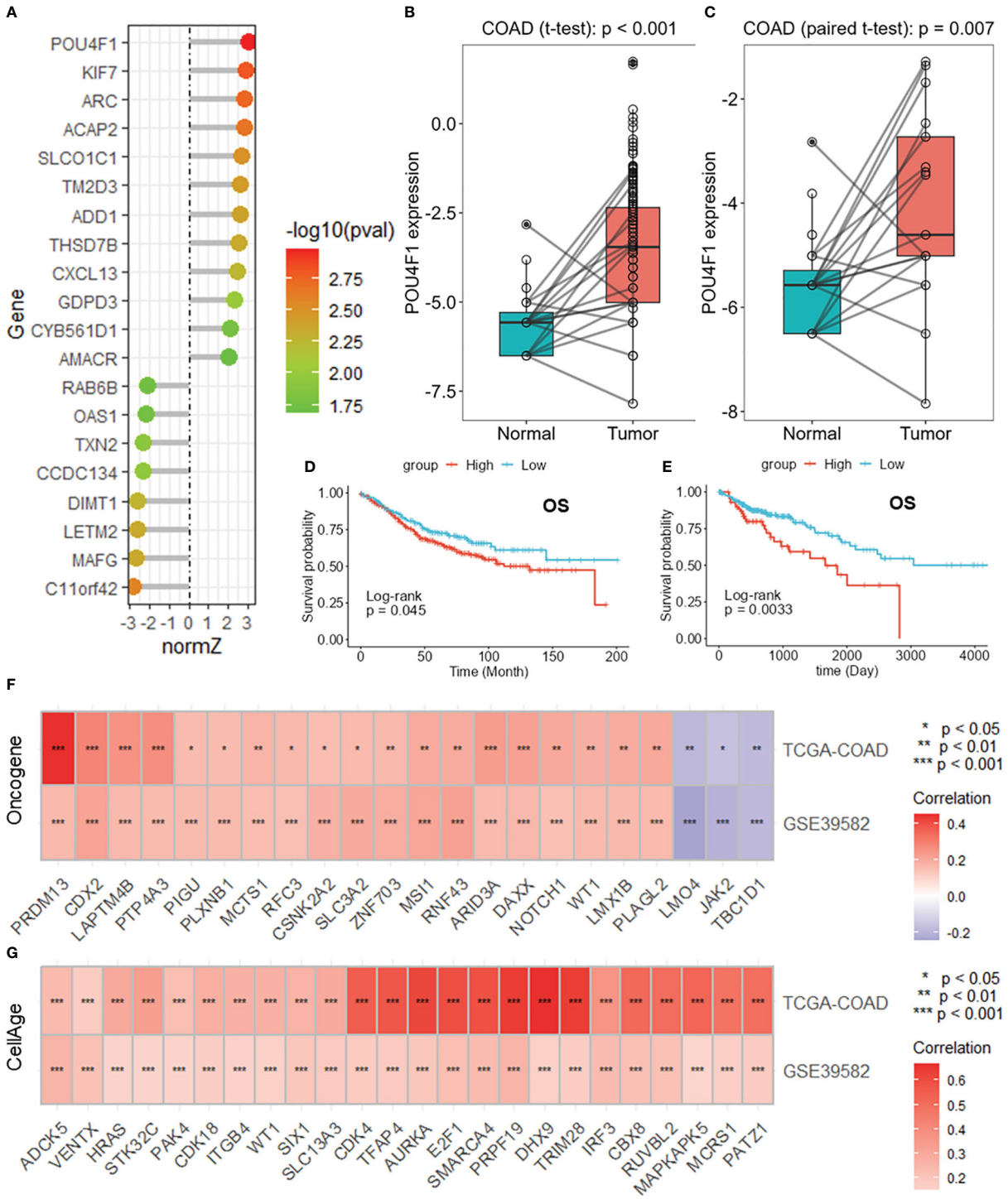

FIGURE 7
POU4F1 is highly expressed in COAD and is related to cancer progression. **(A)** Lollipop plot showing the normalized Z scores of the DRGs in the risk model. Boxplots showing the differential expression of POU4F1 in the whole TCGA-COAD dataset **(B)** and paired samples **(C)**. Survival analysis of POU4F1 for overall survival in the GSE39582 **(D)** and TCGA-COAD **(E)** datasets. Heatmaps showing the intersection of the oncogenes **(F)** and cell senescence-related genes **(G)** correlated with POU4F1 in the GSE39582 and TCGA-COAD datasets. DRGs, disulfidptosis-related genes; COAD, colon adenocarcinoma. * p<0.05,** p<0.01,***p<0.001

cancer-related stromal cells, endothelial cells, and other components (20, 21). Among the various stromal cells within the TME, cancer-related fibroblasts (CAFs) are recognized as key contributors that exhibit tumor-promoting effects and participate in multiple stages of tumor development through various pathways (22, 23). Tumor endothelial cells, another important type of stromal cell in the TME, have been reported to release "angiocrine factors" that promote tumor progression (24). Through a correlation

10.3389/fimmu.2024.1344637

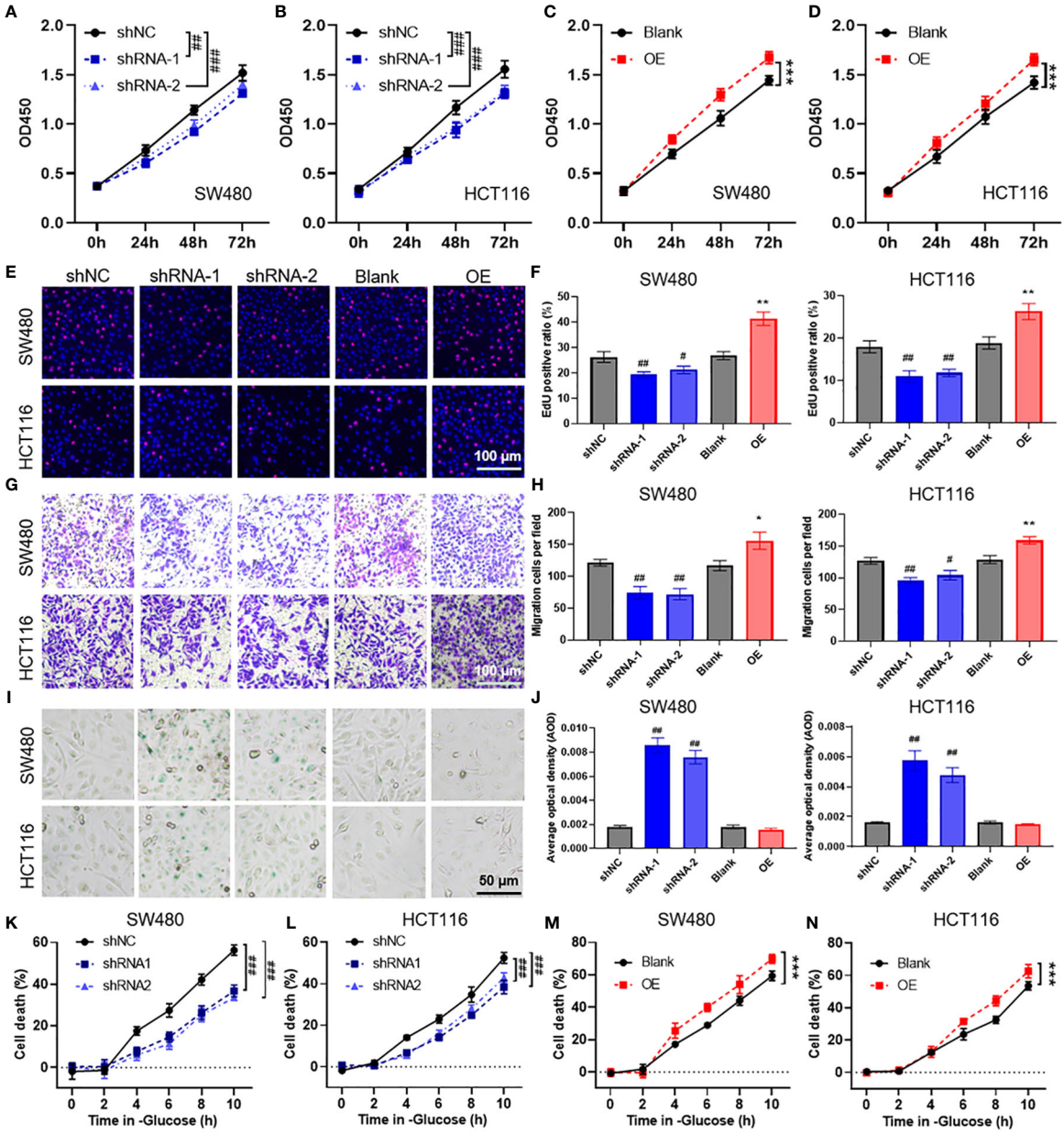

FIGURE 8
POU4F1 promotes cell proliferation, migration, and disulfidptosis in colon adenocarcinoma (COAD). **(A–D)** A CCK-8 assay was used to measure the effect of POU4F1 knockdown or overexpression in SW480 and HCT116 cells. Representative images **(E)** and the quantified results **(F)** of the EdU cell proliferation assay for COAD cells with POU4F1 knockdown or knockdown. Representative images **(G)** and the quantified results **(H)** of the Transwell cell migration assay for COAD cells with POU4F1 knockdown or knockdown. Representative images **(I)** and the quantified results **(J)** of the β-galactosidase staining assay for COAD cells with POU4F1 knockdown or knockdown. **(K–N)** A CCK-8 assay was used to measure the cell death induced by glucose deprivation in COAD cells with POU4F1 knockdown or knockdown. Compare with shNC, # p<0.05, ## p<0.01, ### p<0.001; compare with Blank, * p<0.05, ** p<0.01, *** p<0.001.

analysis, we found that the risk score derived from our model was positively correlated with the stromal score and the infiltration of endothelial cells and CAFs. Additionally, the risk score was correlated with the expression of several immune checkpoint molecules, including BTLA, CTLA4, and SIRPA. Immune checkpoint genes regulate the immune system by either stimulating or suppressing immune responses, and this regulatory mechanism is widely observed in tumors under physiological conditions (25). Gene set enrichment analysis (GSEA) revealed potential biological processes associated with the risk score. Our findings indicate that the risk score is correlated with DNA replication, cytochrome complex assembly, and base excision repair. Moreover, we observed a positive correlation between the risk score and the expression of multiple oncogenes and cell senescence-associated genes. Cellular aging, characterized by permanent cell cycle arrest, is characterized by various physiological and pathological processes, such as tissue remodeling, injury, cancer, and aging. While cellular aging acts as an effective barrier

to prevent tumors, there are instances where aged cells can support tumor progression (26). These results suggest that our risk prediction model based on DRGs has potential as an indicator for predicting immune microenvironment homeostasis, evaluating immune checkpoint blockade therapy, and assessing the biological functional status of tumors. Although this study proposes a prognostic prediction model based on DRGs and preliminarily validates the role of POU4F1 in COAD, these findings remain hypothetical and require additional experimental validation and clinical research to confirm their effectiveness in practical clinical applications.

Among the 20 DRGs included in our risk prediction model, we focused on POU4F1, which demonstrated the highest normalized Z score based on CRISPR screening. Our aim was to investigate its role in regulating biological functions and cell death in COAD cells. Previous studies have identified POU4F1 as a factor that induces resistance to trastuzumab in breast cancer cells by mediating the ERK1/2 pathway (27). As a transcription factor, POU4F1 has been shown to transcribe and regulate the expression of MEK in melanoma, thereby reactivating the MAPK pathway and leading to resistance against BRAF inhibitors (28). Our findings indicate that POU4F1 may act as an oncogene due to its upregulation in COAD tumors and its positive correlation with the expression of oncogenes. Furthermore, survival analysis revealed that a high POU4F1 expression was associated with a poor prognosis in COAD patients. Further *in vivo* assays indicated that POU4F1 knockdown significantly attenuated cell proliferation and migration while increasing cell senescence in COAD cells. Our research highlights the nuanced roles of SLC7A11 and POU4F1 in COAD, where SLC7A11 overexpression may inhibit metastasis, in contrast with the ability of POU4F1 to facilitate tumor growth and migration, suggesting that gene functions vary significantly across cancers due to unique genetic and epigenetic landscapes (29). We further evaluated the regulatory effect of the DRGs on disulfidptosis by culturing the cells in a glucose-deprived medium. The results demonstrated that POU4F1 knockdown inhibited glucose deprivation-induced cell death, while POU4F1 overexpression promoted cell death. These results revealed that POU4F1 has important effects on the proliferation, migration, and senescence of COAD cells as well as disulfidptosis. In summary, our study revealed and validated a risk prediction model based on DRGs in COAD patients. Furthermore, we have provided evidence that POU4F1 promotes cell proliferation, migration, and disulfidptosis in COAD.

In conclusion, our study revealed and verified a risk prediction model based on disulfidptosis-related genes (DRGs) in COAD patients. The risk score is related to immune microenvironment homeostasis, expression of immune checkpoints, and tumor biological functions. POU4F1, a crucial component of this model, has been confirmed to promote cell proliferation, migration, and disulfidptosis in COAD cells. This prognostic model not only enhances our understanding of COAD progression mechanisms but also provides a new tool for the stratified management of colorectal cancer patients, allowing clinicians to more accurately predict patient prognosis and formulate personalized treatment plans, thereby improving treatment outcomes and patient survival rates.

Data availability statement

The datasets presented in this study can be found in online repositories. The names of the repository/repositories and accession number(s) can be found in the article/Supplementary Material.

Ethics statement

Ethical approval was not required for the studies on animals in accordance with the local legislation and institutional requirements because only commercially available established cell lines were used.

Author contributions

ML: Conceptualization, Data curation, Formal analysis, Investigation, Methodology, Software, Writing – original draft, Writing – review & editing, Funding acquisition. JW: Conceptualization, Data curation, Methodology, Software, Writing – original draft. YZ: Data curation, Methodology, Writing – original draft, Formal analysis, Investigation, Project administration, Resources, Visualization. CL: Formal analysis, Supervision, Writing – review & editing. JM: Writing – original draft, Methodology, Software. XM: Writing – review & editing, Methodology, Software. ZY: Writing – review & editing, Methodology, Software. CC: Data curation, Writing – review & editing, Software. KT: Writing – original draft, Methodology, Software. PZ: Writing – review & editing. QH: Formal analysis, Writing – original draft. JS: Data curation, Funding acquisition, Methodology, Writing – review & editing. JG: Data curation, Funding acquisition, Methodology, Writing – review & editing, Project administration, Resources, Supervision, Validation, Visualization. SW: Funding acquisition, Methodology, Writing – review & editing, Data curation, Formal analysis, Investigation, Validation, Writing – original draft.

Funding

The author(s) declare financial support was received for the research, authorship, and/or publication of this article. This work was supported in part by the Suzhou “National Mentorship” Training Program for Youth Medical Talent under Grant Qngg2022041, Suzhou Clinical Special Disease Diagnosis and Treatment Program under Grant LCZX202223, Suzhou Science and Technology Development Program under Grant SYS2020138, Suzhou GuSu Medical Talent Program under Grant GSWS2022100, Changshu Health and Technology Development Program under Grant CSWS202108.

Conflict of interest

The authors declare that the research was conducted in the absence of any commercial or financial relationships that could be construed as a potential conflict of interest.

Publisher's note

All claims expressed in this article are solely those of the authors and do not necessarily represent those of their affiliated organizations, or those of the publisher, the editors and the reviewers. Any product that may be evaluated in this article, or claim that may be made by its manufacturer, is not guaranteed or endorsed by the publisher.

Supplementary material

The Supplementary Material for this article can be found online at: https://www.frontiersin.org/articles/10.3389/fimmu.2024.1344637/full#supplementary-material

References

1. Sharma R, Abbasi-Kangevari M, Abd-Rabu R, Abidi H, Abu-Gharbieh E, Acuna JM, et al. Global, regional, and national burden of colorectal cancer and its risk factors, 1990-2019: a systematic analysis for the Global Burden of Disease Study 2019. *Lancet Gastroenterol Hepatol*. (2022) 7:627–47. doi: 10.1016/s2468-1253(22)00044-9

2. Sung H, Ferlay J, Siegel RL, Laversanne M, Soerjomataram I, Jemal A, et al. Global cancer statistics 2020: GLOBOCAN estimates of incidence and mortality worldwide for 36 cancers in 185 countries. *CA Cancer J Clin*. (2021) 71:209–49. doi: 10.3322/caac.21660

3. Siegel RL, Wagle NS, Cercek A, Smith RA, Jemal A. Colorectal cancer statistics, 2023. *CA Cancer J Clin*. (2023) 73:233–54. doi: 10.3322/caac.21772

4. Lui RN, Tsoi KKF, Ho JMW, Lo CM, Chan FCH, Kyaw MH, et al. Global increasing incidence of young-onset colorectal cancer across 5 continents: A joinpoint regression analysis of 1,922,167 cases. *Cancer Epidemiol Biomarkers Prev*. (2019) 28:1275–82. doi: 10.1158/1055-9965.Epi-18-1111

5. Liu X, Nie L, Zhang Y, Yan Y, Wang C, Colic M, et al. Actin cytoskeleton vulnerability to disulfide stress mediates disulfidptosis. *Nat Cell Biol*. (2023) 25:404–14. doi: 10.1038/s41556-023-01091-2

6. Liu X, Olszewski K, Zhang Y, Lim EW, Shi J, Zhang X, et al. Cystine transporter regulation of pentose phosphate pathway dependency and disulfide stress exposes a targetable metabolic vulnerability in cancer. *Nat Cell Biol*. (2020) 22:476–86. doi: 10.1038/s41556-020-0496-x

7. Zheng P, Zhou C, Ding Y, Duan S. Disulfidptosis: a new target for metabolic cancer therapy. *J Exp Clin Cancer Res*. (2023) 42:103. doi: 10.1186/s13046-023-02675-4

8. Yang L, Liu J, Li S, Liu X, Zheng F, Xu S, et al. Based on disulfidptosis, revealing the prognostic and immunological characteristics of renal cell carcinoma with tumor thrombus of vena cava and identifying potential therapeutic target AJAP1. *J Cancer Res Clin Oncol*. (2023) 149(12):9787–804. doi: 10.1007/s00432-023-04877-x

9. Qi C, Ma J, Sun J, Wu X, Ding J. The role of molecular subtypes and immune infiltration characteristics based on disulfidptosis-associated genes in lung adenocarcinoma. *Aging (Albany NY)*. (2023) 15:5075–95. doi: 10.18632/aging.204782

10. Zhao M, Kim P, Mitra R, Zhao J, Zhao Z. TSGene 2.0: an updated literature-based knowledgebase for tumor suppressor genes. *Nucleic Acids Res*. (2016) 44:D1023–1031. doi: 10.1093/nar/gkv1268

11. Charoentong P, Finotello F, Angelova M, Mayer C, Efremova M, Rieder D, et al. Pan-cancer immunogenomic analyses reveal genotype-immunophenotype relationships and predictors of response to checkpoint blockade. *Cell Rep*. (2017) 18:248–62. doi: 10.1016/j.celrep.2016.12.019

12. Aran D, Hu Z, Butte AJ. xCell: digitally portraying the tissue cellular heterogeneity landscape. *Genome Biol*. (2017) 18:220. doi: 10.1186/s13059-017-1349-1

13. Jiang P, Gu S, Pan D, Fu J, Sahu A, Hu X, et al. Signatures of T cell dysfunction and exclusion predict cancer immunotherapy response. *Nat Med*. (2018) 24:1550–8. doi: 10.1038/s41591-018-0136-1

14. Yang W, Soares J, Greninger P, Edelman EJ, Lightfoot H, Forbes S, et al. Genomics of Drug Sensitivity in Cancer (GDSC): a resource for therapeutic biomarker discovery in cancer cells. *Nucleic Acids Res*. (2013) 41:D955–961. doi: 10.1093/nar/gks1111

15. Maeser D, Gruener RF, Huang RS. oncoPredict: an R package for predicting in vivo or cancer patient drug response and biomarkers from cell line screening data. *Brief Bioinform*. (2021) 22(6):bbab260. doi: 10.1093/bib/bbab260

16. Wu M, Li X, Liu R, Yuan H, Liu W, Liu Z. Development and validation of a metastasis-related Gene Signature for predicting the Overall Survival in patients with Pancreatic Ductal Adenocarcinoma. *J Cancer*. (2020) 11:6299–318. doi: 10.7150/jca.47629

17. Hu G, Yao H, Wei Z, Li L, Yu Z, Li J, et al. A bioinformatics approach to identify a disulfidptosis-related gene signature for prognostic implication in colon adenocarcinoma. *Sci Rep*. (2023) 13:12403. doi: 10.1038/s41598-023-39563-y

18. Chen H, Yang W, Li Y, Ma L, Ji Z. Leveraging a disulfidptosis-based signature to improve the survival and drug sensitivity of bladder cancer patients. *Front Immunol*. (2023) 14:1198878. doi: 10.3389/fimmu.2023.1198878

19. Chen F, Zhuang XQ, Lin LY, Yu PF, Wang Y, Shi YF, et al. New horizons in tumor microenvironment biology: challenges and opportunities. *BMC Med*. (2015) 13:45. doi: 10.1186/s12916-015-0278-7

20. Giraldo NA, Sanchez-Salas R, Peske JD, Vano Y, Becht E, Petitprez F, et al. The clinical role of the TME in solid cancer. *Brit J Cancer*. (2019) 120:45–53. doi: 10.1038/s41416-018-0327-z

21. Li HC, Fan XL, Houghton J. Tumor microenvironment: The role of the tumor stroma in cancer. *J Cell Biochem*. (2007) 101:805–15. doi: 10.1002/jcb.21159

22. Fiori ME, Di Franco S, Villanova L, Bianca P, Stassi G, De Maria R. Cancer-associated fibroblasts as abettors of tumor progression at the crossroads of EMT and therapy resistance. *Mol Cancer*. (2019) 18(1):70. doi: 10.1186/s12943-019-0994-2

23. Hinshaw DC, Shevde LA. The tumor microenvironment innately modulates cancer progression. *Cancer Res*. (2019) 79:4557–66. doi: 10.1158/0008-5472.Can-18-3962

24. Maishi N, Hida K. Tumor endothelial cells accelerate tumor metastasis. *Cancer Sci*. (2017) 108:1921–6. doi: 10.1111/cas.13336

25. Morad G, Helmink BA, Sharma P, Wargo JA. Hallmarks of response, resistance, and toxicity to immune checkpoint blockade. *Cell*. (2021) 184:5309–37. doi: 10.1016/j.cell.2021.09.020

26. Calcinotto A, Kohli J, Zagato E, Pellegrini L, Demaria M, Alimonti A. Cellular senescence: aging, cancer, and injury. *Physiol Rev*. (2019) 99:1047–78. doi: 10.1152/physrev.00020.2018

27. Wu D, Jia HY, Wei N, Li SJ. POU4F1 confers trastuzumab resistance in HER2-positive breast cancer through regulating ERK1/2 signaling pathway. *Biochem Biophys Res Commun*. (2020) 533:533–9. doi: 10.1016/j.bbrc.2020.09.003

28. Liu L, Yue Q, Ma J, Liu Y, Zhao T, Guo W, et al. POU4F1 promotes the resistance of melanoma to BRAF inhibitors through MEK/ERK pathway activation and MITF up-regulation. *Cell Death Dis*. (2020) 11:451. doi: 10.1038/s41419-020-2662-2

29. Yan Y, Teng H, Hang Q, Kondiparthi L, Lei G, Horbath A, et al. SLC7A11 expression level dictates differential responses to oxidative stress in cancer cells. *Nat Commun*. (2023) 14:3673. doi: 10.1038/s41467-023-39401-9

frontiers | Frontiers in Immunology

TYPE Original Research
PUBLISHED 01 July 2024
DOI 10.3389/fimmu.2024.1396349

OPEN ACCESS

EDITED BY
Laura Senovilla,
Spanish National Research Council (CSIC), Spain

REVIEWED BY
Udo S. Gaipl,
University Hospital Erlangen, Germany
Luciana Dini,
Sapienza University of Rome, Italy

*CORRESPONDENCE
Dmitri V. Krysko
dmitri.krysko@ugent.be

†These authors have contributed equally to this work and share first authorship

RECEIVED 05 March 2024
ACCEPTED 19 June 2024
PUBLISHED 01 July 2024

CITATION
Naessens F, Demuynck R, Vershinina O, Efimova I, Saviuk M, De Smet G, Mishchenko TA, Vedunova MV, Krysko O, Catanzaro E and Krysko DV (2024) CX3CL1 release during immunogenic apoptosis is associated with enhanced anti-tumour immunity.
Front. Immunol. 15:1396349.
doi: 10.3389/fimmu.2024.1396349

CX3CL1 release during immunogenic apoptosis is associated with enhanced anti-tumour immunity

Faye Naessens[1,2†], Robin Demuynck[1,2†], Olga Vershinina[3], Iuliia Efimova[1,2], Mariia Saviuk[1,2], Greet De Smet[1], Tatiana A. Mishchenko[3], Maria V. Vedunova[3], Olga Krysko[1], Elena Catanzaro[1,2] and Dmitri V. Krysko[1,2*]

[1]Cell Death Investigation and Therapy Laboratory, Anatomy and Embryology Unit, Department of Human Structure and Repair, Faculty of Medicine and Health Sciences, Ghent University, Ghent, Belgium, [2]Cancer Research Institute Ghent, Ghent, Belgium, [3]Institute of Biology and Biomedicine, National Research Lobachevsky State University of Nizhny Novgorod, Nizhny Novgorod, Russia

Introduction: Immunogenic cell death (ICD) has emerged as a novel option for cancer immunotherapy. The key determinants of ICD encompass antigenicity (the presence of antigens) and adjuvanticity, which involves the release of damage-associated molecular patterns (DAMPs) and various cytokines and chemokines. CX3CL1, also known as neurotactin or fractalkine, is a chemokine involved in cellular signalling and immune cell interactions. CX3CL1 has been denoted as a "find me" signal that stimulates chemotaxis of immune cells towards dying cells, facilitating efferocytosis and antigen presentation. However, in the context of ICD, it is uncertain whether CX3CL1 is an important mediator of the effects of ICD.

Methods: In this study, we investigated the intricate role of CX3CL1 in immunogenic apoptosis induced by mitoxantrone (MTX) in cancer cells. The Luminex xMAP technology was used to quantify murine cytokines, chemokines and growth factors to identify pivotal regulatory cytokines released by murine fibrosarcoma MCA205 and melanoma B16-F10 cells undergoing ICD. Moreover, a murine tumour prophylactic vaccination model was employed to analyse the effect of CX3CL1 on the activation of an adaptive immune response against MCA205 cells undergoing ICD. Furthermore, thorough analysis of the TCGA-SKCM public dataset from 98 melanoma patients revealed the role of CX3CL1 and its receptor CX3CR1 in melanoma patients.

Results: Our findings demonstrate enhanced CX3CL1 release from apoptotic MCA205 and B16-F10 cells (regardless of the cell type) but not if they are undergoing ferroptosis or accidental necrosis. Moreover, the addition of recombinant CX3CL1 to non-immunogenic doses of MTX-treated, apoptotically dying cancer cells in the murine prophylactic tumour vaccination model induced a robust immunogenic response, effectively increasing the survival of the mice. Furthermore, analysis of melanoma patient data revealed enhanced survival rates in individuals exhibiting elevated levels of CD8+ T cells expressing CX3CR1.

10.3389/fimmu.2024.1396349

Conclusion: These data collectively underscore the importance of the release of CX3CL1 in eliciting an immunogenic response against dying cancer cells and suggest that CX3CL1 may serve as a key switch in conferring immunogenicity to apoptosis.

KEYWORDS

immunogenic apoptosis, fractalkine, cytokines, immunogenic cell death, chemokines, CX3CL1

1 Introduction

Immunogenic cell death (ICD) has emerged as a paradigm-shifting concept in the field of immunology and cancer therapeutics. It combines the ability to kill cancer cells and restore the lost immunological ability to identify and interact with dying cancer cells. This leads to the stimulation of innate and adaptive immune responses, and thereby establishment of long-term immunological memory (1). ICD is an overarching term that includes cell death modalities such as apoptosis (2), necroptosis (3–5), and ferroptosis (6–8). It can be induced by specific stimuli, including oncolytic viruses (9), conventional chemotherapeutics such as mitoxantrone (MTX) (10), and physical interventions such as radiotherapy, including heavy ions (11) or X-rays radiotherapy (12), or photodynamic therapy (13). Perturbation of endoplasmic reticulum (ER) homeostasis and activation of ER stress pathways, also known as the unfolded protein response (14), together with the generation of reactive oxygen species, are essential components of nearly (15) all scenarios in which ICD occurs (16–18). For cell death to possess immunogenic properties also requires both antigenicity and adjuvanticity (1, 19, 20). Antigenicity refers to the availability of either tumour-specific antigens, tumour-associated antigens, or neo-antigens, which enable the specific recognition and killing of the tumour cells by the immune system. Adjuvanticity involves the spatio-temporal release of damage-associated molecular patterns (DAMPs) and pro-inflammatory cytokines/chemokines from the dying cancer cells. This triggers the recruitment, activation and maturation of antigen-presenting cells (APCs), such as dendritic cells, via their respective pattern recognition receptors (PRRs). Several crucial DAMPs and cytokines have been discovered, including but not limited to high-mobility group B1, surface-exposed calreticulin, extracellular secretion of adenosine triphosphate, annexin A1 and several members of the type 1 interferon family (1, 21). Upon engulfment of dying tumour cells, APCs undergo activation and maturation characterised by upregulation of major histocompatibility complex class II molecules and costimulatory markers, such as CD80 and CD86, while migrating to the tumour-draining lymph nodes to present cancer antigens to $CD8^+$ T cells. The activated cytotoxic $CD8^+$ T lymphocytes then relocate to the tumour site, releasing interferon gamma, promoting eradication of the neoplastic lesion, and stimulating the formation of a long-lasting immunological memory against the tumour (1, 22).

CX3C chemokine ligand 1 (CX3CL1), originally named neurotactin (23) and later fractalkine (24), is a chemokine intricately involved in cell signalling and in immune cell recruitment and activation (25). CX3CL1 can exist as a membrane-bound variant (mCX3CL1) serving as an adhesion protein for cells expressing the CX3CL1 receptor (CX3CR1), including various immune cell types such as NK cells, monocytes, dendritic cells, granulocytes, and $CD3^+$ T cells (24, 26, 27). Conversely, the soluble form of CX3CL1 (sCX3CL1), which is released upon proteolytic cleavage of mCX3CL1, predominantly exerts a potent chemoattractant function (24, 25, 27–30). Importantly, CX3CL1 has been identified as a "find me" signal that attracts immune cells towards dying cells, facilitating efferocytosis (31–35). However, in the context of ICD, it remains uncertain whether CX3CL1 is an important mediator of the effect of ICD or, due to its potential pro-tumourigenic features (36–42), might act as a "keep out" signal, hindering efferocytosis and the initiation of an effective ICD immune cycle (43, 44).

In this study, we assessed the secretion of CX3CL1 from MTX-treated murine fibrosarcoma MC205 and melanoma B16-F10 cells undergoing immunogenic apoptosis (*i.e.*, apoptotic cell death exhibiting ICD characteristics (10, 45)), and explored its potential as a mediator of anti-tumour immunity during ICD. Our results demonstrate that CX3CL1 is released specifically during apoptotic cell death regardless of the cell type. Furthermore, the addition of 1 ng or 10 ng of recombinant CX3CL1 (rCX3CL1) to a non-immunogenic dose of dying/dead cancer cells for prophylactic vaccination of mice significantly increased the tumour-free survival of mice and restored immunogenicity of dying cancer cells. In addition, analysis of publicly available human database (The Cancer Genome Atlas-Skin Cutaneous Melanoma (TCGA-SKCM)) containing data from 98 melanoma patients revealed a correlation between high levels of CX3CR1 expression and higher overall survival probability. Moreover, CX3CR1 was predominantly associated with increased presence of $CD8^+$ T cells, and a high level of CX3CR1 expression was correlated with increased expression of $CD8^+$ T cell signature. These findings identify CX3CL1 as an effective mediator of an adaptive immune response during

immunogenic apoptosis and position it as a promising therapeutic adjuvant in ICD-based treatment.

2 Materials and methods

2.1 Cell lines and cell culture

Murine fibrosarcoma MCA205 cells were cultured in Roswell Park Memorial Institute (RPMI) 1640 (Gibco, 21875–034) supplemented with heat-inactivated foetal bovine serum (FBS, Thermo Fisher Scientific, 10%, 10270–106), penicillin (100 U/mL), and streptomycin (Gibco, 100 µg/L, 15140–122). B16-F10 murine melanoma cells were cultured in Dulbecco's Modified Eagle Medium (DMEM) (Gibco, 10938–025) supplemented with 10% FBS, 1% L-glutamine (Gibco, 25030–024), 1% sodium pyruvate (Gibco, 11360–039) and 1% penicillin/streptomycin. All cells were maintained under constant conditions of 37°C, 5% CO_2, and a humidified atmosphere in a cell culture incubator. The medium was changed every two days, and detaching and splitting of cells were done using trypsin-EDTA (0.05%) (Gibco, 25300–054).

2.2 Cell death assay by flow cytometry

Cells were stimulated with 2 µM mitoxantrone (MTX) (Sigma Aldrich, M6545) or 2.5 µM RAS-selective lethal 3 (RSL3) (Sigma Aldrich, SML2234) for 24 h. The cells were washed in Annexin-V binding buffer (10 mM HEPES, pH 7.4, 0.14 mM NaCl, and 2.5 mM $CaCl_2$), followed by staining with Sytox Blue Nucleic Acid Stain (Molecular Probes, S11348, 2.5 mM), Annexin-V (AnV), and Alexa Fluor 488 conjugate (Molecular Probes, A13201). The cells were run on a Becton Dickinson (BD) LSRII flow cytometer, and the data were analysed by using FlowJo software (V.10.0.8). Flow cytometry experiments were performed at the Core Flow Cytometry (BOF/COR/2022/001) at Ghent University.

2.3 Multiplex analysis of cytokines

Supernatants of treated cells was analysed using the Luminex xMAP technology. The multiplexing analysis was performed using the Luminex™ 200 system (Luminex, Austin, TX, USA) by Eve Technologies Corp (Calgary, Alberta). The samples were simultaneously measured using Eve Technologies' Mouse Cytokine Discovery Assay® (MD44). The assay was run according to the manufacturer's protocol. Assay sensitivities of these markers range from 0.3–30.6 pg/mL. Individual analyte sensitivity values are available in the Millipore Sigma MILLIPLEX® MAP protocol.

2.4 Mice

The *in vivo* experiments were performed on immune-competent C57BL/6J mice (7–9 weeks old) (Janvier Labs, France). The mice were housed in specific pathogen-free conditions. All *in vivo* experiments were conducted according to the guidelines of the local Ethics Committee of Ghent University at the Core ARTH Animal Facilities at Ghent University (Belgium).

2.4.1 Prophylactic tumour vaccination mice model

To confirm the role of CX3CL1 in immunogenic apoptosis, a non-immunogenic dose of MTX-treated MCA205 cells was used in the prophylactic tumour vaccination mouse model. MCA205 cancer cells were seeded at a density of 2 x 10^6 cells per flask and induced to undergo cell death with 2 µM MTX for 24 h. After incubation overnight, 2.5 x 10^5 MTX-treated MCA205 cells (non-immunogenic dose) or 5 x 10^5 dying cancer cells were collected in PBS (200 µL per mouse, Gibco, 14190–144). Cell death analysis was performed using flow cytometry (See 2.2). The cells were injected subcutaneously (s.c.) in the left flank of C57BL/6J mice. After seven days, the mice were challenged with 10^5 viable/untreated MCA205 cells in the opposite (right) flank, and tumour growth on both sides was measured with a digital calliper.

By using a non-immunogenic dose, the recovery of immunogenicity by CX3CL1 was investigated further. MCA205 cancer cells were seeded at a density of 2 x 10^6 cells per flask and induced to undergo apoptosis with 2 µM MTX for 24 h. After incubation overnight, 2.5 x 10^5 dying cancer cells (non-immunogenic dose) were collected and mixed with different doses (0, 1, 10 or 100 ng) of recombinant murine CX3CL1 (R&D system, 472-FF/CF) in PBS at a volume of 200 µL per mouse. Cell death analysis was performed using flow cytometry (See 2.2). The cells were s.c. injected in the left flank of C57BL/6J mice. Mice injected only with PBS or only recombinant murine CX3CL1 (1 ng, 10 ng or 100 ng) served as negative controls. Seven days post-immunisation, the mice were challenged as described above. Tumour growth was monitored with the digital calliper once every two days for up to 21 days after challenge. When a tumour became too big (> 1,500 mm^3) or an open necrotic lesion developed, the mouse was euthanised by cervical dislocation.

2.4.2 Therapeutic tumour mice model

5 x 10^5 MCA205 cells were injected s.c. in the right flank of C57BL/6J mice. After 7 days, when the tumour had reached about 20–45 mm^3, the mice were treated intraperitoneally (i.p.) with 100 µL of 5.2 mg/kg MTX in PBS. 12 h and 24 h after treatment, the mice were injected intratumourally with 1 or 10 ng CX3CL1 in 10 µL of PBS or, for the control mice, with PBS only. This was repeated on day 14. The efficacy of therapy was analysed by monitoring tumour growth with a digital calliper once every two days for up to 29 days after tumour cell injection. When a tumour became too big (> 1,500 mm^3) or became an open necrotic lesion, the mouse was euthanised by cervical dislocation.

2.5 Public dataset

RNA-sequencing (RNA-seq) data and corresponding patient clinical information of the TCGA-SKCM project were downloaded from The Cancer Genome Atlas (https://portal.gdc.cancer.gov/). Patients with no reported vital status (alive or dead), with recurrent

tumour, or with an unknown survival time were excluded. The TCGA-SKCM dataset comprises 98 patients with a primary tumour, of whom 28 have a vital status of 'Dead' and 70 have a vital status of 'Alive'. For analysis, we used STAR-count files containing the number of mapped reads (counts) for each gene. The non-protein-coding genes were filtered out, leaving 19,938 genes. The expression count data were normalised by transcripts per million (TPM) and then transformed to $\log_2$ values.

2.5.1 Survival analysis

Survival analysis of patients from the public dataset was performed in Python using the lifelines v0.27.4 package. For each specific gene, patients were divided into two groups based on median expression level (high or low). Overall survival was estimated using the Kaplan–Meier method. Log-rank test (Mantel-Cox) was used to compare the statistical differences between groups, and a p-value < 0.05 was considered statistically significant. Where survival curves intersected, a weighted log-rank test (Fleming-Harrington test) was additionally used for evaluation. Depending on the values of parameters p and q, this test can determine early ($p > q$) or late ($p < q$) differences in survival. For $p = q = 0$, the test reduces to the unweighted log-rank test.

2.5.2 Estimation of tumour-infiltrating cells

The immunedeconv v2.0.4 (46) R package was used to analyse the abundance of immunocyte infiltration from bulk gene expression data. This package evaluates cell proportions using algorithms such as EPIC (47), TIMER (48), quanTIseq (49), MCP-counter (50) and xCell (51).

2.6 Statistical analysis

Statistics for the public dataset were calculated in Python using the scipy v.1.9.3 package. As the data were often not normally distributed according to the Shapiro–Wilk test, a nonparametric Mann-Whitney U test was used to evaluate the differences between two groups. P-values < 0.05 were considered statistically significant.

Statistical analysis with one-way or two-way Analysis of Variance (ANOVA) and graphs were plotted in GraphPad Prism (V.8.0.1). Kaplan-Meier survival curves showing the timelines of tumour development were analysed by log-rank Mantel-Cox test. Differences between groups were considered significant if the corresponding p-value was < 0.05.

3 Results

3.1 CX3CL1 release is associated with immunogenic apoptosis

Different types of cell death modalities (*i.e.*, apoptosis, ferroptosis and accidental necrosis) were induced in both murine fibrosarcoma (MCA205) (Figures 1A, B) and melanoma (B16-F10) cells (Figures 1D, E). MCA205 and B16-F10 are commonly used cell lines in ICD studies (6, 13, 45, 52). Immunogenic apoptosis was induced with MTX for 24 h (10, 45), ferroptosis (non-immunogenic) was induced with RSL3 (6), and accidental necrosis of low immunogenicity was induced with three freeze/thaw (F/T) cycles (6, 13, 53, 54). The used cell death inducers have already been extensively described and defined (6, 10, 13, 45, 53, 54). Treatment for 24 h with RSL3 or F/T cells were used as negative controls because they do not induce the characteristics of ICD (6). Cell death rates, quantified by AnV and Sytox blue staining, were comparable with previously published data (6), *i.e.* approximately 20% for MTX (Figures 1A, D). Sytox Blue positivity refers to cell membrane permeabilisation and, together with positive AnV staining, detects a late phase of cell death, while single AnV positivity occurs at an early phase of cell death (6). Since B16 cells are resistant to RSL3 (55, 56), it was not used for B16. Supernatants were collected from the dying murine fibrosarcoma MCA205 and melanoma B16-F10 cells, as well as from viable cells as a control, and analysed for cytokine secretion using the Luminex xMAP technology from Eve Technologies. CX3CL1 was associated only with MTX-treatment (*i.e.*, immunogenic apoptosis) despite the limited membrane permeabilisation (Figures 1C, F). This release from both cancer cell types excludes the possibility of effects specific to a particular cancer cell type. During late ferroptosis in MCA205 cells, CX3CL1 levels remained unaltered compared to the viable control, whereas during accidental necrosis, the levels of CX3CL1 even diminished in both MCA205 and B16-F10 cells. These data suggest a strong association of CX3CL1 secretion with the specific induction of immunogenic apoptosis but not with the other cell death modalities.

3.2 CX3CL1 reverts non-immunogenic apoptosis to ICD

To investigate the importance of CX3CL1 secretion in immunogenic apoptosis, the tumour prophylactic vaccination mouse model was used (Figures 2A, C). Mice were vaccinated with MTX-treated MCA205 cells in one flank and one week later challenged in the opposite flank with viable cancer cells of the same cancer type. For this experiment, a non-immunogenic low-dose of MTX-treated MCA205 cells was used for vaccination (Figures 2A, B). Vaccination of mice with 5×10^5 MTX-treated MCA205 cells protected approximately 70% of the mice against tumour challenge, whereas the half-dose of 2.5×10^5 cells protected only 20% of the mice (Figure 2B). Therefore, this so-called non-immunogenic dose of 2.5×10^5 cells was used in the following experiments. Doses of 1 ng, 10 ng or 100 ng of murine rCX3CL1 were added to the non-immunogenic dose of MTX-treated cancer cells to analyse whether the addition of CX3CL1 can enhance the immunogenicity of dying cancer cells (Figure 2C). Indeed, addition of 1 ng or 10 ng of rCX3CL1 effectively increased tumour-free survival ($p = 0.0084$) in mice from 10% (non-immunogenic MCA205 MTX only) to 50%, demonstrating restored immunogenicity (Figure 2D). Interestingly, the addition of a dose of 100 ng rCX3CL1 to the MTX-treated cancer cells did not increase tumour-free survival and vaccination

10.3389/fimmu.2024.1396349

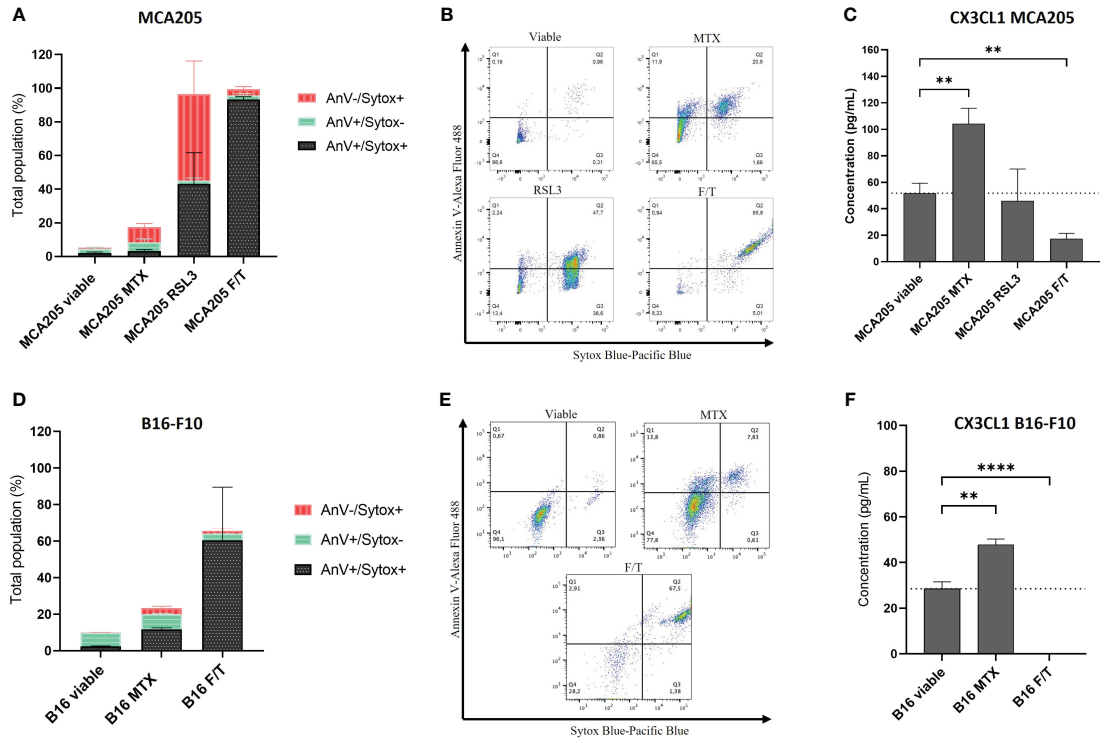

FIGURE 1
CX3CL1 release is associated with immunogenic apoptosis. **(A, D)** Cell death measured by flow cytometry of MCA205 cells **(A)** and B16-F10 cells **(D)** treated with 2 µM or 8 µM MTX (MCA205 and B16-F10 respectively), 2.5 µM RSL3, or three cycles of F/T. Quantification was done by AnV and Sytox Blue staining. The values are the means ± SEM and represent three independent experiments. **(B, E)** Representative dot plots of the cell death measurement shown in **(A, D)**. **(C, F)** The concentration (pg/mL) of CX3CL1 measured in the supernatants of dying cells using Luminex xMAP technology. The values are the means ± SEM and represent three independent experiments. Statistical significance was calculated by one-way ANOVA followed by Tukey's multiple comparisons test: **p < 0.01, ****p < 0.0001. MTX, mitoxantrone; RSL3, RAS-lethal selective 3; F/T, freeze/thaw; AnV, Annexin-V; Sytox, Sytox Blue.

with rCX3CL1 alone (*i.e.*, without MTX-treated cancer cells) did not exhibit any effect (Supplementary Figure S1). These data indicate the importance of CX3CL1 secretion in establishing an effective immune response during immunogenic apoptosis, although this occurs only for an appropriate dose. Of note, the therapeutic effect of CX3CL1 during MTX treatment in MCA205 tumour-bearing mice decreased the tumour size but this decrease was not statistically significant (Supplementary Figure S2).

3.3 CX3CR1 is associated with increased CD8+ T cells and increased patient survival

To understand the relevance of CX3CL1 in human patients, a cohort of 98 SKCM patients was thoroughly screened utilising the publicly available TCGA dataset. We found that the presence of the receptor of CX3CL1, CX3CR1, was associated with a significantly higher five-year survival of melanoma patients (log-rank Mantel-Cox test, p = 0.04) (Figure 3A). Additionally, a late-weighted Fleming-Harrington test also showed a significant difference in survival (p=4.85e-03). Moreover, CX3CR1 was mainly associated with $CD8^+$ cytotoxic T cells (Figure 3B). Finally, a high expression level of CX3CR1 in melanoma patients was correlated with increased abundance of cytotoxic $CD8^+$ T-cells (Figure 3C). Taken together, the increase of CX3CL1 results in mobilisation and recruitment of CX3CR1-positive cells. A heightened abundance of CX3CR1 in melanoma patients, particularly associated with increased presence of $CD8^+$ T cells, was correlated with increased overall survival probability among the individuals with melanoma.

4 Discussion

We examined the secretion of CX3CL1 from MTX-treated cancer cells undergoing immunogenic apoptosis and its potential role as a mediator of anti-tumour immunity during ICD. In our study, CX3CL1 was released exclusively during apoptotic cell death induced by MTX in murine fibrosarcoma MCA205 and melanoma B16-F10 cells. Moreover, in prophylactic vaccination of mice, the addition of 1 ng or 10 ng of rCX3CL1 to non-immunogenic doses of dying/dead cancer cells significantly enhanced tumour-free survival and restored immunogenicity of the dying cancer cells. Furthermore, analysis of the TCGA-SKCM database of data from 98 melanoma patients revealed a significant correlation between increased CX3CR1 expression and the patients' improved overall survival probability. In addition, CX3CR1 was predominantly associated with increased abundance of $CD8^+$ T cells, with high

10.3389/fimmu.2024.1396349

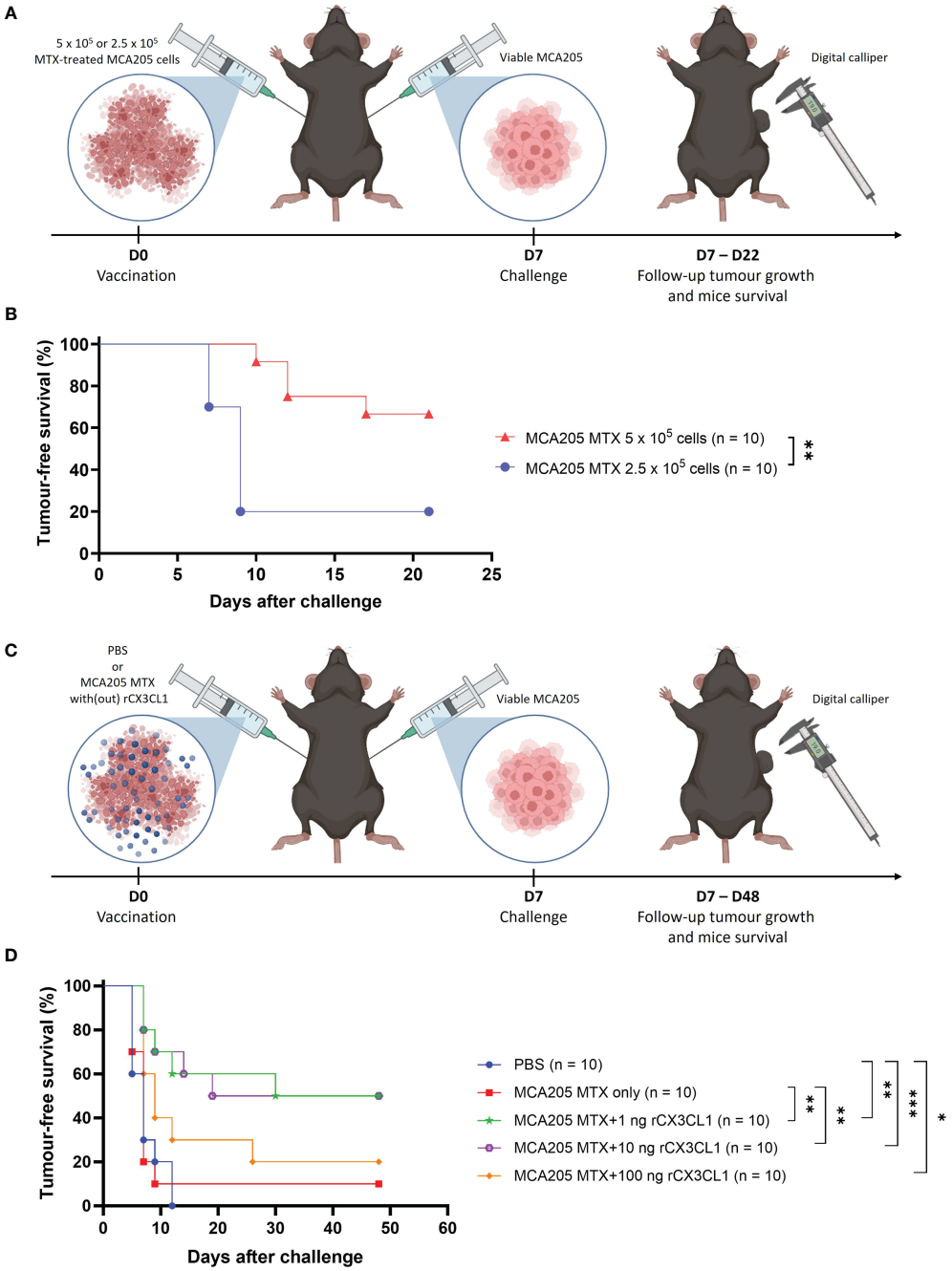

FIGURE 2
CX3CL1 reverts non-immunogenic apoptosis to ICD. **(A)** Schematic representation of the tumour prophylactic vaccination mouse model. On day 0, mice were vaccinated in the left flank with either 5 x 10^5 or 2.5 x 10^5 MTX-treated MCA205 cells. On day 7, the mice were challenged in the opposite flank with 10^5 viable cancer cells of the same type and tumour growth was monitored with a digital calliper. **(B)** Kaplan-Meier curve of the progression of tumour development over time. The reduction of dose of MTX-treated MCA205 cells from 5 x 10^5 cells to 2.5 x 10^5 cells significantly decreased tumour-free survival from 70% to 20%. The statistical differences were calculated by a log-rank (Mantel-Cox) test. Survival curves comparison: **p < 0.01. **(C)** Schematic representation of the tumour prophylactic vaccination mouse model. On day 0, mice were vaccinated in the left flank with either PBS, 2.5 x 10^5 MTX-treated MCA205 cells alone or 2.5 x 10^5 MTX-treated cells in combination with different doses of recombinant CX3CL1 (1 ng, 10 ng or 100 ng). On day 7, mice were challenged in the opposite flank with 10^5 viable cancer cells of the same type and afterwards tumour growth was followed with a digital calliper. **(D)** Kaplan-Meier curve of the progression of tumour development over time. The addition of 1 ng or 10 ng of rCX3CL1 to MTX-treated MCA205 cells significantly increased tumour-free survival from 10% (MCA205 MTX alone) to 50%. Interestingly, 100 ng of rCX3CL1 had no significant effect on tumour-free survival. The statistical differences were calculated by a log-rank (Mantel-Cox) test. Survival curves comparison: *p < 0.05, **p < 0.01, ***p < 0.001. ICD, immunogenic cell death; MTX, mitoxantrone; PBS, phosphate-buffered saline; rCX3CL1, recombinant CX3CL1.

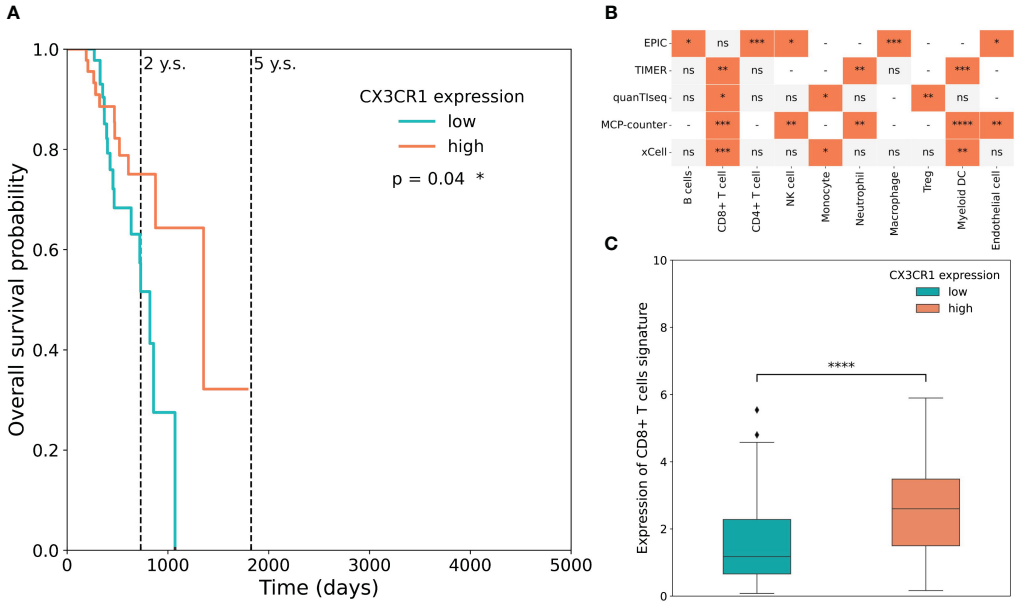

FIGURE 3
CX3CR1 is associated with increased CD8$^+$ T cells and increased patient survival probability. **(A)** The association between CX3CR1 expression and overall survival (OS) in the TCGA-SKCM dataset. OS curves were generated by setting median expression as cut-off. **(B)** Statistical analysis of cell infiltration stratified based on CX3CR1 expression in the TCGA-SKCM dataset. Cellular deconvolution was performed by five algorithms (EPIC, TIMER, quanTIseq, MCP-counter and xCell). The orange square means that the abundance of cells is significantly greater in patients with a high expression level of the receptor than in those with a low expression level. A grey square means that cell proportion does not differ statistically between groups, ns – not significant. A dash means that the method does not determine the proportions of the corresponding cells. Mann-Whitney U test, *p < 0.05, **p < 0.01, ***p < 0.001, ****p < 0.0001. **(C)** Boxplots of CD8+ T-cell signature expression stratified according to CX3CR1 expression in the TCGA-SKCM dataset. High (coral) and low (cyan) expression level groups were generated by setting median expression as cut-off. Mann-Whitney U test, *p < 0.05, **p < 0.01, ***p < 0.001, ****p < 0.0001, ns, not significant.

CX3CR1 expression levels correlating with increased CD8$^+$ T cell signature.

Cytokines and chemokines are recognised as crucial regulators in cancer development, cell dynamics within the tumour microenvironment, and intercellular signalling processes. These molecular mediators are also an integral part of ICD, acting as signals for cellular recruitment ("find me" and "eat me" signals), as well as for immune evasion ("keep out" and "don't eat me" signals) (1). The concept of ICD has gained significant attention as a novel immunotherapeutic strategy and is characterised by the release of DAMPs and pro-inflammatory cytokines/chemokines that can be detected by APCs via their corresponding PRRs (21). This drives the recruitment of APCs to the tumour site, facilitates recognition, engulfment, and subsequent processing and presentation of tumour antigens by APCs, and provides guidance for cytotoxic lymphocytes. CX3CL1 has been described as an important chemokine that can be implicated in the context of cancer, although controversies persist regarding the properties and activities of this chemokine due to its pro- and anti-cancer characteristics (25). But what is the role of CX3CL1 during ICD, in particular during immunogenic apoptosis?

In our experimental findings, we demonstrated that CX3CL1 was only detected in the supernatants of MTX-treated immunogenic apoptotic fibrosarcoma MCA205 and melanoma B16-F10 cells, and to a significantly lesser extent in the supernatants of viable cancer cells, RSL3-treated non-immunogenic late ferroptotic (6) cancer cells and non-immunogenic F/T accidentally necrotic cancer cells (Figures 1C, F). This indicates the exclusivity of CX3CL1 release during immunogenic apoptosis, suggesting its potential role in mediating immunogenicity of cancer cells undergoing apoptotic ICD. The receptor for CX3CL1, CX3CR1, is expressed on various immune cells, including NK cells, monocytes, dendritic cells, granulocytes, and CD3$^+$ T cells, stimulating their adhesion, retention, and transendothelial migration to sites characterised by strong inflammatory reactions (24, 57). It has been shown that sCX3CL1 also serves as a potent chemoattractant for these CX3CR1-expressing immune cells, enabling their chemotaxis towards the cancer niche and activation of their anti-cancer functions (24, 30, 58–61). Moreover, CX3CL1 expression is crucial for dendritic cell migration, maturation, and adhesion to T cells (58), while the presence of CX3CL1 on mature dendritic cells also activates resting NK cells (62). Hence, the release of CX3CL1 by the MTX-induced dying cancer cells (Figures 1C, F) may establish a gradient directed towards the tumour, presumably augmenting CX3CR1$^+$ immune cell migration along the gradient and activation of an anti-tumour immune cycle. Nevertheless, it is important to note that the upregulation of CX3CR1 expression may be associated with increased expression of this protein on the tumour cells, which may result in metastasis when the cancer cells enter the bloodstream and bind CX3CR1 on endothelial cells (25). However, due to the elevated concentration of CX3CL1, cancer cells expressing CX3CR1 might also be retained within the tumour and become the target of immune cells.

Furthermore, we demonstrated that the addition of CX3CL1 to a non-immunogenic dose of MTX-treated dying cancer cells is sufficient to elicit an immunogenic response in a tumour prophylactic mouse model, thereby revealing CX3CL1 as a power switch of immunogenic apoptosis induced by MTX (Figure 2D). Since it has been shown that CX3CL1 enhances efferocytosis of apoptotic thymocytes (34), it is conceivable that the presence of CX3CL1 in the prophylactic vaccine may lead to increased recruitment of phagocytes and clearance of dying cancer cells, consequently culminating in an overall improved anti-tumour immunity. However, the presence of CX3CL1 can also be associated with tolerogenic apoptosis (63). This underscores the nuanced and context-dependent role of CX3CL1 during cell death, where different factors intricately interact to determine the ultimate outcome. During immunogenic apoptosis, the secretion of other DAMPs fosters the anti-tumour effect, whereas during tolerogenic apoptosis DAMPs release is minimal, thus constraining the activation of an adaptive immune response. Therefore, it will be interesting to determine the differences in CX3CL1 secretion between tolerogenic apoptosis and immunogenic apoptosis, as the quantity of CX3CL1 secretion might be the key to shifting tolerogenic cell death towards an immunogenic form. In addition, it is important to note that prophylactic vaccination of mice with CX3CL1 alone (*i.e.*, without any MTX-treated cancer cells) had no effect on the tumour-free survival of the mice (Supplementary Figure S1), logically due to the absence of any antigens (antigenicity) or other DAMPs (adjuvanticity) during vaccination.

Remarkably, our findings from the tumour prophylactic vaccination experiments (Figure 2D) demonstrate that only lower doses (1 ng or 10 ng) of CX3CL1 exhibit an enhanced anti-tumour effect of ICD, whereas use of a high dose (100 ng) leads to almost complete absence of the anti-tumour effect (Figure 2D). This observation might indicate that the inherently inflammatory nature of CX3CL1 could contribute to hyperinflammation at higher doses, potentially promoting a pro-tumourigenic environment. Moreover, lack of sufficient DAMPs (due to a non-immunogenic dose of MTX-treated cancer cells) and excessive influx of immune cells (30, 58, 59) (due to a high CX3CL1 dose) might diminish activation of infiltrating immune cells, leading to an immunosuppressive phenotype and thus loss of the anti-tumour effect in the presence of a high dose of CX3CL1. Although gene therapy involving the transfer of CX3CL1 to cancer cells was demonstrated to induce a robust anti-cancer effect (64–66), we did not see a significant reduction in tumour size following co-treatment with CX3CL1 and MTX in the therapeutic mouse model (Supplementary Figure S2). It is conceivable that the supplementary CX3CL1 introduced alongside the already secreted CX3CL1 by the MTX-treated tumour cells resulted in an excessively high concentration of CX3CL1, which ceases to elicit an additive effect.

Of interest, analysis of RNA-seq data and corresponding patient clinical information of the TCGA-SKCM of 98 melanoma patients demonstrated a positive correlation between increased CX3CR1 levels and increased overall survival probability in the melanoma patients, along with a discernible $CD8^+$ T cell signature (Figure 3). CX3CR1 has been reported to be associated with $CD8^+$ T cells that respond to PD1 therapy while resisting cell death during chemotherapy (67). Moreover, CX3CR1-deficient mice injected with melanoma cells had increased tumour burden, cachexia, and defective anti-tumour responses (68). It has also been shown that an increase in CX3CL1 expression in the tumour is linked to improved prognosis of many cancer patients with breast carcinoma (69), colorectal cancer (70, 71) or lung adenocarcinoma (72), among other cancers (70–75).

In summary, our study indicates that CX3CL1 serves as a potent mediator of immunogenicity during immunogenic apoptosis induced by MTX. CX3CL1 is released by immunogenic apoptotic cancer cells regardless of the cancer cell type. Moreover, the addition of CX3CL1 to non-immunogenic doses of MTX-treated dying cancer cells in mouse prophylactic tumour vaccination models resulted in the activation of an adaptive immune response and effectively lengthened survival. In addition, an increase in CX3CR1 expression was correlated with increased overall survival probability of melanoma patients and increased $CD8^+$ T cell signature. Our data provide a rationale for exploiting CX3CL1 as a future adjuvant to render therapy-induced cell death immunogenic. The addition of CX3CL1 to other treatments could affect their immunogenicity, unleashing their full immunogenic potential during cell death in anti-cancer therapy. However, to achieve an overall favourable immunogenic outcome, accurate dosing of CX3CL1 might be of paramount importance.

Data availability statement

The original contributions presented in the study are included in the article/Supplementary Material, further inquiries can be directed to the corresponding author/s.

Ethics statement

Ethical approval was not required for the study involving humans in accordance with the local legislation and institutional requirements. Written informed consent to participate in this study was not required from the participants or the participants' legal guardians/next of kin in accordance with the national legislation and the institutional requirements. The animal study was approved by Ethics Committee of Ghent University. The study was conducted in accordance with the local legislation and institutional requirements.

Author contributions

FN: Data curation, Formal analysis, Investigation, Methodology, Validation, Writing – original draft, Writing – review & editing. RD: Data curation, Formal analysis, Investigation, Methodology, Writing – original draft, Writing – review & editing. OV: Formal analysis, Software, Writing – review & editing. IE: Writing – review & editing. MS: Writing – review & editing. GD: Data curation, Writing – review & editing. TM: Writing – review & editing. MV: Writing – review & editing. OK: Writing – review & editing. EC: Writing – review & editing.

DK: Funding acquisition, Project administration, Resources, Supervision, Writing – review & editing.

Funding

The author(s) declare financial support was received for the research, authorship, and/or publication of this article. The CDIT laboratory (headed by DK) is supported from the Flanders Research Foundation (FWO) and the Belgian National Fund for Scientific Research (F.R.S.-FNRS) under the Excellence of Science (EOS) program (#40007488), FWO grant (#G016221N), two Special Research Fund (BOF) grants from Ghent University (#BOF/IOP/2022/033, #BOF23/GOA/029), IOF "PULSE" grant (#F2023/IOF-ConcepTT/033) and IOF "IMMUNO-FER-GUARD" grant (#F2023/IOF-ConcepTT/106) from Ghent University. RD holds a Ph.D. fellowship from FWO (#11E3123N). FN holds a Special Research Fund (BOF) fellowship from Ghent University (#BOF22/DOC/012). EC holds a Marie Sklodowska Curie (MSCA) post-doctoral fellowship (HORIZON-MSCA-2022 PF-01).

Acknowledgments

The authors gratefully acknowledge Frédéric Clement, Maarten Verdonckt and Sophie Vermaut of the Core Flow Cytometry (BOF/COR/2022/009) at Ghent University (Belgium) for the use and/or support on following technique/technology/experiment(s): BD LSR II flow cytometer and the BD LSR Fortessa flow cytometer. The authors also gratefully acknowledge Karlijn Debusschere of the Core ARTH Animal Facilities (BOF/COR/2022/007) at Ghent University (Belgium) for the use and/or support on the animal experiments. Figures were created with the use of Biorender.

Conflict of interest

The authors declare that the research was conducted in the absence of any commercial or financial relationships that could be construed as a potential conflict of interest.

The author(s) declared that they were an editorial board member of Frontiers, at the time of submission. This had no impact on the peer review process and the final decision.

Publisher's note

Supplementary material

The Supplementary Material for this article can be found online at: https://www.frontiersin.org/articles/10.3389/fimmu.2024.1396349/full#supplementary-material

References

1. Galluzzi L, Vitale I, Warren S, Adjemian S, Agostinis P, Martinez AB, et al. Consensus guidelines for the definition, detection and interpretation of immunogenic cell death. *J Immunother Cancer*. (2020) 8:e000337. doi: 10.1136/jitc-2019-000337

2. Casares N, Pequignot MO, Tesniere A, Ghiringhelli F, Roux S, Chaput N, et al. Caspase-dependent immunogenicity of doxorubicin-induced tumor cell death. *J Exp Med*. (2005) 202:1691–701. doi: 10.1084/jem.20050915

3. Aaes TL, Kaczmarek A, Delvaeye T, De Craene B, De Koker S, Heyndrickx L, et al. Vaccination with necroptotic cancer cells induces efficient anti-tumor immunity. *Cell Rep*. (2016) 15:274–87. doi: 10.1016/j.celrep.2016.03.037

4. Aaes TL, Verschuere H, Kaczmarek A, Heyndrickx L, Wiernicki B, Delrue I, et al. Immunodominant AH1 antigen-deficient necroptotic, but not apoptotic, murine cancer cells induce antitumor protection. *J Immunol*. (2020) 204:775–87. doi: 10.4049/jimmunol.1900072

5. Yatim N, Jusforgues-Saklani H, Orozco S, Schulz O, Barreira da Silva R, Reis e Sousa C, et al. RIPK1 and NF-κB signaling in dying cells determines cross-priming of CD8+ T cells. *Science*. (2015) 350:328–34. doi: 10.1126/science.aad0395

6. Efimova I, Catanzaro E, van der Meeren L, Turubanova VD, Hammad H, Mishchenko TA, et al. Vaccination with early ferroptotic cancer cells induces efficient antitumor immunity. *J Immunother Cancer*. (2020) 8:e001369. doi: 10.1136/jitc-2020-001369

7. Liu J, Zhu S, Zeng L, Li J, Klionsky DJ, Kroemer G, et al. DCN released from ferroptotic cells ignites AGER-dependent immune responses. *Autophagy*. (2022) 18:2036–49. doi: 10.1080/15548627.2021.2008692

8. Catanzaro E, Demuynck R, Naessens F, Galluzzi L, Krysko DV. Immunogenicity of ferroptosis in cancer: a matter of context? *Trends Cancer*. (2024) 10(5):407–16. doi: 10.1016/j.trecan.2024.01.013

9. Bommareddy PK, Zloza A, Rabkin SD, Kaufman HL. Oncolytic virus immunotherapy induces immunogenic cell death and overcomes STING deficiency in melanoma. *Oncoimmunology*. (2019) 8:1591875. doi: 10.1080/2162402X.2019.1591875

10. Obeid M, Tesniere A, Ghiringhelli F, Fimia GM, Apetoh L, Perfettini JL, et al. Calreticulin exposure dictates the immunogenicity of cancer cell death. *Nat Med*. (2007) 13:54–61. doi: 10.1038/nm1523

11. Zhou H, Tu C, Yang P, Li J, Kepp O, Li H, et al. Carbon ion radiotherapy triggers immunogenic cell death and sensitizes melanoma to anti-PD-1 therapy in mice. *OncoImmunology*. (2022) 11:2057892. doi: 10.1080/2162402X.2022.2057892

12. Frey B, Rückert M, Deloch L, Rühle PF, Derer A, Fietkau R, et al. Immunomodulation by ionizing radiation-impact for design of radio-immunotherapies and for treatment of inflammatory diseases. *Immunol Rev*. (2017) 280:231–48. doi: 10.1111/imr.12572

13. Turubanova VD, Balalaeva IV, Mishchenko TA, Catanzaro E, Alzeibak R, Peskova NN, et al. Immunogenic cell death induced by a new photodynamic therapy based on photosens and photodithazine. *J Immunother Cancer*. (2019) 7:350. doi: 10.1186/s40425-019-0826-3

14. Kozutsumi Y, Segal M, Normington K, Gething MJ, Sambrook J. The presence of malfolded proteins in the endoplasmic reticulum signals the induction of glucose-regulated proteins. *Nature*. (1988) 332:462–4. doi: 10.1038/332462a0

15. Zhang R, Neighbors JD, Schell TD, Hohl RJ. Schweinfurthin induces ICD without ER stress and caspase activation. *OncoImmunology*. (2022) 11:2104551. doi: 10.1080/2162402X.2022.2104551

16. Serrano-del Valle A, Anel A, Naval J, Marzo I. Immunogenic cell death and immunotherapy of multiple myeloma. *Front Cell Dev Biol*. (2019) 7:50. doi: 10.3389/fcell.2019.00050

17. Rufo N, Yang Y, De Vleeschouwer S, Agostinis P. The "Yin and yang" of unfolded protein response in cancer and immunogenic cell death. *Cells januari*. (2022) 11:2899. doi: 10.3390/cells11182899

18. Krysko DV, Demuynck R, Efimova I, Naessens F, Krysko O, Catanzaro E. *In vitro* veritas: from 2D cultures to organ-on-a-chip models to study immunogenic cell death in the tumor microenvironment. *Cells januari*. (2022) 11:3705. doi: 10.3390/cells11223705

19. Demuynck R, Efimova I, Naessens F, Krysko DV. Immunogenic ferroptosis and where to find it? *J Immunother Cancer*. (2021) 9:e003430. doi: 10.1136/jitc-2021-003430

20. Galluzzi L, Vitale I, Aaronson SA, Abrams JM, Adam D, Agostinis P, et al. Molecular mechanisms of cell death: recommendations of the Nomenclature Committee on Cell Death 2018. *Cell Death Differ*. (2018) 25:486–541. doi: 10.1038/s41418-017-0012-4

21. Krysko DV, Garg AD, Kaczmarek A, Krysko O, Agostinis P, Vandenabeele P. Immunogenic cell death and DAMPs in cancer therapy. *Nat Rev Cancer*. (2012) 12:860–75. doi: 10.1038/nrc3380

22. Galluzzi L, Buqué A, Kepp O, Zitvogel L, Kroemer G. Immunogenic cell death in cancer and infectious disease. *Nat Rev Immunol*. (2017) 17:97–111. doi: 10.1038/nri.2016.107

23. Pan Y, Lloyd C, Zhou H, Dolich S, Deeds J, Gonzalo JA, et al. Neurotactin, a membrane-anchored chemokine upregulated in brain inflammation. *Nature*. (1997) 387:611–7. doi: 10.1038/42491

24. Imai T, Hieshima K, Haskell C, Baba M, Nagira M, Nishimura M, et al. Identification and molecular characterization of fractalkine receptor CX3CR1, which mediates both leukocyte migration and adhesion. *Cell*. (1997) 91:521–30. doi: 10.1016/S0092-8674(00)80438-9

25. Korbecki J, Simińska D, Kojder K, Grochans S, Gutowska I, Chlubek D, et al. Fractalkine/CX3CL1 in neoplastic processes. *Int J Mol Sci*. (2020) 21:3723. doi: 10.3390/ijms21103723

26. Haskell CA, Cleary MD, Charo IF. Molecular uncoupling of fractalkine-mediated cell adhesion and signal transduction: RAPID FLOW ARREST OF CX3CR1-EXPRESSING CELLS IS INDEPENDENT OF G-PROTEIN ACTIVATION *. *J Biol Chem*. (1999) 274:10053–8. doi: 10.1074/jbc.274.15.10053

27. Jung S, Aliberti J, Graemmel P, Sunshine MJ, Kreutzberg GW, Sher A, et al. Analysis of fractalkine receptor CX3CR1 function by targeted deletion and green fluorescent protein reporter gene insertion. *Mol Cell Biol*. (2000) 20:4106–14. doi: 10.1128/MCB.20.11.4106-4114.2000

28. Garton KJ, Gough PJ, Blobel CP, Murphy G, Greaves DR, Dempsey PJ, et al. Tumor necrosis factor-α-converting enzyme (ADAM17) mediates the cleavage and shedding of fractalkine (CX3CL1) *. *J Biol Chem*. (2001) 276:37993–8001. doi: 10.1074/jbc.M106434200

29. Dichmann S, Herouy Y, Purlis D, Rheinen H, Gebicke-Härter P, Norgauer J. Fractalkine induces chemotaxis and actin polymerization in human dendritic cells. *Inflamm Res*. (2001) 50:529–33. doi: 10.1007/PL00000230

30. Truman LA, Ford CA, Pasikowska M, Pound JD, Wilkinson SJ, Dumitriu IE, et al. CX3CL1/fractalkine is released from apoptotic lymphocytes to stimulate macrophage chemotaxis. *Blood*. (2008) 112:5026–36. doi: 10.1182/blood-2008-06-162404

31. Bazan JF, Bacon KB, Hardiman G, Wang W, Soo K, Rossi D, et al. A new class of membrane-bound chemokine with a CX3C motif. *Nature*. (1997) 385:640–4. doi: 10.1038/385640a0

32. Sokolowski JD, Chabanon-Hicks CN, Han CZ, Heffron DS, Mandell JW. Fractalkine is a "find-me" signal released by neurons undergoing ethanol-induced apoptosis. *Front Cell Neurosci*. (2014) 8:360. doi: 10.3389/fncel.2014.00360

33. Peter C, Waibel M, Radu CG, Yang LV, Witte ON, Schulze-Osthoff K, et al. Migration to apoptotic "Find-me" Signals is mediated via the phagocyte receptor G2A *. *J Biol Chem*. (2008) 283:5296–305. doi: 10.1074/jbc.M706586200

34. Miksa M, Amin D, Wu R, Dong W, Ravikumar TS, Wang P. Fractalkine-induced MFG-E8 leads to enhanced apoptotic cell clearance by macrophages. *Mol Med*. (2007) 13:553–60. doi: 10.2119/2007-00019.Miksa

35. Tsai WH, Chang SC, Lin YC, Hsu HC. CX3CL1(+) microparticles-induced MFG-E8 enhances apoptotic cell clearance by alveolar macrophages. *Cells*. (2021) 10:2583. doi: 10.3390/cells10102583

36. Tang J, Chen Y, Cui R, Li D, Xiao L, Lin P, et al. Upregulation of fractalkine contributes to the proliferative response of prostate cancer cells to hypoxia via promoting the G1/S phase transition. *Mol Med Rep*. (2015) 12:7907–14. doi: 10.3892/mmr.2015.4438

37. Tardáguila M, Mira E, García-Cabezas MA, Feijoo AM, Quintela-Fandino M, Azcoitia I, et al. CX3CL1 promotes breast cancer via transactivation of the EGF pathway. *Cancer Res*. (2013) 73:4461–73. doi: 10.1158/0008-5472.CAN-12-3828

38. Wang H, Cai J, Du S, Guo Z, Xin B, Wang J, et al. Fractalkine/CX3CR1 induces apoptosis resistance and proliferation through the activation of the AKT/NF-κB cascade in pancreatic cancer cells. *Cell Biochem Funct*. (2017) 35:315–26. doi: 10.1002/cbf.3278

39. Liu P, Liang Y, Jiang L, Wang H, Wang S, Dong J. CX3CL1/fractalkine enhances prostate cancer spinal metastasis by activating the Src/FAK pathway. *Int J Oncol*. (2018) 53:1544–56. doi: 10.3892/ijo

40. Gurler Main H, Xie J, Muralidhar GG, Elfituri O, Xu H, Kajdacsy-Balla AA, et al. Emergent role of the fractalkine axis in dissemination of peritoneal metastasis from epithelial ovarian carcinoma. *Oncogene*. (2017) 36:3025–36. doi: 10.1038/onc.2016.456

41. Liu JF, Tsao YT, Hou CH. Fractalkine/CX3CL1 induced intercellular adhesion molecule-1-dependent tumor metastasis through the CX3CR1/PI3K/Akt/NF-κB pathway in human osteosarcoma. *Oncotarget*. (2016) 8:54136–48. doi: 10.18632/oncotarget.11250

42. Liang Y, Yi L, Liu P, Jiang L, Wang H, Hu A, et al. CX3CL1 involves in breast cancer metastasizing to the spine via the Src/FAK signaling pathway. *J Cancer*. (2018) 9:3603–12. doi: 10.7150/jca.26497

43. Showalter A, Limaye A, Oyer JL, Igarashi R, Kittipatarin C, Copik AJ, et al. Cytokines in immunogenic cell death: Applications for cancer immunotherapy. *Cytokine*. (2017) 97:123–32. doi: 10.1016/j.cyto.2017.05.024

44. Tajbakhsh A, Yousefi F, Abedi SM, Rezaee M, Savardashtaki A, Teng Y, et al. The cross-talk between soluble "Find me" and "Keep out" signals as an initial step in regulating efferocytosis. *J Cell Physiol*. (2022) 237:3113–26. doi: 10.1002/jcp.30770

45. Sukkurwala AQ, Adjemian S, Senovilla L, Michaud M, Spaggiari S, Vacchelli E, et al. Screening of novel immunogenic cell death inducers within the NCI Mechanistic Diversity Set. *OncoImmunology*. (2014) 3:e28473. doi: 10.4161/onci.28473

46. Sturm G, Finotello F, Petitprez F, Zhang JD, Baumbach J, Fridman WH, et al. Comprehensive evaluation of transcriptome-based cell-type quantification methods for immuno-oncology. *Bioinformatics*. (2019) 35:i436–45. doi: 10.1093/bioinformatics/btz363

47. Racle J, de Jonge K, Baumgaertner P, Speiser DE, Gfeller D. Simultaneous enumeration of cancer and immune cell types from bulk tumor gene expression data. *eLife*. (2017) 6:e26476. doi: 10.7554/eLife.26476.049

48. Li B, Severson E, Pignon JC, Zhao H, Li T, Novak J, et al. Comprehensive analyses of tumor immunity: implications for cancer immunotherapy. *Genome Biol*. (2016) 17:174. doi: 10.1186/s13059-016-1028-7

49. Finotello F, Mayer C, Plattner C, Laschober G, Rieder D, Hackl H, et al. Molecular and pharmacological modulators of the tumor immune contexture revealed by deconvolution of RNA-seq data. *Genome Med*. (2019) 11:34. doi: 10.1186/s13073-019-0638-6

50. Becht E, Giraldo NA, Lacroix L, Buttard B, Elarouci N, Petitprez F, et al. Estimating the population abundance of tissue-infiltrating immune and stromal cell populations using gene expression. *Genome Biol*. (2016) 17:218. doi: 10.1186/s13059-016-1070-5

51. Aran D, Hu Z, Butte AJ. xCell: digitally portraying the tissue cellular heterogeneity landscape. *Genome Biol*. (2017) 18:220. doi: 10.1186/s13059-017-1349-1

52. Ramon J, Engelen Y, De Keersmaecker H, Goemaere I, Punj D, Mejía Morales J, et al. Laser-induced vapor nanobubbles for B16-F10 melanoma cell killing and intracellular delivery of chemotherapeutics. *J Control Release*. (2024) 365:1019–36. doi: 10.1016/j.jconrel.2023.12.006

53. Gamrekelashvili J, Ormandy LA, Heimesaat MM, Kirschning CJ, Manns MP, Korangy F, et al. Primary sterile necrotic cells fail to cross-prime CD8+ T cells. *OncoImmunology*. (2012) 1:1017–26. doi: 10.4161/onci.21098

54. Vedunova M, Turubanova V, Vershinina O, Savyuk M, Efimova I, Mishchenko T, et al. DC vaccines loaded with glioma cells killed by photodynamic therapy induce Th17 anti-tumor immunity and provide a four-gene signature for glioma prognosis. *Cell Death Dis*. (2022) 13:1–19. doi: 10.1038/s41419-022-05514-0

55. Ubellacker JM, Tasdogan A, Ramesh V, Shen B, Mitchell EC, Martin-Sandoval MS, et al. Lymph protects metastasizing melanoma cells from ferroptosis. *Nature*. (2020) 585:113–8. doi: 10.1038/s41586-020-2623-z

56. Gagliardi M, Cotella D, Santoro C, Corà D, Barlev NA, Piacentini M, et al. Aldo-keto reductases protect metastatic melanoma from ER stress-independent ferroptosis. *Cell Death Dis*. (2019) 10:1–15. doi: 10.1038/s41419-019-2143-7

57. Johnson LA, Jackson DG. The chemokine CX3CL1 promotes trafficking of dendritic cells through inflamed lymphatics. *J Cell Sci*. (2013) 126:5259–70. doi: 10.1242/jcs.135343

58. Guo J, Zhang M, Wang B, Yuan Z, Guo Z, Chen T, et al. Fractalkine transgene induces T-cell-dependent antitumor immunity through chemoattraction and activation of dendritic cells. *Int J Cancer*. (2003) 103:212–20. doi: 10.1002/ijc.10816

59. Guo J, Chen T, Wang B, Zhang M, An H, Guo Z, et al. Chemoattraction, adhesion and activation of natural killer cells are involved in the antitumor immune response induced by fractalkine/CX3CL1. *Immunol Lett*. (2003) 89:1–7. doi: 10.1016/S0165-2478(03)00101-9

60. Foussat A, Coulomb-L'Hermine A, Gosling J, Krzysiek R, Durand-Gasselin I, Schall T, et al. Fractalkine receptor expression by T lymphocyte subpopulations and in *vivo* production of fractalkine in human. *Eur J Immunol*. (2000) 30:87–97. doi: 10.1002/(ISSN)1521-4141

61. Lavergne E, Combadière B, Bonduelle O, Iga M, Gao JL, Maho M, et al. Fractalkine mediates natural killer-dependent antitumor responses in vivo1. *Cancer Res*. (2003) 63:7468–74.

62. Pallandre JR, Krzewski K, Bedel R, Ryffel B, Caignard A, Rohrlich PS, et al. Dendritic cell and natural killer cell cross-talk: a pivotal role of CX3CL1 in NK cytoskeleton organization and activation. *Blood*. (2008) 112:4420–4. doi: 10.1182/blood-2007-12-126888

63. Garg AD, Martin S, Golab J, Agostinis P. Danger signalling during cancer cell death: origins, plasticity and regulation. *Cell Death Differ*. (2014) 21:26–38. doi: 10.1038/cdd.2013.48

64. Tang L, Hu HD, Hu P, Lan YH, Peng ML, Chen M, et al. Gene therapy with CX3CL1/Fractalkine induces antitumor immunity to regress effectively mouse hepatocellular carcinoma. *Gene Ther*. (2007) 14:1226–34. doi: 10.1038/sj.gt.3302959

65. Kee JY, Arita Y, Shinohara K, Ohashi Y, Sakurai H, Saiki I, et al. Antitumor immune activity by chemokine CX3CL1 in an orthotopic implantation of lung cancer model in *vivo*. *Mol Clin Oncol*. (2013) 1:35–40. doi: 10.3892/mco.2012.30

66. Xin H, Kikuchi T, Andarini S, Ohkouchi S, Suzuki T, Nukiwa T, et al. Antitumor immune response by CX3CL1 fractalkine gene transfer depends on both NK and T cells. *Eur J Immunol*. (2005) 35:1371–80. doi: 10.1002/eji.200526042

67. Yan Y, Cao S, Liu X, Harrington SM, Bindeman WE, Adjei AA, et al. CX3CR1 identifies PD-1 therapy–responsive CD8+ T cells that withstand chemotherapy during cancer chemoimmunotherapy. *JCI Insight*. (2018) 3:e97828. doi: 10.1172/jci.insight.97828

68. Yu YRA, Fong AM, Combadiere C, Gao JL, Murphy PM, Patel DD. Defective antitumor responses in CX3CR1-deficient mice. *Int J Cancer*. (2007) 121:316–22. doi: 10.1002/ijc.22660

69. Park MH, Lee JS, Yoon JH. High expression of CX3CL1 by tumor cells correlates with a good prognosis and increased tumor-infiltrating CD8+ T cells, natural killer cells, and dendritic cells in breast carcinoma. *J Surg Oncol*. (2012) 106:386–92. doi: 10.1002/jso.23095

70. Ohta M, Tanaka F, Yamaguchi H, Sadanaga N, Inoue H, Mori M. The high expression of Fractalkine results in a better prognosis for colorectal cancer patients. *Int J Oncol*. (2005) 26:41–7. doi: 10.3892/ijo

71. Erreni M, Siddiqui I, Marelli G, Grizzi F, Bianchi P, Morone D, et al. The fractalkine-receptor axis improves human colorectal cancer prognosis by limiting tumor metastatic dissemination. *J Immunol*. (2016) 196:902–14. doi: 10.4049/jimmunol.1501335

72. Liu J, Li Y, Zhu X, Li Q, Liang X, Xie J, et al. Increased CX3CL1 mRNA expression level is a positive prognostic factor in patients with lung adenocarcinoma. *Oncol Lett*. (2019) 17:4877–90. doi: 10.3892/ol

73. Hyakudomi M, Matsubara T, Hyakudomi R, Yamamoto T, Kinugasa S, Yamanoi A, et al. Increased expression of fractalkine is correlated with a better prognosis and an increased number of both CD8+ T cells and natural killer cells in gastric adenocarcinoma. *Ann Surg Oncol*. (2008) 15:1775–82. doi: 10.1245/s10434-008-9876-3

74. Ren F, Zhao Q, Huang L, Zheng Y, Li L, He Q, et al. The R132H mutation in IDH1 promotes the recruitment of NK cells through CX3CL1/CX3CR1 chemotaxis and is correlated with a better prognosis in gliomas. *Immunol Cell Biol*. (2019) 97:457–69. doi: 10.1111/imcb.12225

75. Matsubara T, Ono T, Yamanoi A, Tachibana M, Nagasue N. Fractalkine-CX3CR1 axis regulates tumor cell cycle and deteriorates prognosis after radical resection for hepatocellular carcinoma. *J Surg Oncol*. (2007) 95:241–9. doi: 10.1002/jso.20642

frontiers | Frontiers in Immunology

TYPE Original Research
PUBLISHED 15 July 2024
DOI 10.3389/fimmu.2024.1416443

OPEN ACCESS

EDITED BY
Shensi Shen,
Sichuan University, China

REVIEWED BY
Xiaoying Zhou,
Guangxi Medical University, China
Yajie Xiao,
The Chinese University of Hong Kong, Hong Kong SAR, China
Hualin Chen,
Peking Union Medical College Hospital (CAMS), China

*CORRESPONDENCE
Qiongying Zhang
zhangqiongying1993@163.com
Lechi Ye
lancetdream@126.com

†These authors have contributed equally to this work

RECEIVED 12 April 2024
ACCEPTED 28 June 2024
PUBLISHED 15 July 2024

CITATION
Zhu J, Zhang J, Lou Y, Zheng Y, Zheng X, Cen W, Ye L and Zhang Q (2024) Developing a machine learning-based prognosis and immunotherapeutic response signature in colorectal cancer: insights from ferroptosis, fatty acid dynamics, and the tumor microenvironment.
Front. Immunol. 15:1416443.
doi: 10.3389/fimmu.2024.1416443

Developing a machine learning-based prognosis and immunotherapeutic response signature in colorectal cancer: insights from ferroptosis, fatty acid dynamics, and the tumor microenvironment

Junchang Zhu[1†], Jinyuan Zhang[1†], Yunwei Lou[2†], Yijie Zheng[1], Xuzhi Zheng[1], Wei Cen[1], Lechi Ye[1*] and Qiongying Zhang[3*]

[1]Department of Colorectal and Anal Surgery, The First Affiliated Hospital of Wenzhou Medical University, Wenzhou, China, [2]Department of Gastroenterology, The First Affiliated Hospital of Wenzhou Medical University, Wenzhou, China, [3]Department of Pathology, The First Affiliated Hospital of Wenzhou Medical University, Wenzhou, China

Instruction: Colorectal cancer (CRC) poses a challenge to public health and is characterized by a high incidence rate. This study explored the relationship between ferroptosis and fatty acid metabolism in the tumor microenvironment (TME) of patients with CRC to identify how these interactions impact the prognosis and effectiveness of immunotherapy, focusing on patient outcomes and the potential for predicting treatment response.

Methods: Using datasets from multiple cohorts, including The Cancer Genome Atlas (TCGA) and Gene Expression Omnibus (GEO), we conducted an in-depth multi-omics study to uncover the relationship between ferroptosis regulators and fatty acid metabolism in CRC. Through unsupervised clustering, we discovered unique patterns that link ferroptosis and fatty acid metabolism, and further investigated them in the context of immune cell infiltration and pathway analysis. We developed the FeFAMscore, a prognostic model created using a combination of machine learning algorithms, and assessed its predictive power for patient outcomes and responsiveness to treatment. The FeFAMscore signature expression level was confirmed using RT-PCR, and ACAA2 progression in cancer was further verified.

Results: This study revealed significant correlations between ferroptosis regulators and fatty acid metabolism-related genes with respect to tumor progression. Three distinct patient clusters with varied prognoses and immune cell infiltration were identified. The FeFAMscore demonstrated superior prognostic accuracy over existing models, with a C-index of 0.689 in the training cohort and values ranging from 0.648 to 0.720 in four independent validation cohorts. It also responses to immunotherapy and chemotherapy, indicating a sensitive response of special therapies (e.g., anti-PD-1, anti-CTLA4, osimertinib) in high FeFAMscore patients.

Conclusion: Ferroptosis regulators and fatty acid metabolism-related genes not only enhance immune activation, but also contribute to immune escape. Thus, the FeFAMscore, a novel prognostic tool, is promising for predicting both the prognosis and efficacy of immunotherapeutic strategies in patients with CRC.

KEYWORDS

ferroptosis, fatty acid metabolism, TME, colorectal cancer, immunotherapy, machine learning

1 Introduction

Colorectal cancer (CRC) is one of the most prevalent malignant tumors of the digestive system. According to the American Cancer Society, approximately 81,860 patients with CRC were diagnosed and 28,470 deaths occurred in the United States of America in 2023, causing serious problems for patients and public health (1). Although endoscopic screening has reduced the mortality and morbidity rates of CRC in recent years, and recurrence and metastasis remain major challenges (2). Currently, primary treatments for CRC include surgery, chemotherapy, and radiotherapy. Nevertheless, advances in immunotherapies, including anti-PD-1, anti-PD-L1, and anti-CTLA4 treatments, have presented a new and promising therapeutic paradigm for CRC with significant potential efficacy (3). For instance, the successful anti-PD-1 application in patients with CRC and mismatch repair deficiency (dMMR) or high microsatellite instability (MSI-H) significantly causes progression-free survival in CRC (4, 5). A new combination of radiotherapy and immunotherapy promotes robust antitumor immune priming (6, 7). However, these methodologies face constraints arising from spatiotemporal heterogeneity, moderate precision, or limited representation of population subsets (8–10). Consequently, in the context of personalized treatment paradigms, the identification of robust biomarkers is essential for optimizing prognosis and enhancing the efficacy of drug therapies for CRC.

Ferroptosis, driven by biochemical and genetic components, is a programmed cell death pathway reliant on iron and activated by lipid peroxide buildup on cellular membranes. Its involvement extends to tumor advancement and therapeutic responses across various malignancies and is often intertwined with reactive oxygen species (ROS) that participate in cancer-related pathways (10). Fatty acid metabolism is a crucial cellular process that transforms nutrients into metabolic intermediates used for membrane synthesis, energy reservation, and signaling molecule production. This process has garnered significant attention as a potential target for cancer therapy, particularly because it is associated with regulatory and CD8+ T cells (11–13). Glutathione peroxidase 4 (GPx4) and prolyl hydroxylase-3 (PHD3) represent significant regulators of ferroptosis and fatty acid metabolism, respectively, emphasizing the potential role of both in immunotherapy (14, 15). Recent studies indicated a significant association between fatty acid metabolism and ferroptosis. Microsomal triglyceride transfer protein (MTTP)expression increases in the body during fatty acid metabolism, which inhibits ferroptosis and decreases the density of chemotherapy (16). Similar results were observed for phospholipids containing a single polyunsaturated fatty acyl tail (PL-PUFA1s), which are also strongly correlated with ferroptosis (17). Additionally, cytochrome P450 1B1 (CYP1B1) and cyclin-dependent kinase 1 (CDK1) degrade acyl-CoA synthetase long-chain family member 4 (ACSL4), who plays an essential role in fatty acid metabolism and inhibits ferroptosis, thereby inducing resistance to anti-PD-1 and oxaliplatin, respectively (18, 19). Thus, the fatty acid metabolism-related genes appear to regulate ferroptosis and function as intermediates. The relationship between ferroptosis regulators and fatty acid metabolism-related genes, which may significantly influence prognosis and drug resistance in colorectal cancer, has been less explored. The tumor microenvironment (TME), which consists of tumor cells, stromal cells, and immune cells, plays an irreplaceable role in the metastasis and tumor progression and also affects the efficacy of immune checkpoint blockade (ICB) treatment (20, 21). Considering the special relationship between ferroptosis and fatty acid metabolism regulators, a unique TME may induce novel metabolic pathways in CRC. Thus, the interactions between ferroptosis and fatty acid metabolism regulatory molecules should be explored in multicenter cohorts from a multi-omics perspective, including the TME, immunotherapy, and epigenetic mutations.

In this study, we conducted a thorough pan-cancer multi-omics analysis to examine the molecular correlations between ferroptosis and fatty acid metabolism regulators in 33 cancer types. By performing unsupervised clustering, we identified three distinct clusters related to ferroptosis and fatty acid metabolism based on the TME, gene expression, and biological functions. Utilizing a robust combination of 117 machine-learning algorithms, we developed the FeFAMscore, which demonstrated superior predictive performance in both the training cohort and four independent external validation cohorts. It also effectively exhibits potential in forecasting immunotherapy and chemotherapy drug sensitivity in CRC patients. Overall, the FeFAMscore is promising for the advancement of novel treatment strategies, fostering a nuanced and personalized approach to medicine.

2 Methods

2.1 Data acquisition and pre-processing

The workflow is illustrated in Supplementary Figure S1. The Gene Expression Omnibus (GEO) (https://www.ncbi.nlm.nih.gov/geo/) and The Cancer Genome Atlas (TCGA) (https://portal.gdc.cancer.gov/databases were used to obtain the CRC RNA expression profiles, in addition to the associated comprehensive clinical annotations, including TCGA-COAD, TCGA-READ, GSE17536, GSE17537, GSE29621, GSE38832, and GSE39582. The Meta-cohort and Train cohorts (TCGA-COAD, TCGA-READ, and GSE39582) were established and the batch effects were estimated using the "sva" package in R software. Additionally, three immunotherapy cohorts with different immunotherapy efficacies downloaded from the TIGER website (http://tiger.canceromics.org/), including IMVigor210 (anti-PD-L1), Braun (anti-PD-1), and PRJNA23709 (anti-PD-1 + anati-CTLA4) were investigated. The microarray data from the GEO were normalized and corrected background by the "impute" R package. The ferroptosis regulators and fatty acid metabolism-related genes investigated in this study were extracted from FerrDb (22) and MSigDB (https://www.gsea-msigdb.org/gsea/msigdb/) (Supplementary Table S1). Finally, 1448 patients with survival information were acquired from the database. The data of Copy Number Variation (CNV) is extracted from TCGA database in 33 cancers and analyzed by the "matfool" packages.

2.2 Unsupervised clustering of ferroptosis regulators and fatty acid metabolism-related genes

The tumor-related FeFAM genes were obtained from TCGA database using "limma" and "survival" packages in the R software. Univariate Cox analysis was used to filter the 50 prognosis genes in the training cohort based on $p<0.05$. Next, the training cohort was subjected to unsupervised clustering to identify distinct patterns. The potential groupings were delineated using K-means clustering analysis with varying cluster numbers ($k = 2–9$) (23). We then performed the "Nuclst" package to verify the most appropriate clusters with 28 criteria and repeated 1000 times on resample rate of 0.8 to validate the classification stability. Principal component analysis (PCA) was subsequently employed to validate the clustering results using the expression profiles of these genes. This analysis confirmed the co-expression patterns of ferroptosis regulators and fatty acid metabolism-associated genes.

2.3 Cell infiltration estimation

We evaluated the immune cell microenvironment using the CIBERSORT algorithm, EPIC algorithm, MCPCOUNTER algorithm, TIMER algorithm, quantiseq algorithm, and XCELL algorithm of the "IBOR" and "GSVA" R package. Single-sample gene set enrichment analysis (ssGSEA) algorithm was used to verify the results. Additionally, the TIDE algorithm (http://tide.dfci.harvard.edu/) was used to evaluate the tumor immune dysfunction and exclusion (TIDE) score, CAF, dysfunction and exclusion of immune cells, PD-L1, and cytotoxic T cells (CTL) score. A high TIDE score may reflect poor ICI efficacy.

2.4 Pathway enrichment analysis

To investigated the biological difference between three patterns and cancer-related pathways, we downloaded "h.all.v7.5.1.symbols.gmt" and "c2.cp.kegg.v7.4.symbols" from the MsigDB database (c2.cp.kegg.symbols), and analyzed using the GSVA program. We further explored the differences in cancer-, immune-, and metabolism-related patterns as reported previously (24–27). The pathways with the highest expression among the three patterns with $p<0.05$ were considered activated.

2.5 FeFAMscore prognostic model construction

To further explore the biofunction and prognostic value of FeFAM genes, we first randomly combined 10 machine learning algorithms, including random survival forest (RSF), elastic network (Enet), Ridge, Stepwise Cox, Lasso, CoxBoost, partial least squares regression for Cox (plsRcox), generalized boosted regression modelling (GBM), supervised principal components (SuperPC), and survival support vector machine (survival-SVM), as reported previously (28). Then, the training cohorts were input as the training group to the combined 117 algorithms, and each model was detected in four independent datasets (GSE17536, GSE17537, GSE29621, and GSE38832). Next, Harrell's concordance index (C-index) was calculated for each model across all validation cohorts using the FeFAMscore derived from the training cohorts. Based on the average C-index in all validation cohorts, we selected the optimal model and compared the FeFAMscore with those of 69 published models in the past decade, which proved its reliable and robust predictive power.

2.6 Cell culture

Normal colon mucosal epithelial cells (NCM460) and HCT116, DLD-1, and CACO2 cell lines were obtained from the Chinese Academy of Sciences (Shanghai, China), cultured in DMEM supplemented with 10% fetal bovine serum (both from Thermo Fisher Scientific, Waltham, MA, USA), and maintained under standard cell culture conditions (37°C, 5% CO_2) in a cell incubator.

2.7 RNA extraction and RT-qPCR

Cellular and tissue RNA was extracted using TRIzol reagent (R411-01, Vazyme, Nanjing, China), followed by reverse

transcription using HiScript III RT SuperMix (R323, Vazyme). Quantitative PCR analysis was performed using the Universal SYBR Green Fast qPCR Mix (ABclonal, Hong Kong, China, RK21203). The data were analyzed using the 2(−ΔΔCt) method, with GADPH serving as the internal control. The primer sequences are provided in Supplementary Table S1.

2.8 siRNA transfection

siRNA-ACAA2-1 or siRNA-ACAA2 (GenePharma, Shanghai, China) was used to silence the ACAA2 gene. The siRNA sequences were as follows: si-ACAA2-1 (sense: 5′-UGCUGAGACAGU GAUUGUATT-3′; antisense: 5′-UACAAUCACUGUCUCUCATT-3′), and si-ACAA2-2 (sense: 5′-GGGCACTGAAGAAAGCAGGA-3′; antisense: 5′-CGTGAACCAGGTGTGCAGTA-3′). Transfection was performed using Lipofectamine 3000 (Thermo Fisher Scientific) following the manufacturer's instructions.

2.9 Cell viability assay

CRC cell viability was evaluated using the Cell Counting Kit 8 (CCK-8, Dojindo, Japan). Briefly, 3000–5000 cells were seeded per well in 96-well plates. Subsequently, 100 µL medium containing 10 µL CCK-8 solution was added to each well and incubated at 37°C for 3 h. The absorbance at 450 nm was measured.

2.10 Transwell assay

HCT116 and CACO2 cell lines transfected with siRNAs targeting ACAA2 (si-ACAA2-1 and si-ACAA2-2) or non-targeting control siRNA (si-NC) were harvested, washed twice with PBS, and resuspended in DMEM. The suspended cells were then placed in the upper chamber of 24-well chambers equipped with 8 µm pore inserts.

2.11 Colony formation assay

To evaluate colony formation in the monolayer culture, 1000 cells were seeded in 6-well plates. Following two weeks of culture, the colonies were fixed and stained with 4% paraformaldehyde and 0.1% crystal violet for 30 min at room temperature.

2.12 Western blot

Protein concentration was determined using the BCA Protein Assay Kit (Thermo Fisher Scientific, USA). Samples containing 30 µg of protein were separated on a 12% SDS-PAGE gel and transferred onto a PVDF membrane. The membrane was blocked with 5% BSA for 2 hours and then incubated overnight at 4°C with the primary antibody. Afterward, the membranes were incubated for 1 hour with the secondary antibody and washed three times with TBST buffer. Antibody signals were detected using the ECL system (Bio-Rad, California, USA).

2.13 Immunotherapeutic response prediction

We predicted the immunotherapy response of the FeFAMscore by analyzing the expression of tumor mutational burden (TMB), TIDE score, and differences in pathway enrichment. Based on these results, we calculated the FeFAMscore of patients in the training cohort to explore the function of the FeFAMscore in immunotherapy. Subsequently, we used Subclass Mapping (Submap) to determine the relationship between high or low FeFAMscore groups and anti-PD-1 and anti-CTLA4 antibodies. In addition, we utilized immunotherapy cohorts with clinical response information to validate the immunotherapy response. The IMVigor210CoreBiologies R package was used to obtain transcriptome, survival, and immunotherapy efficacy data for the IMVigor210 cohort (29). The anti-PD-1 and anti-CTLA4 cohorts were validated using Braun and PRJNA23709.

2.14 Chemotherapeutic sensitivity prediction

The correlation with FeFAMscore and drug sensitivity was predicted by the GDSC and CTRP datasets with "oncoPredict" packages. The relation with gene expression and drug sensitivity was measured by the "Hmsic" package in R software.

2.15 Statistical analysis

Data processing and visualization were performed using R software (version 4.3.2) and GraphPad Prism 8.0, respectively. Group comparisons were performed using the Wilcoxon test for pairwise comparisons, while ANOVA and Kruskal–Wallis tests were used to assess variable distributions among multiple groups, considering normality assumptions. Categorical variables were analyzed using the chi-square and Fisher's exact tests. Correlations were determined using the Spearman and Pearson techniques. Survival disparities were evaluated using the Kaplan–Meier method and log-rank test. Statistical significance was set at $p<0.05$, and all p-values were two-tailed.

3 Result

3.1 Identification of novel correlations between ferroptosis and fatty acid metabolism regulators

To explore the relationship between cell death and metabolism, we investigated the crosstalk between ferroptosis-associated regulators and fatty acid metabolism-regulating genes. The 486

ferroptosis-associated genes derived from the FerrDb included markers, suppressors, and drivers (Supplementary Table S1). Meanwhile, 272 FAM genes were retained from the MSigDB database. Genome-wide omics data for 33 cancer types were retrieved from the TCGA database for analysis. The frequency of mutations in these genes was significantly correlated between ferroptosis and fatty acid metabolism in the tumors (Figure 1A). PCA was performed to measure the levels of ferroptosis-associated and FAM genes in the 33 cancer types database, then the Spearman's analysis further demonstrated a significant correlation between them (Supplementary Figure S1A). Interestingly, the COREAD database, with the largest number of patients, exhibiting a prominent association between them (R = -0.93) (Figures 1B, C). Consequently, to further explore the colorectal cancer, the top 10 mutations in ferroptosis-associated regulators and fatty acid genes were identified in 480 (95.98%) of 497 patients with COREAD. The highest mutation frequencies were detected in TP53 (67%), KRAS (44%), and PIK3CA (26%) (Supplementary Figure S2B). The exploration of copy number variation (CNV) alteration frequency showed a high incidence of CNV gains in the TCGA cohort, demonstrating the potential for therapy in CRC (Supplementary Figure S2C). The locations of FeFAM genes with CNVs on the chromosomes are marked in the Circle Map (Supplementary Figure S2C). Additionally, co-mutations were common among these genes (Supplementary Figures S2E, F).

Based on the analysis of results, we compared the CRC and normal samples from COREAD databases in TCGA, which finally identified 159 ferroptosis-associated and fatty acid metabolism-related genes according to logFC>1 and FDR <0.05 (Figure 1D). To counterbalance the implications between TCGA and GEO database, we enrolled COREAD database and GSE39582 and adopted the "sva" package to remove batch effects and extract relevant genes as the training cohort. A total of 50 genes were subsequently screened using univariate Cox regression analysis (P <0.05) of the FeFAM genes in the combined database (Supplementary Figure S2G). The KEGG analysis, depicted using a barplot, revealed enrichment of these genes in pathways such as "PPAR signaling pathway", "fatty acid degradation", "fatty acid metabolism", "propanoate metabolism", "tyrosine metabolism", and "p53 signaling pathway". Furthermore, GO analysis of molecular functions (MF), biological processes (BP), and cellular components (CC) highlighted their relevance in fatty acid metabolism, response to oxygen levels, and cancer pathways. (Figure 1E). Network analysis offered a holistic view of the prognostic implications and molecular interactions within the FeFAM framework (Figure 1F). Considering the discernible differences in the transcriptional profiles and the unique interplay between these molecules, dysregulation within the FeFAM network significantly contributes to CRC initiation and progression.

3.2 Discovery of novel FeFAM patterns through unsupervised clustering analysis

To elucidate the potential FeFAM phenotypes in CRC, we utilized K-means-based unsupervised clustering in the training cohort. The R package "ConsensusClusterPlus" was used to initially categorize the patients with CRC into k (k=2–9) FeFAM clusters (Figure 1G; Supplementary Figures S3A-K). The cumulative distribution function (CDF) curves, derived from the consensus score matrix and PAC statistics, elucidated the optimal number of clusters (k=3) across the entire training patient cohort. These clusters, denoted A, B, and C, exhibited discernible segregation patterns (Figure 1H). Nbclust testing, which included 28 criteria, yielded the same results (Supplementary Figure S3L). The PCA demonstrated a clear distinction between the three clusters (Figure 1I). The Kaplan–Meier curve showed that cluster C had better survival prognosis than clusters A and B (p<0.001) (Figure 1J). The expression of FeFAM genes also indicated the ability to differentiate between the three subtypes (Figure 1K).

3.3 TME characterization in different FeFAM patterns

The ssGSEA method, which simulates the entire tumor immune process, was first used to calculate tumor immune cell infiltration in the training cohorts to investigate the differences in the TME (Figure 2A). Next, six different algorithms, such as CIBERSORT, EPIC, MCPCOUNTER, TIMER, QuantiSeq, and XCELL, obtained the same results, verifying the crucial effects of FeFAM genes in the immune system (Supplementary Figure S4A). Meanwhile, according to the Spearman's correlation analysis, almost all FeFAM genes were significantly implicated in the immune microenvironment composition (Figure 2B). Ferroptosis-associated regulators, including ENPP2, CAV1, FABP4, PDK4, ADIPOQ, NOX4, COKN2A, CDO1, WWTR1, DDR2, CPEB1, and TIMP1, are preferentially associated with the most immunosuppressive cells, whereas FAM genes correlated with immune microenvironment activation. Furthermore, Spearman's analysis demonstrated significant co-expression of the Fe and FAM genes (Supplementary Figure S4B). Compared to FeFAM clusters B and C, FeFAM cluster A had a significantly worse prognosis. Analysis of gene signatures revealed an increased presence of immune cells exhibiting notable immunosuppressive functionality, macrophages, regulatory T cells (Tregs), and type 2 T helper cells, including within FeFAMA cluster A across all cohorts. Remarkably, CD4+ T cells, CD8+ T cells, neutrophils, dendritic cells, and natural killer (NK) cells were abundant in the FeFAM cluster A across nearly all the algorithms, suggesting that the immune cells within FeFAM cluster A may concurrently govern immune evasion and anti-tumor activities. Despite having similar prognoses, FeFAM clusters B and C exhibited contrasting levels of immune infiltration, implying that they may have different immunotherapeutic potentials. The XCELL and ESTIMATE algorithms also demonstrated high immune, stroma, and microenvironment scores in FeFAM clusters A and C (Supplementary Figure S4C). Consequently, FeFAM clusters A, B, and C were considered immune-excluded, immune-desert, and immune-activated clusters, respectively. To ensure stability of the results, the TIDE algorithm, which is commonly adopted to measure immune escape levels and ICD treatment efficacy, was

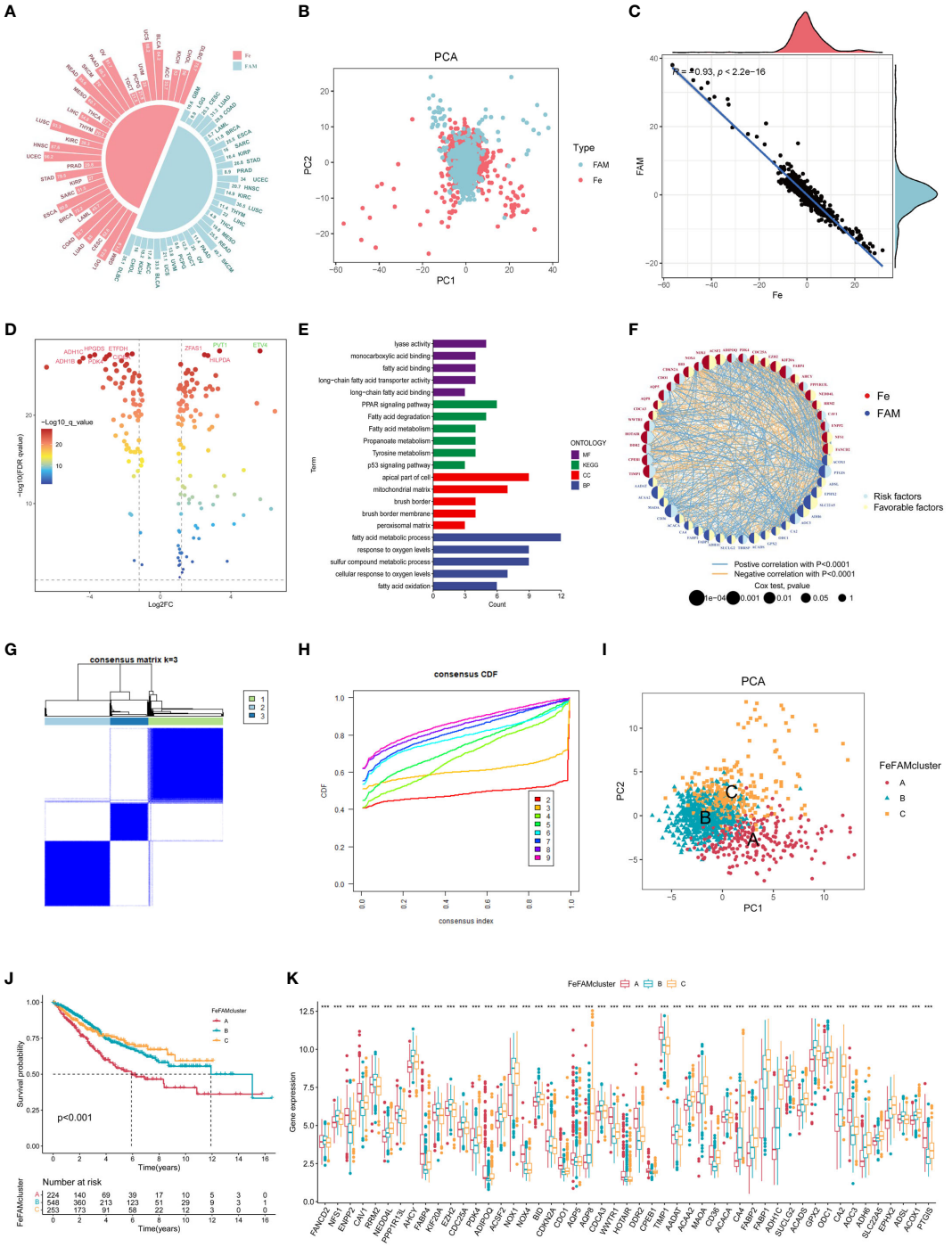

FIGURE 1
Landscape of genetic and relation of FeFAM regulators and discovery of novel FeFAM patterns. **(A)** Mutation frequency of FeFAM regulators in 33 types cancers in TCGA. **(B)** PCA of FeFAM regulators in the CRC. **(C)** Scatter plot showed the spearmen correlation of FeFAM regulators. **(D)** Volcano plot showed the differential FeFAM regulators in CRC. **(E)** KEGG and GO analyze of 50 OS-related FeFAM regulators. **(F)** Network showed the interactions among FeFAM regulators in CRC. **(G)** A The consensus score matrix of all samples when k = 3. **(H)** The CDF curves of consensus matrix for each k (indicated by colors). **(I)** Principal component (PC) analysis revealed remarkable difference between three FeFAM patterns from train cohort (n = 1029). **(J)** Kaplan-Meier curves of survival for three FeFAM patterns based on CRC patients from train cohort. **(K)** This boxplot demonstrates the expression variations in the FeFAM-related genes among three FeFAM patterns. The top portion represented Fisher's precise test. The lower portion indicated the Wilcoxon rank-sum test. ***p < 0.001. FeFAM, ferroptosis and fatty acid metabolism regulators.

10.3389/fimmu.2024.1416443

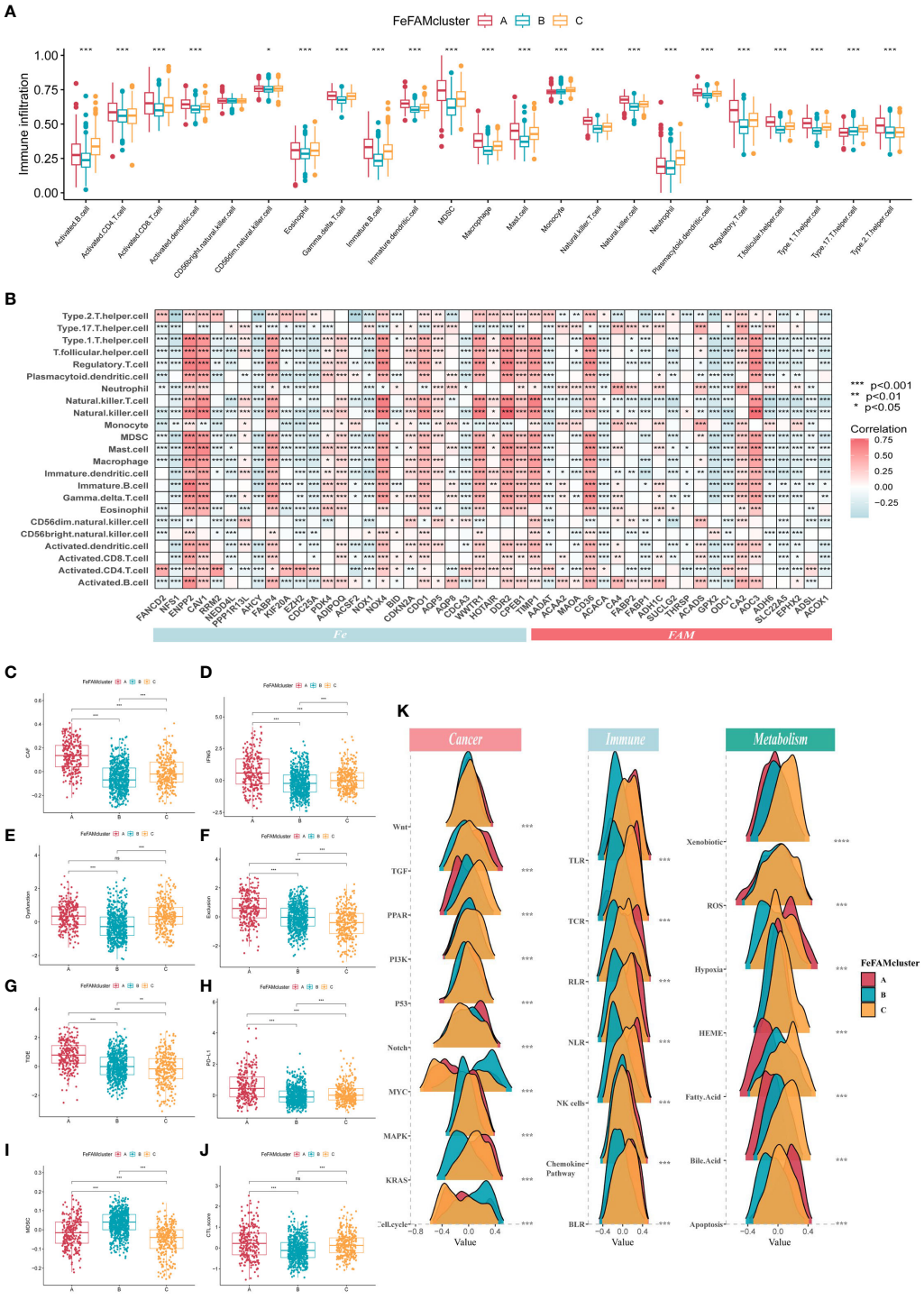

FIGURE 2
Characterization of tumor microenvironment, signing and immune pathways in different FeFAM patterns. **(A)** Characteristics of immune infiltrating cells in different FeFAMclusters. **(B)** Characteristics of immune infiltrating cells in different FeFAM regulators. **(C-J)** Box plots showed the significant difference in CAF **(C)**, IFNG **(D)**, Dyfunction **(E)**, Exclusion **(F)**, TIDE **(G)**, PD-L1 **(H)**, MDSC **(I)**, and CTL.score **(J)**. **(K)** The cancer-related, immune-related and metabolism-related pathways between the three FeFAM subtypes. * $p < 0.05$, ** $p < 0.01$, *** $p < 0.001$, ns, not significant. FeFAM, ferroptosis and fatty acid metabolism regulators.

used. We discovered that FeFAM cluster A showed the highest CAF, IFN, TIDE, PD-L1 and exclusion among the three clusters, consistent with the above analysis results and possibly attributed to immune escape (Figures 2C–J). Interestingly, although FeFAM cluster A had more MDSCs than FeFAM cluster C, their CTL.scores and dysfunction were similar, suggesting that activated ferroptosis and fatty acid pathways may inhibit intratumoral CD8+ T cell effector function and impair their anti-tumor ability, which was similar to previously reported results (12, 30–32). Above all, ferroptosis regulators may cooperate with fatty

acid metabolism-associated genes to contribute to a particular immune microenvironment, thereby presenting potential targets for immunotherapy.

3.4 Signaling and immune pathway differences between the FeFAM patterns

Utilizing the "gsva" package, we executed GSVA-enrichment experiments to investigate various cancer-related signaling pathways across the three patterns within the Hallmarker and KEGG pathways (Supplementary Figure S4D). The findings indicate that FeFAM cluster A was significantly enriched in immune- and tumor-related pathways, such as "apoptosis", "epithelial mesenchymal transition (EMT)", "inflammatory response", and "VEGF signaling pathway". The FeFAM clusters B and C are two distinct groups with specific associations in terms of their biological functions and metabolic pathways. FeFAM cluster B, for instance, is substantially associated with "DNA repair and replication", "protein export", and "spliceosome", while FeFAM cluster C is associated with the metabolic pathway "fatty acid metabolism", "linoleic acid metabolism", "nicotinate and nicotinamide metabolism" and "nitrogen metabolism". Consequently, we further investigated the carcinogen-signaling, immune-related, and metabolic pathways to compare the differences among the three patterns. Wnt, TGF, Notch, MAPK, KRAS, TLR, TCR, RLR, NK cells, chemokine pathway, hypoxia, and apoptosis were activated in cluster A. PPAR, PI3K, P53, xenobiotics, ROS, HEME, fatty acids, and bile acids were activated in cluster C, indicating that ferroptosis and fatty acid metabolism may be upgraded to improve prognosis and prevent immune escape (Figure 2K). These analyses provided additional evidence that FeFAM molecules regulate the immune microenvironment and facilitate immune evasion in patients with CRC through diverse signaling pathways. This underscores the potential of FeFAM as a promising target for immunotherapy.

3.5 Integrated construction and consistent prognostic value of the FeFAMscore

Based on the varying expression levels of FeFAM genes among the three patterns, we subjected the 50 FeFAM-related genes to our machine learning-based integrative approach to construct an FeFAM-related signature, termed the FeFAMscore. In the training cohort, 117 algorithms generated from a random permutation of 10 machine-learning algorithms were employed to compute the C-index using a 10-fold cross-validation framework. The model was subsequently evaluated across four cohorts to gauge its predictive efficacy and to determine its consistency across different datasets. Following this evaluation, the model with the highest average C-index among the validation cohorts was identified. Specifically, the combination of CoxBoost and StepCox (backward and both) yielded the highest average C-index of 0.689, establishing it as the optimal model (Figure 3A; Supplementary Table S2). Fifteen genes were first screened using the CoxBoost model and then subjected to backward Cox proportional hazards regression. A final set of 15 genes was identified, including KIF20A, ACSF2, NOX1, BID, AADAT, ACAA2, FABP1, CA2, SLC22A5, PPP1R13L, AQP5, HOTAIR, DDR2, TIMP1, and CD36 (Figure 3B). Subsequently, the FeFAM score for each patient was determined by employing the expression levels of 15 genes, which were weighted using the regression coefficients obtained from a Cox model (Figure 3B). Subsequently, all patients were dichotomized into high- and low-FeFAMScore groups. These 15 genes significantly distinguished high-risk individuals from low-risk individuals (Figures 3C–H). Patients categorized into the high FeFAMscore group exhibited significantly poorer overall survival (OS) compared to those in the low FeFAMscore group, as determined by Kaplan–Meier survival analysis in both the combined training (N=1029, P<0.001) and four validation datasets: GSE17536 (N=177, P<0.001), GSE17537 (N=55, P=0.003), GSE29621 (N=65, P=0.007), and GSE38832 (N=122, P<0.001). A similar outcome was observed in the meta-cohort (N=1448), thereby affirming the predictive accuracy and reliability of the model. An alluvial diagram illustrates the correlation between FeFAMcluster and FeFAMscore (Figure 3I).

3.6 Consistent prognostic value of FeFAMscore

Receiver operating characteristic (ROC) curve analysis was conducted to evaluate the discriminative ability of the FeFAMscores. In the training cohort, the areas under the ROC curve (AUC) for 1-, 3-, and 5-year survival were 0.701, 0.712, and 0.668, respectively. Furthermore, excellent results were also indicated in the test cohorts, including 0.738, 0.718, and 0.64 in GSE17536; 0.729, 0.684, and 0.687 in GSE17537; 0.769, 0.670, and 0.649 in GSE29621; and 0.799, 0.773, and 0.708 in GSE38832 (Figure 4A). The meta-cohort of these patients showed AUC values of 0.687, 0.683, and 0.644, indicating that the FeFAMscore model is predictive and reliable in multiple independent CRC cohorts (Figure 4A).

The C-index [95% confidence interval] was 0.67 [0.652–0.688], 0.648 [0.617–0.679], 0.684 [0.639–0.807], 0.666 [0.614–0.790], 0.720 [0.649–0.804], 0.649 [0.646–0.711] in the four independent validation cohorts and meta-cohorts, respectively (Figure 4B). To predict patient prognosis, clinical characteristics including age, sex, T stage, N stage, M stage, and stage are widely acknowledged. Therefore, the C-index was applied to measure the predictive accuracy between the FeFAMscore and clinical traits in the training and four independent validation cohorts. The FeFAMscore exhibited significantly higher predictive accuracy than other clinical traits in the training, GSE17536, GSE17537, and GSE38832 cohorts (Figures 4C–G). In contrast, the performance of the FeFAMscore in GSE29621 cohort was similar to that of the M stage and stages, which may have been due to the small sample size and data bias. These results indicate that FeFAMScore may be a prospective alternative biomarker for predicting survival risk in clinical practice.

10.3389/fimmu.2024.1416443

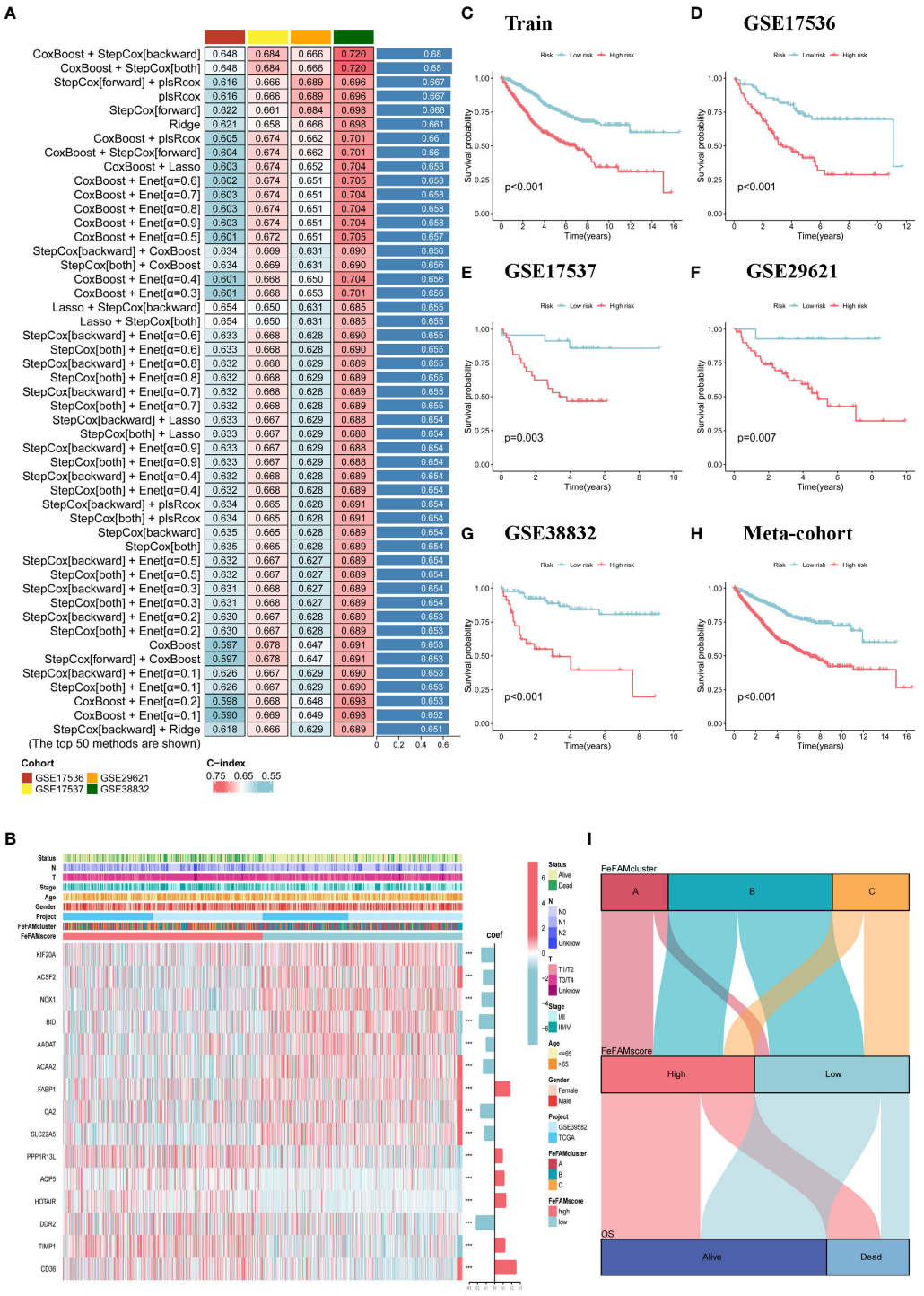

FIGURE 3
Construction of a machine learning-based signature. **(A)** The top C-index of 50 machine learning methods in four validation cohorts. **(B)** The heatmap demonstrates the relationships between the three FeFAM phenotypes, clinicopathologic characteristics, coef value and the expression variations of the FeFAM-related genes in train cohort. **(C–H)** Kaplan-Meier curves of OS according to the FeFAMscore in Train cohorts (log-rank test: p<0.001) **(C)**. GSE17536 (Log-rank test: p<0.001) **(D)**. GSE17537 (Log-rank test: p = 0.003) **(E)**. GSE29621 (Log-rank test: p = 0.007) **(F)**. GSE38832 (Log-rank test: p < 0.001) **(G)**. Meta-cohort (Log-rank test: p < 0.001) **(H)**. **(I)** Alluvial diagram showing the correlation of FeFAMclusters and FeFAMscore. *** p < 0.001. FeFAM, ferroptosis and fatty acid metabolism regulators.

10.3389/fimmu.2024.1416443

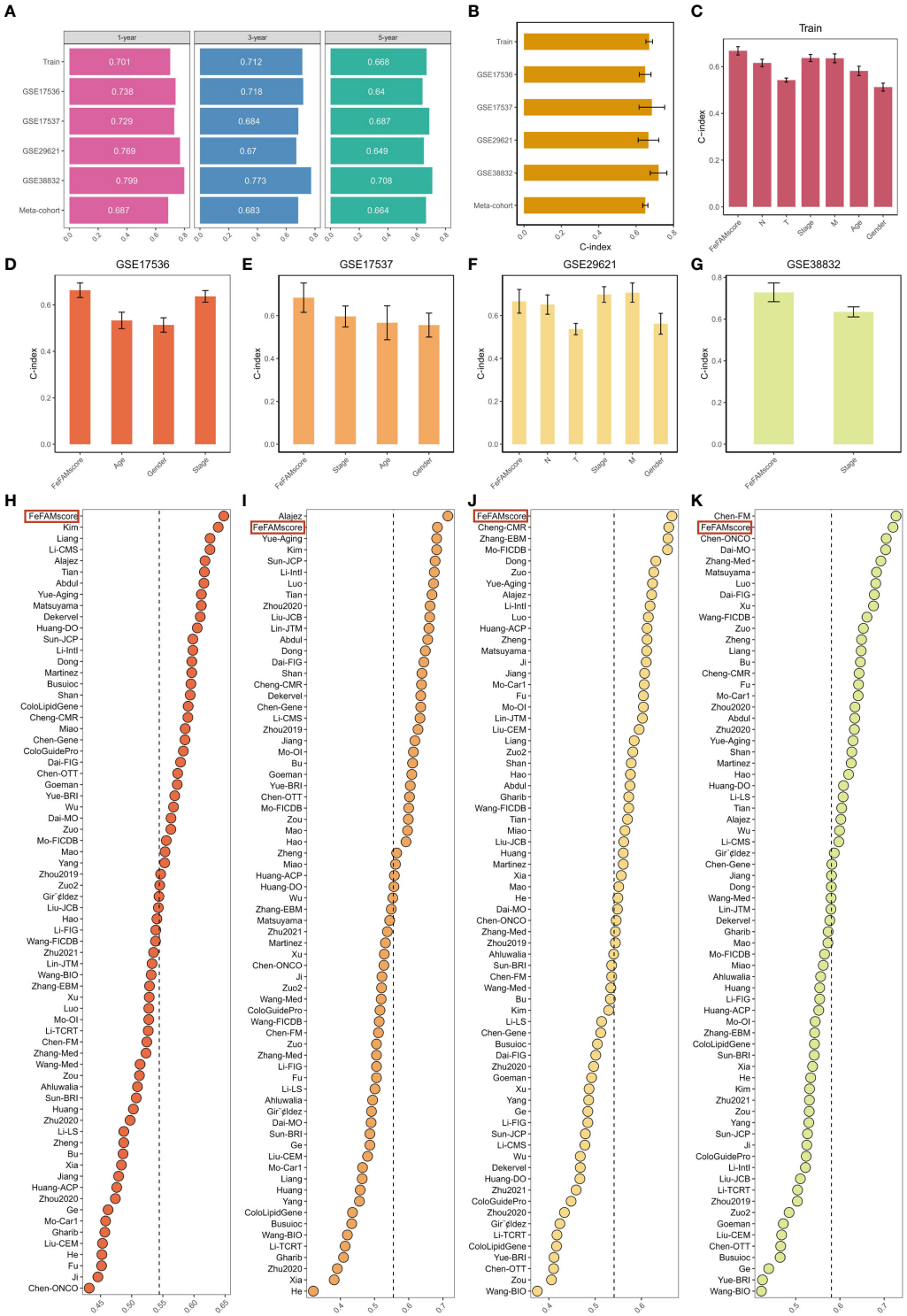

FIGURE 4
Comparison between the FeFAMscore and the other 69 signatures in colorectal cancer. **(A)** Time-dependent ROC analysis for predicting OS at 1,3, and 5 years in train cohort (n = 1029), GSE17536 (n = 177), GSE17537 (n = 55), GSE29621 (n = 65), and GSE38832 (n = 122). **(B)** C-index of FeFAMscore across all datasets. **(C-G)** The performance of FeFAMscore was compared with other clinical variables in predicting prognosis. Train **(C)**, GSE17536 **(D)**, GSE17537 **(E)**, GSE29621 **(F)**, and GSE38832 **(G)**. **(H-K)** C-index of FeFAMscore and 69 published signatures in GSE17536 **(H)**, GSE17537 **(I)**, GSE29621 **(J)**, and GSE38832 **(K)**. *** $p < 0.001$. FeFAM, ferroptosis and fatty acid metabolism regulators.

3.7 Resilient predictive performance of FeFAMscore

As the sequencing depth continually increases, CRC treatment outcomes are well predicted. Machine learning-based prognostic models for CRC have been increasingly developed in recent years. To quantify the performance of the FeFAMscore, we systematically retrieved mRNA signatures from CRC research over the past decade and finally acquired 69 mRNA signatures. We compared the predictive ability of the FeFAMscore using the C-index value in the four independent validation cohorts. The FeFAMscore ranked first in the GSE17536 and GSE29621 datasets, followed by GSE17537 and GSE38832 (Figures 4D-G). However, some models exhibited appreciable predictive performance for the GSE17537 and GSE38832 datasets and performed moderately in other cohorts, further proving the uniqueness and reliability of our models. The Chen-FM model, for instance, showed a better C-index than the FeFAMscore in GSE38832 and was poorly displayed in GSE17536, GSE17537, and GSE38832 with a C-index of less than 0.6. The above results demonstrated the good predictive performance of the FeFAMscore (Figures 4H–K).

3.8 ACAA2 is associated with tumor progression in CRC

To further evaluate the expression and function of the FeFAMscore, we first performed RT-qPCR in cell lines from patients with CRC for the six genes. The other nine genes involved in the FeFAM score have been demonstrated by other researchers (33–41). Compared with those in normal human colonic cells (NCM460 cells), the expression of ACAA2 was significantly higher in HCT116 and CACO2 cells, while the expression of ACSF2, DDR2 and SLC22A5 was significantly increased in the CRC cells (Figures 5A, B). Among the expression and correlation of the genes, ACAA2 was significantly overexpressed in the tumor tissues and strong correlated with ferroptosis regulators. We then used two small interfering RNAs (siRNAs) to downregulate ACAA2 expression in HCT116 and CACO2 CRC cell lines (Figure 5C). The western blot further demonstrated the results (Figure 5D). Cell viability was reduced by ACAA2 downregulation after 72 h (Figures 5E, F). In addition, Cell colony formation experiments demonstrated a significant reduction in colony numbers in HCT116 and CACO2 cell lines following ACAA2 knockdown. (Figure 5G). Transwell assays also confirmed that ACAA2 knockdown significantly reduced the migratory ability of CRC cells (Figures 5H–J). Taken together, these results indicate that ACAA2 not only induces CRC cell proliferation, but also promotes CRC cell migration.

3.9 Mutation status in high and low FeFAMscore groups

To explore the mechanisms underlying the FeFAMScore, somatic mutations in the patients with CRC in the TCGA cohort were further analyzed. As expected, more mutations in top 15 genes were observed in the high FeFAMscore group than that in the low FeFAMscore group (Figures 6A, B). In addition, co-occurrence and mutual exclusion were observed among these genes (Figures 6C, D). The forest plot also revealed that the BRAF gene, which is generally regarded as a potential prognostic risk factor, had more mutations than the low one, which indicates poor prognostic survival and worse ICI efficacy (Figure 6E). Moreover, the high FeFAMscore groups exhibited a higher TMB than the low FeFAMscore groups (Figure 6F). Poor prognosis was also demonstrated by high TMB combined with a high FeFAMscore (Figure 6G).

3.10 Immune characteristics related to FeFAMscore

We first adopted the ssGSEA algorithm to explore the correlation between tumor-infiltrating immune cells and the FeFAMscore in the training cohorts (Supplementary Figure S5A), which indicated that the FeFAMscore had a positive relationship with the immune cells. These findings suggest that the high FeFAMscore group, despite exhibiting a worse prognosis, harbored a higher abundance of immunologically activated cells than the low FeFAMscore group. Additionally, the high FeFAMscore group demonstrated an increased presence of immunosuppressive cells such as MDSCs, macrophages, mast cells, and regulatory T cells (Supplementary Figure S5B). Therefore, ssGSEA and six external algorithms, including CIBERSORT, EPIC, MCPCOUNTER, TIMER, quantiseq, and XCELL were further used, yielding similar results: the high FeFAMscore group had a high ImmuneScore, StromaScore, and MicroenvironmentScore (Supplementary Figure S5C). Next, we investigated the cancer-, immune-, and metabolic-related pathways between the two groups, which means that a high FeFAMscore prefers to be enriched in cancer-related and immune-related pathways (Supplementary Figure S5D). Interestingly, fatty acid metabolism was significantly activated in the low FeFAMscore group, which may improve the prognosis. Based on these findings, the high FeFAMscore groups probably had several targets that may benefit from specifically targeted immunotherapy, even though they had a worse prognosis.

3.11 FeFAMscore predicts CRC response to immunotherapy

We first used TIDE and ESTIMATE algorithms to measure the microenvironment in patients with low and high FeFAMscores (Figures 7A–F; Supplementary Figure S5E). The results indicated that the high FeFAMscore group was associated with high immune infiltration but high TIDE, CTL.score, dysfunction, MSI, and PD-L1, which means that although these individuals with poor survival prognosis contain immunosuppressive cells, this is the main reason for immune evasion and poor ICI efficacy in these individuals. This suggests that the high FeFAMscore group with poor survival may be a special target for activated immune cells, improving survival prognosis. Hence, the submap algorithm was used to assess the feasibility of the FeFAMscore in predicting immunotherapy

10.3389/fimmu.2024.1416443

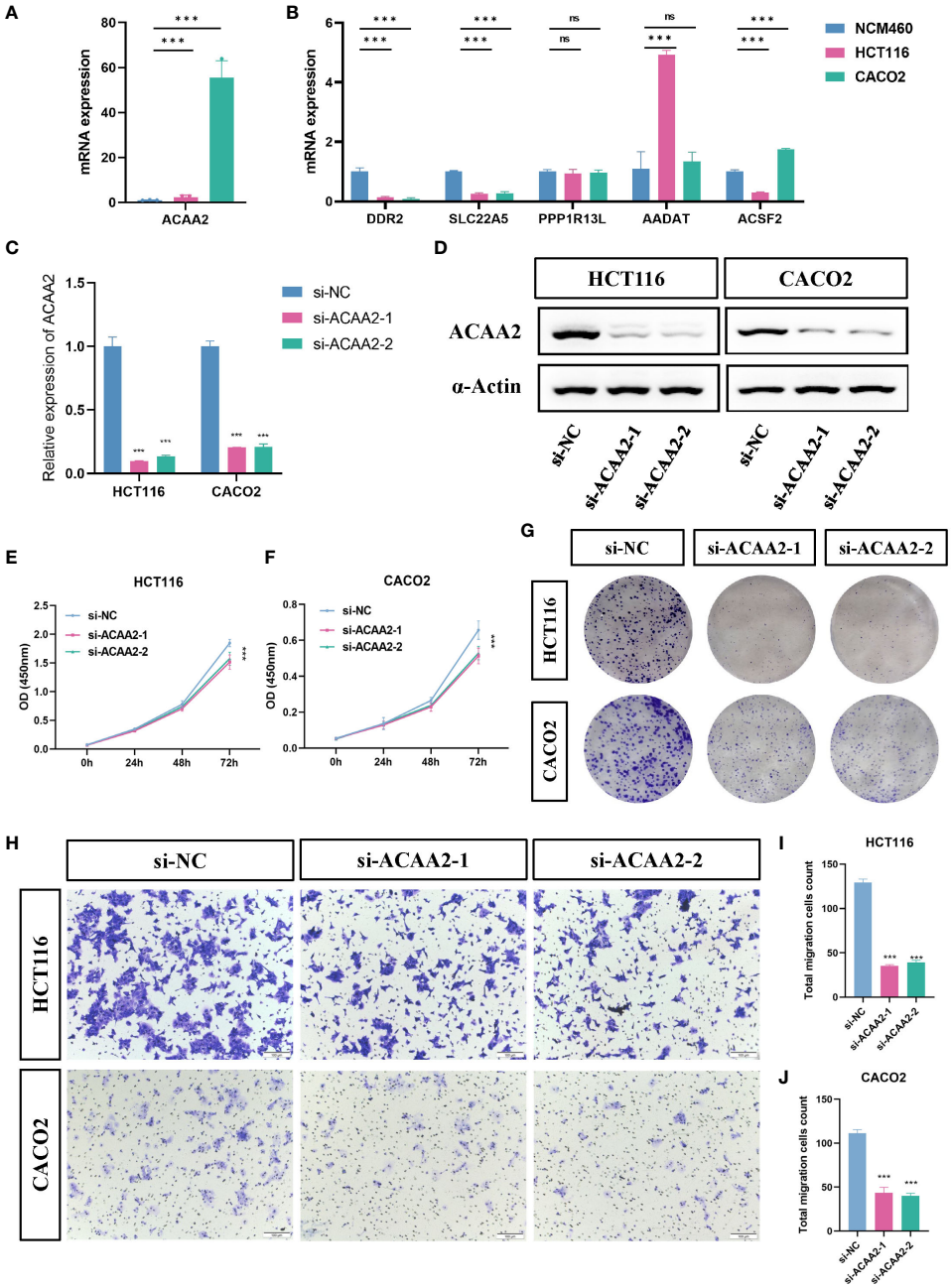

FIGURE 5
ACAA2 promotes colorectal cancer progression. **(A, B)** Comparison of the expression levels of ACAA2, DDR2, SLC22A5, PPP1R13L, AADAT and ACSF2 between NCM460 cells, HCT116 cells, and CACO2 cells. **(C)** The knockdown efficiency of ACAA2 in HCT116 cells and CACO2. **(D)** Representative western blots examined the expression of ACAA2 protein levels after the downregulation of ACAA2 of HCT116 and CACO2 cell lines. **(E, F)** The CCK8 assay detected cell viability after decreased ACAA2 expression in HCT116 **(E)** and CACO2 **(F)** cell lines. **(G)** Knockdown of ACAA2 significantly reduced the number of clones in HCT116 and CACO2 cell lines. **(H)** The transwell assay detected the migration ability of HCT116 and CACO2 cells after decreased ACAA2 expression. **(I-J)** Quantification results of numbers of relative migration rates in transwell assay in HCT116 **(I)** and CACO2 **(J)** cells. *** $p < 0.001$, ns, not significant.

efficacy. These findings affirmed that individuals in the high FeFAMscore group may benefit from both anti-PD-1 and anti-CTLA4 therapies (Figure 7G).

Based on the previous analysis, we determined the FeFAMscore in the IMvigor210 cohorts (anti-PD-L1 therapy) (42), Braun cohorts (anti-PD-1 therapy) (43) and PRJNA23709 (anti-PD-1 therapy + anti-CLTA4 therapy) (44). In the IMvigor210 dataset, patients with low FeFAMscores exhibited better prognoses than those with high FeFAMscores. Additionally, individuals with low FeFAMscores were likely to respond favorably to anti-PD-L1 immunotherapy (Figures 7H,

10.3389/fimmu.2024.1416443

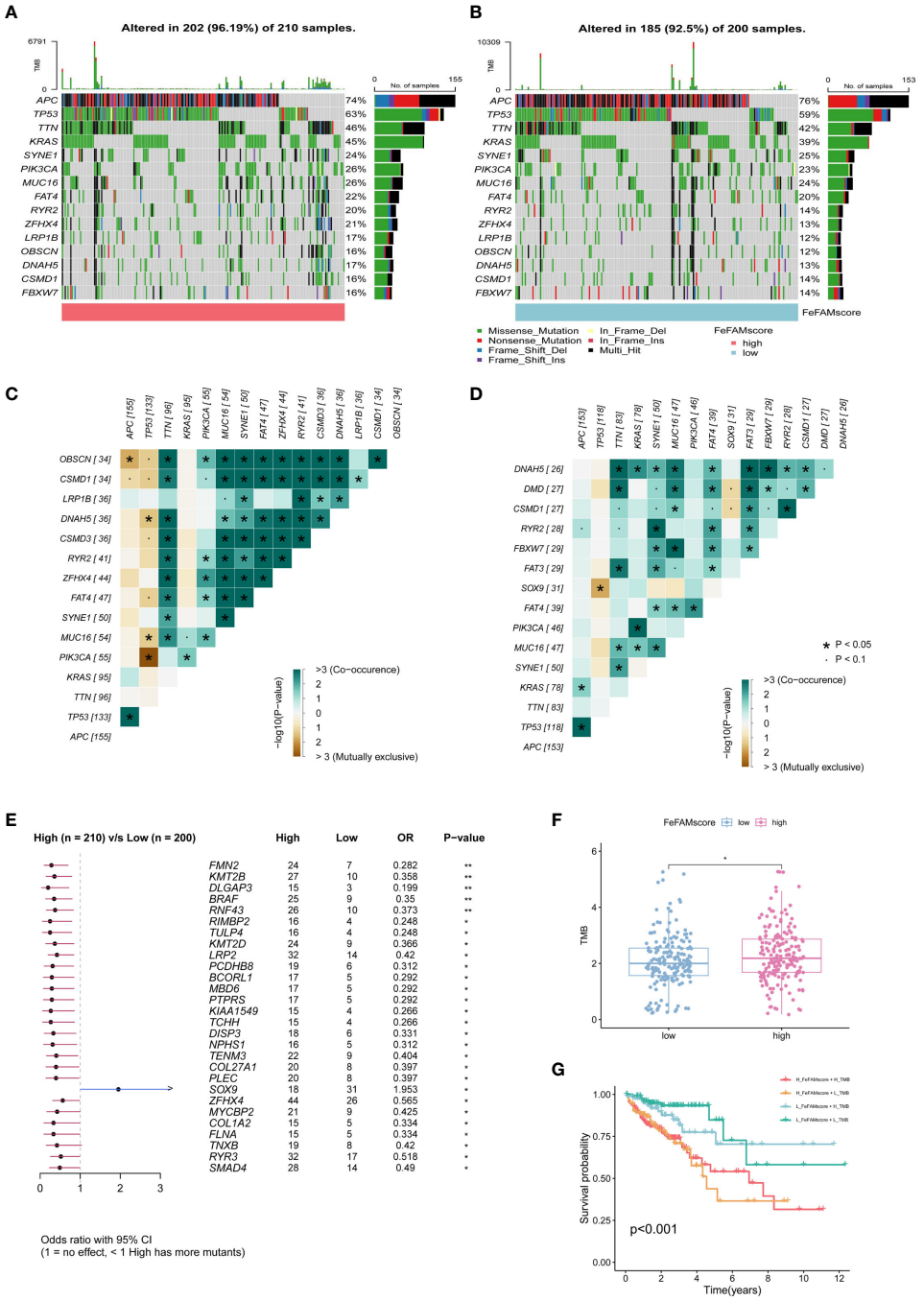

FIGURE 6
The FeFAMscore related to the tumor mutation status. **(A, B)** Visual summary showing common genetic alterations in low **(A)** and high **(B)** FeFAMscore groups. **(C, D)** Interaction effect of genes mutating in the low **(C)** and high **(D)** FeFAMscore groups. **(E)** Forest plot gene mutations in the CRC patients. **(F)** The TMB in low and high FeFAMscore groups. **(G)** Survival analysis for CRC patients measured by both FeFAMscore and TMB using Kaplan-Meier curves. * p < 0.05, ns, not significant. FeFAM, ferroptosis and fatty acid metabolism regulators.

K, N). Interestingly, in the Braun cohort, patients with high FeFAMscores demonstrated the potential for benefit from anti-PD-1 therapy (Figures 7I, L, O). As expected, patients with renal cell carcinoma and high FeFAMscore had significantly improved survival probability and were likely to respond to anti-PD-1 therapy. The results were shown in PRJNA23709 when patients with high FeFAMscore received combined anti-PD-1 and anti-CTLA4 therapy (Figures 7J, M, P). They not only greatly improved survival prognosis, but also acquired a remarkable response rate to immune therapy. These results suggest that individuals with a low FeFAMscore may benefit from immunotherapy, but that individuals with a high FeFAMscore obtain excellent response rates and survival with specific immunotherapies.

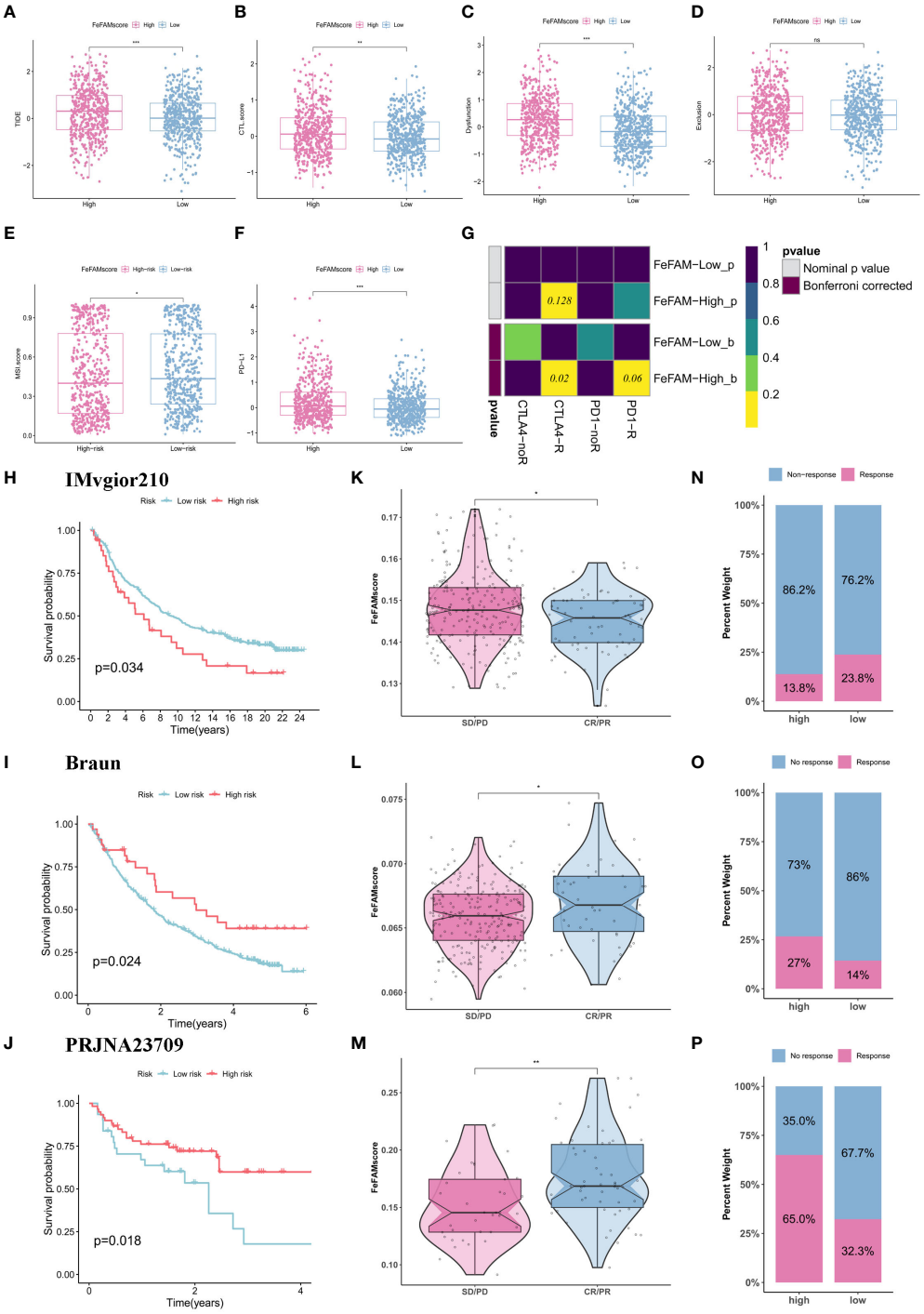

FIGURE 7
FeFAMscore predicts the response of colorectal to immunotherapy. **(A-F)** Box plots showed the significant difference in TIDE **(A)**, CTL.score **(B)**, Dyfunction **(C)**, Exclusion **(D)**, MDSC **(E)**, PD-L1 **(F)**. **(G)** The submap algorithm predicts the probability of anti-PD1 and anti-CTLA4 immunotherapy response in high and low FeFAMscore groups. **(H-J)** The Kaplan–Meier curve exhibited a significant difference in survival rate between the high and low FeFAMscore groups in the IMVgior210 cohort **(H)**, Braun **(I)**, and PRJNA23709 **(J)**. **(K-M)** The Wilcoxon rank-sum test of FeFAMscore variation in the IMVgior210 cohort **(K)**, Braun **(L)**, and PRJNA23709 **(M)**. **(N-P)** The stacked histogram shows the difference in immunotherapy responsiveness between the high and low FeFAMscore groups in the IMVgior210 cohort **(N)**, Braun **(O)**, and PRJNA23709 **(P)**. FeFAM, ferroptosis and fatty acid metabolism regulators. * $p < 0.05$, ** $p < 0.01$, *** $p < 0.001$, ns: not significant.

3.12 FeFAMscore predicts CRC sensitivity to chemotherapeutic response analysis

To assess potentially effective drugs associated with the FeFAMscore, we investigated chemotherapeutic agents using the "oncoPredict" package. With the compared differences between two risk FeFAM groups by the Wilcoxion test with $p<0.05$, we significantly filtered 316 (total: 545) and 95 (total: 224) compounds in the CTRP and GDSC, respectively. Next, we investigated the drug intersections in the two databases (Supplementary Figure S6A). Spearman's method was used to measure the correlation between FeFAM genes and drug sensitivity. Some genes and drugs, such as KIF20A and AADAT, interacted antagonistically (Supplementary Figures S6B, C). However, the ACSF2 and FABP1 interacted synergistically. To validate the irreplaceable role of FeFAM molecules in chemotherapy, we applied the FeFAMscore to guide chemotherapeutic selection for CRC in clinical practice. Exploring in the CRC related chemotherapy drugs, the osimertinib, oxaliplatin, gefitinib, eriotinib, navitoclax, and cyclophosphamide are beneficial for the patients with high FeFAMscore, unlike irinotecan, niraparib, gemcitabine, niraparib, dabrafenib, and selumetinib (Supplementary Figures S6D–O). These findings underscore the availability of diverse chemotherapy modalities tailored to specific patients with CRC, thereby paving the way for precision chemotherapy and personalized treatment approaches.

4 Discussion

Several therapeutic modalities, including surgery, chemotherapy, immunotherapy, radiotherapy, and targeted therapy have emerged as key strategies in CRC research (3, 5, 45, 46). These diverse treatment approaches represent a profound advancement in CRC management, reflecting the multifaceted approach necessitated by disease complexity (47). Among these, immunotherapy is a promising frontier that exploits the intricate interplay between the immune system and malignant cells to elicit therapeutic responses (48). However, a subset of patients with CRC exhibiting deficient mismatch repair or microsatellite instability-high (dMMR/MSI-H) represents a relatively small fraction, comprising approximately 15% and 4% patients with CRC and metastatic colorectal cancer (mCRC), respectively; a proportion of these patients swiftly progress to a state of immune resistance (38, 39). The AJCC staging system is a widely accepted criterion for clinical management and encompasses therapeutic decision-making and surveillance strategies for CRC. The utility of the AJCC staging system is constrained by the variability in clinical outcomes observed among patients classified within the same stage (49). This may not only result in overtreatment and undertreatment, but also make it difficult to reflect the sensitivity of immunotherapy and chemotherapy because it does not reflect the TME. To bridge this gap, identifying novel prognostic and therapeutic targets for CRC is vital.

Cell death is a regulated process in cells and may be related to metabolism during tumor progression, metastasis, and drug resistance. Ferroptosis is an iron-related cell death pathway characterized by lipid peroxide accumulation (50, 51). Fatty acid metabolism plays a pivotal role in tumorigenesis, disease progression, and treatment resistance by facilitating augmented lipid synthesis, storage, and catabolism (52). Numerous studies have demonstrated that ferroptosis is significantly correlated with metabolism, particularly lipid metabolism (50–53). For instance, ASL4, a fatty acid metabolism-related gene, is induced by the T cell-derived interferon (IFN)-γ to change the tumor lipid pattern, which increased arachidonic acid (AA) production to promote ferroptosis (32). SLC47A1, which regulates lipid remodeling and survival during ferroptosis, inhibits the anticancer activity of ferroptosis inducers (54). Moreover, they interact to modulate drug sensitivity (32, 55). Consequently, the influence of ferroptosis regulators and fatty acid molecules on the TME as well as their predictive capacity for prognosis and response to immunotherapy in CRC, remain unclear.

This study elucidated the genetic and transcriptomic diversity of FeFAMs across 33 cancer species using a multi-omics approach. Similar frequencies observed among the ferroptosis and fatty acid metabolism regulators indicate their interconnectedness. Spearman's rank correlation coefficient further demonstrated a strong correlation of ferroptosis and fatty acid metabolism regulators between 33 cancer species, especially in CRC ($R= -0.93$; $p<0.001$). Furthermore, after screening 50 genes using the "limma" package and univariate Cox regression analysis, the patients were stratified into three distinct phenotypes, each exhibiting significant disparities in genetic profiles and immune infiltration within the clusters.

We then distinguished three ferroptosis- and fatty acid metabolism-related patterns, named FeFAM clusters A/B/C. The TME characteristics in the three patterns indicated differential immune cell compositions. FeFAM clusters A and C were correlated with immune cell abundance; however, they displayed disparate prognostic outcomes. The FeFAM cluster A processed with high immune activate, StromaSocre, PD-L1 expression, CAF expression, and high activation of TGF-β signaling pathway proved a strong relation with immune-exclude subtypes, while the FeFAM cluster C associated with excellent prognosis and abundant immune cell was regarded as an immune-inflamed phenotype. Interestingly, FeFAM cluster C exhibited the same levels of dysfunction and CTL.score and high metabolism levels, such as the ROS and fatty acids, than FeFAM cluster A, which indicated that the interaction of ferroptosis and fatty acid metabolism may coordinate with T cell dysfunction (32). MDSC density was the highest in FeFAM cluster B, which is defined as the immune desert subtype. These results demonstrate that FeFAM molecules play a vital role in the TME and may trigger extrinsic immune escape.

Further FeFAM molecule characterization in CRC is imperative. Developing features associated with FeFAM molecules will facilitate prognosis prediction and immune response evaluation in CRC. To avoid model selection bias and confirm model accuracy, we randomly combined 10 classical algorithms and eventually obtained 117 combined algorithms. Subsequently, we developed FeFAMscore, a machine-learning-based FeFAM-related model, which exhibited the best performance among the 117 signatures.

Recognizing the heterogeneity often observed in the patients with CRC, we externally validated the FeFAMscore using four additional CRC databases. The highest C-index among the validations not only confirmed the selection of the optimal model, CoxBoost combined with stepwise Cox (backward direction), but also underscored the accuracy and generalizability of the model. Moreover, a comparison of 69 published CRC signatures showed improved accuracy, exhibiting robustness. To validate model accuracy, we identified ACAA2 as a key FeFAMscore regulator and conducted cellular experiments, which revealed that ACAA2 promotes CRC proliferation and migration.

Furthermore, FeFAMscore demonstrated a robust association with survival outcomes. The adverse prognosis observed in the high FeFAMscore group may be attributed to improved activation of anti-immune components, potentially fostering a TME conducive to immune evasion. Interestingly, the FeFAMscore and tumor immune infiltration extent in CRC is positively correlated. Moreover, mutations leading to tumor neoantigens, along with a high tumor mutational burden (TMB), increase tumor immunogenic neoantigen abundance (56). The patients with high TMB may benefit from immunotherapy, but many patients do not achieve the desired results (42). Similar results were observed in this study. Tide, a computational method developed by Peng Jiang, models T cell dysfunction and exclusion mechanisms of tumor immune evasion by infiltration of cytotoxic T lymphocytes (CTL), showed the same results (42). However, owing to the variances in immune-related pathways between the two cohorts and the primary mechanism of immune evasion being dysfunction, it is plausible that there may be specific therapeutic benefits for the high FeFAMscore group. The Submap algorithm further supported these results, showing that the high FeFAMscore group processes were more sensitive to anti-PD-1 and anti-CTLA4 therapies. According to the results of previous studies, the predominant mechanism suggests that both high and low fatty acid metabolism can affect the expression level of iron death, consequently affecting the mode of action of CTLs (30, 32). The high FeFAMscore group exhibited diminished fatty acid metabolism, potentially regulating ferroptosis to augment CTL sensitivity. To validate these results, we analyzed the FeFAMscores in immunotherapy cohorts receiving anti-PD-L1 therapy, anti-PD-1 therapy, and anti-PD-1 combined with anti-CTLA4 therapy. Similar results were observed in these cohorts, further demonstrating the limitations of TMB and TIDE. Furthermore, regarding chemotherapeutic agents, the FeFAMscore exhibited promising predictive capabilities. Collectively, these findings indicate that FeFAMscore holds promise as a valuable tool for formulating efficacious CRC treatment strategies.

This study had some limitations. First, the intricate regulatory mechanisms governing ferroptosis and fatty acid metabolism remain unclear. Moreover, retrospective cohorts sourced from publicly available online databases were used. Large multicenter prospective clinical investigations are warranted to corroborate these findings. Finally, to validate the predictive utility of the FeFAMscore in immunotherapy response, additional indicators are required, along with prospective cohorts of patients with glioma undergoing immunotherapeutic interventions.

In conclusion, through a comprehensive approach integrating multicenter analysis and machine learning algorithms, we developed a stable and reliable prognostic and immunotherapeutic response predictor, the FeFAMscore, for CRC. Notably, the high FeFAMscore group demonstrated an increased sensitivity to anti-PD-1 and anti-CTLA4 therapies. The FeFAMscore holds promise as a valuable tool for tailoring efficacious treatment regimens for CRC.

Data availability statement

The datasets presented in this study can be found in online repositories. The names of the repository/repositories and accession number(s) can be found below: https://www.ncbi.nlm.nih.gov/, TCGA-COAD, https://www.ncbi.nlm.nih.gov/, TCGA-READ, https://www.ncbi.nlm.nih.gov/, GSE17536, https://www.ncbi.nlm.nih.gov/, GSE17537, https://www.ncbi.nlm.nih.gov/, GSE29621, https://www.ncbi.nlm.nih.gov/, GSE39582, https://www.ncbi.nlm.nih.gov/, GSE38832.

Author contributions

JCZ: Conceptualization, Data curation, Formal Analysis, Investigation, Methodology, Project administration, Resources, Software, Supervision, Visualization, Writing – original draft, Writing – review & editing. JYZ: Conceptualization, Data curation, Formal Analysis, Investigation, Methodology, Validation, Writing – review & editing. YL: Funding acquisition, Investigation, Project administration, Software, Supervision, Writing – review & editing. YZ: Conceptualization, Data curation, Project administration, Writing – review & editing. XZ: Formal Analysis, Investigation, Supervision, Writing – original draft. WC: Data curation, Formal Analysis, Visualization, Writing – review & editing. LY: Funding acquisition, Project administration, Supervision, Visualization, Writing – review & editing. QZ: Data curation, Investigation, Methodology, Resources, Supervision, Validation, Visualization, Writing – review & editing.

Funding

The author(s) declare financial support was received for the research, authorship, and/or publication of this article. The National Natural Science Foundation of China (No. 82172816)

Acknowledgments

We appreciated the support of the First Affiliated Hospital of Wenzhou Medical University.

Conflict of interest

The authors declare that the research was conducted in the absence of any commercial or financial relationships that could be construed as a potential conflict of interest.

Publisher's note

All claims expressed in this article are solely those of the authors and do not necessarily represent those of their affiliated organizations, or those of the publisher, the editors and the reviewers. Any product that may be evaluated in this article, or claim that may be made by its manufacturer, is not guaranteed or endorsed by the publisher.

Supplementary material

The Supplementary Material for this article can be found online at: https://www.frontiersin.org/articles/10.3389/fimmu.2024.1416443/full#supplementary-material

References

1. Siegel RL, Miller KD, Wagle NS, Jemal A. Cancer statistics, 2023. *CA Cancer J Clin*. (2023) 73:17–48. doi: 10.3322/caac.21763

2. Bretthauer M, Løberg M, Wieszczy P, Kalager M, Emilsson L, Garborg K, et al. Effect of colonoscopy screening on risks of colorectal cancer and related death. *N Engl J Med*. (2022) 387:1547–56. doi: 10.1056/NEJMoa2208375

3. Biller LH, Schrag D. Diagnosis and treatment of metastatic colorectal cancer: A review. *JAMA*. (2021) 325:669–85. doi: 10.1001/jama.2021.0106

4. Cercek A, Lumish M, Sinopoli J, Weiss J, Shia J, Lamendola-Essel M, et al. Pd-1 blockade in mismatch repair-deficient, locally advanced rectal cancer. *N Engl J Med*. (2022) 386:2363–76. doi: 10.1056/NEJMoa2201445

5. André T, Shiu K-K, Kim TW, Jensen BV, Jensen LH, Punt C, et al. Pembrolizumab in microsatellite-instability-high advanced colorectal cancer. *N Engl J Med*. (2020) 383:2207–18. doi: 10.1056/NEJMoa2017699

6. Hsieh RC-E, Krishnan S, Wu R-C, Boda AR, Liu A, Winkler M, et al. Atr-mediated cd47 and pd-L1 up-regulation restricts radiotherapy-induced immune priming and abscopal responses in colorectal cancer. *Sci Immunol*. (2022) 7: eabl9330. doi: 10.1126/sciimmunol.abl9330

7. Liu C, Wang X, Qin W, Tu J, Li C, Zhao W, et al. Combining radiation and the atr inhibitor berzosertib activates sting signaling and enhances immunotherapy via inhibiting shp1 function in colorectal cancer. *Cancer Commun (Lond)*. (2023) 43:435–54. doi: 10.1002/cac2.12412

8. Gibney GT, Weiner LM, Atkins MB. Predictive biomarkers for checkpoint inhibitor-based immunotherapy. *Lancet Oncol*. (2016) 17:e542–e51. doi: 10.1016/S1470-2045(16)30406-5

9. Chan TA, Yarchoan M, Jaffee E, Swanton C, Quezada SA, Stenzinger A, et al. Development of tumor mutation burden as an immunotherapy biomarker: utility for the oncology clinic. *Ann Oncol*. (2019) 30:44–56. doi: 10.1093/annonc/mdy495

10. Cortes-Ciriano I, Lee S, Park W-Y, Kim T-M, Park PJ. A molecular portrait of microsatellite instability across multiple cancers. *Nat Commun*. (2017) 8:15180. doi: 10.1038/ncomms15180

11. Röhrig F, Schulze A. The multifaceted roles of fatty acid synthesis in cancer. *Nat Rev Cancer*. (2016) 16:732–49. doi: 10.1038/nrc.2016.89

12. Berod L, Friedrich C, Nandan A, Freitag J, Hagemann S, Harmrolfs K, et al. *De novo* fatty acid synthesis controls the fate between regulatory T and T helper 17 cells. *Nat Med*. (2014) 20:1327–33. doi: 10.1038/nm.3704

13. Bachem A, Makhlouf C, Binger KJ, de Souza DP, Tull D, Hochheiser K, et al. Microbiota-derived short-chain fatty acids promote the memory potential of antigen-activated cd8+ T cells. *Immunity*. (2019) 51:285–97. doi: 10.1016/j.immuni.2019.06.002

14. Conche C, Finkelmeier F, Pešić M, Nicolas AM, Böttger TW, Kennel KB, et al. Combining ferroptosis induction with mdsc blockade renders primary tumours and metastases in liver sensitive to immune checkpoint blockade. *Gut*. (2023) 72:1774–82. doi: 10.1136/gutjnl-2022-327909

15. Fang H, Wu Y, Chen L, Cao Z, Deng Z, Zhao R, et al. Regulating the obesity-related tumor microenvironment to improve cancer immunotherapy. *ACS Nano*. (2023) 17:4748–63. doi: 10.1021/acsnano.2c11159

16. Zhang Q, Deng T, Zhang H, Zuo D, Zhu Q, Bai M, et al. Adipocyte-derived exosomal mttp suppresses ferroptosis and promotes chemoresistance in colorectal cancer. *Adv Sci (Weinh)*. (2022) 9:e220335. doi: 10.1002/advs.202203357

17. Qiu B, Zandkarimi F, Bezjian CT, Reznik E, Soni RK, Gu W, et al. Phospholipids with two polyunsaturated fatty acyl tails promote ferroptosis. *Cell*. (2024) 187:1177–90. doi: 10.1016/j.cell.2024.01.030

18. Chen C, Yang Y, Guo Y, He J, Chen Z, Qiu S, et al. Cyp1b1 inhibits ferroptosis and induces anti-pd-1 resistance by degrading acsl4 in colorectal cancer. *Cell Death Dis*. (2023) 14:271. doi: 10.1038/s41419-023-05803-2

19. Zeng K, Li W, Wang Y, Zhang Z, Zhang L, Zhang W, et al. Inhibition of cdk1 overcomes oxaliplatin resistance by regulating acsl4-mediated ferroptosis in colorectal cancer. *Adv Sci (Weinh)*. (2023) 10:e2301088. doi: 10.1002/advs.202301088

20. Ruan R, Li L, Li X, Huang C, Zhang Z, Zhong H, et al. Unleashing the potential of combining fgfr inhibitor and immune checkpoint blockade for fgf/fgfr signaling in tumor microenvironment. *Mol Cancer*. (2023) 22:60. doi: 10.1186/s12943-023-01761-7

21. Gao Z, Bai Y, Lin A, Jiang A, Zhou C, Cheng Q, et al. Gamma delta T-cell-based immune checkpoint therapy: attractive candidate for antitumor treatment. *Mol Cancer*. (2023) 22:31. doi: 10.1186/s12943-023-01722-0

22. Zhou N, Yuan X, Du Q, Zhang Z, Shi X, Bao J, et al. Ferrdb V2: update of the manually curated database of ferroptosis regulators and ferroptosis-disease associations. *Nucleic Acids Res*. (2023) 51:D571–D82. doi: 10.1093/nar/gkac935

23. Wilkerson MD, Hayes DN. Consensusclusterplus: A class discovery tool with confidence assessments and item tracking. *Bioinformatics*. (2010) 26:1572–3. doi: 10.1093/bioinformatics/btq170

24. Zhang J, Zhang S. Discovery of cancer common and specific driver gene sets. *Nucleic Acids Res*. (2017) 45:e86. doi: 10.1093/nar/gkx089

25. Dhanasekaran R, Deutzmann A, Mahauad-Fernandez WD, Hansen AS, Gouw AM, Felsher DW. The myc oncogene - the grand orchestrator of cancer growth and immune evasion. *Nat Rev Clin Oncol*. (2022) 19:23–36. doi: 10.1038/s41571-021-00549-2

26. Zhou B, Lin W, Long Y, Yang Y, Zhang H, Wu K, et al. Notch signaling pathway: architecture, disease, and therapeutics. *Signal Transduct Target Ther*. (2022) 7:95. doi: 10.1038/s41392-022-00934-y

27. Kroemer G, Pouyssegur J. Tumor cell metabolism: cancer's Achilles' Heel. *Cancer Cell*. (2008) 13:472–82. doi: 10.1016/j.ccr.2008.05.005

28. Liu Z, Liu L, Weng S, Guo C, Dang Q, Xu H, et al. Machine learning-based integration develops an immune-derived lncrna signature for improving outcomes in colorectal cancer. *Nat Commun*. (2022) 13:816. doi: 10.1038/s41467-022-28421-6

29. Mariathasan S, Turley SJ, Nickles D, Castiglioni A, Yuen K, Wang Y, et al. Tgfβ Attenuates tumour response to pd-L1 blockade by contributing to exclusion of T cells. *Nature*. (2018) 554:544–8. doi: 10.1038/nature25501

30. Ma X, Xiao L, Liu L, Ye L, Su P, Bi E, et al. Cd36-mediated ferroptosis dampens intratumoral cd8+ T cell effector function and impairs their antitumor ability. *Cell Metab*. (2021) 33:1001–12. doi: 10.1016/j.cmet.2021.02.015

31. Wang Y, Tian Q, Hao Y, Yao W, Lu J, Chen C, et al. The kinase complex mtorc2 promotes the longevity of virus-specific memory cd4+ T cells by preventing ferroptosis. *Nat Immunol*. (2022) 23:303–17. doi: 10.1038/s41590-021-01090-1

32. Liao P, Wang W, Wang W, Kryczek I, Li X, Bian Y, et al. Cd8+ T cells and fatty acids orchestrate tumor ferroptosis and immunity via acsl4. *Cancer Cell*. (2022) 40:365–78. doi: 10.1016/j.ccell.2022.02.003

33. Xiong M, Zhuang K, Luo Y, Lai Q, Luo X, Fang Y, et al. Kif20a promotes cellular Malignant behavior and enhances resistance to chemotherapy in colorectal cancer through regulation of the jak/stat3 signaling pathway. *Aging (Albany NY)*. (2019) 11:11905–21. doi: 10.18632/aging.v11i24

34. Banskota S, Regmi SC, Kim J-A. Nox1 to nox2 switch deactivates ampk and induces invasive phenotype in colon cancer cells through overexpression of mmp-7. *Mol Cancer*. (2015) 14:1–14. doi: 10.1186/s12943-015-0379-0

35. Seenath MM, Roberts D, Cawthorne C, Saunders MP, Armstrong GR, O'Dwyer ST, et al. Reciprocal relationship between expression of hypoxia inducible factor 1alpha (Hif-1alpha) and the pro-apoptotic protein bid in ex vivo colorectal cancer. *Br J Cancer*. (2008) 99:459–63. doi: 10.1038/sj.bjc.6604474

36. Wood SM, Gill AJ, Brodsky AS, Lu S, Friedman K, Karashchuk G, et al. Fatty acid-binding protein 1 is preferentially lost in microsatellite instable colorectal

carcinomas and is immune modulated via the interferon Γ Pathway. *Mod Pathol*. (2017) 30:123–33. doi: 10.1038/modpathol.2016.170

37. Choi SS, Lee SK, Kim JK, Park H-K, Lee E, Jang J, et al. Flightless-1 inhibits er stress-induced apoptosis in colorectal cancer cells by regulating ca2+ Homeostasis. *Exp Mol Med*. (2020) 52:940–50. doi: 10.1038/s12276-020-0448-3

38. Chen C, Ma T, Zhang C, Zhang H, Bai L, Kong L, et al. Down-regulation of aquaporin 5-mediated epithelial-mesenchymal transition and anti-metastatic effect by natural product cairicoside E in colorectal cancer. *Mol Carcinog*. (2017) 56:2692–705. doi: 10.1002/mc.22712

39. Liu B, Liu Q, Pan S, Huang Y, Qi Y, Li S, et al. The hotair/mir-214/st6gal1 crosstalk modulates colorectal cancer procession through mediating sialylated C-met via jak2/stat3 cascade. *J Exp Clin Cancer Res*. (2019) 38:455. doi: 10.1186/s13046-019-1468-5

40. Song G, Xu S, Zhang H, Wang Y, Xiao C, Jiang T, et al. Timp1 is a prognostic marker for the progression and metastasis of colon cancer through fak-pi3k/akt and mapk pathway. *J Exp Clin Cancer Res*. (2016) 35:148. doi: 10.1186/s13046-016-0427-7

41. Fang Y, Shen Z-Y, Zhan Y-Z, Feng X-C, Chen K-L, Li Y-S, et al. Cd36 inhibits B-catenin/C-myc-mediated glycolysis through ubiquitination of gpc4 to repress colorectal tumorigenesis. *Nat Commun*. (2019) 10:3981. doi: 10.1038/s41467-019-11662-3

42. Balar AV, Galsky MD, Rosenberg JE, Powles T, Petrylak DP, Bellmunt J, et al. Atezolizumab as first-line treatment in cisplatin-ineligible patients with locally advanced and metastatic urothelial carcinoma: A single-arm, multicentre, phase 2 trial. *Lancet*. (2017) 389:67–76. doi: 10.1016/S0140-6736(16)32455-2

43. Braun DA, Hou Y, Bakouny Z, Ficial M, Sant' Angelo M, Forman J, et al. Interplay of somatic alterations and immune infiltration modulates response to pd-1 blockade in advanced clear cell renal cell carcinoma. *Nat Med*. (2020) 26:909–18. doi: 10.1038/s41591-020-0839-y

44. Gide TN, Quek C, Menzies AM, Tasker AT, Shang P, Holst J, et al. Distinct immune cell populations define response to anti-pd-1 monotherapy and anti-pd-1/anti-ctla-4 combined therapy. *Cancer Cell*. (2019) 35. doi: 10.1016/j.ccell.2019.01.003

45. Wyld L, Audisio RA, Poston GJ. The evolution of cancer surgery and future perspectives. *Nat Rev Clin Oncol*. (2015) 12:115–24. doi: 10.1038/nrclinonc.2014.191

46. Zhang N, Ng AS, Cai S, Li Q, Yang L, Kerr D. Novel therapeutic strategies: targeting epithelial-mesenchymal transition in colorectal cancer. *Lancet Oncol*. (2021) 22:e358–e68. doi: 10.1016/S1470-2045(21)00343-0

47. Andrei P, Battuello P, Grasso G, Rovera E, Tesio N, Bardelli A. Integrated approaches for precision oncology in colorectal cancer: the more you know, the better. *Semin Cancer Biol*. (2022) 84:199–213. doi: 10.1016/j.semcancer.2021.04.007

48. Ganesh K, Stadler ZK, Cercek A, Mendelsohn RB, Shia J, Segal NH, et al. Immunotherapy in colorectal cancer: rationale, challenges and potential. *Nat Rev Gastroenterol Hepatol*. (2019) 16:361–75. doi: 10.1038/s41575-019-0126-x

49. Brenner H, Kloor M, Pox CP. Colorectal cancer. *Lancet*. (2014) 383:1490–502. doi: 10.1016/S0140-6736(13)61649-9

50. Li D, Li Y. The interaction between ferroptosis and lipid metabolism in cancer. *Signal Transduct Target Ther*. (2020) 5:108. doi: 10.1038/s41392-020-00216-5

51. Liang D, Minikes AM, Jiang X. Ferroptosis at the intersection of lipid metabolism and cellular signaling. *Mol Cell*. (2022) 82:2215–27. doi: 10.1016/j.molcel.2022.03.022

52. Hoy AJ, Nagarajan SR, Butler LM. Tumour fatty acid metabolism in the context of therapy resistance and obesity. *Nat Rev Cancer*. (2021) 21:753–66. doi: 10.1038/s41568-021-00388-4

53. Zheng J, Conrad M. The metabolic underpinnings of ferroptosis. *Cell Metab*. (2020) 32:920–37. doi: 10.1016/j.cmet.2020.10.011

54. Lin Z, Liu J, Long F, Kang R, Kroemer G, Tang D, et al. The lipid flippase slc47a1 blocks metabolic vulnerability to ferroptosis. *Nat Commun*. (2022) 13:7965. doi: 10.1038/s41467-022-35707-2

55. Yang Y, Gu H, Zhang K, Guo Z, Wang X, Wei Q, et al. Exosomal acadm sensitizes gemcitabine-resistance through modulating fatty acid metabolism and ferroptosis in pancreatic cancer. *BMC Cancer*. (2023) 23:789. doi: 10.1186/s12885-023-11239-w

56. Chabanon RM, Pedrero M, Lefebvre C, Marabelle A, Soria J-C, Postel-Vinay S. Mutational landscape and sensitivity to immune checkpoint blockers. *Clin Cancer Res*. (2016) 22:4309–21. doi: 10.1158/1078-0432.CCR-16-0903

frontiers | Frontiers in Immunology

TYPE Original Research
PUBLISHED 18 July 2024
DOI 10.3389/fimmu.2024.1398802

OPEN ACCESS

EDITED BY
Laura Senovilla,
Spanish National Research Council (CSIC), Spain

REVIEWED BY
Laura Mondragón Martínez,
Josep Carreras Leukemia Research Institute (IJC), Spain
Mehdi Pirooznia,
Johnson & Johnson, United States

*CORRESPONDENCE
Yi Li
liyi3443@hotmail.com
Xinmao Song
muqinger@sina.com

†These authors have contributed equally to this work

RECEIVED 10 March 2024
ACCEPTED 03 July 2024
PUBLISHED 18 July 2024

CITATION
Zhang K, Li G, Wang Q, Liu X, Chen H, Li F, Li S, Song X and Li Y (2024) A disulfidptosis-related glucose metabolism and immune response prognostic model revealing the immune microenvironment in lung adenocarcinoma.
Front. Immunol. 15:1398802.
doi: 10.3389/fimmu.2024.1398802

A disulfidptosis-related glucose metabolism and immune response prognostic model revealing the immune microenvironment in lung adenocarcinoma

Kai Zhang[1†], Gang Li[2†], Qin Wang[2†], Xin Liu[3], Hong Chen[1], Fuqiang Li[4], Shuangyan Li[2], Xinmao Song[5*] and Yi Li[1*]

[1]Department of Oncology, 920th Hospital of Joint Logistics Support Force, Kunming, China, [2]Graduate School, Kunming Medical University, Kunming, China, [3]Department of Thoracic Surgery, Second Affiliated Hospital of Kunming Medical University, Kunming, China, [4]Department of Traditional Chinese Medicine, 920th Hospital of Joint Logistics Support Force, Kunming, China, [5]Department of Radiation Oncology, Ear, Nose & Throat Hospital of Fudan University, Shanghai, China

Background: Lung adenocarcinoma accounts for the majority of lung cancer cases and impact survival rate of patients severely. Immunotherapy is an effective treatment for lung adenocarcinoma but is restricted by many factors including immune checkpoint expression and the inhibitory immune microenvironment. This study aimed to explore the immune microenvironment in lung adenocarcinoma via disulfidptosis.

Methods: Public datasets of lung adenocarcinoma from the TCGA and GEO was adopted as the training and validation cohort. Based on the differences in the expression of disulfidptosis -related genes, a glucose metabolism and immune response prognostic model was constructed. The prognostic value and clinical relationship of the model were further explored. Immune-related analyses were performed according to CIBERSORT, ssGSEA, TIDE, IPS.

Results: We verified that the model could accurately predict the survival expectancy of lung adenocarcinoma patients. Patients with lung adenocarcinoma and a low-risk score had better survival outcomes according to the model. Moreover, the high-risk group tended to have an immunosuppressive effect, as reflected by the immune cell components, phenotypes and functions. We also found that the clinically relevant immune checkpoint CTLA-4 was significantly higher in low-risk group ($P<0.05$), indicating that the high-risk group may suffer worse tumor immunotherapy efficacy. Finally, we found that this model has accurate predictive value for the efficacy of immune checkpoint blockade in non-small cell lung cancer ($P<0.05$).

Conclusion: The prognostic model demonstrated the feasibility of predicting survival and immunotherapy efficacy via disulfidptosis-related genes and will facilitate the development of personalized anticancer therapy.

KEYWORDS

lung adenocarcinoma, tumor microenvironment, disulfidptosis-related genes, immune checkpoint, programmed cell death

Introduction

Lung cancer is one of the most common causes of cancer-related death worldwide, and lung adenocarcinoma (LUAD) accounts for the majority of lung cancer cases among all histological subtypes (1). Because LUAD is prone to metastasis in the early stage, the prognosis of LUAD patients is usually poor, with an average 5-year survival rate less than 20% (2). At present, personalized and precise treatments for lung cancer have been increasingly emphasized (3). Unfortunately, although great progress has been made in targeted therapy, the 5-year overall survival (OS) rate of LUAD patients is still low (4). Therefore, identification of better ways to improve the effectiveness of therapy is urgently needed.

Under normal circumstances, the immune system can identify and eliminate tumor cells in the tumor microenvironment (TME) (5). However, in order to survive and grow, tumor cells will escape the body's immune surveillance in different ways, ultimately resulting in immune escape (6). Therefore, restoring the antitumor immune response to control and eliminate tumor cells is the core idea of tumor immunotherapy (7). In clinical practice, immunotherapy has been successful at enhancing the tumor killing effect of tumor immune cells by inhibiting programmed death proteins (8). A case in point is pablizumab, whose inhibitory site is the PD-1 molecule. Tumor cells express PD-L1 and bind to the PD-1 receptor on effector T cells, thereby inducing programmed cell death (PCD) in effector T cells (9). PCD refers to the process in which cells initiate the expression of death-related genes through targeted signals in the internal and external environment, which promotes cell "suicide", thus removing unnecessary or abnormal cells from the body (10). To date, the PCD family has expanded from apoptosis and necrosis to pyroptosis, ferroptosis, cuproptosis and other forms (11). In the latest research of Gan et al., a new form of PCD—disulfidptosis—was also found to be involved (12).

Disulfidptosis refers to glucose deficiency resulting in the excessive accumulation of disulfide bonds in cells highly expressing SLC7A11, which leads to abnormal crosslinking of disulfide bonds between cytoskeleton proteins (13), ultimately resulting in abnormal contraction of the cytoskeleton, collapse of the actin network and even cell death (14). Tumor cells usually need to highly express the SLC7A11 protein to recruit additional cystine for the synthesis of reduced glutathione, which balances the oxidation caused by the highly active metabolism of tumor cells (15). In addition, glucose metabolism plays an important role in the biochemical energy supply and cell substance transformation. Cystine entry into cells mediated by the SLC7A11 protein needs to be further reduced to cysteine by reduced nicotinamide adenine dinucleotide phosphate (NADPH) produced by the pentose phosphate pathway (PPP) in glucose metabolism (16). This process can reduce the toxicity of cystine and provide raw materials for the synthesis of glutathione. However, when glucose is deficient, NADPH depletion leads to abnormal accumulation of cystine and other disulfides in cells highly expressing SLC7A11 and triggers disulfidptosis (17). As a species of high-metabolism and high-energy-consumption cell, tumor cells with high SLC7A11 expression exhibit a stronger disulfidptosis response when glucose is depleted (18).

Therefore, in this study, we investigated disulfidptosis-related molecules and pathways using immune- and glucose metabolism-related genes by analyzing LUAD patient gene expression in the TCGA database. We established a risk model to predict LUAD patient survival and immunotherapy efficacy based on disulfidptosis-related genes, providing a therapeutic reference for LUAD patients.

Methods

Patients and datasets

The fragments per kilobase of transcript per million mapped reads (FPKM) standardized RNA-seq data of 600 samples, including 59 normal lung tissues and 541 tumor samples and corresponding clinical, prognostic and tumor mutation burden (TMB) data downloaded from The Cancer Genome Atlas (TCGA) website (https://portal.gdc.cancer.gov/projects/TCGA-LUAD), were used to identify DEGs between normal samples and tumor samples. Patients with unknown clinical information or an overall survival time less than 30 days were excluded. Then, three gene expression profiles of LUAD (GSE26939, GSE68465, and GSE72094) were downloaded from the Gene Expression Omnibus (GEO) (http://www.ncbi.nlm.nih.gov/geo) and used to validate the accuracy of the prognostic model. The 32 genomes involved in

glucose metabolism were downloaded from the Molecular Signatures Database (MsigDB) via gene set enrichment analysis (GSEA; https://www.gsea-msigdb.org/gsea/msigdb/index.jsp) and used to identify disulfidptosis-related genes involved in glucose metabolism. Finally, two databases, IMMPORT (https://www.immport.org/) and InnateDB (https://www.innatedb.ca/), were used to obtain immune-related genes (19). The selected genes were subsequently used to identify disulfidptosis-related genes involved in the immune response.

TCGA differential analysis

We performed differential expression analysis of genes encoding proteins (or their active subunits) that affect glucose metabolism in the TCGA cohort by the Wilcoxon test (20). Gene expression profiles were processed by CIBERSORT to determine the cell composition of complex tissues. The Wilcoxon test was subsequently used to analyze the difference in infiltrating immune cell diversity between normal tissues and lung adenocarcinoma tissues. The differential gene mechanism and signaling pathway enrichment analyses were performed by gene set variation analysis (GSVA) based on the Gene Ontology (GO) dataset (c5.go.v2023.1.Hs.symbols.gmt) and Kyoto Encyclopedia of Genes and Genomes (KEGG) dataset (c2.cp.kegg.v2023.1.Hs.symbols.gmt) from the TCGA cohort. We performed correlation analysis to identify disulfidptosis-related genes (DRGs) via the R packages "corrplot" and "circlize". Additionally, heatmaps were constructed to visualize the results of the differential expression gene (DEG) analysis in the TCGA cohort via the R packages "limma" and "pheatmap". Ultimately, immune cell infiltration was analyzed and visualized by correlation analysis between DEGs and immune cells.

Identification of g/i-DRG-DEGs

A total of 24 DRGs were classified from recently published literature (21) to identify g/i-DRG-DEGs (disulfidptosis-related genes involved in glucose metabolism and the immune response). According to previous reports, Pearson analysis was considered an accepted method for revealing the correlation between DRGs and genes involved in glucose metabolism and the immune response in the RNA-seq data of TCGA LUAD patients (22). The cutoff values of $R > 0.4$ and $P < 0.001$ were acceptable. The differences in the expression levels of the g/i-Genes between LUAD tissues and normal tissues from the lungs were subsequently evaluated via the Wilcoxon test. A false discovery rate (FDR) < 0.05 and a fold change (FC)> 1 were set as screening criteria for obtaining differentially expressed g/i-DEGs. The g/i-DEG and g/i-DRGs intersect to obtain the g/i-DRG-DEG. The g-/i-DRG-DEGs were subsequently subjected to univariate Cox analysis to determine the prognostic value of the g-/i-DRG in LUAD patients via the R package "survival". Least absolute shrinkage and selection operator (LASSO) Cox regression analysis was applied to construct a 7-g/i-DRG-DEG predictive signature (23).

Construction of the disulfidptosis-related prognostic signature

Initially, 7 prognostic genes were screened out on the basis of the optimal penalty parameter l determined by tenfold cross-validation following the minimum criteria. Afterwards, Multivariate Cox regression analysis was conducted to establish a seven-gene predictive model. The computational formula used for determining the disulfidptosis-related prognostic risk score was as follows:

Risk score = Coefi gene1 × gene1 expression + Coefi gene2 × gene2 expression + ···· + Coefi gene × gene expression. Coefi represents the coefficient value of the corresponding gene. Patients were divided into low-risk and high-risk groups based on the median risk score (24).

Time-dependent receiver operating characteristic (ROC) analyses and Kaplan–Meier log-rank tests were used to evaluate the performance and prognostic ability of the predictive signature using the TCGA and GEO datasets via the R packages "timeROC" and "survival", respectively. Additionally, univariate and multivariate Cox regression analyses were performed to assess the ability of the risk model to predict patient prognosis independent of other clinicopathological features.

Clinical and functional analysis

A nomogram for predicting the 1-, 3-, and 5-year survival of LUAD patients was developed using the risk model in conjunction with clinicopathological parameters such as age, sex, and stage (25). We employed a calibration curve to determine if the anticipated survival rate was congruent with the observed survival rate. GSEA was performed to determine which pathway genes were enriched mainly between the high- and low-risk groups via the GO dataset and the KEGG dataset from the molecular signature dataset (https://www.gsea-msigdb.org/gsea/msigdb) as references. The criteria for statistical significance were FC>1, nominal $p<0.05$ and FDR<0.25. Then, functional enrichment analyses based on the KEGG dataset and GO dataset were performed separately (26).

Immune infiltration analysis

Twenty-nine different kinds of tumor infiltrating immune cells (TIICs) were examined by ssGSEA (27). The Wilcoxon test was performed to compare the tumor-infiltrating immune cell scores. K–M survival curves and the log-rank test were used to compare the prognostic significance of immune cells with significant differences between the high-infiltration and low-infiltration groups in the TCGA cohort (28). Additionally, the expression levels of immune checkpoint molecules were extracted from 541 LUAD tissues in the TCGA database. The differential expression of immune checkpoint molecules in the high- and low-risk groups was explored using the Wilcoxon test. The same method was used to analyze the difference in HLA expression (29).

Immune analysis

Tumor immune dysfunction and exclusion (TIDE) is a computational framework for evaluating the possibility of tumor immune escape according to the gene expression profiles of tumor samples. We obtained TIDE scores (http://tide.dfci.harvard.edu/) and performed a difference analysis of TIDE scores for the high- and low-risk groups using Wilcox's method to predict immune escape. To further verify the accuracy of the risk score model, we generated ROC curves for the risk score, TIDE score and TIS. First, we calculated the tumor mutation burden (TMB) for each tumor sample in the TCGA cohort and performed differential analysis of the TMB using the Wilcoxon test. Subsequently, we performed combined survival analysis on the same samples by combining TMB and risk score data. We classified tumors into six subtypes based on immunological characteristics (30). The immune checkpoint inhibitor (ICI) sensitivity score of tumor samples from each TCGA cohort was calculated by the R package "oncoPredict". Finally, we downloaded the immune cell proportion score (IPS) from The Cancer Imaging Archive database (TCIA) and combined it with the TCGA expression data. We used the R packages reshape2 and ggpubr to perform a rank sum test on the IPS between the high- and low-risk groups, and the results were visualized with box plots.

Other statistical analyses

RStudio and its associated packages were used to conduct all the statistical analyses. The 'ggplot2' package was used to visualize the graphs. Wilcox analysis was performed through the 'limma' package. The chi-square test was used to examine differences in the proportions of clinical features. A paired t test was used to analyze the difference in the survival of LUAD tissues and adjacent normal tissues. Differences among multiple groups were analyzed by one-way ANOVA. $p<0.05$ was considered to indicate statistical significance.

Results

Selection and differential analysis of the TCGA cohort

The overall data analysis workflow is shown in Figure 1. We selected the TCGA cohort, which included 600 samples (including 541 LUAD cases and 59 normal tissue cases). Samples with duplicate names were removed by quality control (the expression values of the same patient were averaged), and 508 LUAD samples were ultimately obtained. We annotated the standardized RNA-seq data in the TCGA cohort and obtained a total of 59427 genes. By analyzing the differential expression of the genes affecting glucose metabolism, we found that several hypoxia-inducible genes (such as HIF-1A and PDK-1, $P<0.05$) were significantly upregulated. Moreover, glucose transport-, glycolysis-, and pentose phosphate pathway-related genes (such as SLC2A1, PKM, PFKP, IDH2 and G6PDH, $P<0.05$) were significantly upregulated, suggesting that there were additional active glucose transport, glycolysis and pentose phosphate pathway processes in LUAD cells (Figure 2A).

Furthermore, we analyzed the differences in immune cells in the tumor microenvironment in this cohort (Figure 2C). Through gene set variation analysis (GSVA) analysis based on Kyoto Encyclopedia of Genes and Genomes (KEGG) and Gene Ontology (GO) analyses, we found significant differences in immune-related, metabolism-related and tumor-related pathways (Supplementary Figures S1A, B). Moreover, the expression of 24 disulfidptosis-related genes (DRGs) was significantly different in different tumor-infiltrating immune cells (Figure 2D), and most DRGs were expressed at low levels in CD4+ regulatory T cells and plasma cells. We found that there were 22 DRGs in the TCGA cohort (Figure 2B). We performed differential expression analysis of the DRGs, and all the DRGs were significantly different between normal and tumor tissues ($P<0.05$). Among them, SLC7A11, LRPPRC and other genes were significantly expressed at low levels in normal tissues, while MYH10, PDLIM1 and other genes were significantly highly expressed in normal tissues (Supplementary Figure S1C).

Identification and construction of the 7-g/i-DRG-DEG signature model

We selected a total of 1009 genes from 32 glucose metabolism-related gene sets from the GSEA database and then extracted the expression of 1009 genes from the TCGA cohort via Perl scripts. Using the same method, we evaluated the expression of 2328 genes involved in the immune response from the IMMORT and INNATE gene sets. These two gene sets were combined to obtain the total gene set (g/i-Genes) related to glucose metabolism or the immune response (Figure 3A). The expression levels of the g/i-Genes were performed via differential gene analysis and correlation analysis with the DRGs: *a*. Through differential gene expression analysis ($log2|FC|>1$, $FDR<0.01$), we obtained 905 glucose metabolism- and immune-related genes (g/i-DEGs). *b*. A total of 707 DRG-related genes (g/i-DRGs) were screened by Pearson correlation analysis ($R > 0.4$, $P < 0.001$). A total of 128 differentially expressed disulfidptosis-related genes involved in glucose metabolism and the immune response (g/i-DRG-DEG) were obtained by taking the intersection of g/i-DEG and g/i-DRG. Ultimately, we used the overall survival (OS) data of LUAD patients in the TCGA cohort to examine the predictive ability of g/i-DRG-DEGs through univariate Cox regression analysis, and 37 prognostic g/i-DRG-DEGs were identified as "risk genes".

Subsequently, 508 LUAD patients were randomly divided into two groups: the training group and the validation group. We used the expression profiles of 37 prognostic g/i-DRG-DEGs in the training cohort to construct a 7-g/i-DRG-DEG model containing 7 signatures through LASSOCOX regression analysis, including ARRB1、LIFR、PDGFB、LGR4、KIF20A、NT5E、PHKA1 (Figures 3B, C). There were significant differences in the expression of these seven genes in the TCGA cohort (Figure 3D). Multivariate Cox regression was used to analyze the expression risk score of the 7-g/i-DRG-DEG for each sample. Tumor stage and risk score were

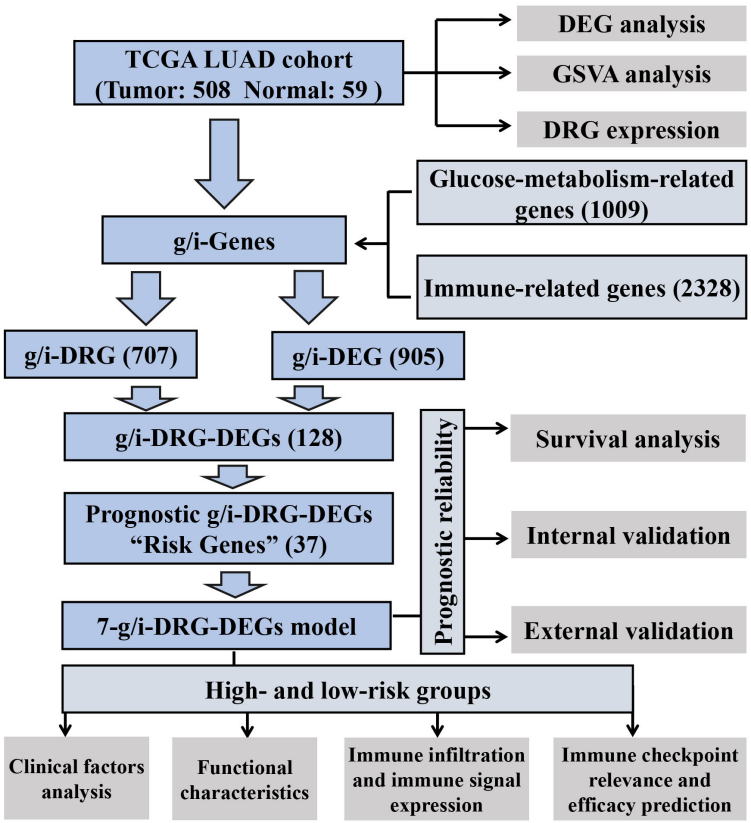

FIGURE 1
Analysis workflow of our work. LUAD, Lung Adenocarcinoma; TCGA, The Cancer Genome Atlas; GSVA, Gene Set Variation Analysis; DEG, Differential Expression Gene; DRG, Disulfidptosis-Related Gene.

found to be important predictors of OS in LUAD patients by univariate Cox regression analysis (Figure 3E, P<0.001). Tumor stage and the risk score were independent determinants of OS in LUAD patients by multivariate Cox analysis (Figure 3F, P<0.001). To better demonstrate the prognostic value of this model for LUAD patients, we used a nomogram to predict the prognosis of LUAD patients at 1, 3, and 5 years (Figure 3G). The calibration curve further verified that the 1-, 3-, and 5-year survival rates were highly consistent with the predicted survival rates (Figure 3H).

Prognostic reliability of 7-g/i-DRG-DEG model

We focused on the prognostic value of the 7-g/i-DRG-DEG signature model and evaluated its performance. Patients in the TCGA training cohort were divided into high-risk and low-risk groups by the median cutoff (Figure 4A), and deaths among LUAD patients increased as risk scores increased (Figure 4D). K–M curve analysis revealed that OS was significantly shorter in the high-risk subgroup than in the low-risk subgroup (P<0.001) (Figure 4G). Moreover, the area under the curve (AUC) values for 1-year, 3-year and 5-year survival were 0.694, 0.706 and 0.749, respectively (Figure 4J). The risk score had greater predictive accuracy than did the other single factors (Figure 4M). To evaluate the prognostic value of OS in the entire TCGA dataset, we further performed confirmatory analyses of the model in the validation cohort and the entire TCGA cohort. Consistent with the results observed in the training cohort, samples from both risk categories were reasonably distributed in the validation cohort (Figures 4B, E, H, K, N) and the entire cohort (Figures 4C, F, I, L, O). Finally, we conducted external validation on three GEO datasets (the GSE26939, GSE68465 and GSE72094 cohorts) to further verify the generalizability of the model. The results demonstrated that the model had the same stable performance (Supplementary Figure S2). The above analyses revealed that the disulfidptosis-related 7-g/i-DRG-DEG signature is a reliable independent predictor of LUAD patients.

The clinical and functional characteristics of risk score based on the 7-g/i-DRG-DEG model

First, we visualized the DEGs between the high-risk and low-risk groups via heatmaps (Supplementary Figure S3). A total of 782 genes were significantly differentially expressed. Among the seven modeling genes, NT5E (log2|FC|=1.06, p<0.05) and KIF20A (|FC|=1.02, p<0.05) were significantly highly expressed in the high-risk group. We divided LUAD patients in the TCGA cohort into different groups randomly according to clinical stage, T stage, age,

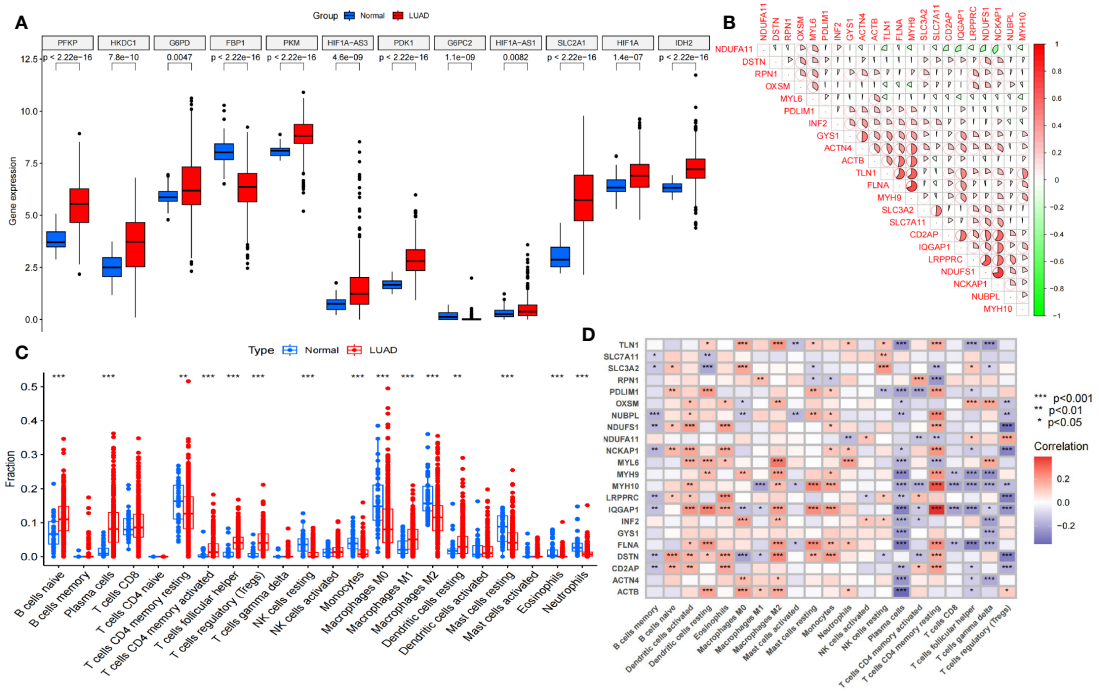

FIGURE 2
Selection and difference analysis of the TCGA cohort. **(A)** Differential expression analysis of the key glycolysis-related genes involved in disulfidptosis. **(B)** Correlation analysis of 22 disulfidptosis-related genes expressed in this TCGA cohort. **(C)** Analysis of immune cells in the tumor microenvironment in this TCGA cohort. **(D)** Disulfidptosis-related genes correlation analysis with different tumor-infiltrating immune cells. NK cells, Natural Killer cells. *P<0.05; **P<0.01; *** P<0.001.

sex, and four representative gene mutations (KRAS, EGFR, TP53, STK11) to study whether the prognostic model could predict LUAD patient OS based on these clinical features (Supplementary Figure S4). We also performed a correlation analysis of risk scores between different clinical variable subgroups and detected significant differences in tumor stage (P<0.001), T stage (P<0.05) and TP53 mutation status (P<0.001). In addition, we found that the OS time of high-risk patients was significantly shorter than that of low-risk patients in every clinical characteristic subgroup (P<0.01). In summary, the 7-g/i-DRG-DEG model can accurately predict the prognosis of LUAD patients without considering certain essential clinical characteristics.

Then, we performed GSEA, KEGG and GO enrichment analyses. Through gene set enrichment analysis (GSEA), we found that several pathways related to tumor development and progression, including the cell cycle, ECM receptor interaction, focal adhesion, actin regulatory, and spliceosome pathways, were upregulated in the high-risk group (Figure 5A), wherein actin regulation is closely related to disulfide denaturation. Moreover, there were also significant differences in several biological processes between the two groups, including intermediate filament, mitotic nuclear, mitotic nuclear regulation, axial filament assembly and ciliary movement (Figures 5B, C). KEGG enrichment analysis revealed significant differences in the cell cycle, motor proteins, complement and coagulation cascades, pancreatic secretion, protein digestion and absorption, metabolism of xenobiotics by cytochrome P450, linoleic acid metabolism and the alpha–linolenic acid metabolism pathway (Figure 5D). GO functional enrichment analysis also revealed significant differences in cytoskeletal motor activity, microtubule motor activity, glycosaminoglycan binding, heparin binding, serine metabolism-related enzyme activities, organelle fission, nuclear division, chromosome segregation, chromosome-associated regions, organelles involved in cell division, and the collagen-containing extracellular matrix (Figure 5E). Importantly, cytoskeletal motor activity and microtubule motor activity are strongly correlated with disulfidptosis.

Immune correlation analysis

To verify whether the signature genes of the 7-g/i-DRG-DEG model are related to tumor immunity, we used the CIBERSORT and ssGSEA algorithms to compare TIICs (31). CIBERSORT analysis demonstrated that there were significant differences in plasma cells, CD8+ T cells, CD4+ memory activated T cells, resting NK cells, M0 macrophages, M1 macrophages, resting dendritic cells, and resting and activated mast cells between the high- and low-risk groups (Figure 6A). K–M analysis further verified that OS was related to different TIIC infiltration levels (P<0.05; Figures 6C–G). Similarly, ssGSEA revealed significant differences in coinhibitory effects on APCs, B cells, CCRs, iDCs, mast cells, class 1 MHC, NK cells, inflammatory cells, T helper cells, TILs, Treg T cells, the type I IFN response and the type II IFN response between the high- and low-risk groups (Figure 6B), as well as in OS time, which was related to different TIIC infiltration levels (Figures 6H–N).

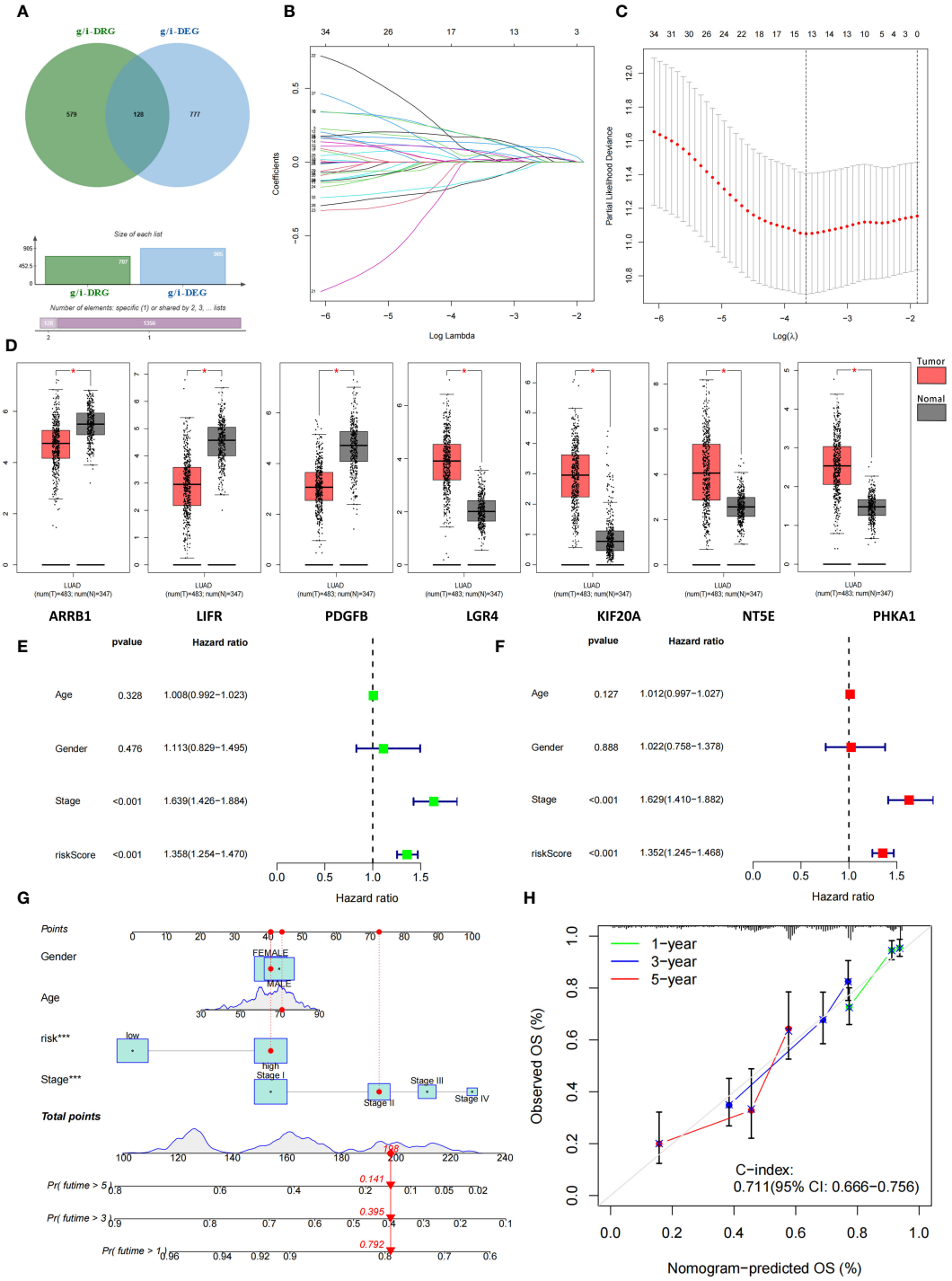

FIGURE 3
Identification and construction of 7-g/i-DRG-DEG signature model. **(A)** Combining two gene sets to obtain the total gene set (g/i-Genes) related to glucose metabolism or the immune response. **(B, C)** Cvfit **(B)** and lambda curves **(C)** demonstrating the generated LASSO regression of 7 signature genes. **(D)** Differential expression of 7 signature genes between tumor and normal tissue. **(E, F)** Univariate **(E)** and multivariate Cox regression analyses **(F)** of overall survival in LUAD patients. **(G, H)** Nomogram analysis **(G)** and calibration curve **(H)** predicting LUAD patient prognosis. *P<0.05.

In addition, we analyzed the tumor mutation burden (TMB) in the TCGA cohort and found that, except for ZNF536 and FLG, the mutation frequency of the remaining genes with the highest mutation frequency was greater in the high-risk group (Figures 7A, B). In detail, the TMB of all samples in the high-risk subgroup was significantly different from that in the low-risk subgroup (P=0.02) (Figure 7F), and the OS time of the high-TMB subgroup was longer than that of the low-TMB subgroup (P=0.024; Figure 7C). The high-TMB plus low-risk subgroup had the longest OS time; in contrast, the low-TMB plus high-risk subgroup had the shortest OS time (P<0.001; Figure 7D). According to Thorsson's study on dividing cancer sample cells into six immune subtypes, we

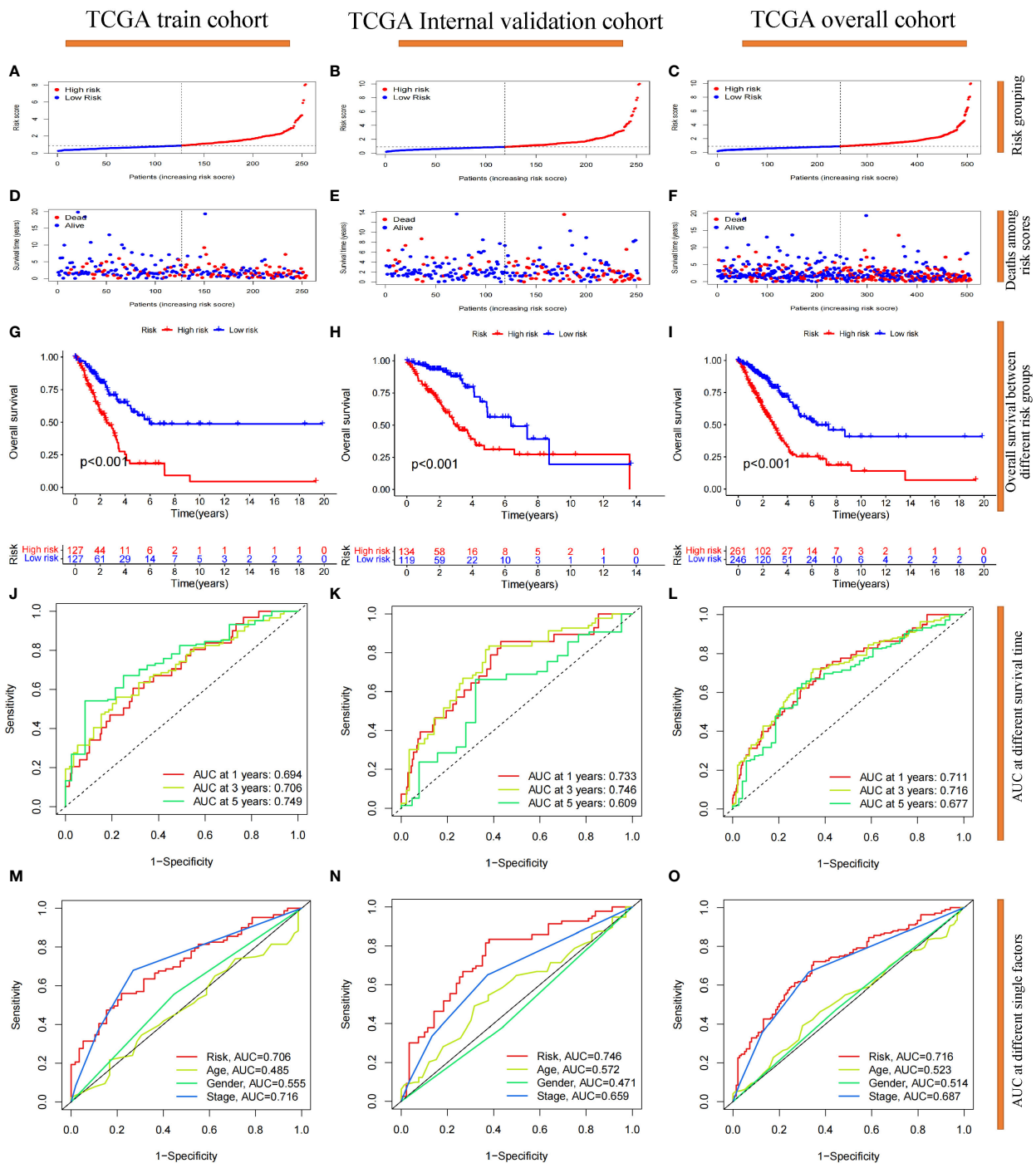

FIGURE 4
Prognostic reliability validation of the 7-g/i-DRG-DEG signature model. **(A–C)** Dividing the cohort into high- and low-risk groups by the median cutoff. **(D–F)** Deaths situation of LUAD patients in the cohort between high- and low-risk groups. **(G–I)** Overall Survival of LUAD patients between the high- and low-risk groups. **(J–L)** Area Under Curve (AUC) at 1-year, 3-year and 5-year survival time. **(M–O)** AUC at risk group, age, gender and tumor stage. **(A, D, G, J, M)** Analysis of the TCGA training cohort. **(B, E, H, K, N)** Analysis of the TCGA internal validation cohort. **(C, F, I, L, O)** Analysis of the TCGA entire cohort.

also found that C1-C6 immunophenotypes were significantly different between the high-risk and low-risk groups (P=0.001) (Figure 7E). Furthermore, we found that there were also significant differences in the expression of immune checkpoint molecules between the high- and low-risk groups (Figures 8A, B). PDC1 and CD274, the most commonly used immune checkpoints, were significantly highly expressed in the high-risk group. Moreover, the HLA gene encoding MHC-I molecules was highly expressed in the high-risk group, while the genes encoding MHC-II were highly expressed in the low-risk group (Figures 8C, D).

Fortunately, the predictive accuracy of our risk-scoring model was comparable to that of the TIDE and TIS models (Figure 8E).

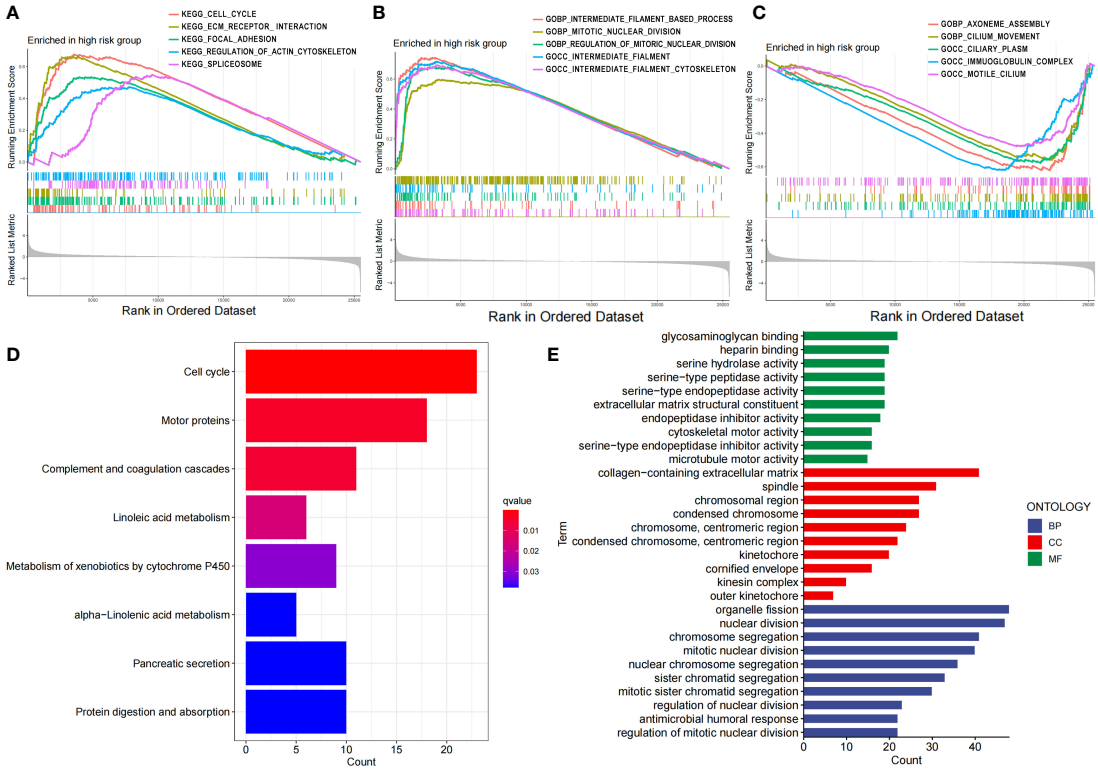

FIGURE 5
Functional characteristics of the risk score based on the 7-g/i-DRG-DEG model. **(A–C)** GSEA analyses between the high- and low-risk groups. **(D, E)** KEGG **(D)** and GO **(E)** analyses between the high- and low-risk groups.

We further verified that the high-risk group in our model had a significantly greater score than the low-risk group by TIDE scoring (P<0.001; Figure 8F), which indicated that the high-risk patients suffered a worse response to immune checkpoint inhibitor (ICI) treatment. However, there was no significant difference in the PD-1-positive group according to the Immunephenoscore (IPS), which indicated that it was difficult for our model to predict the efficacy of PD-1 blockers. The low-risk group with CTLA-4 positive had higher scores than did the high-risk group (P<0.01; Figure 8G), which indicated that the low-risk group might possess stronger CTLA-4 blocker sensitivity. CTLA4 is upregulated in activated regulatory T cells (Tregs) and can bind to CD80 or CD86 on the surface of antigen-presenting cells, thus “shutting down” tumor immunity (32). We noticed that Treg numbers decreased significantly in the high-risk group according to ssGSEA, which further confirmed the predictive effect of our model on CTLA-4 immune checkpoints. To further verify the predictive effect of this risk model on immunotherapy efficacy, we selected data sets (GSE135222 and GSE126044) which contained lung cancer samples after treatment with Ipilimumab, Nivolumab or Pembrolizumab (33). As a result, we found this model had a good predictive effect on immune efficacy, with AUC at 12 and 18 months both exceeding 0.8 (Figure 8H). The PFS of the low-risk group was significantly longer than the high-risk group (P<0.05; Figure 8I). In addition, as the risk score increased, the number of non-responders to ICB treatment was also significantly more than that of responders (P<0.05; Figure 8J). These verifications further illustrated that the 7-g/i-DRG-DEG model could predict the ICB efficacy in NSCLC accurately.

Discussion

From the discovery of aerobic glycolysis to the pentose phosphate pathway (PPP), characterizing the special metabolism of tumor cells has always been a research direction for breakthrough tumor treatment (34). When the oxygen supply cannot meet the energy production needs of mitochondria, tumor cells increase glycolysis to fill the energy gap caused by insufficient ATP, thereby preventing tumor cell death caused by hypoxia (35). Tumor cells steal more glucose by overexpressing glucose transporter proteins, and excess raw material increases glycolysis levels in tumor cells (36). Simply put, tumor cells reprogram the normal process of glucose metabolism to gain an advantage in confronting immune cells and competing with normal tissue cells (37). To further confirm this conclusion, we selected a cohort of 600 samples from the TCGA database and performed differential gene analysis on glucose metabolism-associated genes. We found that genes related to hypoxia, glycolysis, glucose transport, and the PPP were differentially upregulated, which indirectly explained why the hypoxic environment of tumor cells led to a high consumption and low production state in the glucose metabolism pathway. Therefore, the highly expressed glucose transporter (GLUT) plays an important role in maintaining this state of tumor cells.

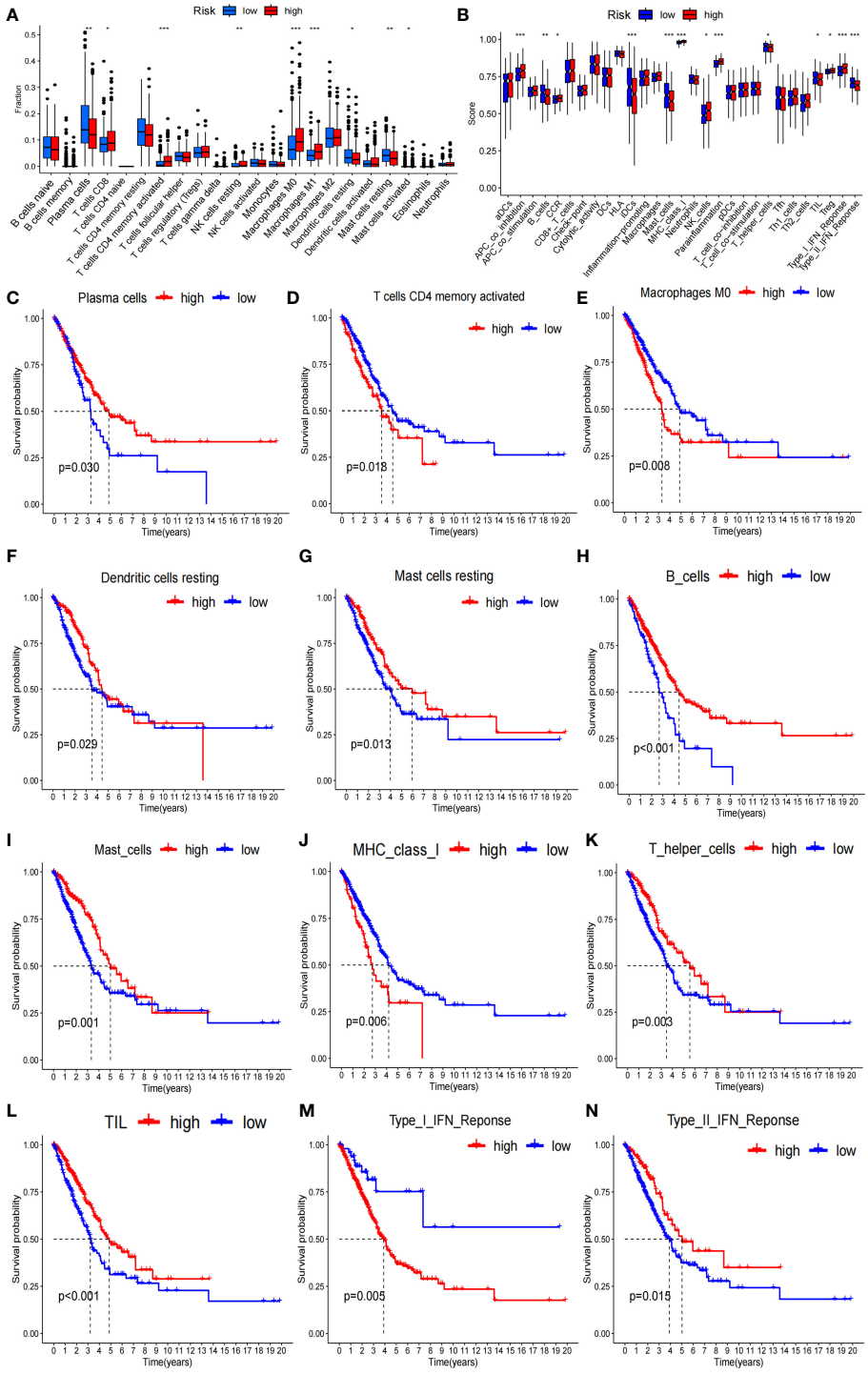

FIGURE 6
Tumor immunity analysis of the 7-g/i-DRG-DEG model. **(A, B)** Immune cell components analyses between the high- and low-risk groups by CIBERSORT analysis **(A)** and ssGSEA analysis **(B)**. **(C–G)** K–M curve between the high- and low-risk groups by CIBERSORT analysis. **(H–N)** K–M curve between the high- and low-risk groups by ssGSEA analysis. APC, Antigen-Presenting Cells; NK cells, Natural Killer cells; IFN, Interferon; DC, Dendritic Cells; TIL, Tumor Infiltrating Lymphocyte. *P<0.05; **P<0.01; *** P<0.001.

Nevertheless, an important reason for the occurrence of disulfidptosis is the insufficient supply of reduced NADPH during glucose starvation, which leads to the abnormal accumulation of cystine and other disulfides in cells with high SLC7A11 expression. As a new form of PCD, disulfidptosis of tumor cells can be further exacerbated by limiting glucose uptake via the use of GLUT inhibitors (38). We further performed differential expression analysis of 22 DRGs, and the results showed that SLC7A11, a key gene involved in disulfidoptosis, was differentially elevated in tumors. Moreover, we found that DRGs expression was also

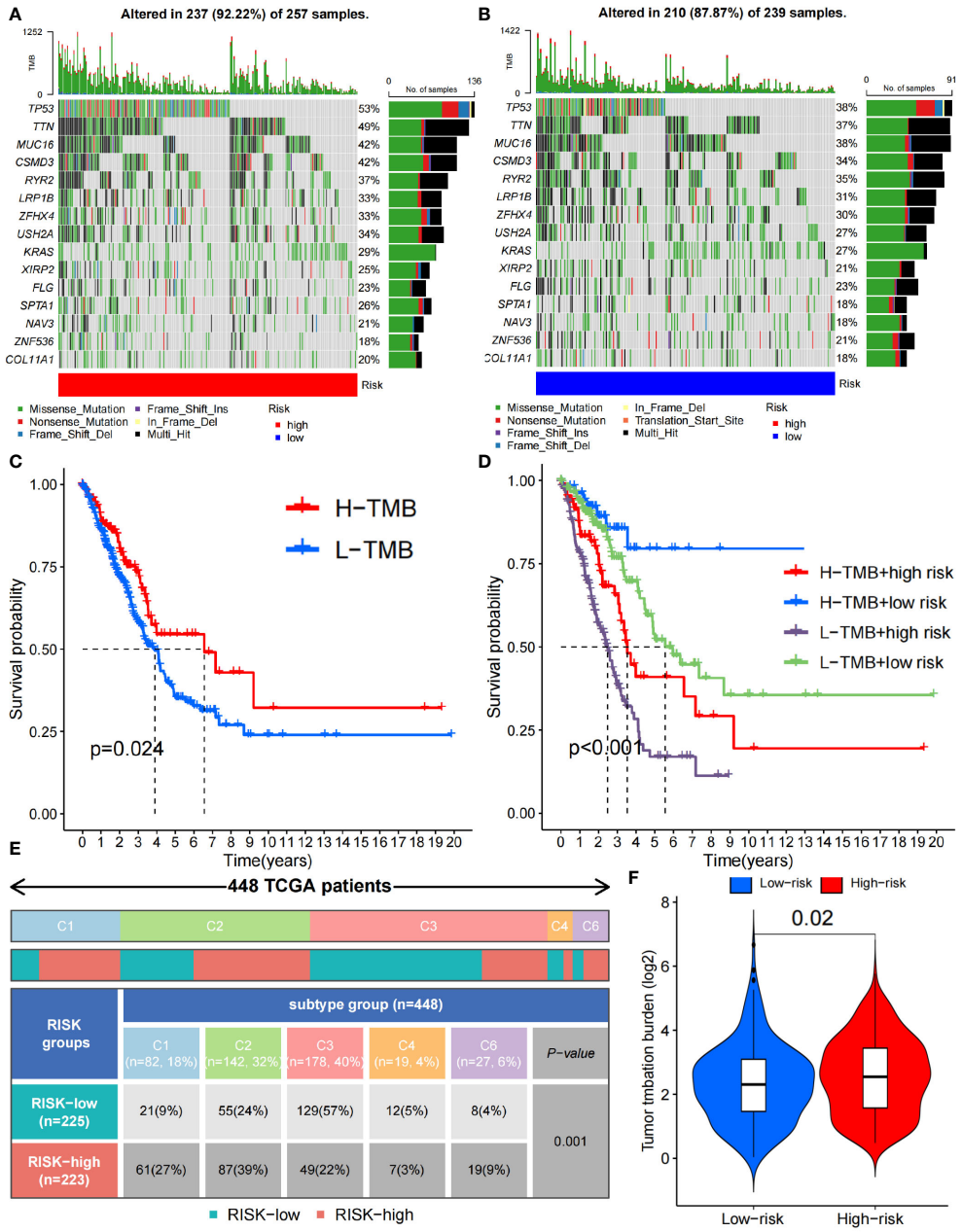

FIGURE 7
Immune characteristics between the high- and low-risk groups. **(A, B)** Waterfall plots depicting the gene mutation landscape of the 15 most frequently mutated genes in the high- **(A)** and low-risk **(B)** groups. **(C)** Survival analysis between high- and low- TMB burden. **(D)** Survival analysis among high- and low- TMB combined with high- and low-risk group. **(E)** C1-C6 immunophenotype analysis between the high- and low-risk groups (C1, wound healing; C2, IFN-γ dominant; C3, inflammatory; C4, lymphocyte depleted; C5, immunologically quiet; C6, TGF-β dominant). **(F)** TMB difference between the high- and low-risk groups. TMB, Tumor Mutational Burden.

differentially increased in several important TIICs involved in tumor suppressive immunity, such as CD4+ T cells and tumor-associated macrophages (TAMs). Therefore, we infer that GLUT inhibitors can also have therapeutic effects on the suppressive tumor immune microenvironment (39).

Immunotherapy plays an irreplaceable role in tumor treatment. However, ICB has great limitations in clinical application. On the one hand, only a few tumors highly express immune checkpoints; on the other hand, the efficacy of ICB is uncertain even in some immune checkpoint-positive tumors (40). Moreover, in some EGFR-mutated tumors, ICB may even lead to tumor hyperprogression (41). There is an urgent need for effective means to predict immune efficacy in the clinic. Therefore, we constructed models related to immunity and glucose metabolism to address this issue.

We extracted a total of 3337 genes through the GSEA, IMMORT and INNATE datasets. We selected 905 genes that were differentially expressed in tumors (g/i-DEG) and 707 genes related to disulfidptosis (g/i-DRG) and then intersected the two gene sets to obtain 128 differentially expressed disulfidptosis-related

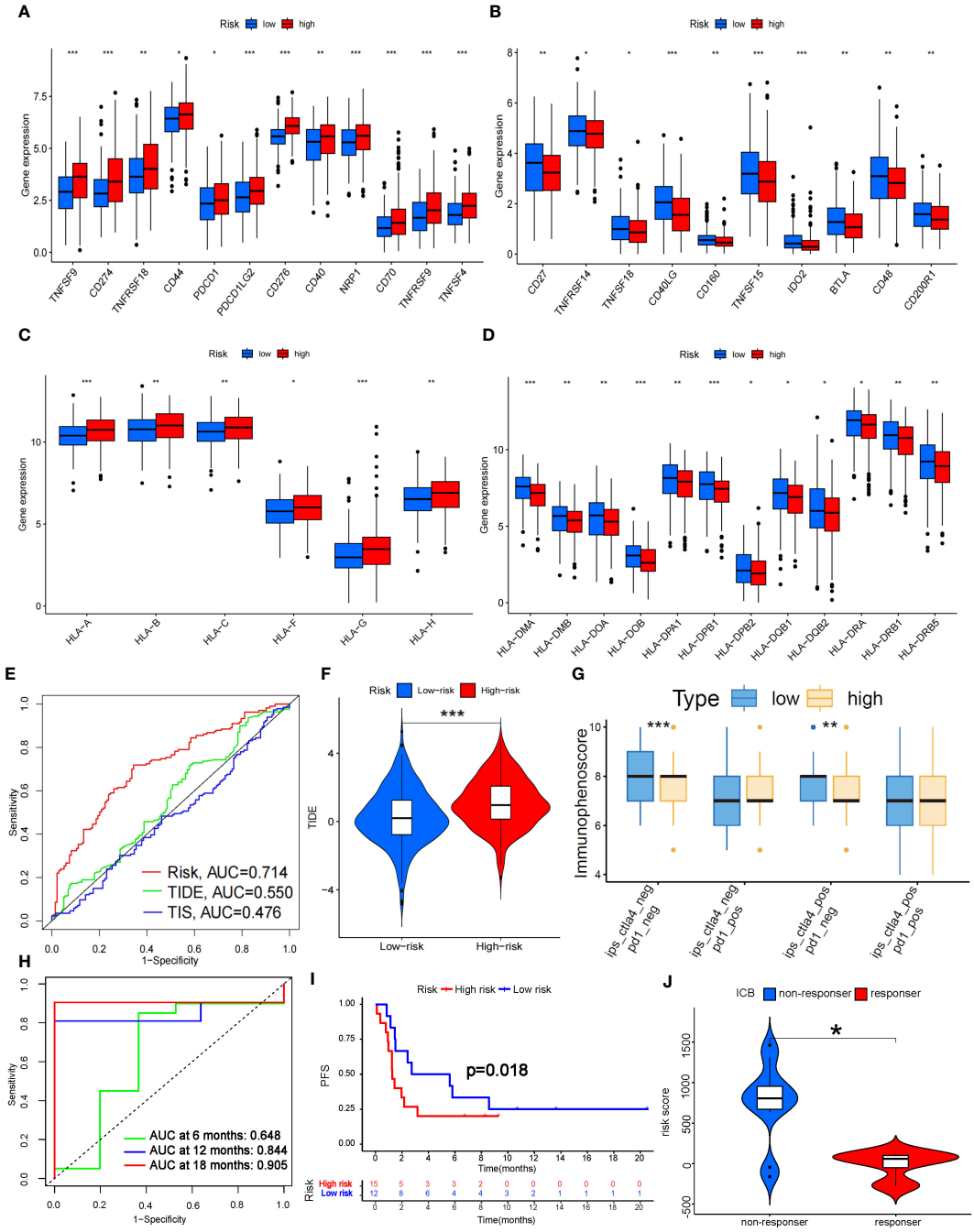

FIGURE 8
Prediction of ICB treatment efficacy. **(A-D)** Differential expression analysis of immune checkpoints **(A, B)** and human leukocyte antigens **(C, D)** between the high- and low-risk groups. **(E)** Prediction accuracy of the risk score model compared to that of the TIDE and TIS models. **(F)** TIDE scoring analysis between the high- and low-risk groups. **(G)** IPS scoring analysis between the high- and low-risk groups. **(H)** Prediction accuracy of ICB efficacy at 6, 12 and 18 months. **(I)** PFS between the high- and low-risk groups. **(J)** Response to ICB with different risk scores. HLA, Human Leukocyte Antigens; PFS, Progression Free Survival; ICB, Immune Checkpoint Blocker; TIDE, Tumor Immune Dysfunction and Exclusion; TIS, Tumor Inflammation Signature. *P<0.05; **P<0.01; *** P<0.001.

genes (g/i-DRG-DEG). Thirty-seven "risk" genes were identified by Cox regression analysis of OS time. Finally, through LASSO Cox regression analysis, we constructed a 7-g/i-DRG-DEG model containing 7 signature genes (ARRB1, LIFR, PDGFB, LGR4, KIF20A, NT5E and PHKA1) in the training cohort. We verified the reliability of the model in the validation set and 3 external GEO datasets stratified by different risk score groups. The results proved that this model can better predict the survival of tumor patients than can the classical TNM staging and risk score models.

We studied the relationship between the 7-g/i-DRG-DEG model risk score and cellular functions. Through differential gene analysis, we found that the NT5E and KIF20A genes, which are highly related to tumor development, were differentially elevated in the high-risk group. The GSEA, KEGG and GO analyses revealed

enrichment of genes involved in various functions and pathways, including the cell cycle, cytoskeleton movement activity, microtubule movement activity, organelle division, nuclear division, chromosome segregation, chromosome-related regions, organelles involved in cell division and extracellular matrix containing collagen. Notably, the genes in the high-risk group were positively correlated with the cell cycle, ECM receptor interaction, regulation of the actin cytoskeleton, and regulation of mitosis, indicating that the genes in the high-risk group had stronger cell proliferation and division functions. This result is consistent with the clinical observation that poorly differentiated and highly proliferative tumor cells usually have a worse prognosis (42). As mentioned before, disulfidptosis relies on abnormal cross-linking of disulfide bonds between cytoskeletal proteins, and the high-risk group also exhibited a greater ability to regulate the actin cytoskeleton (43).

Given that the immune response of the tumor microenvironment is an important factor in determining tumor cell aggressiveness and progression (44), we further verified the immune impact of the 7-g/i-DRG-DEG model. By comparing TIICs through the CIBERSORT and ssGSEA algorithms respectively, we found that immune cells with direct tumor killing functions, such as plasma cells and CD8+ T cells, were significantly reduced in the high-risk group, while immune cells with auxiliary functions, such as M0 macrophages, M1 macrophages, and activated CD4+ T cells, were significantly increased in the high-risk group. However, tumor-associated macrophages (TAMs) have been a hot topic of cancer research in recent years. An increasing number of studies have proven that TAM infiltration is strongly correlated with the poor prognosis of tumor patients due to a series of functions that promote tumor development, such as supporting tumor cell proliferation, invasion, and metastasis (45). We also noted that in another similar disulfidptosis-related model, the expression of signature genes was positively correlated with M1 cell migration and invasion, indicating that there is obvious tropism of M1 cells in the high-risk group (46).

In addition, CD8+ T cells in the high-risk group were more susceptible to immune checkpoint effects. We found that the immune checkpoint molecule CTLA-4, which is currently widely used in clinical applications, was significantly overexpressed in the high-risk group, indicating that the high-risk group may have a suppressive TME that is more unfavorable for tumor immunity. Subsequently, the accuracy of the prediction of ICB efficacy was verified to further illustrate that this model has reference value for the clinical application of ICB. Specifically, The high expression of HLA-I class molecules in the high-risk group also confirmed this conclusion. HLA-I class molecules stimulate cytotoxic immune responses by binding CD8+ T cells, and HLA-II class molecules bind to CD4+ T cells (47). An increase in HLA class I molecules in the high-risk group indicated a decrease in CD8+ T cells. HLA-II class molecules were lower in the high-risk group, further indicating that $CD4^+$ immune cells increased, which proved by immune infiltration analysis. For the immune phenotype, the expression of angiogenic genes was enhanced in the high-risk group, which had a high proliferation rate, and Th2 cells were prone to acquired immune osmosis, which stimulated the proliferation of CD4+ T cells and B cells. These results indicate that the TME in the high-risk group was more inclined to exhibit a “cold immune” phenotype, which is associated with greater tumor malignancy and a more tolerant immune environment (48).

In summary, benefiting from the development of bioinformatics technology, we constructed a 7-gene signature prediction model based on TCGA LUAD patient data and evaluated patient tumor prognosis risk through signature gene expression. We demonstrated the reliability of this model and further validated its value in predicting tumor immunity through immune infiltration analysis. Such studies will help to develop more personalized treatment strategies in the future, promote the development of new drugs, and ultimately extend the survival expectancy of cancer patients.

Data availability statement

The datasets presented in this study can be found in online repositories. The names of the repository/repositories and accession number(s) can be found in the article/Supplementary Material.

Ethics statement

The studies involving humans were approved by 920th Hospital of Joint Logistics Support Force. The studies were conducted in accordance with the local legislation and institutional requirements. Written informed consent for participation was not required from the participants or the participants’ legal guardians/next of kin in accordance with the national legislation and institutional requirements.

Author contributions

KZ: Conceptualization, Writing – original draft. GL: Validation, Visualization, Writing – original draft. QW: Data curation, Formal analysis, Writing – original draft. XL: Conceptualization, Writing – original draft. HC: Resources, Writing – review & editing. FL: Methodology, Project administration, Writing – review & editing. SL: Validation, Visualization, Writing – review & editing. XS: Resources, Supervision, Writing – review & editing. YL: Funding acquisition, Resources, Supervision, Writing – review & editing.

Funding

The author(s) declare financial support was received for the research, authorship, and/or publication of this article. Key project of applied basic research of Yunnan Province (202001AS070241); Innovation team of cancer precision radiotherapy transformation research of Yunnan Province (202305AS350028); Outstanding Youth Fund Project of Yunnan Province (202201AV070009).

Conflict of interest

The authors declare that the research was conducted in the absence of any commercial or financial relationships that could be construed as a potential conflict of interest.

Publisher's note

All claims expressed in this article are solely those of the authors and do not necessarily represent those of their affiliated organizations, or those of the publisher, the editors and the reviewers. Any product that may be evaluated in this article, or claim that may be made by its manufacturer, is not guaranteed or endorsed by the publisher.

Supplementary material

The Supplementary Material for this article can be found online at: https://www.frontiersin.org/articles/10.3389/fimmu.2024.1398802/full#supplementary-material

References

1. Herbst RS, Morgensztern D, Boshoff C. The biology and management of non-small cell lung cancer. *Nature*. (2018) 553:446–54. doi: 10.1038/nature25183

2. Barta JA, Powell CA, Wisnivesky JP. Global epidemiology of lung cancer. *Ann Glob Health*. (2019) 85:8. doi: 10.5334/aogh.2419

3. Liao B-C, Lee J-H, Lin C-C, Chen Y-F, Chang C-H, Ho C-C, et al. Epidermal growth factor receptor tyrosine kinase inhibitors for non-small-cell lung cancer patients with leptomeningeal carcinomatosis. *J Thorac Oncol*. (2015) 10:1754–61. doi: 10.1097/JTO.0000000000000669

4. Westover D, Zugazagoitia J, Cho BC, Lovly CM, Paz-Ares L. Mechanisms of acquired resistance to first- and second-generation EGFR tyrosine kinase inhibitors. *Ann Oncol*. (2018) 29:i10–9. doi: 10.1093/annonc/mdx703

5. Keathley R, Kocherginsky M, Davuluri R, Matei D. Integrated multi-omic analysis reveals immunosuppressive phenotype associated with poor outcomes in high-grade serous ovarian cancer. *Cancers (Basel)*. (2023) 15:3649. doi: 10.3390/cancers15143649

6. Madeddu C, Donisi C, Liscia N, Lai E, Scartozzi M, Macciò A. EGFR-mutated non-small cell lung cancer and resistance to immunotherapy: role of the tumor microenvironment. *Int J Mol Sci*. (2022) 23:3649. doi: 10.3390/ijms23126489

7. Tan Y, Chen Q, Li X, Zeng Z, Xiong W, Li G, et al. Pyroptosis: a new paradigm of cell death for fighting against cancer. *J Exp Clin Cancer Res*. (2021) 40:153. doi: 10.1186/s13046-021-01959-x

8. Lahiri A, Maji A, Potdar PD, Singh N, Parikh P, Bisht B, et al. Lung cancer immunotherapy: progress, pitfalls, and promises. *Mol Cancer*. (2023) 22:40. doi: 10.1186/s12943-023-01740-y

9. Janssen EM, Dy SM, Meara AS, Kneuertz PJ, Presley CJ, Bridges JF. Analysis of patient preferences in lung cancer - estimating acceptable tradeoffs between treatment benefit and side effects. *Patient Prefer Adherence*. (2020) 14:927–37. doi: 10.2147/PPA.S235430

10. Liu J, Hong M, Li Y, Chen D, Wu Y, Hu Y. Programmed cell death tunes tumor immunity. *Front Immunol*. (2022) 13:847345. doi: 10.3389/fimmu.2022.847345

11. Li D, Shi Z, Liu X, Jin S, Chen P, Zhang Y, et al. Identification and development of a novel risk model based on cuproptosis-associated RNA methylation regulators for predicting prognosis and characterizing immune status in hepatocellular carcinoma. *Hepatol Int*. (2023) 17:112–30. doi: 10.1007/s12072-022-10460-2

12. Liu X, Zhuang L, Gan B. Disulfidptosis: disulfide stress-induced cell death. *Trends Cell Biol*. (2024) 34:327–37. doi: 10.1016/j.tcb.2023.07.009

13. Li S, Lu Z, Sun R, Guo S, Gao F, Cao B, et al. The role of SLC7A11 in cancer: friend or foe? *Cancers (Basel)*. (2022) 14:3059. doi: 10.3390/cancers14133059

14. Liu X, Nie L, Zhang Y, Yan Y, Wang C, Colic M, et al. Actin cytoskeleton vulnerability to disulfide stress mediates disulfidptosis. *Nat Cell Biol*. (2023) 25:404–14. doi: 10.1038/s41556-023-01091-2

15. Koppula P, Zhuang L, Gan B. Cystine transporter SLC7A11/xCT in cancer: ferroptosis, nutrient dependency, and cancer therapy. *Protein Cell*. (2021) 12:599–620. doi: 10.1007/s13238-020-00789-5

16. Liu X, Olszewski K, Zhang Y, Lim EW, Shi J, Zhang X, et al. Cystine transporter regulation of pentose phosphate pathway dependency and disulfide stress exposes a targetable metabolic vulnerability in cancer. *Nat Cell Biol*. (2020) 22:476–86. doi: 10.1038/s41556-020-0496-x

17. Li J, Yang C, Zheng Y. A novel disulfidptosis and glycolysis related risk score signature for prediction of prognosis and ICI therapeutic responsiveness in colorectal cancer. *Sci Rep*. (2023) 13:13344. doi: 10.1038/s41598-023-40381-5

18. Machesky LM. Deadly actin collapse by disulfidptosis. *Nat Cell Biol*. (2023) 25:375–6. doi: 10.1038/s41556-023-01100-4

19. Wu P, Zheng Y, Wang Y, Wang Y, Liang N. Development and validation of a robust immune-related prognostic signature in early-stage lung adenocarcinoma. *J Transl Med*. (2020) 18:380. doi: 10.1186/s12967-020-02545-z

20. Zhang Z, Zhu H, Wang X, Lin S, Ruan C, Wang Q. A novel basement membrane-related gene signature for prognosis of lung adenocarcinomas. *Comput Biol Med*. (2023) 154:106597. doi: 10.1016/j.compbiomed.2023.106597

21. Zhang H-B, Pan J-Y, Zhu T. A disulfidptosis-related lncRNA prognostic model to predict survival and response to immunotherapy in lung adenocarcinoma. *Front Pharmacol*. (2023) 14:1254119. doi: 10.3389/fphar.2023.1254119

22. Xiao W, Geng W, Xu J, Huang Q, Fan J, Tan Q, et al. Construction and validation of a nomogram based on N6-Methylandenosine-related lncRNAs for predicting the prognosis of non-small cell lung cancer patients. *Cancer Med*. (2023) 12:2058–74. doi: 10.1002/cam4.4961

23. Yue T, Chen S, Zhu J, Guo S, Huang Z, Wang P, et al. The aging-related risk signature in colorectal cancer. *Aging (Albany NY)*. (2021) 13:7330–49. doi: 10.18632/aging.v13i5

24. Li D, Jin S, Chen P, Zhang Y, Li Y, Zhong C, et al. Comprehensive analysis of cuproptosis-related lncRNAs for prognostic significance and immune microenvironment characterization in hepatocellular carcinoma. *Front Immunol*. (2022) 13:991604. doi: 10.3389/fimmu.2022.991604

25. Iasonos A, Schrag D, Raj GV, Panageas KS. How to build and interpret a nomogram for cancer prognosis. *J Clin Oncol*. (2008) 26:1364–70. doi: 10.1200/JCO.2007.12.9791

26. Hou W, Kong L, Hou Z, Ji H. CD44 is a prognostic biomarker and correlated with immune infiltrates in gastric cancer. *BMC Med Genomics*. (2022) 15:225. doi: 10.1186/s12920-022-01383-w

27. Zhang X, Jiang D, Li S, Zhang X, Zheng W, Cheng B. A signature-based classification of lung adenocarcinoma that stratifies tumor immunity. *Front Oncol*. (2022) 12:1023833. doi: 10.3389/fonc.2022.1023833

28. Luo C, Lei M, Zhang Y, Zhang Q, Li L, Lian J, et al. Systematic construction and validation of an immune prognostic model for lung adenocarcinoma. *J Cell Mol Med*. (2020) 24:1233–44. doi: 10.1111/jcmm.14719

29. Yan Z-J, Yu C-T, Chen L, Wang H-Y. Development of a TMErisk model based on immune infiltration in tumour microenvironment to predict prognosis of immune checkpoint inhibitor treatment in hepatocellular carcinoma. *Brief Bioinform*. (2023) 24:bbad067. doi: 10.1093/bib/bbad067

30. Thorsson V, Gibbs DL, Brown SD, Wolf D, Bortone DS, Ou Yang T-H, et al. The immune landscape of cancer. *Immunity*. (2018) 48:812–830.e14. doi: 10.1016/j.immuni.2018.03.023

31. Yang X, Shi Y, Li M, Lu T, Xi J, Lin Z, et al. Identification and validation of an immune cell infiltrating score predicting survival in patients with lung adenocarcinoma. *J Transl Med*. (2019) 17:217. doi: 10.1186/s12967-019-1964-6

32. Liu Y, Zheng P. Preserving the CTLA-4 checkpoint for safer and more effective cancer immunotherapy. *Trends Pharmacol Sci*. (2020) 41:4–12. doi: 10.1016/j.tips.2019.11.003

33. Huang J, Yuan L, Huang W, Liao L, Zhu X, Wang X, et al. LATPS, a novel prognostic signature based on tumor microenvironment of lung adenocarcinoma to better predict survival and immunotherapy response. *Front Immunol*. (2022) 13:1064874. doi: 10.3389/fimmu.2022.1064874

34. Dasgupta S, Rajapakshe K, Zhu B, Nikolai BC, Yi P, Putluri N, et al. Metabolic enzyme PFKFB4 activates transcriptional coactivator SRC-3 to drive breast cancer. *Nature*. (2018) 556:249–54. doi: 10.1038/s41586-018-0018-1

35. Kierans SJ, Taylor CT. Regulation of glycolysis by the hypoxia-inducible factor (HIF): implications for cellular physiology. *J Physiol*. (2021) 599:23–37. doi: 10.1113/JP280572

36. Ancey P-B, Contat C, Meylan E. Glucose transporters in cancer - from tumor cells to the tumor microenvironment. *FEBS J*. (2018) 285:2926–43. doi: 10.1111/febs.14577

37. Liu Y, Zhou Q, Song S, Tang S. Integrating metabolic reprogramming and metabolic imaging to predict breast cancer therapeutic responses. *Trends Endocrinol Metab*. (2021) 32:762–75. doi: 10.1016/j.tem.2021.07.001

38. Zheng P, Zhou C, Ding Y, Duan S. Disulfidptosis: a new target for metabolic cancer therapy. *J Exp Clin Cancer Res*. (2023) 42:103. doi: 10.1186/s13046-023-02675-4

39. Choi H, Na KJ. Different glucose metabolic features according to cancer and immune cells in the tumor microenvironment. *Front Oncol*. (2021) 11:769393. doi: 10.3389/fonc.2021.769393

40. Anichini A, Perotti VE, Sgambelluri F, Mortarini R. Immune escape mechanisms in non small cell lung cancer. *Cancers (Basel)*. (2020) 12:3605. doi: 10.3390/cancers12123605

41. Negrao MV, Skoulidis F, Montesion M, Schulze K, Bara I, Shen V, et al. Oncogene-specific differences in tumor mutational burden, PD-L1 expression, and outcomes from immunotherapy in non-small cell lung cancer. *J Immunother Cancer*. (2021) 9:e002891. doi: 10.1136/jitc-2021-002891

42. Calderaro J, Ziol M, Paradis V, Zucman-Rossi J. Molecular and histological correlations in liver cancer. *J Hepatol*. (2019) 71:616–30. doi: 10.1016/j.jhep.2019.06.001

43. Wang X, Lin J, Li Z, Wang M. In what area of biology has a "new" type of cell death been discovered? *Biochim Biophys Acta Rev Cancer*. (2023) 1878:188955. doi: 10.1016/j.bbcan.2023.188955

44. Zuo Y-H, Gao W-N, Xie Y-J, Yang S-Y, Zhou J-T, Liang H-H, et al. Tumor PKCδ instigates immune exclusion in EGFR-mutated non-small cell lung cancer. *BMC Med*. (2022) 20:470. doi: 10.1186/s12916-022-02670-0

45. Wang J, Li D, Cang H, Guo B. Crosstalk between cancer and immune cells: Role of tumor-associated macrophages in the tumor microenvironment. *Cancer Med*. (2019) 8:4709–21. doi: 10.1002/cam4.2327

46. Wang Z, Chen X, Zhang J, Chen X, Peng J, Huang W. Based on disulfidptosis-related glycolytic genes to construct a signature for predicting prognosis and immune infiltration analysis of hepatocellular carcinoma. *Front Immunol*. (2023) 14:1204338. doi: 10.3389/fimmu.2023.1204338

47. Anderson P, Aptsiauri N, Ruiz-Cabello F, Garrido F. HLA class I loss in colorectal cancer: implications for immune escape and immunotherapy. *Cell Mol Immunol*. (2021) 18:556–65. doi: 10.1038/s41423-021-00634-7

48. Pan X, Zhang C, Wang J, Wang P, Gao Y, Shang S, et al. Epigenome signature as an immunophenotype indicator prompts durable clinical immunotherapy benefits in lung adenocarcinoma. *Brief Bioinform*. (2022) 23:bbab481. doi: 10.1093/bib/bbab481

frontiers | Frontiers in Immunology

TYPE Review
PUBLISHED 13 August 2024
DOI 10.3389/fimmu.2024.1410018

OPEN ACCESS

EDITED BY
Shensi Shen,
Sichuan University, China

REVIEWED BY
Ankita Leekha,
University of Houston, United States
Qiming Gong,
Southwest Medical University, China

*CORRESPONDENCE
Liancheng Zhu
zhulc@cmu.edu.cn

RECEIVED 31 March 2024
ACCEPTED 24 July 2024
PUBLISHED 13 August 2024

CITATION
Guo K, Lu M, Bi J, Yao T, Gao J, Ren F and Zhu L (2024) Ferroptosis: mechanism, immunotherapy and role in ovarian cancer. *Front. Immunol.* 15:1410018. doi: 10.3389/fimmu.2024.1410018

Ferroptosis: mechanism, immunotherapy and role in ovarian cancer

Ke Guo[1], Miao Lu[1], Jianlei Bi[2], Tianyu Yao[1], Jian Gao[1], Fang Ren[1] and Liancheng Zhu[1]*

[1]Department of Obstetrics and Gynecology, Shengjing Hospital of China Medical University, Shenyang, Liaoning, China, [2]Department of Obstetrics and Gynecology, The Second Hospital of Dalian Medical University, Dalian, Liaoning, China

Ovarian cancer is currently the second most common malignant tumor among gynecological cancers worldwide, primarily due to challenges in early diagnosis, high recurrence rates, and resistance to existing treatments. Current therapeutic options are inadequate for addressing the needs of ovarian cancer patients. Ferroptosis, a novel form of regulated cell death with demonstrated tumor-suppressive properties, has gained increasing attention in ovarian malignancy research. A growing body of evidence suggests that ferroptosis plays a significant role in the onset, progression, and incidence of ovarian cancer. Additionally, it has been found that immunotherapy, an emerging frontier in tumor treatment, synergizes with ferroptosis in the context of ovarian cancer. Consequently, ferroptosis is likely to become a critical target in the treatment of ovarian cancer.

KEYWORDS

ferroptosis, ovarian cancer, Xc system, MDSC, immunotherapy

1 Introduction

Ovarian cancer is one of the most prevalent and deadly subtypes of gynecological malignant tumors. There are several types of ovarian cancer, with epithelial ovarian cancer being the most common (1). Ovarian cancer is typically diagnosed using a combination of therapies, including surgery, chemotherapy, and innovative immunotherapy. Between 1976 and 2015, the death rate from ovarian cancer in the United States declined by 33%, while its incidence fell by 29% between 1985 and 2014 (2). However, the five-year survival rate of patients remained less than thirty percent (2), leading to a higher mortality rate among female reproductive system malignancies, as the majority of ovarian cancers were only discovered in stage III (51%) or stage IV (29%) (3). Furthermore, there is a lack of treatment resistance and early diagnostic targets for ovarian cancer. Therefore, novel therapeutics are urgently needed to improve the early diagnosis, treatment, and prognosis of ovarian cancer.

Ferroptosis is a novel process of iron-dependent regulated cell death induced by erastin, characterized by the accumulation of iron ions, increased lipid peroxide concentration, reduced glutathione peroxidase 4 (GPx4) activity, and often accompanied by large amounts of reactive oxygen species (4). Ferroptosis has been shown to be intimately associated with several biological processes and diseases, including Alzheimer's disease and brain hemorrhage. Furthermore, it has been proposed that ferroptosis may play a role in tumor suppression (5). Recent studies have demonstrated that ferroptosis is closely related to the growth regulation of ovarian cancers through mechanisms involving the transsulfuration pathway, Hippo signaling pathways, and p53. Additionally, the combination of immunotherapy and ferroptosis treatment is becoming a research hotspot in ovarian cancer. This review outlines the current understanding and research on ferroptosis in ovarian cancer, as many specific regulatory processes and mechanisms remain unclear. Further elucidation of the ferroptosis process in ovarian cancer is expected to identify more therapeutic targets and drugs, laying the groundwork for novel treatment approaches and improved prognoses.

2 Mechanism of ferroptosis

Ferroptosis is commonly believed to be regulated primarily by three mechanisms: iron overload, lipid peroxidation, and the oxidized form mediated by the xc-cysteine/glutamate antiporter system (6).Notably, ferroptosis is primarily caused by unbalanced cellular metabolic processes, including dysregulated iron and lipid metabolism, and the production of reactive oxygen species (ROS) (7).This unique characteristic of ferroptosis has led to the discovery of new pathways and mechanisms which closely related to ferroptosis regulation in recent years (Figure 1).

2.1 GPX4-GSH pathway

The XC-system is an amino acid transporter that forms the GPX4-GSH pathway with the functional subunit SLC7A11 and the regulatory subunit SLC3A2, playing a crucial role in the cellular antioxidant system. Through the XC-system, cystine and glutamate are exchanged between the inside and outside of the cell. Inside the cell, cystine is converted to cysteine, which is further transformed into glutathione (GSH). GSH acts as a cofactor for glutathione peroxidase 4 (GPX4), helping to restore polyunsaturated fatty acids (PUFAs) and inhibiting ferroptosis, making it a vital regulator of ferroptosis (8). When GPX4 is suppressed, it promotes the accumulation of lipid ROS, accelerates cell death, induces the occurrence of ferroptosis, and inhibits the growth of tumor cells (9). Studies have found that drugs such as erastin (10), sulfasalazine (11), ssorafenib (12), and p53 (13)can causing the production of GSH by inhibiting the XC system and induce the occurrence of ferroptosis. In ovarian cancer, Luo et al. discovered that PAX8, a gene that suppresses ferroptosis, can be inhibited by PAX8i to induce ferroptosis through the GPX4 pathway in combination with RSL3. This approach increases sensitivity to ferroptosis inducers and inhibits the progression of ovarian cancer (14).

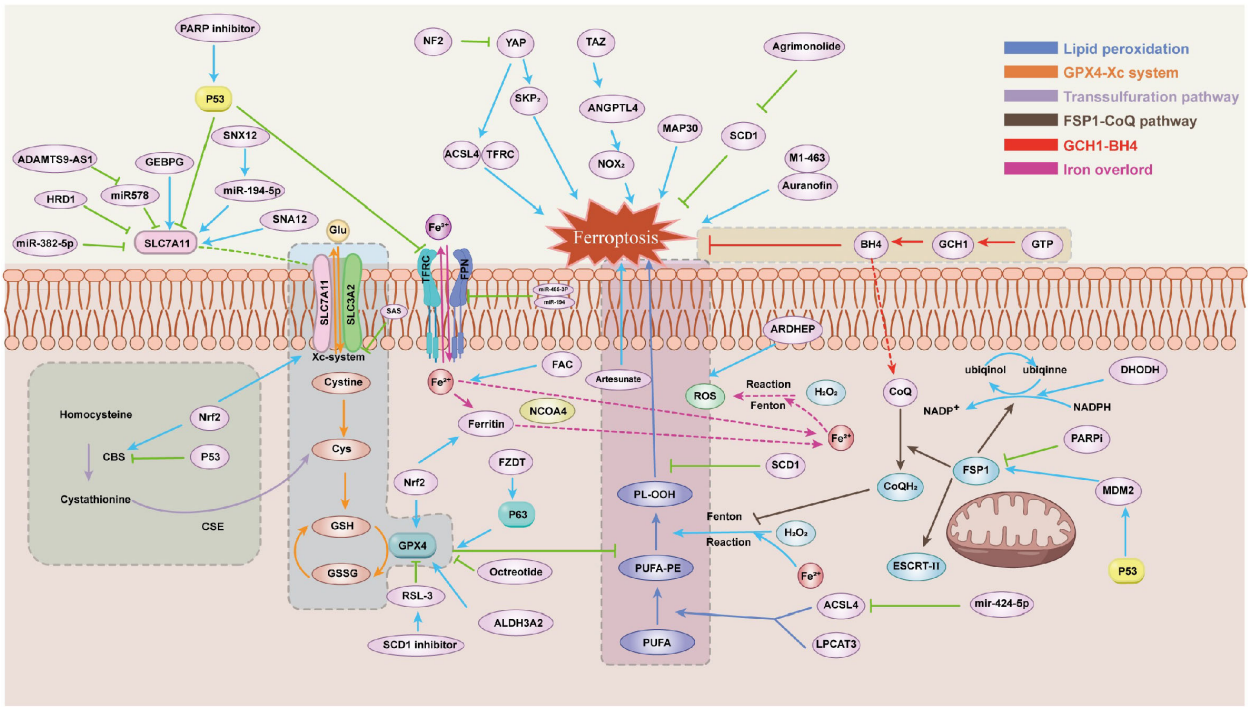

FIGURE 1
The main mechanism of ferroptosis.

Mammal cells can also obtain cysteine through the transsulfuration pathway in certain cases, in addition to their dependence on the XC system (15). Methionine can be converted to cysteine via the catalytic actions of cystathionine β-synthase (CBS) and cystathionine gamma-lyase (CSE). Verschoor and colleagues discovered that blocking the transsulfuration pathway lowers the level of GSH and GPX activity in an ovarian cancer model cell line (16), which ultimately results in ferroptosis.

2.2 Lipid peroxidation

Ferroptosis is primarily caused by the lipid peroxidation of polyunsaturated fatty acids (PUFAs). The acyl-CoA synthetase long-chain family member 4 (ACSL4) and lysophosphatidylcholine acyltransferase 3 (LPCAT3) catalyze the production of polyunsaturated fatty acid-phosphatidylethanolamine (PUFA-PE) from PUFA (17). PUFA-PE is the most susceptible to the oxidation of lipids, which under the influence of the Fenton reaction undergo a series of oxidative reactions, thereby promoting the production of PL-OOH (18).This extensive lipid peroxide reaction induces the occurrence of ferroptosis (19). Sebastian Doll (20) and colleagues found that inhibiting ACSL4 can suppress ferroptosis by regulating lipid peroxidation, suggesting that ACSL4 may be a potential target for preventing ferroptosis-related diseases.

2.3 FSP1-CoQ10-NAD (P) H pathway

A recently identified antioxidant system that controls ferroptosis without relying on the GPX4 pathway is ferroptosis suppressor protein 1 (FSP1) (21). By reducing and restoring coenzyme Q10 (CoQ10), which inhibits lipid peroxide, FSP1 is drawn to the plasma membrane to prevent ferroptosis. FSP1, possessing NAD(P)H oxidase activity (22), can catalyze the conversion of ubiquinone to ubiquinol, with the resulting ubiquinol scavenging free radicals and thereby preventing ferroptosis. However, Kang et al. discovered that in FSP1-knockout cells, CoQ10 cannot reverse the ferroptosis induced by ferroptosis inducers. On the other hand, the ESCRT-III membrane repair system lets the ferroptosis inductor do its job again, which is to cause ferroptosis in FSP-1 cells. Consequently, it is unlikely that FSP1 might also be involved in ESCRT-III-mediated ferroptosis suppression (23). Additionally, it has been shown that dihydroorotate dehydrogenase (DHODH) can prevent ferroptosis in the mitochondrial membrane by converting ubiquinone to ubiquinol. In GPX4-deficient cancer cells, DHODH inactivation leads to extensive lipid peroxidation and ferroptosis (24). However, none of the specific mechanisms are clear enough.

2.4 The BH4-GCH1 pathway

GTP cyclohydrolase 1 (GCH1) produces tetrahydrobiopterin (BH4) from GTP, acting as a speed limit enzyme. GCH1 prevents ferroptosis by acting as an antioxidant through BH4/BH2. High-expressed BH4 cells can prevent oxidative damage by producing CoQ10, which prevents oxidation directly and prevents cellular ferroptosis (25).

2.5 Iron overload

The transferrin receptor (TFRC) recognizes Fe (3+) bound to transferrin (TF) in the serum and facilitates its entry into the cell. Once inside, Fe (3+) is reduced to Fe (2+) and stored in the iron pool. An excess of Fe (2+) activates iron-containing enzymes, which react with H2O2 to generate a significant amount of reactive oxygen species (ROS), leading to ferroptosis (26). When the stored ferritin is recognized by NCOA4, it is recruited into the autophage, causing oxidative damage, a process also known as ferritinophagy, which can help induce ferroptosis (5). Simultaneously, the susceptibility to ferroptosis is increased when ferritinophagy takes place, which results in a significant amount of free iron (27).

3 Regulation of ferroptosis in ovarian cancer

3.1 Signal pathway

3.1.1 HIPPO pathway

The hippo pathway is a tumor-suppressing pathway that can detect and control cell density. The two main transcript coactivators of this pathway are Yes-associated protein 1 (YAP) and transcription coactivator with PDZ-binding motif (TAZ). Transcription enhancement-related domains (TEAD) members can interact with TAP to mediate multi-cancer proliferation, renewal, transfer, and drug resistance (28). The Hippo pathway controls ferroptosis in ovarian cancer through YAP and TAZ. When TAZ is overexpressed, OVCA cells become susceptible to ferroptosis. TAZ also causes ferroptosis by controlling the level of its direct target gene, angiooietin-like 4(ANGPTL4), which in turn controls the activity of NADPH oxidase 2 (NOX2) (29). When TAZ is overexpressed, OVCA cells become susceptible to ferroptosis. When SKP2 or YAP are removed, lipid oxidation is inhibited during the ferroptosis inducer (30).Therefore, the Hippo pathway may be a major target in ovarian tumor cell ferroptosis and play a crucial role in controlling the susceptibility of ferroptosis inducers to ovarian tumor ferroptosis.

3.1.2 Nrf2 pathway

To keep cell metabolism, oxidation restoration, protein sedimentation balance, and antioxidation going, nuclear factor erythroid 2-related factor 2 (NRf2) is a transcription factor that is very important. It has been discovered that numerous significant ferroptosis regulators are NRF2's target genes (31). For example, research has discovered that NRF2 can govern the ferroptosis of tumor cells through many downstream targets such as GPX4 channels (32, 33), HMOX1 (34), ferritinophagy activating proteins (ATG5 etc.) (31), while NRF 2 has also been reported to be connected with the prognosis of tumors (35).

Several studies have found that NRF2 is a regulatory factor in ovarian tumor ferroptosis. Apatinib can induce ferroptosis by combining olaparib with NRf2, inhibiting GPX4 expression (36). Pachymaran can induce ferroptosis by lowering NRF2 mRNA to raise Fe2+ and lower levels of NRF2,HO-1 and GPX4 proteins in ovarian cancer cells (37). Norcantharidin (NCTD) can also regulate ferroptosis by acting on the NRF2/HO-1/GPX4/xCT axis, leading to ferroptosis of ovarian cancer cells by inhibiting NRF2 (38). Tripterygium glycosides, by targeting the NRF2/GPX4 signal axis, disrupt the stability of the oxidation restoration reaction and induce ferroptosis in ovarian tumor cells, thereby enhancing the chemical susceptibility of ovarian cancer to cisplatin (39). Wang et al. found that eryodictyol reduced NRF2 expression in mouse tumor tissue and regulated ferroptosis in ovarian cancer through NRF2/HO-1/NQO1 signal pathways (40). Furthermore, NRF2 can enhance erastin-induced ferroptosis resistance by upgrading the expression of CBS in anti-erastin cells in the transsulfuration pathway (41). Chelerythrine (CHE), widely recognized as an anticancer agent, was found by Jia et al. to exert inhibitory effects on ovarian cancer cell growth. This inhibition was achieved through its action on Nrf2, which mediated the expression of ferroptosis-related proteins and subsequently promoted ferroptosis (42). NRF2 can also play a role in ferritin synthesis and degradation NRF2 regulates ferritin by HECT and RLD domains containing E3 ubiquitin protein ligase 2(HERC2), NCOA4 and vesicle-associated membrane protein 8(VAMP8). In addition, ovarian cancer cells with high NFE2L2/NRF2 expression have been found to increase sensitivity to the ferroptosis inducer (43).This demonstrates that NRF2 is an important treatment target for ovarian cancer and plays a role in a variety of regulatory pathways. While other ferroptosis regulating factors in ovarian cancer that are regulated by NRF2 are not yet fully studied, future studies of NRf2 in ovary cancer are to be expected.

3.1.3 P53 pathway

P53 is a tumor suppressor protein that plays a powerful role in cell aging, death, and DNA damage repair. In recent years, more and more research has found that P53 plays a crucial role in ferroptosis. The regulatory effect of P53 is two-way and has a different effect as the environment changes. When lipid peroxide is slight, it inhibits the occurrence of ferroptosis, helping the cell to survive. However, when lipid peroxide is persistent and severe, it induces ferroptosis, helping tumor cell death (44). For the GPX4-Xc system, P53 can combine and degrade SLC7A11, enhance the expression of SAT1 and GLS2 in cells (5, 13), and reduce the production of GSH by inhibiting CBS (45) expression, thereby suppressing GPX4.When p53 elevates SAT1 expression, it can indirectly promote ALOX15 elevation, promoting lipid peroxide (46).Studies have also shown that p53 can inhibit the development of ferroptosis by blocking dipeptidyl-peptidase-4 (DPP4) activity, limiting the peroxidation of lipids (47). P53 inhibits TFR1 and ZRT/IRT-like Protein 14 (ZIP14),reducing cellular Fe (2+) (48). p53 can also inhibit the occurrence of ferroptosis by reactivating the two-minute binoculars (MDM2) in mice, activating FSP1 (49).

Through p53, PARP inhibitors block SLC7A11 expression in ovarian cancer, which lowers GSH synthesis and increases lipid peroxide and ferroptosis (50). Apatinib combined with olaparib causes ferroptosis in ovarian cancer through p53 dependent way (36). A lack of MEX3A causes the p53 protein to become more stable, which prevents ferroptosis and encourages ovarian cancer (51). To encourage OVCAR-3-cell ferroptosis, ursolic acid (UA) can trigger the JNK/p53 signal pathway (52).

3.2 Gene

3.2.1 SCD1

Stearoyl-CoA Desaturase 1(SCD1) is an enzyme that catalyzes the synthesis of monounsaturated fatty acids in ovarian cancer cells and is highly expressed in ovary tumor cells (53). Inhibition or absence of the SCD1 gene can induce cellular ferroptosis. SCD1/FADS2 has a positive ratio to the level of unsaturated fatty acids, which can regulate lipid peroxide. Inhibiting SCD1/FADS2 can also directly degrade GPX4, thereby inducing the development of ferroptosis (54). Menin-mixed-lineage leukemia(Menin-MLL) inhibitor MI-463 can mediate ferroptosis in cancer cells through lipid peroxide regulated by SCD1 (55). Furthermore, in ovarian cancer cells, agrimonolide can target SCD1 as a new ferroptosis inducer (56). The ferroptosis pathway is one of the SCD1 routes that TP53 (13) can regulate, indicating that ovarian cancer with TP53 mutations may respond better to a SCD1 inhibitor. In addition to increasing ovarian sensitivity to ferroptosis, SCD1 medication suppression may be more advantageous for TP53-mutated ovarian malignancies (57). TESFAY found that ferroptosis inhibitor erastin can be used in conjunction with SCD1-inhibitors A939572 to regulate lipid metabolism, significantly enhancing the anti-tumor effect of the induced ferroptosis inducer in the ovarian cells, increasing ovarian cell susceptibility to ferroptosis inducers (53). Treatment with the SCD1-inhibitors MF-438, CAY10566, and 939572 makes ovarian carcinoma cells more susceptible to the death ferroptosis-inducers RSL3 and Erastin (58). Treatment of ovarian tumor cells with SCD1/FADS2 inhibitors in combination with ferroptosislatin can raise the rate of apoptosis, decrease the rate of cell mobility and tumor metastasis, and increase the sensitivity of ovarian tumor cells to ferroptosislatin (54). According to a number of studies, SCD1 inhibitors in ovarian cancer can dramatically increase the effect of ferroptosis and aid in tumor cell regression, in addition to increasing the sensitivity of ferroptosis inducers. This suggests that SCD1 may one day serve as a novel therapeutic.

3.2.2 FZD7

Wnt receptor Frizzled-7 (FZD7) is a transmembrane receptor that functions beyond the signals of both the canonical pathway and the Wnt/Ca2+ pathway. Overexpression of FZD7 can drive the development of ovarian tumors via the Wnt signal pathway (59). FZD7 directly links to the expression of GSS, GSR, GPX2, and IDH genes related to GSH metabolism. In ovarian cancer tissue, FZD7 can activate the carcinogen P63, enhance the expression of GPX4, prevent tumor cell ferroptosis, and decrease the susceptibility of drug-

resistant ovarian cancer cells to ferroptosis (60). In addition, miR-1-3p significantly improves the sensitivity of ovarian cancer cells to Erastin or RSL3-induced ferroptosis by decreasing FZD7 expression (61). This shows that treating ovarian cancer cells resistant to platinum may benefit from targeting FZD7. Simultaneously, an innovative prospect of combining a ferroptosis inducer with a FZD7 inhibitor emerged.

3.2.3 SNAI2

Research has demonstrated strong expression of SNAI2 in ovarian cancer cells, directly linking this expression to the cells' ability to survive, proliferate, invade, and spread. The promoter area of SLC7A11 is bound by SNAI2, and when SNAI2 is blocked, SLC7A11 expression is down-regulated, which causes ferroptosis in ovarian carcinoma cells (62). A leucine zipper transcription factor called CCAAT/enhancer binding protein gamma(CEBPG) has also been found to enhance transcription in SLC7A11 and promote GPX4 expression, thereby inhibiting ferroptosis in the OC. and leading to tumor cell development. Additionally, at the clinical level, CEBPG expression has been observed to be associated with an adverse prognosis in patients with OC (63). The E3 ubiquitin ligase 3-hydroxy-3-methylglutaryl reductase degradation (HRD1) inhibits the growth of tumors in a variety of cancer forms. HRD1 has the capacity to control ubiquitination and OC cell stability. Through increasing SLC7A11 degradation, HRD1 interacts with SLC7A11 in OC cells to encourage ferroptosis and prevent the growth of OC tumors (64).

3.2.4 PARP

Poly (ADP-ribose) polymerases (PARP) are involved in cellular processes such as DNA repair, transcription, metabolic regulation and cell death (65). PARP inhibitors are currently an effective treatment for BRCA mutant ovarian cancer (66). PARPi reduces the expression of SLC7A11 in a p53 dependent way, thereby reducing the biosynthesis of GSH and promoting lipid peroxide and ferroptosis. It was also found that PARPi was associated with the expression of CBS, FSP-1,etc. (50).Olaparib is a classic PARP inhibitor for treating BRCA mutant ovarian cancer. The combined treatment of olaparib and arsenic trioxide (ATO) activates the AMPKα pathway and inhibits SCD1 expression, resulting in a significant increase in lipid peroxide in ovarian cancer cells, which induces the occurrence of ferroptosis (67).However, BRCA (wild type) ovarian cancer can produce olaparib resistance by repairing PARPi-induced DNA damage. On this basis, PARPi combined with FINS targeting SLC7A11 or GPX4 can synergistically enhance ferroptosis, thereby producing an effective tumor suppression effect against BRCA (wild type) ovarian cancer (50).Similarly, Apatinib combined with olaparib reduced GPX4 by inhibiting expression of NRF2 and autophagy, inducing ferroptosis in ovarian cancer. However, in P53 (wild type) ovarian cancer cells, the p53 activator RITA can increase the sensitivity of resistant cells to ferroptosis, enhancing the effect of ferroptosis (36).PARP inhibitors, in addition to their therapeutic effects on BRCA mutant ovarian cancer cells, have also been combined with ferroptosis inducers or critical factors to enhance the sensitivity of mutant ovary cancer to ferroptosis.

3.2.5 ARDHEP 15

In the clinical treatment of malignancies, microtubule-targeted agents (MTA) are useful chemotherapeutic agents, and the interaction of microtubulin with VDAC provides a novel target for inducing ferroptosis in cancer cells (68). Tubulin polymerization can be inhibited by the newly synthesized novel aroyl diheterocyclic pyrrole (ARDHEP) 15. ARDHEP may induce ferroptosis in ovarian tumor cells and prevent tumor cell growth by upregulating GPX4, increasing intracellular ROS and Fe(2+) buildup, and stimulating cellular oxidative damage (69). It is a novel therapeutic target for tumors.

ALDH3A2 is a member of the ALDH family. Studies have shown that removing ALDH3A2 boosts lipid metabolism and, when combined with GPX4, helps prevent ferroptosis. Additionally, the expression of ALDH3A2 is directly correlated with the ferroptosis susceptibility of ovarian cancer cells, which can prevent ferroptosis in ovarian cancerous cells (69).

3.2.6 RNA

Microscopic RNAs (miRNAs) are a class of endogenous expressions of non-coding RNA that are highly significant in biological processes such as differentiation, proliferation, mortality, etc. Recent research has also discovered that miRNAs regulate ferroptosis, connecting them to numerous diseases, including cancer (70). By directly combining the 3' Untranslated Regions (UTR) with ACSL4, mir-424-5p inhibits the expression of ACSL4, thereby reducing the ferroptosis induced by erastin and RSL3, thereby lowering the sensitivity of ovarian cancer tissue to ferroptosis, ultimately leading to the malignant progression of OC (71). Researchers found that Extrinsic Fe and DFO target miR-485-3P and miR-194 to regulate the expression of FPN. Large-scale induction of miR-485-3P expression can reduce intraocular FPN, which raises Fe2+ in ovarian cancer cells and causes the cells to undergo ferroptosis (72). By boosting miR-382-5p to lower SLC7A11 and so preventing the proliferation, invasion, and transfer of ovarian cancer cells, lidocaine also causes a buildup of iron content and reactive oxygen species (ROS) in the OC. cells (73). lncRNA is a non-coding RNA with a length longer than 200 nucleocarbons and plays a significant role in epigenetic regulation, cell cycle regulation, and cell differentiation regulation (67).lncRNA ADAMTS9-AS1 can block the process of ferroptosis in OC cells via modulating the mir-587/SLC7A11 axis, which can further the malignant growth of OC cells (73). JIN et al. found that LncRNA CACNA1G-AS1 can stimulate the growth and transfer of ovarian cancer cells through the FTH1-IGF2BP1 axis to regulate the expression of FTH1 and inhibit ferritinophagy (74). According to recent research, circRNA regulates ferroptosis, anemia, metabolism, tumor growth, and anemia (75). CircRNASnx12 improves immunomodulatory resistance in ovarian cancer by targeting miR-194-5p/SLC7A11 pathways to block ferroptosis. CircRNASnx12 can therefore serve as an effective therapeutic target for overcoming cisplatin resistance (76) (Table 1).

TABLE 1 Genes involved in ferroptosis of ovarian cancer cell.

Gene	Mechanism	Function	Reference
TAZ	Target ANGPTL4/NOX2	induce ferroptosis and increase sensitivity	(29)
YAP	Target SKP2	induce ferroptosis and increase sensitivity	(30)
NRF2	Target GPX4/HO-1/HMOX1/CBS	inhibit ferroptosis	(41)
P53	GPX4/Xc system	induce ferroptosis	(77)
PARP	GPX4/Xc system/ P53/FSP-1	induce ferroptosis and increase sensitivity	(50)
MEX3A	Target P53	induce ferroptosis	(51)
SCD1	Target GPX4	inhibit ferroptosis	(54, 57)
F7D7	Target Wnt/ GPX4/TP63	inhibit ferroptosis and decrease sensitivity	(60)
miR-1-3p	Target F7D7	induce ferroptosis and increase sensitivity	(61)
SNAI2	Target SLC7A11	inhibit ferroptosis	(62)
GEBPG	Target SLC7A11	inhibit ferroptosis	(63)
HRD1	Target SLC7A11	induce ferroptosis	(64)
ALDH3A2	Target GPX4	inhibit ferroptosis and decrease sensitivity	(78)
mir-424-5p	Target ACSL4	inhibit ferroptosis and decrease sensitivity	(71)
miR-485-3P	Target FPN	induce ferroptosis	(72)
miR-194	Target FPN	induce ferroptosis	(76)
miR-382-5p	Target SLC7A11	induce ferroptosis	(73)
lncRNA ADAMTS9-AS1	mir-587/SLC7A11	inhibit ferroptosis	(79)
lncRNA CACNA1G-AS1	Target FTH1-IGF2BP1	inhibit ferroptosis	(74)
circRNASnx12	Target miR-194-5p/SLC7A11	inhibit ferroptosis and increase sensitivity	(76)
HNF1	Target P53	inhibit ferroptosis and increase sensitivity	(80, 81)
FDX1	Target ROS	inhint ferroptosis and decrease sensitivity	(82)
c-myc	Target NCOA4/HMGB1	inhibit ferroptosis	(83)
MTHFR	Target HMOX1	inhibit ferroptosis	(84)

3.3 Drug therapy

Researchers are still studying the development of ferroptosis-related drugs for ovarian cancer despite the increasing clarity on many mechanisms of ferroptosis. The thioredoxin reductase auranofin, is used in conjunction with the MENIN-MLL inhibitor MI-463 to induce ferroptosis in ovarian tumor cells (55). Artesunate (ART) is a widely used anti-malaria drug that has been studied to find multiple cellular responses involved in tumor cells, such as mortality, malnutrition, ferroptosis, etc. (85). Greenshields and others found that ART treatment induces ovarian cancer cells to produce a large amount of ROS, which exerts a potent anti-proliferative and cell-toxic effect on ovarian cancers. At the same time, neither the use of mortality inhibitors nor ferroptosis related-inhibitors can completely eliminate the effect of ART, indicating that ART has a combined inhibitory effect on ovarian cancer tumor cells in a variety of ways (86).Octreotide, an FDA-approved medication that is commonly used in the clinical treatment of ovarian cancer, can directly decrease the expression of GPX4 inducing ferroptosis (87). A rating system of ferroptosis-related genes constructed using TCGA mRNA expression data found Dimethyloxalylglycine (DMOG) to be a potentially sensitive drug for ovarian cancer (88). Large doses of selenium induce cell death mediated by ferroptosis through abnormal GPx4 and lipid peroxide mechanisms, thereby producing anti-cancer effects. High doses of selenium have been speculated to lead to GPx4 deficiency through the Wnt/β-catenin signal pathway (89). After the treatment of ovarian cancer stem cells (OCSCs) with anisomycin, the levels of triphosadenine and total glutathione were found to be significantly reduced, Fe2+ levels increased, lipid peroxide increased, and the activity of OCSCs significantly decreased. Furthermore, anisomycin reduces the level of transcription of gene clusters that encode pathways related to the regulation of ferroptosis, such as glutathione metabolism and the autophagy signal transduction pathway. The genes of the core factor ATF4 of these two pathways are significantly expressed in ovarian cancer tissue and are associated with a poor prognosis. Thus, anisomycin may induce ferroptosis in ovarian cancer stem cells by reducing ATF4 to regulate glutathione metabolism (90). Leukemia inhibitory factor (LIF) and its receptor (LIFR) can induce ferroptosis via the GPX4 system. Additionally, LIF and LIFR have been found to act on M1 macrophages, enhancing the activity of CD8+ T cells and thereby regulating the immunogenicity of ovarian cancer cells. However, the specific mechanisms and pathways involved in this process remain unclear (91).

As a new direction in ferroptosis applications, nanomaterials are safer, more durable and more accurate in applications that induce ferroptosis to produce ovarian tumor suppression (92). In addition, nanomaterials have been found to enhance the immunotherapy effect of induced ferroptosis (93). Superparamagnetic iron oxid spio-serum can effectively induce lipid peroxide and produce a large amount of toxic ROS by reducing the expression of the ferroptosis related proteins SLC7A11 and GPX4 in OVCA cells, play synergies with p53 and promote the occurrence of ferroptosis in ovarian cancer cells (77). Biomimetic magnetic nanoparticles Fe3O4-SAS @ PLT are constructed by Fe3O4 and a platelet membrane covering containing sulfasalazine (SAS), which can increase the sensitivity to ferroptosis, inducing ferroptosis by inhibiting the Xc-system. In addition, Fe3O4-SAS @ PLT can also produce mild immunogenicity that triggers the immunotherapy response to ovarian cancer (94). Chemokinetic therapy (CDT) is considered one of the most promising cancer treatments, mainly through the Fenton reaction. As a Fenton

reagent, iron nitroprusside, (FeNP) has a therapeutic effect on ovarian cancer organs originating from high-grade serous ovarian carcinoma (HGSOC) by inhibiting GPX4's involvement in ferroptosis (95) (Table 2).

Although research on medications linked to ferroptosis is still ongoing, there is still hope for significant future developments in ovarian cancer management.

TABLE 2 The drug that regulate ferroptosis and sensitivity of ovarian tumor cell to chemotherapy.

DRUG	Mechanism	Function	Reference
erastin	target ROS	induce ferroptosis	(96)
Apatinib	target NRF2/ GPX4/p53	inhibit ferroptosis	(36)
pachymaran	target NRF2/ HO-1	inhibit ferroptosis	(37)
NCTD	target NRF2/GPX4	induce ferroptosis	(38)
tripterygium glycosides	target NRF2/ HO-1/NQO1	induce ferroptosis and increase sensitivity	(39)
eriodictyol	target Nrf2/HO-1/NQO1	induce ferroptosis	(40)
UA	target JNK/P53	induce ferroptosis	(52)
MI-463	target SCD1	induce ferroptosis	(54)
Agrimonolide	target SCD1	induce ferroptosis	(56)
ARDHEP15	target GPX4	induce ferroptosis	(69)
ART	target mTOR/ROS	induce ferroptosis	(86)
Octreotide	target GPX4	induce ferroptosis	(87)
Sodium Selenite	target Wnt/β-catenin/GPX4	induce ferroptosis	(97)
Anisomycin	target ATF4/GPX4	induce ferroptosis	(90)
spio=serum	target SLC7A11/GPX4	induce ferroptosis	(77)
Fe3O4 - SAS @ PL	target Xc system	induce ferroptosis	(98)
FeNP	target GPX4	induce ferroptosis	(95)
ferlixit	target Fe2+	induce ferroptosis	(99)
Sorafenib	target SLC7A11/GPX8	induce ferroptosis	(100)
MAP30	target Ca2+	induce ferroptosis and increase sensitivity	(101)
oncolytic vaccinia virus	target CXCR4	induce ferroptosis and increase sensitivity	(102)
GALNT14	EGFR/mTOR	induce ferroptosis and increase sensitivity	(103)
Chelerythrine	target Nrf2	induce ferroptosis	(42)
LIF	Target GPX4	induce ferroptosis	(91)

3.4 Enhancement of chemoresistance

Currently, the main clinical treatments for ovarian cancer are surgery and chemotherapy with paclitaxel combined with platinum drugs. However, the prognosis for ovarian cancer patients who are susceptible to chemotherapy resistance is poor. Nevertheless, research has shown that ferroptosis inducers can improve the chemotherapy sensitivity of ovarian cancer cells (104). The ferroptosis inducer erastin has been shown to activate the apoptosis pathway, which may increase the sensitivity of HEY and SKOV3 cells to cisplatin (105). Furthermore, expression due to ATP binding cassette subfamily B member 1 (ABCB1) in OVCA cells that are resistant to another chemotherapeutic drug, dositase, erastin exhibits a strong reversal effect of ABCB1, increasing the susceptibility of OVCAC cells to docetaxel (94).

The sensitivity of cells to ferroptosis and ferroptosis conditions is strongly correlated, and the iron compound ferlixit joint erastin can overcome the chemotherapeutic resistance of ferroptosis ovarian cancer (99). Studies have also demonstrated that the acquired synthesis of cystine and glutathione impacts carboplatin resistance in ovarian cancer. Hepatocyte nuclear factor-1-beta (HNF1) can promote glutathione synthesis to avoid carboplatin resistance to ovarian clear cell carcinoma (80). Simultaneously, P53 was identified as a key pathway in the bioinformatic analysis of the resistance of HNF1 to ovarian cancer (81). The loss of Fdx1 mediated by siRNA in cisplatin-resistant cells is potentiated by an elevation in mitochondrial membrane potential and cisplatin-induced lipid peroxidation, ultimately leading to ferroptosis. Immunohistochemical analysis of clinical specimens from ovarian cancer patients revealed higher expression levels of Fdx1 in cisplatin-resistant specimens compared to cisplatin-sensitive ones. Fdx1 may be a new and appropriate diagnostic and prognostic marker and therapeutic molecular target for the treatment of COVID-19 (82). SLC7A11 and GPX4 high expression levels linked to platinum resistance in EOC patients. The combined expression of SLC7A11 and GPX4 may be a significant independent prognostic factor and a potential treatment target for EOC patients (106). For example, Tripterygium glycosides target the NRF2/GPX4 signal axis and mess up the stable reaction of oxidation restoration. They also cause ferroptosis in A2780/DDP cells and make ovarian cancer more likely to respond to cisplatin (39).

Statistics for progression-free survival and clinically significant improvement were found in patients with ovary cancer who were treated with sorafenib combined with topotecan maintenance therapy (100). MAP30 protein from Momordica charantia and cisplatin can synergistically induce ferroptosis in ovarian cancer cells by altering metabolism (101). GALNT14, a member of the acetylgalactosaminyltransferases family, which can regulate the stability of EGFR proteins to inhibit the EGFR/mTOR pathway, has significantly higher levels of GALNT14 in cisplatin resistance ovarian cancer tissue compared to cisplatin sensitive ovarian cancer tissue. The combination of cisplatin and the mTOR inhibitor GALNT14 had a cumulative effect by promoting apoptosis and ferroptosis of ovarian cancer cells, which may offer a new target for overcoming cisplatin resistance in ovarian cancer (103).By increasing ROS, lipid peroxidation, and iron homeostasis in high-

OXPHOS high-grade serous ovarian cancer (HGSOC), the promyelocytic leukemia protein-peroxisome proliferator-activated receptor gamma coactivator-1a (PML-PGC-1a) axis can help make ovarian cancer more sensitive to chemotherapy. These features are regulatory mechanisms for ferroptosis. It is therefore suspected that this mechanism may improve resistance in ovarian cancer by modulating ferroptosis (107). Furthermore, it was discovered in Zhang 's study that chemotherapeutic drugs can also result in lipid peroxidation through an excess of ROS, which can lead to ferroptosis in normal ovarian cells (108). Figuring out the exact way ferroptosis works and what it targets in chemotherapy could help make ovarian cancer cells more sensitive to chemotherapy drugs while keeping healthy ovarian tissue as safe as possible.

4 Immunotherapy

The study of immunotherapy in the field of ovarian cancer is a hot topic right now. The three main approaches are tumor antigen vaccines, monoclonal antibodies that target the expression of immune checkpoint inhibitors, and immunostimulatory cytokines. Cancer cells can escape immune therapy by modulating immune checkpoint pathways. The study found that when TYRO3 inhibits ferroptosis by regulating ferroptosis pathways such as NRF2, Xc system, tumor cells express high resistance to anti-PD-1/PD-L1 therapy (109).In addition, IFN γ released by CD8(+)T cells has been found to promote ferroptosis by acting on SLC3A2 and SLC7A11 on cancer cells, which also enhances anti-tumor immunotherapy against PD-L1 (110). Studies have shown that ovarian cancer is immunogenic (111), and that immunotherapy can extend the survival period of patients with ovarian cancer while lowering the recurrence rate (111). This means that using ferroptosis inducers along with immune checkpoint inhibitors might work well to treat ovarian tumors.

4.1 DAMPs

When tumor cells die due to external stimuli, the process from the non-immunogenic to the immunogenic immune response of the mediated organism is known as immune cell death (ICD). Tumor cells experiencing ICD can release large amounts of cell content into the extracellular space through sudden and uncontrolled cell death. The damage signal molecule is called the damage-associated molecular pattern (DAMPs). The presence of DAMPs in extracellular space triggers a strong immune response, drawing in more phagocytes and other immune cells to eliminate the threat and encourage tissue repair (112). Some anti-tumor drugs can induce ICD through DAMPs (112), recruit immune-inflammatory cells, release a large amount of inflammatory agents, and cause inflammation responses that cause the destruction of normal surrounding tissue, stimulate the formation of neonatal blood vessels, increase vascular permeability, weaken adaptive immune responses, promote tumor development, cancer transfer and tumor resistance (113). Ferroptosis kills cancer cells by enhancing immune cell activity (114). The DAMPs that primarily contribute to ferroptosis include HMGB1, CRT, ATP, and others. The release of ATP from dead cells is a self-dependent process. The presence of ATP serves as a "find me" signal in extracellular space, which is a chemoattractant of the DC precursor. ATP binds to the P2RX7 receptor on DCs, facilitating inflammasome mediated secretion of interleukin 1β (IL-1β), and the binding signals stimulate the production of the pro-inflammatory cytokine IL8 (115), and increase the recruitment of neutrophils and phagocytic potential.CRT is also a recognized DAMP molecule that plays a key role in the onset of immune cell death. The CRT on the membrane of the dead cell serves as a "eat me" signal to the APCs and triggers immune stimulation. HMGB1 is currently mainly believed to play a role through the promotion of inflammatory mediators, achieving inflammation responses, and initiating immunotherapy in ferroptosis (116) (Figure 2).

4.2 Immune cells

Immunol cells can perform anti-tumor immune functions by releasing cytokines that promote the ferroptosis activity of tumor cells. CTL-released IFNγ activates the Janus kinase (JAK) signal and signal transducer and activator of transcription 1 (STAT1) pathways, thereby reducing the expression of SLC3A2 and SLC7A11 to inhibit Xc system expression, increasing the iron content stored in the cell, and thus inducing ferroptosis (117). IFNγ released by CD8(+)T cells inhibits the expression of SLC7A11 synergistically, leading to the activation of ferroptosis, thereby enhancing anti-PD-L1 anti-tumor immunotherapy, enhancing lipid oxidation and ferroptosis in tumors, and improving tumor control (110). Similarly, the transformed growth factor-β (TGF-β1) released by macrophageal cells can inhibit transcription of the Xc system through SMAD signals, thereby promoting ferroptosis (118). The SAPE-OOH on the surface of the deferrous cell, as an eat-me signal, guides swallowing by targeting TLR 2 on the macrophageal cell (119) (Figure 2).

4.3 Immunosuppressive cells

Some immunosuppressive cells can antagonize ferroptosis through high expression of GPX4 or other components (110). In addition, Gpx4 can suppress anti-tumor immunity by promoting Treg cell survival in the tumor (120). In Tregs with TCR/CD28 co-stimulation activation,GPX4 expression was promoted, thereby reducing the occurrence of ferroptosis (121).With the absence of GPX4,M1 cells express high amounts of nitric oxide synthase (iNOS) and create more NO free radicals (NO-), which can have an impact akin to GPX4. (NO-) down-regulates the expression of ferroptosis (122). Intratumoral prostaglandin E2 (PGE2) is an immunosuppressive mediator that directly inhibits cytotoxic T cell activity (123). It also decreases the number of DCs infiltrating into the TME by inhibiting the chemokines CCL5 and XCL1 (124). The release of PGE2 is linked to the induction of ferroptosis in tumor cell (8, 125, 126). PGE2 overproduction inhibits the tumor immune response and promotes tumor immune evasion (127).

10.3389/fimmu.2024.1410018

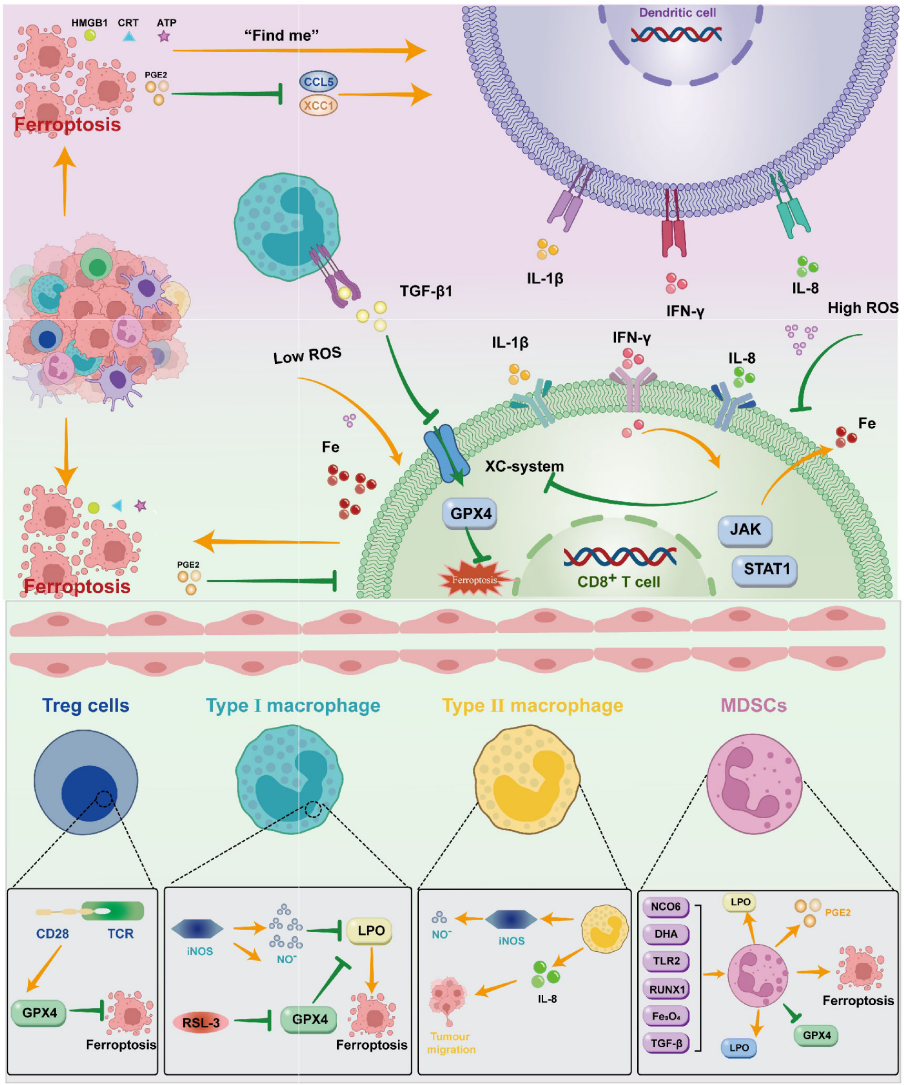

FIGURE 2
DAMPs such as HMGB1, CRT, ATP, and PGE2 are created when ferroptosis occurs in ovarian cancer cells. These molecules primarily operate on DC through various signals; DC can also act on CD8+T cells by releasing cytokines like IL-1β, IFN-γ, IL-8, and so on. T cells can control the incidence of ferroptosis by inhibiting the Xc system through JAK/STAT1 and promoting Fe through the release of IFN-γ. Macrophages mainly influence the Xc system by means of TGF-β1. To control ferroptosis, immunosuppressive cells can operate on the GPX4 system in a variety of ways.

Immunocytosuppressive tumors, or "cold tumors," do not have tumor-infiltrating T cells, which do not respond to immune checkpoint inhibitors. In cold tumors, T cells lack cystathionase and Xc transporters, while myeloid-derived suppressor cells (MDSCs) lack ASC neutral amino acid transporters and limiting extracellular cysteine, inhibiting T cell activation (128), and its TME is immersed in various immunosuppressive cells (129, 130). We are aware that MDSC is an immunosuppressive cell in ovarian tumor cells. Several studies have demonstrated that MDSC has an immunosuppressive impact by preventing CD8+T cells from infiltrating TME (131, 132), increasing PGE2 to induce PD-L1 expression in ovarian tumor cells (133). As the research goes deeper, there are greater expectations for the combination of ICIs with ferroptosis inducers. Immunosuppressant M2 can be re-polarized to M1 (98, 134) when ferroptosis is caused by certain circumstances, providing an environment for ICIs. Research has demonstrated that CD36 facilitates the absorption of fatty acids by CD8 T cells in TME that have invaded tumors, inducing lipid peroxide and ferroptosis, resulting in reduced cytotoxic cytokine generation and impaired anti-tumor capacity. Blocking CD36 or inhibiting ferroptosis in CD8 T cells effectively restores its anti-tumor activity. More importantly, it has a greater antitumor effect when combined with anti-PD-1 antibodies (135). As an inducer of ferroptosis, erastin has little effect on autoimmune activity. However, when combined with oncolytic vaccinia virus (OVV), erastin promotes therapeutic effectiveness and anti-tumor immunity by increasing the number of activated DCs and promoting the activity of tumor-specific CD8+T cells in the tumor (102). The combination also led to increased expression of PD-1 and CTLA-4 in the TME. It provides a molecular basis for

future ICIS combination therapy. Therefore, the combination of ferroptosis inducers with ICIs enhances tumor immunotherapy.

However, the combination of ferroptosis inducers with ICIs is also likely to increase immunosuppression, which is mainly the role played by MDSC. Ferroptosis of PMN MDSCs in TME gives them stronger immunosuppressive capabilities that are sufficient to convert non-inhibiting PMNs into immune-inhibitory PMN-MDSCs. Even though ferroptosis lowers the number of PMN MDSCs in the TME, it also increases the release of molecules that weaken the immune system, which stops T cells from working. In addition, PMN MDSCs in TME are known to produce PGE2, which undermines the anti-tumor function of innate and adaptive immune cells, inhibits ferroptosis, protects PMN MDSC, and blocks the release of immunosuppressive factors, thereby facilitating the conversion of PMN MDSC to classical non-inhibitory PMN. In some models, the immunosuppressive effects of ferroptosis in PMN-MDSC can exceed its tumor-suppressive effect on cancer cell death. PMN-MDSCs can also rely on peroxide enzymes for lipid peroxidation and transfer lipid to DC cells, blocking the cross-presentation of DC, thus exerting pro-tumor activity (136). The study found that GPx4 deficiency did not inhibit the development of tumors, instead, the GPx4-related ferroptosis caused the cytotoxic CD8+T cell CXCL10 dependent immersion, which was offset by the PD-L1 upgradation of the tumor cell and the significant HMGB1-mediated MDSC infiltration, resulting in a tumor-inhibiting immune response. Therefore, the combination of ferroptosis inducers with ICIs has not yet been clearly concluded. However, there are also ferroptosis inducers that can inhibit MDSC. Dihydroartemisinin (DHA) has a marked anti-tumor and inducing ferroptosis function in tumors, which can be achieved using the PDAC orthotopic tumor model, which significantly inhibits MDSC (137). TLR2 and Runx1 can also regulate MDSC through the ferroptosis path (124). The combination of induced ferroptosis with PD-L1 and MDSC blockage induced ferroptosis doesn't rely on the presence of particular mutations in tumor cells, meaning that any type of tumor may be treated with this combination therapy. The TME reaction to ferroptosis will determine how well the therapy works (138). Zhu et al. found that Asah2 is highly expressed in tumor-infiltrating MDSCs, which can regulate the ferroptosis of MDSCs through the P53-HMOX1 pathway. The use of the Asah2 inhibitor NC06 to target ASAH2 to induce MDSC ferroptosis is a potentially effective therapy for inhibiting the MDSC accumulation in cancer immunotherapy (139). In addition, Zhang and others constructed a biomimetic magnetosome composed of Fe3O4 magnetic nanocluster (NC) as a core, loaded with TGF-β inhibitors and PD-1 antibodies (Pa).When entering the tumor, Pa and Ti synergistically form an immunogenic micro-environment that increases the amount of H2O2 in the polarized M1 macrophage cells, thereby promoting the Fenton reaction released with NCs. Meanwhile, the produced (OH) induces the ferroptosis of ovarian tumor cells, and the micro-environmental immunogenicity is increased by the exposed tumor antigen. The synergistic effect of ferroptosis and immune therapy in ovarian cancer was generated (140). This gives us the clue that it may be possible to use the ferroptosis inducer in conjunction with ICIs for immunotherapy of tumors in cases where MDSC is suppressed.

It also gives us new ideas for ovarian cancer immunotherapy. The study discovered that ferroptosis was closely associated with ovarian tumor immunity (141). However, in contrast to other tumors, current studies on ferroptosis in immunotherapy are more likely to induce ferroptosis release of DAMP, causing tumor development and a poor prognosis. For instance, C-MYC inhibits ferroptosis induced HMGB1 release mediated by NCOA4 in ovarian cancer cells (83). Low-concentration erastin by STAT3 mediated M2 polarization of macrophage cells increased ferroptosis resistance to ovarian cancer. The macrophage cells processed by erastin also secrete the key cytokines IL-8, which encourage the invasion and migration of anti-ferroptosis O.C. cells (96). However, studies have also found that immune cells can have an anti-tumor effect by inducing the ferroptosis of ovarian cells. ICIs can induce CD8+ T cells to trigger ferroptosis in mouse ovarian tumor cells (142). Immunotherapy-activated CD8+T cells can release IFN-γ and enhance the anti-tumor effect of immunotherapy by inducing ovarian cancer cell ferroptosis. IFN-γ kills mouse OVCA cells ID8 through inhibiting the Xc system, increasing lipid ROS, and reducing tumor growth (117). The study found that inhibition of ovarian cancer metastasis was achieved through targeted MDSC immersion TME (143). By encouraging the release of C5 by ovarian cancer cells and their interaction with PPIP5K2, LncOVM can aid in the infiltration of MDSCs in TME, which leads to lymphatic metastasis in ovarian cancer cells. By blocking this pathway, the C5aR antibody or inhibitor (CCX168) can prevent the recruitment of MDSCs and reinstate the *in vivo* suppression of tumor genesis and metastasis (143). Ferroptosis inducers in conjunction with ICDs for ovarian cancer have not been investigated for their precise process and effectiveness, but this combination might represent a potent target for ovarian cancer therapy. Due to its unique way of competing with T cells for cysteine, glutamine metabolism will be targeted by MDSC to lower its activity and down-regulate the immunosuppressive tumor microenvironment at the same time. Ferroptosis inducers that affect the Xc-system could be more important in promoting immunity and preventing immunological escape.

DAMPs such as HMGB1, CRT, ATP, and PGE2 are created when ferroptosis occurs in ovarian cancer cells. These molecules primarily operate on DC through various signals; DC can also act on CD8+T cells by releasing cytokines like IL-1β, IFN-γ, IL-8, and so on. T cells can control the incidence of ferroptosis by inhibiting the Xc system through JAK/STAT1 and promoting Fe through the release of IFN-γ. Macrophages mainly influence the Xc system by means of TGF-β1. To control ferroptosis, immunosuppressive cells can operate on the GPX4 system in a variety of ways (Figure 2).

4.4 Related gene prediction models

Using bioinformation technology, several researchers have constructed prediction models for ovarian cancer and discovered ferroptosis genes that are associated with both tumor inhibition and ovarian cancer prediction. The ferroptosis driving gene ALOX12, for instance, was found to be overexpressed in ovarian cancer cells and induce lipid production, showing high sensitivity and specificity for serous ovarian cystadenocarcinoma (144). Its

increased expression was associated with a poor prognosis in OC patients, according to multiple studies using the mRNA expression data of TCGA, IGCG, GTEx, and clinical OC patients. ALOX12 may be a possible risk factor for OC, as inhibition of ALOX12 decreases the migration and proliferation of ovarian cancer cells (145, 146). Comprehensive evaluation of gene expression, related signaling pathways, and immunomodulatory functions also found that the ferroptosis related gene PRNP also played a tumor suppressor role in OC. It may be a potential new biomarker for OC diagnosis, prognosis, and immunotherapy response (147).

The identification of appropriate and effective immune prediction targets will significantly increase the practicality of immunotherapy for ovarian cancer. The realization and implementation of ovarian cancer immunotherapy must take into consideration the immunosuppressive network of ovarian cancer. Researchers are increasingly developing immunotherapy bio-information technology models that utilize ferroptosis-related genes to predict the effects, side-effects, and prognosis of immunotherapies. Studies have constructed a model containing nine ferroptosis-related genes, showing that ferroptosis is closely linked to tumor immunity through the ssGSEA method, but further experimental validation is needed (141). When paired with clinical variables, the risk model developed by YE et al. based on five ferroptosis-related characteristics linked to tumor immunity can more accurately predict the prognosis of OC patients (146). A model of 15 FRGs (c) divided patients into high- and low-risk groups, showing good survival differences. Additionally, in the low-risk group, characteristic enrichment sets were detected with immunity pathways related to ovarian cancer, which suggests that the model can be used to precisely treat immunotherapy for ovarian cancer and for prognosis (148). Using Cox analysis, three prognostic genes were identified from 63 FRGs. Significant differences were found in activated DCs, plasma cells, M0 infiltration, and important immune checkpoint molecules between the two groups when the CIBERSORT algorithm was applied to the various tumor immune microenvironments between the two groups based on the grouping of prognostic genes. The low-risk group also responded better to immunotherapy and chemotherapy at the same time, which was predictive of prognosis and immune response (149). Similar outcomes were achieved by Wang et al. when they developed a risk score model based on various prognostic signal FRGS. Additionally, it has been proposed that in high-risk patients, the combination of immunity and ferroptosis may result in a worse prognosis (150). A clinical risk stratification tool based on four DEG (differentially expressed genes from immune and ferroptosis) has been developed for serous ovarian cancer. It can exhibit a strong correlation with immune markers and induced pluripotent stem cells (IPS). Encourage additional clinical judgment in the areas of personalized treatment planning, prognostic assessment, and follow-up scheduling (151). A risk model established by finding significantly differentially expressed genes associated with ferroptosis was found to have favorable immune cell and prognostic associations (152). Furthermore, ferroptosis and oxidative stress-related genes (FORGs) have been found to be associated with immunotherapy in ovarian cancer. Based on the expressive characteristics of 19 FORGs, ovarian cancer patients were divided into two FORG subtypes. The high-risk group had immunosuppression and a poor prognosis. The risk scores significantly correlated with immunosurgery expression and chemotherapy sensitivity, demonstrating the usefulness of prognostication and chemotherapy for O.C (153). Xiang et al. conducted molecular subtyping of ferroptosis-related genes in ovarian cancer and developed a predictive model. They discovered that high-risk patients exhibited a tumor immune microenvironment with increased infiltration of M2 macrophages and reduced numbers of CD8+ T cells, which impaired immune responses and led to poor prognoses (154). Li and colleagues also construct risk models in conjunction with genes related to ferroptosis and cuprotosis, which can predict individual sensitivity to various immunotherapies and chemotherapy drugs based on specific groups, and have strong immune prediction and prognostic ability (155) (Table 3).

TABLE 3 The role of ferroptosis related gene in prediction and immunotherapy of ovarian cancer cell.

ferroptosis-related genes	Prognostic function	Related to immune response	reference
PRNP	√	√	(147)
15-FRG (CYBB, VDAC2, SOCS1, LINC00472, ELAVL1, IFNG, IDH1; NRAS, MT1G, ACSL3, SLC3A2; PTGS2, SLC1A4, PCK2, XBP1)	√	√	(148)
CXCL11、CX3CR1、FH、DNAJB6	√	√	(151)
SLC7A11, ZFP36、TTBK2	√	√	(149)
ALOX12、ACACA、SLC7A11、FTH1、CD44	√	√	(146)
FORG	√	√	(153)
HIC1、LPCAT3、DUOX1	√	√	(150)
LPCAT3、ACSL3、CRYAB、PTGS2、ALOX12、HSBP1、SLC1A5、SLC7A11, ZEB1	√	×	(141)
CDKN1B、CXCR4、FAS、FOS、FOXO1、GABARAPL1、HDAC1、IFNG、IL24、MTMR14、NFKB1、PEX3、PPP1R15A、RB1, SIRT2	√	×	(156)
GFPT2, VSIG4, HOXA5, CXCL9, and LYPD1.	√	√	(155)
ALOX12、RB1、DNAJB6、STEAP3, SELENOS	√	×	(145)

(Continued)

TABLE 3 Continued

ferroptosis-related genes	Prognostic function	Related to immune response	reference
DNAJB6、RB1、VIMP/SELENOS、STEAP3、BACH1 and ALOX12	√	×	(144)
LAMP2, NOS2, ALOX5, CD44, CHMP5, FH, GOT1, DUOX2, SLC7A11, and DDIT3	√	√	(152)
PDP1, FCGBP, EPHA4, GAS1, SLC7A11, BLOC1S1, SPOCK2, and CXCL9	√	√	(154)

√, provided; × : not provided.

5 Conclusion and perspectives

As a new type of cell death found to be used to suppress tumor cells, ferroptosis is significant and has recently become a hotspot in the field of tumors. The regulatory role of specific mechanisms such as the GPX4 (157) and Xc system in ferroptosis and related pathways and targets has been gradually clarified. Many new mechanisms for ferroptosis, pathways and genes have been gradually discovered, but further research is still to be undertaken. Many of the currently known treatments for ovarian cancer are highly toxic and ineffective. Studies have found that ferroptosis combination therapy can help increase ovarian cancer sensitivity to the drug and improve the prognosis. The mechanism of ferroptosis is closely related to oxidative stress and ROS production, with research often focusing on mitochondria. Ferroptosis is characterized by distinct morphological changes, including smaller mitochondria, shriveled mitochondrial membranes, and reduced or absent mitochondrial cristae, while the cell membrane remains intact and the cell nucleus size remains normal (10). In ovarian cancer, PML-PGC-1α (107) can promote mitochondrial respiration, cysteine (158) restriction affects Fe-S cluster synthesis in mitochondria, and compounds like eriodictyol (40) and SPIO-serum (40) exacerbate mitochondrial dysfunction, all of which regulate ferroptosis. Recent studies have identified Mitotic Arrest Deficient 2 Like 2 (MAD2L2), an important tumor-associated protein primarily located in ribosomes, as having a potential role in mitochondrial elongation. MAD2L2 can promote ovarian cancer proliferation and migration by inhibiting ferroptosis and is closely associated with various immune cells. However, the specific and complete mechanisms and pathways of ferroptosis in mitochondria remain unclear. Future research in this area is expected to provide a more comprehensive understanding of ferroptosis (157).Furthermore, due to the immunosuppressive nature of ovarian cancer, single immunotherapy currently has good therapeutic effects in only a fraction of ovarian cancer patients, therapy combined with other new tumor treatments is a new research trend. Ferroptosis, as a new type of treatment, can not only play a role in suppressing ovarian tumors but also induce immunotherapy. However, immunosuppression of ovarian cancer has been found to reduce this combined effect and even lead to bad side effects. The study also found that it may be possible to inhibit the immunosuppressive microenvironment of ovarian tumors by targeting immune cells, thereby helping in the combination of ferroptosis inducers and immunotherapy. The application of nanomaterials in this field has endless potential and can be targeted therapeutically, inducing ferroptosis to produce the effect of immunotherapy and play more accurate, longer-lasting, and with fewer side effects. However, the specific mechanisms are not clear enough. In recent years, considerable research has been undertaken on immuno-predictive models built from bioinformatics and ferroptosis-related genes, which may help in the research and development of targets and drugs for ovarian cancer treatment. In the future, the association of ferroptosis-related inducers and inhibitors with other treatments for ovarian cancer is still worth exploring.

Author contributions

KG: Writing – original draft, Writing – review & editing. ML: Writing – review & editing. JB: Conceptualization, Writing – review & editing. TY: Writing – review & editing. JG: Writing – review & editing. FR: Conceptualization, Writing – review & editing. LZ: Writing – review & editing, Funding acquisition.

Funding

The author(s) declare financial support was received for the research, authorship, and/or publication of this article. The present study was supported by scientific research fund project of Liaoning Provincial Department of Education (general project, 2021, Grant No. LJKZ0752); 345 Talent Project of Shengjing Hospital.

Conflict of interest

The authors declare that the research was conducted in the absence of any commercial or financial relationships that could be construed as a potential conflict of interest.

Publisher's note

References

1. Cho KR, Shih I-M. Ovarian cancer. *Annu Rev Pathol Mech Dis*. (2009) 4:287–313. doi: 10.1146/annurev.pathol.4.110807.092246

2. Yeung T-L, Leung CS, Yip K-P, Au Yeung CL, Wong STC, Mok SC. Cellular and molecular processes in ovarian cancer metastasis. A Review in the Theme: Cell and Molecular Processes in Cancer Metastasis. *Am J Physiol Cell Physiol*. (2015) 309:C444–456. doi: 10.1152/ajpcell.00188.2015

3. Siegel RL, Miller KD, Fuchs HE, Jemal A. Cancer statistics, 2021. *CA Cancer J Clin*. (2021) 71:7–33. doi: 10.3322/caac.21654

4. Yang WS, Stockwell BR. Ferroptosis: death by lipid peroxidation. *Trends Cell Biol*. (2016) 26:165–76. doi: 10.1016/j.tcb.2015.10.014

5. Stockwell BR, Angeli JPF, Bayir H, Bush AI, Conrad M, Dixon S, et al. Ferroptosis: a regulated cell death nexus linking metabolism, redox biology, and disease. *Cell*. (2017) 171:273–85. doi: 10.1016/j.cell.2017.09.021

6. Dixon SJ, Stockwell BR. The hallmarks of ferroptosis. *Annu Rev Cancer Biol*. (2019) 3:35–54. doi: 10.1146/annurev-cancerbio-030518-055844

7. Cao JY, Dixon SJ. Mechanisms of ferroptosis. *Cell Mol Life Sci*. (2016) 73:2195–209. doi: 10.1007/s00018-016-2194-1

8. Yang WS, SriRamaratnam R, Welsch ME, Shimada K, Skouta R, Viswanathan VS, et al. Regulation of ferroptotic cancer cell death by GPX4. *Cell*. (2014) 156:317–31. doi: 10.1016/j.cell.2013.12.010

9. Li D, Zhang M, Chao H. Significance of glutathione peroxidase 4 and intracellular iron level in ovarian cancer cells—"utilization" of ferroptosis mechanism. *Inflammation Res*. (2021) 70:1177–89. doi: 10.1007/s00011-021-01495-6

10. Dixon SJ, Lemberg KM, Lamprecht MR, Skouta R, Zaitsev EM, Gleason CE, et al. Ferroptosis: an iron-dependent form of nonapoptotic cell death. *Cell*. (2012) 149:1060–72. doi: 10.1016/j.cell.2012.03.042

11. Guan J, Lo M, Dockery P, Mahon S, Karp CM, Buckley AR, et al. The xc- cystine/glutamate antiporter as a potential therapeutic target for small-cell lung cancer: use of sulfasalazine. *Cancer Chemother Pharmacol*. (2009) 64:463–72. doi: 10.1007/s00280-008-0894-4

12. Sun X, Niu X, Chen R, He W, Chen D, Kang R, et al. Metallothionein-1G facilitates sorafenib resistance through inhibition of ferroptosis. *Hepatology*. (2016) 64:488–500. doi: 10.1002/hep.28574

13. Jiang L, Kon N, Li T, Wang S-J, Su T, Hibshoosh H, et al. Ferroptosis as a p53-mediated activity during tumor suppression. *Nature*. (2015) 520:57–62. doi: 10.1038/nature14344

14. Luo Y, Liu X, Chen Y, Tang Q, He C, Ding X, et al. Targeting PAX8 sensitizes ovarian cancer cells to ferroptosis by inhibiting glutathione synthesis. *Apoptosis*. (2024). doi: 10.1007/s10495-024-01985-y

15. Sbodio JI, Snyder SH, Paul BD. Regulators of the transsulfuration pathway. *Br J Pharmacol*. (2019) 176:583–93. doi: 10.1111/bph.14446

16. Verschoor ML, Singh G. Ets-1 regulates intracellular glutathione levels: key target for resistant ovarian cancer. *Mol Cancer*. (2013) 12:138. doi: 10.1186/1476-4598-12-138

17. MeiFang W, De-Guan L. Research progress of ferroptosis in cardiovascular and cerebrovascular diseases. *Chin Bullet Life Sci*. (2019) 31(09):886–93. doi: 10.13376/j.cbls/2019109

18. Jiang X, Stockwell BR, Conrad M. Ferroptosis: mechanisms, biology and role in disease. *Nat Rev Mol Cell Biol*. (2021) 22:266–82. doi: 10.1038/s41580-020-00324-8

19. Agmon E, Stockwell BR. Lipid homeostasis and regulated cell death. *Curr Opin Chem Biol*. (2017) 39:83–9. doi: 10.1016/j.cbpa.2017.06.002

20. Doll S, Proneth B, Tyurina YY, Panzilius E, Kobayashi S, Ingold I, et al. ACSL4 dictates ferroptosis sensitivity by shaping cellular lipid composition. *Nat Chem Biol*. (2017) 13:91–8. doi: 10.1038/nchembio.2239

21. Bersuker K, Hendricks JM, Li Z, Magtanong L, Ford B, Tang PH, et al. The CoQ oxidoreductase FSP1 acts parallel to GPX4 to inhibit ferroptosis. *Nature*. (2019) 575:688–92. doi: 10.1038/s41586-019-1705-2

22. Marshall KR, Gong M, Wodke L, Lamb JH, Jones DJL, Farmer PB, et al. The human apoptosis-inducing protein AMID is an oxidoreductase with a modified flavin cofactor and DNA binding activity. *J Biol Chem*. (2005) 280:30735–40. doi: 10.1074/jbc.M414018200

23. Dai E, Zhang W, Cong D, Kang R, Wang J, Tang D. AIFM2 blocks ferroptosis independent of ubiquinol metabolism. *Biochem Biophys Res Commun*. (2020) 523:966–71. doi: 10.1016/j.bbrc.2020.01.066

24. Mao C, Liu X, Zhang Y, Lei G, Yan Y, Lee H, et al. DHODH-mediated ferroptosis defense is a targetable vulnerability in cancer. *Nature*. (2021) 593:586–90. doi: 10.1038/s41586-021-03539-7

25. Kraft VAN, Bezjian CT, Pfeiffer S, Ringelstetter L, Müller C, Zandkarimi F, et al. GTP cyclohydrolase 1/tetrahydrobiopterin counteract ferroptosis through lipid remodeling. *ACS Cent Sci*. (2020) 6:41–53. doi: 10.1021/acscentsci.9b01063

26. Shen Z, Liu T, Li Y, Lau J, Yang Z, Fan W, et al. Fenton-reaction-acceleratable magnetic nanoparticles for ferroptosis therapy of orthotopic brain tumors. *ACS Nano*. (2018) 12:11355–65. doi: 10.1021/acsnano.8b06201

27. Bellelli R, Federico G, Matte' A, Colecchia D, Iolascon A, Chiariello M, et al. NCOA4 deficiency impairs systemic iron homeostasis. *Cell Rep*. (2016) 14:411–21. doi: 10.1016/j.celrep.2015.12.065

28. Dey A, Varelas X, Guan K-L. Targeting the Hippo pathway in cancer, fibrosis, wound healing and regenerative medicine. *Nat Rev Drug Discovery*. (2020) 19:480–94. doi: 10.1038/s41573-020-0070-z

29. Yang W-H, Huang Z, Wu J, Ding C-KC, Murphy SK, Chi J-T. A TAZ-ANGPTL4-NOX2 axis regulates ferroptotic cell death and chemoresistance in epithelial ovarian cancer. *Mol Cancer Res*. (2020) 18:79–90. doi: 10.1158/1541-7786.MCR-19-0691

30. Yang W-H, Lin C-C, Wu J, Chao P-Y, Chen K, Chen P-H, et al. The hippo pathway effector YAP promotes ferroptosis via the E3 ligase SKP2. *Mol Cancer Res*. (2021) 19:1005–14. doi: 10.1158/1541-7786.MCR-20-0534

31. Anandhan A, Dodson M, Schmidlin CJ, Liu P, Zhang DD. Breakdown of an ironclad defense system: The critical role of NRF2 in mediating ferroptosis. *Cell Chem Biol*. (2020) 27:436–47. doi: 10.1016/j.chembiol.2020.03.011

32. Wang Y, Yan S, Liu X, Deng F, Wang P, Yang L, et al. PRMT4 promotes ferroptosis to aggravate doxorubicin-induced cardiomyopathy via inhibition of the Nrf2/GPX4 pathway. *Cell Death Differ*. (2022) 29:1982–95. doi: 10.1038/s41418-022-00990-5

33. Dang R, Wang M, Li X, Wang H, Liu L, Wu Q, et al. Edaravone ameliorates depressive and anxiety-like behaviors via Sirt1/Nrf2/HO-1/Gpx4 pathway. *J Neuroinflamm*. (2022) 19:41. doi: 10.1186/s12974-022-02400-6

34. Chang L-C, Chiang S-K, Chen S-E, Yu Y-L, Chou R-H, Chang W-C. Heme oxygenase-1 mediates BAY 11–7085 induced ferroptosis. *Cancer Lett*. (2018) 416:124–37. doi: 10.1016/j.canlet.2017.12.025

35. Kerins MJ, Ooi A. The roles of NRF2 in modulating cellular iron homeostasis. *Antioxidants Redox Signaling*. (2018) 29:1756–73. doi: 10.1089/ars.2017.7176

36. Yue W, Yupeng G, Jun C, Kui J. Apatinib combined with olaparib induces ferroptosis via a p53-dependent manner in ovarian cancer. *J Cancer Res Clin Oncol*. (2023) 149(11):681–9. doi: 10.1007/s00432-023-04811-1

37. Jing T, Guo Y, Wei Y. Carboxymethylated pachyman induces ferroptosis in ovarian cancer by suppressing NRF1/HO-1 signaling. *Oncol Lett*. (2022) 23:161. doi: 10.3892/ol.2022.13281

38. Zhu X, Chen X, Qiu L, Zhu J, Wang J. Norcantharidin induces ferroptosis via the suppression of NRF2/HO-1 signaling in ovarian cancer cells. *Oncol Lett*. (2022) 24:359. doi: 10.3892/ol.2022.13479

39. Ma B, Zhong Y, Chen R, Zhan X, Huang G, Xiong Y, et al. Tripterygium glycosides reverse chemotherapy resistance in ovarian cancer by targeting the NRF2/GPX4 signal axis to induce ferroptosis of drug-resistant human epithelial ovarian cancer cells. *Biochem Biophys Res Commun*. (2023) 665:178–86. doi: 10.1016/j.bbrc.2023.04.111

40. Wang X, Chen J, Tie H, Tian W, Zhao Y, Qin L, et al. Eriodictyol regulated ferroptosis, mitochondrial dysfunction, and cell viability via Nrf2/HO-1/NQO1 signaling pathway in ovarian cancer cells. *J Biochem Mol Toxicol*. (2023) 37(7):e23368. doi: 10.1002/jbt.23368

41. Liu N, Lin X, Huang C. Activation of the reverse transsulfuration pathway through NRF2/CBS confers erastin-induced ferroptosis resistance. *Br J Cancer*. (2020) 122:279–92. doi: 10.1038/s41416-019-0660-x

42. Zhou J, Wang Y, Fu Y, Lin Z, Lin H, Lv G, et al. Chelerythrine induces apoptosis and ferroptosis through Nrf2 in ovarian cancer cells. *Cell Mol Biol (Noisy-le-grand)*. (2024) 70:174–81. doi: 10.14715/cmb/2024.70.3.26

43. Anandhan A, Dodson M, Shakya A, Chen J, Liu P, Wei Y, et al. NRF2 controls iron homeostasis and ferroptosis through HERC2 and VAMP8. *Sci Adv*. (2023) 9:eade9585. doi: 10.1126/sciadv.ade9585

44. Xu R, Wang W, Zhang W. Ferroptosis and the bidirectional regulatory factor p53. *Cell Death Discovery*. (2023) 9:197. doi: 10.1038/s41420-023-01517-8

45. Guo X, Liu N, Liu M. Long non-coding RNA LINC00336 as an independentprognostic indicator and an oncogenic lncRNA in bladder cancer. *Arch Med Sci*. (2019) 19(2):478–87. doi: 10.5114/aoms.2019.89661

46. Ou Y, Wang S-J, Li D, Chu B, Gu W. Activation of SAT1 engages polyamine metabolism with p53-mediated ferroptotic responses. *Proc Natl Acad Sci U.S.A*. (2016) 113:E6806–12. doi: 10.1073/pnas.1607152113

47. Xie Y, Zhu S, Song X, Sun X, Fan Y, Liu J, et al. The tumor suppressor p53 limits ferroptosis by blocking DPP4 activity. *Cell Rep*. (2017) 20:1692–704. doi: 10.1016/j.celrep.2017.07.055

48. Liu Y, Gu W. p53 in ferroptosis regulation: the new weapon for the old guardian. *Cell Death Differ*. (2022) 29:895–910. doi: 10.1038/s41418-022-00943-y

49. Venkatesh D, O'Brien NA, Zandkarimi F, Tong DR, Stokes ME, Dunn DE, et al. MDM2 and MDMX promote ferroptosis by PPARα-mediated lipid remodeling. *Genes Dev*. (2020) 34:526–43. doi: 10.1101/gad.334219.119

50. Hong T, Lei G, Chen X, Li H, Zhang X, Wu N, et al. PARP inhibition promotes ferroptosis via repressing SLC7A11 and synergizes with ferroptosis inducers in BRCA-

proficient ovarian cancer. *Redox Biol*. (2021) 42:101928. doi: 10.1016/j.redox.2021.101928

51. Wang C-K, Chen T-J, Tan GYT, Chang F-P, Sridharan S, Yu C-HA, et al. MEX3A mediates p53 degradation to suppress ferroptosis and facilitate ovarian cancer tumorigenesis. *Cancer Res*. (2023) 83:251–63. doi: 10.1158/0008-5472.CAN-22-1159

52. Fang R, Yunfei W, Jishui W. Exploration on role and mechanism of ursolic acid - Induced iron death in ovarian cancer cell line OVCAR-3 based on JNK / p53 pathway. *Chin Arch Traditional Chin Med*. (2021) 39:62–64+267. doi: 10.13193/j.issn.1673-7717.2021.07.016

53. Tesfay L, Paul BT, Konstorum A, Deng Z, Cox AO, Lee J, et al. Stearoyl-coA desaturase 1 protects ovarian cancer cells from ferroptotic cell death. *Cancer Res*. (2019) 79:5355–66. doi: 10.1158/0008-5472.CAN-19-0369

54. Xuan Y, Wang H, Yung MM, Chen F, Chan W-S, Chan Y-S, et al. SCD1/FADS2 fatty acid desaturases equipoise lipid metabolic activity and redox-driven ferroptosis in ascites-derived ovarian cancer cells. *Theranostics*. (2022) 12:3534–52. doi: 10.7150/thno.70194

55. Kato I, Kasukabe T, Kumakura S. Menin–MLL inhibitors induce ferroptosis and enhance the anti–proliferative activity of auranofin in several types of cancer cells. *Int J Oncol*. (2020) 57(4):1057–71. doi: 10.3892/ijo.2020.5116

56. Liu Y, Liu X, Wang H, Ding P, Wang C. Agrimonolide inhibits cancer progression and induces ferroptosis and apoptosis by targeting SCD1 in ovarian cancer cells. *Phytomedicine*. (2022) 101:154102. doi: 10.1016/j.phymed.2022.154102

57. Carbone M, Melino G. Stearoyl coA desaturase regulates ferroptosis in ovarian cancer offering new therapeutic perspectives. *Cancer Res*. (2019) 79:5149–50. doi: 10.1158/0008-5472.CAN-19-2453

58. McCabe KE, Bacos K, Lu D, Delaney JR, Axelrod J, Potter MD, et al. Triggering necroptosis in cisplatin and IAP antagonist-resistant ovarian carcinoma. *Cell Death Dis*. (2014) 5:e1496–6. doi: 10.1038/cddis.2014.448

59. Do M, Wu CCN, Sonavane PR, Juarez EF, Adams SR, Ross J, et al. A FZD7-specific antibody-drug conjugate induces ovarian tumor regression in preclinical models. *Mol Cancer Ther*. (2022) 21:113–24. doi: 10.1158/1535-7163.MCT-21-0548

60. Wang Y, Zhao G, Condello S, Huang H, Cardenas H, Tanner EJ, et al. Frizzled-7 identifies platinum-tolerant ovarian cancer cells susceptible to ferroptosis. *Cancer Res*. (2021) 81:384–99. doi: 10.1158/0008-5472.CAN-20-1488

61. Zhang D, Qu B, Hu B, Cao K, Shen H. MiR-1-3p enhances the sensitivity of ovarian cancer cells to ferroptosis by targeting FZD7. *Zhong Nan Da Xue Xue Bao Yi Xue Ban*. (2022) 47:1512–21. doi: 10.11817/j.issn.1672-7347.2022.210800

62. Jin Y, Chen L, Li L, Huang G, Huang H, Tang C. SNAI2 promotes the development of ovarian cancer through regulating ferroptosis. *Bioengineered*. (2022) 13:6451–63. doi: 10.1080/21655979.2021.2024319

63. Zhang X, Zheng X, Ying X, Xie W, Yin Y, Wang X. CEBPG suppresses ferroptosis through transcriptional control of SLC7A11 in ovarian cancer. *J Transl Med*. (2023) 21:334. doi: 10.1186/s12967-023-04136-0

64. Wang Y, Wang S, Zhang W. HRD1 functions as a tumor suppressor in ovarian cancer by facilitating ubiquitination-dependent SLC7A11 degradation. *Cell Cycle*. (2023) 22:1116–26. doi: 10.1080/15384101.2023.2178102

65. Bai P, Cantó C. The role of PARP-1 and PARP-2 enzymes in metabolic regulation and disease. *Cell Metab*. (2012) 16:290–5. doi: 10.1016/j.cmet.2012.06.016

66. Konstantinopoulos PA, Ceccaldi R, Shapiro GI, D'Andrea AD. Homologous recombination deficiency: exploiting the fundamental vulnerability of ovarian cancer. *Cancer Discovery*. (2015) 5:1137–54. doi: 10.1158/2159-8290.CD-15-0714

67. Tang S, Shen Y, Wei X, Shen Z, Lu W, Xu J. Olaparib synergizes with arsenic trioxide by promoting apoptosis and ferroptosis in platinum-resistant ovarian cancer. *Cell Death Dis*. (2022) 13:826. doi: 10.1038/s41419-022-05257-y

68. Zhou J, Pang Y, Zhang W, OuYang F, Lin H, Li X, et al. Discovery of a novel stilbene derivative as a microtubule targeting agent capable of inducing cell ferroptosis. *J Med Chem*. (2022) 65:4687–708. doi: 10.1021/acs.jmedchem.1c01775

69. Puxeddu M, Wu J, Bai R, D'Ambrosio M, Nalli M, Coluccia A, et al. Induction of ferroptosis in glioblastoma and ovarian cancers by a new pyrrole tubulin assembly inhibitor. *J Med Chem*. (2022) 65:15805–18. doi: 10.1021/acs.jmedchem.2c01457

70. Zuo Y-B, Zhang Y-F, Zhang R, Tian J-W, Lv X-B, Li R, et al. Ferroptosis in cancer progression: role of noncoding RNAs. *Int J Biol Sci*. (2022) 18:1829–43. doi: 10.7150/ijbs.66917

71. Ma L-L, Liang L, Zhou D, Wang S-W. Tumor suppressor miR-424-5p abrogates ferroptosis in ovarian cancer through targeting ACSL4. *neo*. (2021) 68:165–73. doi: 10.4149/neo_2020_200707N705

72. Sangokoya C, Doss JF, Chi J-T. Iron-responsive miR-485-3p regulates cellular iron homeostasis by targeting ferroportin. *PloS Genet*. (2013) 9:e1003408. doi: 10.1371/journal.pgen.1003408

73. Sun D, Li Y-C, Zhang X-Y. Lidocaine promoted ferroptosis by targeting miR-382-5p /SLC7A11 axis in ovarian and breast cancer. *Front Pharmacol*. (2021) 12:681223. doi: 10.3389/fphar.2021.681223

74. Jin Y, Qiu J, Lu X, Ma Y, Li G. LncRNA CACNA1G-AS1 up-regulates FTH1 to inhibit ferroptosis and promote Malignant phenotypes in ovarian cancer cells. *Oncol Res*. (2023) 31:169–79. doi: 10.32604/or.2023.027815

75. Zhou X, Zhan L, Huang K, Wang X. The functions and clinical significance of circRNAs in hematological Malignancies. *J Hematol Oncol*. (2020) 13:138. doi: 10.1186/s13045-020-00976-1

76. Qin K, Zhang F, Wang H, Wang N, Qiu H, Jia X, et al. circRNA circSnx12 confers Cisplatin chemoresistance to ovarian cancer by inhibiting ferroptosis through a miR-194-5p/SLC7A11 axis. *BMB Rep*. (2023) 56:184–9. doi: 10.5483/BMBRep.2022-0175

77. Zhang Y, Xia M, Zhou Z, Hu X, Wang J, Zhang M, et al. p53 promoted ferroptosis in ovarian cancer cells treated with human serum incubated-superparamagnetic iron oxides. *IJN*. (2021) 16:283–96. doi: 10.2147/IJN.S282489

78. Dong H, He L, Sun Q, Zhan J, Li J, Xiong X, et al. Inhibit ALDH3A2 reduce ovarian cancer cells survival via elevating ferroptosis sensitivity. *Gene*. (2023) 876:147515. doi: 10.1016/j.gene.2023.147515

79. Cai L, Hu X, Ye L, Bai P, Jie Y, Shu K. Long non-coding RNA ADAMTS9-AS1 attenuates ferroptosis by Targeting microRNA-587/solute carrier family 7 member 11 axis in epithelial ovarian cancer. *Bioengineered*. (2002) 13:8226–39. doi: 10.1080/21655979.2022.2049470

80. Yamaguchi K, Kitamura S, Furutake Y, Murakami R, Yamanoi K, Taki M, et al. Acquired evolution of mitochondrial metabolism regulated by HNF1B in ovarian clear cell carcinoma. *Cancers (Basel)*. (2021) 13:2413. doi: 10.3390/cancers13102413

81. Li J, Zhang Y, Gao Y, Cui Y, Liu H, Li M, et al. Downregulation of HNF1 homeobox B is associated with drug resistance in ovarian cancer. *Oncol Rep*. (2014) 32 (3):979–88. doi: 10.3892/or.2014.3297

82. Takahashi R, Kamizaki K, Yamanaka K, Terai Y, Minami Y. Expression of Ferredoxin1 in cisplatin–resistant ovarian cancer cells confers their resistance against ferroptosis induced by cisplatin. *Oncol Rep*. (2023) 49:124. doi: 10.3892/or.2023.8561

83. Jin Y, Qiu J, Lu X, Li G. C-MYC inhibited ferroptosis and promoted immune evasion in ovarian cancer cells through NCOA4 mediated ferritin autophagy. *Cells*. (2022) 11:4127. doi: 10.3390/cells11244127

84. Wang X, Xu Z, Ren X, Chen X, Yi Q, Zeng S, et al. MTHFR inhibits TRC8-mediated HMOX1 ubiquitination and regulates ferroptosis in ovarian cancer. *Clin Transl Med*. (2022) 12:e1013. doi: 10.1002/ctm2.1013

85. Efferth T. From ancient herb to modern drug: Artemisia annua and artemisinin for cancer therapy. *Semin Cancer Biol*. (2017) 46:65–83. doi: 10.1016/j.semcancer.2017.02.009

86. Greenshields AL, Shepherd TG, Hoskin DW. Contribution of reactive oxygen species to ovarian cancer cell growth arrest and killing by the anti-malarial drug artesunate. *Mol Carcinog*. (2017) 56:75–93. doi: 10.1002/mc.v56.1

87. Woo JH, Shimoni Y, Yang WS, Subramaniam P, Iyer A, Nicoletti P, et al. Elucidating compound mechanism of action by network perturbation analysis. *Cell*. (2015) 162:441–51. doi: 10.1016/j.cell.2015.05.056

88. You Y, Fan Q, Huang J, Wu Y, Lin H, Zhang Q. Ferroptosis-related gene signature promotes ovarian cancer by influencing immune infiltration and invasion. *J Oncol*. (2021) 2021:9915312. doi: 10.1155/2021/9915312

89. Choi J-A, Lee EH, Cho H, Kim J-H. High-dose selenium induces ferroptotic cell death in ovarian cancer. *Int J Mol Sci*. (2023) 24:1918. doi: 10.3390/ijms24031918

90. Xiong Y, Liu T, Chen J. Anisomycin has the potential to induce human ovarian cancer stem cell ferroptosis by influencing glutathione metabolism and autophagy signal transduction pathways. *J Cancer*. (2023) 14:1202–15. doi: 10.7150/jca.83355

91. Ebrahimi B, Viswanadhapalli S, Pratap UP, Rahul G, Yang X, Pitta Venkata P, et al. Pharmacological inhibition of the LIF/LIFR autocrine loop reveals vulnerability of ovarian cancer cells to ferroptosis. *NPJ Precis Oncol*. (2024) 8:118. doi: 10.1038/s41698-024-00612-y

92. Shen Z, Song J, Yung BC, Zhou Z, Wu A, Chen X. Emerging strategies of cancer therapy based on ferroptosis. *Adv Mater*. (2018) 30:e1704007. doi: 10.1002/adma.201704007

93. Lu J, Tai Z, Wu J, Li L, Zhang T, Liu J, et al. Nanomedicine-induced programmed cell death enhances tumor immunotherapy. *J Adv Res*. (2024) 14:199–217. doi: 10.1016/j.jare.2023.09.018

94. Zhou H-H, Chen X, Cai L-Y, Nan X-W, Chen J-H, Chen X-X, et al. Erastin reverses ABCB1-mediated docetaxel resistance in ovarian cancer. *Front Oncol*. (2019) 9:1398. doi: 10.3389/fonc.2019.01398

95. Asif K, Adeel M, Rahman MM, Caligiuri I, Perin T, Cemazar M, et al. Iron nitroprusside as a chemodynamic agent and inducer of ferroptosis for ovarian cancer therapy. *J Mater Chem B*. (2023) 11:3124–35. doi: 10.1039/D2TB02691K

96. Cang W, Wu A, Gu L, Wang W, Tian Q, Zheng Z, et al. Erastin enhances metastatic potential of ferroptosis-resistant ovarian cancer cells by M2 polarization through STAT3/IL-8 axis. *Int Immunopharmacol*. (2022) 113:109422. doi: 10.1016/j.intimp.2022.109422

97. Mao G, Xin D, Wang Q, Lai D. Sodium molybdate inhibits the growth of ovarian cancer cells via inducing both ferroptosis and apoptosis. *Free Radical Biol Med*. (2022) 182:79–92. doi: 10.1016/j.freeradbiomed.2022.02.023

98. Jiang Q, Wang K, Zhang X, Ouyang B, Liu H, Pang Z, et al. Platelet membrane-camouflaged magnetic nanoparticles for ferroptosis-enhanced cancer immunotherapy. *Small*. (2020) 16:2001704. doi: 10.1002/smll.202001704

99. Battaglia AM, Sacco A, Perrotta ID, Faniello MC, Scalise M, Torella D, et al. Iron administration overcomes resistance to erastin-mediated ferroptosis in ovarian cancer cells. *Front Oncol*. (2022) 12:868351. doi: 10.3389/fonc.2022.868351

100. Chekerov R, Hilpert F, Mahner S, El-Balat A, Harter P, De Gregorio N, et al. Sorafenib plus topotecan versus placebo plus topotecan for platinum-resistant ovarian cancer (TRIAS): a multicenter, randomized, double-blind, placebo-controlled, phase 2 trial. *Lancet Oncol*. (2018) 19:1247–58. doi: 10.1016/S1470-2045(18)30372-3

101. Chan DW, Yung MM, Chan Y-S, Xuan Y, Yang H, Xu D, et al. MAP30 protein from Momordica charantia is therapeutic and has synergic activity with cisplatin against ovarian cancer in *vivo* by altering metabolism and inducing ferroptosis. *Pharmacol Res*. (2020) 161:105157. doi: 10.1016/j.phrs.2020.105157

102. Liu W, Chen H, Zhu Z, Liu Z, Ma C, Lee YJ, et al. Ferroptosis inducer improves the efficacy of oncolytic virus-mediated cancer immunotherapy. *Biomedicines*. (2022) 10:1425. doi: 10.3390/biomedicines10061425

103. Li H, Liu M, Jiang X, Song T, Feng S, Wu J, et al. GALNT14 regulates ferroptosis and apoptosis of ovarian cancer through the EGFR/mTOR pathway. *Future Oncol*. (2022) 18:149–61. doi: 10.2217/fon-2021-0883

104. Lin C-C, Chi J-T. Ferroptosis of epithelial ovarian cancer: genetic determinants and therapeutic potential. *Oncotarget*. (2020) 11:3562–70. doi: 10.18632/oncotarget.v11i39

105. Cang W, Wu A, Divin, Qiu L, et al. Ferroptosis inducer Erastin enhances cisplatin sensitivity in human epithelial ovarian cancer cells by activating apoptosis. *Department Obstetrics Gynecology*. (2020) 29:730–3. doi: 10.13283/j.cnki.xdfckjz.2020.10.030

106. Wu X, Shen S, Qin J, Fei W, Fan F, Gu J, et al. High co-expression of SLC7A11 and GPX4 as a predictor of platinum resistance and poor prognosis in patients with epithelial ovarian cancer. *BJOG: Int J Obstetrics Gynecology*. (2022) 129:40–9. doi: 10.1111/1471-0528.17327

107. Gentric G, Kieffer Y, Mieulet V, Goundiam O, Bonneau C, Nemati F, et al. PML-regulated mitochondrial metabolism enhances chemosensitivity in human ovarian cancers. *Cell Metab*. (2019) 29:156–173.e10. doi: 10.1016/j.cmet.2018.09.002

108. Zhang S, Liu Q, Chang M, Pan Y, Yahaya BH, Liu Y, et al. Chemotherapy impairs ovarian function through excessive ROS-induced ferroptosis. *Cell Death Dis*. (2023) 14:340. doi: 10.1038/s41419-023-05859-0

109. Jiang Z, Lim S-O, Yan M, Hsu JL, Yao J, Wei Y, et al. TYRO3 induces anti–PD-1/PD-L1 therapy resistance by limiting innate immunity and tumoral ferroptosis. *J Clin Invest*. (2021) 131:e139434. doi: 10.1172/JCI139434

110. Lang X, Green MD, Wang W, Yu J, Choi JE, Jiang L, et al. Radiotherapy and immunotherapy promote tumoral lipid oxidation and ferroptosis via synergistic repression of SLC7A11. *Cancer Discovery*. (2019) 9:1673–85. doi: 10.1158/2159-8290.CD-19-0338

111. Morand S, Devanaboyina M, Staats H, Stanbery L, Nemunaitis J. Ovarian cancer immunotherapy and personalized medicine. *Int J Mol Sci*. (2021) 22(12):6532. doi: 10.3390/ijms22126532

112. Chen J, Wei Z, Fu K, Duan Y, Zhang M, Li K, et al. Non-apoptotic cell death in ovarian cancer: Treatment, resistance and prognosis. *Biomedicine Pharmacotherapy*. (2022) 150:112929. doi: 10.1016/j.biopha.2022.112929

113. Hänggi K, Vasilikos L, Valls AF, Yerbes R, Knop J, Spilgies LM, et al. RIPK1/RIPK3 promotes vascular permeability to allow tumor cell extravasation independent of its necroptotic function. *Cell Death Dis*. (2017) 8:e2588. doi: 10.1038/cddis.2017.20

114. Song J, Liu T, Yin Y, Zhao W, Lin Z, Yin Y, et al. The deubiquitinase OTUD1 enhances iron transport and potentiates host antitumor immunity. *EMBO Rep*. (2021) 22(2):e51162. doi: 10.15252/embr.202051162

115. Säve S, Persson K. Extracellular ATP and P2Y receptor activation induce a proinflammatory host response in the human urinary tract. *Infect Immun*. (2010) 78:3609–15. doi: 10.1128/IAI.00074-10

116. Wen Q, Liu J, Kang R, Zhou B, Tang D. The release and activity of HMGB1 in ferroptosis. *Biochem Biophys Res Commun*. (2019) 510:278–83. doi: 10.1016/j.bbrc.2019.01.090

117. Wang W, Green M, Choi JE, Gijón M, Kennedy PD, Johnson JK, et al. CD8+ T cells regulate tumor ferroptosis during cancer immunotherapy. *Nature*. (2019) 569(7755):270–4. doi: 10.1038/s41586-019-1170-y

118. Kim DH, Kim WD, Kim SK, Moon DH, Lee SJ. TGF-β1-mediated repression of SLC7A11 drives vulnerability to GPX4 inhibition in hepatocellular carcinoma cells. *Cell Death Dis*. (2020) 11:406. doi: 10.1038/s41419-020-2618-6

119. Luo X, Gong H-B, Gao H-Y, Wu Y-P, Sun W-Y, Li Z-Q, et al. Oxygenated phosphatidylethanolamine navigates phagocytosis of ferroptotic cells by interacting with TLR2. *Cell Death Differ*. (2021) 28:1971–89. doi: 10.1038/s41418-020-00719-2

120. Xu C, Sun S, Johnson T, Qi R, Zhang S, Zhang J, et al. The glutathione peroxidase Gpx4 prevents lipid peroxidation and ferroptosis to sustain Treg cell activation and suppression of antitumor immunity. *Cell Rep*. (2021) 35:109235. doi: 10.1016/j.celrep.2021.109235

121. Drijvers JM, Gillis JE, Muijlwijk T, Nguyen TH, Gaudiano EF, Harris IS, et al. Pharmacologic screening identifies metabolic vulnerabilities of CD8+ T cells. *Cancer Immunol Res*. (2021) 9:184–99. doi: 10.1158/2326-6066.CIR-20-0384

122. Kapralov AA, Yang Q, Dar HH, Tyurina YY, Anthonymuthu TS, Kim R, et al. Redox lipid reprogramming commands susceptibility of macrophages and microglia to ferroptotic death. *Nat Chem Biol*. (2020) 16:278–90. doi: 10.1038/s41589-019-0462-8

123. Wang D, DuBois RN. Immunosuppression associated with chronic inflammation in the tumor microenvironment. *Carcinogenesis*. (2015) 36:1085–93. doi: 10.1093/carcin/bgv123

124. Böttcher JP, Bonavita E, Chakravarty P, Blees H, Cabeza-Cabrerizo M, Sammicheli S, et al. NK Cells Stimulate Recruitment of cDC1 into the Tumor Microenvironment Promoting Cancer Immune Control. *Cell*. (2018) 172:1022–1037.e14. doi: 10.1016/j.cell.2018.01.004

125. Veglia F, Tyurin VA, Blasi M, De Leo A, Kossenkov AV, Donthireddy L, et al. Fatty acid transport protein 2 reprograms neutrophils in cancer. *Nature*. (2019) 569:73–8. doi: 10.1038/s41586-019-1118-2

126. Kalinski P. Regulation of immune responses by prostaglandin E2. *J Immunol*. (2012) 188:21–8. doi: 10.4049/jimmunol.1101029

127. Tang R, Xu J, Zhang B, Liu J, Liang C, Hua J, et al. Ferroptosis, necroptosis, and pyroptosis in anticancer immunity. *J Hematol Oncol*. (2020) 13:110. doi: 10.1186/s13045-020-00946-7

128. Srivastava MK, Sinha P, Clements VK, Rodriguez P, Ostrand-Rosenberg S. Myeloid-derived suppressor cells inhibit T-cell activation by depleting cystine and cysteine. *Cancer Res*. (2010) 70:68–77. doi: 10.1158/0008-5472.CAN-09-2587

129. O'Donnell JS, Teng MWL, Smyth MJ. Cancer immunoediting and resistance to T cell-based immunotherapy. *Nat Rev Clin Oncol*. (2019) 16:151–67. doi: 10.1038/s41571-018-0142-8

130. Bear AS, Vonderheide RH, O'Hara MH. Challenges and opportunities for pancreatic cancer immunotherapy. *Cancer Cell*. (2020) 38:788–802. doi: 10.1016/j.ccell.2020.08.004

131. Baert T, Vankerckhoven A, Riva M, Van Hoylandt A, Thirion G, Holger G, et al. Myeloid derived suppressor cells: key drivers of immunosuppression in ovarian cancer. *Front Immunol*. (2019) 10:1273. doi: 10.3389/fimmu.2019.01273

132. Horikawa N, Abiko K, Matsumura N, Hamanishi J, Baba T, Yamaguchi K, et al. Expression of vascular endothelial growth factor in ovarian cancer inhibits tumor immunity through the accumulation of myeloid-derived suppressor cells. *Clin Cancer Res*. (2017) 23:587–99. doi: 10.1158/1078-0432.CCR-16-0387

133. Komura N, Mabuchi S, Shimura K, Yokoi E, Kozasa K, Kuroda H, et al. The role of myeloid-derived suppressor cells in increasing cancer stem-like cells and promoting PD-L1 expression in epithelial ovarian cancer. *Cancer Immunol Immunother*. (2020) 69:2477–99. doi: 10.1007/s00262-020-02628-2

134. Guo P, Wang L, Shang W, Chen J, Chen Z, Xiong F, et al. Intravesical *in situ* immunostimulatory gel for triple therapy of bladder cancer. *ACS Appl Mater Interfaces*. (2020) 12:54367–77. doi: 10.1021/acsami.0c15176

135. Ma X, Xiao L, Liu L, Ye L, Su P, Bi E, et al. CD36-mediated ferroptosis dampens intratumoral CD8+ T cell effector function and impairs their antitumor ability. *Cell Metab*. (2021) 33:1001–1012.e5. doi: 10.1016/j.cmet.2021.02.015

136. Ugolini A, Tyurin VA, Tyurina YY, Tcyganov EN, Donthireddy L, Kagan VE, et al. Polymorphonuclear myeloid-derived suppressor cells limit antigen cross-presentation by dendritic cells in cancer. *JCI Insight*. (2020) 5:e138581. doi: 10.1172/jci.insight.138581

137. Zhang H, Zhuo Y, Li D, Zhang L, Gao Q, Yang L, et al. Dihydroartemisinin inhibits the growth of pancreatic cells by inducing ferroptosis and activating antitumor immunity. *Eur J Pharmacol*. (2022) 926:175028. doi: 10.1016/j.ejphar.2022.175028

138. Conche C, Finkelmeier F, Pešić M, Nicolas AM, Böttger TW, Kennel KB, et al. Combining ferroptosis induction with MDSC blockade renders primary tumors and metastases in liver sensitive to immune checkpoint blockade. *Gut*. (2023) 72(9):1774–82. doi: 10.1136/gutjnl-2022-327909

139. Zhu H, Klement JD, Lu C, Redd PS, Yang D, Smith AD, et al. Asah2 represses the p53-hmox1 axis to protect myeloid-derived suppressor cells from ferroptosis. *J Immunol*. (2021) 206:1395–404. doi: 10.4049/jimmunol.2000500

140. Zhang F, Li F, Lu G-H, Nie W, Zhang L, Lv Y, et al. Engineering magnetosomes for ferroptosis/immunomodulation synergism in cancer. *ACS Nano*. (2019) 13:5662–73. doi: 10.1021/acsnano.9b00892

141. Yang L, Tian S, Chen Y, Miao C, Zhao Y, Wang R, et al. Ferroptosis-related gene model to predict overall survival of ovarian carcinoma. *J Oncol*. (2021) 2021:6687391. doi: 10.1155/2021/6687391

142. Immunotherapy activates unexpected cell death mechanism. *Cancer Discovery*. (2019) 9:OF2. doi: 10.1158/2159-8290.CD-NB2019-058

143. Li Y, Zhang Q, Wu M, Zhang P, Huang L, Ai X, et al. Suppressing MDSC infiltration in tumor microenvironment serves as an option for treating ovarian cancer metastasis. *Int J Biol Sci*. (2022) 18:3697–713. doi: 10.7150/ijbs.70013

144. Yu Z, He H, Chen Y, Ji Q, Sun M. A novel ferroptosis related gene signature is associated with prognosis in patients with ovarian serous cystadenocarcinoma. *Sci Rep*. (2021) 11:11486. doi: 10.1038/s41598-021-90126-5

145. Cheng Z, Chen Y, Huang H. Identification and validation of a novel prognostic signature based on ferroptosis-related genes in ovarian cancer. *Vaccines (Basel)*. (2023) 11:205. doi: 10.3390/vaccines11020205

146. Ye Y, Dai Q, Li S, He J, Qi H. A novel defined risk signature of the ferroptosis-related genes for predicting the prognosis of ovarian cancer. *Front Mol Biosci*. (2021) 8:645845. doi: 10.3389/fmolb.2021.645845

147. Hu K, Zhang X, Zhou L, Li J. Downregulated PRNP facilitates cell proliferation and invasion and has effect on the immune regulation in ovarian cancer. *J Immunol Res*. (2022) 2022:3205040. doi: 10.1155/2022/3205040

148. Liu Y, Du S, Yuan M, He X, Zhu C, Han K, et al. Identification of a novel ferroptosis-related gene signature associated with prognosis, the immune landscape, and biomarkers for immunotherapy in ovarian cancer. *Front Pharmacol*. (2022) 13:949126. doi: 10.3389/fphar.2022.949126

149. Yang J, Wang C, Cheng S, Zhang Y, Jin Y, Zhang N, et al. Construction and validation of a novel ferroptosis-related signature for evaluating prognosis and immune

microenvironment in ovarian cancer. *Front Genet*. (2022) 13:1094474. doi: 10.3389/fgene.2022.1094474

150. Wang H, Cheng Q, Chang K, Bao L, Yi X. Integrated analysis of ferroptosis-related biomarker signatures to improve the diagnosis and prognosis prediction of ovarian cancer. *Front Cell Dev Biol*. (2022) 9:807862. doi: 10.3389/fcell.2021.807862

151. Yuan X, Zhou Q, Zhang F, Zheng W, Liu H, Chen A, et al. Identification of immunity- and ferroptosis-related genes for predicting the prognosis of serous ovarian cancer. *Gene*. (2022) 838:146701. doi: 10.1016/j.gene.2022.146701

152. Xiong T, Wang Y, Zhu C. A risk model based on 10 ferroptosis regulators and markers established by LASSO-regularized linear Cox regression has a good prognostic value for ovarian cancer patients. *Diagn Pathol*. (2024) 19:4. doi: 10.1186/s13000-023-01414-9

153. Li S, Cao T, Wu T, Xu J, Shen C, Hou S, et al. Identification of a ferroptosis- and oxidative stress-associated gene signature for prognostic stratification of ovarian cancer. *Am J Transl Res*. (2023) 15:2645–55.

154. Sun X, He W, Lin B, Huang W, Ye D. Defining three ferroptosis-based molecular subtypes and developing a prognostic risk model for high-grade serous ovarian cancer. *Aging (Albany NY)*. (2024) 16:9106–26. doi: 10.18632/aging.v16i10

155. Li Y, Fang T, Shan W, Gao Q. Identification of a novel model for predicting the prognosis and immune response based on genes related to cuproptosis and ferroptosis in ovarian cancer. *Cancers (Basel)*. (2023) 15:579. doi: 10.3390/cancers15030579

156. Zhang J, Xi J, Huang P, Zeng S. Comprehensive analysis identifies potential ferroptosis-associated mRNA therapeutic targets in ovarian cancer. *Front Med*. (2021) 8:644053. doi: 10.3389/fmed.2021.644053

157. Xu K, Zheng X, Shi H, Ou J, Ding H. MAD2L2, a key regulator in ovarian cancer and promoting tumor progression. *Sci Rep*. (2024) 14:130. doi: 10.1038/s41598-023-50744-7

158. Novera W, Lee Z-W, Nin DS, Dai MZ-Y, Binte Idres S, Wu H, et al. Cysteine deprivation targets ovarian clear cell carcinoma via oxidative stress and iron-sulfur cluster biogenesis deficit. *Antioxid Redox Signal*. (2020) 33:1191–208. doi: 10.1089/ars.2019.7850

frontiers | Frontiers in Immunology

TYPE Original Research
PUBLISHED 07 October 2024
DOI 10.3389/fimmu.2024.1412277

OPEN ACCESS

EDITED BY
Laura Senovilla,
Spanish National Research Council (CSIC), Spain

REVIEWED BY
Luis Castro-Sánchez,
University of Colima, Mexico
Omar Motiño,
University of Valladolid, Spain

*CORRESPONDENCE
Xiaolong Liu
12218318@zju.edu.cn
Xiaoxiao Fan
fanxx_gs@zju.edu.cn

†These authors have contributed equally to this work

RECEIVED 04 April 2024
ACCEPTED 19 September 2024
PUBLISHED 07 October 2024

CITATION
Zheng H, Cheng J, Zhuang Z, Li D, Yang J, Yuan F, Fan X and Liu X (2024) A disulfidptosis-related lncRNA signature for analyzing tumor microenvironment and clinical prognosis in hepatocellular carcinoma. *Front. Immunol.* 15:1412277. doi: 10.3389/fimmu.2024.1412277

A disulfidptosis-related lncRNA signature for analyzing tumor microenvironment and clinical prognosis in hepatocellular carcinoma

Haishui Zheng[1†], Jigan Cheng[1†], Ziyun Zhuang[2,3†], Duguang Li[1], Jing Yang[1], Fan Yuan[1], Xiaoxiao Fan[1*] and Xiaolong Liu[1*]

[1]Department of General Surgery, Sir Run Run Shaw Hospital, School of Medicine, Zhejiang University, Hangzhou, China, [2]Shantou University Medical College, Shantou, China, [3]Department of Breast Cancer, Cancer Center, Guangdong Provincial People's Hospital.Guangdong Academy of Medical Sciences, Guangzhou, China

Introduction: Disulfidptosis is a recently identified form of non-apoptotic programmed cell death which distinguishes itself from classical cell death pathways. However, the prognostic implications of disulfidptosis-related long non-coding RNAs (DRLs) and their underlying mechanisms in hepatocellular carcinoma (HCC) remain largely unexplored.

Methods: In this study, we leveraged RNA-sequencing data and clinical information of HCC patients from the TCGA database. Through expression correlation and prognostic correlation analyses, we identified a set of top-performing long non-coding RNAs. Subsequently, a 5-DRLs predictive signature was established by conducting a Lasso regression analysis.

Results: This signature effectively stratified patients into high- and low-risk groups, revealing notable differences in survival outcomes. Further validation through univariate and multivariate Cox regression analyses confirmed that the risk score derived from our signature independently predicted the prognosis of HCC patients. Moreover, we observed significant disparities in immune cell infiltration and tumor mutation burden (TMB) between the two risk groups, shedding light on the potential connection between immune-related mechanisms and disulfidptosis. Notably, the signature also exhibited predictive value in the context of chemotherapeutic drug sensitivity and immunotherapy efficacy for HCC patients. Finally, we performed experimental validation at both cellular and patient levels and successfully induced a disulfidptosis phenotype in HCC cells.

Discussion: In general, this multifaceted approach provides a comprehensive overview of DRLs profiles in HCC, culminating in the establishment of a novel risk signature that holds promise for predicting prognosis and therapy outcomes of HCC patients.

KEYWORDS

hepatocellular carcinoma, disulfidptosis, lncRNA, tumor microenvironment, SLC7A11

1 Introduction

Hepatocellular carcinoma (HCC) is a multifaceted, globally impactful disease (1). Owing to its inconspicuous clinical symptoms in the early stages and the presence of numerous risk factors, it poses a significant clinical challenge. Primary liver cancer is the sixth most common cancer in the world and the third leading cause of cancer-related deaths in 2022, according to global cancer statistics published in 2024 (2). HCC accounts 80-90% of primary liver cancer cases and is the most common type (3). In recent years, enormous strides in targeted therapies and immunotherapies have been developed, offering renewed hope for better patient outcomes (4). However, patients with HCC continue to experience high rates of recurrence, metastasis, and drug resistance, contributing to an unfavorable prognosis (5). This underlines the necessity for early detection and a multidisciplinary approach for managing this formidable malignancy. Therefore, it is imperative to explore the intricate molecular mechanisms underlying HCC. The development of innovative therapies is indispensable in the ongoing battle against HCC.

Cell death is crucial for the development and homeostasis of multicellular organisms, and its dysregulation can lead to various diseases including cancer (6). A comprehensive understanding of programmed cell death modes could potentially pave the way for the targeted elimination of cancer cells, thereby improving cancer treatment outcomes (7). For example, the apoptotic signaling pathway has been the focal point of tumor chemotherapy in the past few decades. Some chemotherapeutic drugs, such as Paclitaxel and Vinca Alkaloids, can induce apoptosis of tumor cells by targeting microtubules and oxidative phosphorylation, thus achieving a therapeutic effect on tumors (8, 9). However, these therapies are associated with a high rate of drug resistance, posing significant challenges. Therefore, it is necessary to expand our understanding of regulated cell death modes beyond apoptosis to facilitate the discovery of potential therapeutic targets. In recent years, research has increasingly shown that many forms of non-apoptotic cell death are also executed in a regulated manner, which are collectively referred to as "regulated non-apoptotic cell death modes" (10). These newly named cell death modes include necroptosis, oxytosis, pyroptosis, parthanatos, NETosis, ferroptosis and cuproptosis (11–16). Recently, Gan et al. proposed a novel form of cell death known as disulfidptosis, which opens a promising avenue for cancer treatment. Disulfidptosis is triggered by the significant accumulation of disulfide molecules within cancer cells in the absence of glucose, particularly in those with elevated SLC7A11 expression. This phenomenon results in abnormal disulfide bonding between actin cytoskeletal proteins, disrupting their organization, and ultimately leading to the collapse of the actin protein network and cell death. Gan et al. treated cancer cells with a glucose transporter (GLUT) inhibitor and observed that the outcome was similar to that under glucose-deprived conditions (17). This inventive discovery has immense potential for developing targeted therapies for cancer treatment. It is crucial to acknowledge that the comprehension of distinct forms of cell death, including apoptosis, necrosis, ferroptosis, and the newly discovered disulfidptosis, remains an evolving frontier in the realm of cell biology and cancer research. Further investigations are warranted to comprehensively elucidate disulfidptosis, its relevance in the context of cancer, and its potential as a target for therapeutic interventions.

LncRNAs are a class of non-coding RNA molecules with a length exceeding 200 nucleotides. This type of RNA lacks an open reading frame (ORF) and does not encode proteins, leading to the belief that it exists solely as a transcriptional byproduct. However, extensive research has demonstrated that lncRNAs participate in various biological processes including DNA methylation, histone modification, post-transcriptional regulation of RNA, and protein translation (18). Additionally, lncRNAs play pivotal roles in processes related to immunology, neurobiology, inflammatory responses, and cancer (19). Furthermore, lncRNAs are critical regulators of cellular proliferation and programmed cell death. Sun et al. discovered that lncRNA-ATB regulates the formation of tumor metastasis foci by modulating the stability of IL-11 mRNA and STAT3 phosphorylation (20). Concerning regulated cell death, lncRNA-HEPFAL was found to promote ferroptosis by reducing SLC7A11 expression and increasing levels of lipid reactive oxygen species (ROS) and iron ions (21). The association between lncRNAs and HCC has been extensively explored, notably in the regulation of cell death processes in HCC. For example, Chen et al. revealed that lncRNA DUXAP8 decreased the sensitivity of HCC to sorafenib-induced ferroptosis by interacting with SLC7A11 (22). In the era of precision medicine, identification of precise lncRNAs that regulate disulfidptosis in HCC, along with a thorough elucidation of their mechanisms, could offer innovative insights and perspectives for the treatment of HCC.

In this study, we collected HCC data from The Cancer Genome Atlas (TCGA) database to elucidate the prognostic and biological functions of disulfidptosis-related long non-coding RNAs (DRLs) through various bioinformatic analyses. Our 5-DRLs signature

Abbreviations: DRLs, Disulfidptosis-related long non-coding RNAs; HCC, Hepatocellular carcinoma; TMB, Tumor mutation burden; GLUT, Glucose transporter; ORF, Open reading frame; ROS, Lipid reactive oxygen species; TCGA, The cancer genome atlas; TME, Tumor microenvironment; FPKM, Fragments per kilobase of transcript per million mapped reads; OS, Overall survival; DCLs, Disulfidptosis co-expressed lncRNAs; DELs, Differentially expressed lncRNAs; LASSO, Least absolute shrinkage and selection operator; IPS, Immunophenoscore; MAF, Mutation annotation format; IC50, The semi-inhibitory concentration; DAVID, Database for annotation, visualization, and integrated discovery; GSEA, Gene set enrichment analysis; KEGG, Kyoto encyclopedia of genes and genomes analysis; GO, Gene ontology analysis; FBS, Fetal bovine serum; SRRSH, Sir run run shaw hospital; GAPDH, Glyceraldehyde 3-phosphate dehydrogenase; RIPA, Radioimmunoprecipitation assay; BCA, Bicinchoninic acid; PVDF, Polyvinylidene difluoride; ECL, Enhanced chemiluminescence; DRGs, Disulfidptosis-related genes; DCDELs, Disulfidptosis co-expressed and differentially expressed lncRNAs; PCA, Principal component analysis; PFS, Progression-free survival; t-SNE, t-Distributed stochastic neighbor embedding; AUC, Area under curve; DCA, Decision curve analysis; ICB, Immune checkpoint blockade; DEGs, Differentially expressed genes; TMEM9, Transmembrane protein 9; GSH, Cysteine-dependent glutathione; ECs, Endothelial cells; M1, Type 1-polarized macrophages; M2, Type 2-polarized macrophages.

exhibited excellent performance in predicting patient survival and remarkable superiority over the other clinically independent variables. Additionally, we established a potential relationship between the risk signature and tumor microenvironment (TME), as well as tumor mutation burden (TMB), through immune infiltration analysis and TMB analysis. Furthermore, KEGG and GO analyses were performed between the high- and low-risk groups to identify the potential molecular pathways. Overall, our findings shed light on the understanding of molecular mechanisms related to disulfidptosis in HCC and could help to develop individualized therapies for patients with HCC.

2 Materials and methods

2.1 Data acquisition

A total of 374 HCC samples and 50 adjacent normal hepatic sample fragments per kilobase of transcript per million mapped reads (FPKM)-standardized RNA-seq data were downloaded from The Cancer Genome Atlas(TCGA) (https://portal.gdc.cancer.gov/projects/TCGA-LIHC). Ensembl IDs were processed and converted to official gene symbols encompassing various elements, such as lncRNAs, protein-coding genes, and miRNAs. Additional information, including clinical data, was also acquired from patients with HCC in the TCGA database. Samples lacking survival information and those with an overall survival (OS) of less than 30 days were excluded from subsequent analysis. Ten Disulfidptosis-related Genes (DRGs) were obtained in a recent study (Table 1) (17).

2.2 Identification of disulfidptosis co-expressed lncRNAs

Pearson's correlation analysis was chosen as a widely accepted method to explore the correlation between coding genes and lncRNAs. Using a cutoff criterion of R > 0.3 and $P < 0.001$, Pearson correlation analysis was applied to identify lncRNAs that were co-expressed with the 10 DRGs from the RNA-seq data of TCGA HCC samples.

TABLE 1 Disulfidptosis-related genes.

Official Symbol	Official Full Name
GYS1	Glycogen Synthase 1
NDUFS1	NADH Dehydrogenase Fe-S Protein 1
OXSM	3-Oxoacyl-ACP Synthase, Mitochondrial
LRPPRC	Leucine Rich Pentatricopeptide Repeat Containing
NDUFA11	NADH: Ubiquinone Oxidoreductase Subunit A11
NUBPL	NUBP Iron-Sulfur Cluster Assembly Factor, Mitochondrial
NCKAP1	NCK Associated Protein 1
RPN1	Ribophorin I
SLC3A2	Solute Carrier Family 3 Member 2
SLC7A11	Solute Carrier Family 7 Member 11

2.3 Identification of differentially expressed lncRNAs

Differentially expressed lncRNAs between HCC and normal patients from TCGA were identified using the R package "Limma." The significance criterion for identifying DEGs was set as $|\log_2(\text{fold-change})| > 1$ and $p < 0.001$.

2.4 Univariate cox analysis for prognostic lncRNAs

By using the 'survival' R package and defining $p < 0.05$ as screening criteria, the intersecting lncRNAs of DCLs and DELs were subsequent to univariate cox analysis for obtaining prognostic DRLs in HCC patients.

2.5 Construction and validation of the disulfidptosis-related prognostic signature

To construct a disulfidptosis-related prognostic signature, least absolute shrinkage and selection operator (LASSO) Cox regression analysis was used to select the most appropriate lncRNAs and estimate and weight the regression coefficients of the optimal DRLs (23). Initially, nine prognostic lncRNAs were screened based on the optimal penalty parameter λ determined by tenfold cross-validation following the minimum criteria. Afterwards, a multivariate Cox regression analysis was conducted to establish a five-lncRNA predictive model. The Risk score of each HCC patient was calculated using the following formula: Risk score = (Coef.DRL1 × DRL1 exp.) + (Coef.DRL2 × DRL2 exp.) + (…) + (Coef. DRLn × DRLn exp.). Patients were categorized into low- and high-risk groups based on the median risk score. The performance and prognostic ability of the predictive signature were evaluated using time-dependent receiver operating characteristic (ROC) analyses and Kaplan-Meier log-rank tests. These analyses were conducted with the R packages "timeROC" and "survival," respectively (24). Furthermore, in combination with the DRL prognostic signature, the clinical characteristics of patients with HCC from TCGA were analyzed using univariate and multivariate Cox regression analyses.

2.6 Establishment of a nomogram

Package "rms" was utilized to create a nomogram, offering valuable clinical prognostic insights for HCC patients, including their risk scores and various clinicopathological attributes, particularly about 1-, 3-, and 5-year OS (25). Subsequently, we

conducted calibration curve analysis to validate the clinical accuracy of the nomogram.

2.7 Relationship of DRL risk signature with tumor microenvironment in HCC

The immune and stromal scores of each HCC patient were calculated using the ESTIMATE algorithm (26). Next, the levels of 22 immune cell subtypes of each patient were computed using the CIBERSORT algorithm (27). The differentially expressed immune checkpoint genes between high- and low- risk groups were identified using R package "Limma." Immunophenoscore (IPS) was obtained from the TCIA database (https://tcia.at/home) to predict the relative immune response (28).

2.8 Tumor mutation burden analysis

To delineate the mutational profiles of HCC patients within two distinct risk groups, the Mutation Annotation Format (MAF) was generated using the "maftools" package (29). This MAF served to characterize the mutational landscape of patients with HCC from different DRL risk groups.

2.9 Drug sensitivity analysis

The semi-inhibitory concentration (IC50) values for commonly used chemotherapy agents in HCC patients were calculated using the "pRRophetic" package to predict the clinical performance of chemotherapy agents in different DRL risk groups for HCC patients (30).

2.10 Gene set enrichment analysis, Kyoto encyclopedia of genes and genomes and gene ontology analysis

To identify the potential molecular pathways between the high- and low-risk groups, KEGG, GO, and GSEA were performed. Firstly, R package "Limma" was performed to classified differential expressed genes between high- and low-risk groups ($|\log_2 FC| > 1$, $p < 0.05$). Significant genes were inserted into the Database for Annotation, Visualization, and Integrated Discovery (DAVID, https://david.ncifcrf.gov/) to enrich closely related metabolic pathways. GSEA was performed using GSEA software with c5.all.v7.4 symbols.gmt as a template. The criteria for statistical significance were nominal $p < 0.05$ and FDR< 0.25.

2.11 Cell culture and human samples

The normal human liver cell line MIHA and the human hepatocellular carcinoma cell lines HA22T, HCCLM3, HepG2, and JHH-7 were purchased from the Cell Bank of the Chinese Academy of Sciences. All cell lines were cultured in DMEM medium (Gibco, USA) containing 10% fetal bovine serum (FBS, Gibco) at 37°C in humidified air with 5% CO_2. A total of 16 HCC samples and adjacent normal tissues were collected from patients with HCC who underwent surgical resection at the Sir Run Run Shaw Hospital (SRRSH), in accordance with the principles of the Declaration of Helsinki. Written informed consent was obtained from all the patients. All human samples were obtained after obtaining informed consent as approved by the Institutional Review Board of SRRSH, School of Medicine, Zhejiang University, Hangzhou, China (ethical code: 20210729-282).

2.12 RNA extraction and quantitative real-time PCR

RNA extraction was performed using an RNA-Quick Purification Kit (AG21023, Accurate Biology). Reverse transcription was conducted according to the protocol of the Eco M-MLV RT Premix Kit (AG11706, Accurate Biology). RT-qPCR was conducted on a QuantStudio 1 (Applied Biosystems, Thermo Fisher Scientific, USA) using the SYBR Green Premix Pro Tag HS qPCR kit (AG11701, Accurate Biology). Target gene expression was normalized to the endogenous control gene glyceraldehyde 3-phosphate dehydrogenase (GAPDH). The primers used in this study was listed in Table 2.

2.13 Cell counting kit-8 assay

HepG2 and JHH-7 cell viability was assessed using the CCK-8 reagent (Meilunbio, China), following the manufacturer's instructions. Cells were seeded in 96-well plates at a density of

TABLE 2 Primers for RT-qPCR in this study.

Primer name	Sequence (5′-3′)
TMCC1-AS1-F	GGTAGGGTAGCAGGTCAGCATATC
TMCC1-AS1-R	TTGTCACAGGCCAGACTACCAG
FOXD2-AS1-F	TATGTGGTAGGGGACTCGCT
FOXD2-AS1-R	GGTTTCAAGTGGCGCTGTTT
LINC01063-F	CCTGAGCCTGGAAGGTGATT
LINC01063-R	TGACTGAGGTTCGCTGTGAC
SLC25A30-AS1-F	CAAGTGCCCCTCAGGATCTTC
SLC25A30-AS1-R	AATTTCTCTTCCACCTCCCAGTC
AC009283.1-F	GCATCTGAGCAGCTGTGCAGCA
AC009283.1-R	CCTCCTCATCATCCTCCTGTGGGT
GAPDH-F	CTCTGCTCCTCCTGTTCGAC
GAPDH-R	ACCAAATCCGTTGACTCCGA
SLC7A11-F	TCTCCAAAGGAGGTTACCTGC
SLC7A11-R	AGACTCCCCTCAGTAAAGTGAC

3000 cells/well in 100 µL of medium. Subsequently, CCK8 solution (10 µL) was added to each well at 3, 6, 12, 24, 36, and 48 hours after treatment with glucose-free DMEM. The cells were then further incubated at 37°C for 2 h. The absorbance of each well was measured at 450 nm wavelength using a spectrophotometer.

2.14 Confocal microscopic imaging of F-actin staining

HepG2 and JHH-7 cells were seeded in 24-well plates at a density of 20000 cells per well and treated with DMEM Medium without glucose for 24 h. For actin filament staining, cells were fixed for 30 min at room temperature with 4% paraformaldehyde and then permeabilized for 10 min with permeabilization buffer (0.1% Triton X-100 in PBS). Subsequently, the cells were incubated in darkness at room temperature for 1-2 hours with TRITC Phalloidin (Solarbio, CA1610). Afterward, the cells were then washed twice and mounted with antifade mounting medium containing DAPI (Beyotime, P0131). Finally, all fluorescence images were captured using a confocal microscope (LSM 880, Zeiss).

2.15 Drugs and reagents

Z-VAD-FMK (ZVF, S7023), ferrostatin-1 (Fer-1, S7243), necrostatin-1 (Nec-1, S8037), and N-acetyl cysteine (NAC, S5804) were purchased from Selleck. Tetrathiomolybdate (TTM, 323446) was purchased from Sigma. Tris (2-carboxyethyl) phosphine (TCEP, T2556) was purchased from Thermo Fisher. The concentration of ZVF, Fer-1, Nec-1, NAC, TTM and TCEP were 30µM, 10µM, 20µM, 1mM, 20µM, 1mM.

2.16 Western blotting

Proteins from cells were extracted using radioimmunoprecipitation assay (RIPA) buffer (Fude Biotech, China) containing protease inhibitors. Subsequently, protein concentrations were determined using a Bicinchoninic Acid (BCA) Protein Assay Kit (Meilunbio, China). A total of 20 µg of protein was subjected to sodium dodecyl sulfate–polyacrylamide gel electrophoresis and transferred to a 0.22 or 0.45 µm polyvinylidene difluoride (PVDF) membrane. PVDF membranes were then blocked in 5% skim milk for 2 h. Subsequently, samples were incubated with specific primary antibodies at 4°C overnight. The primary antibodies were as follows: SLC7A11 (82115-2-RR, Proteintech, Wuhan, China), GAPDH (AC002, Abclonal, Wuhan, China). Following this, membranes were incubated with the appropriate secondary antibodies for 2 h at room temperature. Finally, the protein bands were visualized with enhanced chemiluminescence (ECL) Western blotting substrate (Fude Biotech, China).

2.17 RNA interference

The small interference RNAs (siRNAs) was designed and synthesized in GenePharma(China), which could effectively knock down lncRNAs effectively. Cells were transfected with 100 nM of smart silencer for each well using the Lipofectamine™ 3000 transfection reagent (L3000015; Thermo Fisher, USA). After 48 hours of transfection, cells were collected and processed for RT-qPCR and other experiments. The sequences of the lncRNA siRNA were listed in Table 3.

2.18 Statistical analysis

All statistical analyses were conducted using R software (Version 4.1.2). Wilcox test was used to compare lncRNA expression levels between HCC and para-noncancerous tissues sourced from TCGA. Differences in the proportions of clinical features were assessed using the chi-square test. A paired t-test was used to compare data between HCC and adjacent normal tissues obtained in-house. Variances among multiple groups were analyzed using one-way ANOVA. Statistical significance was defined as a p-value < 0.05.

3 Results

3.1 Identification of disulfidptosis-related differentially expressed and prognostic lncRNAs in HCC

Initially, we retrieved data from 374 patients diagnosed with HCC from TCGA database, consisting of transcriptomes and clinical information. Subsequently, we identified ten DRGs, as previously reported (Table 1) (17). The flowchart was presented

TABLE 3 Sequences of siRNAs for related lncRNAs.

LncRNA name	sense(5′-3′)	antisense(5′-3′)
FOXD2-AS1-Homo-1	GAGGGACAGCCAAGAAUACTT	GUAUUCUUGGCUGUCCCUCTT
FOXD2-AS1-Homo-2	AGUCCCAGACAGGGUAACUTT	AGUUACCCUGUCUGGGACUTT
FOXD2-AS1-Homo-3	GUCAGGAACUAAAGGACUGTT	CAGUCCUUUAGUUCCUGACTT
LINC01063-Homo-1	AUCAAGCGGUGGCAGUUCATT	UGAACUGCCACCGCUUGAUTT
LINC01063-Homo-2	GGAAGGUGAUUGGCUAGAGTT	CUCUAGCCAAUCACCUUCCTT
LINC01063-Homo-3	UGCGAGCAUCAUGUUGCCUTT	AGGCAACAUGAUGCUCGCATT

in Figure 1. Figure 2A illustrated the correlation network diagram and provided insights into the interactions among these 10 DRGs in patients with HCC. To assess clinical relevance, we conducted a comparative analysis of gene expression between HCC tissues and adjacent normal tissues. A total of 3261 Differentially Expressed lncRNAs (DELs) were identified based on the criteria of $|\log_2 FC|>1$, $p<0.001$. Detailed information on these DEGs were provided in Supplementary Table 1, and the volcano plot in Figure 2B depicted the variation in lncRNA expression levels between HCC and adjacent normal tissues. To investigate the relationship between DRGs and lncRNAs, we performed Pearson correlation analysis with a threshold of R>0.3 and $p<0.001$, leading to the identification of 863 DCLs, as shown in Supplementary Figure 1. The correlation between DRGs and lncRNAs were shown in Supplementary

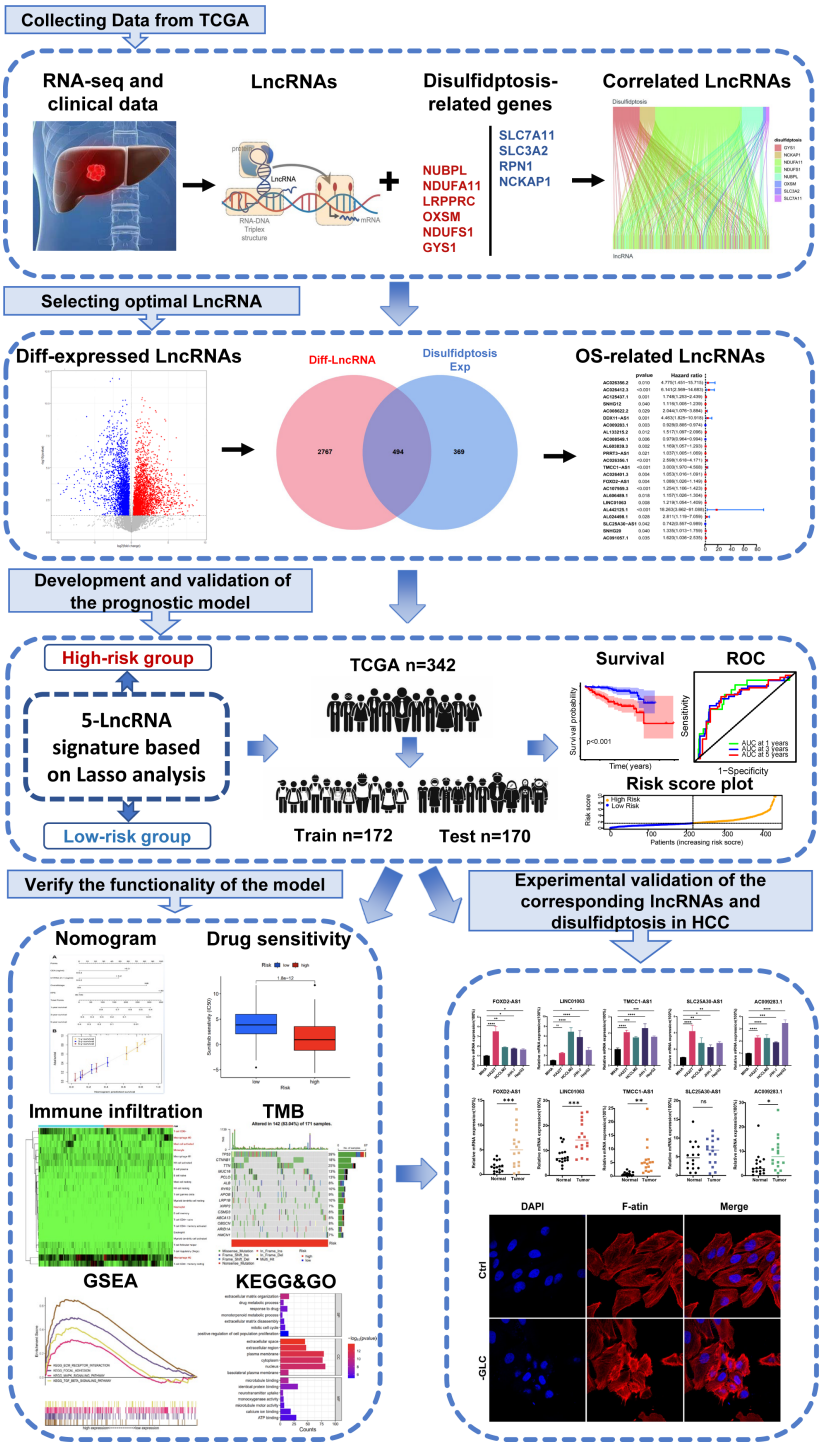

FIGURE 1
The flow chart of this study.

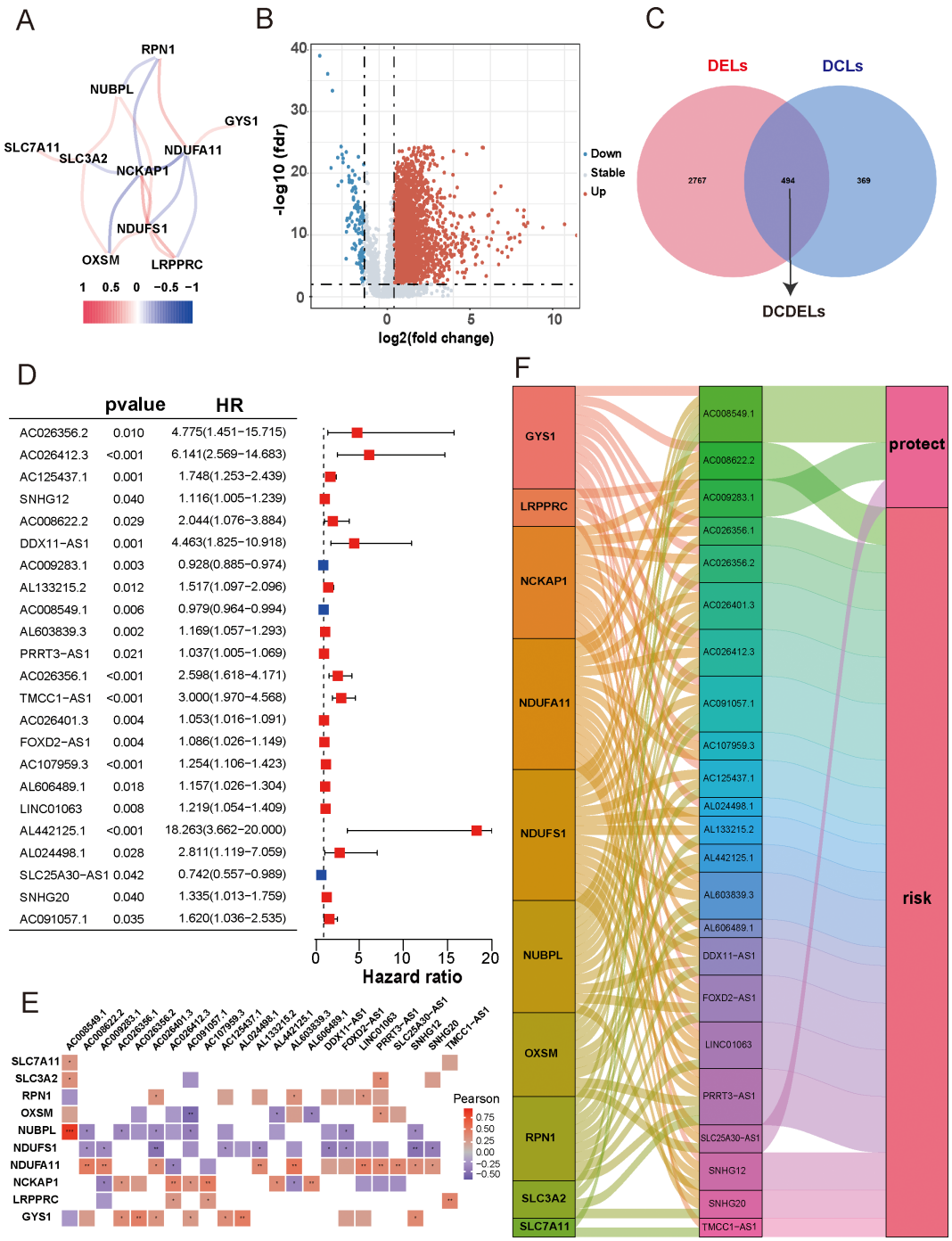

FIGURE 2
Identification of disulfidptosis-related differentially expressed and prognostic lncRNAs in HCC. **(A)** Co-expression network of 10 DRGs. (Red and blue colors represent a positive correlation and a negative correlation, respectively) **(B)** Volcano plot showed the differentially expressed lncRNA between the HCC tissues and adjacent normal tissues. (red: upregulated, blue: downregulated, grey: no significant) **(C)** Venn diagram displayed the lncRNAs shared by DCLs and DELs. **(D)** Forest plots presented the results of the univariate cox regression analysis of the 23 prognostic DCDELs. **(E)** Correlation of 23 prognostic DCDELs with 10 DRGs in TCGA-HCC Cohort. The color of each unit showed an indication of the degree of correlation. (Red implied a positive relationship, while blue indicated the opposite.) **(F)** The Sankey diagram demonstrated the roles of DCDELs and DRGs in HCC based on of Pearson's R>0.3and p<0.001. HCC, hepatocellular carcinoma; DRGs, disulfidptosis-related genes; lncRNAs, long noncoding RNAs; DRLs, disulfidptosis-related long non-coding RNAs; DCLs, disulfidptosis co-expressed lncRNAs; DELs, differentially expressed lncRNAs; *p < 0.05, **p < 0.01, and ***p < 0.001.

Table 2. We further integrated the DCLs and DELs, resulting in a set of 494 lncRNAs that were both differentially expressed and correlated, which named "DCDELs" (Figure 2C). Subsequently, we conducted a univariate Cox regression analysis to evaluate the prognostic ability of these DCDELs based on overall survival (OS) data from the TCGA clinical database. This analysis identified 23 prognostic DCDELs (Figure 2D, Supplementary Table 3). The correlation and differential expression between these prognostic DCDELs and DRGs were illustrated in Figure 2E, red indicates a positive correlation, while blue indicates a negative correlation. Furthermore, we generated a Sankey diagram (Figure 2F) to visually represent the roles of DCDELs and DRGs in HCC, providing a clear depiction of their correlation and prognostic significance in the context of patients with HCC.

3.2 Construction and validation of prognostic DRLs signature in HCC

First, we randomly divided 342 patients into training and test cohorts at a 1:1 ratio. Next, we conducted LASSO regression and multivariate Cox regression analyses to construct a prognostic signature based on the expression profiles of the previously identified 23 prognostic DCDELs (Figure 3A). Figure 3B illustrated the lambda curves obtained from LASSO regression analysis. LASSO regression selected nine lncRNAs based on the optimal penalty parameter λ, and multivariate Cox regression analysis further refined these to five lncRNAs, which were ultimately used to build the disulfidptosis-related prognostic signature. Ultimately, we identified five prognostic DRLs using the optimal penalty parameter λ determined through tenfold cross-validation following the minimum criteria. The risk score for each HCC patient was calculated using the following formula: Risk score = (1.583×TMCC1-AS1 expression) + (0.515×FOXD2-AS1 expression) + (0.577×LINC01063 expression) + (-0.698×AC009283.1 expression) + (-0.890×SLC25A30-AS1 expression) (detailed in Supplementary Table 4).

Based on the median risk score, patients were categorized into low- and high-risk groups (Figures 3C-E). To evaluate the feasibility and universality of the prognostic signature, we validated it in the train, test, and all cohorts. All cohorts exhibited a similar distribution in that the mortality rate increased in the high-risk score group, whereas the mortality rate decreased in the low-risk score group (Figures 3F-H). Furthermore, we compared the OS between the high-risk and low-risk groups using the Kaplan-Meier method, and the results revealed that the high-risk group had a significantly shorter OS than the low-risk group ($p < 0.001$) (Figures 3I-K). Principal Component Analysis (PCA) effectively discriminated the two risk subgroups in the train cohort, test cohort, and all cohorts (Figures 3L-N). The signature showed good performance in predicting survival in all cohorts (1, 3, and 5 years: AUC, 0.782, 0.735, and 0.734), in the train cohort (1, 3, and 5 years: AUC, 0.798, 0.761, and 0.713), and in the test cohort (1, 3, and 5 years: AUC, 0.762, 0.709, and 0.712) (Figures 3O-Q). Taken together, these findings demonstrated that this DRLs signature could serve as a reliable independent predictive tool for patients with HCC.

Additionally, when we compared progression-free survival (PFS) between the high- and low-risk groups, we observed that the PFS of the high-risk group was significantly lower than that of the low-risk group (Supplementary Figures 2A, C, E). Moreover, t-distributed Stochastic Neighbor Embedding (t-SNE) analysis revealed significant differences in distributions between the high- and low-risk groups in the overall dataset, test cohort, and train cohort (Supplementary Figures 2B, D, F).

3.3 Correlation between DRLs signature and clinicopathological features in HCC patients

To explore the association between the 5-DRLs signature and disulfidptosis, we compared the expression levels of 10 DRGs between the low-risk and high-risk groups. The results indicated that the majority of DRGs expression exhibited distinct differences with significant p-values (Supplementary Figure 3). We further analyzed the connections in clinicopathological parameters between the two risk groups (Figure 4A). Significant variations were analyzed in factors such as Survival Status ($p<0.001$), gender ($p<0.01$), grade ($p<0.05$), T stage ($p<0.05$), stage ($p<0.01$) and AFP level ($p<0.05$) between the low- and high-risk groups and the differences were shown in Supplementary Figure 4. In addition, the 5-DRLs exhibited different distributions. AC009283.1 and SLC25A30-AS1 had higher expression levels in the low-risk group, while FOXD2-AS1, LINC01063, and TMCC1-AS1 showed the opposite trend. To further validate the performance of the 5-DRLs prognostic signature, we constructed ROC curves to demonstrate its superiority in terms of predictive accuracy compared to other clinicopathological parameters (Figures 4B-D). The results revealed that our risk signature exhibited excellent predictive performance, with AUC values of 0.782, 0.798, and 0.762 for the total, train, and test groups, respectively, which were significantly higher than those of other clinical univariate variables.

In addition, patients with HCC were categorized into different groups based on their age, gender, AFP level, tumor grade, TNM stage, and vascular invasion to verify whether our predictive model could be an effective supplement to the current staging system. For each group, the overall survival of the high-risk patients was remarkably lower than that of the low-risk group (Figures 4E–P). Model validation in different clinical subgroups indicated that the performance and predictive capability of the prognostic signature remained stable and effective under specific clinical conditions. However, if the model excels in a particular clinical subgroup, it may suggest that patients in that subgroup are more suitable for our predictive signature. For instance, our prognostic signature showed superior predictive performance in patients with advanced HCC (stages II-IV) compared to those in the early stage ($p<0.001$ vs. $p=0.015$) (Figures 4K, L), indicating its suitability for advanced HCC patients. In summary, validation of our novel signature in clinical subgroups is a pivotal step, ensuring the reliability of research outcomes and providing profound insights for the practical application of the model in clinical practice.

10.3389/fimmu.2024.1412277

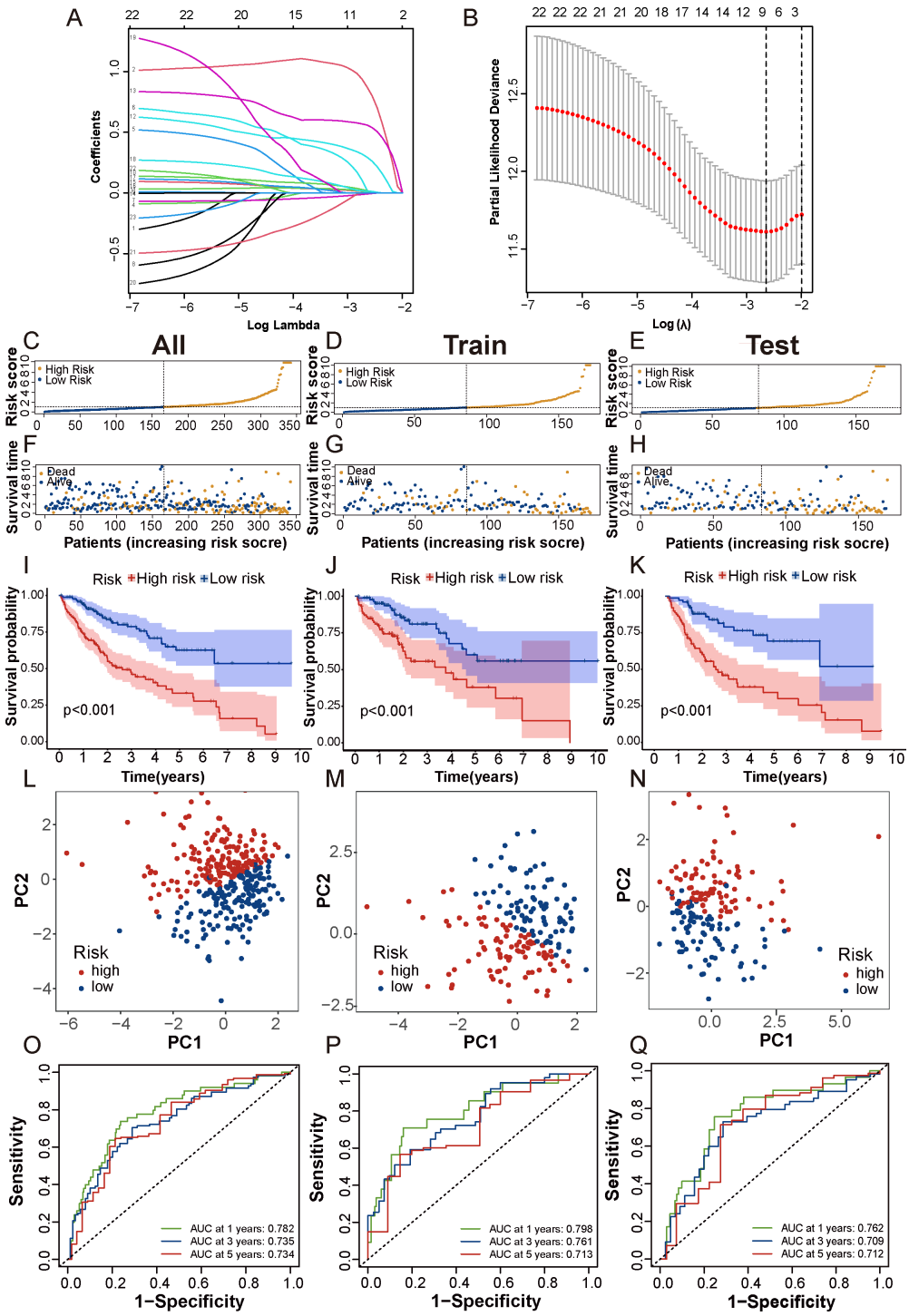

FIGURE 3
Construction and validation of prognostic DRLs signature in HCC. **(A, B)** Cvfit and lambda curves showed LASSO regression, constructed by the 10-fold cross-validation. **(C-E)** The distribution and median risk scores in the overall, train and test cohorts. **(F-H)** The distribution of overall survival status, survival time, and risk score in each cohort. **(I-K)** The Kaplan-Meier curves depicted the survival status and survival time of the overall, train and test cohorts. **(L-N)** PCA analysis showed a significant distinction in each cohort. **(O-Q)** AUC of the time-dependent ROC curves illustrated the ability of the signature consisting of DRLs to predict the 1-, 3- and 5-year OS in each cohort. lncRNAs, long noncoding RNAs; ROC, receiver operating characteristic; AUC, area under the curve; OS, overall survival.

10.3389/fimmu.2024.1412277

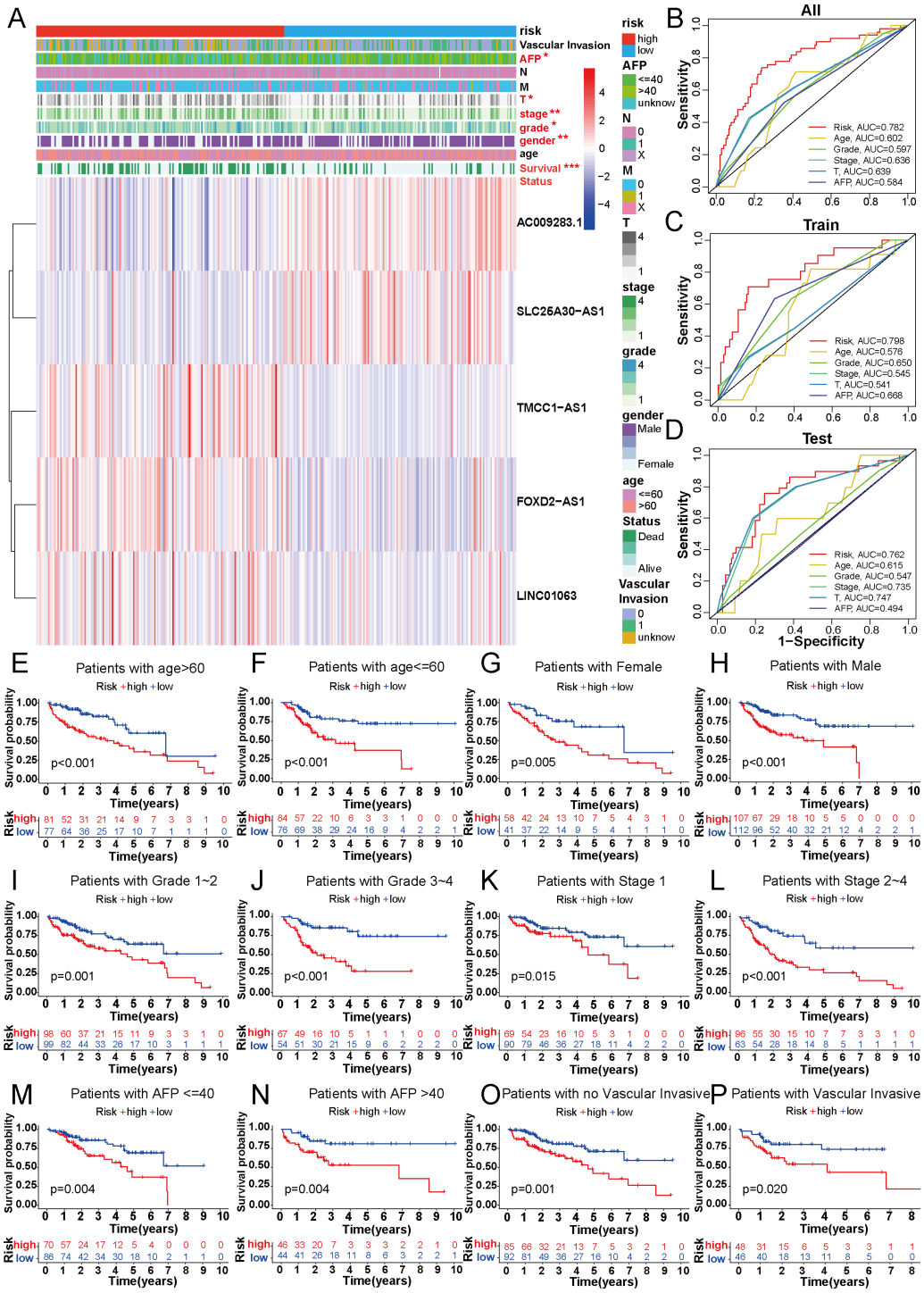

FIGURE 4
Correlation between DRLs signature and clinicopathological features in HCC patients. **(A)** The heatmap showed the distribution of ten specific clinicopathological characteristics and the corresponding risk score for the individual patient based on the predictive signature. Clinicopathological features highlighted in red indicated significant distinction in distribution between the high- and low-risk groups. **(B-D)** The ROC curves were performed to compare the prognostic accuracy of the signature and other prognostic parameters in overall, train and test cohorts. **(E-P)** Kaplan-Meier survival curves based on age, gender, grade classification, TNM stage, AFP and vascular invasive for high-risk and low-risk patient groups. *$p < 0.05$, **$p < 0.01$ and ***$p < 0.001$.

3.4 The predictive value evaluation of the 5-DRLs signature, and the construction and validation of the predictive nomogram

Univariate and multivariate Cox regression analyses were used to explore whether the risk score calculated by the predictive signature could be an independent prognostic indicator for predicting the outcomes of HCC patients. Univariate Cox regression analysis showed that the risk score (hazard ratio [HR] = 1.349, 95%CI = 1.215-1.496, $p < 0.001$) was a prominent predictor of patients' prognosis. In addition, gender, grade, stage, T stage, and M stage were all related to prognosis by univariate Cox regression analysis (Figure 5A). However, in the multivariate Cox regression analysis, only grade (HR=2.117, 95%CI=1.216-3.686, $p< 0.008$) and risk score (HR=1.277, 95%CI=1.142-1.148, $p< 0.001$) were significant predictors of patients' prognosis (Figure 5B). The C-index was used to evaluate the discrimination ability of our predictive model. The risk score calculated by our signature exhibited a higher C-index than other clinical variables, underscoring the superiority of our signature (Figure 5C). Additionally, decision curve analysis (DCA) was employed to validate the performance of the prognostic signature. The positive

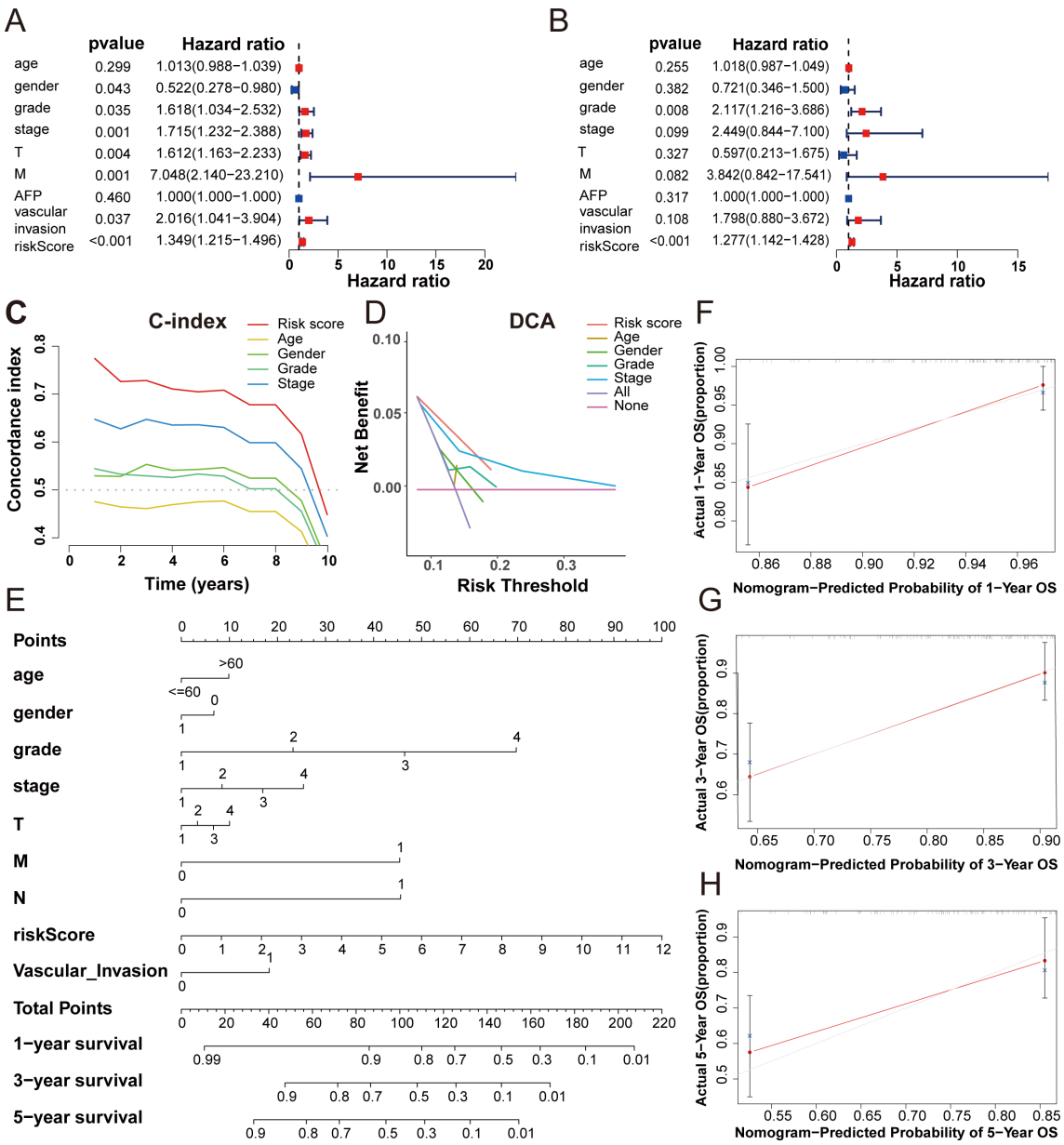

FIGURE 5
The predictive value evaluation of the 5-DRLs signature, and the construction and validation of the predictive nomogram. **(A, B)** The univariate cox and the multivariate cox regression analysis between risk score and other clinicopathological variables in HCC patients. **(C)** The concordance index of five indicators for OS in patients with HCC. **(D)** Decision-curve analysis for five indicators for OS in patients with HCC. **(E)** A nomogram combined risk score with other clinicopathologic variables (age, gender, grade, pathological tumor stage, T stage, M stage and N stage and vascular invasion) to predict overall survival time in HCC patients. **(F-H)** Nomogram-predicted probability of 1, 3, 5-year OS.

clinical net benefit interval of the risk scores surpassed others in the risk threshold range of 0.1-0.2, which also indicated the superior performance of our five DRLs signature (Figure 5D).

A nomogram, a common tool to estimate the personal prognosis of tumors, was able to create an individual numerical probability of a clinical event by calculating many prognostic and crucial factors (31). To simplify our model into an easy numerical estimate of the probability of 1-, 3-, and 5-year OS of HCC, a nomogram based on age, gender, grade, stage, T stage, M stage, N stage, vascular invasion, and risk score was established (Figure 5E) (25). The 1-, 3-, and 5-year calibration curves revealed that the predictive outcome was close to the actual OS rate, suggesting a notable predictive value of our signature (Figures 5F-H).

3.5 5-DRLs prognostic signature for immune microenvironment and immunotherapy response discrimination in HCC

Besides the crucial roles of gene mutations and epigenetic alterations in cancer, further investigations have found that the tumor immune microenvironment (TME) play an increasingly pivotal role in tumor physiology (32). The different characteristics of tumors were determined by distinctive stromal cell types and various sub-cell types (33). To explore the correlation between the 5-DRLs signature and TME, the CIBERSORT algorithm, which can estimate the abundance of immune cell types, was used (34). It could be found in the heatmap that various immune cells were significantly distinguished between the low-risk group and the high-risk group (Figure 6A). Specifically, M0 macrophages ($p < 0.05$), M2 macrophages ($p < 0.001$), and neutrophils ($p < 0.01$) were more abundant in the high-risk group, whereas CD8+ T cells ($p < 0.01$), activated mast cells ($p < 0.01$), and monocytes ($p < 0.05$) were more percentage in the low-risk group (Figure 6D). Spearman's correlation test was used to determine the relationship between the immune score and risk score (R=0.05, p=0.36) and between the stromal score and risk score (R=0.037, p=0.49). However, neither had an apparent relationship (Figures 6B, C).

The expression levels of CD200R1, CD200, TNFSF4, CD80, VTCN1, CD276, LGALS9, HHLA2, TNFRSF18, CD86, HAVCR2, TNFSF15, and LAIR1 were all significantly higher in the high-risk group, with the exception of ADORA2A (Figure 6E). Remarkably, the expression of CD276 was considerably higher in the high-risk group than in the low-risk group ($p < 0.001$). Simultaneously, immunophenoscore (IPS), a score based on immunogenicity to predict immunotherapy potential, was used to assess the potential effects of two common immune treatment targets, CTLA-4 and PD-1 (35). As shown in the violin plot, IPS, IPS-CTLA4, IPS-PD1, and IPS-PD1+CTLA4+ were all significantly higher in the low-risk group than in the high-risk group. ($P< 0.01$) (Figures 6F-I). Therefore, the 5-DRLs signature established in this study has potential immunotherapy predictive value for clinical HCC treatment.

3.6 Correlation between 5-DRLs signature and TMB, and predictive analysis of drug sensitivity

Tumor mutation burden (TMB), which is based on the generation of immunogenic neoantigens from tumor gene mutations, had been regarded as a predictive biomarker for the response to immune checkpoint blockade (ICB) (36). Therefore, we analyzed the correlation between the 5-DRLs signature and TMB and found that their mutative frequencies were similar (high-risk group, 83.04%; low-risk group, 80.25%). Specifically, TP53 (39%), TTN (25%), CTNNB1(18%), MUC16(13%), and PCLO (13%) were the five most frequently mutated genes in the high-risk group, whereas CTNNB1(33%), TTN (20%), MUC16 (19%), TP53 (14%), and ALB (12%) were the top five genes in the low-risk group (Figures 7A, B). Meanwhile, we explored the OS rates between the high-TMB and low-TMB groups and further explored them by considering different risk scores separately. As depicted in Figures 7C, D, the high-TMB group had a relatively more unfavorable outcome (P<0.025) (Figure 7C). In addition, the low-TMB plus low-risk group was the most favorable one among the four groups (P<0.001) (Figure 7D).

To predict the potential for medical treatment and achieve precise individualized oncology therapy, drug-sensitivity analysis based on the different risk groups was performed. The IC50 values of Elesclomol, Docetaxel and Vinblastine were lower in the low-risk group than in the high-risk group, which indicated that they were probably more sensitive to low-risk HCC patients (Figures 7E-G). Conversely, the IC50 values for Sunitinib, Gemcitabine and Paclitaxel were higher in the low-risk group, suggesting a higher likelihood of obtaining better responses in the high-risk group (Figures 7H-J).

3.7 Pathway and functional enrichment analyses of DEGs

To elucidate the potentially different mechanisms in the high- and low-risk groups, we selected differentially expressed genes (DEGs). KEGG pathway enrichment and GO functional annotation analyses were conducted based on the DEGs between the low- and high-risk groups. In KEGG pathway enrichment, many signaling pathways were significantly enriched, and the top 20 involved pathways, including pathways in cancer, cellular senescence, PPAR signaling pathway, and ECM-receptor interaction pathway, were depicted (Figure 8A). The top 100 pathways in the KEGG analysis of the DEGs were shown in Supplementary Table 5. The top 20 pathways enriched by GO functional annotation analysis of DEGs were shown in Figure 8B, which show that pathways such as extracellular matrix organization, nucleus, and identical protein binding were enriched. The top 100 pathways in the GO analysis of the DEGs were shown in Supplementary Table 6.

10.3389/fimmu.2024.1412277

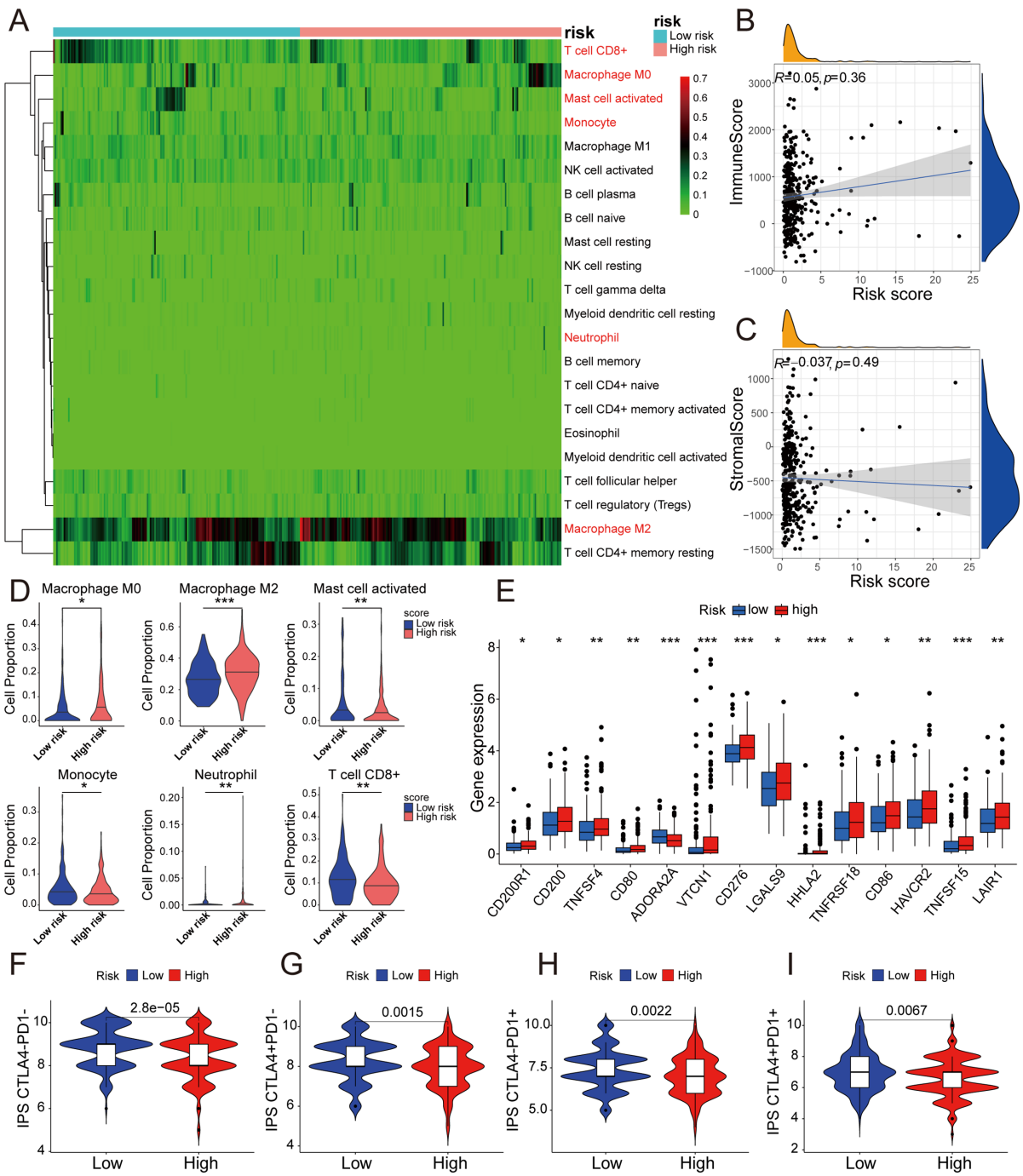

FIGURE 6
5-DRLs prognostic signature for immune microenvironment and immunotherapy response discrimination in HCC. **(A)** Relative proportion of 22 different immune cells based on CIBERSORT in the low-risk group and the high-risk group. Immune cells in red indicated that there was a significant difference between two groups. **(B)** The relationship between the risk score and immune Score. **(C)** The relationship between the risk score and Stromal Score. **(D)** The proportion of M0 macrophages, M2 macrophages, activated mast cell, monocyte, neutrophil, and CD8+ T cell in the low-risk group and the high-risk group. **(E)** Differential expressions of immune checkpoint genes between high- and low-risk groups. **(F-I)** Immunophenoscore predicts response to immunotherapy with CTLA-4 and PD-1 blockers. *$p < 0.05$, **$p < 0.01$, and ***$p < 0.001$.

Furthermore, GSEA was performed to reveal potential biological processes and mechanistic pathways between the different risk groups. The top 100 pathways in the GSEA-KEGG and GSEA-GO analyses between the high- and low-risk groups were shown in Supplementary Table 7. Surprisingly, it was revealed that the regulation of the actin cytoskelet.

on and microtubule motor activity were enriched in the high-risk group (Figures 8C, D). Previous studies had demonstrated that actin, microtubules, and intermediate filaments were integral components of the cytoskeleton. The formation of disulfide bonds in actin cytoskeleton proteins that led to F-actin collapse and generation of forces within cells, ultimately inducing disulfidptosis

10.3389/fimmu.2024.1412277

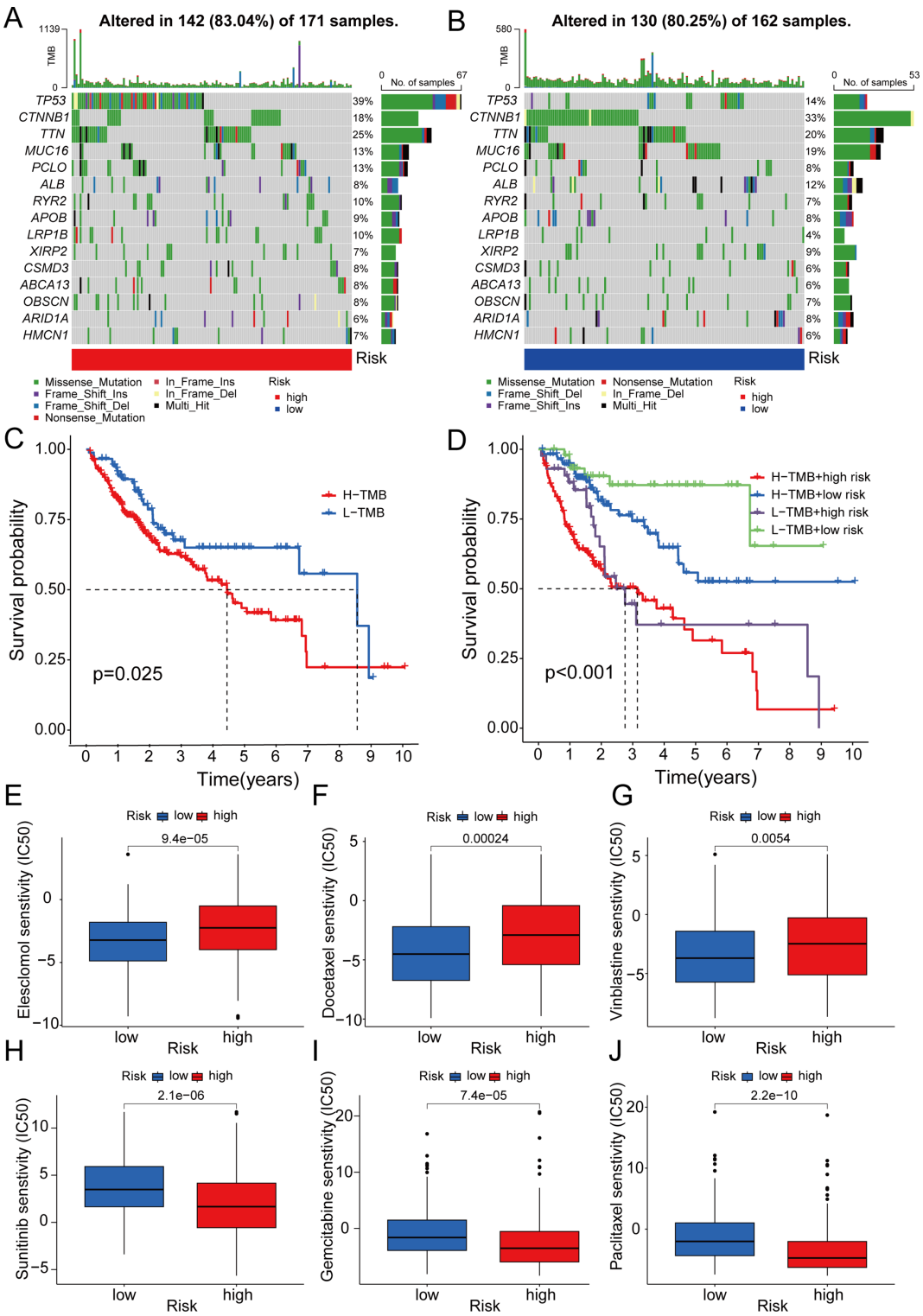

FIGURE 7
Correlation between 5-DRLs signature and TMB and drug sensitivity analysis. **(A, B)** Waterfall plot of the TMB in the high- and low-groups revealed the top 15 most frequent mutation genes. **(C)** The Kaplan–Meier curve for survival status and survival time in the high-and low-TMB groups. **(D)** The Kaplan–Meier curve for survival status and survival time in the high-TMB + high-risk, low-TMB + high-risk, high-TMB + low-risk and low-TMB + low-risk groups. **(E-J)** IC50 of elesclomol, docetaxel, vinblastine, sunitinib, gemcitabine and, paclitaxel between the two risk groups. TMB, tumor mutational burden; IC50, half-maximal inhibitory concentration.

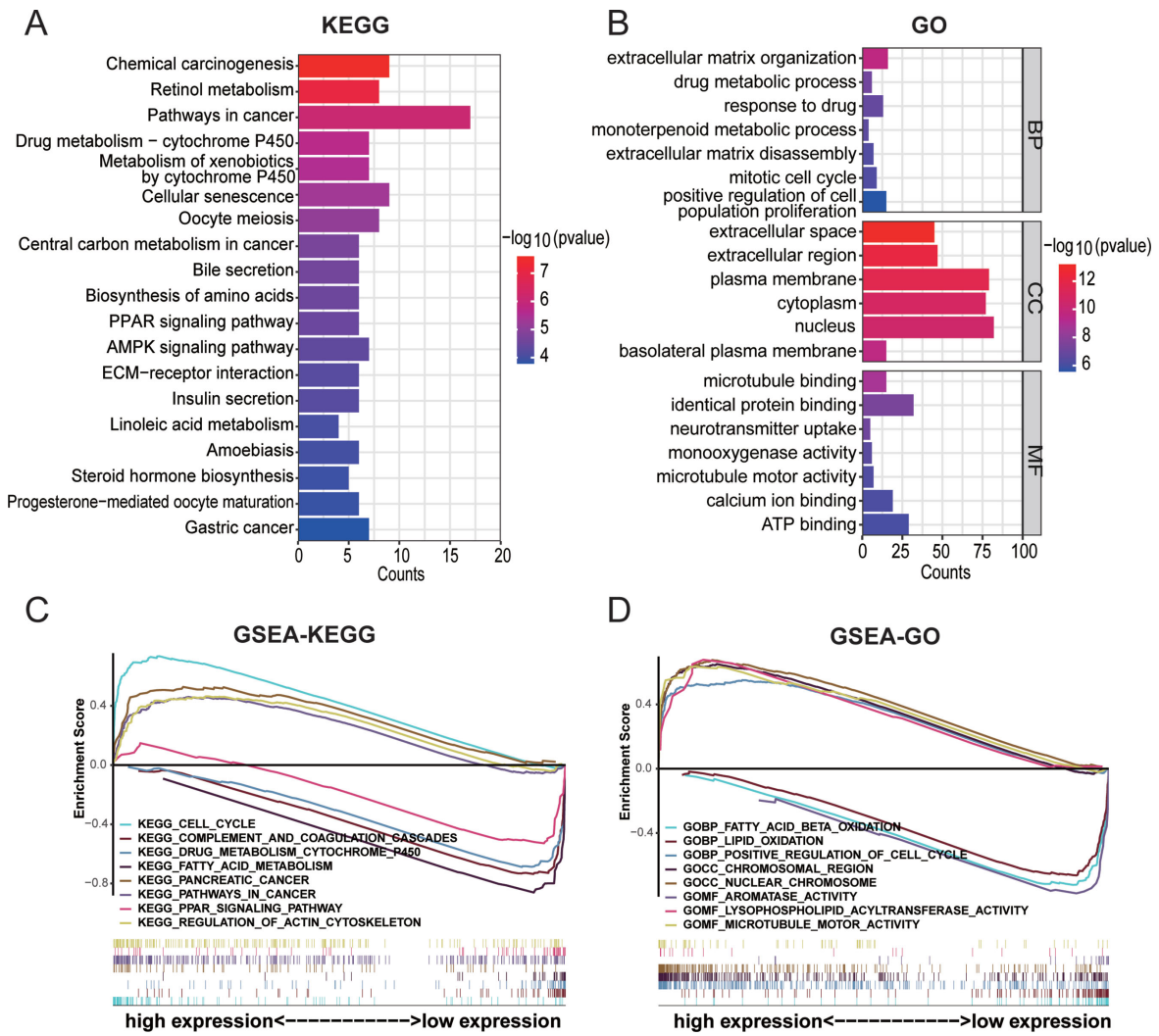

FIGURE 8
Pathway and functional enrichment analyses of DEGs between high- and low- risk group. **(A)** KEGG pathway enrichment of DEGs between high- and low- risk group. **(B)** GO functional annotation analysis of DEGs between high- and low- risk group. **(C, D)** Gene set enrichment analysis between high- and low- risk group.

(17, 37). Hence, it could be inferred that the 5-DRLs signature is closely associated with disulfidptosis.

3.8 Verification of 5 DRLs expressions in HCC cell lines and tissues

According to the data presented in Figure 9A, there were significantly higher expression levels of the five DRLs in HCC tissues than in normal tissues from TCGA database. To further verify this finding, we conducted experiments using a normal liver cell line MIHA and four distinct liver cancer cell lines: HA22T, JHH-7, HCCLM3, and HepG2. Subsequently, we extracted RNA from each cell line and used RT-qPCR to confirm the expression levels of these lncRNAs. The results demonstrated that the five DRLs exhibited higher expression levels in HCC cells than in normal liver cells (Figures 9B-F). For further corroboration, we collected 16 pairs of HCC tissues and adjacent normal tissues from patients with HCC who had undergone surgical resection. Similar results were observed in these clinical samples, indicating higher expression levels of the aforementioned lncRNAs in HCC tissues, except SLC25A30-AS1 (Figures 9G-K).

3.9 Validation of disulfidptosis phenotype in HCC cell lines

To verify the phenomenon of disulfidptosis could be repeated in HCC, we induced disulfidoptosis in selected HCC cell lines through glucose deprivation. Initially, we compared the expression levels of SLC7A11 gene among different liver cell lines and HCC cell lines in mRNA level and protein level. The result revealed that all of HCC cell lines exhibited higher expression levels than the normal liver cell line MIHA. Among the HCC cell lines, HepG2 and HCCLM3 displayed significantly elevated expression, whereas HA22T and JHH-7 had relatively lower levels (Figures 10A, B). Subsequently,

10.3389/fimmu.2024.1412277

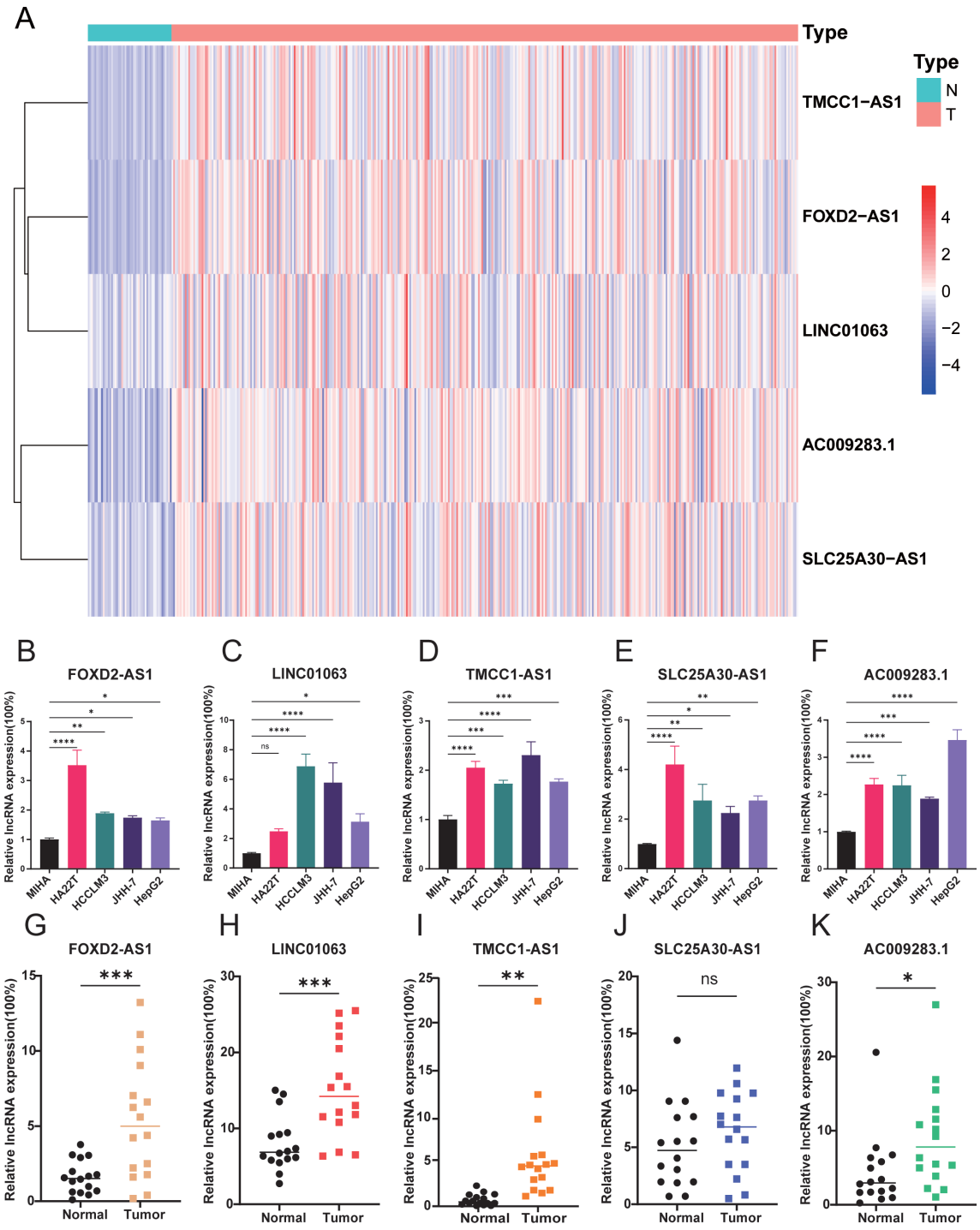

FIGURE 9
Verification of 5 DRLs expressions in HCC cell lines and tissues. **(A)** The heatmap of the expression of 5 DRLs in HCC tissues and adjacent tissues from TCGA database. **(B-F)** 5 lncRNAs' (FOXD2-AS1, LINC01063, TMCC1-AS1, SLC25A30-AS1, AC009283.1) expression levels in liver cell lines and different HCC cell lines including MIHA, HA22T, HCCLM3, JHH-7, HepG2 (n=3) (One-way ANOVA). **(G-K)** 5 lncRNAs' expression levels in HCC tissues and adjacent normal tissues (T-test). *p < 0.05, **p < 0.01, ***p < 0.001 and ****p<0.0001. ns, no significance.

we selected HepG2, characterized by high SLC7A11 expression level, and JHH-7, characterized by low SLC7A11 expression level, to validate the disulfidoptosis phenotype in HCC. The cell viability curve indicated that HepG2 was more sensitive to disulfidoptosis (Figure 10C). Besides, after exposing both cell lines in glucose deprivation for 12 hours, we fixed those cells in 4% formaldehyde and stained them with phalloidin. HepG2 cells exhibited substantially morphological changes, including intensified cytoskeletal staining. Compared with normal cells, treated cells displayed contraction, actin filament accumulation and reduced cell volume (Figure 10D). Relatively lesser changes were observed in JHH-7 cells (Figure 10E).

10.3389/fimmu.2024.1412277

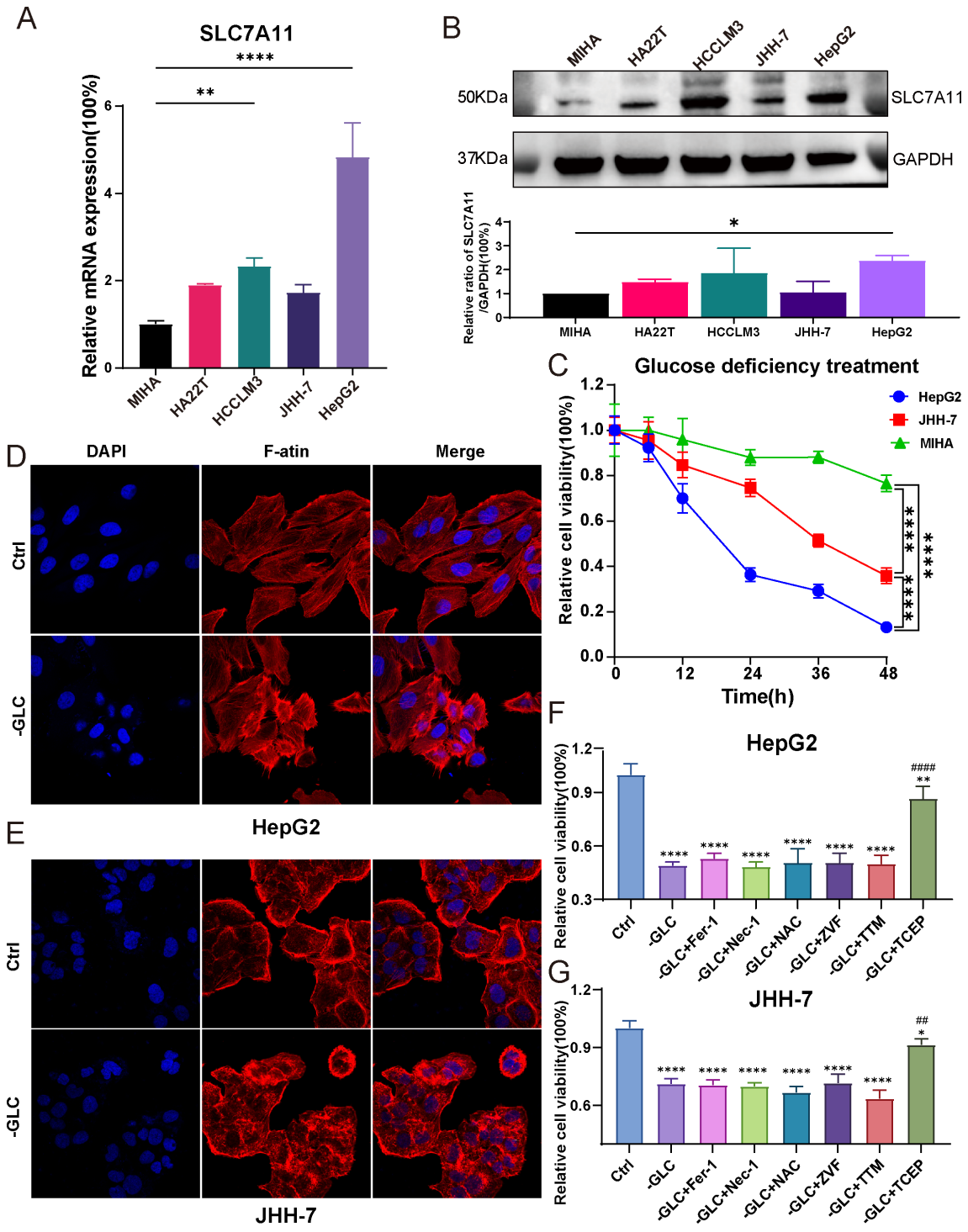

FIGURE 10
Validation of disulfidptosis phenotype between HCC cell lines. **(A)** The expression levels of SLC7A11 gene in 5 cell lines (n=3) (One-way ANOVA). **(B)**The Western blot bands of SLC7A11 and GAPDH protein in 5 cell lines (n=3) (One-way ANOVA). **(C)** Cell viability curve of HepG2 and JHH-7 about 6, 12, 18 and 24 h after glucose starvation treatment, respectively (Two-way ANOVA). **(D, E)** F-actin staining by phalloidin of HepG2 and JHH-7. **(F, G)** The rescue effect of cell death inhibitors in HepG2 and JHH-7 undergoing disulfidptosis for 12 hours was explored through CCK8 assay (One-way ANOVA). ZVF, Z-VAD-FMK; Fer-1, ferrostatin-1; Nec-1, necrostatin-1; NAC, N-acetyl cysteine; TTM, Tetra thiomolybdate; TCEP, Tris(2-carboxyethyl) phosphine. * $p < 0.05$, ** $p < 0.01$, and **** $p < 0.0001$. ##p<0.01, ####p<0.0001. (*means compared with group Ctrl; #means compared with group -GLC).

We also explored the expression of ten disulfidptosis-related genes in the TCGA database and in 16 HCC patients. As shown in Supplementary Figures 5 and 6, we presented the expression of these ten genes in TCGA and HCC patients, respectively. It was observed that most of the disulfidptosis-related genes were more highly expressed in HCC tissues compared to normal tissues. This indicates that these genes could potentially be targeted to induce disulfidptosis and serve as treatment targets for HCC in future.

To further confirm that cell death induced by glucose deficiency was not caused by other forms of cell death, we introduced various cell death inhibitors, such as Ferrostatin-1 (Fer-1, a ferroptosis inhibitor), Necrostatin-1 (Nec-1, a necroptosis inhibitor), Z-VAD-FMK (ZVF, an apoptosis inhibitor), N-acetyl cysteine (NAC, an antioxidant), Tetra thiomolybdate (TTM, a cuproptosis inhibitor) to the treatment groups during the 12-hour glucose starvation and detected the cell viability. However, these inhibitors did not alleviate cells death. Surprisingly, the addition of Tris(2-carboxyethyl) phosphine (TCEP), a non-thiol reducing agent, resulted in a remarkable rescue in cell death (Figures 10F, G). In summary, our study conclusively showed that glucose deprivation could trigger disulfidptosis in HCC. The extent of this novel cell death was directly correlated with the expression level of the SLC7A11 gene. Besides, this cellular damage resulting from sulfide accumulation could be mitigated by TCEP.

3.10 Disulfidptosis regulated by LINC01063 and FOXD2-AS1

According to the disulfidptosis-related lncRNA signature, five lncRNAs (AC009283.1, SLC25A30-AS1, FOXD2-AS1, LINC01063, and TMCC1-AS1) were identified as central components within this network, suggesting their potential significance in the disulfidptosis of HCC.

We selected two lncRNAs, FOXD2-AS1 and LINC01063, for further investigation. Initially, we designed silencing RNAs to knock down the expression of FOXD2-AS1 and LINC01063 in the HepG2 cell line. The knockdown efficiency was confirmed via RT-qPCR, revealing that LIN010613 siRNA1 and FOXD2-AS1 siRNA2 achieved greater than 70% knockdown efficiency (Figures 11A, D). Subsequent cell viability assays demonstrated that the depletion of FOXD2-AS1 and LINC01063 sensitized HCC cells to disulfidptosis (Figures 11B, E). After 24 hours of glucose starvation, cells with LINC01063 and FOXD2-AS1 knockdown showed significantly lower viability compared to the control group. Additionally, fluorescence microscopy with F-actin staining further demonstrated that, after 12 hours of glucose starvation, cells with LINC01063 and FOXD2-AS1 knockdowns displayed more markedly abnormal cell morphology (Figures 11C, F). Specifically, these HepG2 cells exhibited substantial morphological changes, including intensified cytoskeletal staining, pronounced cytoskeletal shrinkage, actin filament accumulation, and reduced cell volume (Figures 11G, H).

These findings corroborate our bioinformatics analysis, which indicated that the lncRNAs within the prognostic signature play a regulatory role in disulfidptosis. Specifically, the downregulation of lncRNAs such as LINC01063 and FOXD2-AS1 enhances the sensitivity of HCC cells to disulfidptosis. The precise regulatory mechanisms underlying this effect warrant further investigation.

4 Discussion

HCC is the sixth most common cancer worldwide and is known for its high mortality rate and aggressiveness (38). Therefore, understanding the pathogenesis of HCC and exploring new diagnostic and prognostic markers are crucial. Meanwhile, disulfidptosis has provided a new theoretical foundation for the development of innovative antitumor treatments (17). In this study, we conducted a comprehensive analysis of the transcriptional expression of 10 disulfidptosis-related genes (DRGs) in HCC patients based on the TCGA database. Subsequently, we identified the co-expressed lncRNAs associated with these DRGs and developed a novel scoring system based on five co-expressed prognostic-related lncRNAs (FOXD2-AS1, SLC25A30-AS1, TMCC1-AS1, LINC01063, and AC009283.1). ROC, C-index, and DCA analyses revealed that the risk signature had high accuracy and excellent sensitivity. Moreover, univariate and multivariate Cox analyses confirmed it to be an independent prognostic factor for patients according to univariate and multivariate Cox analyses. In addition, we created a nomogram by combining the risk score with other clinicopathological features. This nomogram provided an intuitive and quick individualized risk assessment for patients with HCC. We established a signature of lncRNAs associated with disulfidptosis, providing a potential strategy for guiding individualized treatment and contributing to the prediction of prognosis and immune response in HCC patients. Finally, we validated the relative expression of the five lncRNAs in both cell lines and HCC tissues and verified the disulfidptosis phenotype of HCC under glucose deprivation.

The five DRLs, components of our signature, were identified as potentially associated with HCC and disulfidptosis in the existing literature. We discovered that these lncRNAs had been previously studied in various types of cancers. For instance, Miranda's research indicated that lncRNA AC009283.1 may be causally related to carcinogenesis. It has been suggested that AC009283.1, contributes to the malignant phenotype of the HER2-rich subtype of breast cancer, leading to an upregulation of tumor cell proliferation capacity and resistance to apoptosis (39). However, in our risk signature, AC009283.1 exhibited higher expression levels in the lower-risk group (Figure 4A). The heterogeneity of tumors may be responsible for this inconsistency. For LINC01063, Xu's al. reported that it acted as an oncogene in melanoma by functioning as a sponge for miR-5194, leading to increased cancer cell proliferation, migration, invasion, and epithelial-mesenchymal transition (40). TMCC1-AS1 has also been implicated as a tumor promoter; its suppression led to increased E-cadherin expression and decreased proliferating cell nuclear antigen Ki67 expression in HCC cells (41). Mechanistic insights into FOXD2-AS1 have been extensively explored in gastric cancer, colorectal cancer, breast cancer, and other malignancies, primarily focusing on its cancer-promoting properties. For example, Xu et al. revealed that the knockdown of FOXD2-AS1 reduced transmembrane protein 9

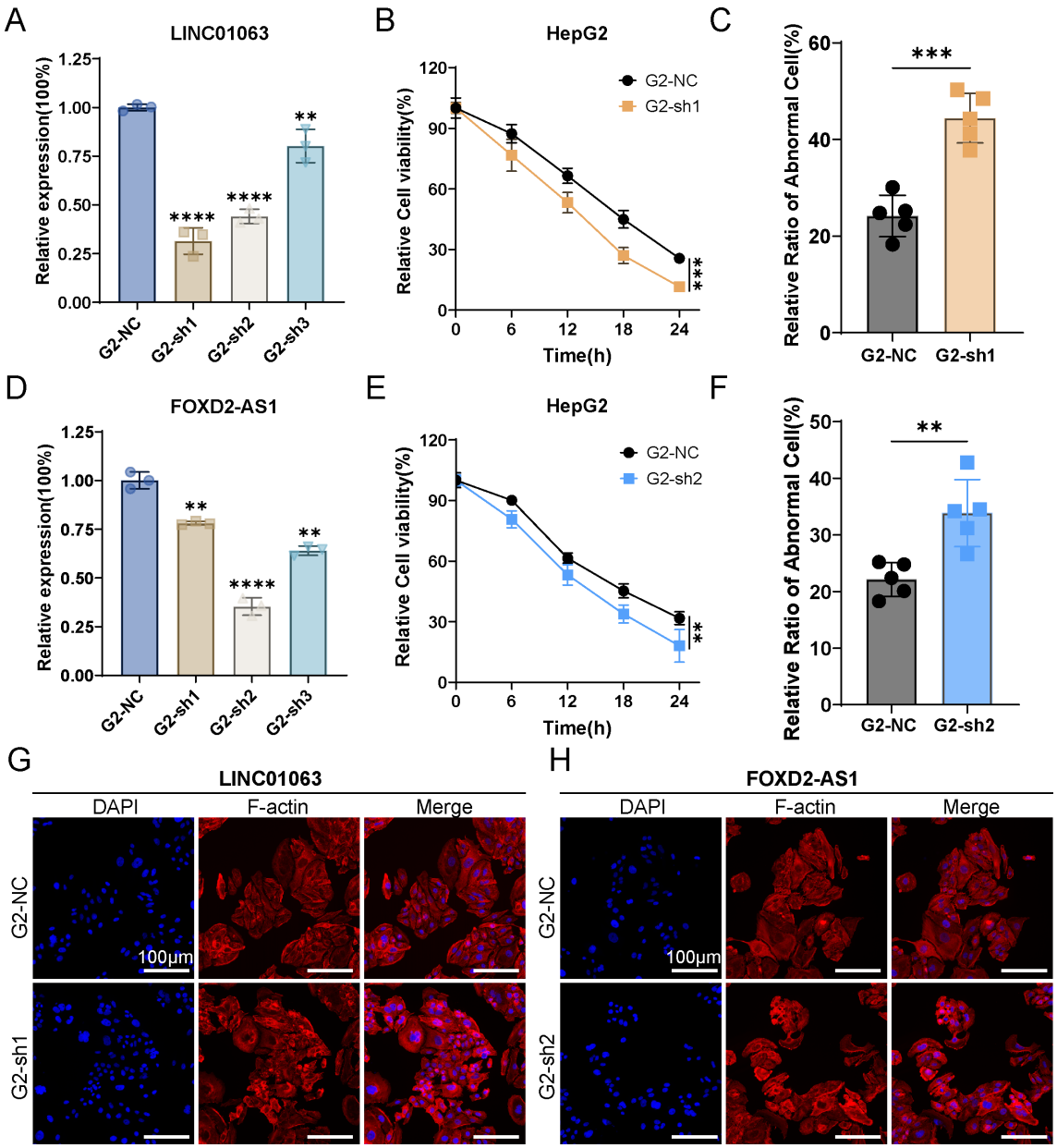

FIGURE 11
LINC01063 and FOXD2-AS knockdown increases susceptibility to disulfidptosis in HepG2 cells. **(A, D)** The expression levels of LINC01063 and FOXD2-AS lncRNAs in HepG2 cells, with or without siRNA treatment, are shown (n=3) (One-way ANOVA). **(B, E)** HepG2 cells with or without LINC01063 and FOXD2-AS knockdown were subjected to glucose starvation for 0, 6, 12, 18, and 24 hours, followed by assessment using the CCK8 reagent (Two-way ANOVA). **(C, F)** The proportion of abnormal cells in different groups was quantified using F-actin staining images obtained with a fluorescence microscope (T-test). **(G, H)** Representative fluorescence images of F-actin staining after 12 hours of glucose starvation are shown for HepG2 cells with or without LINC01063 and FOXD2-AS knockdown. $^{**}p < 0.01$, $^{***}p < 0.001$ and $^{****}p < 0.0001$.

(TMEM9) expression and increased the sensitivity of HCC cells to sorafenib (42). In addition, SLC25A30-AS1 showed a lower expression level in the high-risk group of our risk signature, which correlated with poor prognosis (Figure 4A). Hence, further experiments are required to elucidate how SLC25A30-AS1 regulates the malignant behavior of HCC.

TMB, associated with neoantigens present on the surface of cancerous cells, complements conventional biomarkers for predicting the effectiveness of ICB (43). Previous studies have reported that patients with high TMB tend to have poorer survival and better response to ICB (44). In this study, there was a significant disparity in TP53 and CTNNB1 gene mutations between the two groups: the high-risk group exhibited a higher frequency of TP53 gene mutations, whereas the low-risk group showed an elevated frequency of CTNNB1 gene mutations. CTNNB1-mutated HCC has been proven to be a homogeneous subtype of non-proliferative tumors with well-differentiated characteristics such as an intact tumor capsule, cholestasis, microtrabecular, and pseudoglandular architectural patterns (45, 46). Conversely, TP53-mutated tumors were poorly differentiated, with a compact pattern, multinucleated

and pleomorphic cells, and vascular invasion (46). Additionally, previous studies have shown that TP53 could inhibit the expression of SLC7A11 (a key component of the cystine/glutamate antiporter), reducing the uptake of cystine and synthesis of cysteine-dependent glutathione (GSH), destroying cellular antioxidant defenses, ultimately accelerating ROS accumulation, and inducing ferroptosis (15, 47). However, high expression of SLC7A11 combined with glucose starvation could result in disulfidptosis (47, 48). Therefore, the cellular and molecular mechanism of how TP53 regulated the disulfidptosis and the balance between disulfidptosis and ferroptosis require further exploration.

Tumor cells under continuous evolution driven by constant selection and mutual interaction within the entire cellular ecosystem, ultimately giving rise to adaptive cellular phenotypes within the tumor microenvironment (TME) (49, 50). In our study, M2 macrophages were highly recruited to the high-risk group. Macrophages, which are versatile and heterogeneous innate immune cells, possessed plasticity that allows them to interact with a wide range of cell type including tumor cells, T lymphocytes, endothelial cells (ECs), and fibroblasts. This interaction can subsequently promote tumor tolerance and progression (51). Recent research has revealed a correlation between an unfavorable prognosis and M0 macrophages in HCC (52). In addition, there were two distinct types of polarized macrophages. Type 1-polarized macrophages (M1), identified by the expression of CD80, CD86, MHC II, iNOS, and CD68, were phagocytic and could impede tumor progression. In contrast, type 2-polarized macrophages (M2), induced under the influence of IL-4, IL-13, IL-10, and M-CSF, were immunosuppressive cells characterized by the expression of CD206, CD204, VEGF, CD163, and Arg-1. These actions can suppress the anti-cancer immune response (32, 53). Therefore, the high-risk group with higher recruitment of M2 macrophages in our study may have a relatively worse anticancer immune response, highlighting the predictive value of the prognostic signature in the TME.

In recent years, immune checkpoint inhibitors have been vigorously developed for cancer therapy. Atezolizumab plus Bevacizumab and Tremelimumab plus Durvalumab have been widely approved as standard-of-care first-line therapies for HCC (54). Tremelimumab, an anti-CTLA-4 antibody, inhibit the interaction between CTLA-4 and B7-1 (CD80) and CTLA-4 and B7-2 (CD86), reactivating T lymphocytes (55). As illustrated in Figure 6E, the gene expression of CD80 and CD86 was higher in the high-risk group, suggesting that Tremelimumab may be more effective in this group. In addition, the expression of CD276 (B7-H3) was significantly higher in the high-risk group. CD276, which is selectively expressed in tumor and immune cells, was associated with tumor cell proliferation, metastasis, and therapeutic resistance (56). Therefore, our 5-DRLs signature may have the potential to predict the expression of immune checkpoint genes and related immunotherapeutic responses.

However, this study remained several limitations. Firstly, our analysis relied on retrospective patient information available from public datasets. No external database was available to validate the reliability of the signature in terms of lncRNA expression and clinical prognostic data. Additional verification using prospective multicenter real-world data is required for this risk signature. Secondly, we only verified the differential expression of five lncRNAs in HCC compared to normal subjects using a small sample size. Thirdly, we only confirmed that disulfidptosis could be induced in HCC, without further investigation into the mechanisms and applications of this signature. Therefore, further studies are needed to thoroughly elucidate the function of disulfidptosis-related lncRNAs in HCC in future research.

5 Conclusion

In summary, we developed a novel 5-DRLs signature with excellent specificity and sensitivity, serving as a reliable prognostic indicator for patients with HCC. The nomogram, which includes age, clinical TNM staging, and risk scores, provides a straightforward tool for predicting the survival period of patients with HCC. Additionally, our signature has the potential to predict the effectiveness of immunotherapy and targeted therapies. We believe that our signature can build a bridge between HCC and disulfidptosis, ultimately serving as a clinically applicable diagnostic and therapeutic tool.

Data availability statement

The original contributions presented in the study are included in the article/Supplementary Material. Further inquiries can be directed to the corresponding authors.

Ethics statement

The studies involving humans were approved by Sir Run Run Shaw Hospital (SRRSH), School of Medicine, Zhejiang University, Hangzhou, China. The studies were conducted in accordance with the local legislation and institutional requirements. The participants provided their written informed consent to participate in this study.

Author contributions

HZ: Data curation, Formal analysis, Investigation, Methodology, Software, Visualization, Writing – original draft. JC: Data curation, Formal analysis, Investigation, Methodology, Software, Writing – original draft. ZZ: Data curation, Formal analysis, Investigation, Methodology, Resources, Software, Visualization, Writing – original draft. DL: Formal analysis, Investigation, Methodology, Software, Supervision, Visualization, Writing – review & editing. JY: Formal analysis, Investigation, Methodology, Project administration, Resources, Writing – review & editing. FY: Data curation, Formal analysis, Investigation, Methodology, Writing – original draft. XF: Conceptualization, Funding acquisition, Supervision, Validation, Visualization, Writing – review & editing. XL: Conceptualization, Investigation, Methodology, Supervision, Validation, Writing – original draft, Writing – review & editing, Software.

Funding

The author(s) declare financial support was received for the research, authorship, and/or publication of this article. This work was supported by the National Natural Science Foundation of China (82102105) and Natural Science Foundation of Zhejiang Province (LQ22H160017).

Conflict of interest

The authors declare that the research was conducted in the absence of any commercial or financial relationships that could be construed as a potential conflict of interest.

Publisher's note

Supplementary material

The Supplementary Material for this article can be found online at: https://www.frontiersin.org/articles/10.3389/fimmu.2024.1412277/full#supplementary-material

References

1. Llovet JM, Kelley RK, Villanueva A, Singal AG, Pikarsky E, Roayaie S, et al. Hepatocellular carcinoma. *Nat Rev Dis Primers*. (2021) 7:7.

2. Bray F, Laversanne M, Sung H, Ferlay J, Siegel RL, Soerjomataram I, et al. Global cancer statistics 2022: GLOBOCAN estimates of incidence and mortality worldwide for 36 cancers in 185 countries. *CA: Cancer J For Clin*. (2024) 74:229–63. doi: 10.3322/caac.21834

3. Rumgay H, Arnold M, Ferlay J, Lesi O, Cabasag CJ, Vignat J, et al. Global burden of primary liver cancer in 2020 and predictions to 2040. *J Hepatol*. (2022) 77:1598–606. doi: 10.1016/j.jhep.2022.08.021

4. Yang C, Zhang H, Zhang L, Zhu AX, Bernards R, Qin W, et al. Evolving therapeutic landscape of advanced hepatocellular carcinoma. *Nat Rev Gastroenterol Hepatol*. (2023) 20:203–22. doi: 10.1038/s41575-022-00704-9

5. Llovet JM, Pinyol R, Kelley RK, El-Khoueiry A, Reeves HL, Wang XW, et al. Molecular pathogenesis and systemic therapies for hepatocellular carcinoma. *Nat Cancer*. (2022) 3:386–401. doi: 10.1038/s43018-022-00357-2

6. Ke B, Tian M, Li J, Liu B, He G. Targeting programmed cell death using small-molecule compounds to improve potential cancer therapy. *Med Res Rev*. (2016) 36:983–1035. doi: 10.1002/med.2016.36.issue-6

7. Peng F, Liao M, Qin R, Zhu S, Peng C, Fu L, et al. Regulated cell death (RCD) in cancer: key pathways and targeted therapies. *Signal Transduct Target Ther*. (2022) 7:286. doi: 10.1038/s41392-022-01110-y

8. Wong RS. Apoptosis in cancer: from pathogenesis to treatment. *J Exp Clin Cancer Res*. (2011) 30:87. doi: 10.1186/1756-9966-30-87

9. Diepstraten ST, Anderson MA, Czabotar PE, Lessene G, Strasser A, Kelly GL. The manipulation of apoptosis for cancer therapy using BH3-mimetic drugs. *Nat Rev Cancer*. (2022) 22:45–64. doi: 10.1038/s41568-021-00407-4

10. Hadian K, Stockwell BR. The therapeutic potential of targeting regulated non-apoptotic cell death. *Nat Rev Drug Discovery*. (2023) 22:723–42. doi: 10.1038/s41573-023-00749-8

11. Degterev A, Huang Z, Boyce M, Li Y, Jagtap P, Mizushima N, et al. Chemical inhibitor of nonapoptotic cell death with therapeutic potential for ischemic brain injury. *Nat Chem Biol*. (2005) 1:112–9. doi: 10.1038/nchembio711

12. Shi J, Zhao Y, Wang K, Shi X, Wang Y, Huang H, et al. Cleavage of GSDMD by inflammatory caspases determines pyroptotic cell death. *Nature*. (2015) 526:660–5. doi: 10.1038/nature15514

13. Andrabi SA, Dawson TM, Dawson VL. Mitochondrial and nuclear cross talk in cell death: parthanatos. *Ann N Y Acad Sci*. (2008) 1147:233–41. doi: 10.1196/nyas.2008.1147.issue-1

14. Remijsen Q, Vanden Berghe T, Wirawan E, Asselbergh B, Parthoens E, De Rycke R, et al. Neutrophil extracellular trap cell death requires both autophagy and superoxide generation. *Cell Res*. (2011) 21:290–304. doi: 10.1038/cr.2010.150

15. Dixon SJ, Lemberg KM, Lamprecht MR, Skouta R, Zaitsev EM, Gleason CE, et al. Ferroptosis: an iron-dependent form of nonapoptotic cell death. *Cell*. (2012) 149:1060–72. doi: 10.1016/j.cell.2012.03.042

16. Tsvetkov P, Coy S, Petrova B, Dreishpoon M, Verma A, Abdusamad M, et al. Copper induces cell death by targeting lipoylated TCA cycle proteins. *Science*. (2022) 375:1254–61. doi: 10.1126/science.abf0529

17. Liu X, Nie L, Zhang Y, Yan Y, Wang C, Colic M, et al. Actin cytoskeleton vulnerability to disulfide stress mediates disulfidptosis. *Nat Cell Biol*. (2023) 25:404–14. doi: 10.1038/s41556-023-01091-2

18. Batista PJ, Chang HY. Long noncoding RNAs: cellular address codes in development and disease. *Cell*. (2013) 152:1298–307. doi: 10.1016/j.cell.2013.02.012

19. Li D, Fan X, Li Y, Yang J, Lin H. The paradoxical functions of long noncoding RNAs in hepatocellular carcinoma: Implications in therapeutic opportunities and precision medicine. *Genes Dis*. (2022) 9:358–69. doi: 10.1016/j.gendis.2020.11.014

20. Yuan JH, Yang F, Wang F, Ma JZ, Guo YJ, Tao QF, et al. A long noncoding RNA activated by TGF-beta promotes the invasion-metastasis cascade in hepatocellular carcinoma. *Cancer Cell*. (2014) 25:666–81. doi: 10.1016/j.ccr.2014.03.010

21. Zhang B, Bao W, Zhang S, Chen B, Zhou X, Zhao J, et al. LncRNA HEPFAL accelerates ferroptosis in hepatocellular carcinoma by regulating SLC7A11 ubiquitination. *Cell Death Dis*. (2022) 13:734. doi: 10.1038/s41419-022-05173-1

22. Shi Z, Li Z, Jin B, Ye W, Wang L, Zhang S, et al. Loss of LncRNA DUXAP8 synergistically enhanced sorafenib induced ferroptosis in hepatocellular carcinoma via SLC7A11 de-palmitoylation. *Clin Transl Med*. (2023) 13:e1300. doi: 10.1002/ctm2.v13.6

23. Tibshirani R. The lasso method for variable selection in the Cox model. *Stat Med*. (1997) 16:385–95. doi: 10.1002/(SICI)1097-0258(19970228)16:4<385::AID-SIM380>3.0.CO;2-3

24. Rich JT, Neely JG, Paniello RC, Voelker CC, Nussenbaum B, Wang EW. A practical guide to understanding Kaplan-Meier curves. *Otolaryngol Head Neck Surg*. (2010) 143:331–6. doi: 10.1016/j.otohns.2010.05.007

25. Iasonos A, Schrag D, Raj GV, Panageas KS. How to build and interpret a nomogram for cancer prognosis. *J Clin Oncol*. (2008) 26:1364–70. doi: 10.1200/JCO.2007.12.9791

26. Meng Z, Ren D, Zhang K, Zhao J, Jin X, Wu H. Using ESTIMATE algorithm to establish an 8-mRNA signature prognosis prediction system and identify immunocyte infiltration-related genes in Pancreatic adenocarcinoma. *Aging (Albany NY)*. (2020) 12:5048–70. doi: 10.18632/aging.102931

27. Wei C, Wei Y, Cheng J, Tan X, Zhou Z, Lin S, et al. Identification and verification of diagnostic biomarkers in recurrent pregnancy loss via machine learning algorithm and WGCNA. *Front Immunol*. (2023) 14:1241816. doi: 10.3389/fimmu.2023.1241816

28. Zanfardino M, Pane K, Mirabelli P, Salvatore M, Franzese M. TCGA-TCIA impact on radiogenomics cancer research: A systematic review. *Int J Mol Sci*. (2019) 20:6033. doi: 10.3390/ijms20236033

29. Mayakonda A, Lin DC, Assenov Y, Plass C, Koeffler HP. Maftools: efficient and comprehensive analysis of somatic variants in cancer. *Genome Res*. (2018) 28:1747–56. doi: 10.1101/gr.239244.118

30. Geeleher P, Cox N, Huang RS. pRRophetic: an R package for prediction of clinical chemotherapeutic response from tumor gene expression levels. *PloS One*. (2014) 9:e107468. doi: 10.1371/journal.pone.0107468

31. Balachandran VP, Gonen M, Smith JJ, DeMatteo RP. Nomograms in oncology: more than meets the eye. *Lancet Oncol*. (2015) 16:e173–80. doi: 10.1016/S1470-2045(14)71116-7

32. Pitt JM, Marabelle A, Eggermont A, Soria JC, Kroemer G, Zitvogel L. Targeting the tumor microenvironment: removing obstruction to anticancer immune responses and immunotherapy. *Ann Oncol*. (2016) 27:1482–92. doi: 10.1093/annonc/mdw168

33. Hanahan D, Coussens LM. Accessories to the crime: functions of cells recruited to the tumor microenvironment. *Cancer Cell*. (2012) 21:309–22. doi: 10.1016/j.ccr.2012.02.022

34. Newman AM, Liu CL, Green MR, Gentles AJ, Feng W, Xu Y, et al. Robust enumeration of cell subsets from tissue expression profiles. *Nat Methods*. (2015) 12:453–7. doi: 10.1038/nmeth.3337

35. Charoentong P, Finotello F, Angelova M, Mayer C, Efremova M, Rieder D, et al. Pan-cancer immunogenomic analyses reveal genotype-immunophenotype relationships and predictors of response to checkpoint blockade. *Cell Rep*. (2017) 18:248–62. doi: 10.1016/j.celrep.2016.12.019

36. McGrail DJ, Pilié PG, Rashid NU, Voorwerk L, Slagter M, Kok M, et al. High tumor mutation burden fails to predict immune checkpoint blockade response across all cancer types. *Ann Oncol*. (2021) 32:661–72. doi: 10.1016/j.annonc.2021.02.006

37. Lappalainen P, Kotila T, Jégou A, Romet-Lemonne G. Biochemical and mechanical regulation of actin dynamics. *Nat Rev Mol Cell Biol*. (2022) 23:836–52. doi: 10.1038/s41580-022-00508-4

38. Sung H, Ferlay J, Siegel RL, Laversanne M, Soerjomataram I, Jemal A, et al. Global cancer statistics 2020: GLOBOCAN estimates of incidence and mortality worldwide for 36 cancers in 185 countries. *CA Cancer J Clin*. (2021) 71:209–49. doi: 10.3322/caac.21660

39. Cedro-Tanda A, Rios-Romero M, Romero-Cordoba S, Cisneros-Villanueva M, Rebollar-Vega RG, Alfaro-Ruiz LA, et al. A lncRNA landscape in breast cancer reveals a potential role for AC009283.1 in proliferation and apoptosis in HER2-enriched subtype. *Sci Rep*. (2020) 10:13146. doi: 10.1038/s41598-020-69905-z

40. Xu J, Ou R, Nie G, Wen J, Ling L, Mo L, et al. LINC01063 functions as an oncogene in melanoma through regulation of miR-5194-mediated SOX12 expression. *Melanoma Res*. (2022) 32:218–30. doi: 10.1097/CMR.0000000000000803

41. Chen C, Su N, Li G, Shen Y, Duan X. Long non-coding RNA TMCC1-AS1 predicts poor prognosis and accelerates epithelial-mesenchymal transition in liver cancer. *Oncol Lett*. (2021) 22:773. doi: 10.3892/ol.2021.13034

42. Sui C, Dong Z, Yang C, Zhang M, Dai B, Geng L, et al. LncRNA FOXD2-AS1 as a competitive endogenous RNA against miR-150-5p reverses resistance to sorafenib in hepatocellular carcinoma. *J Cell Mol Med*. (2019) 23:6024–33. doi: 10.1111/jcmm.14465

43. Chan TA, Yarchoan M, Jaffee E, Swanton C, Quezada SA, Stenzinger A, et al. Development of tumor mutation burden as an immunotherapy biomarker: utility for the oncology clinic. *Ann Oncol*. (2019) 30:44–56. doi: 10.1093/annonc/mdy495

44. Valero C, Lee M, Hoen D, Wang J, Nadeem Z, Patel N, et al. The association between tumor mutational burden and prognosis is dependent on treatment context. *Nat Genet*. (2021) 53:11–5. doi: 10.1038/s41588-020-00752-4

45. Calderaro J, Ziol M, Paradis V, Zucman-Rossi J. Molecular and histological correlations in liver cancer. *J Hepatol*. (2019) 71:616–30. doi: 10.1016/j.jhep.2019.06.001

46. Calderaro J, Couchy G, Imbeaud S, Amaddeo G, Letouzé E, Blanc J-F, et al. Histological subtypes of hepatocellular carcinoma are related to gene mutations and molecular tumor classification. *J Hepatol*. (2017) 67:727–38. doi: 10.1016/j.jhep.2017.05.014

47. Jiang L, Kon N, Li T, Wang S-J, Su T, Hibshoosh H, et al. Ferroptosis as a p53-mediated activity during tumor suppression. *Nature*. (2015) 520:57–62. doi: 10.1038/nature14344

48. Liu X, Zhuang L, Gan B. Disulfidptosis: disulfide stress-induced cell death. *Trends Cell Biol*. (2023) 34(4):327–37. doi: 10.1016/j.tcb.2023.07.009

49. Polyak K, Haviv I, Campbell IG. Co-evolution of tumor cells and their microenvironment. *Trends Genet*. (2009) 25:30–8. doi: 10.1016/j.tig.2008.10.012

50. Anderson ARA, Weaver AM, Cummings PT, Quaranta V. Tumor morphology and phenotypic evolution driven by selective pressure from the microenvironment. *Cell*. (2006) 127:905–15. doi: 10.1016/j.cell.2006.09.042

51. Kloosterman DJ, Akkari L. Macrophages at the interface of the co-evolving cancer ecosystem. *Cell*. (2023) 186:1627–51. doi: 10.1016/j.cell.2023.02.020

52. Zhang Y, Zou J, Chen R. An M0 macrophage-related prognostic model for hepatocellular carcinoma. *BMC Cancer*. (2022) 22:791. doi: 10.1186/s12885-022-09872-y

53. Christofides A, Strauss L, Yeo A, Cao C, Charest A, Boussiotis VA. The complex role of tumor-infiltrating macrophages. *Nat Immunol*. (2022) 23:1148–56. doi: 10.1038/s41590-022-01267-2

54. Greten TF, Villanueva A, Korangy F, Ruf B, Yarchoan M, Ma L, et al. Biomarkers for immunotherapy of hepatocellular carcinoma. *Nat Rev Clin Oncol*. (2023) 20:780–98. doi: 10.1038/s41571-023-00816-4

55. Keam SJ. Tremelimumab: first approval. *Drugs*. (2023) 83(3):93–102. doi: 10.1007/s40265-022-01827-8

56. Getu AA, Tigabu A, Zhou M, Lu J, Fodstad Ø, Tan M. New frontiers in immune checkpoint B7-H3 (CD276) research and drug development. *Mol Cancer*. (2023) 22:43. doi: 10.1186/s12943-023-01751-9

Frontiers in Immunology

Explores novel approaches and diagnoses to treat immune disorders.

The official journal of the International Union of Immunological Societies (IUIS) and the most cited in its field, leading the way for research across basic, translational and clinical immunology.

Discover the latest Research Topics

See more →

Frontiers

Avenue du Tribunal-Fédéral 34
1005 Lausanne, Switzerland
frontiersin.org

Contact us

+41 (0)21 510 17 00
frontiersin.org/about/contact